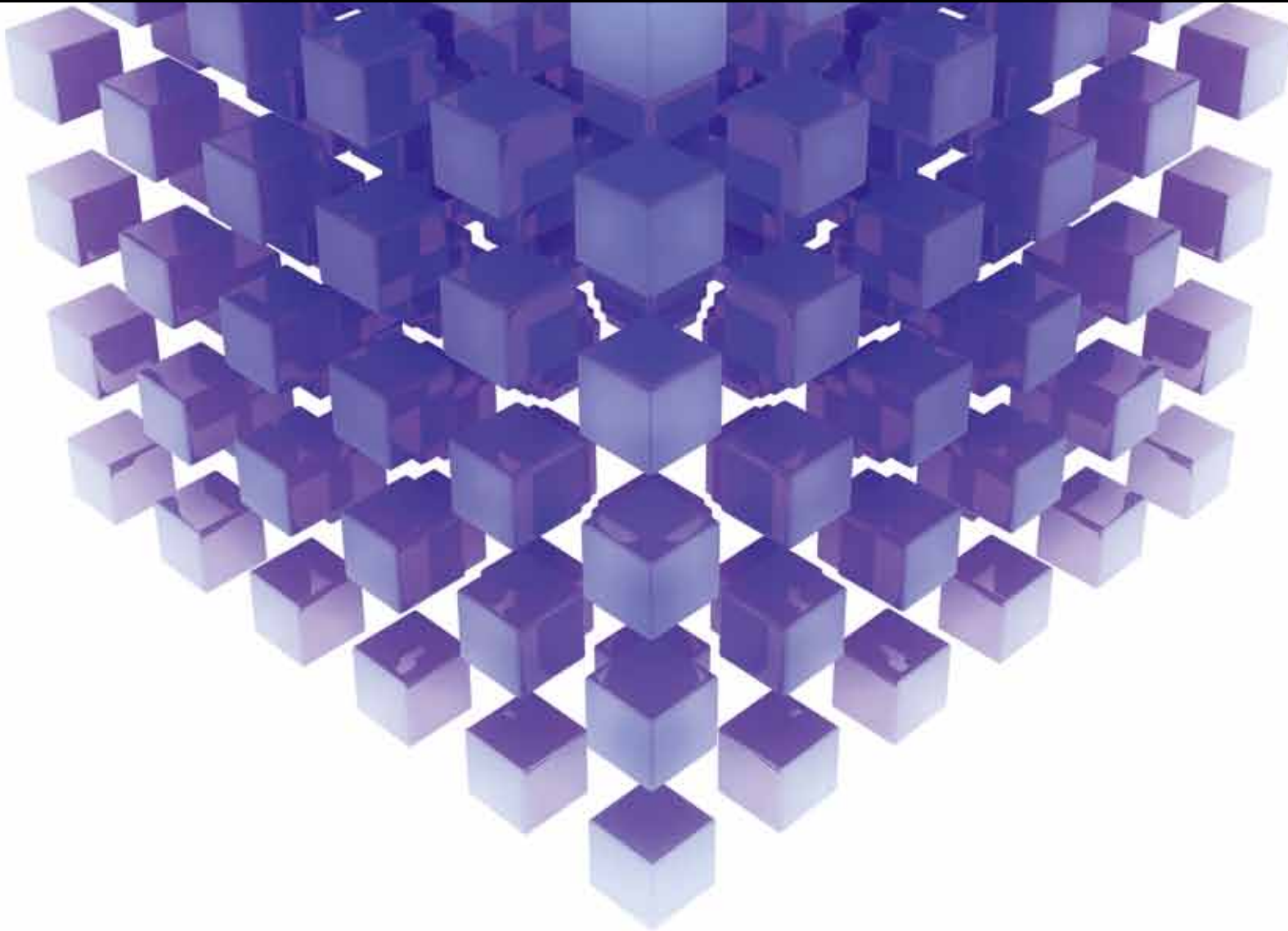


MATHEMATICAL PROBLEMS IN ENGINEERING

STRUCTURAL HEALTH MONITORING-ORIENTED DATA MINING, FEATURE EXTRACTION, AND CONDITION ASSESSMENT

GUEST EDITORS: TING-HUA YI, STATHIS C. STIROS, XIAO-WEI YE, AND JUN LI





**Structural Health Monitoring-Oriented
Data Mining, Feature Extraction,
and Condition Assessment**

Mathematical Problems in Engineering

**Structural Health Monitoring-Oriented
Data Mining, Feature Extraction,
and Condition Assessment**

Guest Editors: Ting-Hua Yi, Stathis C. Stiros, Xiao-Wei Ye,
and Jun Li



Copyright © 2014 Hindawi Publishing Corporation. All rights reserved.

This is a special issue published in “Mathematical Problems in Engineering.” All articles are open access articles distributed under the Creative Commons Attribution License, which permits unrestricted use, distribution, and reproduction in any medium, provided the original work is properly cited.

Editorial Board

- M. Abd El Aziz, Egypt
E. M. Abdel-Rahman, Canada
R. K. Abu Al-Rub, USA
Sarp Adali, South Africa
Salvatore Alfonzetti, Italy
Igor Andrianov, Germany
Sebastian Anita, Romania
W. Assawinchaichote, Thailand
Erwei Bai, USA
Ezzat G. Bakhoum, USA
José M. Balthazar, Brazil
R. K. Bera, India
C. Bérenguer, France
Jonathan N. Blakely, USA
Stefano Boccaletti, Spain
Stephane P.A. Bordas, USA
Daniela Boso, Italy
M. Boutayeb, France
Michael J. Brennan, UK
Salvatore Caddemi, Italy
Piermarco Cannarsa, Italy
Jose E. Capilla, Spain
Carlo Cattani, Italy
Marcelo M. Cavalcanti, Brazil
Diego J. Celentano, Chile
Mohammed Chadli, France
Arindam Chakraborty, USA
Yong-Kui Chang, China
Michael J. Chappell, UK
Kui Fu Chen, China
Xinkai Chen, Japan
Kue-Hong Chen, Taiwan
Jyh-Horng Chou, Taiwan
Slim Choura, Tunisia
Cesar Cruz-Hernandez, Mexico
Swagatam Das, India
Filippo de Monte, Italy
Antonio Desimone, Italy
Yannis Dimakopoulos, Greece
Baocang Ding, China
Joao B. R. Do Val, Brazil
Daoyi Dong, Australia
B. Dubey, India
Horst Ecker, Austria
M. Onder Efe, Turkey
Elmetwally Elabbasy, Egypt
A. Elías-Zúñiga, Mexico
Anders Eriksson, Sweden
Vedat S. Erturk, Turkey
Moez Feki, Tunisia
Ricardo Femat, Mexico
Robertt A. Valente, Portugal
C. Fuerte-Esquivel, Mexico
Zoran Gajic, USA
Ugo Galvanetto, Italy
Furong Gao, Hong Kong
Xin-Lin Gao, USA
Behrouz Gatmiri, Iran
Oleg V. Gendelman, Israel
Didier Georges, France
Paulo B. Gonçalves, Brazil
Oded Gottlieb, Israel
Fabrizio Greco, Italy
Quang Phuc Ha, Australia
M. R. Hajj, USA
Tony S. W. Hann, Taiwan
Thomas Hanne, Switzerland
K. R. (Stevanovic) Hedrih, Serbia
M.I. Herreros, Spain
Wei-Chiang Hong, Taiwan
Jaromir Horacek, Czech Republic
Huabing Huang, China
Chuangxia Huang, China
Gordon Huang, Canada
Yi Feng Hung, Taiwan
Hai-Feng Huo, China
Asier Ibeas, Spain
Anuar Ishak, Malaysia
Reza Jazar, Australia
Zhijian Ji, China
Jun Jiang, China
J. J. Judice, Portugal
Tadeusz Kaczorek, Poland
Tamas Kalmar-Nagy, USA
Tomasz Kapitaniak, Poland
Hamid Reza Karimi, Norway
Metin O. Kaya, Turkey
Nikolaos Kazantzis, USA
Farzad Khani, Iran
K. Krabbenhoft, Australia
Ren-Jieh Kuo, Taiwan
Jurgen Kurths, Germany
Claude Lamarque, France
Usik Lee, Korea
Marek Lefik, Poland
Stefano Lenci, Italy
Roman Lewandowski, Poland
Shanling Li, Canada
Ming Li, China
Jian Li, China
Shihua Li, China
Teh-Lu Liao, Taiwan
Panos Liatsis, UK
Shueei M. Lin, Taiwan
Yi-Kuei Lin, Taiwan
Jui-Sheng Lin, Taiwan
Yuji Liu, China
Wanquan Liu, Australia
Bin Liu, Australia
Paolo Lonetti, Italy
V. C. Loukopoulos, Greece
Junguo Lu, China
Chien-Yu Lu, Taiwan
Alexei Mailybaev, Brazil
Manoranjan K. Maiti, India
O. D. Makinde, South Africa
R. Martinez-Guerra, Mexico
Driss Mehdi, France
Roderick Melnik, Canada
Xinzhu Meng, China
Yuri V. Mikhlin, Ukraine
G. Milovanovic, Serbia
Ebrahim Momoniat, South Africa
Trung Nguyen Thoi, Vietnam
Hung Nguyen-Xuan, Vietnam
Ben T. Nohara, Japan
Sotiris K. Ntouyas, Greece
Gerard Olivar, Colombia
Claudio Padra, Argentina
Bijaya Ketan Panigrahi, India
Francesco Pellicano, Italy
Matjaz Perc, Slovenia
Vu Ngoc Phat, Vietnam
M. do Rosário Pinho, Portugal
A. Pogromsky, The Netherlands

Seppo Pohjolainen, Finland
Stanislav Potapenko, Canada
Sergio Preidikman, USA
Carsten Proppe, Germany
Hector Puebla, Mexico
Justo Puerto, Spain
Dane Quinn, USA
K. R. Rajagopal, USA
Gianluca Ranzi, Australia
Sivaguru Ravindran, USA
G. Rega, Italy
Pedro Ribeiro, Portugal
J. Rodellar, Spain
R. Rodriguez-Lopez, Spain
A. J. Rodriguez-Luis, Spain
Ignacio Romero, Spain
Hamid Ronagh, Australia
Carla Roque, Portugal
Rubén R. García, Spain
Manouchehr Salehi, Iran
Miguel A. Sanjuán, Spain
Ilmar F. Santos, Denmark
Nickolas S. Sapidis, Greece
E. J. Sapountzakis, Greece
Bozidar Sarler, Slovenia
Andrey V. Savkin, Australia
Massimo Scalia, Italy
Mohamed A. Seddeek, Egypt
A. P. Seyranian, Russia
Leonid Shaikhet, Ukraine

Cheng Shao, China
Bo Shen, Germany
Jian-Jun Shu, Singapore
Zhan Shu, UK
Dan Simon, USA
Luciano Simoni, Italy
Grigori M. Sisoiev, UK
Christos H. Skiadas, Greece
Davide Spinello, Canada
Sri Sridharan, USA
Rolf Stenberg, Finland
Changyin Sun, China
Jitao Sun, China
Xi-Ming Sun, China
Andrzej Swierniak, Poland
Yang Tang, Germany
Allen Tannenbaum, USA
Cristian Toma, Romania
Irina N. Trendafilova, UK
Alberto Trevisani, Italy
Jung-Fa Tsai, Taiwan
K. Vajravelu, USA
Victoria Vampa, Argentina
Josep Vehi, Spain
Stefano Vidoli, Italy
Xiaojun Wang, China
Dan Wang, China
Youqing Wang, China
Yongqi Wang, Germany
Cheng C. Wang, Taiwan

Moran Wang, China
Yijing Wang, China
Gerhard-Wilhelm Weber, Turkey
J. A. S. Witteveen, The Netherlands
Kwok-Wo Wong, Hong Kong
Ligang Wu, China
Zhengguang Wu, China
Gongnan Xie, China
Wang Xing-yuan, China
Xi Frank Xu, USA
Xuping Xu, USA
Jun-Juh Yan, Taiwan
Xing-Gang Yan, UK
Suh-Yuh Yang, Taiwan
Mahmoud T. Yassen, Egypt
Mohammad I. Younis, USA
Bo Yu, China
Huang Yuan, Germany
S.P. Yung, Hong Kong
Ion Zaballa, Spain
Ashraf M. Zenkour, Saudi Arabia
Jianming Zhan, China
Xu Zhang, China
Yingwei Zhang, China
Lu Zhen, China
Liancun Zheng, China
Jian Guo Zhou, UK
Zexuan Zhu, China
Mustapha Zidi, France

Contents

Structural Health Monitoring-Oriented Data Mining, Feature Extraction, and Condition Assessment, Ting-Hua Yi, Stathis C. Stiros, Xiao-Wei Ye, and Jun Li
Volume 2014, Article ID 941780, 3 pages

A Time-Domain Structural Damage Detection Method Based on Improved Multiparticle Swarm Coevolution Optimization Algorithm, Shao-Fei Jiang, Si-Yao Wu, and Li-Qiang Dong
Volume 2014, Article ID 232763, 11 pages

Complete Inverse Method Using Ant Colony Optimization Algorithm for Structural Parameters and Excitation Identification from Output Only Measurements, Jun Chen, Xin Chen, and Wei Liu
Volume 2014, Article ID 185487, 18 pages

Innovative Data Fusion Enabled Structural Health Monitoring Approach, Xiukuan Zhao, Ruolin Wang, Haichang Gu, Gangbing Song, and Y. L. Mo
Volume 2014, Article ID 369540, 10 pages

Structural System Identification with Extended Kalman Filter and Orthogonal Decomposition of Excitation, Y. Ding, B. Y. Zhao, and B. Wu
Volume 2014, Article ID 987694, 10 pages

A State-of-the-Art Review on Fatigue Life Assessment of Steel Bridges, X. W. Ye, Y. H. Su, and J. P. Han
Volume 2014, Article ID 956473, 13 pages

PZT-Based Detection of Compactness of Concrete in Concrete Filled Steel Tube Using Time Reversal Method, Shi Yan, Jinzhi Fu, Wei Sun, Baohui Qi, and Fuxue Liu
Volume 2014, Article ID 909682, 11 pages

Intelligent Platform for Model Updating in a Structural Health Monitoring System, Danhui Dan, Tong Yang, and Jiongxin Gong
Volume 2014, Article ID 628619, 11 pages

A Method of Data Recovery Based on Compressive Sensing in Wireless Structural Health Monitoring, Sai Ji, Yajie Sun, and Jian Shen
Volume 2014, Article ID 546478, 9 pages

Structural Damage Identification Based on the Minimum System Realization and Sensitivity Analysis, W. R. Li, Y. F. Du, S. Y. Tang, and L. J. Zhao
Volume 2014, Article ID 405760, 12 pages

A Three-Dimensional Model of the Effective Electromechanical Impedance for an Embedded PZT Transducer, Chunyuan Zuo, Xin Feng, and Jing Zhou
Volume 2013, Article ID 218026, 10 pages

Review of Physical Based Monitoring Techniques for Condition Assessment of Corrosion in Reinforced Concrete, Ying Lei and Zhu-Peng Zheng
Volume 2013, Article ID 953930, 14 pages

GPS and InSAR Time Series Analysis: Deformation Monitoring Application in a Hydraulic Engineering Resettlement Zone, Southwest China, Ruya Xiao and Xiufeng He
Volume 2013, Article ID 601209, 11 pages

FBG-Based Creep Analysis of GFRP Materials Embedded in Concrete, Guo-Wei Li, Cheng-Yu Hong, Jian Dai, Liang Yu, and Wan-Huan Zhou
Volume 2013, Article ID 631216, 9 pages

Condition Assessment on Thermal Effects of a Suspension Bridge Based on SHM Oriented Model and Data, Bo Chen, Zhi-wei Chen, Yu-zhou Sun, and Sheng-lin Zhao
Volume 2013, Article ID 256816, 18 pages

Slope Stability Analysis Based on Measured Strains along Soil Nails Using FBG Sensing Technology, Hua-Fu Pei, Chao Li, Hong-Hu Zhu, and Yu-Jie Wang
Volume 2013, Article ID 561360, 5 pages

Field Measurement of Wind Speeds and Wind-Induced Responses atop the Shanghai World Financial Center under Normal Climate Conditions, Yong Quan, Shuai Wang, Ming Gu, and Jun Kuang
Volume 2013, Article ID 902643, 14 pages

Analysis on Factors Affecting the Self-Repair Capability of SMA Wire Concrete Beam, Li Sun, Dezhi Liang, Qianqian Gao, and Jianhong Zhou
Volume 2013, Article ID 138162, 6 pages

Analysis of Precursors Prior to Rock Burst in Granite Tunnel Using Acoustic Emission and Far Infrared Monitoring, Zhengzhao Liang, Xiangxin Liu, Yanbo Zhang, and Chunan Tang
Volume 2013, Article ID 214340, 10 pages

Statistical Estimation of Changes in the Dominant Frequencies of Structures in Long Noisy Series of Monitoring Data, Fanis Moschas and Eva Steirou
Volume 2013, Article ID 216860, 11 pages

Recent Developments on Wireless Sensor Networks Technology for Bridge Health Monitoring, Guang-Dong Zhou and Ting-Hua Yi
Volume 2013, Article ID 947867, 33 pages

Safety Monitoring Index of High Concrete Gravity Dam Based on Failure Mechanism of Instability, Shaowei Wang, Chongshi Gu, and Tengfei Bao
Volume 2013, Article ID 732325, 14 pages

Construction of Stiffness and Flexibility for Substructure-Based Model Updating, Shun Weng, Hong-Ping Zhu, Yong Xia, Ling Ye, and Xian-Yan Hu
Volume 2013, Article ID 706798, 14 pages

Real-Time Dry Beach Length Monitoring for Tailings Dams Based on Visual Measurement, Jun Hu, Shan Hu, Fei Kang, and Jianhua Zhang
Volume 2013, Article ID 935371, 7 pages

Experimental Study of Aerodynamic Damping of Typical Tall Buildings, Peng Huang, Yong Quan,
and Ming Gu

Volume 2013, Article ID 731572, 9 pages

An Improved Negative Pressure Wave Method for Natural Gas Pipeline Leak Location Using FBG Based Strain Sensor and Wavelet Transform, Qingmin Hou, Liang Ren, Wenling Jiao, Pinghua Zou,
and Gangbing Song

Volume 2013, Article ID 278794, 8 pages

Editorial

Structural Health Monitoring-Oriented Data Mining, Feature Extraction, and Condition Assessment

Ting-Hua Yi,¹ Stathis C. Stiros,² Xiao-Wei Ye,³ and Jun Li⁴

¹ School of Civil Engineering, Dalian University of Technology, Dalian 116023, China

² Department of Civil Engineering, Patras University, 26500 Patras, Greece

³ Department of Civil Engineering, Zhejiang University, Hangzhou 310058, China

⁴ School of Civil and Resource Engineering, University of Western Australia, Perth, WA 6009, Australia

Correspondence should be addressed to Xiao-Wei Ye; cexwye@zju.edu.cn

Received 13 February 2014; Accepted 13 February 2014; Published 17 March 2014

Copyright © 2014 Ting-Hua Yi et al. This is an open access article distributed under the Creative Commons Attribution License, which permits unrestricted use, distribution, and reproduction in any medium, provided the original work is properly cited.

Structural health monitoring (SHM) is the usage of modern sensing technologies, communication algorithms, and advanced data mining and management systems to monitor the operational environments and loadings as well as the structural responses in real time, to effectively evaluate the structural health condition and safety performance and to instruct the daily structural inspection and maintenance, which is a multidiscipline and cutting-edge research field in civil engineering [1–3]. In the past several decades, a great amount of long-term SHM systems have been designed and implemented worldwide on civil engineering structures such as large-scale bridges and high-rise buildings [4]. With these SHM systems, a vast ocean of information relevant to the structural responses and behavior can be continuously obtained in real time. The measurement data are valuable in detecting structural anomalies and damage at an early stage to ensure operational safety and in providing authentic information for timely assessment after disasters and extreme events.

A critical issue of great concern is how to extract the features inherent in the monitoring data for structural performance assessment targeting life-cycle safety, reliability, durability, and sustainability. Therefore, intelligent computational methodologies and approaches, such as artificial neural networks, fuzzy logic systems, and genetic algorithms, are always desired. Numerous investigators worldwide were invited to contribute their original papers and review articles on the theme of this special issue.

A total of 44 technical papers are received and 25 out of them are finally accepted for publication in this special issue. The first seven papers address novel sensing technologies in SHM. The paper “Recent developments on wireless sensor networks technology for bridge health monitoring” by G.-D. Zhou and T.-H. Yi summarizes the recent technology developments in the field of bridge health monitoring with the use of the wireless sensor networks. The paper “Review of physical based monitoring techniques for condition assessment of corrosion in reinforced concrete” by Y. Lei and Z.-P. Zheng reviews the physical based steel corrosion monitoring techniques developed in the last decade. In the paper “Analysis on factors affecting the self-repair capability of SMA wire concrete beam” by L. Sun et al., the authors investigate the influential factors on the self-repair capability of shape memory alloy wire concrete beam. The paper “Analysis of precursors prior to rock burst in granite tunnel using acoustic emission and far infrared monitoring” by Z. Liang et al. investigates the progressive failure of a rock tunnel model by use of the acoustic emission and far-infrared techniques. The paper “A three-dimensional model of the effective electromechanical impedance for an embedded PZT transducer” by C. Zuo et al. proposes a three-dimensional model for the embedded PZT sensor by considering the interaction between the PZT and the host structure. The paper “GPS and InSAR time series analysis: deformation monitoring application in a hydraulic engineering resettlement zone, Southwest China” by R. Xiao and X. He presents the application of the GPS and InSAR for

deformation measurement in hydraulic engineering. In the paper “*FBG-based creep analysis of GFRP materials embedded in concrete*” by G.-W. Li et al., the authors investigate the creep interaction behavior between prestressed GFRP bar and concrete using the fiber Bragg grating sensors.

The subsequent four papers focus on the research pertaining on structural condition assessment. The paper “*A state-of-the-art review on fatigue life assessment of steel bridges*” by X. W. Ye et al. presents a summary on the development history and current status of fatigue condition assessment of steel bridges. The paper “*Condition assessment on thermal effects of a suspension bridge based on SHM oriented model and data*” by B. Chen et al. carries out the condition assessment on temperature distribution and thermal effects of a long span suspension bridge by use with both the numerical simulation and monitoring data. In the paper “*Statistical estimation of changes in the dominant frequencies of structures in long noisy series of monitoring data*” by F. Moschas and E. Steirou, the authors adapt a statistical approach for identification of the dominant frequencies of structures targeting structural health condition assessment. The paper “*Safety monitoring index of high concrete gravity dam based on failure mechanism of instability*” by S. Wang et al. presents the establishment process of safety monitoring index for high concrete gravity dams based on the failure mechanism of instability.

The next four papers address the research on structural damage detection and model updating. The paper “*A time-domain structural damage detection method based on improved multiparticle swarm coevolution optimization algorithm*” by S.-F. Jiang et al. proposes an improved multiparticle swarm coevolution optimization method for structural damage localization and quantification. The paper “*Innovative data fusion enabled structural health monitoring approach*” by X. Zhao et al. proposes a data fusion enabled method based on the Dempster-Shafer evidence theory for structural damage detection. In the paper “*Structural damage identification based on the minimum system realization and sensitivity analysis*” by W. R. Li et al., the authors develop a new method for damage detection by combing the minimum system realization and sensitivity analysis. The paper “*PZT-based detection of compactness of concrete in concrete filled steel tube using time reversal method*” by S. Yan et al. develops a wave-based smart sensing system for concrete compactness detection by use with the piezoceramic-based smart aggregates.

The following four papers present the achievements on system and parameter identification. The paper “*Construction of stiffness and flexibility for substructure-based model updating*” by S. Weng et al. conducts the research on the substructuring methods by taking a deeper look at the analysis of a free-free substructure. The paper “*Intelligent platform for model updating in a structural health monitoring system*” by D. Dan et al. develops an automated smart software platform to improve the time-consuming and laborious process in model updating. In the paper “*Complete inverse method using ant colony optimization algorithm for structural parameters and excitation identification from output only measurements*” by

J. Chen et al., the authors integrate the ant colony optimization algorithm with the complete inverse method for simultaneous identification of unknown structural parameters and input time histories using output-only measurements. The paper “*Structural system identification with extended Kalman filter and orthogonal decomposition of excitation*” by Y. Ding et al. proposes a system identification method in the time domain for simultaneous evaluation of structural parameters and external excitations.

The remaining six papers in this special issue are on the topics of field and laboratory measurements. The paper “*An improved negative pressure wave method for natural gas pipeline leak location using FBG based strain sensor and wavelet transform*” by Q. Hou et al. develops an FBG based strain sensor for measurement and detection of the negative pressure wave signal produced by leakage in pipelines. The paper “*Real-time dry beach length monitoring for tailings dams based on visual measurement*” by J. Hu et al. presents a method for dry beach length measurement through the ordinary camera and the effectiveness of which has been verified by the experimental study. The paper “*Field measurement of wind speeds and wind-induced responses atop the Shanghai World Financial Center under normal climate conditions*” by Y. Quan et al. presents the field measurement data of wind velocities and wind-induced accelerations at the top of the Shanghai World Financial Center under normal climate conditions. In the paper “*Slope stability analysis based on measured strains along soil nails using FBG sensing technology*” by H.-F. Pei et al., the authors evaluate the safety factor of a slope by measurement of the strains on the soil nails with the fiber Bragg grating sensors. The paper “*Experimental study of aerodynamic damping of typical tall buildings*” by P. Huang et al. conducts an experimental study on aerodynamic damping measurements by use of the aeroelastic models of tall buildings with typical cross-sections in a wind tunnel. The paper “*A method of data recovery based on compressive sensing in wireless structural health monitoring*” by S. Ji et al. proposes a method of recovering lost data in wireless sensor networks based on compressive sensing and validates the proposed method through measurements. Without a doubt, the papers reflect the state-of-the-art researches and developments of this subject.

Acknowledgments

The guest editors would like to express their sincere appreciation to all the authors for contributing their latest research work to this special issue. We are grateful to the reviewers for their constructive and insightful comments. This meaningful work was jointly supported by the National Natural Science Foundation of China (Grants nos. 51121005, 51222806, and 51327003) and the Specialized Research Fund for the Doctoral Program of Higher Education (Grant no. 20130041110031).

Ting-Hua Yi
Stathis C. Stiros
Xiao-Wei Ye
Jun Li

References

- [1] T.-H. Yi, H.-N. Li, and M. Gu, "Optimal sensor placement for structural health monitoring based on multiple optimization strategies," *The Structural Design of Tall and Special Buildings*, vol. 20, no. 7, pp. 881–900, 2011.
- [2] T. H. Yi, H. N. Li, and X. D. Zhang, "Sensor placement on Canton Tower for health monitoring using asynchronous-climbing monkey algorithm," *Smart Materials and Structures*, vol. 21, no. 12, Article ID 125023, 12 pages, 2012.
- [3] T.-H. Yi, H.-N. Li, and M. Gu, "Characterization and extraction of global positioning system multipath signals using an improved particle-filtering algorithm," *Measurement Science and Technology*, vol. 22, no. 7, Article ID 075101, 11 pages, 2011.
- [4] T.-H. Yi, H.-N. Li, and M. Gu, "Recent research and applications of GPS-based monitoring technology for high-rise structures," *Structural Control and Health Monitoring*, vol. 20, no. 5, pp. 649–670, 2013.

Research Article

A Time-Domain Structural Damage Detection Method Based on Improved Multiparticle Swarm Coevolution Optimization Algorithm

Shao-Fei Jiang, Si-Yao Wu, and Li-Qiang Dong

College of Civil Engineering, Fuzhou University, Fuzhou 350108, China

Correspondence should be addressed to Shao-Fei Jiang; cejsf@163.com

Received 28 October 2013; Revised 24 January 2014; Accepted 25 January 2014; Published 5 March 2014

Academic Editor: Jun Li

Copyright © 2014 Shao-Fei Jiang et al. This is an open access article distributed under the Creative Commons Attribution License, which permits unrestricted use, distribution, and reproduction in any medium, provided the original work is properly cited.

Optimization techniques have been applied to structural health monitoring and damage detection of civil infrastructures for two decades. The standard particle swarm optimization (PSO) is easy to fall into the local optimum and such deficiency also exists in the multiparticle swarm coevolution optimization (MPSCO). This paper presents an improved MPSCO algorithm (IMPSCO) firstly and then integrates it with Newmark's algorithm to localize and quantify the structural damage by using the damage threshold proposed. To validate the proposed method, a numerical simulation and an experimental study of a seven-story steel frame were employed finally, and a comparison was made between the proposed method and the genetic algorithm (GA). The results show threefold: (1) the proposed method not only is capable of localization and quantification of damage, but also has good noise-tolerance; (2) the damage location can be accurately detected using the damage threshold proposed in this paper; and (3) compared with the GA, the IMPSCO algorithm is more efficient and accurate for damage detection problems in general. This implies that the proposed method is applicable and effective in the community of damage detection and structural health monitoring.

1. Introduction

Structural health monitoring (SHM) systems offer the possibility to detect the damage for large civil infrastructures accurately and immediately so as to ensure structural integrity and safety. Among the techniques adopted for SHM, vibration-based structural damage detection (SDD) has attracted considerable attention for two decades [1–3]. However, with an increasing amount of vibration data collected from the SHM system, it is still challenging to develop more efficient and robust detection algorithms in respect of variation in structural parameters due to deterioration or damage.

In particular, time-domain analysis techniques have been studied for a relatively long time and proven to be useful for SDD. Mathematically, SDD is a highly nonlinear inverse problem and for time-domain identification it is usually solved by minimizing an objective function, which is defined in terms of the discrepancies between time-series responses measured from the laboratory or in-site and those computed from the analytical model. However, conventional optimization methods, such as the conjugate gradient, usually lead to

a local optimum. Hence, a global optimization technique is needed to develop so as to obtain a more accurate and reliable solution [4]. In recent years, many computational intelligence methods have been proposed and applied to SDD, such as genetic algorithm (GA) [5–8], artificial neural network (ANN) [9, 10], and swarm intelligence techniques [11, 12]. Particle swarm optimization (PSO) proposed in 1995 [13] is a popular swarm intelligence method, which mimics the collective motion of insects and birds, known as “swarm behavior.” PSO has achieved to date tremendous progress and has been successfully applied to SDD due to its simplicity, fast convergence speed, and outstanding performance.

Similar to other evolutionary algorithms, however, standard PSO also has the problem of premature convergence and can be trapped into some local optima. As a result, a number of improved PSO methods have been developed [14–16]. In recent years, the multiparticle swarm coevolution optimization (MPSCO) by integrating the collaborative theory in ecology with the principle of automatic adjustment has become a popular hotspot [17–19]. Nevertheless, such efforts cannot

completely solve the problem of local optimum. Therefore, an improved MPSCO algorithm called IMPSCO is proposed and applied to SDD in this study. In IMPSCO the evolutionary theory is integrated with MPSCO so as to reduce the possibility of falling into the local optimum.

To develop an effective time-domain SDD method, this paper proposes an optimization-based damage strategy by integrating IMPSCO with Newmark's algorithm, and a damage threshold is also developed to accurately quantify damage. Numerical simulations and experimental test of a 7-floor steel frame are conducted to validate the efficiency of the proposed approach; furthermore, the proposed method is also compared with other methods like GA. Both simulation and experimental results have demonstrated that (1) the proposed method uses any kinds of structural time-series responses and only requires very few sensors in practical applications; and (2) after the damage threshold is determined by hypothesis testing, damage location and damage extent can be identified quickly and accurately with the enormous data polluted by measurement noise which is induced by the complicated operating environment of structures.

The organization of the paper is as follows. Section 2 provides the basic theory of IMPSCO. Section 3 describes the damage detection strategy based on IMPSCO and Newmark's algorithm. Numerical simulations are carried out in Section 4, while experimental study is presented in Section 5. Section 6 gives the concluding remarks.

2. Basic Theory

2.1. Improved Multiparticle Swarm Coevolution Optimization Algorithm. With basic MPSCO, multisubpopulations are divided into two layers. All particles from the upper-layer follow the optimum of the entire population so as to obtain a faster convergence speed, while all particles from the lower-layer follow the optimum of the subpopulation to which it belongs, so as to ensure the population diversity. Although the performance of basic MPSCO is better than standard PSO in some aspects, the subpopulations in lower-layer still perform the process of standard PSO, which makes its falling into the local optimum possible. To solve this problem, the IMPSCO algorithm is proposed and applied to locate and quantify damage of a structure in this study.

In nature, some species disappear because of environmental variation, while some new species will emerge at the same time so that the species diversity is balanced. Accordingly, the searching procedure of PSO can be regarded as a natural selection process of species in biology. If a particle is recorded as the worst particle for many times in the iteration of the algorithm, it indicates that this particle is unable to adapt to the current environment and needs to be eliminated. As a consequence, the improved strategy is presented, in which the particles to be deleted are replaced with the gravity position of the selected excellent particles in current entire population. After the replacement, the particles can quickly get out of the local optimum. All in all, the proposed IMPSCO algorithm is described as follows.

Step 1 (population initialization). Generate m subpopulations randomly, and each of them contains n particles. Then divide them into the upper-layer with only one subpopulation and the lower-layer with $m - 1$ subpopulations. Meanwhile, set the iteration index k to zero.

Step 2 (fitness calculation). Evaluate the fitness of each particle and save the personal best and its corresponding fitness as $pbest$ and $pbestval$. Simultaneously, record the best individual of each subpopulation and the corresponding fitness as $gbest_j$ and $gbestval_j$ ($j = 1, 2 \dots m$); meanwhile record the best individual in the entire population and its corresponding fitness as $gbest$ and $gbestval$.

Step 3 (particles updating). Update the particles in the upper layer and the lower layer according to (1) and (2), respectively, and the worst particle in the entire population is recorded:

$$\begin{aligned} v_i^{k+1} &= wv_i^k + c_1r_1(p_i - z_i^k) + c_2r_2(p_g - z_i^k) \\ z_i^{k+1} &= z_i^k + v_i^{k+1} \end{aligned} \quad (1)$$

$$\begin{aligned} v_i^{k+1} &= wv_i^k + c_1r_1(p_i - z_i^k) + c_2r_2(p_{lg} - z_i^k) \\ z_i^{k+1} &= z_i^k + v_i^{k+1}, \end{aligned} \quad (2)$$

where i is the particle's index in the swarm; z_i and v_i represent the position and velocity of the particle, respectively; p_i represents the optimal position of the particle; p_g and p_{lg} represent the optimal position of the entire population and the subpopulation to which the particle belongs, respectively; r_1 and r_2 are the random numbers between zero and one; c_1 and c_2 are the learning factors; w is the inertia weight.

Additionally, the maximum velocity of each particle cannot exceed V_{max} which is set to be 20% of the length of the search space.

Step 4 (optimum updating). Calculate the fitness of each updated particle and compare it with the values above. If it is preferable, then update $pbest$, $pbestval$, $gbest$, $gbestval$, $gbest_j$ and $gbestval_j$, correspondingly. Let $k = k + 1$.

Step 5 (worst particle replacement). Repeat Steps 3-4. When the particle is recorded as the worst for the predetermined times I_w , replace it with G_g as shown in (3), and its worst record returns to zero:

$$G_g = \frac{\sum_{j=1}^s z_j}{s}, \quad (3)$$

where s and z_j represent the number of the selected excellent particles and their position, respectively.

Step 6. Go to Step 3, and repeat until the maximum iteration times k_{max} is reached.

2.2. The Newmark Integration Method. The Newmark method is a commonly used numerical integration method to solve differential equations and has been widely applied

to numerical evaluation of the dynamic responses for structures. It is based on the following assumptions:

$$\dot{X}_{i+1} = \dot{X}_i + \left[(1 - \gamma) \ddot{X}_i + \gamma \ddot{X}_{i+1} \right] \Delta t \quad (4)$$

$$X_{i+1} = X_i + \dot{X}_i \Delta t + \left[\left(\frac{1}{2} - \beta \right) \ddot{X}_i + \beta \ddot{X}_{i+1} \right] \Delta t^2, \quad (5)$$

where X , \dot{X} , and \ddot{X} are the displacement, velocity, and acceleration, respectively; Δt is the time step; γ and β are the parameters which determine the accuracy and stability, respectively. When $\gamma = 1/2$ and $\beta = 1/4$, it is Newmark's constant-average acceleration method.

The equilibrium equation at time $i + 1$ is also represented with

$$\mathbf{M}\ddot{X}_{i+1} + \mathbf{C}\dot{X}_{i+1} + \mathbf{K}X_{i+1} = F_{i+1}, \quad (6)$$

where \mathbf{M} is the mass matrix; \mathbf{C} is the damping matrix; \mathbf{K} is the stiffness matrix; F_{i+1} is the external force at time $i + 1$. After X_0 , \dot{X}_0 , and \ddot{X}_0 are initialized; the structural responses X , \dot{X} , and \ddot{X} at each time step can be calculated using (4)–(6).

2.3. Rayleigh Damping. In this study, the damping matrix \mathbf{C} is obtained according to the assumption of Rayleigh damping model:

$$\mathbf{C} = \alpha \mathbf{M} + \beta \mathbf{K}, \quad (7)$$

where α and β represent the mass and stiffness damping coefficient, respectively, which can be calculated by

$$\alpha = \frac{2w_i w_j (w_i \zeta_j - w_j \zeta_i)}{w_i^2 - w_j^2}, \quad \beta = \frac{2(w_i \zeta_i - w_j \zeta_j)}{w_i^2 - w_j^2}, \quad (8)$$

where w_i and w_j are the natural frequencies of the i th mode and j th mode; ζ_i and ζ_j are the corresponding damping ratios.

3. Damage Detection Strategy

On the basis of the abovementioned, this section proposes a time-domain damage detection strategy by integrating the IMPSCO and Newmark's algorithm. The schematic diagram of the damage detection strategy is depicted in Figure 1.

From Figure 1, it is found that two steps are significant for the damage detection strategy, namely, *Determination of Damage Threshold* and *Parameter Identification with IMPSCO and Newmark's algorithm* [20]. Generally, it involves parameters encoding, establishment of fitness function, and parameters setting for the IMPSCO algorithm.

3.1. Parameters Encoding. The first task is to encode parameters involving the IMPSCO. For a frame, generally, the floor stiffness is encoded directly as the parameter to be optimized in the intact state. However the actual stiffness values cannot be obtained accurately, so we turn to focus on detecting the stiffness reduction for damage scenarios. Therefore the floor stiffness ratio of the damaged structure to the undamaged structure, which is defined as the rigidity

coefficient, is introduced and encoded in order to make the detection results simple and clear. In addition, with the Rayleigh damping taken into consideration, the mass and stiffness damping coefficients α and β should also be encoded.

3.2. Parameters Setting in IMPSCO. To implement optimization, some parameters should be set and initialized in advance for the IMPSCO. Usually, 3~5 subpopulations having 30 to 100 particles in total are sufficient, and the maximum iteration times k_{\max} can be set to 50~500. When the inertia weight w is set linearly to a range from 0.9 to 0.4 in variation and learning factors c_1 and c_2 are set to 2 simultaneously, the PSO algorithm exhibits excellent performance. In addition, the limited times for the worst record I_w and the number of the selected excellent particles s are both empirically set to 5~10.

In this study, the parameters are set as follows: the total number of subpopulations $m = 3$; each population size $n = 10$; learning factors $c_1 = c_2 = 2$; limited times for the worst record $I_w = 5$; maximum iteration times $k_{\max} = 60$; the number of the selected excellent particles $s = 6$; the inertia weight w is linearly decreased from 0.9 to 0.4 before the 45th iteration and afterwards it maintains at 0.4 to enhance the local search capability.

3.3. Establishment of Fitness Function. The most important task is to determine the fitness function for the IMPSCO. Firstly, the structural mass matrix \mathbf{M} , stiffness matrix \mathbf{K} , and damping matrix \mathbf{C} are constructed with the generation of particles. And then the simulated time-series responses can be obtained by using Newmark's constant-average acceleration method. Only if the analytical responses are close to the measured ones can it be determined that the structural properties represented with the particles agree well with actual damage situations. Consequently, the fitness function can be represented with

$$F(\boldsymbol{\theta}) = \frac{1}{\sum_i^N \sum_l^L (X_{i,l}^{\text{mea}} - X_{i,l}^{\text{sim}})^2}, \quad (9)$$

where $\boldsymbol{\theta}$ is the parameters vector; N is the number of measuring points; L is the length of response data; $X_{i,l}^{\text{mea}}$ and $X_{i,l}^{\text{sim}}$ are the measured and simulated time-series responses, respectively.

When $F(\boldsymbol{\theta})$ reaches the maximum, the values of $\boldsymbol{\theta}$ are the optimal solution.

3.4. Determination of Damage Threshold and Results Output. It is a difficult and significant task to determine the damage threshold because the threshold is usually used to judge damage. If the identification results are higher than the threshold, it indicates that the damage occurs; otherwise the damage is excluded because of the inevitable measurement noise. Eventually the damage detection is performed.

In this study, the damage threshold is set to 2% validated by the statistical hypothesis testing, which is a method for testing a hypothesis regarding a population parameter, such as the mean from measured sampling data. It usually involves four steps. Firstly, extract the frequency sample set of the

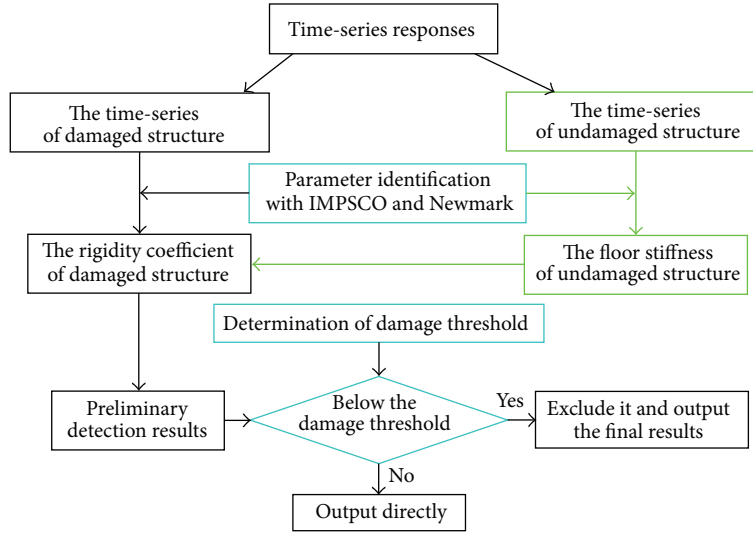


FIGURE 1: The procedure of damage detection.

structure before and after 2% damage, representing with \mathbf{X}_1 and \mathbf{X}_2 , respectively; secondly, design the null hypothesis (H_0) : $\mu_1 = \mu_2$, in which μ_1 and μ_2 represent the means of \mathbf{X}_1 and \mathbf{X}_2 , respectively; thirdly, construct a test statistic using the obtained frequency samples and determine the rejection region on the basis of the predetermined significance level α ; finally, decide whether to accept H_0 or not by comparing the value of the test statistic and the rejection region. If accept H_0 , it indicates that the mean of the frequency samplings does not change significantly when 2% damage is introduced, implying that the floor with identified damage extent below 2% is intact for the structure. More details can be seen in Section 4.2 (2).

4. Numerical Study

4.1. Numerical Model and Analysis. (1) Numerical model: in order to validate the effectiveness of the proposed strategy, a numerical model of a 7-floor shear frame is simplified as a 7-DOF Mass-Spring-Damper system and established by the software of ANSYS, as shown in Figure 2. The mass of each floor $M_1 = \dots = M_6 = 3.78$ kg and $M_7 = 3.31$ kg, which is simulated using mass element MASS21. The floor stiffness K_i ($i = 1, 2, \dots, 7$) is 375 kN/m, which is simulated using the 1-D COMBIN14 spring element. The Rayleigh damping is employed with the damping ratio of 2%. Then the natural frequencies of the first two modes w_1 and w_2 can be obtained by modal analysis and therefore the damping coefficients α , β can be calculated by (8). The model is subjected to random excitation at the seventh floor.

(2) Damage scenarios: damage is simulated by reduction of the stiffness for each floor via

$$DK_i = \frac{K_{ui} - K_{di}}{K_{ui}} \times 100\% \quad (i = 1, 2, \dots, 7), \quad (10)$$

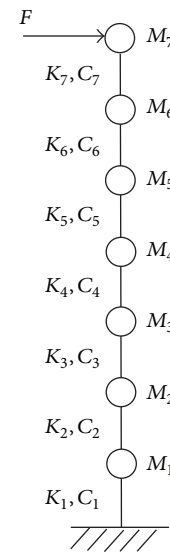


FIGURE 2: Seven-floor shear-type frame simplified model.

where DK represents the damage magnitude; K_{ui} and K_{di} represent the stiffness in the i th floor of the undamaged structure and damaged structure, respectively. Two magnitudes of damage and three damage locations are used to validate the proposed approach. The damage magnitudes are classified quantitatively as small (4.1%) and large (16.7%), while the damage locations are denoted by their corresponding floor numbers. Thus six damage patterns are simulated (as shown in Table 1) and are discussed further later.

(3) **Data Acquisition.** The random force is input to the numerical model based on the vibration exciter of the experiment in Section 5.2. By setting the time step $\Delta t = 0.0002$ s and the loading time $t = 0.1$ s, the structural responses can be calculated, and 500 acceleration data points can be collected

TABLE 1: Damage scenarios.

Damage scenario	Small damage	Large damage
D1	4th floor	—
D2	—	4th floor
D3	6th floor	4th floor
D4	3rd and 6th floors	4th floor
D5	3rd floor	4th and 6th floors
D6	—	3rd, 4th, and 6th floors

at each floor for the structure in the intact and damaged cases, respectively.

In order to simulate the operating environment, 10% Gaussian white noise is added to all the acceleration responses using (11):

$$y_i = y_i^a \times (1 + \varepsilon R), \quad (11)$$

where y_i and y_i^a represent the contaminated and theoretical accelerations, respectively; R is a normally distributed random variable with zero mean and a derivation of 1; ε is an index representing the noise level, which is set to 10% here.

4.2. Damage Detection. (1) Identification of undamaged structure: for the intact structural model, each floor stiffness and damping coefficient are encoded as $\theta = [K_1, K_2, \dots, K_7, \alpha, \beta]$. The search range of K_i ($i = 1, 2, \dots, 7$) is within the interval of $[0, 800 \text{ kN/m}]$, and the search range of α and β is within the intervals of $[0, 4] \text{ s}^{-1}$ and $[0, 0.001] \text{ s}$, respectively. Following the steps presented in Section 3, the floor stiffness of the intact structure can be identified.

Because the IMPSCO algorithm is a probabilistic optimization algorithm, the evolutionary process is always accompanied with randomness. Consequently, it is difficult to judge whether the detection result is correct from a single test. In this study the detection results with bad fitness values are eliminated and ten results are kept in total. Finally the average values are regarded as the final results, as presented in Table 2.

It can be seen that the identification results agree well with the theoretical values, and then the rigidity coefficients can be calculated and introduced to identify the damaged structure by using the identification results. In addition, it is seen that there is a significant difference between the identified damping coefficients and the theoretical values. Since the damping of the structure is reasonably small and only a short time-history is required, this damping is unlikely to have a significant effect on the simulated structural responses when calculating the fitness function. Therefore, the identification results of floor stiffness are considered reliable, which indicates that the accurate assumption of structural damping model is not necessary and the assumption of Rayleigh damping model meets the requirements.

(2) The hypothesis testing of damage threshold: as presented in Section 3.4, the damage threshold is set to 2% in this paper. In order to prove its reasonability, the natural frequencies of the first 7 modes are regarded as the sensitivity indices to carry out the hypothesis testing. The specific process is as follows.

Step 1. Extract the natural frequencies of the undamaged structure using the acceleration responses of each floor by Fast Fourier Transform (FFT). Take the average values as the final natural frequencies of the first 7 modes in the intact state.

Step 2. Repeat Step 1 for 30 times to obtain 30 frequency samples of the undamaged structure. The statistical theory shows that the samples follow the Gaussian distributions approximately if the sample size is large enough.

Step 3. Introduce 2% damage to any floor of the structure (the 4th floor is chosen here) and then calculate the corresponding acceleration responses by using the developed finite element model. Similarly, repeat Step 2 to obtain 30 frequency samples of the damaged structure with 2% damage.

Step 4. Employ the natural frequencies of the second mode for hypothesis testing because their variation is the maximum for all seven modes. Therefore, the frequency sample set of the undamaged structure is represented with $\mathbf{X}_1 = \{244.1, 240.9, 241.1, 241.4, 240.1, 243.6, 242.4, 237.2, 243.8, 243.3, 242.8, 245.3, 246.1, 242.1, 249.0, 239.8, 244.8, 239.3, 243.9, 241.7, 242.8, 242.5, 242.3, 240.8, 246.9, 240.7, 239.6, 243.6, 242.5, 244.9\}$ rad/s; the frequency sample set of the damaged structure is represented with $\mathbf{X}_2 = \{249.3, 239.7, 244.9, 237.3, 238.5, 242.4, 243.1, 241.7, 240.3, 241.0, 244.3, 241.2, 241.6, 241.4, 243.5, 239.1, 241.6, 238.0, 239.9, 237.4, 245.6, 241.6, 244.0, 240.3, 243.0, 245.0, 242.3, 241.6, 239.5, 244.6\}$ rad/s.

Step 5. Assume that $\mathbf{X}_1 \sim N(\mu_1, \sigma_1^2)$, $\mathbf{X}_2 \sim N(\mu_2, \sigma_2^2)$, and $\mathbf{Y} = \mathbf{X}_1 - \mathbf{X}_2$, so $\mathbf{Y} \sim N(\mu, \sigma^2)$ ($\mu = \mu_1 - \mu_2$, $\sigma^2 = \sigma_1^2 + \sigma_2^2$), in which μ_1 , μ_2 , and σ_1^2 , σ_2^2 represent the mean and the variance of \mathbf{X}_1 and \mathbf{X}_2 , respectively.

Step 6. Assume $H_0 : \mu = 0$, $H_1 : \mu \neq 0$. Then the T -statistic is constructed and represented with

$$T = \frac{\sqrt{n}(\bar{Y} - \mu)}{S}, \quad (12)$$

where \bar{Y} , S^2 , and n represent the mean, the variance, and the size of the samples, respectively, so the T -statistic follows the t -distribution with the degree of freedom of $n - 1$; that is, $T \sim t(n - 1)$.

Step 7. In this example, the confidence level $(1 - \alpha)$ is set to 0.99, then the critical value $t_{\alpha/2} = 2.76$, and the rejection region can be represented with $W = \{|T| \geq 2.76\}$ on account of the t -distribution. Meanwhile, the T -statistic value can be obtained from (12), and the value is 1.54. It can be seen that the T -statistic value is out of the rejection region; that is, $T = 1.54 \notin W$, so accept H_0 and reject H_1 . It indicates that no significant change of the frequency has occurred before and after 2% damage, implying intact structure.

As a consequence, the damage threshold of 2% is reasonable from the above demonstration.

(3) Identification of damaged structure: the identification procedure is similar to that of undamaged structure, except that the parameters encoded are replaced by $\theta =$

TABLE 2: Identification results in intact state.

Parameters	Floor stiffness (kN/m)							α (s ⁻¹)	β ($\times 10^{-4}$ s)
	K_1	K_2	K_3	K_4	K_5	K_6	K_7		
Identification	380	372	371	370	377	371	375	3.10	5.99
Theoretical values	375	375	375	375	375	375	375	2.00	1.51

TABLE 3: Detection results of all scenarios.

Damage scenarios	R_1	R_2	R_3	R_4	R_5	R_6	R_7
D1							
Identification	0.996	0.997	0.998	0.962	0.997	1.000	0.999
Theoretical values	1.000	1.000	1.000	0.959	1.000	1.000	1.000
Relative error (%)	0.4	0.3	0.2	0.3	0.3	0.0	0.1
D2							
Identification	0.999	0.990	0.990	0.846	0.994	1.000	0.998
Theoretical values	1.000	1.000	1.000	0.833	1.000	1.000	1.000
Relative error (%)	0.1	1.0	1.0	1.6	0.6	0.0	0.2
D3							
Identification	0.994	0.994	0.995	0.843	0.992	0.966	1.000
Theoretical values	1.000	1.000	1.000	0.833	1.000	0.959	1.000
Relative error (%)	0.6	0.6	0.5	1.2	0.8	0.7	0.0
D4							
Identification	0.990	0.986	0.958	0.843	0.999	0.963	1.000
Theoretical values	1.000	1.000	0.959	0.833	1.000	0.959	1.000
Relative error (%)	1.0	1.4	0.1	1.2	0.1	0.4	0.4
D5							
Identification	0.994	0.989	0.967	0.836	0.994	0.837	0.998
Theoretical values	1.000	1.000	0.959	0.833	1.000	0.833	1.000
Relative error (%)	0.6	1.1	0.8	0.4	0.6	0.5	0.2
D6							
Identification	0.988	0.995	0.835	0.836	1.000	0.839	1.000
Theoretical values	1.000	1.000	0.833	0.833	1.000	0.833	1.000
Relative error (%)	1.2	0.5	0.2	0.4	0.4	0.7	0.2

$[R_1, R_2, \dots, R_7, \alpha, \beta]$, in which R_i ($i = 1, 2, \dots, 7$) represents the rigidity coefficient and belongs to $[0, 1]$. The final identification results are presented in Table 3.

It can be seen that although 10% Gaussian white noise is added to the accelerations, the maximum relative error is 1.6% for all damage scenarios. This implies that structural damage can be detected effectively and accurately even in the case of a noisy environment.

4.3. Comparison and Discussion. To validate the efficiency and robustness, a comparison was made between the theoretical damage extent, identification results by the genetic algorithm (GA), and IMPSCO. It is noted that the number of species group is 80 and the number of generation is 100 in the GA employed in the literature [20]. Other parameters in GA are the same as IMPSCO. The identification results are depicted in Figure 3.

According to the damage threshold determined in Section 4.2 (2), the structure whose damage extent is lower than 2% is regarded as intact structure. Consequently the following observation can be found.

- (1) The damage locations of all scenarios are detected correctly using two different optimization techniques, even for multidamage patterns like D4, D5, and D6.
- (2) Although the detection of damage extent is also reasonable and reliable using GA, IMPSCO is better than GA in terms of identification accuracy in general. It is noted that GA is better than IMPSCO in the detection of damage extent for D2 and D4 at the cost of longer running time.
- (3) Regarding the running time, IMPSCO costs 100 CPU seconds to implement the damage detection only half of the GA.

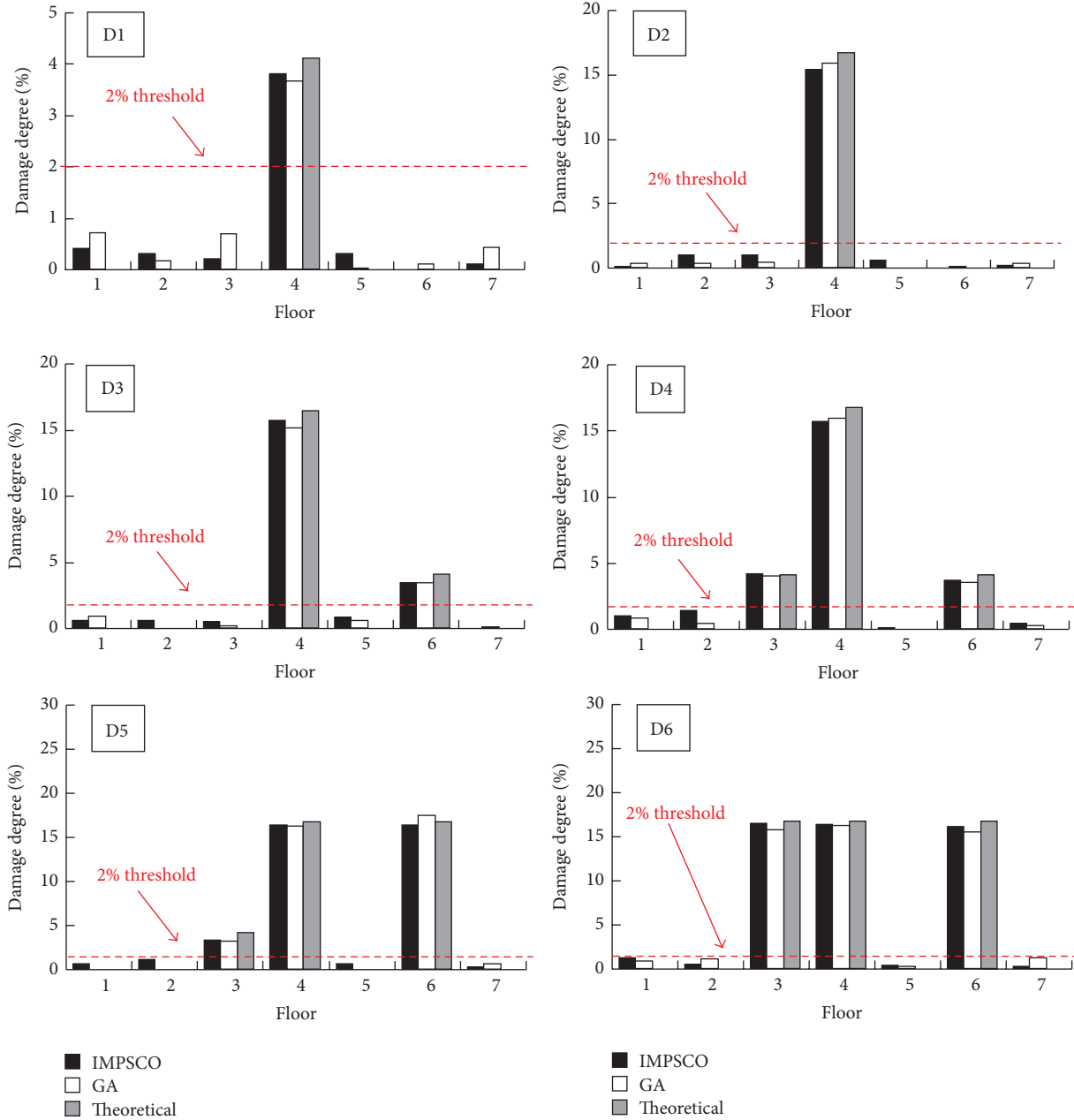


FIGURE 3: The detection results of all scenarios.

5. Experimental Study

5.1. Steel Frame. A seven-floor steel frame of 1.4125 m in height is constructed and tested in the laboratory [21]. The model is designed with flexible columns and relatively rigid beams to simulate a shear building, as shown in Figure 4. The cross-section properties of the structural members are listed in Table 4. The mass of the structure is concentrated at the floors, and the structural model is regarded as a lumped mass model. Therefore, the steel frame can be simplified as a 7-DOF spring-mass system with the masses $M_1, M_2, \dots, M_6 = 3.78$ kg and $M_7 = 3.31$ kg.

5.2. Dynamic Test. (1) Damage scenarios: as the structure is constructed with six columns per floor, damage is simulated by cutting the center column partially or completely in order to keep the symmetry of the model. Small damage is produced by four partial cuts near the top and bottom of the column, whereas large damage is simulated by a complete cut at the mid-height of the column, as indicated in Figure 5. The expected reduction of floor stiffness due to the small damage is estimated by the software of ABAQUS. The finite element models of both the undamaged and damaged columns are established, and the displacements under the same nodal loads are calculated and compared in order to determine the

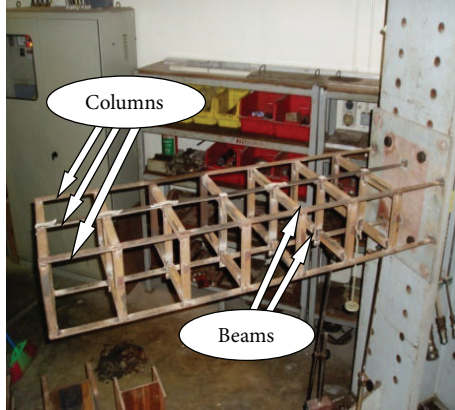


FIGURE 4: Seven-floor steel frame model.

TABLE 4: Section properties of the frame members.

Parameter	Beam	Column
Section size (mm)	$25 \times 25 \times 3$	25×4.6
Sectional area A (m ²)	286×10^{-6}	115×10^{-6}
Moment of inertia I (m ⁴)	2.41×10^{-8}	7.78×10^{-10}
Elasticity modulus E (Pa)	206×10^9	206×10^9
Volume density ρ (kg/m ³)	7850	7850

TABLE 5: Identification results of floor stiffness in intact state.

Floor stiffness	K_1	K_2	K_3	K_4	K_5	K_6	K_7
Identification (kN/m)	300	626	553	566	547	574	519

change in column stiffness. As there are 6 columns in each floor, the small damage results in a reduction in the floor stiffness with 4.1%. As for the case of large damage, the column damage is 100% resulting in a reduction in floor stiffness of $1/6 \approx 16.7\%$. More details can be seen in the literature [21]. The six damage scenarios are shown in Table 1.

(2) Experimental data acquisition: Figure 6 illustrates the dynamic testing and data acquisition system. For ease of setup, the model is mounted horizontally and excited by vibration exciter vertically at the seventh floor. The force generated is measured by an ICP (Integrated Circuit Piezoelectric) force sensor (model PCB-208C02). Meanwhile, the structural responses are measured using the ICP accelerometers mounted at each floor. The data is recorded at a sampling frequency of 5000 Hz.

5.3. Damage Detection. (1) Identification of undamaged structure: firstly, 500 data points of the acceleration responses at each floor and the corresponding force are extracted by the installed sensors when the structure is intact. Then follow the steps presented in Section 4.2 (1). Consequently the floor stiffness is identified for the intact structure.

The detection process is repeated for 15 times using the same method in order to improve the identification precision. The average values for the 15 times are regarded as the final results, as shown in Table 5.

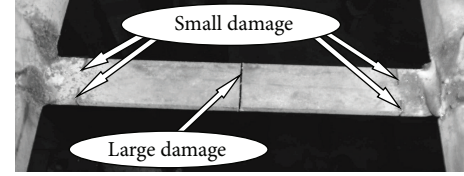


FIGURE 5: Damage applied to the column.

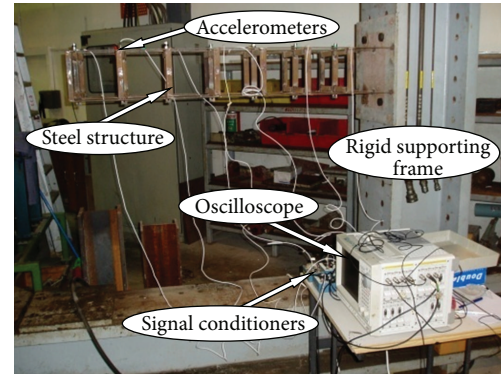


FIGURE 6: Test setup.

It can be seen from Table 5 that the identification result of K_1 is significantly lower, and this is due to the less rigid connection at the base of the structure or the modeling errors of the initial numerical model. In addition, the identification results of α and β are 0.75102223 and 0.00000286, respectively. Then the acceleration responses can be calculated by the identified results according to (4)–(6), which is plotted along with the measured values in Figure 7. For the simplicity, only the comparison results of the second and fifth floors are given as shown in Figure 7. It indicates that the identified and measured acceleration responses are in good agreement, which validates the reasonability of applying the identified floor stiffness of the undamaged structure to the detection of the rigidity coefficients under the different damage scenarios.

(2) Identification of damaged structure: the identification procedure is similar to that of intact structure in Section 5.3 (1), except that the parameters encoded are replaced with $\theta = [R_1, R_2, \dots, R_7, \alpha, \beta]$ as Section 4.2 (3). The final identification results are listed in Table 6.

It is seen from Table 6 that the maximum relative error of identification results is 1.7%, which occurs in the third floor for the multidamage pattern D4. As the rigidity coefficient introduced in the parameter encoding reflects the structural stiffness reduction, the effect on the damage identification results owing to the modeling error of the initial numerical model can be reduced to a great extent. This implies that the proposed structural damage detection strategy is effective and reliable.

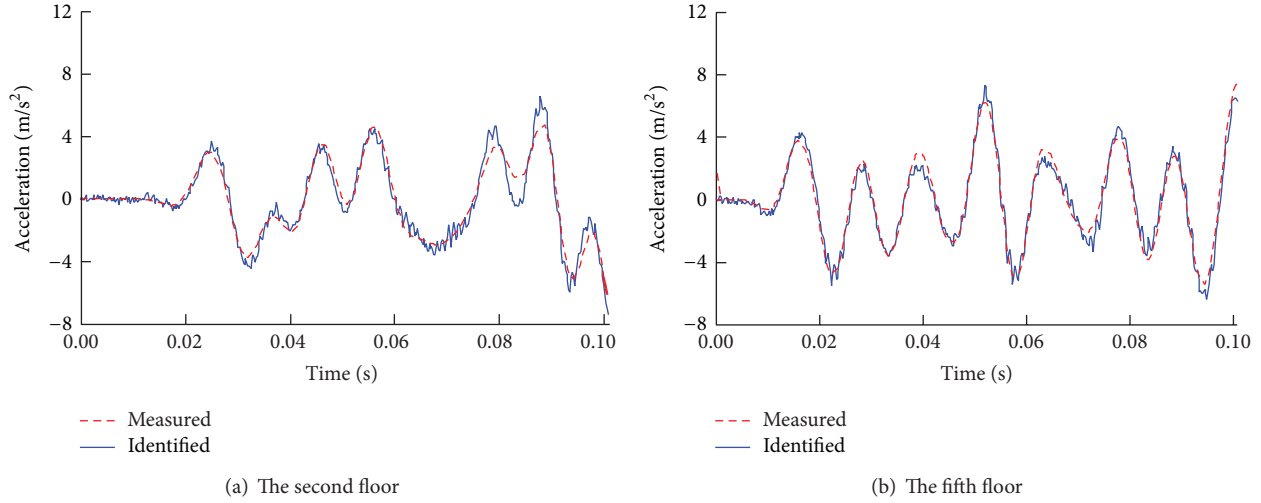


FIGURE 7: The comparison results of acceleration responses.

TABLE 6: Identification results of all damage scenarios.

Damage scenarios	R_1	R_2	R_3	R_4	R_5	R_6	R_7
D1							
Identification	0.988	0.999	0.997	0.968	0.999	0.998	0.998
Theoretical values	1.000	1.000	1.000	0.959	1.000	1.000	1.000
Relative error (%)	1.2	0.1	0.3	0.9	0.1	0.2	0.2
D2							
Identification	0.993	0.986	0.993	0.839	0.999	0.993	0.998
Theoretical values	1.000	1.000	1.000	0.833	1.000	1.000	1.000
Relative error (%)	0.7	1.4	0.7	0.7	0.1	0.7	0.2
D3							
Identification	0.983	0.987	0.993	0.836	0.999	0.953	0.999
Theoretical values	1.000	1.000	1.000	0.833	1.000	0.959	1.000
Relative error (%)	1.7	1.3	0.7	0.4	0.1	0.6	0.1
D4							
Identification	0.998	0.990	0.943	0.829	1.000	0.958	1.000
Theoretical values	1.000	1.000	0.959	0.833	1.000	0.959	1.000
Relative error (%)	0.2	1.0	1.7	0.5	0.0	0.1	0.0
D5							
Identification	0.999	0.983	0.962	0.840	0.999	0.821	1.000
Theoretical values	1.000	1.000	0.959	0.833	1.000	0.833	1.000
Relative error (%)	0.1	1.7	0.3	0.8	0.1	1.4	0.0
D6							
Identification	0.999	0.984	0.822	0.838	1.000	0.825	1.000
Theoretical values	1.000	1.000	0.833	0.833	1.000	0.833	1.000
Relative error (%)	0.1	1.6	1.3	0.5	0.0	1.0	0.0

5.4. Comparison and Discussion. Just as Section 4.3, a comparison is also made among the theoretical damage extent, identification results by genetic algorithm (GA), and IMPSCO, and the results are shown in Figure 8.

On the basis of damage threshold determined in Section 4.2 (2), the floor whose damage extent is lower than 2% is intact. It is found from Figure 7 that damage locations

can be correctly localized using IMPSCO and GA for all damage scenarios. In addition, the detection of damage extent is also accurate and reliable using the two optimization methods. Furthermore, IMPSCO is more efficient and accurate than GA in general. Just as the numerical example, although GA is capable of detecting damage, it costs more running time than IMPSCO.

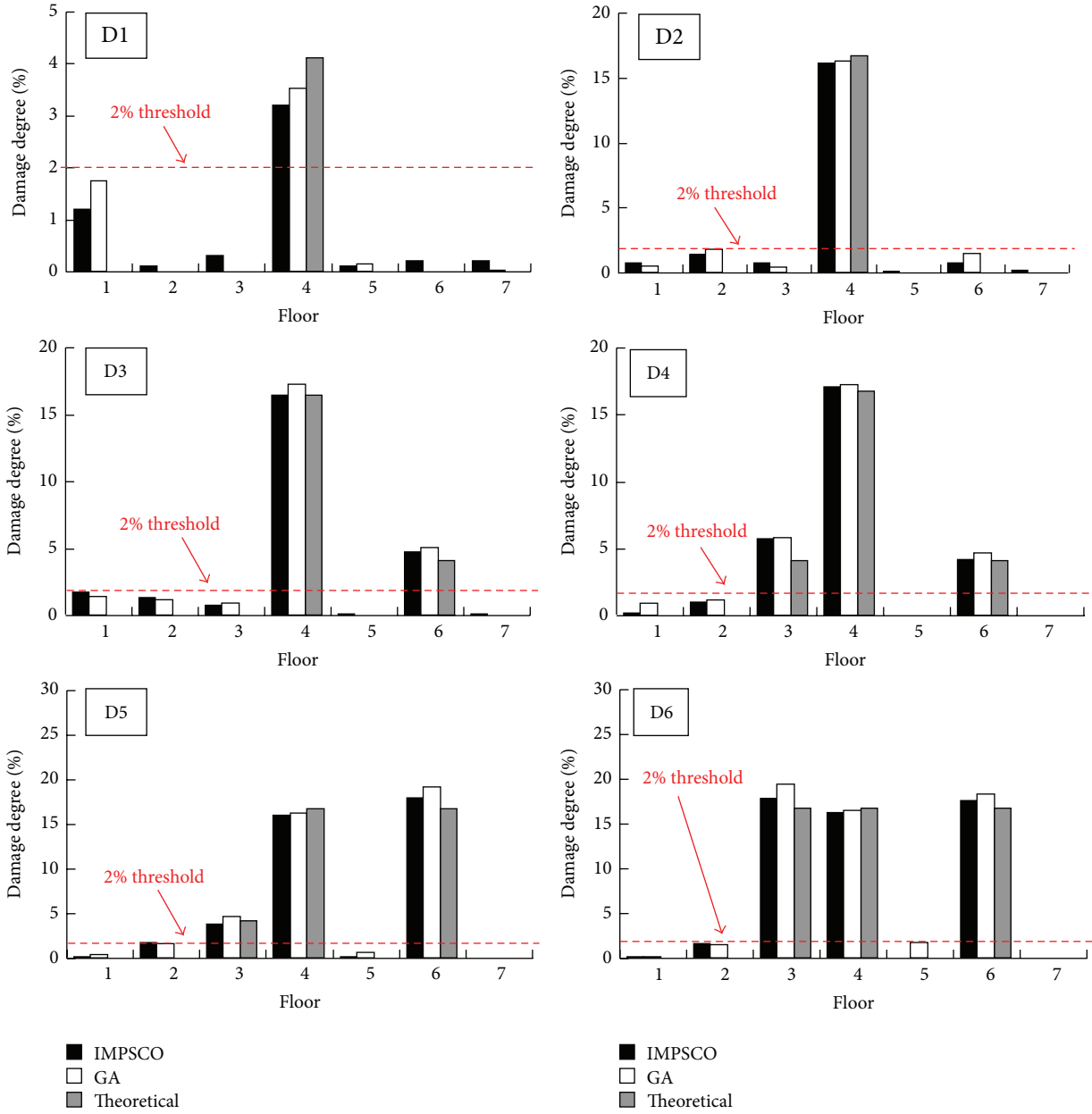


FIGURE 8: Identification results of all damage scenarios.

All in all, the proposed damage detection strategy can not only localize the damage correctly but also quantify damage precisely.

6. Conclusions

This paper proposes a new method by combining the IMPSCO algorithm and Newmark’s constant-average acceleration for the structural damage detection. From the damage detection results of a seven-floor frame model, some conclusions can be drawn as follows.

- (1) The proposed damage detection strategy is applicable and effective for detecting and quantifying damages

using the noise polluted measured data. It is noted that the proposed strategy is implemented only by using any kinds of structural time-series responses and the excitation force.

- (2) Both the numerical simulation and laboratory test of a 7-floor steel frame have proven the feasibility and efficiency of the damage threshold proposed in damage localization.
- (3) On the basis of the damage threshold developed by hypothesis testing, the proposed IMPSCO is capable of accurately detecting damage and reducing the possibility of falling into the local optimum owing to the fact of integrating the evolutionary theory with

MPSCO. Compared with the GA, the proposed damage detection strategy by integrating the IMPSCO and Newmark's algorithm is better than GA in accuracy and runtime.

In summary, the proposed damage detection strategy-based IMPSCO is effective and robust for the numerical simulation and laboratory test of a 7-floor steel frame. However, more experiments are to be conducted to further validate its efficiency.

Conflict of Interests

The authors declare that there is no conflict of interests regarding the publication of this paper.

Acknowledgments

The work was supported by the National Natural Science Foundation of China (Grant no. 51278127), the Ph.D. Programs Foundation of Ministry of Education (Grant no. 20093514110005), and the National 12th Five-Year Research Program of China (Grant no. 2012BAJ14B05).

References

- [1] S. W. Doebling, C. R. Farrar, M. B. Prime, and D. W. Shevitz, "A review of damage identification methods that examine changes in dynamic properties," *Shock and Vibration Digest*, vol. 30, no. 2, pp. 91–105, 1998.
- [2] J. Humar, A. Bagchi, and H. Xu, "Performance of vibration-based techniques for the identification of structural damage," *Structural Health Monitoring*, vol. 5, no. 3, pp. 215–241, 2006.
- [3] W. Fan and P. Z. Qiao, "Vibration-based damage identification methods: a review and comparative study," *Structural Health Monitoring*, vol. 10, no. 1, pp. 83–111, 2011.
- [4] F. Kang, J.-J. Li, and Q. Xu, "Damage detection based on improved particle swarm optimization using vibration data," *Applied Soft Computing*, vol. 12, no. 8, pp. 2329–2335, 2012.
- [5] J.-H. Chou and J. Ghaboussi, "Genetic algorithm in structural damage detection," *Computers & Structures*, vol. 79, no. 14, pp. 1335–1353, 2001.
- [6] H. Hao and Y. Xia, "Vibration-based damage detection of structures by genetic algorithm," *Journal of Computing in Civil Engineering*, vol. 16, no. 3, pp. 222–229, 2002.
- [7] R. R. Tripathy and D. Maity, "Damage assessment of structures from changes in natural frequencies using genetic algorithm," *Structural Engineering and Mechanics*, vol. 19, no. 1, pp. 21–42, 2005.
- [8] C. Na, S.-P. Kim, and H.-G. Kwak, "Structural damage evaluation using genetic algorithm," *Journal of Sound and Vibration*, vol. 330, no. 12, pp. 2772–2783, 2011.
- [9] N. Bakhary, H. Hao, and A. J. Deeks, "Damage detection using artificial neural network with consideration of uncertainties," *Engineering Structures*, vol. 29, no. 11, pp. 2806–2815, 2007.
- [10] V. Vallabhaneni and D. Maity, "Application of radial basis neural network on damage assessment of structures," *Procedia Engineering*, vol. 14, pp. 3104–3110, 2011.
- [11] S. Moradi, P. Razi, and L. Fatahi, "On the application of bees algorithm to the problem of crack detection of beam-type structures," *Computers & Structures*, vol. 89, no. 23–24, pp. 2169–2175, 2011.
- [12] A. Majumdar, D. K. Maiti, and D. Maity, "Damage assessment of truss structures from changes in natural frequencies using ant colony optimization," *Applied Mathematics and Computation*, vol. 218, no. 19, pp. 9759–9772, 2012.
- [13] J. Kennedy and R. Eberhart, "Particle swarm optimization," in *Proceedings of the IEEE International Conference on Neural Networks*, pp. 1942–1948, IEEE Service Center, Piscataway, NJ, USA, 1995.
- [14] D. Chen and C. Zhao, "Particle swarm optimization with adaptive population size and its application," *Applied Soft Computing*, vol. 9, no. 1, pp. 39–48, 2009.
- [15] M.-R. Chen, X. Li, X. Zhang, and Y.-Z. Lu, "A novel particle swarm optimizer hybridized with extremal optimization," *Applied Soft Computing*, vol. 10, no. 2, pp. 367–373, 2010.
- [16] A. Nickabadi, M. M. Ebadzadeh, and R. Safabakhsh, "A novel particle swarm optimization algorithm with adaptive inertia weight," *Applied Soft Computing*, vol. 11, no. 4, pp. 3658–3670, 2011.
- [17] A. G. Li, "Particle swarms cooperative optimizer," *Journal of Fudan University*, vol. 43, no. 5, pp. 923–925, 2004.
- [18] K. Xu and D. Liu, "Algorithm of multi-PSO co-evolution based on GA and PSO," *Computer Engineering and Applications*, vol. 45, no. 3, pp. 51–54, 2009.
- [19] C. T. Man and C. M. Sheng, "An improved algorithm based on cooperative particle swarm optimization," *Journal of Harbin University of Science and Technology*, vol. 15, no. 6, pp. 51–53, 2010.
- [20] S. F. Jiang, L. Q. Dong, and F. Xu, "Intelligent damage detection of frames based on vibration time-series responses," *Journal of Shenyang Jianzhu University*, vol. 28, no. 4, pp. 598–605, 2012.
- [21] C. G. Koh and M. J. Perry, *Structural Identification and Damage Detection Using Genetic Algorithms*, Structures and Infrastructures Series, Taylor & Francis, London, UK, 2010.

Research Article

Complete Inverse Method Using Ant Colony Optimization Algorithm for Structural Parameters and Excitation Identification from Output Only Measurements

Jun Chen, Xin Chen, and Wei Liu

State Key Laboratory for Disaster Reduction in Civil Engineering, Tongji University, Shanghai 200092, China

Correspondence should be addressed to Jun Chen; cejchen@tongji.edu.cn

Received 10 November 2013; Accepted 18 January 2014; Published 4 March 2014

Academic Editor: Jun Li

Copyright © 2014 Jun Chen et al. This is an open access article distributed under the Creative Commons Attribution License, which permits unrestricted use, distribution, and reproduction in any medium, provided the original work is properly cited.

In vibration-based structural health monitoring of existing large civil structures, it is difficult, sometimes even impossible, to measure the actual excitation applied to structures. Therefore, an identification method using output-only measurements is crucial for the practical application of structural health monitoring. This paper integrates the ant colony optimization (ACO) algorithm into the framework of the complete inverse method to simultaneously identify unknown structural parameters and input time history using output-only measurements. The complete inverse method, which was previously suggested by the authors, converts physical or spatial information of the unknown input into the objective function of an optimization problem that can be solved by the ACO algorithm. ACO is a newly developed swarm computation method that has a very good performance in solving complex global continuous optimization problems. The principles and implementation procedure of the ACO algorithm are first introduced followed by an introduction of the framework of the complete inverse method. Construction of the objective function is then described in detail with an emphasis on the common situation wherein a limited number of actuators are installed on some key locations of the structure. Applicability and feasibility of the proposed method were validated by numerical examples and experimental results from a three-story building model.

1. Introduction

Structural health monitoring (SHM) has remained an active research topic in structural engineering since the 1970s. SHM identifies the occurrence, location, and severity of structural damage via significant adverse changes of structural parameters or properties. Thus, the core part of an SHM system is the algorithm used to accurately identify the structural parameters. A number of methods are available nowadays for us to accomplish this identification task. Housner [1] presented an extensive summary on the state-of-the-art methods in the vibration control and health monitoring of civil engineering structures. Zou et al. [2] summarized the methods of vibration-based damage detection and health monitoring for composite structures. Very recent reviews on identification methods used in SHM can be found in Ou and Li [3] and Fan and Qiao [4] among several others. Traditional identification algorithms are generally based on the

assumption that the system's input (excitations) and output (responses) are completely known (measured). However, in vibration-based structural health monitoring of existing large civil structures, it is difficult, sometimes even impossible, to measure the actual excitation applied to the structures. Therefore, output-only structural parameter identification methods are of great significance for practical application of SHM.

In contrast to a number of publications on structural parameter identification with complete output and input information, there is a paucity of publications addressing the identification method using responses only. Since the input/excitation is unknown, assumptions on the input are necessary in order to make the traditional identification method applicable. The most commonly adopted assumption is treating the input as a white-noise process, whose power spectrum is theoretically known. The classical Ibrahim method plus random decrement technique, for instance, is

TABLE 1: The basic parameters of the frame structure model.

Node number	1	2	3	4	5	6
Mass (kg)	610000	580000	530000	530000	530000	360000
Stiffness (kN/m)	271390	290360	282690	252480	233540	229940
Damping (kN·s/m)	2469.65	2874.56	2572.48	2297.57	2265.33	2092.45

based on this assumption. This assumption, however, is not tenable for excitation like earthquakes or strong winds that are in fact a nonstationary random process. Moreover, the time history of the real input cannot be directly identified. The second common way is assuming that the input has some special features. For instance, Toki et al. [5] assumed that the coda of the measured structural responses during an earthquake could be treated as free vibration responses from which the structural parameters could be easily identified. Wang and Haldar [6] identified the unknown earthquake input and structural parameters using output-only measurements through a recursive identification procedure consisting mainly of three steps. Step 1: The unknown structural parameters were identified by assuming that the input excitations were zero at the beginning building up to four time instants, say t_0 to t_4 . Step 2: The input excitation was conjectured by the measured structural responses and the parameters estimated in the first step. Step 3: Replace excitation at t_0 to t_4 in step 1 with new values obtained at step 2, and then repeat step 1 and 2 until the identified input excitation at t_0 to t_4 converged within a preset tolerance limit. For unknown wind load, Law et al. [7] assumed the wind load model was known even though the time histories of the wind load had not been recorded. Based on this assumption, the time history of wind load and the structural parameters could be identified using the response measurements. More recently, Yang et al. [8] suggested a recursive least squares estimation with unknown inputs to identify the stiffness, damping, and other nonlinear parameters at element level. The locations of the unknown excitations are assumed known in their approach. The ASCE structural damage benchmark structure was used to show the feasibility of the method. Yang and Huang [9] further extended this method to situations where external excitations and some acceleration responses are not measured.

To deal with the unknown input identification problem, we have proposed the concept of complete inverse problem, which means identification of structural parameters and the input's time histories simultaneously from the output-only measurements as per Chen and Li [10, 11], Li and Chen [12, 13], and Zhao et al. [14, 15]. Within the framework of complete inverse problem, we have suggested a series of identification methods named as complete inverse methods (CIM) addressing different types of unknown excitations. The core idea of CIM is to convert any additional information of the excitations (whose time histories are unknown) into mathematical constraint conditions that can be further integrated into an iteration identification procedure based on least square technique. For instance, when the locations of the excitations are known, the spatial information of the external excitation can be used in the parameter identification method [10, 11]. For ground motion excitation like that

TABLE 2: Parameters used by ACO_R for HIM.

Parameters	Symbol	Value
Speed of convergence	ξ	0.85
Locality of the search process	q	0.2
Archive size	k	40
Number of dimensions	N	12

resulting from an earthquake, its mechanical features indicate that the inertial force proportional to the mass can be introduced into the interaction procedure as a mathematical constraint to ensure a stable and unique solution [12, 13]. For a proportional-type excitation, like wind loads, the ratio of forces at different structural heights can be used as a mathematical condition to identify the structural parameters and inputs. For shear-type building under earthquake excitation and with limited response measurements, we proposed a hybrid identification method where the unknown structural parameters for the first floor are identified using measured modal shapes, and parameters of all the other stories are identified using measured acceleration responses [14, 15]. We have also provided strict mathematical proofs from Chen and Li [11] and Li and Chen [13] to demonstrate the unconditional convergence features of the proposed complete identification methods.

Despite CIM's success, it does have several limitations. This paper thus tries to improve the CIM in two directions. The first arises from replacing the least square method with another efficient and more robust optimization method. The recently emerged ant colony optimization algorithm (ACO) has been adopted in this paper to identify the structural parameter. The second improvement aims to validate the proposed method by experimental examples. The feasibility and effectiveness of all the aforementioned identification methods have already been demonstrated by different kinds of numerical examples. However, few experimental investigations have been conducted to assess the practical application of these methods. The effect of measurement noise and modeling error cannot be fully investigated in a numerical simulation. However, time-domain identification methods are known to be sensitive to measurement noise.

To this end, the paper first presents the principle of ACO for solving both discrete optimization problems and continuous optimization problems as well. Then, the ACO is integrated into the CIM methods by constructing the objective function according to the type of excitation. After that, the proposed method is applied to numerical model and an experimental model. The results show that the CIM+ACO algorithm performs very well for a noise-free and

TABLE 3: Identified results with noise-free measurements.

Parameters and its real values		Case 1		Case 2		Case 3	
		θ_0	θ^\diamond	θ_0	θ^\diamond	θ_0	θ^\diamond
k_1	271390	[1, 1E6]	271390.00	[1, 1E6]	271390.00	[1, 1E7]	271389.99
k_2	290360	[1, 1E6]	290360.00	[1, 1E6]	290360.00	[1, 1E7]	290360.00
k_3	282690	[1, 1E6]	282690.00	[1, 1E6]	282690.00	[1, 1E7]	282689.99
k_4	252480	[1, 1E6]	252490.00	[1, 1E6]	252479.99	[1, 1E7]	252479.99
k_5	233540	[1, 1E6]	233540.00	[1, 1E6]	233540.00	[1, 1E7]	233540.00
k_6	229940	[1, 1E6]	229939.99	[1, 1E6]	229940.00	[1, 1E7]	229940.00
c_1	2469.65	[1, 1E6]	2469.6499	[1, 1E6]	2469.6499	[1, 1E7]	2469.6500
c_2	2874.56	[1, 1E6]	2874.5600	[1, 1E6]	2874.5600	[1, 1E7]	2874.5599
c_3	2572.48	[1, 1E6]	2572.4800	[1, 1E6]	2572.4799	[1, 1E7]	2572.4799
c_4	2297.57	[1, 1E6]	2297.5699	[1, 1E6]	2297.5700	[1, 1E7]	2297.5700
c_5	2265.33	[1, 1E6]	2265.3300	[1, 1E6]	2265.3300	[1, 1E7]	2265.3299
c_6	2092.45	[1, 1E6]	2092.4499	[1, 1E6]	2092.4499	[1, 1E7]	2092.4500
L			100		20		100
Iteration number			410		417		968

θ_0 : initial values range of the parameter vector, generate k solutions by uniform random sampling for archive T ; θ^\diamond : identified parameter vector, L : number of sampling points used.

TABLE 4: Identified results with noise-pollution measurements.

Parameters and its real values		Case 1		Case 2		Case 3		Case 4	
		(Noise = 1%)		(Noise = 5%)		(Noise = 10%)		(Noise = 15%)	
		θ^\diamond	Error (%)						
$k_1 k_1$	271390	271212	-0.07	270655	-0.27	267110	-1.58	251259	-7.42
k_2	290360	290206	-0.05	288793	-0.54	288103	-0.78	273108	-5.94
k_3	282690	282877	0.07	281526	-0.41	278466	-1.49	276999	-2.01
k_4	252480	252271	-0.08	252238	-0.10	249497	-1.18	246445	-2.39
k_5	233540	233605	0.03	232816	-0.31	230917	-1.12	229261	-1.83
k_6	229940	229767	-0.08	229776	-0.07	230418	0.21	222248	-3.35
c_1	2469.65	2451.16	-0.75	2484.77	0.61	2061.82	-16.51	1591.87	-35.54
c_2	2874.56	2878.74	0.15	2865.31	-0.32	3047.32	6.01	3293.65	14.58
c_3	2572.48	2564.28	-0.32	2601.61	1.13	2124.07	-17.43	2192.95	-14.75
c_4	2297.57	2297.05	-0.02	2273.31	-1.06	2468.87	7.46	2490.99	8.42
c_5	2265.33	2266.12	0.03	2246.78	-0.82	2231.8	-1.48	2191.78	-3.25
c_6	2092.45	2095.25	0.13	2107.04	0.70	2134.34	2.00	2038.22	-2.59
L		200		300		200		300	

For all cases, identical initial values range [1, 1E7] is used for all stiffness and damping parameters; θ^\diamond : identified parameter vector; Error: relative error, L : number of sampling points used.

noise-polluted case and has good identification accuracy in parameters and inputs.

2. Ant Colony Optimization

Inspired by the ants' foraging behavior, Dorigo [16] proposed the ant colony optimization algorithm (ACO). ACO emulates the behavior of a group of ants in searching food from their nest to the food sources. Every ant leaves an amount of pheromone on the path that it passes and chooses the path with more pheromone left on it from the previous ants. Then, after more and more ants pass, the path having the maximum pheromone will be the best (shortest) way from the nest to the food source. ACO algorithms have already been

successfully applied for solving combinatorial optimization problems, including the traveling salesman problem (TSP) [17], the routing problem in a computer network [18], the quadratic assignment problem (QAP) [19], and structural health monitoring problems [20, 21]. ACO algorithms for continuous optimization have been proposed in the literature [22–24]. All the above work has proven ACO to be an efficient and versatile tool for solving various continuous optimization problems. The ACO algorithm has already been well established so far. Principal and application procedures of ACO are briefly summarized in Section 2.1.

2.1. *Ant System Model* [22]. As mentioned earlier, ACO emulates the behavior of a group of ants in searching for

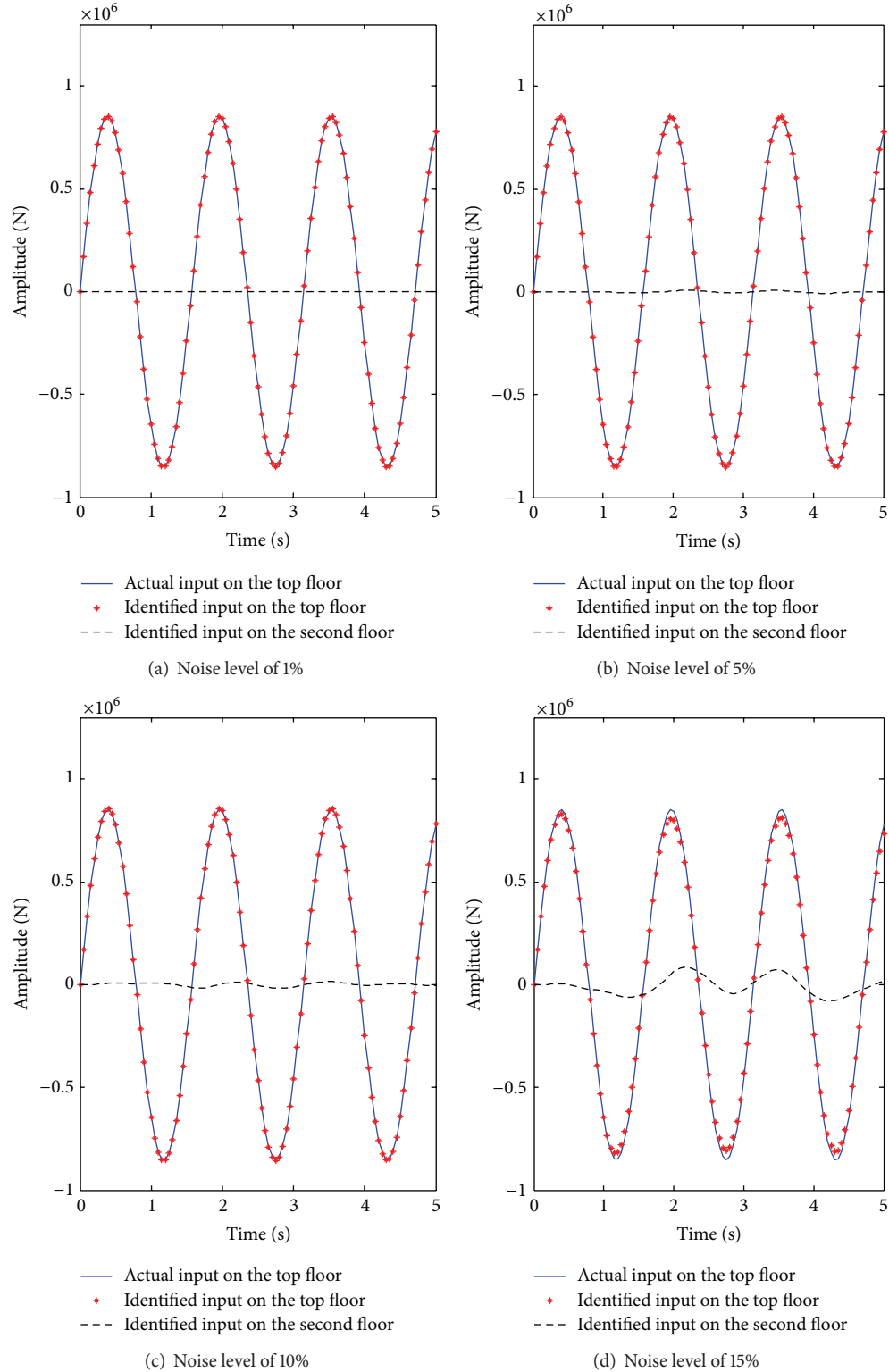


FIGURE 1: Comparison of identified time histories of inputs with real input at different floor.

food. Modeling of the ant system and the pheromone left by ants on the path are of great importance for application of ACO. When ACO is used for discrete optimization problems, ants construct solutions incrementally. That is, each ant starts

with an empty solution S^0 and a component of the solution is added at each construction step. If C^i denotes all the available solutions at step i , we need to choose one best solution from C^i and add the solution to previous solution S^{i-1} leading to



FIGURE 2: The 3-story building model in the test.

the new solution as S^i . The definition of the available solution component depends on the problem tackled. For instance, in the popular travelling salesman problem (TSP), a component of the solution is a city that is added to a tour. The solution components may be defined differently for other problems.

A probability-based strategy is adopted to choose the best solution components from C^i for constructing the current partial solution S^i . This decision is usually influenced by amount of pheromone τ associated with available choices and by heuristic information about the problem. To avoid the loss of generality, in the following problem, no heuristic information is used. Assuming that the partial solution constructed is S^i so far, the probability p is used to choose a solution component $c \in C^i$ at step i in iteration t as calculated by the following:

$$p_{S^i c}^i(t) = \frac{\tau_{S^i c}(t)}{\sum_{j \in C^i} \tau_{S^i j}(t)}, \quad (1)$$

where τ is the pheromone, the subscript S denotes the solution domain, and i means the i th iteration step. Hence, in case of discrete optimization problems, the ants make a probabilistic decision according to some discrete probability distribution at each construction step. For continuous optimization problems, the domain changes from discrete to continuous. The logical adaptation also would be moved from using the discrete probability distribution to a continuous one—the probability density function (PDF). Instead of choosing a component $c \in C^i$ at step i , the ants would generate a random number according to a certain PDF $P(x)$.

2.2. ACO for Continuous Domain: ACO_R [22, 23]. The original ACO algorithm applies only to discrete domain and cannot be directly introduced into continuous domain optimization problems. Structural identification in nature is an optimization problem that aims to find the best parameters for a given objective function defined in a continuous

domain. The ACO for continuous domain is, therefore, necessary. We adopted the method suggested by Socha [22] and Socha and Dorigo [23], which is an ACO for continuous domain (ACO_R) based on Gaussian probability density functions. Application of ACO_R is briefly summarized here for the purpose of completion. More technical details of ACO_R can be found in Socha [22] and Socha and Dorigo [23].

A Gaussian kernel PDF is used in ACO_R to account for the multiple-peaks (multiple optimization solutions) domain. Suppose the optimization problem on hand is $i = 1, 2, \dots, n$ dimensions; for the i th dimension, the Gaussian kernel PDF $G^i(x)$ is defined as a weighted sum of several one-dimensional Gaussian functions as follows:

$$G^i(x) = \sum_{l=1}^k \omega_l g_l^i(x) = \sum_{l=1}^k \omega_l \frac{1}{\sigma_l^i \sqrt{2\pi}} \exp\left(-\frac{(x - \mu_l^i)^2}{2(\sigma_l^i)^2}\right), \quad (2)$$

where, $i = 1, 2, \dots, N$ is the number of dimensions of the problem; $l = 1, 2, \dots, k$ is the number of single Gaussian functions constituting the Gaussian kernel PDF; ω_l is the weight associated with the l th individual Gaussian function; μ_l^i and σ_l^i are the mean and standard deviation for the l th function in the i th dimension. They can also be expressed in vector form as $\{\mu^i\}$ and $\{\sigma^i\}$ whose cardinality is equal to k .

For an N -dimension problem, an ant constructs a solution in N steps. At each step, an ant gets a value for the unknown variable x_i . For each solution s_j , ACO_R will store the current results of N as unknown variables and the value of the objective function $f(s_j)$ in an archive T . All the solutions are ordered in T according to their qualities, that is, $f(s_1) \leq f(s_2) \leq \dots \leq f(s_l) \leq \dots \leq f(s_k)$. Each solution has an associated weight ω that is proportional to the solution quality, $\omega_1 \geq \omega_2 \geq \dots \geq \omega_l \geq \dots \geq \omega_k$. The PDF G^i is constructed using only the i th coordinates of all k solutions from the archive.

For each dimension $i = 1, 2, \dots, N$ of the problem, there is a different Gaussian kernel PDF $G^i(x)$ defined. For each $G^i(x)$, the values of the i th variable of all the solutions in the archive T become the elements of the vector μ^i :

$$\mu^i = \{\mu_1^i, \dots, \mu_k^i\} = \{s_1^i, \dots, s_k^i\}. \quad (3)$$

Before each solution is added to the archive T , it must be evaluated and ranked. The solutions in the archive are sorted according to their rank—that is, solution s_j has rank l . Better solutions will have a higher weight. The weight ω_l of the solution s_j is calculated by the following:

$$\omega_l = \frac{1}{q\sqrt{2\pi}} \exp\left(-\frac{(l-1)^2}{2q^2}\right). \quad (4)$$

The weight is for the Gaussian function with argument l , mean 1.0, and standard deviation q . In the ACO_R , q is in fact a parameter to balance between diversification and intensification. When q is small, the best-ranked solutions

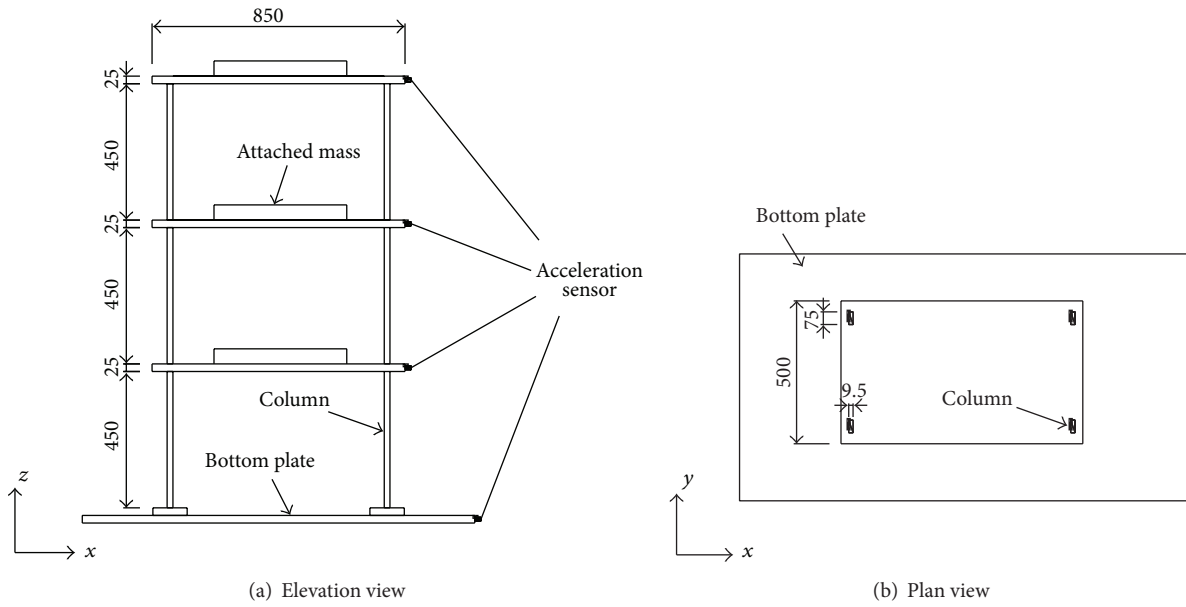


FIGURE 3: Dimensions of the building model.

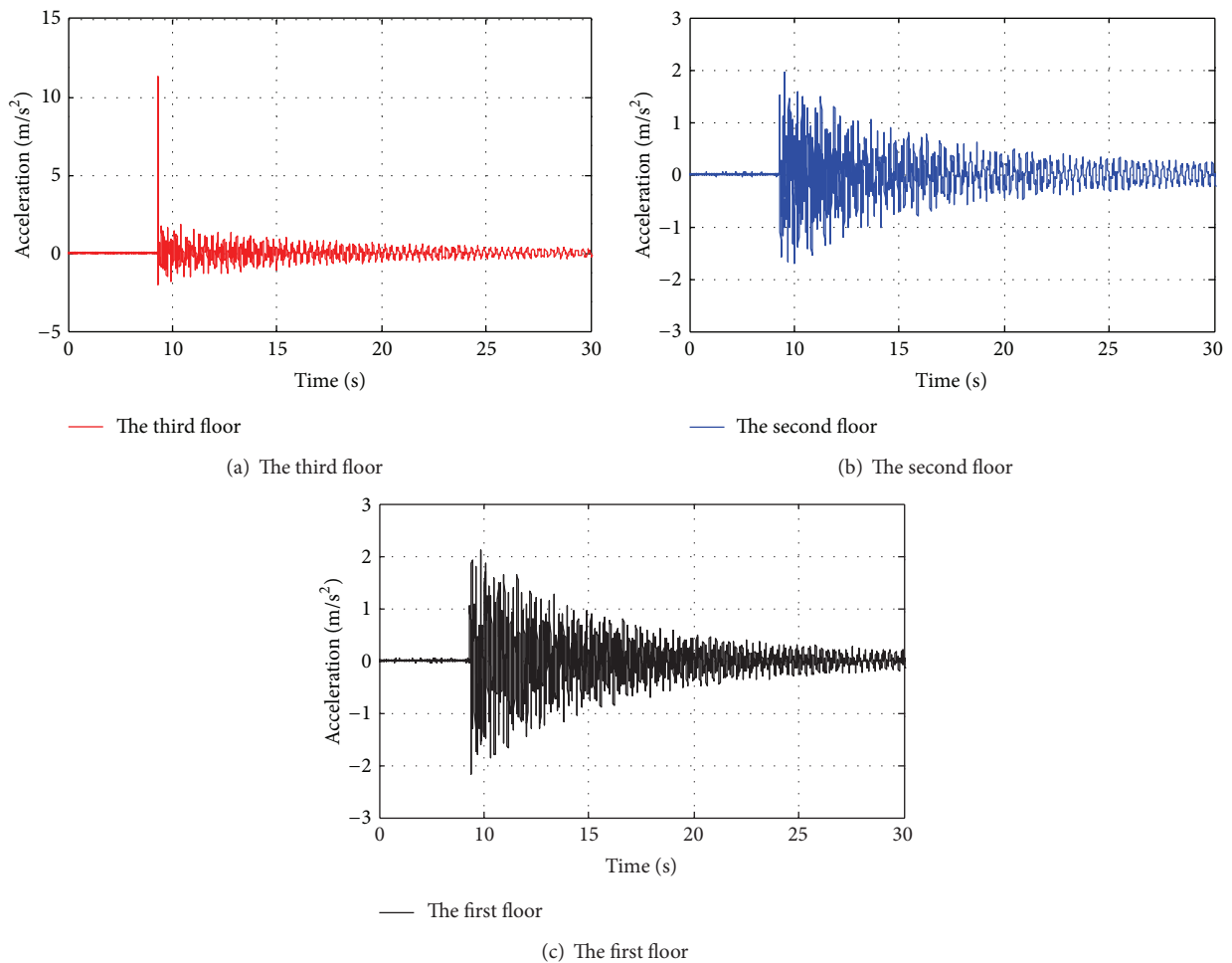


FIGURE 4: The recorded acceleration responses of each floor for impact test case.

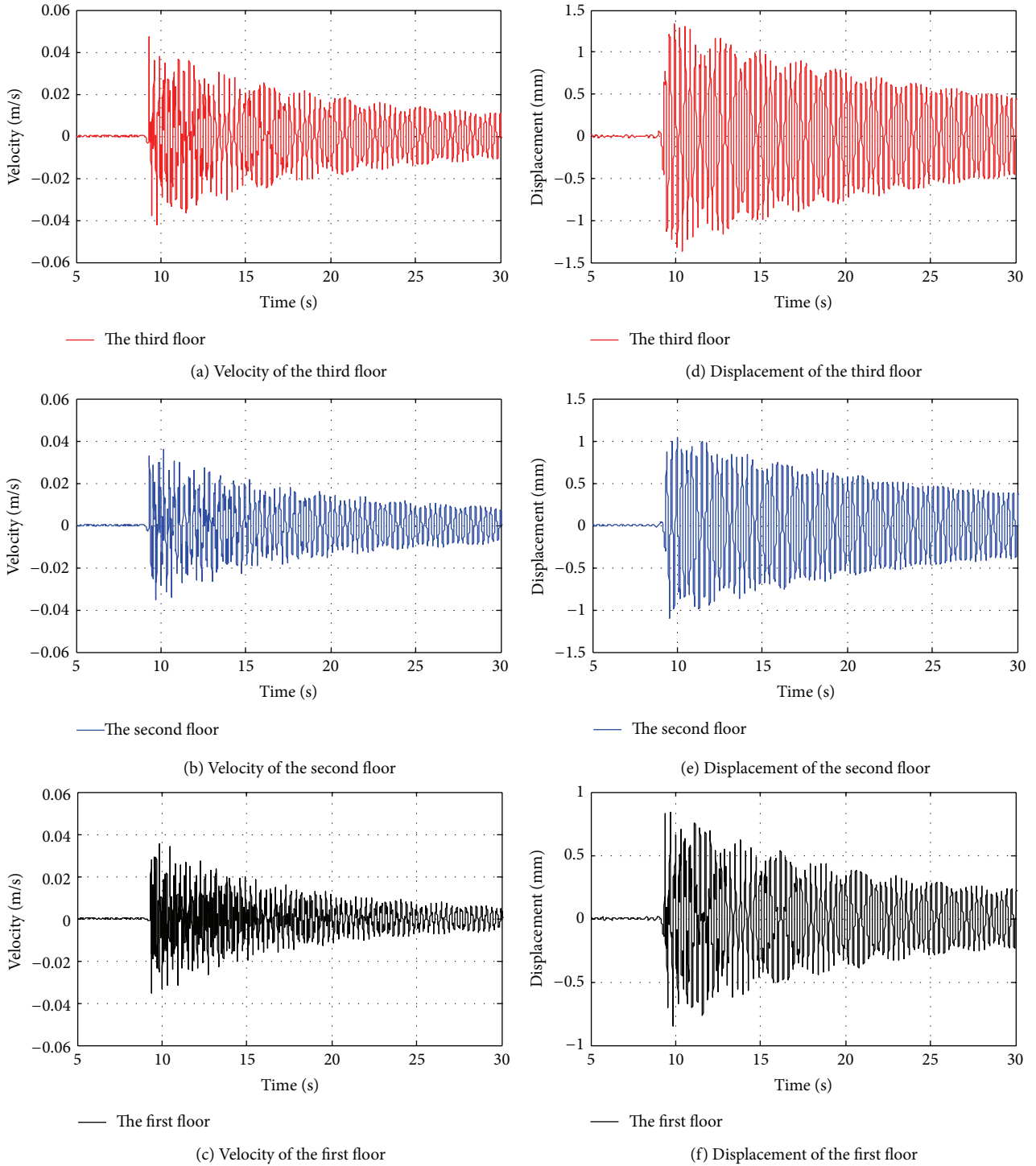


FIGURE 5: The integrated velocity and displacement from accelerations shown in Figure 4.

are strongly preferred, and when it is large, the probability becomes uniform.

In practice, generating the Gaussian kernel PDF is accomplished as follows. First, choose one of the individual Gaussian functions that compose the Gaussian kernel with

probability p_l given by (5). Then generate the chosen Gaussian function

$$p_l = \frac{\omega_l}{\sum_{r=1}^k \omega_r}. \tag{5}$$

TABLE 5: (a) Identified results for single hammer hit on the top floor (computation points = 60). (b) Identified results for single hammer hit on the top floor (computational points = 100). (c) Identified results for single hammer hit on the top floor (computation points = 300). (d) Identified results for single hammer hit on the top floor (computation points = 100 with different initial values for parameters).

(a)						
Computation response segments	Identification results ($\times 10^5$) and identification errors					
	k_1	Error	k_2	Error	k_3	Error
10.0~10.2 s	5.6027	-0.60	5.5243	-1.99	5.6330	-0.06
10.4~10.6 s	5.5882	-0.86	5.5804	-1.00	5.6430	0.12
10.8~11.0 s	5.5042	-2.35	5.7150	1.39	5.6406	0.07
11.2~11.4 s	5.6356	-0.02	5.4636	-3.07	5.6258	-0.19
11.6~11.8 s	5.4920	-2.56	5.6482	0.21	5.6706	0.60
12.0~12.2 s	5.5471	-1.59	5.6079	-0.51	5.6128	-0.42
12.4~12.6 s	5.6005	-0.64	5.5197	-2.07	5.6233	-0.23
12.8~13.0 s	5.4536	-3.25	5.6930	1.00	5.5977	-0.69
13.2~13.4 s	5.5688	-1.20	5.6138	-0.40	5.6182	-0.32
13.6~14.0 s	5.6279	-0.15	5.4499	-3.31	5.5719	-1.15
Average value	5.5621	-1.32	5.5816	-0.97	5.6237	-0.23

(b)						
Computation response segments	Identification results ($\times 10^5$) and identification errors					
	k_1	Error	k_2	Error	k_3	Error
10.0~10.33 s	5.5985	-0.67	5.6083	-0.50	5.6364	0.00
10.2~10.53 s	5.5308	-1.88	5.5969	-0.70	5.6462	0.17
10.4~10.73 s	5.5931	-0.77	5.5587	-1.38	5.6623	0.46
10.6~10.93 s	5.5365	-1.77	5.6322	-0.08	5.6652	0.51
10.8~11.13 s	5.5277	-1.93	5.6426	0.11	5.6669	0.54
11.0~11.33 s	5.5702	-1.18	5.5808	-0.99	5.6591	0.40
11.2~11.53 s	5.5274	-1.94	5.5934	-0.76	5.6655	0.51
11.4~11.73 s	5.5155	-2.15	5.6174	-0.34	5.6615	0.44
11.6~11.93 s	5.5655	-1.26	5.5664	-1.24	5.6284	-0.14
11.8~12.13 s	5.5815	-0.98	5.5713	-1.16	5.5944	-0.75
Average value	5.5547	-1.45	5.5968	-0.70	5.6486	0.21

(c)						
Computation response segments	Identification results ($\times 10^5$) and identification errors					
	k_1	Error	k_2	Error	k_3	Error
10.0~11.0 s	5.5588	-1.38	5.6011	-0.63	5.6436	0.13
10.4~11.4 s	5.5589	-1.38	5.6011	-0.63	5.6436	0.13
10.8~11.8 s	5.5202	-2.06	5.626	-0.19	5.6538	0.31
11.2~12.2 s	5.546	-1.61	5.5637	-1.29	5.6396	0.05
11.6~12.6 s	5.5457	-1.61	5.5805	-0.99	5.6326	-0.07
12.0~13.0 s	5.5195	-2.08	5.6151	-0.38	5.6089	-0.49
12.4~13.4 s	5.5409	-1.70	5.5773	-1.05	5.5951	-0.73
12.8~13.8 s	5.5409	-1.70	5.5773	-1.05	5.5951	-0.73
13.2~14.2 s	5.5392	-1.73	5.5713	-1.16	5.5805	-0.99
13.6~14.6 s	5.5578	-1.40	5.5061	-2.31	5.5519	-1.50
Average value	5.5428	-1.66	5.5820	-0.97	5.6145	-0.39

(d)						
Computation response segments	Identification results ($\times 10^5$) and identification errors					
	k_1	Error	k_2	Error	k_3	Error
10.0~10.33 s	5.5985	-0.67	5.6083	-0.50	5.6364	0.00
12.0~12.33 s	5.5665	-1.24	5.5997	-0.65	5.5795	-1.01

(d) Continued.

Computation response segments	Identification results ($\times 10^5$) and identification errors					
	k_1	Error	k_2	Error	k_3	Error
14.0~14.33 s	5.5667	-1.24	5.5997	-0.65	5.5795	-1.01
16.0~16.33 s	5.5005	-2.41	5.5325	-1.85	5.5381	-1.75
18.0~18.33 s	5.5362	-1.78	5.5068	-2.30	5.4753	-2.86
20.0~20.33 s	5.5362	-1.78	5.5068	-2.30	5.4752	-2.86
22.0~22.33 s	5.3287	-5.46	5.2234	-7.33	5.0971	-9.57
24.0~24.33 s	5.1685	-8.30	5.0521	-10.37	4.8238	-14.42
26.0~26.33 s	5.0674	-10.10	4.9758	-11.72	4.6406	-17.67
28.0~28.33 s	4.8131	-14.61	4.8464	-14.02	4.0776	-27.66

We consider the chosen Gaussian function given in (5) with μ_i^j a standard solution for other ant solutions to explore. To establish the value of the standard deviation σ_i^j at step i , we calculate the average distance from μ_i^j to all solutions in the archive T , and multiply it by the parameter ξ :

$$\sigma_i^j = \xi \sum_{e=1}^k \frac{|s_e^i - s_i^j|}{k-1}, \quad (6)$$

where the parameter $\xi > 0$ has a similar effect to the pheromone evaporation rate in traditional ACO. The higher the value of ξ , the lower the convergence speed of the algorithm.

At the start of the algorithm, the solution archive T is initialized generating k solutions by uniform random sampling. Pheromone update is accomplished by adding the set of newly generated solutions to the solution archive T and then removing the same number of the worst solutions so that the total size of the archive does not change. This process ensures that only the best solutions are kept in the archive, so that they effectively guide the ants in the search process. When the algorithm is completed, the solutions are ordered in the archive according to their quality, and the best solution is $\mathbf{s}_1 = \{s_1^1, s_1^2, \dots, s_1^l, \dots, s_1^N\}$.

3. Integration of ACO_R with CIM

3.1. Introduction of CIM. The equation of motion of a n -DOFs system can be expressed as follows:

$$\mathbf{M}\ddot{\mathbf{X}}(t) + \mathbf{C}\dot{\mathbf{X}}(t) + \mathbf{K}\mathbf{X}(t) = \mathbf{F}(t), \quad (7)$$

where \mathbf{M} , \mathbf{C} , and \mathbf{K} represent, respectively, mass, damping, and stiffness matrices of the structures, $\mathbf{X}(t)$ and $\dot{\mathbf{X}}(t)$, while $\ddot{\mathbf{X}}(t)$ represents, respectively, the displacements, velocities, and accelerometers response vector of the structure; $\mathbf{F}(t)$ is the external excitation on the structures. Equation (7) can be rewritten as (8), which can be further rearranged as (9) at time instant t_i [10]:

$$\mathbf{C}\dot{\mathbf{X}}(t) + \mathbf{K}\mathbf{X}(t) = \mathbf{F}(t) - \mathbf{M}\ddot{\mathbf{X}}(t), \quad (8)$$

$$\mathbf{H}(t_i)\boldsymbol{\theta} = \mathbf{Y}(t_i), \quad (9)$$

where vector $\boldsymbol{\theta}$ contains all the unknown parameters to be identified; matrix \mathbf{H} consists of the measured structural responses; and vector \mathbf{Y} is the system input. To assemble (9) at all the sampling time instants t_i , $i = 1, 2, \dots, Q$ together, will give

$$\mathbf{H}_Q\boldsymbol{\theta} = \mathbf{Y}_Q. \quad (10)$$

The components of matrix \mathbf{H} and \mathbf{Y} depend on the type of structure. For a shear-type structure, the expressions for \mathbf{H} , \mathbf{Y} , and $\boldsymbol{\theta}$ are

$$\boldsymbol{\theta} = [c_1, k_1, c_2, k_2, \dots, c_n, k_n]^T, \quad (11)$$

$$\mathbf{H}_Q = [\mathbf{H}(t_1), \mathbf{H}(t_2), \dots, \mathbf{H}(t_Q)]^T, \quad (12)$$

$$\mathbf{H}(t_i) = \begin{bmatrix} \dot{x}_1(t_i) & x_1(t_i) & \dot{x}_1(t_i) - \dot{x}_2(t_i) & x_1(t_i) - x_2(t_i) & \dots & 0 \\ 0 & 0 & \dot{x}_2(t_i) - \dot{x}_1(t_i) & x_2(t_i) - x_1(t_i) & \dot{x}_2(t_i) - \dot{x}_3(t_i) & x_2(t_i) - x_3(t_i) \\ \dots & \dots & \dots & \dots & \dots & \dots \\ 0 & \dots & \dots & \dots & \dot{x}_n(t_i) - \dot{x}_{n-1}(t_i) & x_n(t_i) - x_{n-1}(t_i) \end{bmatrix}, \quad (13)$$

$$\mathbf{Y}_Q = [\mathbf{Y}(t_1), \mathbf{Y}(t_2), \dots, \mathbf{Y}(t_Q)]^T, \quad (14)$$

$$\mathbf{Y}(t_i) = [f_1(t_i) - m_1\ddot{x}_1(t_i) \quad f_2(t_i) - m_2\ddot{x}_2(t_i) \quad \dots \quad f_n(t_i) - m_n\ddot{x}_n(t_i)]^T, \quad (15)$$

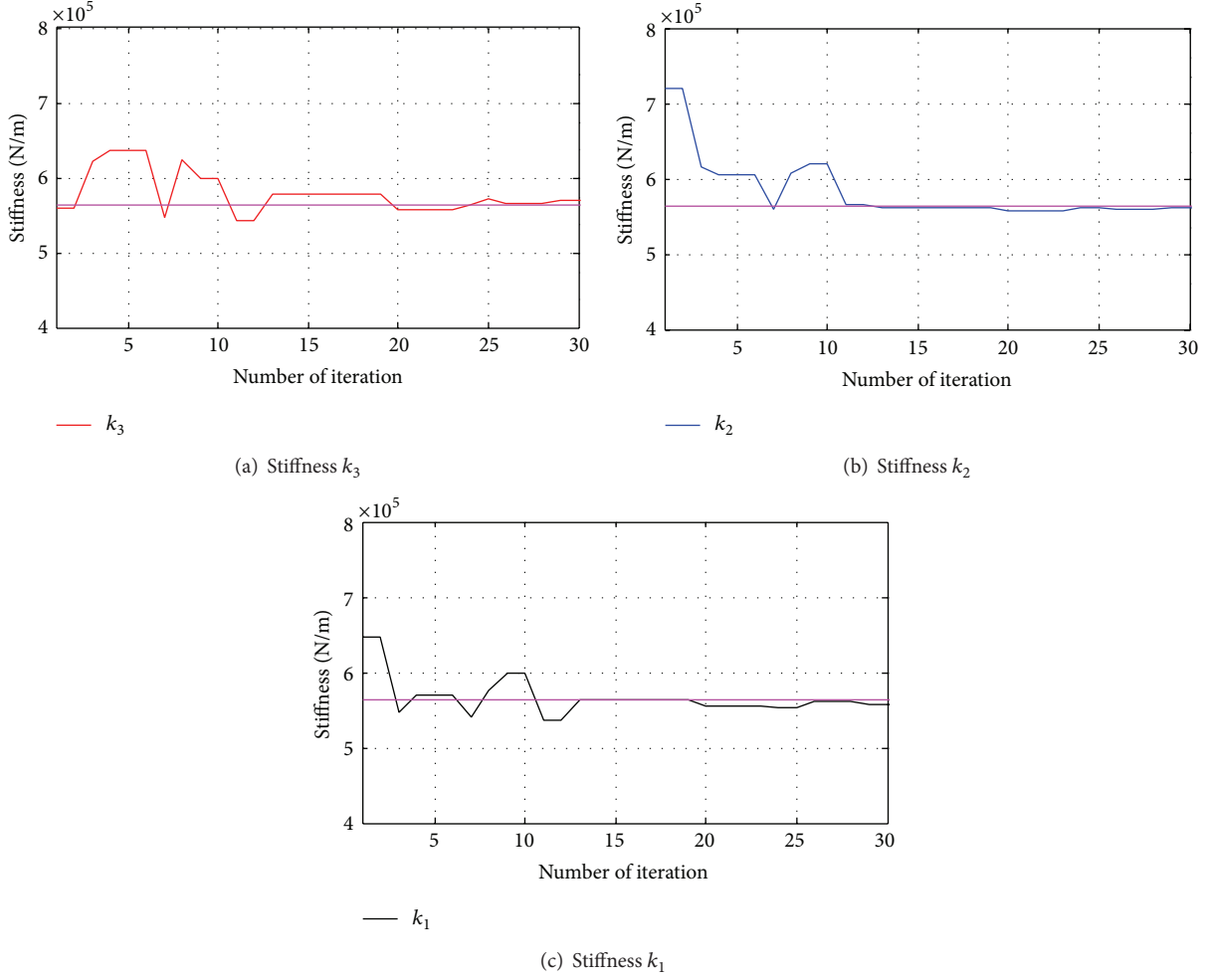


FIGURE 6: Parameter identification convergence procedure for Segments 10.2–10.53 sec in Table 5(b).

where k_1, k_2, \dots, k_n , and c_1, c_2, \dots, c_n represent, respectively, the stiffness and damping coefficients of the structure for each story, and $x_j(t_i)$ and $f_j(t_i)$ are the displacement response and external excitation force of the j th DOF ($j = 1, 2, \dots, n$) at the time instant t_i .

In traditional calculations, the parameters of the structure can be identified from (10) by the least-squares technique as

$$\theta = [\mathbf{H}_Q^T \mathbf{H}_Q]^{-1} \mathbf{H}_Q^T \mathbf{Y}_Q. \quad (16)$$

However, (16) cannot be easily solved to determine the stiffness and damping parameters since there are unknown quantities involved in calculating \mathbf{H}_Q and \mathbf{Y}_Q .

As mentioned earlier, we have suggested the complete inverse method to tackle the unknown input situation in structural identification. Following the framework of CIM, Chen and Li [11] suggested the total compensation method. The total compensation method rests on the assumption that the locations of the external forces are known even though their time histories are unknown, and the number of DOF with applied (unknown) forces is less than the number of DOF whose responses are measured. This assumption reflects

the situation of a forced vibration survey of structure where a limited number of one or several actuator(s) are installed on key locations of the structure to excite it. In this case, the input excitations in (15) can be further expressed into two parts:

$$\begin{aligned} y_u(t_i) &= f_u(t_i) - m_u(t_i) \ddot{x}_u(t_i), \quad i = 1, 2, \dots, Q, \\ y_l(t_i) &= f_l(t_i) - m_l(t_i) \ddot{x}_l(t_i) = -m_l(t_i) \ddot{x}_l(t_i), \quad (17) \\ & \quad i = 1, 2, \dots, Q, \end{aligned}$$

where $y_u(t_i)$ denotes those DOFs with unknown external excitation and $y_l(t_i)$ stands for those DOFs without applied force, that is, $f_l(t_i) \equiv 0$.

3.2. Objective Function. In order to identify structural parameters and the input time history from output-only measurements, an objective function is defined as minimizing discrepancies between the force $y_l(t)$ and the calculated force $y_l^\diamond(t)$. The minimization of the objective function is

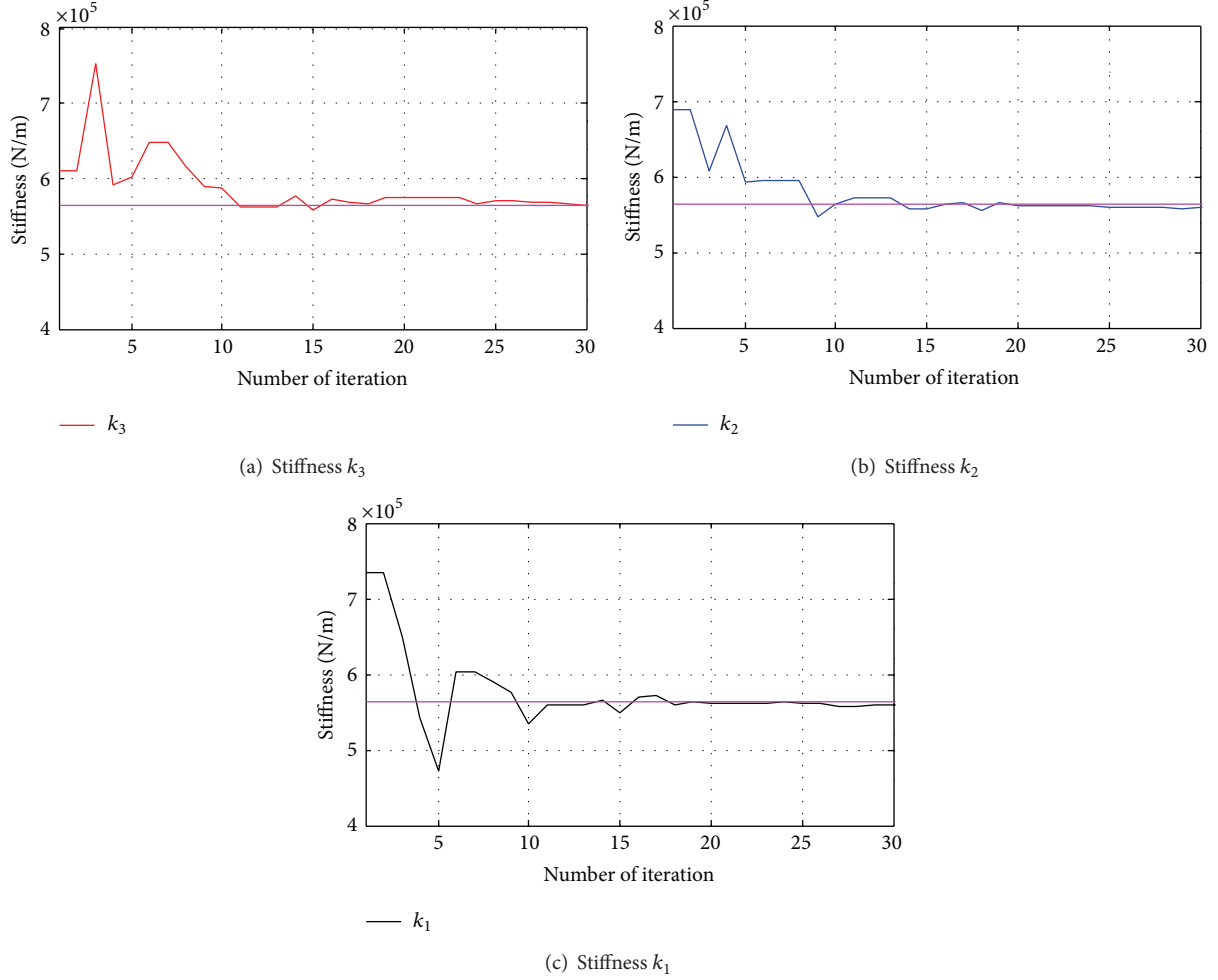


FIGURE 7: Parameter identification convergence procedure for Segments 11.0–11.33 sec in Table 5(b).

expressed as a bound-constrained nonlinear least squares problem:

$$\min \sum_{t_i=t_1}^{t_Q} z(t_i) = \sum_{t_i=t_1}^{t_Q} \sum_{l \in L} \|y_l(t_i) - y_l^\diamond(t_i)\|^2, \quad i = 1, 2, \dots, Q, \quad (18)$$

where L is the set of l and the identified force $y_l^\diamond(t_i)$ is given by

$$y_l^\diamond(t_i) = \mathbf{H}_l(t_i) \boldsymbol{\theta}^\diamond, \quad i = 1, 2, \dots, Q, \quad (19)$$

where $\mathbf{H}_l(t_i)$ is l th row of the matrix $\mathbf{H}(t_i)$, and $\boldsymbol{\theta}^\diamond$ is the result of identified parameters based on ACO_R with the details as

$$\boldsymbol{\theta}^\diamond = [c_1^\diamond, k_1^\diamond, c_2^\diamond, k_2^\diamond, \dots, c_n^\diamond, k_n^\diamond]^T = [s_1^1, s_1^2, \dots, s_1^{2n-1}, s_1^{2n}]^T, \quad (20)$$

where s_1^r , $r = 1, 2, \dots, 2n$ is the value of the first row of the archive T , which is the best solution for (18).

Once the iterative procedure converges, the updated parameter vectors in (20) will give the final identification result of all the structural parameters, whilst the time history of the input $\mathbf{F}(t)$ can be easily determined by (7).

4. Numerical Examples

The suggested algorithm has been applied to several numerical examples including a truss structure, a 6-story shear frame, and a 12-story shear frame structure [25]. Since the observations for all numerical examples are similar, only the results for the 6-story shear frame structure are presented here in detail. The mass, stiffness, and damping coefficient of each story of the structure are shown in Table 1. Sinusoidal excitations are applied on the 4th and the 6th floor, which are $\mathbf{f}_4(t) = 6.74 \times 10^5 \sin(6t)$ and $\mathbf{f}_6(t) = 8.53 \times 10^5 \sin(4t)$, respectively. Therefore the set L in (18) is $L = \{1, 2, 3, 5\}$ for this example. The dynamic responses of all six stories are first calculated in terms of displacement, velocity, and acceleration using the Newmark- β method [26]. Twenty ants are used in each iteration of the ACO_R algorithm, and the convergence threshold in the objective function is set as 1.0×10^{-6} for all the cases. All the computation parameters used for ACO_R are summarized in Table 2.

4.1. Noise-Free Measurements. The proposed ACO_R method is first applied to noise-free measurements. The parameter

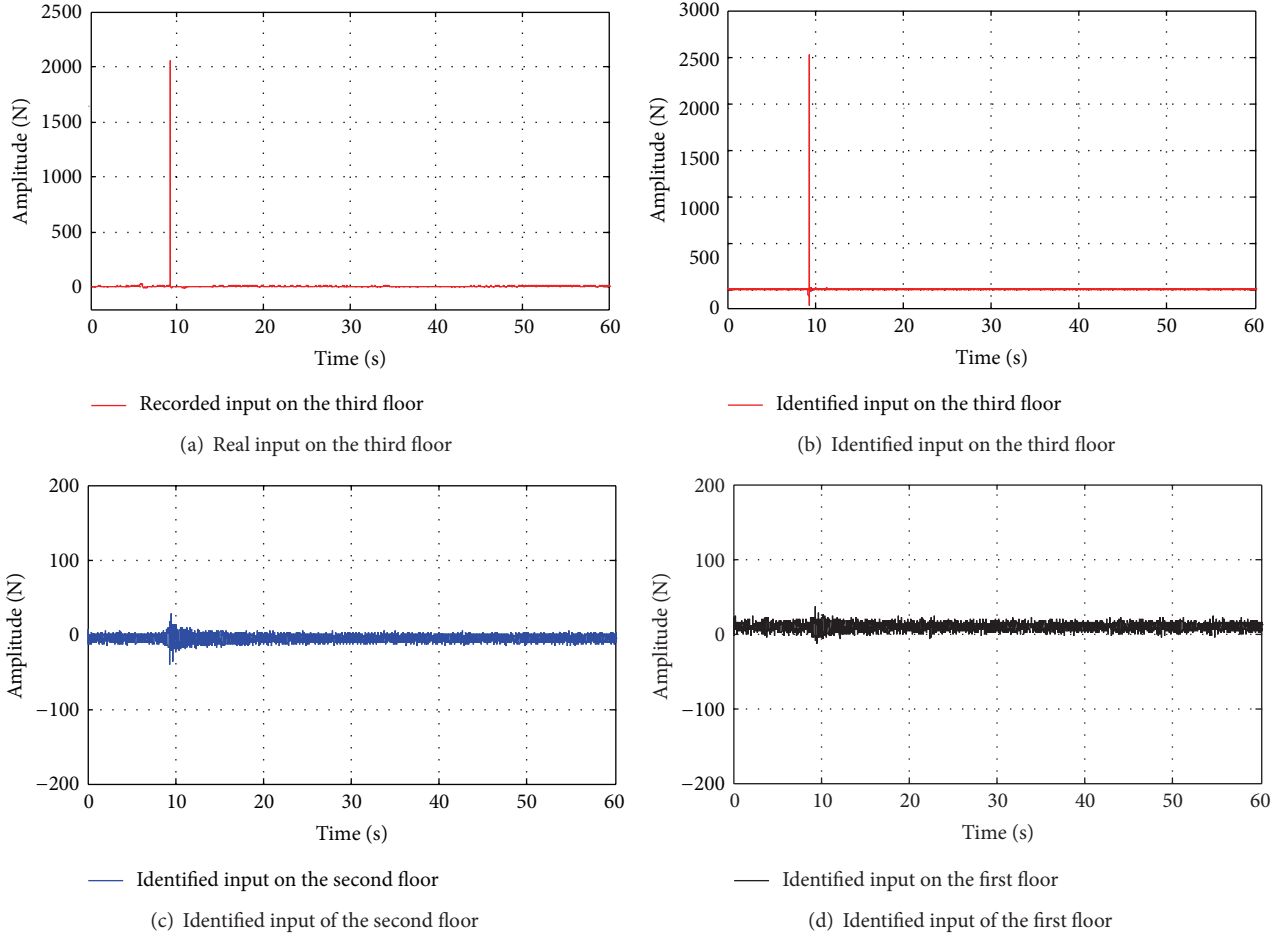


FIGURE 8: The real input on the top floor and the identified inputs of each floor.

identification results of the three cases are shown in Table 3, where Cases 1 and 2 have the same initial parameters' estimate but different measurement durations, and Cases 1 and 3 have the same measurement duration but different initial parameters. It is seen from Table 3 that, for all cases, the unknown parameters can be accurately identified by the proposed method with short duration of measurements and if the method is robust to obtain the initial estimated parameters. The input excitation can also be accurately identified by the ACO_R method in the noise-free case.

4.2. Noise-Pollution Measurements. White noise is numerically added to the calculated responses to simulate noisy measured data by the following equation:

$$\hat{\ddot{x}} = \ddot{x} + E_p N_{\text{noise}} \text{Max}[\ddot{x}], \quad (21)$$

where E_p is the noise level expressed as a percentage, N_{noise} is a uniform distribution vector with interval $[-1, 1]$, and $\text{Max}(\ddot{x})$ is the maximum value of the calculated acceleration response. Four different noise levels at 1%, 5%, 10%, and 15% were considered in the calculation.

The identification results are summarized in Table 4, from which we can see that the proposed method can accurately identify the stiffness parameters for a noise-level

up to 10%. The maximum parameter identification error of the stiffness parameter is lower than 0.1%, 0.6%, 1.6%, and 7.5% for noise levels 1%, 5%, 10%, and 15%, respectively. The identification accuracy for the damping ratio, however, is relatively low. This is not surprise since damping is very sensitive to measurement noise.

It is interesting to compare the inverse input time history of the top floor with that of the second floor where no external force was applied. The identified input forces of the two floors for different noise levels are shown in Figure 1, where the solid blue is the actual force curve and the dotted black line is the identified time history. Visually, even for noise level of 15% the identified force of the top floor matches well with the actual force. Amplitude of the identified curve of the second floor, on the other hand, is approximately zero compared with that of the top floor for noise level of 10%. This and several other numerical examples [25] have demonstrated the applicability and accuracy of the proposed identification method.

5. Experimental Example

The experimental data from a hammer test on a 3-story steel frame structure was adopted to further validate the applicability of the proposed identification method. The structural

TABLE 6: Identified results for continuous hammer hits on the top floor.

Computation response segments	Identification results ($\times 10^5$) and identification errors					
	k_1	Error	k_2	Error	k_3	Error
12.0~12.33 s	5.5252	-1.97	5.5454	-1.62	5.6421	0.10
13.0~13.33 s	5.5462	-1.60	5.6372	0.01	5.6888	0.93
27.0~27.33 s	5.5804	-1.00	5.6745	0.67	5.6446	0.14
28.0~28.33 s	5.5929	-0.77	5.4982	-2.45	5.7204	1.49
39.4~39.73 s	5.5038	-2.35	5.4916	-2.57	5.5697	-1.19
40.4~40.73 s	5.4955	-2.50	5.5077	-2.29	5.6238	-0.23
43.4~43.73 s	5.4719	-2.92	5.6114	-0.45	5.5332	-1.83
Average value	5.5308	-1.87	5.5666	-1.24	5.6318	-0.08

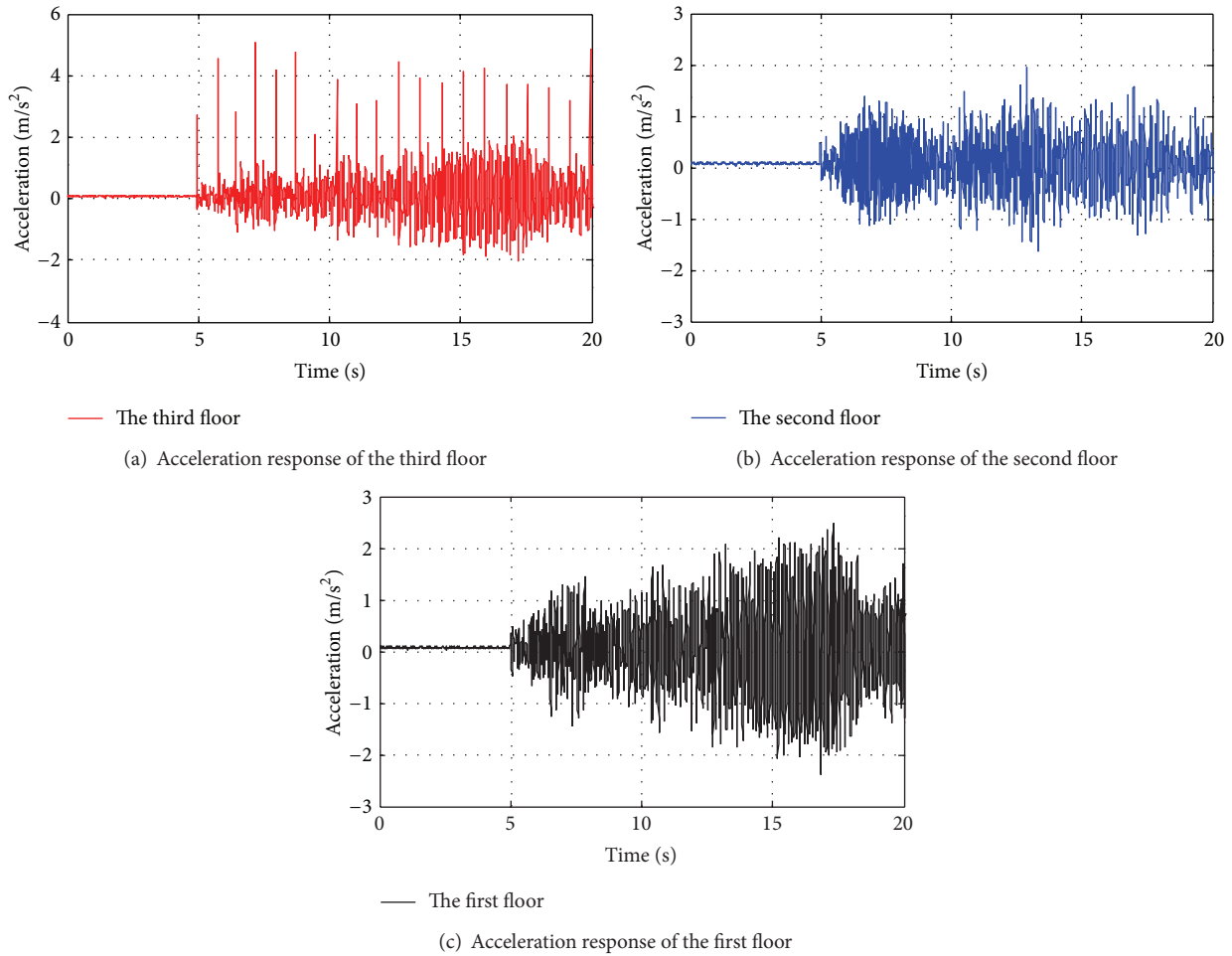


FIGURE 9: The recorded acceleration responses of each floor for continuous hammer test.

model is shown in Figure 2 and dimensions of the model are given in Figure 3. The strength of the steel of the model was tested as 435 Mpa, and the elastic module was 200 Gpa. The overall dimension of the structure is 850 * 500 * 1450 mm (Figure 3). The structure's column was made of a 9.5 * 75 mm steel plate and the floor was made by an 850 * 500 * 25 mm steel plate. Additional mass of 130 kg was installed on each floor leading a total floor mass to 230.3 Kg. The

structural model can be treated as a shear-type building, and the shear stiffness of each floor was computed as 563651 N/m. Hammer tests, hand-shaking tests, and shaking table tests were conducted on the model. Only hammer tests and hand-shaking tests data are adopted in this paper. The hammer tests can be broadly divided into two categories. The first is an impact test where a certain floor of the building is hit once by a force hammer and then the building vibrates freely.

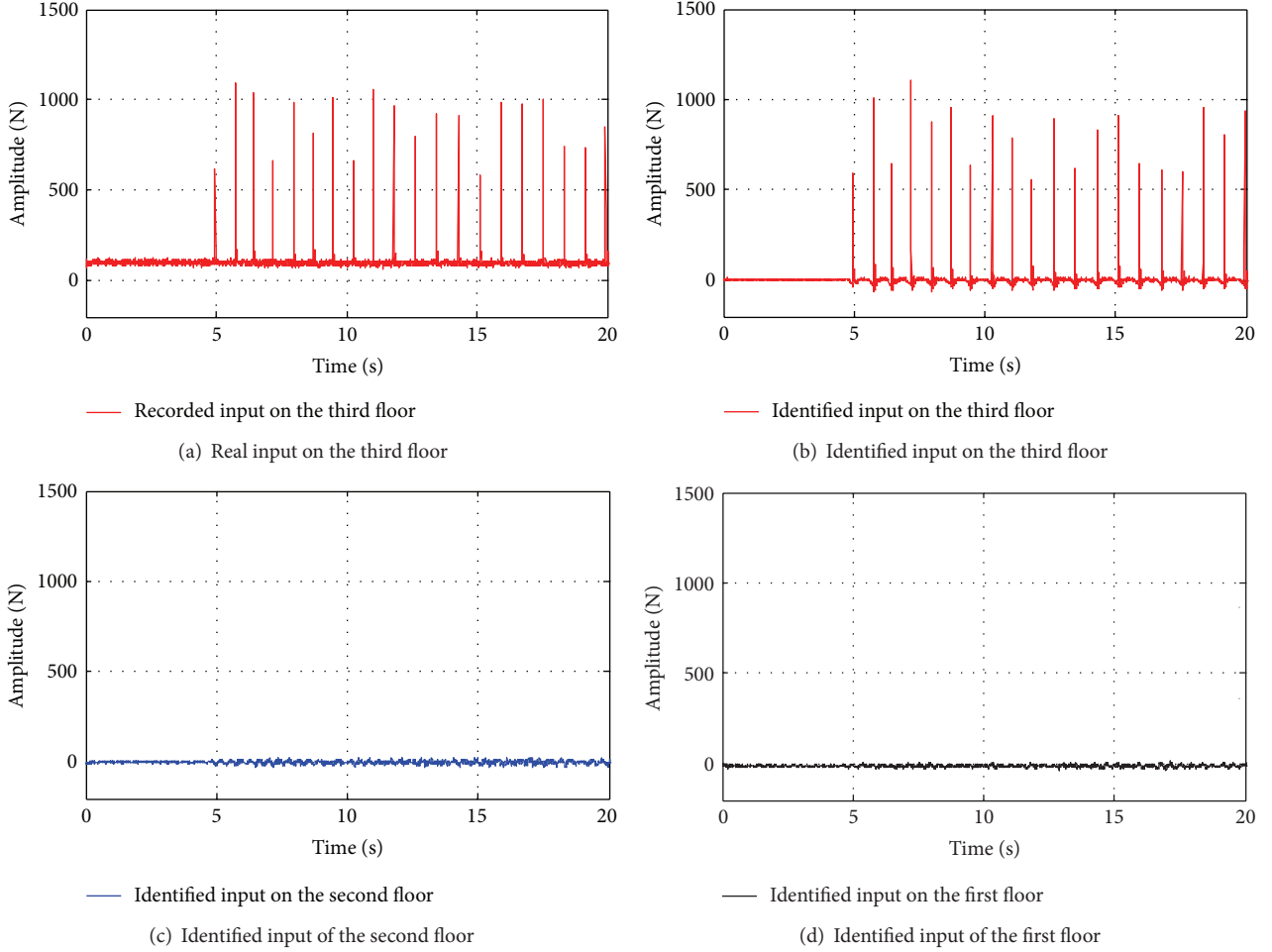


FIGURE 10: The real input on the top floor and the identified inputs of each floor.

The second is a continuous test wherein a certain floor of the building is hit continuously by the hammer.

5.1. Impact Test. In this test, the building model was hit by a hammer once on the 3rd floor and was then released for free decayed vibration in the x direction. Figure 4(a) shows the recorded accelerations for each floor. The accelerations were then integrated to obtain the corresponding velocity and displacement as shown in Figure 5. To reduce the measurement noise, the high-pass Butterworth signal filter was applied to the integration with the filter order $N = 4$ where the lower cut-off frequency = 0.16 rad/sec.

The known information for this case is $f_1(t) \equiv 0.0$ and $f_2(t) \equiv 0.0$, and the structural parameters are to be identified by the proposed ACO_R method with the following objective function:

$$\min \sum_{i=1}^Q z(t_i) = \sum_{i=1}^Q \|y_1(t_i) - y_1^\diamond(t_i)\|^2 + \sum_{i=1}^Q \|y_2(t_i) - y_2^\diamond(t_i)\|^2. \quad (22)$$

Tables 5(a), 5(b), and 5(c) show, respectively, the identified stiffness parameters from ten different response segments. Each has the same duration of 0.2, 0.33 and 1.0 second (i.e., 60, 100, and 300 data points for a sampling frequency 300 Hz). The same initial values for all the unknown parameters were used in the calculation. The maximum average identification error for all three cases is less than 2%, and the maximum identification error for a single parameter is less than 4%. Comparison between Tables 5(a), 5(b), and 5(c) also demonstrates that the identification accuracy is not sensitive to the duration of the response segment. Table 5(d) shows the identification results for response duration of 0.33 second (100 data points) and different initial values of unknown parameters. Comparison between Tables 5(b) and 5(d) shows that the proposed method is not sensitive to the initial estimates of the unknown parameters. All the above results indicate a very good identification accuracy achieved by the proposed method for a very short response duration, which has potential application for online structural health monitoring. It should be noted that the damping identification results are not satisfied in this case. The damping properties can be identified by other effective identification

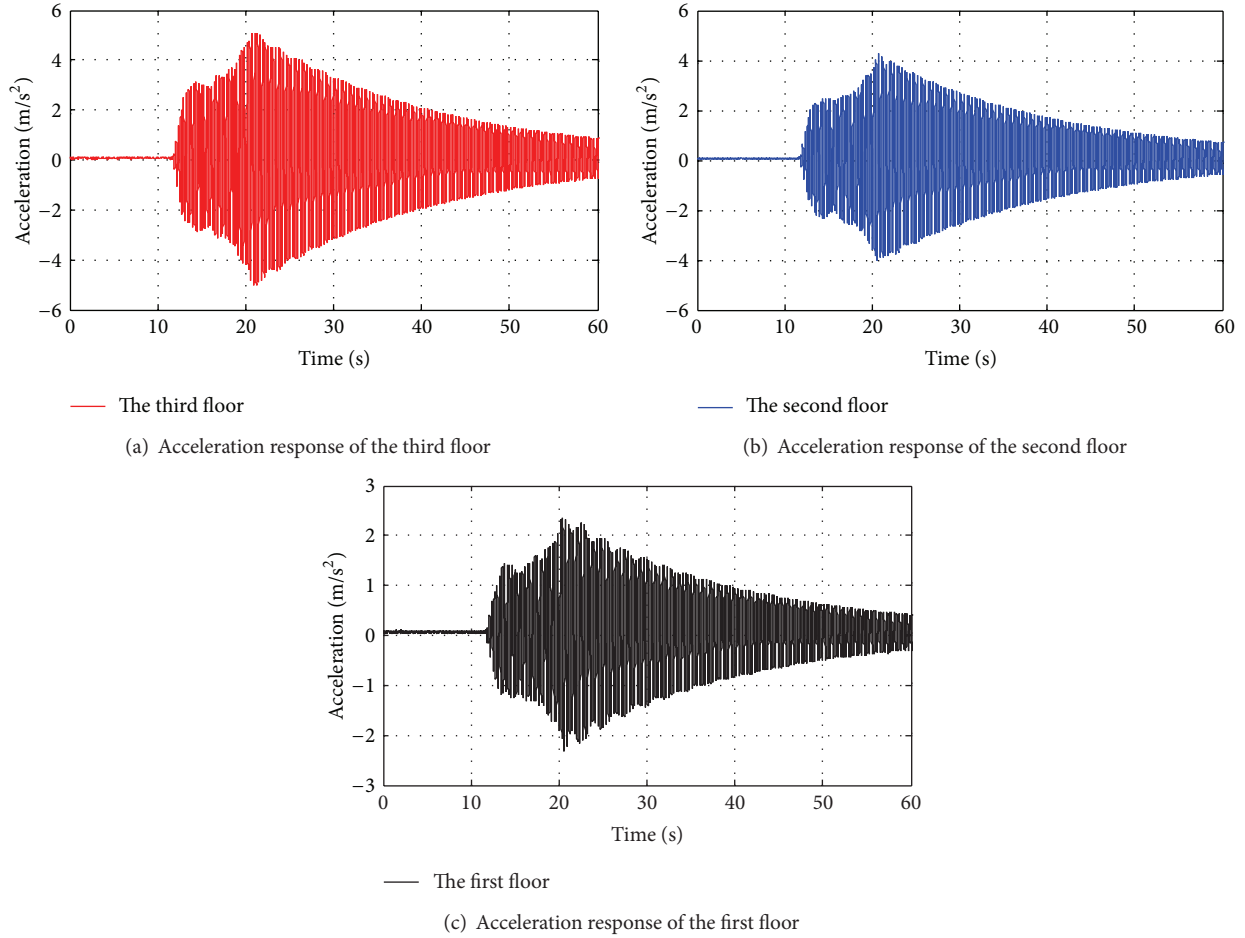


FIGURE 11: The recorded acceleration responses of each floor for hand-shaked test.

techniques such as the empirical mode decomposition plus Hilbert transform method suggested by the authors [27].

Figures 6 and 7 show the convergence procedure of all the stiffness parameters for the computational segments as 10.2~10.53 s and 11.0~11.33 s in Table 5(b). Note that the unknown stiffness parameters can be accurately identified using a short duration of response and the results are robust to the parameters' initial guess.

Figure 8(a) shows the time history of the actual hammer force on the 3rd floor, and Figures 8(b) to 8(c) show the identified time histories of forces for the 3rd, 1st, and 2nd floor, respectively. Note that the identified input on the 3rd floor has a spike at the same time instant as the real input. The amplitudes of the identified inputs on the 1st and 2nd floor are almost zero compared to that of the 3rd floor.

5.2. Continuous Hammer Test. In this test case, the hammer hit the 3rd floor continuously, and the resulting accelerations for each floor are shown in Figure 9. The actual test duration was 60 seconds, but only the first 20 seconds were plotted for the sake of clarity. Using the same objective function as (22), the structural parameters were identified by the ACO_R method, and the results are summarized in Table 6.

Note that the average identification error for each of the seven response segments is less than 2%, and the maximum identification error for each single parameter is less than 3%. Using the global average value of all the identified parameters, the inputs of each floor can be identified. Figures 10(a) and 10(b) compare the identified input and real input on the 3rd floor. It is clear that the identified input has the continued impact spikes (peaks) at the same time as instants for the real input. The amplitudes of the identified inputs of the 2nd and 1st floor are almost zero compared to that of the 3rd floor. The result is consistent with the real test situation.

5.3. Push the Building for a While and Release It to Free Vibration. In this test, the model was hand-shaked on the 2nd floor to vibrate for a while and was then released for free vibration. Figure 11 shows the acceleration responses of each floor for this case. The known information is $f_1(t) \equiv 0.0$ and $f_3(t) \equiv 0.0$, where the objective function can then be established as follows:

$$\min \sum_{i=1}^Q z(t_i) = \sum_{i=1}^Q \|y_1(t_i) - y_1^\diamond(t_i)\|^2 + \sum_{i=1}^Q \|y_3(t_i) - y_3^\diamond(t_i)\|^2. \quad (23)$$

TABLE 7: Identified results for hand-shaked tests on the second floor.

Computation response segments	Identification results ($\times 10^5$) and identification errors					
	k_1	Error	k_2	Error	k_3	Error
19.0~19.33 s	5.6022	-0.61	5.5341	-1.82	5.6282	-0.15
20.0~20.33 s	5.5308	-1.88	5.5969	-0.70	5.6462	0.17
24.0~24.33 s	5.6062	-0.54	5.6089	-0.49	5.6598	0.41
30.0~30.33 s	5.6013	-0.62	5.6068	-0.53	5.6424	0.10
40.0~40.33 s	5.6181	-0.33	5.6101	-0.47	5.6444	0.14
50.0~50.33 s	5.5968	-0.70	5.6174	-0.34	5.6403	0.07
60.0~60.33 s	5.5837	-0.94	5.6017	-0.62	5.6009	-0.63
Average value	5.5913	-0.80	5.5966	-0.71	5.6375	0.02

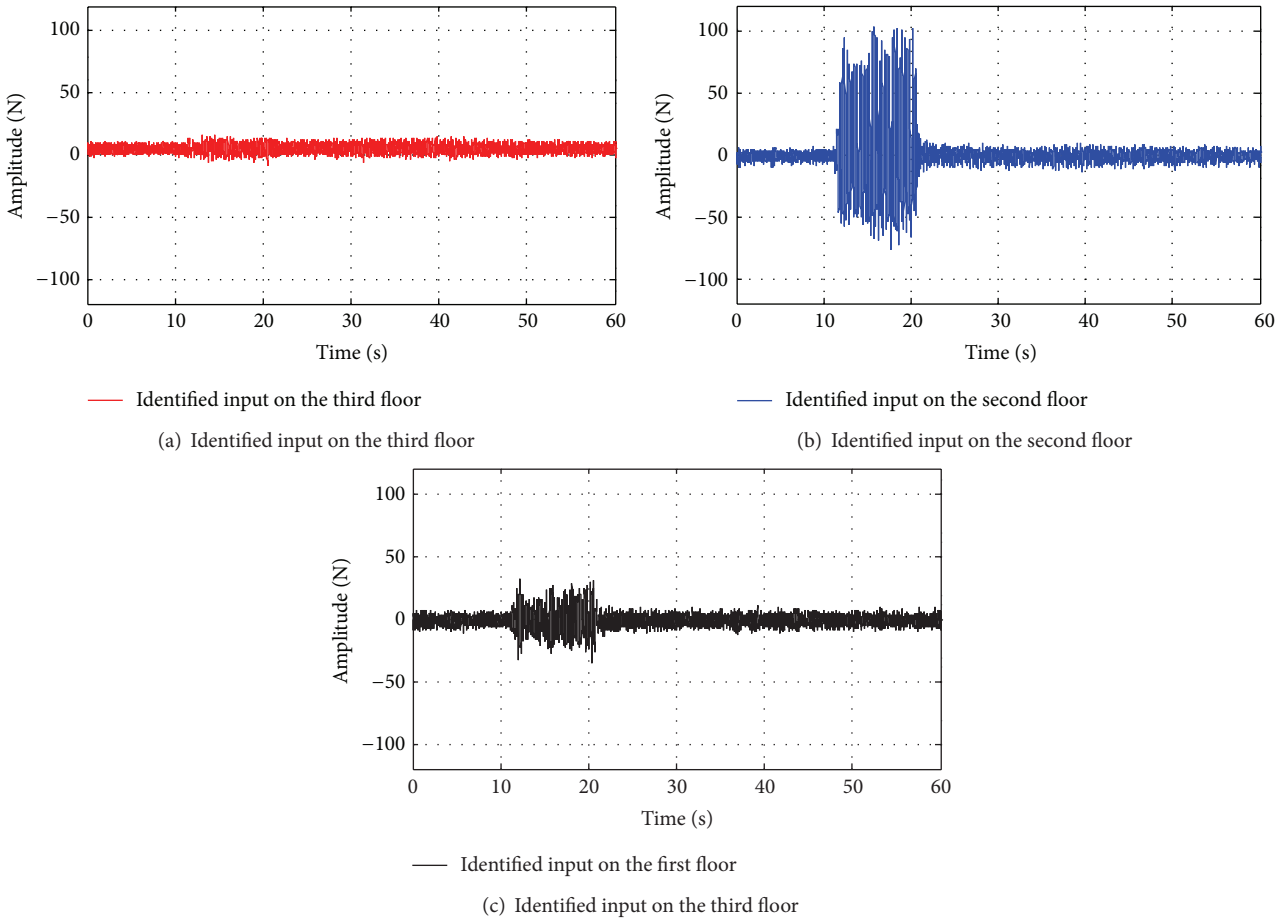


FIGURE 12: The identified inputs of each floor.

Table 7 shows the identification results for this case for seven different response segments. The maximum identification error is less than 1%. It is interesting to compare the identified results of input with the real input. Figures 12(a) to 12(c) show the identified inputs of 1st to 3rd floors, respectively. It is interesting to find that the input of the 2nd floor (Figure 12(b)) has a relatively large excitation force for the duration of 12 to 22 seconds. That is consistent with the test at that duration where the model was hand-shaked. The amplitudes of the inputs from the 1st and 3rd floor are relatively small compared to that of the 2nd floor. The above

three cases demonstrate the applicability and feasibility of the proposed hybrid identification method using response-only measurements.

6. Conclusions

This paper combines the complete inverse method with the ant colony optimization algorithm to identify the input excitation and the structural parameters from the output-only measurements. The core idea of the complete inverse method is to convert the physical features of the excitation

into a mathematical confinement condition. In theory, the proposed method has no limitation on the type of excitation. This paper applies the method to the situation where spatial locations of a limited number of excitations are known. Numerical examples were carried out to evaluate the feasibility of the proposed method. For the situation of noise-free output measurements, numerical studies show that the proposed method can reliably and efficiently identify both the structural parameters and the input time history using a short duration of measurements. Moreover, the accuracy and convergence of the method are robust to the initial values selected for the unknown parameters. For f noise-pollution measurements, the stiffness parameters as well as the input excitation were identified satisfactorily even with high noise level. The identification accuracy of the damping coefficients is broadly acceptable at low noise level and become relatively poor at high noise level. The proposed method is then applied to experimental results of a three-story building model and the results also prove the feasibility of the method.

Conflict of Interests

The authors declare that there is no conflict of interests regarding the publication of this paper.

Acknowledgment

Professor Jun Chen gratefully acknowledges financial support for the research represented by this paper, which came from The Project of National Key Technology R&D Program in the 12th Five Year Plan of China (2012BAJ11B02).

References

- [1] G. W. Housner, L. A. Bergman, T. K. Caughey et al., "Structural control: past, present, and future," *Journal of Engineering Mechanics*, vol. 123, no. 9, pp. 897–971, 1997.
- [2] Y. Zou, L. Tong, and G. P. Steven, "Vibration-based model-dependent damage (delamination) identification and health monitoring for composite structures—a review," *Journal of Sound and Vibration*, vol. 230, no. 2, pp. 357–378, 2000.
- [3] J. Ou and H. Li, "Structural health monitoring in mainland china: review and future trends," *Structural Health Monitoring*, vol. 9, no. 3, pp. 219–231, 2010.
- [4] W. Fan and P. Qiao, "Vibration-based damage identification methods: a review and comparative study," *Structural Health Monitoring*, vol. 10, no. 1, pp. 83–111, 2011.
- [5] K. Toki, T. Stao et al., "Identification of structural parameters and input ground motion from response time histories," *The Journal of Structural Engineering/Earthquake Engineering*, vol. 6, no. 2, pp. 413–421, 1989.
- [6] D. Wang and A. Haldar, "Element-level system identification with unknown input," *Journal of Engineering Mechanics*, vol. 120, no. 1, pp. 159–176, 1994.
- [7] S. S. Law, J. Q. Bu, and X. Q. Zhu, "Time-varying wind load identification from structural responses," *Engineering Structures*, vol. 27, no. 10, pp. 1586–1598, 2005.
- [8] J. N. Yang, S. Pan, and S. Lin, "Least-squares estimation with unknown excitations for damage identification of structures," *Journal of Engineering Mechanics*, vol. 133, no. 1, pp. 12–21, 2007.
- [9] J. N. Yang and H. Huang, "Sequential non-linear least-square estimation for damage identification of structures with unknown inputs and unknown outputs," *International Journal of Non-Linear Mechanics*, vol. 42, no. 5, pp. 789–801, 2007.
- [10] J. Chen and J. Li, "Study of structural system identification with incomplete input information," *Journal of Earthquake Engineering and Engineering Vibration*, vol. 18, no. 4, pp. 40–47, 1998 (Chinese).
- [11] J. Chen and J. Li, "Simultaneous identification of structural parameters and input time history from output-only measurements," *Computational Mechanics*, vol. 33, no. 5, pp. 365–374, 2004.
- [12] J. Li and J. Chen, "Study on identification of structural dynamic parameters with unknown input information," *Chinese Journal of Computational Mechanics*, vol. 16, no. 1, pp. 32–40, 1999 (Chinese).
- [13] J. Li and J. Chen, "A statistical average algorithm for the dynamic compound inverse problem," *Computational Mechanics*, vol. 30, no. 2, pp. 88–95, 2003.
- [14] X. Zhao, Y. L. Xu, J. Chen, and J. Li, "Hybrid identification method for multi-story buildings with unknown ground motion: experimental investigation," *Engineering Structures*, vol. 27, no. 8, pp. 1234–1247, 2005.
- [15] X. Zhao, Y. L. Xu, J. Li, and J. Chen, "Hybrid identification method for multi-story buildings with unknown ground motion: theory," *Journal of Sound and Vibration*, vol. 291, no. 1-2, pp. 215–239, 2006.
- [16] M. Dorigo, *Optimization, learning and natural algorithms (in Italian) [Ph.D. thesis]*, Dipartimento di Electronica, Politecnico di Milano, Italy, 1992.
- [17] M. Dorigo and L. M. Gambardella, "Ant colonies for the travelling salesman problem," *BioSystems*, vol. 43, no. 2, pp. 73–81, 1997.
- [18] G. Di Caro and M. Dorigo, "AntNet: distributed stigmergetic control for communications networks," *Journal of Artificial Intelligence Research*, vol. 9, pp. 317–365, 1998.
- [19] L. M. Gambardella, É. D. Taillard, and M. Dorigo, "Ant colonies for the quadratic assignment problem," *Journal of the Operational Research Society*, vol. 50, no. 2, pp. 167–176, 1999.
- [20] L. Yu and P. Xu, "Structural health monitoring based on continuous ACO method," *Microelectronics Reliability*, vol. 51, no. 2, pp. 270–278, 2011.
- [21] L. Yu, P. Xu, and X. A. Chen, "A SI-based algorithm for structural damage detection," in *Proceedings of 3rd International Conference on Swarm Intelligence (ICSI '12)*, Y. Tan, Y. Shi, and Z. Ji, Eds., vol. 7331 of LNCS, pp. 21–28, ICIS, Shenzhen, China, June 2012.
- [22] K. Socha, "ACO for continuous and mixed-variable optimization," in *Ant Colony Optimization and Swarm Intelligence*, Proceedings, 3172, pp. 25–36, 2004.
- [23] K. Socha and M. Dorigo, "Ant colony optimization for continuous domains," *European Journal of Operational Research*, vol. 185, no. 3, pp. 1155–1173, 2008.
- [24] J. Xiao and L. Li, "A hybrid ant colony optimization for continuous domains," *Expert Systems with Applications*, vol. 38, no. 9, pp. 11072–11077, 2011.
- [25] X. Chen, J. Chen, and W. Liu, "Hybrid identification method based on ant colony optimization algorithm," in *Proceedings of the 1st International Conference on Performance-Based and Life-Cycle Structural Engineering*, pp. 1211–1219, Hong Kong, December 2012.

- [26] R. W. Clough and P. Joseph, *Dynamics of Structure*, Computers & Structures, 3rd edition, 1995.
- [27] J. Chen and Y. L. Xu, "Identification of modal damping ratios of structures with closely spaced modal frequencies," *Structural Engineering and Mechanics*, vol. 14, no. 4, pp. 417–434, 2002.

Research Article

Innovative Data Fusion Enabled Structural Health Monitoring Approach

Xiukuan Zhao,^{1,2} Ruolin Wang,³ Haichang Gu,⁴ Gangbing Song,^{4,5} and Y. L. Mo⁶

¹ Key Laboratory of Ionospheric Environment, Institute of Geology and Geophysics, Chinese Academy of Sciences, Beijing 100029, China

² Beijing National Observatory of Space Environment, Institute of Geology and Geophysics, Chinese Academy of Sciences, Beijing 100029, China

³ School of Civil Engineering, Wuhan University, Wuhan, Hubei 430072, China

⁴ Department of Mechanical Engineering, University of Houston, Houston, TX 77204, USA

⁵ School of Civil Engineering, Dalian University of Technology, Dalian, Liaoning 116024, China

⁶ Department of Civil and Environmental Engineering, University of Houston, Houston, TX 77204, USA

Correspondence should be addressed to Ruolin Wang; rl.wang@whu.edu.cn

Received 10 October 2013; Accepted 23 December 2013; Published 19 February 2014

Academic Editor: Xiao-Wei Ye

Copyright © 2014 Xiukuan Zhao et al. This is an open access article distributed under the Creative Commons Attribution License, which permits unrestricted use, distribution, and reproduction in any medium, provided the original work is properly cited.

Piezoceramic-based active sensing is a useful approach to structural health monitoring. This approach often involves a large number of distributed piezoceramic transducers. It may be confusing to incorporate each sensor data. It is desired to develop an automated health monitoring approach to obtain a comprehensive and accurate health monitoring result by simultaneously interpreting data from all sensors. In this paper, an innovative data fusion enabled structural health monitoring (SHM) approach based on the Dempster-Shafer (D-S) evidence theory is proposed to obtain comprehensive SHM results for a distributed sensor network in a civil infrastructure. Considering that evidence from multiple different information sources (sensor data) has different levels of significance, not all evidence is equivalently effective for the final decision. A weighted fusion damage index (WFDI) is proposed to perform damage identification based on the authors' recently developed piezoceramic-based smart aggregates. Experimental data of a two-story concrete frame was used to study the effectiveness of the proposed weighted fusion damage index. Analyses show that the proposed weighted fusion damage index can reveal the damage status of different areas of the frame. The results are consistent with the visual inspection of the cracks on the concrete frame.

1. Introduction

Health monitoring of civil infrastructures has received considerable attention in recent years. Many events, such as impacts, earthquakes, or hurricanes, cause damage to structures. It is important to provide accurate and comprehensive health monitoring results after such an event to decision-makers. Using piezoelectric transducers, there are many health monitoring approaches, such as the electromechanical (E/M) impedance method (Soh et al. [1], Naidu and Soh [2], Fu and Xu [3], and Kral et al. [4]) and the active-sensing method (Ihn and Chang [5], Song et al. [6, 7], Laskar et al. [8], and Yu et al. [9]). Often multiple sensors are employed in a structural health monitoring (SHM) system [10–12]. The

interpretation of health monitoring data from each individual sensor may be confusing and may not lead to accurate structural health status. It is desired to develop an automated approach to obtain final comprehensive structural health status based on multiple sensors (information sources). In this paper, data fusion technique is proposed to process the data obtained from multiple piezoceramic transducers in a complex civil structure to provide an accurate and comprehensive health monitoring result.

Data fusion combines and processes data from multiple information sources and related information from associated databases to achieve improved accuracies and more specific inferences than the results derived by the use of a single source alone. It has attracted increasing attention in structural

health monitoring due to its inherent capabilities in extracting information from different sources and integrating them into a consistent, accurate, and intelligible dataset. Some researchers studied damage identification methods using data fusion techniques to improve accuracy and obtain more specific inferences. Guo and Zhang [13] and Guo [14] regarded the changes of frequencies and mode shapes as two different information sources and used the data fusion method to detect the damage of two-dimensional truss structures. Three main fusion approaches were studied in this research. Vanniamparambil et al. [15] proposed a novelty detector based on the Mahalanobis distance which was implemented in a data fusion scheme to assess the extent of damage. Their results proved the effectiveness by combining real-time optical and acoustic nondestructive testing, while Bao and Li [16] employed the Dempster-Shafer (D-S) evidence theory and Shannon entropy to decrease the uncertainty and improve the accuracy of damage identification. In addition, data fusion technology is improved by integrating with artificial intelligence, such as fuzzy logic and genetic algorithms. Fan and Zuo [17] improved the D-S theory through the introduction of a fuzzy membership function, importance index, and conflict factor in order to address the issues of evidence sufficiency, evidence importance, and conflicting evidence in the practical application of the D-S evidence theory. Guo and Li [18] presented a two-stage method in determining the location and extent of multiple structural damages by using the information fusion technique and genetic algorithm. Thenozhi et al. [19] used numerical integrator and convex-concave hull classification for structural health monitoring of tall buildings. Zhao et al. [20] introduced a hierarchical ensemble scheme to the data fusion field. Health monitoring of a small-scale two-story frame structure with different types of damage subject to shaking table tests was used as an example to validate the efficiency of their proposed scheme.

Piezoceramic-based active sensing is a useful approach to structural health monitoring. This approach often involves a large number of distributed piezoceramic transducers. It may be confusing to incorporate each sensor data. It is desired to develop an automated health monitoring approach to obtain a final, comprehensive, and accurate health monitoring result by simultaneously interpreting data from all sensors. In this paper, an innovative data fusion enabled structural health monitoring (SHM) approach based on the Dempster-Shafer (D-S) evidence theory is proposed to obtain comprehensive SHM results for a distributed sensor network in a civil infrastructure. Considering that evidence from multiple different information sources (sensor data) has different levels of significance, not all evidence is equivalently effective for the final decision. Different important levels were considered for evidence by assigning weighted coefficients. A weighted fusion damage index (WFDI) is proposed to perform damage identification based on the authors' recently developed piezoceramic-based smart aggregates. Experimental data of a two-story concrete frame was used to study the effectiveness of the proposed weighted fusion damage index. The results indicate that the proposed method can improve damage identification accuracy and increase the reliability of damage identification.

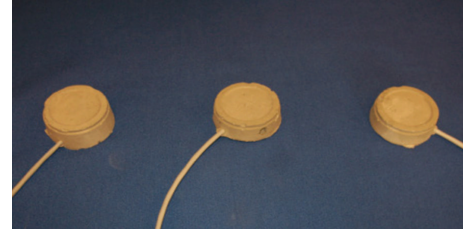


FIGURE 1: Three fabricated smart aggregates.

In this paper, data fusion is used to process structural health monitoring data from multiple sensors to provide an accurate and final interpretation of the structural health status. In the proposed approach, based on the D-S evidence theory, a weighted fusion damage index is proposed by comparing the transmission energy difference between the signatures of healthy and damaged states. To verify the effectiveness of the proposed innovative approach, the data fusion method was used to analyze the experimental data obtained in a structural push-over test of a two-story concrete frame. These experimental data were obtained through an active structural health monitoring approach using piezoceramic-based smart aggregates. Analyses show that the proposed weighted fusion damage index can reveal the damage status of different areas of the frame. The results are consistent with the visual inspection of the cracks on the concrete frame, which indicate that the proposed method can provide an accurate and comprehensive interpretation of the structural health status by using data from multiple sensors.

2. Active Structural Health Monitoring Using Embedded Smart Aggregates

In this study, experimental health monitoring data were obtained by smart aggregates in active-sensing tests and then analyzed by data fusion method to get results with improved accuracy. The developed smart aggregate can either be used as an actuator to excite stress waves to propagate through concrete structure or used as a sensor to detect the wave response.

2.1. Piezoceramic-Based Smart Aggregate. The developed piezoceramic-based smart aggregates are low cost, multifunctional devices which are capable of performing early-age strength monitoring, impact detection, and structural health monitoring for concrete structures [7]. PZT (lead zirconate titanate), a type of piezoceramic material with strong piezoelectric effect, is used to develop the smart aggregates. Smart aggregates (SAs), as shown in Figure 1, are formed by embedding a waterproof PZT patch with lead wires, as shown in Figure 2, into a small concrete block before installing smart aggregates into a larger concrete structure. The materials used to build the small concrete block have the same mixture ratio of cement, sand, and water as the host concrete structure. This way, the smart aggregates will have almost no effect in changing the material and structural properties of the host concrete structures.

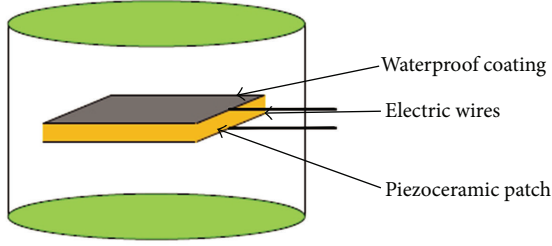


FIGURE 2: Illustration of a smart aggregate.

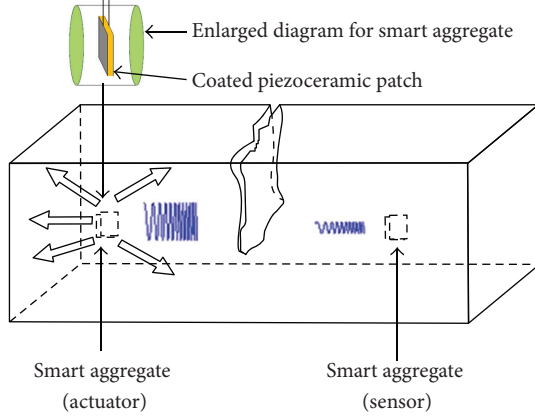


FIGURE 3: Active sensing enabled by smart aggregates.

For concrete structural health monitoring, a smart aggregate enabled active-sensing system was developed as illustrated in Figure 3. In the proposed active-sensing system, one smart aggregate is used as an actuator to generate a sweep sine signal, while the other smart aggregates are used as sensors to detect the sweep sine responses. The crack or damage inside the concrete structure acts as stress relief in the wave propagation path. The amplitude of the wave and the transmission energy will decrease due to the existence of the crack. The drop value of the transmission energy will be correlated with the degree of the damage inside. In this paper, PZTA stands for the smart aggregate used as an actuator and PZTS stands for the smart aggregate used as a sensor.

2.2. Root-Mean-Square Deviation and Damage Index. Various kinds of damage indices have been developed for health monitoring of civil structures in recent years [21, 22]. The root-mean-square deviation (RMSD) is commonly used as a damage index to compare the difference between the signatures of healthy and damaged states.

In this research, wavelet packet analysis is used as a signal-processing tool to analyze the sensor signal of the embedded PZT patches in the concrete structure. The advantage of wavelet packet analysis is that it enables the inspection of relatively narrow frequency bands over a relatively short-time window. The sensor signal S is decomposed by an n -level wavelet packet decomposition into 2^n signal sets $\{X_1, X_2, \dots, X_{2^n}\}$. X_j can be expressed as $X_j = [x_{j,1}, x_{j,2}, \dots, x_{j,m}]$, where j is the frequency band ($j = 1, \dots, 2^n$) and m is

the amount of sampling data. The energy of the decomposed signal is defined as $E_{i,j} = \|X_j\|_2^2 = x_{j,1}^2 + x_{j,2}^2 + \dots + x_{j,m}^2$, where i is the time index and j is the frequency band ($j = 1, \dots, 2^n$). The energy vector at time index i is defined as $E_i = [E_{i,1}, E_{i,2}, \dots, E_{i,2^n}]$.

In the proposed approach, the damage index is formed by calculating the RMSD between the energy vectors of the healthy state and the damaged state. The energy vector for healthy data is $E_h = [E_{h,1}, E_{h,2}, \dots, E_{h,2^n}]$, and the energy vector E_i for the damaged state at time index i is defined as $E_i = [E_{i,1}, E_{i,2}, \dots, E_{i,2^n}]$. The damage index at time i is defined as

$$I_i = \sqrt{\frac{\sum_{j=1}^{2^n} (E_{i,j} - E_{h,j})^2}{\sum_{j=1}^{2^n} (E_{h,j})^2}}. \quad (1)$$

The proposed damage index represents the transmission energy loss portion caused by structural damage. When the damage index is close to 0, the concrete structure is in a healthy state. However, when the damage index is larger than a certain threshold value, damage begins to appear in the concrete structure. The proposed damage index is used to quantitatively evaluate the damage severity. The greater the index is, the more severe the damage that emerges is.

3. Weighted Fusion Damage Index (WFDI)

3.1. Dempster-Shafer Evidence Theory. The Dempster-Shafer (D-S) theory is a mathematical theory of evidence, introduced in the 1960s by Dempster [23] and developed in the 1970s by Shafer [24]. Yager and Liu [25] summarized the classic works of the Dempster-Shafer theory, and the evidence theory is briefly summarized as follows.

For a finite set of mutually exclusive and exhaustive propositions, Θ is called a frame of discernment, where 2^Θ is the set of all the subsets of Θ : $2^\Theta = \{A \mid A \subseteq \Theta\}$. The subset A includes two special cases, which are the null set ϕ and the full set Θ .

The evidence theory allows the basic probability assignment (BPA) to individual propositions and also to any subsets of the power set provided that the sum of all basic probability is equal to one:

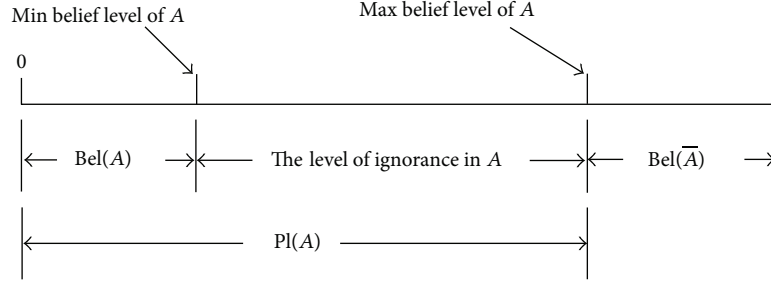
$$m(\phi) = 0, \quad \sum_{A \subseteq \Theta} m(A) = 1, \quad \Theta = \{A_i \mid i = 1, 2, \dots, N\}. \quad (2)$$

The belief function (Bel) is a belief measure of proposition A , and it sums the mass value of all the nonempty subsets of A as

$$\text{Bel}(A) = \sum_{B \subseteq A} m(B). \quad (3)$$

The plausibility function (Pl) takes into account all the elements related to A as

$$\text{Pl}(A) = \sum_{B \cap A \neq \emptyset} m(B). \quad (4)$$

FIGURE 4: Relationship between $\text{Bel}(A)$ and $\text{Pl}(A)$.

The belief function represents the lower limit of the probability, and the plausibility function provides the upper limit of the probability. $[\text{Bel}(A), \text{Pl}(A)]$ is the confidence interval which describes the uncertainty of A . The relationships between Bel value, Pl value, and uncertainty are described in Figure 4.

Multiple evidence can be fused using Dempster's combination rule, which is also called the orthogonal sum of evidence, as shown below:

$$\begin{aligned} (m_1 \oplus \cdots \oplus m_n)(A) &= \frac{1}{K} \sum_{A_1 \cap \cdots \cap A_n = A} m_1(A_1) \cdots m_n(A_n), \\ K &= \sum_{A_1 \cap \cdots \cap A_n \neq \emptyset} m_1(A_1) \cdots m_n(A_n) \\ &= 1 - \sum_{A_1 \cap \cdots \cap A_n = \emptyset} m_1(A_1) \cdots m_n(A_n). \end{aligned} \quad (5)$$

3.2. Weighted Fusion Damage Index. To fuse the information of the same location sensor received from different actuators, each piece of the information received from different actuators can be considered as a piece of evidence for that sensor. In reality, evidence has varying degrees of importance. The conventional D-S evidence theory does not differentiate this. In structural health monitoring, since different evidence makes different contributions to different damage detection, evidence importance should be considered for specific damage detection.

In the piezoceramic-based active-sensing system for structural health monitoring, consider one PZTS (the PZT transducer is utilized as a sensor) data received from different PZTAs (the PZT transducer is utilized as an actuator) as the multidata in data fusion. The structure has two statuses: failure (F_1) and healthy (F_2). The full set is $\Theta = \{F_1, F_2\}$. The original BPA can be obtained from the damage index, $m_{i,j}(F_1) = I_{i,j}$, $m_{i,j}(F_2) = 1 - I_{i,j}$, $m_{i,j}(\Theta) = 0$, where i is the i th PZTS and j is the j th PZTA.

Since the PZTS has different distances between different PZTAs, the contributions of the data from different PZTAs for specific damage detection are also different. To fuse the data of PZTS from different PZTAs, the importance index of the

evidence from PZTA(j) can be written as v_j , which can be obtained by the distance between PZTS and PZTA(j):

$$v_j = \frac{1}{d_j}, \quad (6)$$

where d_j is the distance between PZTS and PZTA(j). Compared with other factors, the distance is more important in extracting the damage location information and evaluating the severity of damage. The smaller the distance between an actuator-sensor pair is, the more important the data of this actuator-sensor pair is in providing the location information and quantitatively evaluating damage. In Section 4.2, we will show how the distance d_j influences the evaluation of the structural health status.

For each PZTS, the largest important index will be taken as the denominator. The weighted index of BPA for PZTS, denoted by w_j , can be expressed as

$$w_j = \frac{v_j}{\max\{v_j \mid j = 1, 2, \dots, n\}}. \quad (7)$$

The matrix W of the weighted index for each PZTS can be obtained by using (7) as

$$W = \begin{matrix} & \{F_1\} & \{F_2\} & \Theta \\ \begin{matrix} E_1 \\ E_2 \\ \vdots \\ E_n \end{matrix} & \begin{bmatrix} w_1 & w_1 & w_1 \\ w_2 & w_2 & w_2 \\ \vdots & \vdots & \vdots \\ w_n & w_n & w_n \end{bmatrix} \end{matrix}, \quad (8)$$

where E_j ($j = 1, \dots, n$) is the evidence from PZTA(j). The new BPA denoted by $m'_j(A)$, as shown in (9), can be recalculated by the matrix W to be

$$m'_j(A) = \begin{cases} w_j \cdot m_j(A), & A \subset \Theta \\ 1 - \sum_{B \subset \Theta} w_j \cdot m_j(A), & B \subset \Theta, A = \Theta. \end{cases} \quad (9)$$

The term $w_j \cdot m_j(A)$ in (9) indicates the BPA of $A \subset \Theta$ is reduced (as $0 < w_j \leq 1$). And the term $1 - \sum_{B \subset \Theta} w_j \cdot m_j(A)$ indicates the loss of BPA will be added to the BPA of Θ . Based on the D-S evidence theory, the BPA for the hypothesis supported by less importance will be significantly reduced. By

TABLE 1: Adjusted BPAs by the weighted index.

	$m(F_1)$ (weighted index) $m'(F_1)$	$m(F_2)$ (weighted index) $m'(F_2)$	$m(\Theta)$ (weighted index) $m'(\Theta)$
m_1	0.8	0.2	0.0
m'_1	$(0.9/0.9 = 1)$ $0.8 * 1 = 0.8$	$(0.9/0.9 = 1)$ $0.2 * 1 = 0.2$	$(0.9/0.9 = 1)$ $1 - 0.8 - 0.2 = 0.0$
m_2	0.1	0.9	0.0
m'_2	$(0.3/0.9 = 0.3333)$ $0.1 * 0.3333 = 0.0333$	$(0.3/0.9 = 0.3333)$ $0.9 * 0.3333 = 0.3$	$(0.3/0.9 = 0.3333)$ $1 - 0.0333 - 0.3 = 0.6667$

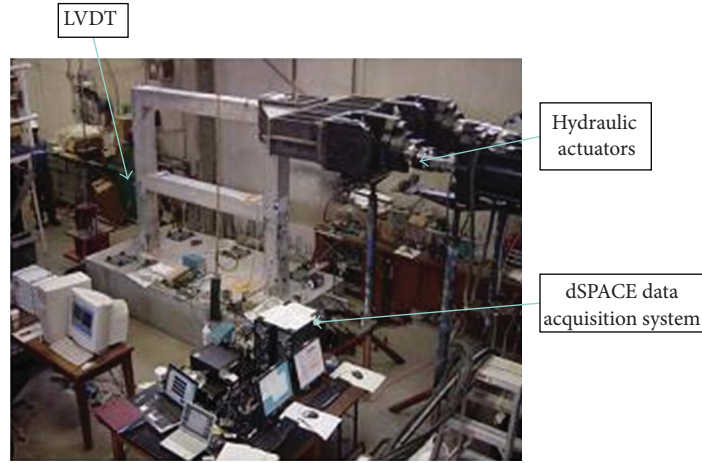


FIGURE 5: Concrete frame for the structural health monitoring test.

fusing the new BPA, the fusion result $m(A)$, $A \in \{F_1, F_2, \Theta\}$, can be obtained by Dempster's combination rule shown in (5). The $m(F_1)$ can be regarded as the weighted fusion damage index.

The following example shows how the WFDI can be calculated. Assume that one PZTS obtains different data from two PZTAs. The RMSD can be calculated through the data, and then the BPAs are shown as follows:

$$\begin{aligned} m_1(F_1) &= 0.8, & m_1(F_2) &= 0.2, & m_1(\Theta) &= 0.0. \\ m_2(F_1) &= 0.1, & m_2(F_2) &= 0.9, & m_2(\Theta) &= 0.0. \end{aligned} \quad (10)$$

Assume that the first evidence importance is larger than the second evidence importance, or $v_1 = 0.9$, and $v_2 = 0.3$ (in reality, these can be calculated based on the distances between the PZTS and the two PZTAs). That means the first evidence is more reliable than the second.

The new BPAs are calculated and shown in Table 1. The losses of $m_2(F_1)$ and $m_2(F_2)$ are added to $m_2(\Theta)$. The second evidence's influence on the fusion result is reduced.

By using (5), the fusion results are obtained as follows:

$$\begin{aligned} K &= 1 - \sum_{A_1 \cap \dots \cap A_n = \emptyset} m_1(A_1) \cdots m_n(A_n) \\ &= 1 - (0.8 * 0.3 + 0.2 * 0.0333) = 0.75334, \end{aligned}$$

$$\begin{aligned} m(F_1) &= (m_1 \oplus m_2)(F_1) \\ &= \frac{1}{K} \sum_{A_1 \cap A_2 = F_1} m_1(A_1) \cdot m_2(A_2) \\ &= \frac{0.8 * 0.0333 + 0.8 * 0.6667}{0.75334} = 0.7434, \end{aligned}$$

$$\begin{aligned} m(F_2) &= (m_1 \oplus m_2)(F_2) \\ &= \frac{1}{K} \sum_{A_1 \cap A_2 = F_2} m_1(A_1) \cdot m_2(A_2) \\ &= \frac{0.2 * 0.3 + 0.2 * 0.6667}{0.75334} = 0.2566, \end{aligned}$$

$$m(\Theta) = 1 - m(F_1) - m(F_2) = 1 - 0.7434 - 0.2566 = 0. \quad (11)$$

It is shown that the fusion result depends more on the first evidence ($m(F_1) = 0.7434$ is close to $m_1(F_1) = 0.8$ as compared to $m_2(F_1) = 0.1$). $m(F_1) = 0.7434$ is the WFDI. It indicates that the structure is seriously damaged, which is a conclusion similar to the first evidence ($m_1(F_1) = 0.8$). The WFDI can avoid the disturbance of the second evidence, which is less reliable. In this paper, the developed weighted fusion damage will be used to quantitatively evaluate the health status and provide more precise monitoring results for a push-over test of a concrete frame.

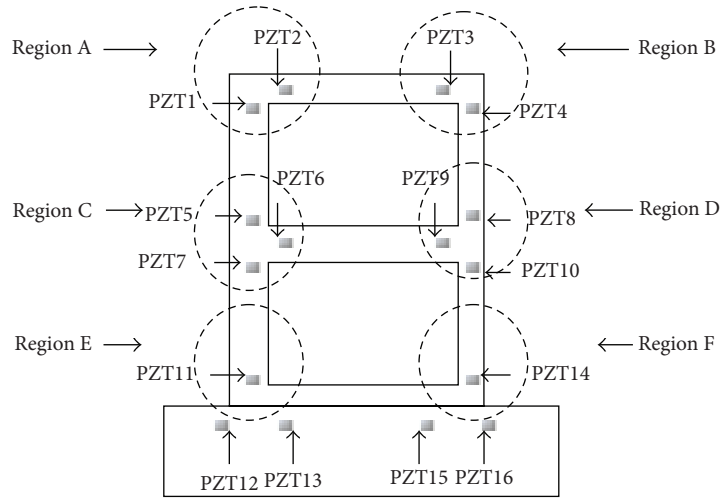


FIGURE 6: Locations of the smart aggregates.



(a) Cracks at region A



(b) Cracks at region B



(c) Cracks at region C



(d) Cracks at region D



(e) Cracks at region E



(f) Cracks at region F

FIGURE 7: Damage status of concrete frame after failure.

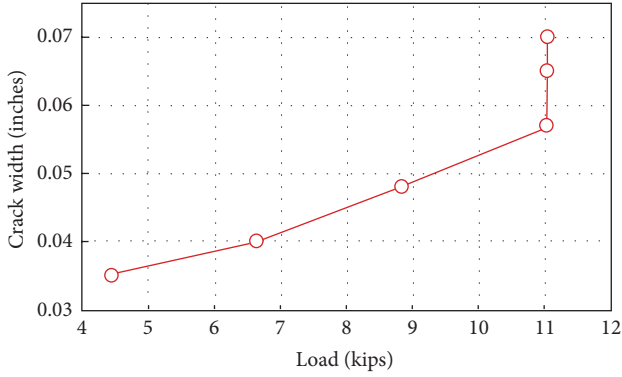


FIGURE 8: Crack width versus the load for a crack which first appears in the concrete frame.

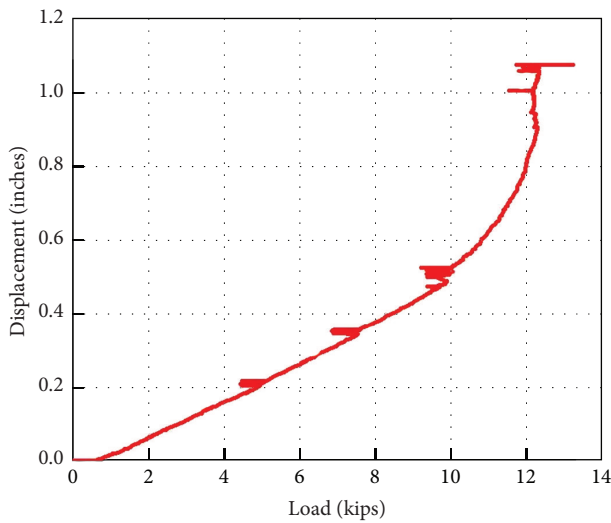


FIGURE 9: Displacement versus load.

4. Test Frame and Instrumentation Details

4.1. *Experimental Program of Structural Health Monitoring.* The data of structural health monitoring of a two-story concrete frame instrumented with piezoceramic-based smart aggregates, as shown in Figure 5 [7, 8], are used in this study. The locations of the smart aggregates are shown in Figure 6. Two hydraulic actuators were used to apply load to the frame structure at its right corner to conduct the so-called push-over test. The load was increasingly applied to the frame until its structural failure. Linear variable differential transformers (LVDTs) were used to measure the displacement at different locations of the concrete frame. In addition, hand-held microscopes were also used to measure the crack width.

During the push-over test, the active-sensing based structural health monitoring enabled by smart aggregates was implemented to evaluate the damage status of the concrete frame. Before the appearance of a major crack, the loading protocol was the force control mode. After the appearance of a major crack, the loading protocol was set to the displacement control mode. During the force control mode, the load (force) was increased gradually at a fixed rate until the major crack appears. During the displacement control mode, the concrete

TABLE 2: Details for each test during the loading process.

Test number	Description
1	Health status
2	Load = 4.41 kips
3	Load = 6.61 kips
4	Load = 8.82 kips
5	Load = 11.02 kips
6	Displacement = 1.6 inches
7	Displacement = 1.9 inches
8	Displacement = 1.9 inches
9	Displacement = 2.5 inches
10	Displacement = 3 inches
11	Displacement = 3 inches
12	Displacement = 3.5 inches
13	Displacement = 4 inches
14	Failed

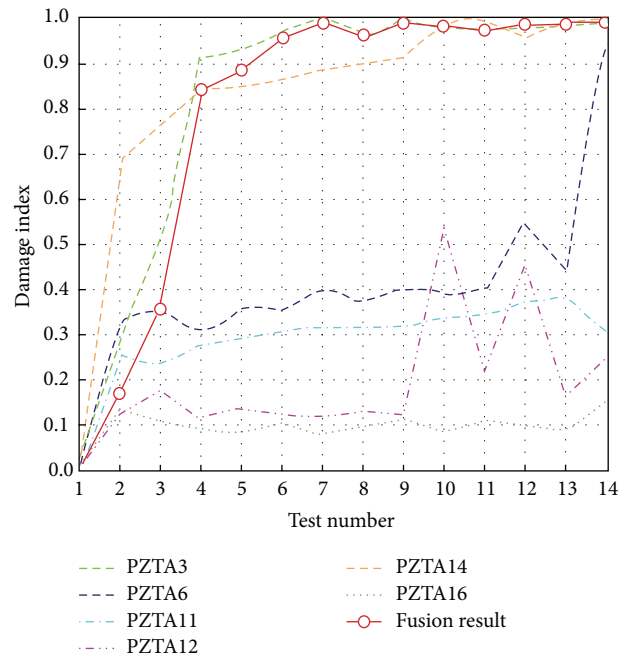


FIGURE 10: Damage index of PZTS2 with fusion result.

frame was pushed by the hydraulic actuators to a certain position at a specified rate and these positions were held for a certain time for data acquisition. During both load control and displacement control modes, the data of the active-sensing based structural health monitoring enabled by smart aggregates were recorded at different time intervals, which are designated as different test numbers. The detailed loading information at each structural health monitoring test is shown in Table 2. After the failure of the concrete frame, the damages at different locations are shown in Figure 7.

The width for the first crack was continuously measured by a hand-held microscope, and the data is plotted versus the load, as shown in Figure 8, which clearly reveals that the relationship between the crack width and the load value is close to a linear one before the load of 11.02 kips. After the load value

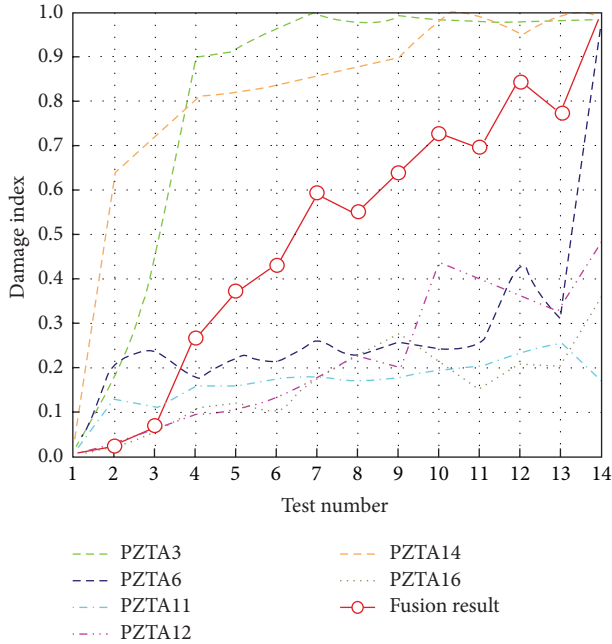


FIGURE 11: Damage index of PZTS8 with fusion result.

reaches 11.02 kips, the crack width increases dramatically due to yielding of the reinforcing steel bars in the concrete frame. In Figure 9, the results of the LVDT measurements show that the relationship between displacement and load was highly nonlinear after the load value reached 11.02 kips. This LVDT was positioned at the top of the concrete frame. The LVDT data also verified that the concrete frame yielded at a load value of 11.02 kips.

4.2. Structural Health Monitoring Using the Weighted Fusion Damage Index. During the active-sensing health monitoring experiment, PZT3, PZT6, PZT11, PZT12, PZT14, and PZT16 were alternately used as actuators. When one smart aggregate was chosen as an actuator (PZTA) to generate sweep sine waves, the other smart aggregates were used as sensors (PZTSs). The PZTSs detected the sweep sine responses. To obtain more reliable results, the developed WFDI was used to process multiple datasets with different smart aggregates. The damage indices were calculated by (1) from the data of PZTSs and the weighted index was calculated by (6) and (7). The BPA in the D-S evidence theory can be obtained from the damage index and adjusted by the weighted index. Then the WFDI can be calculated using (5).

As illustrated in Figure 10, the solid line is the WFDI based on the PZTS2's data. The other dashed lines represent the damage indices without using data fusion when PZT2 was used as the sensor and each of the other smart aggregates was alternatively used as an actuator. Figures 11 and 12 show the WFDI results of PZTS8 and PZTS15. Comparing among WFDI results of PZTS2, PZTS8, and PZTS15, the PZTS2's WFDI has the largest fusion value, PZTS15 has the lowest fusion value, and PZTS8 has the medium fusion value. These results show that among PZT2, PZT8, and PZT15, the area around PZT2 had the most severe damage and the area

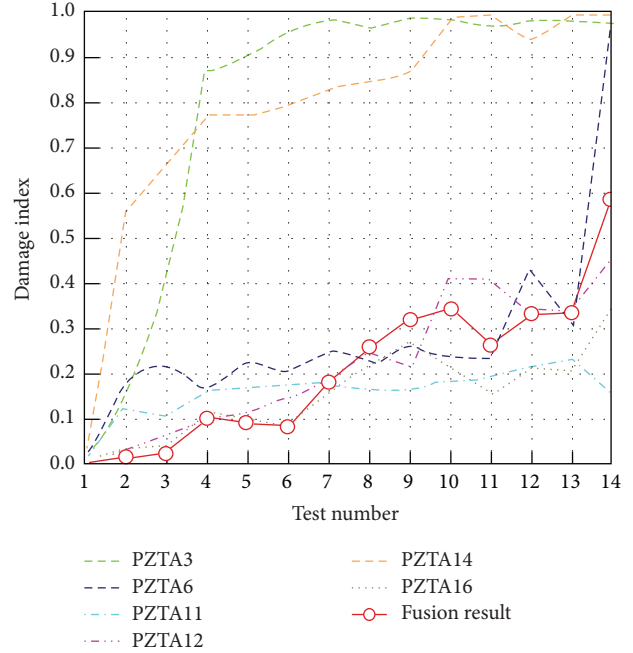


FIGURE 12: Damage index of PZTS15 with fusion result.

around PZT15 had the least severe damage, which are all confirmed by visual inspection of the specimen. PZT15 was embedded inside the base where damage was less likely to happen.

From the WFDI comparison results shown in Figure 13, PZTS2, PZTS6, and PZTS14 have much higher WFDI values than PZT9S and PZT11S. This demonstrates that the damage statuses around PZT2, PZT6, and PZT14 were more severe than those around PZT9 and PZT11, which was verified by the visual inspection results shown in Figure 7. Additionally, the yielding point obtained from the WFDI results was verified by the hand-held microscope data shown in Figure 8 and the LVDT data shown in Figure 9. As shown in Figures 8 and 9, the structure yielded when the load was over 11.02 kips. From Table 2, the load of 11.02 kips corresponds to the test number 5. From the WFDI results shown in Figure 13, the prediction point (WFDI is over 0.9) for yielding is at test number 3, which corresponds to the 6.61-kip load value. The proposed fusion damage index is more sensitive in predicting yielding point than the observation based on measurements from the microscope and the LVDT.

Figure 14 shows the comparison between the WFDI results and the displacement of the top part of the structure when the load was increasingly applied to the structure until failure. PZTS2 and PZTS6 were selected for the comparison as they were located in the most seriously damaged and structurally important parts of the structure. As shown in the figure, the fusion damage indices are consistent with the structure's displacement-load relationship and are more sensitive than the LVDT measured displacement as fusion damage indices reach saturation much earlier than the displacement. By comparing the WFDI results and the load-displacement curve, it can be seen that the proposed weighted fusion damage index quantitatively evaluates the damage status

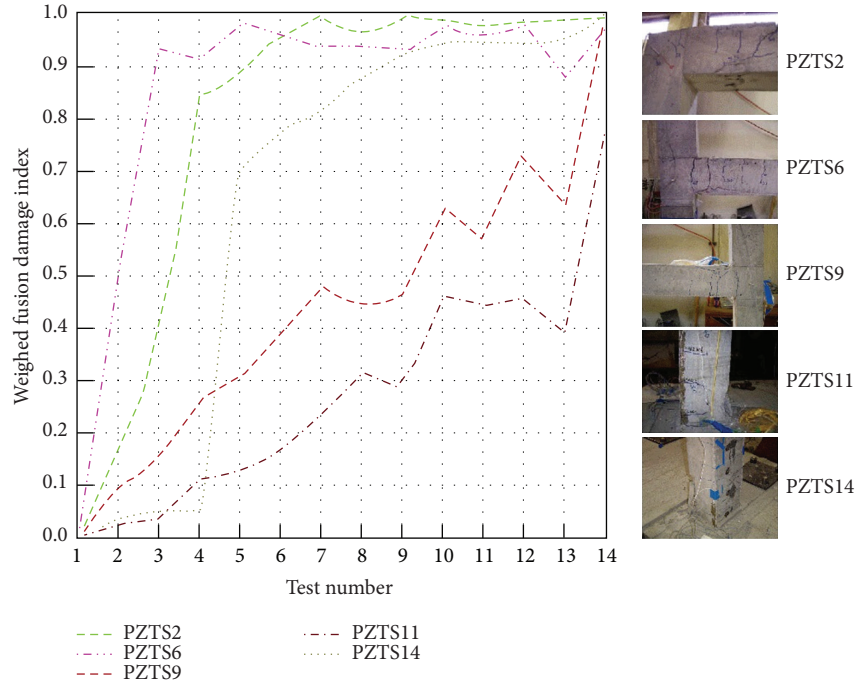


FIGURE 13: Weighted fusion damage index versus damage status at different locations.

during the loading process. Furthermore, the experimental results verify that proposed WFDI is more sensitive in detecting the yielding point than the traditional displacement-load curve. From the traditional displacement-load curve shown in Figure 14, the curve becomes nonlinear when the load was 11.2 kips. This shows that the frame yielded at a load value of 11.2 kips. From the WFDI results shown in Figure 14, the WFDI curve of PZTS2 reached a critical value around a load value of 6.5 kips and the WFDI curve of PZTS6 reached a critical value at a load value of 8.5 kips. The critical point detected by WFDI was ahead of the yielding point detected by traditional displacement-load curve which experimentally verified the effectiveness and the sensitiveness of the proposed WFDI.

5. Conclusions

In this paper, an innovative data fusion-based structural health monitoring approach is proposed to provide accurate and comprehensive health monitoring results. In the proposed approach, a weighted fusion damage index is developed based on the D-S evidence theory and the wavelet packet analysis. Structural health monitoring data of a two-story concrete frame instrumented with smart aggregates were used for this study. The weighted fusion damage indices were developed and applied to analyze and interpret the experimental data. Analyses show that the proposed weighted fusion damage index can reveal the damage status of different areas of the frame. The results are consistent with the visual inspection of the cracks on the concrete frame. Furthermore, analyses also demonstrate that the weighted fusion damage index not only evaluates the damage severity but also is more sensitive than traditional health monitoring approaches that

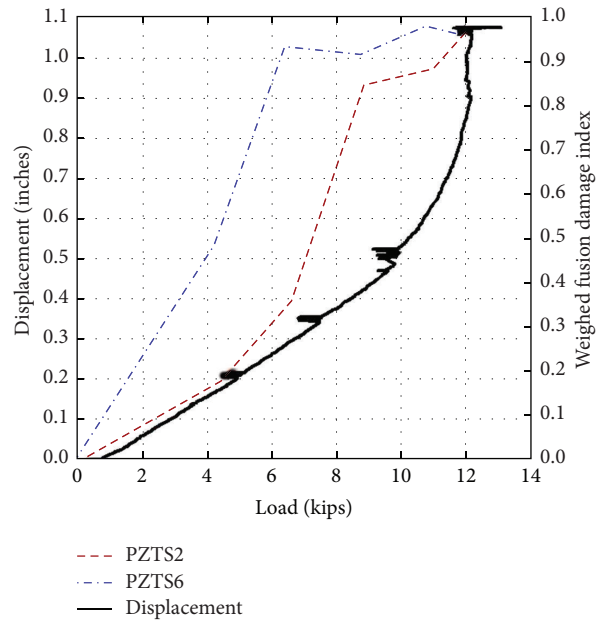


FIGURE 14: Weighted fusion damage index and displacement versus load.

use hand-held microscopes or LVDTs. In addition, the damage location information can be extracted by the proposed approach.

Conflict of Interests

The authors declare that there is no conflict of interests regarding the publication of this paper.

Acknowledgments

This work was partially funded by the National Science Foundation (NSF) via Research Grants (nos. CMMI-0724190 and CNS-0832089), the National Natural Science Foundation of China (no. 41104106, no. 51278387, and no. 51278084), and the Science Fund for Creative Research Groups Grant no. 51121005. The opinions expressed in this study are those of the authors and do not necessarily reflect the views of the sponsor.

References

- [1] C. K. Soh, K. K.-H. Tseng, S. Bhalla, and A. Gupta, "Performance of smart piezoceramic patches in health monitoring of a RC bridge," *Smart Materials and Structures*, vol. 9, no. 4, pp. 533–542, 2000.
- [2] A. S. K. Naidu and C. K. Soh, "Identifying damage location with admittance signatures of smart piezo-transducers," *Journal of Intelligent Material Systems and Structures*, vol. 15, no. 8, pp. 627–642, 2004.
- [3] H. Fu and Q. Xu, "Locating impact on structural plate using principal component analysis and support vector machines," *Mathematical Problems in Engineering*, vol. 2013, Article ID 352149, 8 pages, 2013.
- [4] Z. Kral, W. Horn, and J. Steck, "Crack propagation analysis using acoustic emission sensors for structural health monitoring systems," *The Scientific World Journal*, vol. 2013, Article ID 823603, 13 pages, 2013.
- [5] J.-B. Ihn and F.-K. Chang, "Pitch-catch active sensing methods in structural health monitoring for aircraft structures," *Structural Health Monitoring*, vol. 7, no. 1, pp. 5–19, 2008.
- [6] G. Song, H. Gu, Y. L. Mo, T. T. C. Hsu, and H. Dhonde, "Concrete structural health monitoring using embedded piezoceramic transducers," *Smart Materials and Structures*, vol. 16, no. 4, pp. 959–968, 2007.
- [7] G. Song, H. Gu, and Y.-L. Mo, "Smart aggregates: multi-functional sensors for concrete structures—a tutorial and a review," *Smart Materials and Structures*, vol. 17, no. 3, Article ID 033001, 2008.
- [8] A. Laskar, H. Gu, Y. L. Mo, and G. Song, "Progressive collapse of a two-story reinforced concrete frame with embedded smart aggregates," *Smart Materials and Structures*, vol. 18, no. 7, Article ID 075001, 2009.
- [9] L. Yu, V. Giurgiutiu, J. Wang, and Y.-J. Shin, "Corrosion detection with piezoelectric wafer active sensors using pitch-catch waves and cross-time-frequency analysis," *Structural Health Monitoring*, vol. 11, no. 1, pp. 83–93, 2012.
- [10] Z. Sun, B. Rocha, K. T. Wu, and N. Mrad, "A Methodological review of piezoelectric based acoustic wave generation and detection techniques for structural health monitoring," *International Journal of Aerospace Engineering*, vol. 2013, Article ID 928627, 22 pages, 2013.
- [11] Y. Q. Ni, X. W. Ye, and J. M. Ko, "Monitoring-based fatigue reliability assessment of steel bridges: analytical model and application," *Journal of Structural Engineering*, vol. 136, no. 12, pp. 1563–1573, 2010.
- [12] Y. Q. Ni, X. W. Ye, and J. M. Ko, "Modeling of stress spectrum using long-term monitoring data and finite mixture distributions," *Journal of Engineering Mechanics*, vol. 138, no. 2, pp. 175–183, 2011.
- [13] H. Guo and L. Zhang, "A weighted balance evidence theory for structural multiple damage localization," *Computer Methods in Applied Mechanics and Engineering*, vol. 195, no. 44–47, pp. 6225–6238, 2006.
- [14] H. Y. Guo, "Structural damage detection using information fusion technique," *Mechanical Systems and Signal Processing*, vol. 20, no. 5, pp. 1173–1188, 2006.
- [15] P. A. Vanniamparambil, I. Bartoli, K. Hazeli et al., "An integrated structural health monitoring approach for crack growth monitoring," *Journal of Intelligent Material Systems and Structures*, vol. 23, no. 14, pp. 1563–1573, 2012.
- [16] Y. Bao and H. Li, "Application of information fusion and Shannon entropy in structural damage detection," in *Health Monitoring of Structural and Biological Systems*, Proceedings of SPIE, San Diego, Calif, USA, March 2007.
- [17] X. Fan and M. J. Zuo, "Fault diagnosis of machines based on D-S evidence theory. Part I: D-S evidence theory and its improvement," *Pattern Recognition Letters*, vol. 27, no. 5, pp. 366–376, 2006.
- [18] H. Y. Guo and Z. L. Li, "A two-stage method to identify structural damage sites and extents by using evidence theory and micro-search genetic algorithm," *Mechanical Systems and Signal Processing*, vol. 23, no. 3, pp. 769–782, 2009.
- [19] S. Thenozhi, W. Yu, A. L. López Chau, and X. Li, "Structural health monitoring of tall buildings with numerical integrator and convex-concave hull classification," *Mathematical Problems in Engineering*, vol. 2012, Article ID 212369, 15 pages, 2012.
- [20] X. Zhao, M. Li, G. Song, and J. Xu, "Hierarchical ensemble-based data fusion for structural health monitoring," *Smart Materials and Structures*, vol. 19, no. 4, Article ID 045009, 2010.
- [21] K. K.-H. Tseng and A. S. K. Naidu, "Non-parametric damage detection and characterization using smart piezoceramic material," *Smart Materials and Structures*, vol. 11, no. 3, pp. 317–329, 2002.
- [22] G. Park, H. Sohn, C. R. Farrar, and D. J. Inman, "Overview of piezoelectric impedance-based health monitoring and path forward," *The Shock and Vibration Digest*, vol. 35, no. 6, pp. 451–463, 2003.
- [23] A. P. Dempster, "A generalization of Bayesian inference," *Journal of the Royal Statistical Society B*, vol. 30, pp. 205–247, 1968.
- [24] G. Shafer, *A Mathematical Theory of Evidence*, Princeton University Press, Princeton, NJ, USA, 1976.
- [25] R. R. Yager and L. Liu, *Classic Works of the Dempster-Shafer Theory of Belief Functions*, Springer, New York, NY, USA, 2008.

Research Article

Structural System Identification with Extended Kalman Filter and Orthogonal Decomposition of Excitation

Y. Ding,^{1,2} B. Y. Zhao,^{1,2} and B. Wu^{1,2}

¹ Key Lab of Structures Dynamic Behavior and Control (Harbin Institute of Technology), Ministry of Education, Heilongjiang, Harbin 150090, China

² School of Civil Engineering, Harbin Institute of Technology, Harbin 150090, China

Correspondence should be addressed to Y. Ding; dingyong@hit.edu.cn

Received 10 November 2013; Accepted 25 December 2013; Published 17 February 2014

Academic Editor: Xiao-Wei Ye

Copyright © 2014 Y. Ding et al. This is an open access article distributed under the Creative Commons Attribution License, which permits unrestricted use, distribution, and reproduction in any medium, provided the original work is properly cited.

Both the structural parameter and external excitation have coupling influence on structural response. A new system identification method in time domain is proposed to simultaneously evaluate structural parameter and external excitation. The method can be used for linear and hysteresis nonlinear structural condition assessment based on incomplete structural responses. In this method, the structural excitation is decomposed by orthogonal approximation. With this approximation, the strongly time-variant excitation identification is transformed to gentle time-variant, even constant parameters identification. Then the extended Kalman filter is applied to simultaneously identify state vector including the structural parameters and excitation orthogonal parameters in state space based on incomplete measurements. The proposed method is validated numerically with the simulation of three-story linear and nonlinear structures subject to external force. The external force on the top floor and the structural parameters are simultaneously identified with the proposed system identification method. Results from both simulations indicate that the proposed method is capable of identifying the dynamic load and structural parameters fairly accurately with contaminated incomplete measurement for both of the linear and nonlinear structural systems.

1. Introduction

The evaluation of the structural parameter and external excitation are two main parts of structural health monitoring, which contribute efficiently to structural maintenance and management. After the severe external excitation, infrastructures always suffer from structural damages and some components may perform nonlinearly. The nonlinearities in structural system may have adversely influence on structural health monitoring (SHM) and structural control. Both the structural parameter and external excitation have coupling influence on structural response. Therefore, the evaluation of one aspect without considering another aspect may cause error in the identification result. Exact knowledge of structural parameter and the excitation time history are essential to the rapid postevent structural condition assessment and the prediction of load-bearing capacity.

Vibration-based SHM methods are investigated actively for decades [1–3]. An extensive summary of health monitoring and vibration-based structural condition assessment

of civil engineering structures are provided [1, 4]. Zou et al. [5] summarized the methods on vibration-based damage detection and health monitoring for composite structures, especially in delamination modelling techniques and delamination detection. More recently, Chen and Li [6] presented methods to identify structural parameters and input time history from output-only measurements iteratively. Lu and Law [7] identify the physical parameters and the input excitation force of linear structures based on the sensitivities of dynamic response. Law and Yong [8] proposed substructural condition assessment method for structural damage detection and external force identification of linear structural system. Online identification methods for linear substructures have been developed by Ding [9] and the local damage can be accurately identified. Sun and Betti [10] proposed a simultaneous identification method for linear structure with artificial bee colony algorithm. Lei et al. [11] successfully identified the shear building based on partial output measurements with EKF and least-squares estimator.

However, the target structures investigated above are almost linear and time-invariant.

In the past few decades, numerous methods have been developed for structural model updating and external excitation of nonlinear structures. The Kalman filter is an effective means of parameter identification and input estimation for a linear or nonlinear structure. Two forms of the extended recursive least-squares algorithm were considered for the identification of system parameter and the tracking of a chirped sinusoid with additive noise [12]. Other time-variant parameter identification methods are the online identification of nonlinear hysteretic structure with an adaptive tracking techniques based on least-squares estimation [13], nonlinear normal mode analysis which considered the nonlinearity of structural system [14–16], an online sequential weighted least-squares support vector machine technique to quantify the structural parameter changes when the measurement involves damage events [17], and an adaptive tracking technique based on extended Kalman filter for identifying the structural parameters and their increments [18]. These methods do not require a priori knowledge of the time of occurrence of the anomalies. Hence, these methods could be applied to conduct the structural condition assessment online. However, most existing methods for time-variant parameter identification may require the complete measurement of structural response.

In this paper, a simultaneous identification method for structural parameter and external excitation is proposed for both linear and nonlinear structures based on the extended Kalman filter. The structural parameters include stiffness, damping, and the parameters of nonlinear model. In this study, the excitation time history is decomposed by orthogonal polynomial. The coefficients of orthogonal polynomial and structural parameter are taken as state variables. With extended Kalman filter the state vector is identified recursively. The proposed method was validated numerically with the simulation of a linear shear frame and a hysteretic nonlinear shear frame. Results from the numerical simulations indicate that the proposed method can be used to identify structural parameter and external excitations effectively based on incomplete contaminated structural responses measurements.

2. Equation of Motion in State Space

The equation of motion of an N dofs linear structural system subject to external excitation is

$$\mathbf{M}\ddot{\mathbf{x}}(t) + \mathbf{C}\dot{\mathbf{x}}(t) + \mathbf{K}\mathbf{x}(t) = \mathbf{L}\mathbf{F}, \quad (1)$$

where \mathbf{M} , \mathbf{C} , and \mathbf{K} are the mass, damping, and stiffness matrices of the structural system, respectively. \mathbf{F} is the external force acting on the structure and \mathbf{L} is the location matrix of external force. $\ddot{\mathbf{x}}$, $\dot{\mathbf{x}}$, and \mathbf{x} are, respectively, the vectors of acceleration, velocity, and displacement responses of the structural system. The equation of motion of the linear structural system shown in (1) can also be expressed in the state space generally as the following equation:

$$\dot{\mathbf{Z}}(t) = \mathbf{A}\mathbf{Z}(t) + \mathbf{B}\mathbf{L} \times \mathbf{F}(t), \quad (2)$$

where

$$\mathbf{Z} = \begin{bmatrix} \mathbf{x} \\ \dot{\mathbf{x}} \end{bmatrix}, \quad \mathbf{A} = \begin{bmatrix} 0 & \mathbf{I} \\ -\mathbf{M}^{-1}\mathbf{K} & -\mathbf{M}^{-1}\mathbf{C} \end{bmatrix}, \quad \mathbf{B} = \begin{bmatrix} 0 \\ \mathbf{M}^{-1} \end{bmatrix}. \quad (3)$$

The equation of motion of a hysteretic nonlinear structural system subject to excitation can be written as

$$\mathbf{M}\ddot{\mathbf{x}}(t) + \mathbf{C}\dot{\mathbf{x}}(t) + \mathbf{K}\mathbf{z}(t) = \mathbf{L}\mathbf{F}(t), \quad (4)$$

where $\mathbf{z}(t) = [\mathbf{z}_1(t) \ \mathbf{z}_2(t) \ \cdots \ \mathbf{z}_i(t)]^T$ is the hysteretic component vector, and the hysteretic component can be represented as

$$\dot{z}_i = \dot{x}_i - \beta_i |\dot{x}_i| |z_i|^{\alpha_i - 1} z_i - \gamma_i \dot{x}_i |z_i|^{\alpha_i}, \quad (5)$$

where subscript i represent the i th story. \dot{x}_i and z_i are, respectively, the i th story velocity and hysteretic component. β_i and γ_i are nondimensional parameters which decide the shape of the hysteresis loop of the i th story. α_i is a nondimensional parameter that controls the smoothness of the hysteresis loop of the i th story. The equation of motion of the nonlinear structural system shown in (5) can also be expressed in the state space generally as the following equation:

$$\begin{aligned} \dot{\mathbf{Z}}(t) &= f(\mathbf{Z}, \mathbf{F}, t) \\ &= \begin{bmatrix} \dot{\mathbf{x}}(t) \\ \mathbf{M}^{-1} [\mathbf{L}\mathbf{F}(t) - (\mathbf{C}\mathbf{X}(t) + \mathbf{K}\mathbf{Z}(t))] \\ \dot{\mathbf{x}}(t) - \boldsymbol{\beta} |\dot{\mathbf{x}}(t)| |\mathbf{z}(t)|^{\alpha-1} \mathbf{z} - \boldsymbol{\gamma} \dot{\mathbf{x}}(t) |\mathbf{z}(t)|^\alpha \end{bmatrix}, \end{aligned} \quad (6)$$

where $f(\mathbf{Z}, \mathbf{F}, t)$ is a nonlinear function of \mathbf{Z} in state space. For the linear and nonlinear structures, responses can be recursively calculated by (4) or (6), respectively. The identification method proposed in this paper is based on these two types of state space equations.

3. Extended Kalman Filter for Structural System Identification

The equation of motion of an N dofs structure under load excitation can be written as

$$\mathbf{M}\ddot{\mathbf{x}}(t) + \mathbf{F}_c[\dot{\mathbf{x}}(t)] + \mathbf{F}_s[\mathbf{x}(t)] = \mathbf{L}\mathbf{F}(t), \quad (7)$$

where $\mathbf{F}_c[\dot{\mathbf{x}}(t)]$ denotes damping force vector and $\mathbf{F}_s[\mathbf{x}(t)]$ denotes stiffness force vector. Introducing an extended state vector with a dimension of $2n + m$,

$$\mathbf{Z}(t) = [\mathbf{x}(t), \dot{\mathbf{x}}(t), \boldsymbol{\theta}]^T, \quad (8)$$

where n denote the dimension of original state vector and $\boldsymbol{\theta} = [\theta_1, \theta_2, \dots, \theta_m]^T$ denote m -unknown parameter of the structure, including damping, stiffness, or nonlinear parameters. Equation (8) can be written in continuous state space as

$$\dot{\mathbf{Z}}(t) = f(\mathbf{Z}, \mathbf{F}, t) + \mathbf{w}(t), \quad (9)$$

where \mathbf{Z} , \mathbf{F} , and \mathbf{w} are the state, the external force, and the process noise vectors which are assumed to be zero-mean Gaussian noise. The observation equation at discrete time steps $t_k = k\Delta t$ can be written as

$$\mathbf{y}(t_k) = h(\mathbf{Z}(t_k)) + \mathbf{v}(t_k), \quad (10)$$

where $\mathbf{y}(t_k)$ and $\mathbf{v}(t_k)$ are the measurement response and measurement noise vectors. Both process and measurement noises are assumed to be uncorrelated zero-mean Gaussian random processes. With the EKF, (9) and (10) can be linearized as

$$\begin{aligned} f(\mathbf{Z}, \mathbf{F}, t) &\approx f(\widehat{\mathbf{Z}}_{k|k}, \mathbf{F}, t) + \mathbf{A}_{k|k}(\mathbf{Z} - \widehat{\mathbf{Z}}_{k|k}), \\ h(\mathbf{Z}_{k+1}) &\approx h(\widehat{\mathbf{Z}}_{k+1|k}) + \mathbf{H}_{k+1|k}(\mathbf{Z}_{k+1} - \widehat{\mathbf{Z}}_{k+1|k}), \end{aligned} \quad (11)$$

in which $\mathbf{A}_{k|k}$ is the linearized matrix of $f(\widehat{\mathbf{Z}}_{k|k}, \mathbf{F}, t)$ and $\mathbf{H}_{k+1|k}$ is the linearized matrix of $h(\widehat{\mathbf{Z}}_{k+1|k})$ as follows:

$$\mathbf{A}_{k|k} = \left[\frac{\partial f}{\partial \mathbf{Z}} \right]_{\widehat{\mathbf{Z}}_{k|k}}, \quad (12)$$

$$\mathbf{H}_{k+1|k} = \left[\frac{\partial h}{\partial \mathbf{Z}} \right]_{\widehat{\mathbf{Z}}_{k+1|k}}. \quad (13)$$

Equation (11) constitutes a classical system with continuous time evolution of states and discrete measurements. The hybrid EKF can estimate the states of $\mathbf{Z}((k+1)\Delta t)$ at $t = k\Delta t$ from the contaminated measurements through the following set of equations:

$$\widehat{\mathbf{Z}}_{k+1|k} = \widehat{\mathbf{Z}}_{k|k} + \int_{k\Delta t}^{(k+1)\Delta t} f(\widehat{\mathbf{Z}}_{t|k}) dt. \quad (14)$$

And the recursive optimal solution for $\mathbf{Z}((k+1)\Delta t)$ at $t = (k+1)\Delta t$ is shown as follows:

$$\widehat{\mathbf{Z}}_{k+1|k+1} = \widehat{\mathbf{Z}}_{k+1|k} + \mathbf{K}_{k+1} [\mathbf{Y}_{k+1} - h(\widehat{\mathbf{Z}}_{k+1|k})], \quad (15)$$

where \mathbf{K}_{k+1} is the Kalman gain matrix:

$$\mathbf{K}_{k+1} = \mathbf{P}_{k+1|k} \mathbf{H}_{k+1|k}^T [\mathbf{H}_{k+1|k} \mathbf{P}_{k+1|k} \mathbf{H}_{k+1|k}^T + \mathbf{R}_{k+1}]^{-1}, \quad (16)$$

where $\mathbf{P}_{k+1|k}$ is the error covariance matrix of a posteriori state vector $\widehat{\mathbf{Z}}_{k+1|k}$:

$$\mathbf{P}_{k+1|k} = \Phi_{k+1|k} \mathbf{P}_{k|k} \Phi_{k+1|k}^T + \mathbf{Q}_k, \quad (17)$$

where \mathbf{Q}_k is the covariance matrix of process noise at $t = k\Delta t$. $\Phi_{k+1|k}$ is the state transition matrix of the linearized system given by

$$\Phi_{k+1|k} \approx \mathbf{I} + \Delta t \times \mathbf{A}_{k|k}, \quad (18)$$

in which \mathbf{I} is the unit matrix of dimension $2n + m$. $\mathbf{P}_{k|k}$ in (17) is the error covariance matrix of a priori state vector $\widehat{\mathbf{Z}}_{k|k}$ given by $\Phi_{k+1|k} \approx \mathbf{I} + \Delta t \times \mathbf{A}_{k|k}$ as follows:

$$\mathbf{P}_{k|k} = [\mathbf{I} - \mathbf{K}_k \mathbf{H}_{k|k-1}] \mathbf{P}_{k|k-1} [\mathbf{I} - \mathbf{K}_k \mathbf{H}_{k|k-1}]^T + \mathbf{K}_k \mathbf{R}_k \mathbf{K}_k^T. \quad (19)$$

4. Orthogonal Decomposition of Excitation

The external force is always difficult to be directly identified with extended Kalman filter since it is nonstationary and time-variant. However, the input F is a kind of random process which can be decomposed by standard orthogonal polynomial. Since the orthogonal is constant, the input history will be reconstructed as if the orthogonal parameters can be identified. Therefore, the input identification transforms to the polynomial parameters identification based on input orthogonal decomposition method. The input in (7) can be decomposed as follows:

$$F^i(t) = \sum_{i=1}^{N_f} \sum_{m=1}^{N_m} w_m^i T_m^i(t), \quad (20)$$

where w_m^i is the polynomial coefficients of the i th input. T_m^i is the m th orthogonal polynomial of the i th input. N_m is the order of input decomposition. N_f is the number of inputs. The orthogonal polynomial T_m^i and order of input decomposition N_m can affect the accuracy of input approximation. The order of input decomposition N_m is closely related to input history length and complexity. The orthogonal polynomial T_m^i can be determined in different kinds based on different decomposition methods. The Chebyshev decomposition method is one of the most accuracy methods of random input fitting. The Chebyshev decomposition orthogonal polynomial can be written as follows:

$$\begin{aligned} T_1 &= \frac{1}{\sqrt{\pi}}, \\ T_2 &= \sqrt{\frac{2}{\pi}} \left(\frac{2t}{T} - 1 \right), \\ T_{n+1}(t) &= 2 \left(\frac{2t}{T} - 1 \right) T_n(t) - T_{n-1}(t) \\ &\quad (n = 2, 3, \dots, N_m - 1), \end{aligned} \quad (21)$$

where T is the length of the input history and N_m is the order of decomposition. Based on the Chebyshev standard orthogonal polynomial decomposition, (7) can be written as follows:

$$\mathbf{M}\ddot{\mathbf{x}}(t) + \mathbf{F}_c [\dot{\mathbf{x}}(t)] + \mathbf{F}_s [\mathbf{x}(t)] = \sum_{i=1}^{N_f} \sum_{m=1}^{N_m} w_m^i T_m^i(t). \quad (22)$$

The input can be reconstructed if the polynomial parameters w_m^i can be identified.

5. Simultaneous Identification of Structural System

A new time domain simultaneous identification method is proposed in this section based on orthogonal decomposition of excitation and extended Kalman filter. The input history is firstly decomposed by the Chebyshev standard orthogonal polynomial as shown in (20). The number of decomposition

order is based on the input length and complexity. Then, the structural parameters and polynomial parameters will be identified by extended Kalman estimator based on structural measurements, as shown from (12) to (19).

5.1. *N-Storey Linear Structure.* The equation of motion is given by

$$\mathbf{M} \begin{Bmatrix} \ddot{x}_1(t) \\ \ddot{x}_2(t) \\ \vdots \\ \ddot{x}_n(t) \end{Bmatrix} + \mathbf{C} \begin{Bmatrix} \dot{x}_1(t) \\ \dot{x}_2(t) \\ \vdots \\ \dot{x}_n(t) \end{Bmatrix} + \mathbf{K} \begin{Bmatrix} x_1(t) \\ x_2(t) \\ \vdots \\ x_n(t) \end{Bmatrix} = \mathbf{L} \left(\sum_{i=1}^{N_f} \sum_{m=1}^{N_m} w_m^i T_m^i(t) \right), \quad (23)$$

where

$$\mathbf{M} = \begin{bmatrix} m_1 & & & \\ & m_2 & & \\ & & \ddots & \\ & & & m_n \end{bmatrix}, \quad (24)$$

$$\mathbf{C} = \begin{bmatrix} c_1 + c_2 & -c_2 & & \\ -c_2 & c_2 + c_3 & & \\ & & \ddots & -c_n \\ & & & -c_n & c_n \end{bmatrix},$$

$$\mathbf{K} = \begin{bmatrix} k_1 + k_2 & -k_2 & & \\ -k_2 & k_2 + k_3 & & \\ & & \ddots & -k_n \\ & & & -k_n & k_n \end{bmatrix}.$$

Beside $\mathbf{w} = [w_1, w_2, \dots, w_i]^T$, $i = (1, 2, \dots, N_f)$, is the polynomial coefficients vector. In (23), $x_i(t)$ is the absolute structural response. T_m^i is the orthogonal polynomial which is given by (21). The state vector is defined as

$$\mathbf{Z}(t) = [x_{1 \sim n}, \dot{x}_{1 \sim n}, k_{1 \sim n}, c_{1 \sim n}, w_{1 \sim N_m}]^T. \quad (25)$$

Consider that $\dot{k}_{1 \sim n} = \dot{c}_{1 \sim n} = \dot{w}_{1 \sim N_m} = 0$. Equation (23) can be written in state space as follows:

$$\begin{bmatrix} \dot{\mathbf{x}} \\ \ddot{\mathbf{x}} \\ \dot{\mathbf{k}} \\ \dot{\mathbf{c}} \\ \dot{\mathbf{w}} \end{bmatrix} = \begin{bmatrix} \mathbf{x} \\ \mathbf{M}^{-1} \left[\mathbf{L} \sum_{i=1}^{N_f} \sum_{m=1}^{N_m} w_m^i T_m^i - (\mathbf{F}_c [\mathbf{c}, \dot{\mathbf{x}}] + \mathbf{F}_s [\mathbf{k}, \mathbf{x}]) \right] \\ \mathbf{0} \\ \mathbf{0} \\ \mathbf{0} \end{bmatrix}. \quad (26)$$

The measurement can be obtained in the discrete time step from displacements or accelerations. The observation

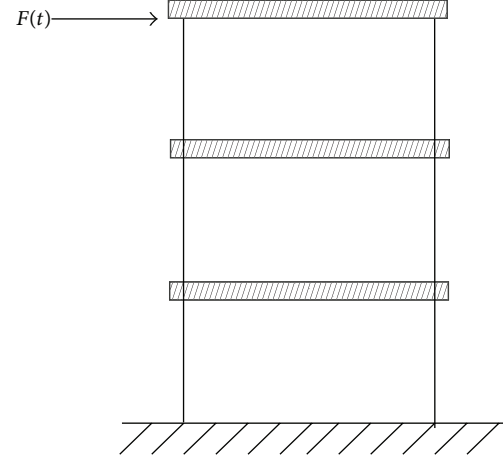


FIGURE 1: Three-storey frame.

equation can be written with the measurement of the displacement as

$$\begin{bmatrix} y_1 \\ y_2 \\ \vdots \\ y_n \end{bmatrix} = [\mathbf{I} \ \mathbf{0} \ \mathbf{0} \ \mathbf{0} \ \mathbf{0}] \begin{bmatrix} \mathbf{x} \\ \dot{\mathbf{x}} \\ \mathbf{k} \\ \mathbf{c} \\ \mathbf{w} \end{bmatrix}. \quad (27)$$

In which \mathbf{I} is the unit matrix of dimension n .

5.2. *N-Story Hysteretic Structure.* The equation of motion is given by

$$\mathbf{M} \begin{Bmatrix} \ddot{x}_1(t) \\ \ddot{x}_2(t) \\ \vdots \\ \ddot{x}_n(t) \end{Bmatrix} + \mathbf{C} \begin{Bmatrix} \dot{x}_1(t) \\ \dot{x}_2(t) \\ \vdots \\ \dot{x}_n(t) \end{Bmatrix} + \mathbf{K} \begin{Bmatrix} z_1(t) \\ z_2(t) \\ \vdots \\ z_n(t) \end{Bmatrix} = \mathbf{L} \left(\sum_{i=1}^{N_f} \sum_{m=1}^{N_m} w_m^i T_m^i(t) \right), \quad (28)$$

in which

$$\mathbf{M} = \begin{bmatrix} m_1 & & & \\ \vdots & m_2 & & \\ \vdots & \vdots & \ddots & \\ m_n & m_n & \dots & m_n \end{bmatrix}, \quad (29)$$

$$\mathbf{C} = \begin{bmatrix} c_1 & -c_2 & & \\ & c_2 & -c_3 & \\ & & \ddots & \ddots & \\ & & & c_{n-1} & -c_n \\ & & & & c_n \end{bmatrix},$$

$$\mathbf{K} = \begin{bmatrix} k_1 & -k_2 & & \\ & k_2 & -k_3 & \\ & & \ddots & \ddots & \\ & & & k_{n-1} & -k_n \\ & & & & k_n \end{bmatrix}.$$

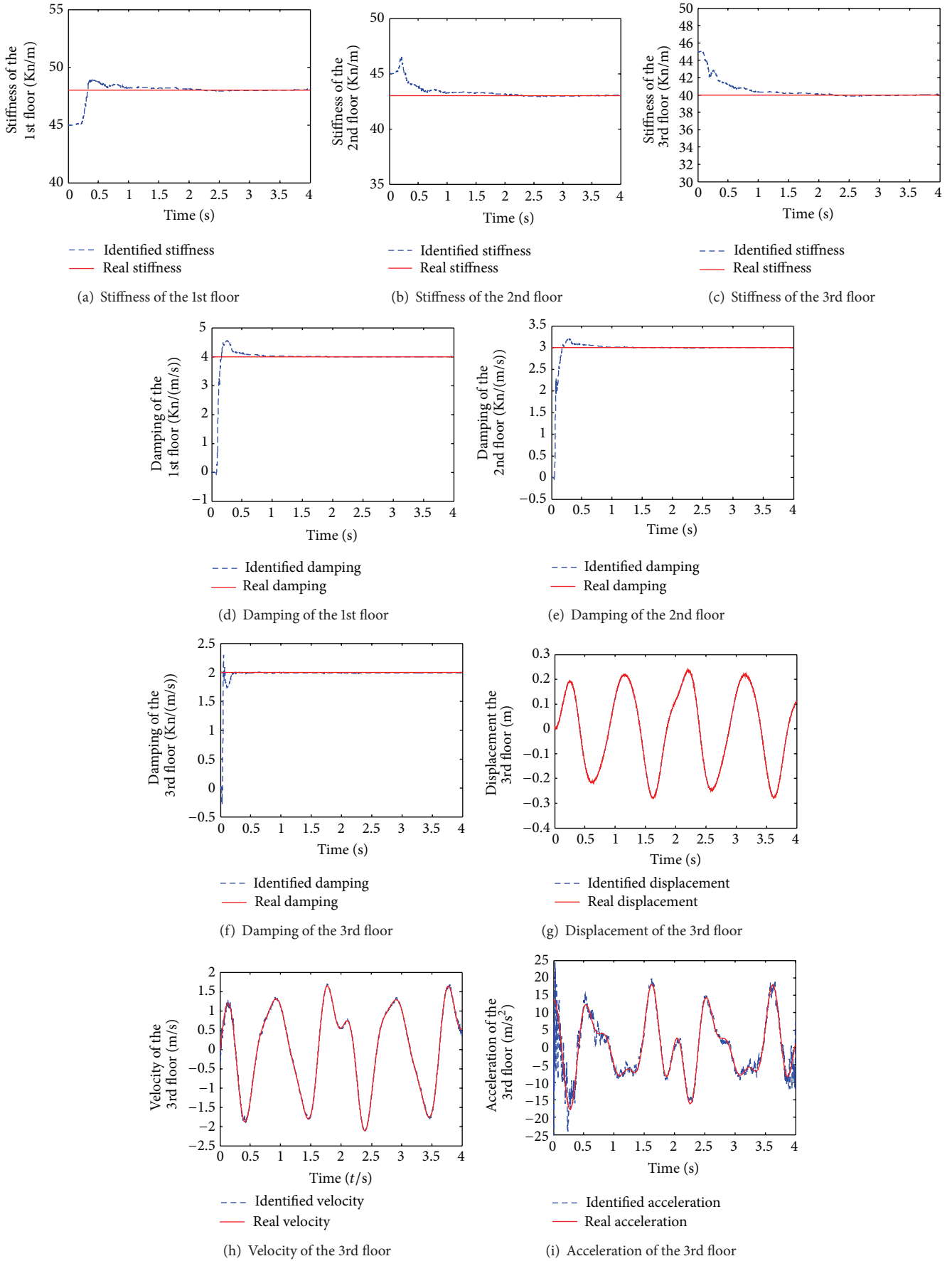


FIGURE 2: Continued.

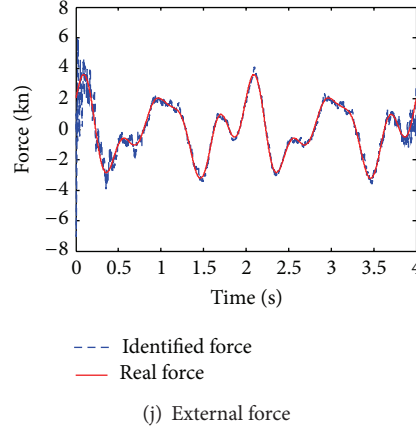


FIGURE 2: Identification results for linear structural system.

Beside $\mathbf{w} = [w_1, w_2, \dots, w_i]^T$, $i = (1, 2, \dots, N_f)$, is the polynomial parameter vector. The responses $x_i(t)$ and $z_i(t)$ in (28) are the interstorey response and hysteretic component of i th storey unit, respectively. In this paper $z_i(t)$ is defined as (5). T_m^i is the orthogonal polynomial which is given by (20). The state vector is defined as

$$\mathbf{Z}(t) = [x_{1 \sim n}, z_{1 \sim n}, \dot{x}_{1 \sim n}, k_{1 \sim n}, c_{1 \sim n}, \beta_{1 \sim n}, \gamma_{1 \sim n}, w_{1 \sim N_m}]^T. \quad (30)$$

Consider that $\dot{k}_{1 \sim n} = \dot{c}_{1 \sim n} = \dot{w}_{1 \sim N_m} = 0$. Equation (28) can be written in state space as follows:

$$\begin{bmatrix} \dot{\mathbf{x}} \\ \ddot{\mathbf{x}} \\ \dot{\mathbf{z}} \\ \dot{\mathbf{k}} \\ \dot{\mathbf{c}} \\ \dot{\boldsymbol{\beta}} \\ \dot{\boldsymbol{\gamma}} \\ \dot{\mathbf{w}} \end{bmatrix} = \begin{bmatrix} \dot{\mathbf{x}} \\ \mathbf{M}^{-1} \left[\mathbf{L} \sum_{i=1}^{N_f} \sum_{m=1}^{N_m} w_m^i T_m^i - (f_c [\mathbf{c}, \dot{\mathbf{x}}] + f_s [\mathbf{k}, \mathbf{z}]) \right] \\ \dot{\mathbf{x}}_i - \beta_i |\dot{\mathbf{x}}_i| |\mathbf{z}_i|^{\alpha_i - 1} \mathbf{z}_i - \gamma_i \dot{\mathbf{x}}_i |\mathbf{z}_i|^{\alpha_i} \\ \mathbf{0} \\ \mathbf{0} \\ \mathbf{0} \\ \mathbf{0} \\ \mathbf{0} \end{bmatrix}. \quad (31)$$

The observation equation is nonlinear in state space with the measurement of acceleration. The discrete linearized observation matrix can be calculated by (13).

6. Implementation Procedure

Step 1. Decompose structural excitation by using the Chebyshev standard orthogonal polynomial. The excitation is represented as orthogonal polynomial approximation. The accuracy of the approximation is according to the order of decomposition.

Step 2. Obtain the mass, damping, and stiffness matrices of the initial structural model, which may be inaccurate with model errors or initial structural damage.

Step 3. Conduct measurement on the structure. The “measured” data for the simulation studies is obtained from the solution of (1) or (6).

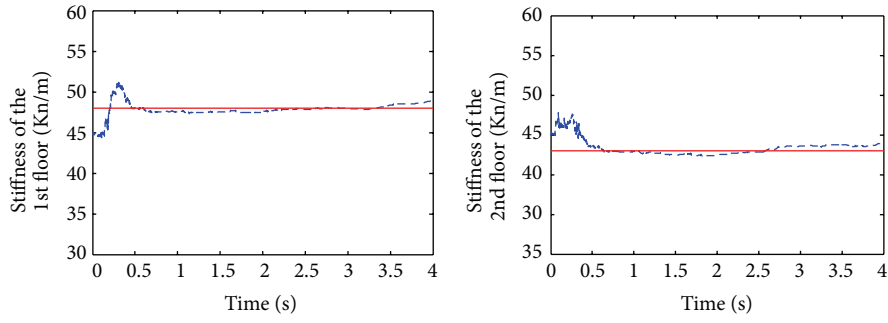
Step 4. Simultaneously identify structural parameter and polynomial parameters with the proposed EKF algorithm as shown in Section 3 from (12) to (19).

7. Numerical Simulation Studies

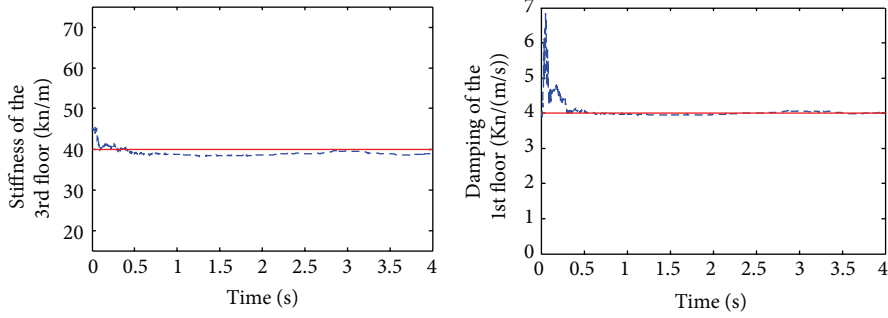
In this Section the proposed system identification method is validated numerically by the investigation of linear and nonlinear 3-storey shear frame as shown in Figure 1. The structural parameters and external force are simultaneously identified with incomplete contaminated measurement for the two cases. The sampling rate is 1000 Hz and 4-second measurements are collected for the identification.

7.1. Case 1: Three-Storey Linear Structure. A linear three-storey shear frame subject to $F(t) = \sin(4\pi t) + 2 \cos(2\pi t) + \sin(5\pi t)$ kN on the top of the floors is studied in this case. The equation of motion with excitation decomposition is shown in (25). The values of structural real parameters are $m_1 = m_2 = m_3 = 500$ kg, $c_1 = 4$ kNs/m, $c_2 = 3$ kNs/m, $c_3 = 2$ kNs/m, $k_1 = 48$ kN/m, $k_2 = 43$ kN/m, and $k_3 = 40$ kN/m. The horizontal displacements of all floors are measured. The “measured” displacements for this simulation are obtained from the solution of (1) with 5% RMS noise process.

In this simulation, the mass of each floor is taken as known constant. The excitation history is decomposed by forty-order orthogonal polynomial. The unknown parameters are k_i , c_i and w_j ($i = 1, 2, 3$ and $j = 1, 2, \dots, 40$). The extended state vector is expressed as $\mathbf{Z}(t) = [x_{1 \sim 3}, \dot{x}_{1 \sim 3}, k_{1 \sim 3}, c_{1 \sim 3}, w_{1 \sim 40}]^T$. The initial guess for k_i , c_i , and w_j are $k_i = 45$ kN/m, $c_i = 0$ kNs/m, ($i = 1, 2, 3$), and $w_j = 0$ ($j = 1, 2, \dots, 40$). The initial guess of displacement and velocity in state variables are supposed as zero. Figure 2 shows the identified structural parameters and excitations. The stiffness and damping as shown in Figures 2(a)–2(f) are accurately identified. The value of the stiffness converges

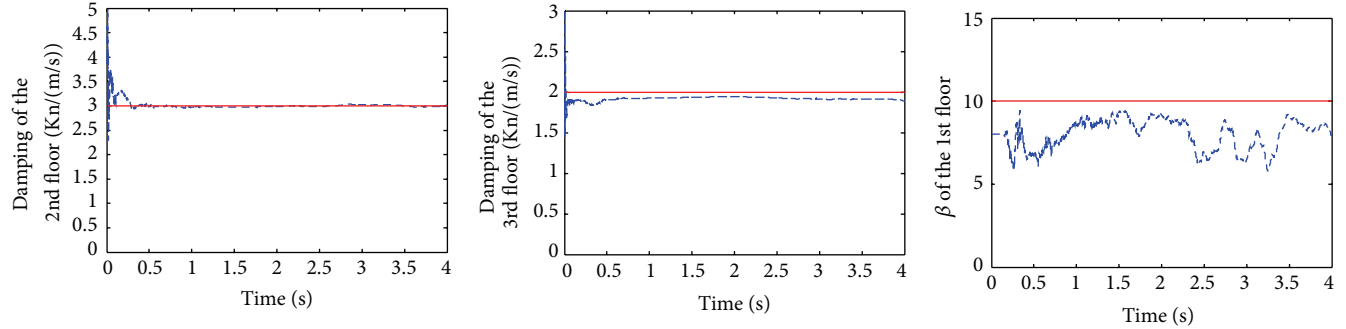


-- Identified stiffness
 — Real stiffness



-- Identified stiffness
 — Real stiffness

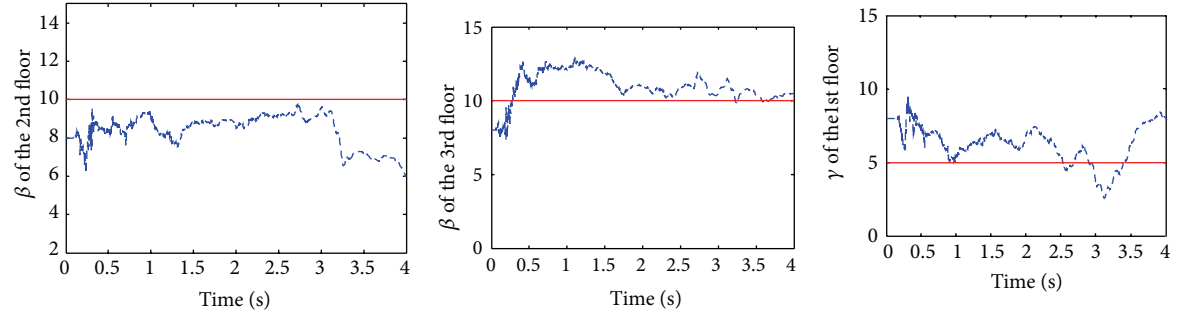
-- Identified damping
 — Real damping



-- Identified damping
 — Real damping

-- Identified damping
 — Real damping

-- Identified β
 — Real β



-- Identified β
 — Real β

-- Identified β
 — Real β

-- Identified γ
 — Real γ

FIGURE 3: Continued.

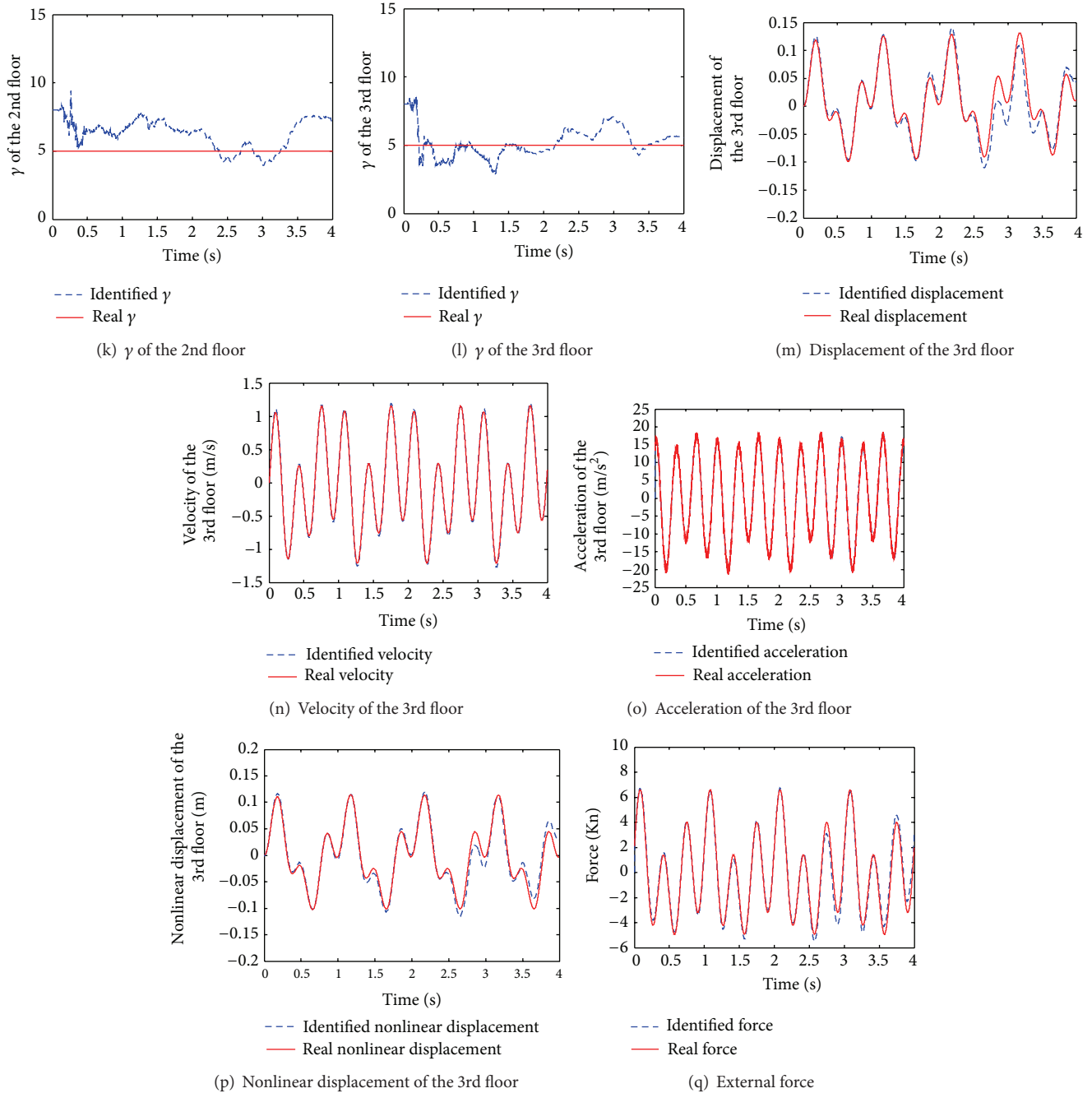


FIGURE 3: Identification results for nonlinear structural system.

to the real value in a short time even with the polluted measurement. In this study only the 3rd floor's displacement, velocity, and acceleration are listed as shown in Figures 2(g), 2(h), and 2(i). The identified and real displacement is nearly overlapping as shown in Figure 2(g). There are some fluctuations at the beginning and the end of the time history of identified velocity though the identified velocity is very close to the real velocity as shown in Figure 2(h). The identified acceleration fluctuates severely at the beginning and the end compared to the real acceleration as shown in Figure 2(i). The displacement is identified with high

accuracy, while the acceleration is identified with lower accuracy. The force can also be identified with contaminated measurement with some fluctuations at the beginning and end of the time history. It is demonstrated that the structural parameter and excitation can be fairly accurately identified with contaminated measurement.

7.2. Three-Storey Hysteretic Nonlinear Structure. A three-storey hysteretic nonlinear shear frame subject to $F(t) = 4 \sin(6\pi t) + 2 \cos(2\pi t) + \sin(4\pi t)$ kN on the top of the floors is investigated. The real values of the structure are

$m_1 = m_2 = m_3 = 500$ kg, $c_1 = 4$ kNs/m, $c_2 = 3$ kNs/m, $c_3 = 2$ kNs/m, $k_1 = 48$ kN/m, $k_2 = 43$ kN/m, $k_3 = 40$ kN/m, $\beta_1 = \beta_2 = \beta_3 = 10$, $\gamma_1 = \gamma_2 = \gamma_3 = 5$, and $n_1 = n_2 = n_3 = 2$. The mass and parameter n are also taken as known constant. The other parameters including stiffness, damping, and the parameters of Bouc-Wen model [19] are the unknowns to be identified. Only the horizontal acceleration of each floor is measured for the identification in this case study. The “measured” accelerations for this simulation are obtained from the solution of (4) with 5% RMS noise. The excitation history is also decomposed by forty-order orthogonal polynomial. The unknown parameters are k_i , c_i , and w_j , ($i = 1, 2, 3$ and $j = 1, 2, \dots, 40$), the extended state vector is $\mathbf{Z}(t) = [x_{1-3}, \dot{x}_{1-3}, z_{1-3}, k_{1-3}, c_{1-3}, \beta_{1-3}, \gamma_{1-3}, w_{1-40}]^T$, and the initial guess for k_i , c_i , w_m , β_i , and γ_i is $k_i = 45$ kN/m, $c_i = 0$ kNs/m, $w_m = 0$, and $\beta_i = \gamma_i = 8$. The initial values of state variables are zero.

Figure 3 shows the identification results for the nonlinear structural system. Though there are a large number of fluctuations at the beginning of the identified time history, the stiffness and damping are fairly accurately identified with contaminated measurement as shown in Figures 3(a)–3(f). The nonlinear parameters of Bouc-wen model are also identified with acceptable accuracy as shown from Figures 3(g) to 3(l). The fluctuation at the beginning is also a little large in the time history of the nonlinear parameters, β and γ . Similarly, in this case only the 3rd floor’s displacement, nonlinear displacement, velocity and acceleration are listed as shown in Figures 3(m)–3(p). There are some errors in the amplitude of the identified displacement and nonlinear displacement. The identified velocity is nearly overlapping with the real velocity as shown in Figure 3(n). There are severe fluctuations in the peak of identified acceleration as shown in Figure 3(o), which is consistent with the linear case study. The external force is also identified accurately as shown in Figure 3(q). It is indicated that the system identification method with EKF and excitation decomposition can conduct the nonlinear structural system identification including structural parameter and external force with contaminated measurement.

8. Conclusions

A new method in time domain was proposed in this paper for simultaneous identification of structural parameters and loads based on limited output information with extended Kalman filter and orthogonal polynomials decomposition. The structural excitation is decomposed by orthogonal approximation. Then the structural parameters and coefficients of orthogonal polynomial are simultaneously identified with EKF. Numerical simulations of linear and nonlinear structures are utilized to study the effectiveness of the proposed method. From the simulation result, the proposed system identification method can conduct the structural system identification accurately and effectively with contaminated measurement. However, the severe nonlinear parameter, such as the nonlinear parameter n of Bouc-Wen model, is taken as known in this paper. New identification method dealing with

the severe nonlinear system identification will be developed in the future research.

Conflict of Interests

The authors declare that there is no conflict of interests regarding the publication of this paper.

Acknowledgments

The work described in this paper was supported by Project number 01319406 of Natural Scientific Research Innovation Foundation in Harbin Institute of Technology, Projects numbers 51161120360, 51308160, and 91315301 of National Natural Science Foundation of China, and Project 2013M541383 of China Postdoctoral Science Foundation.

References

- [1] S. W. Doebling, C. R. Farrar, and M. B. Prime, “A summary review of vibration-based damage identification methods,” *Shock and Vibration Digest*, vol. 30, no. 2, pp. 91–105, 1998.
- [2] Y. Q. Ni, X. W. Ye, and J. M. Ko, “Monitoring-based fatigue reliability assessment of steel bridges: analytical model and application,” *Journal of Structural Engineering*, vol. 136, no. 12, pp. 1563–1573, 2010.
- [3] Y. Q. Ni, X. W. Ye, and J. M. Ko, “Modeling of stress spectrum using long-term monitoring data and finite mixture distributions,” *Journal of Engineering Mechanics*, vol. 138, no. 2, pp. 175–183, 2011.
- [4] G. W. Housner, L. A. Bergman, T. K. Caughey et al., “Structural control: past, present, and future,” *Journal of Engineering Mechanics*, vol. 123, no. 9, pp. 897–971, 1997.
- [5] Y. Zou, L. Tong, and G. P. Steven, “Vibration-based model-dependent damage (delamination) identification and health monitoring for composite structures—a review,” *Journal of Sound and Vibration*, vol. 230, no. 2, pp. 357–378, 2000.
- [6] J. Chen and J. Li, “Simultaneous identification of structural parameters and input time history from output-only measurements,” *Computational Mechanics*, vol. 33, no. 5, pp. 365–374, 2004.
- [7] Z. R. Lu and S. S. Law, “Identification of system parameters and input force from output only,” *Mechanical Systems and Signal Processing*, vol. 21, no. 5, pp. 2099–2111, 2007.
- [8] S. S. Law and D. Yong, “Substructure methods for structural condition assessment,” *Journal of Sound and Vibration*, vol. 330, no. 15, pp. 3606–3619, 2011.
- [9] Y. Ding, *Structural control and condition assessment with substructure method [Ph.D. thesis]*, The Hong Kong Polytechnic University, 2012.
- [10] H. Sun and R. Betti, “Simultaneous identification of structural parameters and dynamic input with incomplete output-only measurements,” *Structural Control and Health Monitoring*, 2013.
- [11] Y. Lei, C. Liu, and L. J. Liu, “Identification of multistory shear buildings under unknown earthquake excitation using partial output measurements: numerical and experimental studies,” *Structural Control and Health Monitoring*, 2013.
- [12] S. Haykin, A. H. H. Sayed, J. R. Zeidler, P. Yee, and P. C. Wei, “Adaptive tracking of linear time-variant systems by extended

- RLS algorithms,” *IEEE Transactions on Signal Processing*, vol. 45, no. 5, pp. 1118–1128, 1997.
- [13] J. N. Yang and S. Lin, “On-line identification of non-linear hysteretic structures using an adaptive tracking technique,” *International Journal of Non-Linear Mechanics*, vol. 39, no. 9, pp. 1481–1491, 2004.
- [14] G. Kerschen, K. Worden, A. F. Vakakis, and J.-C. Golinval, “Past, present and future of nonlinear system identification in structural dynamics,” *Mechanical Systems and Signal Processing*, vol. 20, no. 3, pp. 505–592, 2006.
- [15] G. Kerschen, M. Peeters, J. C. Golinval, and A. F. Vakakis, “Nonlinear normal modes, Part I: a useful framework for the structural dynamicist,” *Mechanical Systems and Signal Processing*, vol. 23, no. 1, pp. 170–194, 2009.
- [16] M. Peeters, R. Viguié, G. Sérandour, G. Kerschen, and J.-C. Golinval, “Nonlinear normal modes, Part II: toward a practical computation using numerical continuation techniques,” *Mechanical Systems and Signal Processing*, vol. 23, no. 1, pp. 195–216, 2009.
- [17] H.-S. Tang, S.-T. Xue, R. Chen, and T. Sato, “Online weighted LS-SVM for hysteretic structural system identification,” *Engineering Structures*, vol. 28, no. 12, pp. 1728–1735, 2006.
- [18] J. N. Yang, S. Pan, and S. Lin, “Least-squares estimation with unknown excitations for damage identification of structures,” *Journal of Engineering Mechanics*, vol. 133, no. 1, pp. 12–21, 2007.
- [19] Y. K. Wen, “Equivalent linearization for hysteretic systems under random excitations,” *Journal of Applied Mechanics, Transactions ASME*, vol. 47, no. 1, pp. 150–154, 1980.

Review Article

A State-of-the-Art Review on Fatigue Life Assessment of Steel Bridges

X. W. Ye,¹ Y. H. Su,² and J. P. Han²

¹ Department of Civil Engineering, Zhejiang University, Hangzhou 310058, China

² Key Laboratory of Disaster Prevention and Mitigation in Civil Engineering of Gansu Province, Lanzhou University of Technology, Lanzhou 730050, China

Correspondence should be addressed to X. W. Ye; cexwye@zju.edu.cn

Received 15 October 2013; Revised 23 December 2013; Accepted 29 December 2013; Published 10 February 2014

Academic Editor: Stathis C. Stiros

Copyright © 2014 X. W. Ye et al. This is an open access article distributed under the Creative Commons Attribution License, which permits unrestricted use, distribution, and reproduction in any medium, provided the original work is properly cited.

Fatigue is among the most critical forms of damage potentially occurring in steel bridges, while accurate assessment or prediction of the fatigue damage status as well as the remaining fatigue life of steel bridges is still a challenging and unsolved issue. There have been numerous investigations on the fatigue damage evaluation and life prediction of steel bridges by use of deterministic or probabilistic methods. The purpose of this review is devoted to presenting a summary on the development history and current status of fatigue condition assessment of steel bridges, containing basic aspects of fatigue, classical fatigue analysis methods, data-driven fatigue life assessment, and reliability-based fatigue condition assessment.

1. Introduction

Fatigue is a localized and progressive process in which structural damage accumulates continuously due to the repetitive application of external loadings such as vehicles for steel bridges, winds for high-rise buildings, waves for offshore platforms, and temperature for turbine engines, while these applied loadings may be well below the structural resistance capacity. This kind of process is extraordinarily dangerous because a single application of the load would not create any abnormal effects, whereas a conventional structural stress analysis might lead to a conclusion of safety that does not exist. Over a long period of time, the strength and serviceability modes of failure have been well investigated in the professional engineering communities. However, as one of the most critical forms of damage and principal failure modes for steel structures, fatigue is still less understood in terms of the cause of formation and failure mechanism. It is therefore essential to seek novel methodologies and develop advanced technologies for seizing the fatigue phenomenon and conducting reliable assessment of fatigue damage status of steel bridges which serve as vital components in the transportation infrastructure of a nation.

Two approaches are commonly employed for fatigue damage evaluation and life prediction of bridge structures. The first approach is the traditional $S-N$ curve method, in which the relationship between the constant-amplitude stress range, S , and the number of cycles to failure, N , is determined by appropriate fatigue experiments and described by an $S-N$ curve. The Palmgren-Miner linear damage hypothesis, also called Miner's rule [1], extends this approach to variable-amplitude loadings. The second method is the fracture mechanics approach which is dominantly dedicated to exploring the features and disciplines of crack initiation and growth in consideration of stress field at the crack tip. In general, the two approaches are applied sequentially, with the $S-N$ curve method being used at the bridge design stage or preliminary evaluation of fatigue life and the fracture mechanics approach for more refined crack-based remaining fatigue life assessment or effective decision-making on inspection and maintenance strategies [2].

There have been a lot of investigations and applications on fatigue damage evaluation and life prediction of bridge structures using the traditional $S-N$ method or the fracture mechanics approach. Some specifications [3–5] adopt the traditional nominal $S-N$ method to guide bridge fatigue

design or evaluation. According to these specifications, the fatigue life prediction of stochastically loaded structures is to determine the correlation between the stress spectrum and the material endurance. The material endurance is generally given in the form of $S-N$ curves for constant-amplitude loadings. The stress spectrum is generally unknown and needs to be evaluated by means of experiments or simulations. In the process of fatigue life prediction, the stress spectrum is derived by extracting the stress cycles from a measured or simulated stress time history with a suitable cycle counting method. Next, a proper fatigue damage accumulative rule is chosen and the fatigue damage caused by individual stress cycle is calculated. The total fatigue damage equals the sum of damage resulting from individual stress cycle. One of the most widely used damage accumulative rules is the Miner's rule, and a rainflow cycle counting method is generally used for extracting the stress cycles from the stress time histories [6, 7].

The nature of fatigue process and uncertainties associated with the load histories and the estimation of future loads require field inspection as a necessary tool for fatigue damage detection and prevention. The fatigue damage condition and fatigue crack growth in bridge components are then assessed with data and information collected from regular field inspection. Inspection may involve the visual examination of structural components and/or the use of a variety of nondestructive evaluation (NDE) techniques, such as dynamic testing method, radiographic inspection method, electric inspection method, sonic and ultrasonic method, acoustic emission method, and dye penetration method [8]. They are conducted typically after observing deterioration and damage such as fatigue cracking in local areas and often expensive, time-consuming, and labor intensive to execute on large-scale bridges. When visual inspections without NDE techniques are used, the effectiveness of the inspection program primarily depends on the inspector's experience and the type of damage observed in generic classes of structures inspected. In cases where NDE techniques are used, the effectiveness of the inspection process, to a great extent, depends on the reliability of the selected technique in fatigue damage detection. These tests may reveal a snapshot of the operating loads and the corresponding responses of the bridge to assess the fatigue life at fatigue-sensitive (especially at fracture-critical) details. However, some of the tests will restrict normal operation of bridges.

Recently, long-term structural health monitoring (SHM) of bridges has been one of the major interests for researchers and engineers in civil, mechanical, material, and computer science fields [9]. Design and implementation of such a system are an integration of analytical skills and instrumentation technologies with the knowledge and experience in bridge design, construction, inspection, maintenance, and management. On-line SHM system is able to provide reliable information pertaining to the integrity, durability, and reliability of bridges. The information can then be incorporated into bridge management and maintenance system (BMMS) for optimizing the maintenance actions and to improve design standards, specifications, codes, and guidelines. SHM is, in fact, an augment but not a substitute of current practice

in bridge maintenance and management, not only through the use of advanced technologies in sensing, data acquisition, computing, communication, and data and information management, but also through effective integration of these technologies into an intelligent system. An accurate estimation of the actual situation in fatigue and remaining life of the critical components is an important task of the SHM system, which can be achieved by use of the continuously measured data of dynamic strain from the long-term SHM system.

Fatigue performance of steel bridges depends on a number of factors such as material characteristics, stress history, and environment, and all these factors exhibit uncertainty and randomness during the service life of the bridge. On the other hand, when the field measurement data are used for fatigue condition assessment, the uncertainties related to the field-measured data and the inaccuracies due to data processing techniques are subsistent and hardly avoidable. In view of these facts, it is more appropriate to conduct fatigue life assessment in a probabilistic way than deterministic procedures.

2. Basic Aspects of Fatigue

As a well-known phenomenon in metallic structures, fatigue failures in service were already observed in the 19th century. The word "fatigue" was introduced in the 1840s and 1850s to describe failures occurring from repeated loads. The first noteworthy investigation on fatigue is generally dated from the engineering research work of August Wöhler, a technologist in the German railroad system in the early 1850s. Wöhler was concerned with the failure of railroad axles after various times in service at loads considerably less than the static strength of the structures and undertook the first systematic study of fatigue by performing many laboratory fatigue tests under cyclic stresses. However, in the 19th century, fatigue was thought to be a mysterious phenomenon in the material of an engineering structure because fatigue damage could not be seen and failure apparently occurred without any early warning. In the 20th century, it has been observed that repeated load applications can start a fatigue mechanism in the engineering material leading to nucleation of a microcrack, crack growth, and ultimately to complete failure of a structure.

The history of fatigue covering a time span from 1837 to 1994 was reviewed in a survey paper by Schütz [10]. Mann [11] compiled 21,075 literature sources about fatigue problems on engineering materials, components, and structures covering the period from 1838 to 1990 in four books with an index on subjects, authors, and years. A comprehensive survey of the historical development of the contributions to fatigue on metallic materials, nonmetallic materials, and composites can also be found in Suresh [12]. Cui [13] carried out a state-of-the-art review of metal fatigue with particular emphasis on the latest developments in fatigue life prediction methods.

2.1. Significance of Fatigue. Fatigue is one of the main causes involved in fatal mechanical failures of a wide range of structures and infrastructures, such as aircrafts, ships, vehicles, offshore structures, pipelines, machinery, pressure vessels,

cranes, power turbines, transmission towers, bridges, or other engineering structures of high visibility. Such devastating events occur suddenly and result in heavy losses of life and property. Even though no exact percentage is available on the mechanical failures due to fatigue, many studies have suggested that 50 to 90 percent of all mechanical failures are fatigue failures [14]. American Society of Civil Engineers (ASCE) Committee on Fatigue and Fracture Reliability stated that about 80 to 90 percent of failures in metallic structures are related to fatigue fracture [15–18].

The fact that most mechanical failures are associated with fatigue is also testified by the results of an extensive study reported in 1983 by Battelle Columbus Laboratories in conjunction with the National Bureau of Standards (currently NIST, National Institute of Standards and Technology) [19]. It is reported that 141 out of the 230 failures (nearly 61%) were associated with fatigue and three main causes of fatigue are improper maintenance, fabrication defects, and design deficiencies. The investigation also emphasized that the cost of fatigue-induced fracture could be dramatically reduced by using proper fatigue analysis methods and technologies. However, fatigue failure of metal materials, components, and structures is very recondite and not well understood, nor readily predicted, by designers and engineers due to the complex nature of the fatigue mechanism.

2.2. Mechanism of Metal Fatigue. The mechanism of the fatigue process is quite complicated and controversial which is still only partially understood. However, understanding the fatigue mechanism is a prerequisite for considering various factors which affect fatigue life and fatigue crack growth, such as the material surface quality, residual stress, and environmental influence. This knowledge is essential for the analysis of fatigue properties of an engineering structure. Generally, fatigue is understood as a crack initiation process followed by a crack growth period. Fatigue cracks caused by the repeated application of loads, which individually would be too small to cause failure, usually start from the surface of a structural component where fatigue damage initiates as microscopic shear cracks on crystallographic slip planes as intrusions and extrusions, which is the first stage called crack initiation (stage I). The crack may then propagate from the localized plastic deformation to a macroscopic size in a direction perpendicular to the applied load, which is a crack propagation process (stage II). Finally the crack becomes unstable and the component may fracture. Usually, it is difficult to make an exact description and distinction of the transition between two phases of the fatigue process since this distinction depends upon many factors, such as component size, material, and the methods used to detect cracks.

Typically, the crack initiation period accounts for most of the fatigue life of a component made of steels, particularly in the high-cycle fatigue (HCF) regime (approximately larger than 10,000 cycles). In the low-cycle fatigue (LCF) regime (approximately less than 10,000 cycles), most of the fatigue life is spent on crack propagation. Modern fatigue theories provide separate analyses for each phase of the fatigue process. Crack initiation theories are based on the assumption that fatigue cracks are initiated by the local strains and stresses

concentrating on the surface of a structural component due to geometric shapes such as holes, discontinuities, and fillet radii. Crack propagation and final failure stages are analyzed by relating crack growth to the stresses in the component using fracture mechanics.

3. Classical Fatigue Analysis Methods

Historically, two overriding considerations have promoted the development of fatigue analysis methods. The first has been the need to provide designers and engineers with methods that are practical, easily implemented, and cost effective. The second consideration has been the need to reconcile these analytical approaches with physical observations. One of the most important physical observations is that the fatigue process can generally be broken into two distinct phases: initiation life and propagation life. This paper introduces three fatigue analysis methods including stress-life ($S-N$) method, the fracture mechanics approach, and strain-life ($\epsilon-N$) method. These methods have their own region of application with some degree of overlap among them.

3.1. Fatigue Analysis Using Stress-Life Method. Stress-life method is suited for HCF and mainly used for long fatigue life prediction where stresses and strains are elastic. It does not distinguish between crack initiation and propagation but deals with a total life or the life to failure of a structural component. Stress-life method represents a relationship between the stress range and fatigue failure in the form of $S-N$ curves, attained by cycling test specimens at constant-amplitude stresses until visible cracking occurs. Such tests are repeated several times at different stress levels to establish the $S-N$ curves. Running fatigue tests is an expensive and time-consuming process and curve fitting of fatigue data is also time-consuming. Fatigue analytical models can link theoretical ideas with the observed data to provide a good prediction of future observations. Wöhler was the pioneer researcher who tried to quantify the fatigue strength in accordance with the experimental results of the metal endurance and investigated the fatigue failure in railroad axles for German Railway Industry. His work also led to the characterization of fatigue behavior as the applied stress versus the cycles to failure and to the concept of fatigue limit [20].

Basquin [21] represented the finite life region of the Wöhler curve as $\log N$ on the abscissa and $\log S$ on the ordinate. The Basquin function can be expressed mathematically by

$$NS^m = A \quad (1)$$

or

$$\log N = -m \log S + \log A, \quad (2)$$

where m and A are positive empirical material constants. Obviously, $\log A$ and m are the intercept on the $\log N$ axis and the constant slope of (2), respectively.

Considering the existence of fatigue limit, Stromeyer [22] modified (2) by introducing an extra parameter F_l as

$$\log N = -m \log (S - F_l) + \log A. \quad (3)$$

In cases where the optimum value of the parameter F_l is negative or insignificant, it should be omitted since F_l represents the fatigue limit stress.

To show the effect of stress ratio R_s or mean stress S_m on the fatigue life, Walker [23] proposed the equivalent stress S_q model which is given by

$$\log N = -m \log(S_q - F_l) + \log A, \quad (4)$$

where

$$S_q = S(1 - R_s)^C. \quad (5)$$

Consider

$$S_m = \frac{S}{2}(1 + R_s). \quad (6)$$

Substituting R_s in (5) with S_m , then

$$S_q = S \left(2 - \frac{2S_m}{S} \right)^C, \quad (7)$$

where C is a constant parameter.

The stress-life methods usually can be divided into different categories depending on the stress analysis of the structural details, mainly including nominal stress method, hot spot stress method, and effective notch stress method [24, 25].

3.1.1. Nominal Stress Method. As a common method for estimating the fatigue life of steel bridges, the nominal stress method has been widely used in most existent codes and standards [3–5]. This method is based on a global consideration focusing on the average stress in the studied cross section according to the fundamental theory of structural mechanics. It is noted that the nominal stress is calculated disregarding the local stress but involving the relative large stress of macrogeometric shape of studied component in the vicinity of welded joints. The nominal stress can be determined using linear elastic structural mechanics for simple structural components or finite element method for relatively complicated structures. Also, the nominal stress can be measured by use of strain gauges which are deployed outside the stress concentration field of the welded joints.

In each code or standard, a variety of S - N curves relevant to specific structural details and loading conditions are of great importance and necessity for fatigue life assessment of steel bridges by use of the nominal stress method. However, the nominal stress method is not suitable for the structural joint if the object detail is extraordinary complicated and incomparable to any classified joints, or the loadings are complex to make it difficult or impossible to determine the nominal stress [26]. Moreover, it has an obvious drawback in that it largely ignores the actual dimensional variations of a specific structural detail [27]. Therefore, as to some structural components of steel bridges, the fatigue life predicted by use of the nominal stress may be unreliable.

3.1.2. Hot Spot Stress Method. An alternative method for fatigue analysis of complicated welded joints is the hot spot

stress method which is more reasonable and accurate than the nominal stress method. The International Institute of Welding (IIW) provides comprehensive rules and explicit recommendations in computation of the hot spot stress involving the detailed process of experiments and modeling. Steel bridges are usually composed of lots of longitudinal and transverse plate-type structural members with welded joints at their intersections, for example, joints of main girders and floor beams, floor beams and stringers in plate girder bridges, and longitudinal ribs and transverse ribs in steel deck plates. Investigations on the fatigue behavior of welded joints as well as fundamentals of fatigue strength assessment together with design rules and applications are numerous [28–31]. The welded joints contain some form of geometrical or microstructural discontinuities, and the weld toes in welded joints are the positions with the maximum local stresses where fatigue cracks are most likely to occur. The hot spot stress is the value of the structural stress at the hot spot usually located at a weld toe, which can be calculated by multiplying the nominal stress by a stress concentration factor (SCF) commonly obtained from the finite element analysis or experimental measurements using strain gauges or experiential formulae [32].

Numerical analyses have the distinct advantage of giving the exact positions, directions, and magnitudes of high stresses and the patterns of stress distribution in the entire zone of the specific joint being considered. When using the finite element method to analyze the SCF, the structural behavior can be analyzed by a global finite element model (FEM). A part of the structure including the studied detail, that is large enough to prevent boundary interaction on stress distribution at the welded joint with adequate boundary conditions, is extracted for a more detailed analysis. This selected area should be newly modeled, in which the meshing is refined to obtain enough fine meshes at the welded connection provided with the boundary conditions from the global FEM calculation. The local stress concentration at the weld toe is heavily dependent, in physical models, on the local weld profile and, in numerical analysis, on the mesh refinement [33]. Therefore, it is necessary to find a compromise between the refinement of the meshing and the size in degrees of freedom of the numerical model.

When tests are performed and strain measurements are used to determine the SCF, an elaborate and reasonable instrumentation scheme of strain gauges is crucial [34]. The selection of hot spot locations for instrumentation with strain gauges is improved and refined based on experiences from a number of finite element analyses of the typical details such as rib-to-diaphragm, rib-to-bulkhead, rib-to-stiffener, and diaphragm-to-deck connections [35–40]. The hot spot stress is calculated by extrapolation or regression of stress distribution outside of the weld to the weld toe. For example, Puthli et al. [41] investigated strain/stress concentration factors numerically and experimentally on X, T, and K joints using square hollow steel sections and obtained parametric strain/stress concentration factor formulae using regression analyses. Fung et al. [42] studied the SCFs of double plate reinforced tubular T-joints subjected to various types of basic loadings such as axial tension, axial compression, and in-plane and

out-of-plane bending by using numerical and experimental methods. Other investigations can also be found in Iida [43], Karamanos et al. [44], Gho et al. [45], and Gao et al. [46].

The IIW recommendations for determining the structural hot spot stress are based on the principle of surface extrapolation. Niemi [47] and Niemi et al. [48] gave detailed recommendations concerning stress determination for the fatigue analysis of welded components and proposed distances of 0.4 and 1 times plate thickness T from the weld toe and also distances of 0.5 and 1 times plate thickness for coarser meshes. Yagi et al. [49] proposed a definition of hot spot stress for fatigue design of plate-type structures, and the hot spot stress should be obtained by means of the linear extrapolation of the specific two points at $1.57\sqrt[4]{T^3}$ and $4.9\sqrt[4]{T^3}$ to the weld toe. Nonlinear extrapolation instead of the linear extrapolation is occasionally applied by considering that the structural stress increase in front of the welded joint occurs with various gradients and nonlinearities [50].

Another method for determining structural hot spot stress is through thickness-at-weld-toe method. Radaj [25] demonstrated that structural hot spot stress could be evaluated either by surface extrapolation or by linearization through the plate thickness. Dong [51] proposed an alternative structural hot spot stress computation method combining the features of the surface extrapolation methods with those of the through thickness methods. Doerk et al. [52] explained and compared various procedures for evaluating structural hot spot stress at different types of welded joints. Poutiainen et al. [27] investigated the limits and accuracy of different methods for hot spot stress determination and compared them with finite element analysis results from simple 2D and precise 3D models. Xiao and Yamada [26] proposed a new method of determining structural hot spot stress in welded constructions based on the computed stress 1 mm below the surface in the direction corresponding to the expected crack path.

Analysis and assessment of the hot spot stress with respect to fatigue have had a rather long history. Pioneering investigations were made in the 1960s by several researchers to relate the fatigue strength to the local stress measured at a certain point close to the weld toe [53]. In 1970s, the development of the hot spot stress method with the definition of reference points for stress evaluation and extrapolation at certain distances away from the weld toe was reviewed by van Wingerde et al. [50], which was particularly successful for fatigue strength assessment of tubular joints. First attempts to apply the approach to welded joints at plates were seen in the early 1980s, and CEN [5] extended the hot spot stress method to plate-type structures due to the increasing demand although only limited guidance was provided [27]. Up to now, the hot spot stress method has been well accepted and recommended by several national and international codes and standards [5, 54–58].

Little research has been performed on the application of the hot spot stress method to fatigue damage evaluation of the welded plate joint of steel structures, especially for cable-supported steel bridge fatigue evaluation [59]. Miki and Tateishi [60] studied the fatigue strength and local stress

for cope hole details existing in I-section beams by fatigue tests, stress measurements, and stress analyses and proposed a simple equation for estimation of SCF based on the results of finite element analysis which was verified by experimental results and confirmed to be accurate. Savaidis and Vormwald [61] investigated numerically and experimentally the hot spot stress and fatigue life of four different welded joints from the floor structure of city buses under bending and tensional cyclic loadings. Han and Shin [62] derived a consistent and unified $S-N$ curve by using the hot spot stress method through a numerical and experimental analysis which can be applied for fatigue strength estimation and fatigue design for general welded steel structures. Chan et al. [59, 63] reported that the hot spot stress method gave a more appropriate fatigue life prediction than the nominal stress method for a steel suspension bridge.

3.1.3. Effective Notch Stress Method. In contrast to the nominal stress method and the hot spot stress method, the effective notch stress method focuses on initiation life prediction for a crack at the root of a notch. This method was proposed by Radaj et al. [53, 64] who were concerned with crack initiation and early growth phase on high-cycle regime using Neuber rule with a fictitious radius of 1 mm for plate thicknesses of 5 mm and above. Zhang and Richter [65] developed a new approach by considering the relationship between the stress intensity factor and the notch stress for numerical fatigue life prediction of spot welded structures using a fictitious radius of 0.05 mm. Sonsino et al. [66] investigated the applicability of four examples from different industrial sectors in terms of notch stress concept with the reference radius of 1 mm for thick walled and 0.05 mm for thin walled welded steel connections. Aygül et al. [67] conducted a comparative study on five selected welded joints frequently used in steel bridges to investigate the accuracy of three different stress-life methods, that is, nominal stress method, hot spot stress method, and effective notch stress method, and the results revealed that the effective notch stress method, despite its more efforts for both modeling and computation, provides an inconspicuous improvement in estimation of the fatigue strength.

3.2. Fatigue Analysis Using Fracture Mechanics Approach. The fracture mechanics approach is usually applied to predict the propagation life from an initial crack or defect. The method of linear elastic fracture mechanics (LEFM) relates the growth of an initial crack of size a to the number of fatigue cycles, N . The fatigue crack growth is generally described by Paris's rule which is expressed by Paris and Erdogan [68]

$$\frac{da}{dN} = C(\Delta K)^m, \quad (8)$$

where C and m are material-related parameters and the range of stress intensity factor ΔK can be determined by Broek [69]

$$\Delta K = SY(a) \sqrt{\pi a}, \quad (9)$$

where $Y(a)$ is a function of the crack geometry and S is the stress range.

Many investigations have been performed on bridge fatigue condition assessment using fracture mechanics approach. Fisher [70] illustrated more than twenty-five case studies on fatigue crack phenomena in steel bridges using fracture mechanics approach and other theories. Agerskov and Nielsen [71] carried out an investigation on fatigue damage accumulation of steel bridges under random loadings and determined the fatigue life of welded joints in steel highway bridges by a fracture mechanics analysis. Applying a LEFM model to predict crack growth, MacDougall et al. [72] quantified the differences in fatigue life of a short-span and a medium-span bridge under successive passages of either a steel-sprung vehicle or an air-sprung vehicle. Xiao et al. [73] pointed out that lack of penetration zones of 2-3 mm resulted in low fatigue strength of the butt welded joints with the aid of obtained experimental data of the structural components in Kinuura Bridge and theoretical predictions based on LEFM.

3.3. Fatigue Analysis Using Strain-Life Method. The strain-life method developed in the 1960s is mainly concerned with the crack initiation stage. It is used when the strain is no longer totally elastic but has a plastic component. Short fatigue lives in LCF regime generally occur under these conditions. There have been some investigations on fatigue performance assessment of steel bridges through low-cycle fatigue tests and theoretical strain-life method [74, 75]. Jesus et al. [76] presented crack propagation fatigue data from five Portuguese ancient metallic riveted bridges, and the strain-life fatigue data were correlated using both deterministic and probabilistic models. Up to now, only very limited amount of research has been conducted on fatigue life assessment of steel bridges based on the strain-life method, and the lack of such investigations is mainly because most of the fatigue issues in steel bridges pertain to HCF regime.

3.4. Fatigue Analysis Using Field Measurement Data. When the stress-life method is adopted for bridge fatigue damage evaluation and life prediction, the engineer must have the most realistic and precise load and resistance information to make an accurate fatigue assessment, particularly when the live load stresses are used in cubic equations [77]. In this type of analysis, a small variation in live load stress range will induce drastically different fatigue assessment results. Analysis using computational models of load and structure cannot attempt to mimic the variation in stress range that a typical structural element will experience. Additionally, it would be extremely time-consuming and almost impossible to attempt to account for all of the variables in a conventional simulation analysis. The only way to obtain precise information that accounts for these variables is through the field measurement, where sensors are attached to the bridge elements and the actual stresses and distribution of stresses that the structural element experiences can be measured and recorded. Consequently, it is considered that the field-measured data would provide the simplest and most accurate basis for fatigue assessment. This section provides a comprehensive overview of fatigue analysis of bridge structures based on field-measured data from load-controlled diagnostic load testing and short-term in-service monitoring using NDE

techniques and long-term monitoring strategy dominated by SHM technologies.

3.4.1. NDE-Based Fatigue Life Assessment. As the traffic volume and truck weight continue to increase and as bridge conditions continue to deteriorate, a lot of existing steel bridges need to be strengthened, repaired, or reconstructed to insure an acceptable level of safety considering present and future traffic conditions [78]. Furthermore, because of lack of funds and the high cost of reconstruction, NDE technology has been developed to improve the accuracy of bridge condition evaluation [79, 80]. Among the methods, diagnostic load testing with controlled loadings and short-term in-service monitoring under normal traffic loadings currently are mainly used and the fatigue condition of bridges is then assessed with the obtained data and information from the deployed sensors and data acquisition systems.

The load-controlled diagnostic load testing has the advantages of using known loadings, which allows relatively accurate quantification of the bridge response and the determination of a fairly comprehensive baseline model for a bridge. The limitation to this type of testing, as opposed to in-service monitoring, is that one must use some level of traffic control during testing. The time used for setup is longer, and the response represents only a snapshot in time. The short-term in-service monitoring, on the other hand, has the advantages of not requiring traffic control during monitoring, having a very rapid setup time, and recording the response due to ambient traffic, thereby providing statistical information about actual responses and allowing the response to be tracked over time. The limitation of in-service monitoring is that the weight and the classification of the truck loadings are not specifically known, and the limited data will not allow bridge parameters to be evaluated explicitly [81].

Some investigations on bridge fatigue analysis by use of NDE techniques have been made in recent years. For example, Hahin et al. [82] presented the application of field strain data to condition assessment and prediction of the fatigue life of fifteen highway bridges located in Illinois, and the results were further used to study the significance of truck weight increase and traffic volume growth on the fatigue life of the bridges. DeWolf et al. [83] evaluated the fatigue life for a variety of bridges using field monitoring data by a portable computer-based strain gauge data acquisition system which has been extensively used in Connecticut to assist the Department of Transportation in evaluation and renewal of the state's bridge infrastructure and identified cost-effective maintenance, repair, and replacement strategies [84]. Peil [85] studied the precision on life cycle prediction of steel bridges under live loadings using strain monitoring at the real critical points. Distortion-induced fatigue problems in steel bridges have been investigated by use of the field measurement [40, 86].

Chajes and Mertz [87] discussed the diagnostic load tests performed at various stages throughout the process on determining the circumstances leading up to the fatigue crack and its cause and presented the temporary and permanent repair strategies. Zhou [88] proved that the fatigue evaluation based on field-measured stress range histograms under actual traffic

loads was a more accurate and efficient method for existing bridges and applied this approach in assessing the remaining fatigue life of aged riveted steel bridges. Ermopoulos and Spyarakos [89] identified the structural components in need of strengthening or replacement for a 19th century railway bridge through static and dynamic field measurements as well as laboratory tests and proposed the strengthening schemes and predicted the remaining fatigue life of the bridge in its present condition and after the suggested strengthening. Investigations into fatigue evaluation of steel bridges by use of NDE techniques were also reported by Moses et al. [90], Roeder et al. [91], Abdou et al. [92], Spyarakos et al. [93], Alampalli and Lund [94], and Malm and Andersson [95].

3.4.2. SHM-Based Fatigue Life Assessment. To secure structural and operational safety throughout the bridge life-cycles and issue early warnings on any deterioration or damage of bridges prior to costly repair or even catastrophic collapse, the significance of implementing long-term SHM systems for bridges has been increasingly recognized in USA [96–98], Europe [99–104], Japan [105, 106], Korea [107, 108], Hong Kong [109, 110], Chinese mainland [111–116], and Canada [117–119], among others. A review of the literature indicates that there is a growing trend in incorporation of computer- and sensor-based long-term health monitoring systems into bridges especially for long-span bridges due to their large investments, their significant roles in economics, and innovative techniques used to design and construct such bridges.

An important function of SHM systems is to monitor structural health and performance, as well as accurately estimating the actual status in fatigue and remaining life of the bridge [120]. It has become an important issue of high research interest with the development of SHM systems for large complicated structures. However, little work on fatigue analysis and condition assessment of bridge structures based on long-term monitoring data has been made in the past decade because SHM is a relatively new technology for applications in civil engineering communities, and even a comprehensive definition of SHM and the system design guidelines have yet to be standardized; another important reason is that such a complicated system has not been extensively installed in most of the bridges worldwide due to high cost.

However, investigations on fatigue condition assessment based on long-term monitoring data still can be found. Li et al. [121] developed a methodology and strategy for fatigue damage analysis and life prediction, and fatigue condition assessment of bridge-deck sections of the Tsing Ma Bridge was carried out taking full advantage of the on-line SHM data. Connor et al. [122] developed and implemented an in-depth instrumentation, testing, and monitoring program on the Bronx-Whitestone Bridge as part of a comprehensive fatigue evaluation for the replacement orthotropic bridge deck. Xu et al. [123] developed a systematic framework for assessing long-term buffeting-induced fatigue damage to a long suspension bridge by integrating a few important wind and structural components with continuum damage mechanics-based fatigue damage assessment method. Ye et al. [124] presented a study on fatigue life assessment of the Tsing Ma Bridge using the standard daily stress spectrum method.

4. Reliability-Based Fatigue Condition Assessment

In October 1945, a paper entitled “The Safety of Structures” appeared in the Proceedings of the ASCE. This historical paper was written by Freudenthal, and its purpose was to analyze the safety factor in engineering structures in order to establish a rational method of evaluating its magnitude. It was selected for inclusion with many discussions in the 1947 Transactions of the ASCE [125]. The publication of this paper marked the beginning of structural reliability studies in the United States [15]. Over the past several decades, the concepts and methods of structural reliability have developed rapidly and become more widely understood and accepted. There have been a lot of studies and applications [126–132] and comprehensive books [133–139] on reliability-based structure analysis.

Fatigue reliability evaluation is a very important task for the design and management of bridges. For highway and railway bridges, the techniques of fatigue reliability have been applied mainly in Mohammadi and Polepeddi [140] and Lukić and Cremona [141]: (i) condition assessment and estimation of the remaining lifetime of bridges, where probabilistic methods can be used to obtain estimates of the adequacy of the existing structure, need for increased inspection in the future to prevent failure, and approximate remaining fatigue lifetime based on projections of the future loads, and (ii) development of probability-based design stress ranges for fatigue-critical bridge components, where accurate traffic load data can be acquired through weigh-in-motion (WIM) systems, from which an extensive amount of data are available showing distribution of loads by its time of appearance, transversal position, speed, number of axles, gross weight of axles, and distance between axles.

Most of the research work on reliability-based fatigue analysis has focused on steel bridges. A comprehensive literature review on the existing fatigue reliability approaches for reassessment of steel structures, including railway and highway bridges, is available in Byers et al. [142, 143]. The general approach for analyzing reliability against fatigue failure is first to formulate a mathematical model, whether on the basis of mechanics or extensive observations of the phenomenon, which incorporates as many of the variables as practical that are known to affect fatigue behavior. The probabilistic and statistical analysis method then is performed within this provided analytical framework.

4.1. Fatigue Reliability Assessment Using Stress-Life Method.

Fatigue load and resistance are two main variables when the stress-life method is chosen for developing fatigue reliability analytical models. The fatigue load model should be determined not only by magnitude but also by frequency of occurrence which can be obtained by WIM measurements [144, 145], and resistance model should be derived from a lot of fatigue tests under varying amplitude loading [146]. Usually, the log-normal distribution and the Weibull distribution are used for load and strength probability distribution [147–151]. Murty et al. [152] proposed a method to deal with the derivation of the fatigue strength distribution as a function

of number of cycles to failure. Zhao et al. [153] developed an approach to determine an appropriate distribution from four possible assumed distributions of the fatigue life under limited data. Lorén [154] presented a model for calculating the fatigue limit distribution based on the inclusion size.

Research efforts have been devoted by a number of investigators for modeling the stress range data by using various single theoretical probability distributions. Beta distribution has been suggested as a theoretical stress range distribution model to describe the field data by Ang and Munse [155] and Walker [156]. Based on 106 recorded stress range histograms, Yamada and Albrecht [157] presented that the probability distribution of dimensionless stress range normalized by the maximum stress range could be expressed by a polynomial distribution. In order to select a single nondimensional mathematical expression that can be used to represent the stress histogram of highway bridges, a continuous two-parameter Rayleigh curve was used to model the probability distribution of stress range in the fatigue test program [158]. Wirsching [159] assumed that the long-term stress range data were Weibull distributed and Madsen [160] took the nominal stress range as a random variable with normal distribution. Park et al. [161] successfully expressed the stress range frequency distribution of 400 block loadings by a log-normal probability distribution. Ni et al. [162] proposed a method for modeling of the stress spectrum using finite mixture distributions and long-term monitoring data of dynamic strain.

There have been a number of studies on the reliability analysis for fatigue damage and life prediction of bridges [163–171]. Imam et al. [172] presented a probabilistic fatigue assessment methodology for riveted railway bridges and applied this method to a typical, short-span, riveted UK railway bridge under historical and present-day train loading. Kwon and Frangopol [173] performed fatigue reliability assessment of steel bridges using the probability density function of the equivalent stress range obtained by monitoring data. Ni et al. [174] developed a fatigue reliability model for fatigue life and reliability evaluation of steel bridges with long-term monitoring data, which integrates the probability distribution of hot spot stress range with a continuous probabilistic formulation of Miner's damage cumulative rule. Research efforts on probabilistic fatigue life estimation of steel bridges by use of a bilinear $S-N$ approach can be found in Kwon et al. [175] and Soliman et al. [176].

4.2. Fatigue Reliability Assessment Using Fracture Mechanics Approach. A significant number of investigations on fatigue reliability assessment of bridges have been conducted by use of the fracture mechanics approach [161, 163, 177]. Based on field-measured data from nondestructive inspections, Zhao and Haldar [78] proposed a LEFM-based reliability model considering uncertainties in different aspects including initial crack size, crack aspects ratio, material properties, and number of stress cycles. Lukić and Cremona [141] presented a probabilistic assessment procedure of steel components damaged by fatigue using a fracture mechanics-based crack growth model, which was applied to a transverse-stiffer-to-bottom-flange welded joint of a typical steel bridge. Righiniotis and Chryssanthopoulos [178] conducted an

investigation on the application of probabilistic fracture mechanics approach to predict the fatigue life of welded joints with initiation cracks through a bilinear crack growth law. Pipinato et al. [179] applied a LEFM approach in a probabilistic content to evaluate the fatigue reliability of steel bridges in the presence of seismic loading. Wang et al. [180] presented a procedure for assessing and updating the fatigue reliability of existing steel bridge components using nondestructive inspection techniques and Bayes theorem based on the probabilistic fracture mechanics method. Guo and Chen [181] performed an investigation on fatigue reliability assessment of welded details of a 40-year-old steel box-girder bridge integrating the LEFM approach and field data obtained from the long-term stress monitoring.

5. Conclusions

This paper provides a summary of research developments in the area of fatigue life assessment of steel bridges. Based on the overall review of fatigue-relevant theories, methods, technologies, and applications, the following conclusions are made: (i) the nominal stress-life method is widely used for fatigue-related design and evaluation of steel bridges; however, the estimated fatigue life by use of the hot spot stress method has been proved to be more accurate and effective; (ii) field measurement data will provide the most accurate information for derivation of the key physical parameters and their statistical properties in fatigue condition assessment, and therefore it is crucial and desirable to develop data-driven methods for fatigue life assessment of steel bridges; and (iii) in recognition of the uncertainties and randomness inherent in the nature of fatigue phenomenon and measurement data, investigations for probabilistic fatigue life assessment of steel bridges are deemed to be reasonable. By so doing, reliable fatigue condition assessment can be achieved for instrumented steel bridges and rational strategies on bridge inspection and maintenance can be executed in accordance with the correlativity between reliability indices and predefined inspection and/or maintenance actions.

Conflict of Interests

The authors declare that there is no conflict of interests regarding the publication of this paper.

Acknowledgments

The work described in this paper was supported by the National Science Foundation of China under Grant nos. 51308493 and U1234204, the Research Fund for the Doctoral Program of Higher Education of China under Grant no. 20130101120080, the Fundamental Research Funds for the Central Universities of China under Grant no. 2013QNA4023, and the Department of Education of Zhejiang Province, China, under Grant no. Y201328906.

References

- [1] M. A. Miner, "Cumulative damage in fatigue," *Journal of Applied Mechanics*, vol. 12, no. 3, pp. 159–164, 1945.

- [2] M. K. Chryssanthopoulos and T. D. Righiniotis, "Fatigue reliability of welded steel structures," *Journal of Constructional Steel Research*, vol. 62, no. 11, pp. 1199–1209, 2006.
- [3] BSI, *BS 5400: Steel, Concrete and Composite Bridges—Part 10: Code of Practice for Fatigue*, British Standards Institution, London, UK, 1980.
- [4] AASHTO, *Guide Specifications for Fatigue Evaluation of Existing Steel Bridges*, American Association of State Highway and Transportation Officials, Washington, DC, USA, 1990.
- [5] CEN, *Eurocode 3: Design of Steel Structures, Part 1-9: Fatigue*, European Committee for Standardization, Brussels, Belgium, 1992.
- [6] M. Matsuishi and T. Endo, "Fatigue of metals subjected to varying stress," *Japan Society of Mechanical Engineers*, pp. 37–40, 1968.
- [7] S. D. Downing and D. F. Socie, "Simple rainflow counting algorithms," *International Journal of Fatigue*, vol. 4, no. 1, pp. 31–40, 1982.
- [8] J. D. Achenbach, "Quantitative nondestructive evaluation," *International Journal of Solids and Structures*, vol. 37, no. 1-2, pp. 13–27, 2000.
- [9] D. Balageas, C. P. Fritzen, and A. Guemes, *Structural Health Monitoring*, Wiley-ISTE, London, UK, 2006.
- [10] W. Schütz, "A history of fatigue," *Engineering Fracture Mechanics*, vol. 54, no. 2, pp. 263–300, 1996.
- [11] J. Y. Mann, *Bibliography on the Fatigue of Materials, Components and Structures*, vol. 1–4, Pergamon Press, Oxford, UK, 1990.
- [12] S. Suresh, *Fatigue of Materials*, Cambridge University Press, New York, NY, USA, 1998.
- [13] W. Cui, "A state-of-the-art review on fatigue life prediction methods for metal structures," *Journal of Marine Science and Technology*, vol. 7, no. 1, pp. 43–56, 2002.
- [14] R. I. Stephens, A. Fatemi, R. R. Stephens, and H. O. Fuchs, *Metal Fatigue in Engineering*, John Wiley & Sons, New York, NY, USA, 2001.
- [15] ASCE Committee on Fatigue and Fracture Reliability, "Fatigue reliability: introduction," *ASCE Journal of the Structural Division*, vol. 108, no. 1, pp. 3–23, 1982.
- [16] ASCE Committee on Fatigue and Fracture Reliability, "Fatigue reliability: quality assurance and maintainability," *ASCE Journal of the Structural Division*, vol. 108, no. 1, pp. 25–46, 1982.
- [17] ASCE Committee on Fatigue and Fracture Reliability, "Fatigue reliability: variable amplitude loading," *ASCE Journal of the Structural Division*, vol. 108, no. 1, pp. 47–69, 1982.
- [18] ASCE Committee on Fatigue and Fracture Reliability, "Fatigue reliability: development of criteria for design," *ASCE Journal of the Structural Division*, vol. 108, no. 1, pp. 71–88, 1982.
- [19] R. P. Reed, J. H. Smith, and B. W. Christ, *The Economic Effects of Fracture in the United States*, vol. 647-1 of *National Bureau of Standards Special Publication*, U.S. Department of Commerce, Gaithersburg, Md, USA, 1983.
- [20] K. S. Al-Rubaia, "A general model for stress-life fatigue prediction," *Materialwissenschaft und Werkstofftechnik*, vol. 39, no. 6, pp. 400–406, 2008.
- [21] O. H. Basquin, "The exponential law of endurance tests," in *Proceedings of American Society for Testing and Materials*, vol. 10, pp. 625–630, West Conshohocken, Pa, USA, 1910.
- [22] C. E. Stromeyer, "The determination of fatigue limits under alternating stress conditions," *Proceedings of the Royal Society of London A*, vol. 90, no. 620, pp. 411–425, 1914.
- [23] E. K. Walker, "The effect of stress ratio during crack propagation and fatigue for 2024-T3 and 7075-T6 aluminum," in *Effects of Environment and Complex Load History on Fatigue Life*, vol. 462 of *ASTM Special Technical Publication*, pp. 1–14, American Society for Testing and Materials, Philadelphia, Pa, USA, 1970.
- [24] W. Fricke, "Fatigue analysis of welded joints: state of development," *Marine Structures*, vol. 16, no. 3, pp. 185–200, 2003.
- [25] D. Radaj, "Review of fatigue strength assessment of nonwelded and welded structures based on local parameters," *International Journal of Fatigue*, vol. 18, no. 3, pp. 153–170, 1996.
- [26] Z.-G. Xiao and K. Yamada, "A method of determining geometric stress for fatigue strength evaluation of steel welded joints," *International Journal of Fatigue*, vol. 26, no. 12, pp. 1277–1293, 2004.
- [27] I. Poutiainen, P. Tanskanen, and G. Marquis, "Finite element methods for structural hot spot stress determination—a comparison of procedures," *International Journal of Fatigue*, vol. 26, no. 11, pp. 1147–1157, 2004.
- [28] T. R. Gurney, *Fatigue of Welded Structures*, Cambridge University Press, Cambridge, UK, 2nd edition, 1979.
- [29] D. R. V. van Delft, "Two dimensional analyses of stress at the vicinity of weld toes of tubular structures," Stevin Report 6-81-8, Stevin Laboratory, Delft University of Technology, Delft, The Netherlands, 1981.
- [30] S. J. Maddox, *Fatigue Strength of Welded Structures*, Abington, Cambridge, UK, 1991.
- [31] A. Hobbacher, "Fatigue design of welded joints and components," IIW Document XIII-1539-96/XV-845-96, Abington, Cambridge, UK, 1996.
- [32] W. D. Pilkey, *Peterson's Stress Concentration Factors*, John Wiley & Sons, New York, NY, USA, 3rd edition, 2008.
- [33] M. R. Morgan and M. M. K. Lee, "New parametric equations for stress concentration factors in tubular K-joints under balanced axial loading," *International Journal of Fatigue*, vol. 19, no. 4, pp. 309–317, 1997.
- [34] X. W. Ye, Y. Q. Ni, and J. M. Ko, "Experimental evaluation of stress concentration factor of welded steel bridge T-joints," *Journal of Constructional Steel Research*, vol. 70, pp. 78–85, 2012.
- [35] M. R. Kaczinski, F. E. Stokes, P. Lugger, and J. W. Fisher, "Williamsburg Bridge, orthotropic deck fatigue tests," ATLSS Report No. 97-04, Department of Civil and Environmental Engineering, Lehigh University, Bethlehem, Pa, USA, 1997.
- [36] A. S. G. Barth and M. D. Bowman, "Fatigue behavior of welded diaphragm-to-beam connections," *ASCE Journal of Structural Engineering*, vol. 127, no. 10, pp. 1145–1152, 2001.
- [37] P. A. Tsakopoulos and J. W. Fisher, "Fatigue resistance investigation for the orthotropic deck on the Bronx-Whitestone Bridge," ATLSS Report No. 02–05, Department of Civil and Environmental Engineering, Lehigh University, Bethlehem, Pa, USA, 2002.
- [38] R. J. Connor, "Influence of cutout geometry on stresses at welded rib-to-diaphragm connections in steel orthotropic bridge decks," *Transportation Research Record*, vol. 1892, pp. 78–87, 2004.
- [39] M. Al-Emrani, "Fatigue performance of stringer-to-floor-beam connections in riveted railway bridges," *ASCE Journal of Bridge Engineering*, vol. 10, no. 2, pp. 179–185, 2005.
- [40] R. J. Connor and J. W. Fisher, "Identifying effective and ineffective retrofits for distortion fatigue cracking in steel bridges using field instrumentation," *ASCE Journal of Bridge Engineering*, vol. 11, no. 6, pp. 745–752, 2006.

- [41] R. S. Puthli, J. Wardenier, C. H. M. de Koning, A. M. van Wingerde, and F. J. van Dooren, "Numerical and experimental determination of strain (stress) concentration factors of welded joints between square hollow sections," *Heron*, vol. 33, no. 2, pp. 1–50, 1988.
- [42] T. C. Fung, C. K. Soh, T. K. Chan, and E. Erni, "Stress concentration factors of doubler plate reinforced tubular T joints," *ASCE Journal of Structural Engineering*, vol. 128, no. 11, pp. 1399–1412, 2002.
- [43] K. Iida, "Application of the hot spot strain concept to fatigue life prediction," *Welding in the World*, vol. 22, no. 9–10, pp. 222–247, 1984.
- [44] S. A. Karamanos, A. Romeijn, and J. Wardenier, "Stress concentrations in tubular DT-joints for fatigue design," *ASCE Journal of Structural Engineering*, vol. 126, no. 11, pp. 1320–1330, 2000.
- [45] W. M. Gho, T. C. Fung, and C. K. Soh, "Stress and strain concentration factors of completely overlapped tubular K(N) joints," *ASCE Journal of Structural Engineering*, vol. 129, no. 1, pp. 21–29, 2003.
- [46] F. Gao, Y. B. Shao, and W. M. Gho, "Stress and strain concentration factors of completely overlapped tubular joints under lap brace IPB load," *Journal of Constructional Steel Research*, vol. 63, no. 3, pp. 305–316, 2007.
- [47] E. Niemi, *Stress Determination for Fatigue Analysis of Welded Components: IIS/IIW-1221-93*, Abington, Cambridge, UK, 1995.
- [48] E. Niemi, W. Fricke, and S. J. Maddox, "Structural hot-spot stress approach to fatigue analysis of welded components," IIW Document, XIII-1819-00/XV-1090-01/ XIII-WG3-06-99, International Institute of Welding, Villeurbanne, France, 2003.
- [49] J. Yagi, S. Machida, Y. Tomita, M. Matoba, and T. Kawasaki, "Definition of hot spot stress in welded plate type structure for fatigue assessment," IIW Document XIII-1414-91, International Institute of Welding, Villeurbanne, France, 1991.
- [50] A. M. van Wingerde, J. A. Packer, and J. Wardenier, "Criteria for the fatigue assessment of hollow structural section connections," *Journal of Constructional Steel Research*, vol. 35, no. 1, pp. 71–115, 1995.
- [51] P. Dong, "A structural stress definition and numerical implementation for fatigue analysis of welded joints," *International Journal of Fatigue*, vol. 23, no. 10, pp. 865–876, 2001.
- [52] O. Doerk, W. Fricke, and C. Weissenborn, "Comparison of different calculation methods for structural stresses at welded joints," *International Journal of Fatigue*, vol. 25, no. 5, pp. 359–369, 2003.
- [53] D. Radaj, C. M. Sonsino, and W. Fricke, *Fatigue Assessment of Welded Joints by Local Approaches*, Abington, Cambridge, UK, 2nd edition, 2006.
- [54] ECCS, *Recommendations for the Fatigue Design of Steel Structures*, European Convention for Constructional Steelwork, Brussels, Belgium, 1985.
- [55] API, "Recommended practice for planning, designing, and constructing fixed offshore platforms," API RP2A-LRFD, American Petroleum Institute, Washington, DC, USA, 1993.
- [56] BSI, *BS 7608: Code of Practice for Fatigue Design and Assessment of Steel Structures*, British Standards Institution, London, UK, 1993.
- [57] AWS, *Structural Welding Code: Steel: ANSI/AWS D1.1 98*, American Welding Society, Miami, Fla, USA, 1998.
- [58] IIW, "Fatigue design procedures for welded hollow section joints," IIW Document XIII-1804-99/XV-1035-99, Recommendations for IIW Subcommission XV-E, Abington, Cambridge, UK, 2000.
- [59] T. H. T. Chan, T. Q. Zhou, Z. X. Li, and L. Guo, "Hot spot stress approach for Tsing Ma Bridge fatigue evaluation under traffic using finite element method," *Structural Engineering and Mechanics*, vol. 19, no. 3, pp. 261–279, 2005.
- [60] C. Miki and K. Tateishi, "Fatigue strength of cope hole details in steel bridges," *International Journal of Fatigue*, vol. 19, no. 6, pp. 445–455, 1997.
- [61] G. Savaidis and M. Vormwald, "Hot-spot stress evaluation of fatigue in welded structural connections supported by finite element analysis," *International Journal of Fatigue*, vol. 22, no. 2, pp. 85–91, 2000.
- [62] S. Han and B. Shin, "Use of hot spot stress for estimating the fatigue strength of welded components," *Steel Research*, vol. 71, no. 11, pp. 466–473, 2000.
- [63] T. H. T. Chan, L. Guo, and Z. X. Li, "Finite element modelling for fatigue stress analysis of large suspension bridges," *Journal of Sound and Vibration*, vol. 261, no. 3, pp. 443–464, 2003.
- [64] D. Radaj, *Design and Analysis of Fatigue Resistant Welded Structures*, Abington, Cambridge, UK, 1990.
- [65] G. Zhang and B. Richter, "New approach to the numerical fatigue-life prediction of spot-welded structures," *Fatigue & Fracture of Engineering Materials & Structures*, vol. 23, no. 6, pp. 499–508, 2000.
- [66] C. M. Sonsino, W. Fricke, F. De Bruyne, A. Hoppe, A. Ahmadi, and G. Zhang, "Notch stress concepts for the fatigue assessment of welded joints—background and applications," *International Journal of Fatigue*, vol. 34, no. 1, pp. 2–16, 2012.
- [67] M. Aygül, M. Bokesj, M. Heshmati, and M. Mohammad, "A comparative study of different fatigue failure assessments of welded bridge details," *International Journal of Fatigue*, vol. 49, pp. 62–72, 2013.
- [68] P. C. Paris and F. Erdogan, "A critical analysis of crack propagation laws," *Journal of Basic Engineering*, vol. 85, no. 4, pp. 528–534, 1963.
- [69] D. Broek, *Elementary Engineering Fracture Mechanics*, Martinus Nijhoff, Dordrecht, The Netherlands, 4th edition, 1986.
- [70] J. W. Fisher, *Fatigue and Fracture in Steel Bridges: Case Studies*, John Wiley & Sons, New York, NY, USA, 1984.
- [71] H. Agerskov and J. A. Nielsen, "Fatigue in steel highway bridges under random loading," *ASCE Journal of Structural Engineering*, vol. 125, no. 2, pp. 152–162, 1999.
- [72] C. MacDougall, M. F. Green, and S. Shillinglaw, "Fatigue damage of steel bridges due to dynamic vehicle loads," *ASCE Journal of Bridge Engineering*, vol. 11, no. 3, pp. 320–328, 2006.
- [73] Z.-G. Xiao, K. Yamada, J. Inoue, and K. Yamaguchi, "Fatigue cracks in longitudinal ribs of steel orthotropic deck," *International Journal of Fatigue*, vol. 28, no. 4, pp. 409–416, 2006.
- [74] M. Sakano and M. A. Wahab, "Extremely low cycle (ELC) fatigue cracking behaviour in steel bridge rigid frame piers," *Journal of Materials Processing Technology*, vol. 118, no. 1–3, pp. 36–39, 2001.
- [75] H. B. Ge, L. Kang, and Y. Tsumura, "Extremely low-cycle fatigue tests of thick-walled steel bridge piers," *ASCE Journal of Bridge Engineering*, vol. 18, no. 9, pp. 858–870, 2013.
- [76] A. M. P. D. Jesus, A. L. L. da Silva, M. V. Figueiredo, J. A. F. O. Correia, A. S. Ribeiro, and A. A. Fernandes, "Strain-life and crack propagation fatigue data from several Portuguese old metallic riveted bridges," *Engineering Failure Analysis*, vol. 18, no. 1, pp. 148–163, 2011.
- [77] R. R. Sartor, M. P. Culmo, and J. T. DeWolf, "Short-term strain monitoring of bridge structures," *ASCE Journal of Bridge Engineering*, vol. 4, no. 3, pp. 157–164, 1999.

- [78] Z. Zhao and A. Haldar, "Bridge fatigue damage evaluation and updating using non-destructive inspections," *Engineering Fracture Mechanics*, vol. 53, no. 5, pp. 775–788, 1996.
- [79] F. M. Russo, T. J. Wipf, and F. W. Klaiber, "Diagnostic load tests of a prestressed concrete bridge damaged by overheight vehicle impact," *Transportation Research Record*, vol. 1696, pp. 103–110, 2000.
- [80] H. W. Shenton III, M. J. Chajes, B. Sivakumar, and W. W. Finch, "Field tests and in-service monitoring of Newburgh-Beacon Bridge," *Transportation Research Record*, vol. 1845, pp. 163–170, 2003.
- [81] M. J. Chajes, H. W. Shenton, and D. O'Shea, "Bridge-condition assessment and load rating using nondestructive evaluation methods," *Transportation Research Record*, vol. 1696, pp. 83–91, 2000.
- [82] C. Hahin, J. M. South, J. Mohammadi, and R. K. Polepeddi, "Accurate and rapid determination of fatigue damage in steel bridges," *ASCE Journal of Structural Engineering*, vol. 119, no. 1, pp. 150–168, 1993.
- [83] J. T. DeWolf, R. G. Lauzon, and M. P. Culmo, "Monitoring bridge performance," *Structural Health Monitoring*, vol. 1, no. 2, pp. 129–138, 2002.
- [84] S. Chakraborty and J. T. Dewolf, "Development and implementation of a continuous strain monitoring system on a multi-girder composite steel bridge," *ASCE Journal of Bridge Engineering*, vol. 11, no. 6, pp. 753–762, 2006.
- [85] U. Peil, "Assessment of bridges via monitoring," *Structure and Infrastructure Engineering*, vol. 1, no. 2, pp. 101–117, 2005.
- [86] Y. Shifferaw and F. S. Fanous, "Field testing and finite element analysis of steel bridge retrofits for distortion-induced fatigue," *Engineering Structures*, vol. 49, pp. 385–395, 2013.
- [87] M. J. Chajes and D. R. Mertz, "Fracture analysis and retrofit design for the I-95 bridge over the Brandywine River," in *Recent Developments in Bridge Engineering*, K. M. Mahmoud, Ed., pp. 205–220, Balkema, Lisse, The Netherlands, 2003.
- [88] Y. E. Zhou, "Assessment of bridge remaining fatigue life through field strain measurement," *ASCE Journal of Bridge Engineering*, vol. 11, no. 6, pp. 737–744, 2006.
- [89] J. Ermopoulos and C. C. Spyarakos, "Validated analysis and strengthening of a 19th century railway bridge," *Engineering Structures*, vol. 28, no. 5, pp. 783–792, 2006.
- [90] F. Moses, J. P. Lebet, and R. Bez, "Applications of field testing to bridge evaluation," *ASCE Journal of Structural Engineering*, vol. 120, no. 6, pp. 1745–1762, 1994.
- [91] C. W. Roeder, G. MacRae, P. Crocker, K. Arima, and S. Wong, "Dynamic response and fatigue of steel tied-arch bridge," *ASCE Journal of Bridge Engineering*, vol. 5, no. 1, pp. 14–21, 2000.
- [92] S. Abdou, W. Zhang, and J. W. Fisher, "Orthotropic deck fatigue investigation at Triborough Bridge," *Transportation Research Record*, vol. 1845, pp. 153–162, 2003.
- [93] C. C. Spyarakos, I. G. Raftoyiannis, and J. C. Ermopoulos, "Condition assessment and retrofit of a historic steel-truss railway bridge," *Journal of Constructional Steel Research*, vol. 60, no. 8, pp. 1213–1225, 2004.
- [94] S. Alampalli and R. Lund, "Estimating fatigue life of bridge components using measured strains," *ASCE Journal of Bridge Engineering*, vol. 11, no. 6, pp. 725–736, 2006.
- [95] R. Malm and A. Andersson, "Field testing and simulation of dynamic properties of a tied arch railway bridge," *Engineering Structures*, vol. 28, no. 1, pp. 143–152, 2006.
- [96] D. J. Pines and A. E. Aktan, "Status of structural health monitoring of long-span bridges in the United States," *Progress in Structural Engineering and Materials*, vol. 4, no. 4, pp. 372–380, 2002.
- [97] P. C. Chang, A. Flatau, and S. C. Liu, "Review paper: health monitoring of civil infrastructure," *Structural Health Monitoring*, vol. 2, no. 3, pp. 257–267, 2003.
- [98] M. Q. Feng, "Application of structural health monitoring in civil infrastructure," *Smart Structures and Systems*, vol. 5, no. 4, pp. 469–482, 2009.
- [99] F. Casciati, "An overview of structural health monitoring expertise within the European Union," in *Structural Health Monitoring and Intelligent Infrastructure*, Z. S. Wu and M. Abe, Eds., pp. 31–37, Balkema, Lisse, The Netherlands, 2003.
- [100] J. M. W. Brownjohn, "Structural health monitoring of civil infrastructure," *Philosophical Transactions of the Royal Society A*, vol. 365, no. 1851, pp. 589–622, 2007.
- [101] J. C. Matos, O. Garcia, A. A. Henriques, J. R. Casas, and J. Vehi, "Health monitoring system (HMS) for structural assessment," *Smart Structures and Systems*, vol. 5, no. 3, pp. 223–240, 2009.
- [102] F. Moschas and S. Stiros, "Measurement of the dynamic displacements and of the modal frequencies of a short-span pedestrian bridge using GPS and an accelerometer," *Engineering Structures*, vol. 33, no. 1, pp. 10–17, 2011.
- [103] P. A. Psimoulis and S. C. Stiros, "Measuring deflections of a short-span railway bridge using a Robotic Total Station," *ASCE Journal of Bridge Engineering*, vol. 18, no. 2, pp. 182–185, 2013.
- [104] F. Moschas and S. C. Stiros, "Three-dimensional dynamic deflections and natural frequencies of a stiff footbridge based on measurements of collocated sensors," *Structural Control and Health Monitoring*, vol. 21, no. 1, pp. 23–42, 2014.
- [105] A. Mita, "Emerging needs in Japan for health monitoring technologies in civil and building structures," in *Structural Health Monitoring 2000*, F. K. Chang, Ed., pp. 56–68, Technomic, Lancaster, UK, 1999.
- [106] Y. Fujino, "Vibration, control and monitoring of long-span bridges—recent research, developments and practice in Japan," *Journal of Constructional Steel Research*, vol. 58, no. 1, pp. 71–97, 2002.
- [107] H. M. Koh, J. F. Cho, S. K. Kim, and C. Y. Kim, "Recent application and development of structural health monitoring systems and intelligent structures in Korea," in *Structural Health Monitoring and Intelligent Infrastructure*, Z. S. Wu and M. Abe, Eds., pp. 99–111, Balkema, Lisse, The Netherlands, 2003.
- [108] C. B. Yun, J. J. Lee, S. K. Kim, and J. W. Kim, "Recent R&D activities on structural health monitoring for civil infrastructures in Korea," *Journal of Civil Engineering*, vol. 7, no. 6, pp. 637–651, 2003.
- [109] J. M. Ko and Y. Q. Ni, "Technology developments in structural health monitoring of large-scale bridges," *Engineering Structures*, vol. 27, no. 12, pp. 1715–1725, 2005.
- [110] K.-Y. Wong, "Design of a structural health monitoring system for long-span bridges," *Structure and Infrastructure Engineering*, vol. 3, no. 2, pp. 169–185, 2007.
- [111] G. Chen and N. Li, "Research on the health monitoring for long span bridge in China," in *Proceedings of the International Conference on Electric Technology and Civil Engineering (ICETCE '11)*, pp. 6814–6816, Hong Kong, China, April 2011.
- [112] Q. Zhang and Y. Zhou, "Investigation of the applicability of current bridge health monitoring technology," *Structure and Infrastructure Engineering*, vol. 3, no. 2, pp. 159–168, 2007.

- [113] J. P. Ou and H. Li, "Structural health monitoring in mainland China: review and future trends," *Structural Health Monitoring*, vol. 9, no. 3, pp. 219–231, 2010.
- [114] T.-H. Yi, H.-N. Li, and M. Gu, "Recent research and applications of GPS-based monitoring technology for high-rise structures," *Structural Control and Health Monitoring*, vol. 20, no. 5, pp. 649–670, 2013.
- [115] T. H. Yi, H. N. Li, and M. Gu, "Wavelet based multi-step filtering method for bridge health monitoring using GPS and accelerometer," *Smart Structures and Systems*, vol. 11, no. 4, pp. 331–348, 2013.
- [116] T. H. Yi, H. N. Li, and H. M. Sun, "Multi-stage structural damage diagnosis method based on "energy-damage" theory," *Smart Structures and Systems*, vol. 12, no. 3-4, pp. 345–361, 2013.
- [117] M. S. Cheung, G. S. Tadros, T. Brown, W. H. Dilger, A. Ghali, and D. T. Lau, "Field monitoring and research on performance of the confederation bridge," *Canadian Journal of Civil Engineering*, vol. 24, no. 6, pp. 951–962, 1997.
- [118] A. A. Mufti, "Structural health monitoring of innovative Canadian civil engineering structures," *Structural Health Monitoring*, vol. 1, no. 1, pp. 89–103, 2002.
- [119] S. L. Desjardins, N. A. Londoño, D. T. Lau, and H. Khoo, "Real-time data processing, analysis and visualization for structural monitoring of the confederation bridge," *Advances in Structural Engineering*, vol. 9, no. 1, pp. 141–157, 2006.
- [120] T. H. T. Chan, Z. X. Li, and J. M. Ko, "Fatigue analysis and life prediction of bridges with structural health monitoring data—part II: application," *International Journal of Fatigue*, vol. 23, no. 1, pp. 55–64, 2001.
- [121] Z. X. Li, T. H. T. Chan, and J. M. Ko, "Fatigue analysis and life prediction of bridges with structural health monitoring data—part I: methodology and strategy," *International Journal of Fatigue*, vol. 23, no. 1, pp. 45–53, 2001.
- [122] R. J. Connor, S. O. Richards, and J. W. Fisher, "Long-term remote monitoring of prototype orthotropic deck panels on the Bronx-Whitestone Bridge for fatigue evaluation," in *Recent Developments in Bridge Engineering*, K. M. Mahmoud, Ed., pp. 257–268, Balkema, Lisse, The Netherlands, 2003.
- [123] Y. L. Xu, T. T. Liu, and W. S. Zhang, "Buffeting-induced fatigue damage assessment of a long suspension bridge," *International Journal of Fatigue*, vol. 31, no. 3, pp. 575–586, 2009.
- [124] X. W. Ye, Y. Q. Ni, K. Y. Wong, and J. M. Ko, "Statistical analysis of stress spectra for fatigue life assessment of steel bridges with structural health monitoring data," *Engineering Structures*, vol. 45, pp. 166–176, 2012.
- [125] A. M. Freudenthal, "Safety of structures," *Transactions of ASCE*, vol. 112, pp. 125–180, 1947.
- [126] R. Rackwitz and B. Flessler, "Structural reliability under combined random load sequences," *Computers & Structures*, vol. 9, no. 5, pp. 489–494, 1978.
- [127] P.-L. Liu and A. Der Kiureghian, "Finite element reliability of geometrically nonlinear uncertain structures," *ASCE Journal of Engineering Mechanics*, vol. 117, no. 8, pp. 1806–1825, 1991.
- [128] P. C. Das, "Application of reliability analysis in bridge management," *Engineering Structures*, vol. 20, no. 11, pp. 957–959, 1998.
- [129] D. M. Frangopol and K. Imai, "Geometrically nonlinear finite element reliability analysis of structural systems. II: applications," *Computers & Structures*, vol. 77, no. 6, pp. 693–709, 2000.
- [130] K. Imai and D. M. Frangopol, "Geometrically nonlinear finite element reliability analysis of structural systems. I: theory," *Computers & Structures*, vol. 77, no. 6, pp. 677–691, 2000.
- [131] M. G. Stewart, "Reliability-based assessment of ageing bridges using risk ranking and life cycle cost decision analyses," *Reliability Engineering & System Safety*, vol. 74, no. 3, pp. 263–273, 2001.
- [132] A. H. S. Ang and D. De Leon, "Modeling and analysis of uncertainties for risk-informed decisions in infrastructures engineering," *Structure and Infrastructure Engineering*, vol. 1, no. 1, pp. 19–31, 2005.
- [133] P. Thoft-Christensen and M. J. Baker, *Structural Reliability Theory and Its Applications*, Springer, Berlin, Germany, 1982.
- [134] D. Kececioglu, *Reliability Engineering Handbook*, vol. 1, Prentice-Hall, Englewood Cliffs, NJ, USA, 1991.
- [135] O. Ditlevsen and H. O. Madsen, *Structural Reliability Methods*, John Wiley & Sons, New York, NY, USA, 1996.
- [136] A. Haldar and S. Mahadevan, *Probability, Reliability, and Statistical Methods in Engineering Design*, John Wiley & Sons, New York, NY, USA, 2000.
- [137] A. Haldar and S. Mahadevan, *Reliability Assessment Using Stochastic Finite Element Analysis*, John Wiley & Sons, New York, NY, USA, 2000.
- [138] B. M. Ayyub, R. H. McCuen, and Probability, *Statistics, and Reliability for Engineers and Scientists*, Chapman & Hall/CRC, Boca Raton, Fla, USA, 2nd edition, 2003.
- [139] J. E. Hurtado, *Structural Reliability: Statistical Learning Perspectives*, Springer, New York, NY, USA, 2004.
- [140] J. Mohammadi and R. Polepeddi, "Bridge rating with consideration for fatigue damage from overloads," *ASCE Journal of Bridge Engineering*, vol. 5, no. 3, pp. 259–265, 2000.
- [141] M. Lukić and C. Cremona, "Probabilistic assessment of welded joints versus fatigue and fracture," *ASCE Journal of Structural Engineering*, vol. 127, no. 2, pp. 211–218, 2001.
- [142] W. G. Byers, M. J. Marley, J. Mohammadi, R. J. Nielsen, and S. Sarkani, "Fatigue reliability reassessment procedures: state-of-the-art paper," *ASCE Journal of Structural Engineering*, vol. 123, no. 3, pp. 271–276, 1997.
- [143] W. G. Byers, M. J. Marley, J. Mohammadi, R. J. Nielsen, and S. Sarkani, "Fatigue reliability reassessment applications: state-of-the-art paper," *ASCE Journal of Structural Engineering*, vol. 123, no. 3, pp. 277–285, 1997.
- [144] T.-L. Wang, C. Liu, D. Huang, and M. Shahawy, "Truck loading and fatigue damage analysis for girder bridges based on weigh-in-motion data," *ASCE Journal of Bridge Engineering*, vol. 10, no. 1, pp. 12–20, 2005.
- [145] P. Chotickai and M. D. Bowman, "Truck models for improved fatigue life predictions of steel bridges," *ASCE Journal of Bridge Engineering*, vol. 11, no. 1, pp. 71–80, 2006.
- [146] M. M. Szerszen, A. S. Nowak, and J. A. Laman, "Fatigue reliability of steel bridges," *Journal of Constructional Steel Research*, vol. 52, no. 1, pp. 83–92, 1999.
- [147] P. H. Wirsching and J. T. P. Yao, "Statistical methods in structural fatigue," *ASCE Journal of the Structural Division*, vol. 96, no. 6, pp. 1201–1219, 1970.
- [148] B. R. Ellingwood, "Fatigue reliability," *ASCE Journal of the Structural Division*, vol. 108, no. 1, pp. 3–23, 1982.
- [149] X.-L. Zheng, B. Lü, and H. Jiang, "Determination of probability distribution of fatigue strength and expressions of P-S-N curves," *Engineering Fracture Mechanics*, vol. 50, no. 4, pp. 483–491, 1995.
- [150] J. H. Yan, X. L. Zheng, and K. Zhao, "Prediction of fatigue life and its probability distribution of notched friction welded

- joints under variable-amplitude loading,” *International Journal of Fatigue*, vol. 22, no. 6, pp. 481–494, 2000.
- [151] H. Jakubczak, W. Sobczykiewicz, and G. Glinka, “Fatigue reliability of structural components,” *International Journal of Materials and Product Technology*, vol. 25, no. 1–3, pp. 64–83, 2006.
- [152] A. S. R. Murty, U. C. Gupta, and A. Radha, “A new approach to fatigue strength distribution for fatigue reliability evaluation,” *International Journal of Fatigue*, vol. 17, no. 2, pp. 85–89, 1995.
- [153] Y.-X. Zhao, Q. Gao, and J.-N. Wang, “An approach for determining an appropriate assumed distribution of fatigue life under limited data,” *Reliability Engineering & System Safety*, vol. 67, no. 1, pp. 1–7, 2000.
- [154] S. Lorén, “Estimating fatigue limit distributions under inhomogeneous stress conditions,” *International Journal of Fatigue*, vol. 26, no. 11, pp. 1197–1205, 2004.
- [155] A. H. S. Ang and W. H. Munse, “Practical reliability basis for structural fatigue,” in *Proceedings of the ASCE National Structural Engineering Conference*, New Orleans, La, USA, April 1975.
- [156] W. H. Walker, “An interim report on studies of stress histories in highway bridges, volume I and II,” Report No. UIUC-Eng-80-2005, University of Illinois at Urbana Champaign, Urbana, Ill, USA, 1978, Structural Research Series No. 448.
- [157] K. Yamada and P. Albrecht, “Fatigue design of welded bridge details for service stresses,” *Transportation Research Record*, vol. 607, pp. 25–30, 1976.
- [158] C. G. Schilling, K. H. Klippstein, J. M. Barson, and G. T. Blake, “Fatigue of welded steel bridge members under variable-amplitude loadings,” NCHRP Report No. 188, Transportation Research Board, Washington, DC, USA, 1978.
- [159] P. H. Wirsching, “Fatigue reliability for offshore structures,” *ASCE Journal of Structural Engineering*, vol. 110, no. 10, pp. 2340–2356, 1984.
- [160] H. O. Madsen, “Bayesian fatigue life prediction,” in *Probabilistic Method in the Mechanics of Solids and Structures*, S. Eggwertz and N. C. Lind, Eds., pp. 395–406, Springer, Berlin, Germany, 1984.
- [161] Y.-S. Park, S.-Y. Han, and B.-C. Suh, “Fatigue reliability analysis of steel bridge welding member by fracture mechanics method,” *Structural Engineering and Mechanics*, vol. 19, no. 3, pp. 347–359, 2005.
- [162] Y. Q. Ni, X. W. Ye, and J. M. Ko, “Modeling of stress spectrum using long-term monitoring data and finite mixture distributions,” *ASCE Journal of Engineering Mechanics*, vol. 138, no. 2, pp. 175–183, 2011.
- [163] Z. Zhao, A. Haldar, and F. L. Breen Jr., “Fatigue-reliability evaluation of steel bridges,” *ASCE Journal of Structural Engineering*, vol. 120, no. 5, pp. 1608–1623, 1994.
- [164] C. Crespo-Minguillón and J. R. Casas, “Fatigue reliability analysis of prestressed concrete bridges,” *ASCE Journal of Structural Engineering*, vol. 124, no. 12, pp. 1458–1466, 1998.
- [165] H.-N. Cho, J.-K. Lim, and H.-H. Choi, “Reliability-based fatigue failure analysis for causes assessment of a collapsed steel truss bridge,” *Engineering Failure Analysis*, vol. 8, no. 4, pp. 311–324, 2001.
- [166] S.-H. Kim, S.-W. Lee, and H.-S. Mha, “Fatigue reliability assessment of an existing steel railroad bridge,” *Engineering Structures*, vol. 23, no. 10, pp. 1203–1211, 2001.
- [167] M. S. Cheung and W. C. Li, “Probabilistic fatigue and fracture analyses of steel bridges,” *Structural Safety*, vol. 25, no. 3, pp. 245–262, 2003.
- [168] S. Pourzeynali and T. K. Datta, “Reliability analysis of suspension bridges against fatigue failure from the gusting of wind,” *Journal of Bridge Engineering*, vol. 10, no. 3, pp. 262–271, 2005.
- [169] M. Liu, D. M. Frangopol, and K. Kwon, “Fatigue reliability assessment of retrofitted steel bridges integrating monitored data,” *Structural Safety*, vol. 32, no. 1, pp. 77–89, 2010.
- [170] T. Guo, D. M. Frangopol, and Y. W. Chen, “Fatigue reliability assessment of steel bridge details integrating weigh-in-motion data and probabilistic finite element analysis,” *Computers & Structures*, vol. 112–113, pp. 245–257, 2012.
- [171] A. Sahrpeyma, A. Hosseini, and M. S. Marefat, “Life-cycle prediction of steel bridges using reliability-based fatigue deterioration profile: case study of Neka Bridge,” *International Journal of Steel Structures*, vol. 13, no. 2, pp. 229–242, 2013.
- [172] B. M. Imam, T. D. Righiniotis, and M. K. Chryssanthopoulos, “Probabilistic fatigue evaluation of riveted railway bridges,” *ASCE Journal of Bridge Engineering*, vol. 13, no. 3, pp. 237–244, 2008.
- [173] K. Kwon and D. M. Frangopol, “Bridge fatigue reliability assessment using probability density functions of equivalent stress range based on field monitoring data,” *International Journal of Fatigue*, vol. 32, no. 8, pp. 1221–1232, 2010.
- [174] Y. Q. Ni, X. W. Ye, and J. M. Ko, “Monitoring-based fatigue reliability assessment of steel bridges: analytical model and application,” *ASCE Journal of Structural Engineering*, vol. 136, no. 12, pp. 1563–1573, 2010.
- [175] K. Kwon, D. M. Frangopol, and M. Soliman, “Probabilistic fatigue life estimation of steel bridges by using a bilinear S-N approach,” *ASCE Journal of Bridge Engineering*, vol. 17, no. 1, pp. 58–70, 2012.
- [176] M. Soliman, D. M. Frangopol, and K. Kwon, “Fatigue assessment and service life prediction of existing steel bridges by integrating SHM into a probabilistic bilinear S-N approach,” *ASCE Journal of Bridge Engineering*, vol. 139, no. 10, pp. 1728–1740, 2013.
- [177] H. O. Madsen, “Probabilistic and deterministic models for predicting damage accumulation due to time varying loading,” DIALOG 5-82, Danish Engineering Academy, Lyngby, Denmark, 1983.
- [178] T. D. Righiniotis and M. K. Chryssanthopoulos, “Probabilistic fatigue analysis under constant amplitude loading,” *Journal of Constructional Steel Research*, vol. 59, no. 7, pp. 867–886, 2003.
- [179] A. Pipinato, C. Pellegrino, and C. Modena, “Fatigue assessment of highway steel bridges in presence of seismic loading,” *Engineering Structures*, vol. 33, no. 1, pp. 202–209, 2011.
- [180] C. S. Wang, L. Hao, and B. N. Fu, “Fatigue reliability updating evaluating of existing steel bridges,” *ASCE Journal of Bridge Engineering*, vol. 17, no. 6, pp. 955–965, 2012.
- [181] T. Guo and Y. W. Chen, “Fatigue reliability analysis of steel bridge details based on field-monitored data and linear elastic fracture mechanics,” *Structure and Infrastructure Engineering*, vol. 9, no. 5, pp. 496–505, 2013.

Research Article

PZT-Based Detection of Compactness of Concrete in Concrete Filled Steel Tube Using Time Reversal Method

Shi Yan,¹ Jinzhi Fu,² Wei Sun,¹ Baohui Qi,³ and Fuxue Liu³

¹ School of Civil Engineering, Shenyang Jianzhu University, Shenyang, Liaoning 110168, China

² Shenzhen China Overseas Construction Limited, Shenzhen, Guangdong 518057, China

³ Building Research Institute, Angang Construction Group, Anshan, Liaoning 114001, China

Correspondence should be addressed to Jinzhi Fu; fujinzhil@126.com

Received 11 October 2013; Revised 20 December 2013; Accepted 21 December 2013; Published 9 February 2014

Academic Editor: Ting-Hua Yi

Copyright © 2014 Shi Yan et al. This is an open access article distributed under the Creative Commons Attribution License, which permits unrestricted use, distribution, and reproduction in any medium, provided the original work is properly cited.

A smart aggregate-based approach is proposed for the concrete compactness detection of concrete filled steel tube (CFST) columns. The piezoceramic-based smart aggregates (SAs) were embedded in the predetermined locations prior to the casting of concrete columns to establish a wave-based smart sensing system for the concrete compactness detection purpose. To evaluate the efficiency of the developed approach, six specimens of the CFST columns with the rectangular cross-section were produced by placing some artificial defects during casting of concrete for simulating various uncompacted voids such as cavities, cracks, and debond. During the test, the time reversal technology was applied to rebuild the received signals and launch the reversed signals again by SAs, to overcome the issue of the lack of the prototype. Based on the proposed nonprototype, two indices of time reversibility (TR) and symmetry (SYM) were applied to relatively evaluate the level of concrete compactness in the range of the two SAs. The experimental results show that the developed method can effectively detect the compactness of concrete in CFST columns.

1. Introduction

In civil engineering, concrete-filled steel tube (CFST) structures have extensively been applied due to advantages of high load bearing capacity, well seismic performance, good durability, and convenient construction. The unique mechanical property of a CFST structure makes it more competitive than concrete or steel structure. However, the comprehensive performance of a CFST member is associated with the compactness of concrete. The poor compactness of concrete for the CFST member may come from various defects such as cavities, cracks, and debond between steel and concrete due to the poor casting of concrete in site, shrinkage and creep development of concrete, weakening the overall performance of the CFST component. The defects are difficult to be evaluated since they hide in the steel tube. Therefore, the development of reliable monitoring techniques for the concrete compactness of CFST members has drawn extensive attention and some methods using nondestructive technology (NDT) are developed.

At present, the most commonly used technologies for nondestructive detection of concrete defect are ultrasonic pulse method, acoustic emission method, pulse echo method, ray method, radar method, infrared spectroscopy method, and so forth. However, the aforementioned methods are usually impractical and inconvenient for CFST structures. Therefore, further researches on the effectiveness for the concrete compactness detection of CFST structures are needed.

The piezoelectric-based approach has been widely recognized as one of the most promising active structural health monitoring (SHM) techniques for engineering structures in recent years due to the advantages of the availability in different shapes, quick response, broadband frequency, low price, and the ability of being employed as actuators and sensors simultaneously for damage detection. An array of piezoelectric transducers to a structure can be used to detect and localize disbands and debonding of advanced composite reinforcement from concrete structures according to the difference between the current transfer function and baseline transfer function for each actuator/sensor, as discussed by

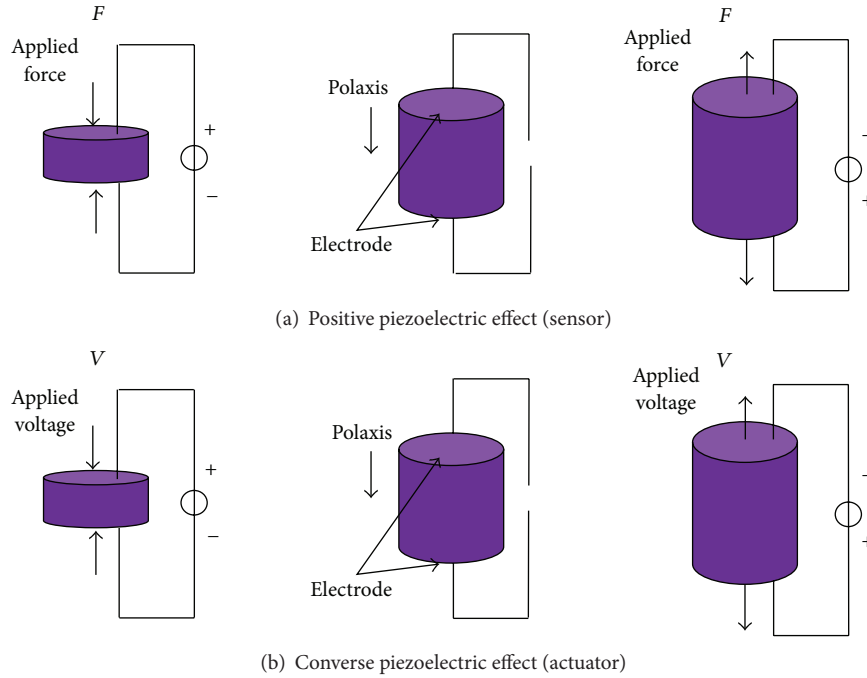


FIGURE 1: The schematic of piezoelectric effects.

Saafi and Sayyah [1]. An active diagnostic system was applied to detect embedded damage in fiber reinforced composite and steel reinforced concrete based on changes of sensor signal strength and arrival time before and after the introduction of damage. The results demonstrated the feasibility of using active sensing diagnostics for detecting deboning inside the structures, as discussed by Wang et al. [2]. An investigation was performed to detect deboning in reinforced concrete structures utilizing built-in piezoelectric patches as transducers in a pitch-catch mode to generate sensor data, which are sensitive to deboning in reinforced concrete structures, and the test results clearly indicated that deboning between concrete and rebar and yielding in rebar can be detected with the proposed method, as discussed by Wu and Chang [3]. A method was proposed for crack online monitoring of concrete compression columns based on piezoelectric sensors. The experimental results showed that the generation and development of the cracks are obviously accompanying with the phenomena of acoustic emission which can be detected by PZT sensors, as discussed by Yan and Sun [4]. A launch-receive interactive method to launch and receive signals was discussed by Qi et al. [5]. Euclidean distance was applied as an index to evaluate the concrete compactness. A validation test in situ was performed and the results showed that the worse concrete compactness in the location of the specimen clipboard was detected.

Usually, piezoelectric ceramic wave-based method for SHM needs a health status of the prototype structure to compare with the damaged one. However, it is very difficult to obtain the health status information of the structure. As a promising method, the time reversal technology (TRT) in signal processing theory needs no information of the prototype structure, and the state of the structure can be

evaluated only by the information of the detected structure. Time reversibility of acoustic or body waves can be applied in lithotripsy, ultrasonic brain surgery, acoustic communications, and other nondestructive evaluations, as discussed by Fink [6]. The developed method opened a new way for SHM in civil engineering, as discussed by Song et al. [7, 8].

This study aimed at the detection of the compactness of concrete in CFST specimens by the use of both the piezoelectric ceramics (lead zirconate titanate, PZT) and the time reversal technology (TRT). For the validation of the proposed approach, six CFST specimens with various artificial defects were tested by using the PZT-based method, and two damage indices of time reversibility (TR) and symmetry (SYM) were applied. The results showed the feasibility and efficiency of the developed approach.

2. Piezoelectric Effect and Smart Aggregates

2.1. Piezoelectric Effect. Piezoelectric ceramic material such as PZT has the positive and converse piezoelectric effect, which can be used as both actuators and sensors, shown in Figures 1(a) and 1(b). Piezoelectric equations are expressed as follows.

Positive piezoelectric effect equation:

$$\{T\} = [c^E] \{S\} - [e^t] \{E\}; \quad (1)$$

converse piezoelectric effect equation:

$$\{D\} = [e] \{S\} + [\epsilon^S] \{E\}, \quad (2)$$

where $[c^E]$ is the elastic stiffness constant matrix; $[\epsilon^S]$ is clamping dielectric constant matrix; $[e]$ is piezoelectric stress

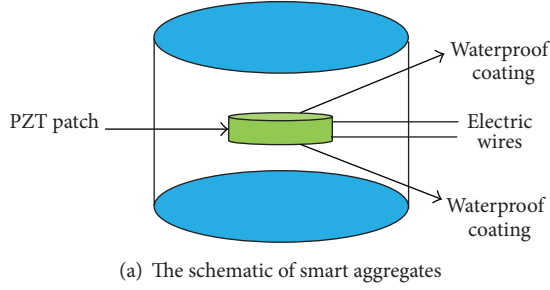


FIGURE 2: PZT-based smart aggregates.

constant matrix; $[e^t]$ is $[e]$ the transposed matrix; $\{T\}$ is the PZT stress vector; $\{S\}$ is the PZT strain vector; $\{E\}$ is the PZT electric field strength vector; and $\{D\}$ is the PZT electric displacement vector.

2.2. Smart Aggregates. PZT-based smart aggregates (SAs) are produced by embedding a waterproof piezoelectric patch with shielded lead wires into a small concrete block, shown in Figure 2. The SA working as a real aggregate in a concrete structure plays a role in protecting PZT sheets. The SAs were embedded in the predetermined locations prior to the casting of concrete columns to establish a wave-based smart sensing system. SAs have properties of fast response, high sensitivity, and sensing and actuation double effect and are widely used in structural health monitoring research in the field of measurement [9–14].

3. Algorithm of Concrete Compactness Detection Using Time Reversal Method (TRM)

3.1. Time Reversal Method. Time reversal method (TRM) is a kind of adaptive technology that can lead beam focus and image in inhomogeneous medium. The French scientists Fink transformed the successful experience in optical application field into the acoustic one. So far, many experts and scholars have carried out a large number of theories and test research work. In recent years, time reversal lamb wave technology has been mature in the quality test of the infinite free boundary plate.

Because of adaptability of time reversal focusing and its automatic compensation of energy loss in the defect, it is

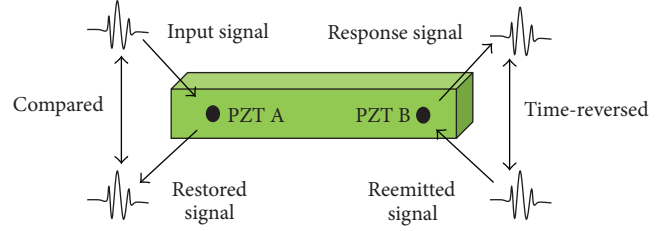


FIGURE 3: The schematic of damage detection using TRM.

suitable for any geometrical type of sensors. In addition, time reversal technology is based on the theory of guided wave propagation of the reciprocity principle, as discussed by Park et al. [15]. Therefore, this method is also applicable to the heterogeneous medium. Though sound field shape of each sensor vibration may not be the same, each time reversal sound wave reaches the maximum in the same place R_0 at the same time T , and a greater focus signal is obtained in the place R_0 . Therefore, time reversal focusing becomes the first choice in heterogeneous medium.

Propagation principle of wave signal based on the time reversal technology is as shown in Figure 3.

When an arbitrary PZT patch (PZTA) is used as an actuator and another distinct PZT patch (PZTB) is used as a sensor, the response voltage at the sensing PZTB can be represented as follows:

$$V_B(r, \omega) = I(\omega) K_B(\omega) K_A(\omega) G(r, \omega), \quad (3)$$

where r , I , $K_A(\omega)$, $K_B(\omega)$, and G are the wave propagation distance from the center of the actuating PZTA to the sensing PZTB, the input voltage at PZTA, the mechanical-electroefficiency constant of PZTA and PZTB, and the frequency response function of PZTB as a result of the input at PZTA, respectively.

As shown in Figure 3, once a response signal, propagating as the original input signal from PZTA, is measured at PZTB, the restored input signal at PZTA can be obtained by reemitting the time-reversed response signal at PZTB. Note that the time reversal operation of a signal in the time domain is equivalent to taking the complex conjugate of the Fourier transform of the signal in the frequency domain. Therefore, the time reverse operation on the response signal at PZTB is equivalent to taking the complex conjugate of (3) in the frequency domain:

$$\widehat{V}_B^*(r, \omega) = I^*(\omega) K_A^*(\omega) K_B^*(\omega) G^*(r, \omega), \quad (4)$$

where a superscript $*$ denotes a complex conjugate.

The restored signal at PZTA from the reemitted signal at PZTB can be represented in a similar form as (3):

$$\begin{aligned} V_A(r, \omega) &= K_A \widehat{V}_B^*(r, \omega) K_B(\omega) G(r, \omega) \\ &= I^*(\omega) K_A^*(\omega) K_B^*(\omega) K_A(\omega) \\ &\quad \times K_B(\omega) G(r, \omega) G^*(r, \omega) \\ &= I^*(\omega) K_{AB}^*(\omega) K_{AB}(\omega) G(r, \omega) G^*(r, \omega), \end{aligned} \quad (5)$$

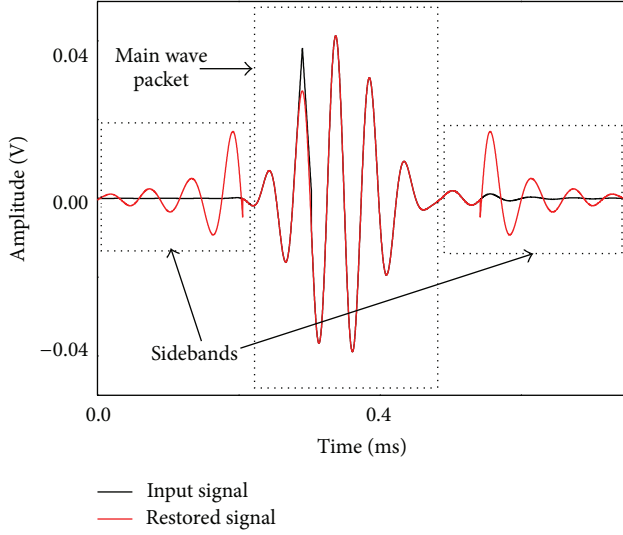


FIGURE 4: Comparison between restored signal and input one.

where $K_{AB}(\omega)$ denotes the product between $K_A(\omega)$ and $K_B(\omega)$. Therefore, the original input signal cannot be properly restored if abroad band input signal is used.

3.2. Compactness Index. Compactness detection of concrete using the time reversal process is based on the premise that, if there are certain types of defects along the wave propagation path, time reversibility breaks down. More precisely, the shape of the restored signal's main wave packet will depart from that of the original input signal and the symmetry of the restored signal is violated. By examining the deviation of the restored signal's main wave packet from the known input signal or the violation of the restored signal's symmetry as shown in Figure 4, certain type of damage can be identified without requiring any previously obtained baseline signals.

Based on this premise, two indices of time reversibility TR and symmetry SYM are applied for damage identification [16]. For the experimental study presented in the paper, a five-peak pulse signal is used for excitation; t_l and t_r represent the starting and ending time points of the five-peak pulse signal, respectively, as defined in Figure 5.

The TR index, defined below, compares the waveform of the original input with that of the restored signal:

$$TR = 1 - \sqrt{\frac{\left[\int_{t_l}^{t_r} I(t) V(t) dt \right]^2}{\left[\int_{t_l}^{t_r} I(t)^2 dt \int_{t_l}^{t_r} V(t)^2 dt \right]}}, \quad (6)$$

where $I(t)$ and $V(t)$ represent the known input signal and the main wave packet in the restored signal, respectively. The value of the TR index becomes zero when the shape of the main wave packet in the restored signal is identical to that of the original input signal. The amplitude scaling difference between $I(t)$ and $V(t)$ does not affect the TR value. If $V(t)$ deviates from $I(t)$, the TR index value increases and approaches 1.0, indicating the existence of damage along the wave propagation path.

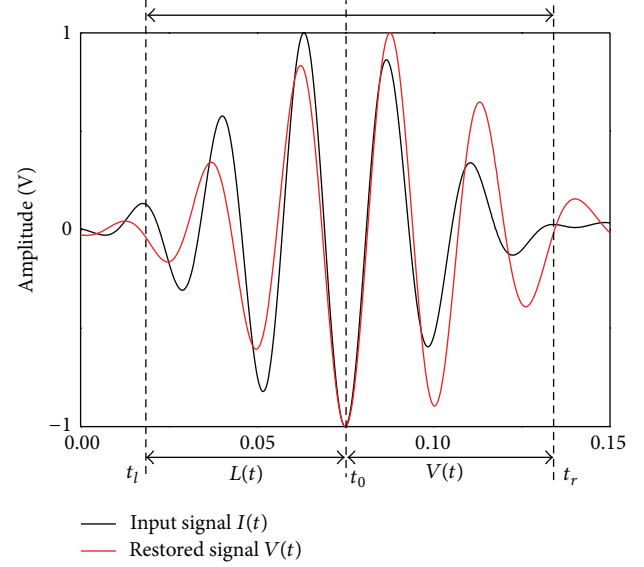


FIGURE 5: Parameter definition in the damage index.

The SYM index measures the degree of symmetry of the restored signal with respect to the main wave packet in the middle:

$$SYM = 1 - \sqrt{\frac{\left[\int_{t_0}^{t_r} L(-t) R(t) dt \right]^2}{\left[\int_{t_l}^{t_0} L(t)^2 dt \int_{t_0}^{t_r} R(t)^2 dt \right]}}, \quad (7)$$

where $L(t)$ and $R(t)$ represent left-hand and right-hand sides of the restored signal with respect to the main wave packet; t_0 is center time point of the main wave packet; t_l and t_r are same as those defined for the TR index. All terms are shown in Figure 5. Because time reversibility is based on the linear reciprocity of elastic waves, one propagating from PZTA to PZTB and the other from PZTB to PZTA should be identical for the same input signal when the system stays in a linear regime. This linear reciprocity is shown to break down when there is damage along the wave path.

4. Results and Discussion

4.1. Verification Experiment

4.1.1. Basic Introduction. In order to validate the feasibility of the proposed method, a full size CFSTC is produced. The size of the column is $300 \times 300 \times 3000$ mm. The tube is divided into three parts linked by two partitions, shown in Figure 6.

For comparison of the compactness of concrete in the CFSTC, two artificial defects ($100 \times 100 \times 10$ mm) are fixed at the bottom of the tube, while the top of the tube is cast in the normal process. Five SAs are buried in the concrete as actuators and sensors for active health monitoring. The location of the SAs and the photo of the specimen are shown in Figures 6 and 7, respectively.

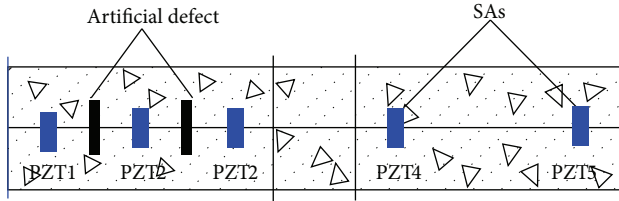


FIGURE 6: The artificial defects and the location of SAs.



FIGURE 7: The specimen.

4.1.2. *Experimental Setup.* In this experiment, a five-peak pulse signal of 10 kHz, which is generated by RIGOL DG1022 arbitrary waveform/function generator, is used to excite the SAs in the center of the columns. The other SAs in the CFST column are used as sensors, whose signals are recorded through DS1000E digital oscilloscope. An amplifier for driving the piezoelectric ceramic is used for increasing the amplitude of the test signal. Figure 8 shows the experimental setup. The five-peak pulse signal is shown in Figure 9.

4.1.3. *Test Results Analysis.* Here are the three settled test groups, PZT1-PZT2 (group A), PZT2-PZT3 (group B), and PZT4-PZT5 (group C). Based on the above-mentioned test principle, an input signal is applied to PZTA, the corresponding response is measured at PZTB, the response at PZTB is reversed in the time domain and applied back to PZTB, and the final response is measured at PZTA. Before comparison, the restored signal is scaled so that the shape of the main wave packet in the restored signal can be better compared with that of the input signal. The results are shown in Figure 10.

We can find that the shape of the restored signal's main wave packet of group A and group B departs from that of the original input signal. Because there exist artificial defects between the two test groups, the amplitude attenuation occurs in the process of spread. Therefore, the symmetry of the restored signal is violated. The restored signal's main wave packet of group C is almost identical to the original input signal, and the symmetry of the restored signal is good. This is because the compactness of the concrete in group C is good. Linear reciprocity of this method has no damage. The validity of this method is proved.

The two compactness indices of the specimen are shown in Figures 11 and 12, respectively.

TR index values of the test groups A and B are 0.531 and 0.497, respectively, while that of group C is 0.143. The values of groups A and B are three times that of group C.

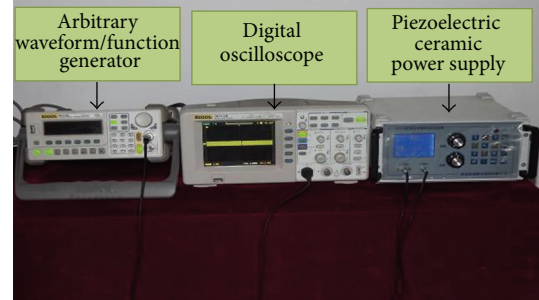


FIGURE 8: The experimental setup.

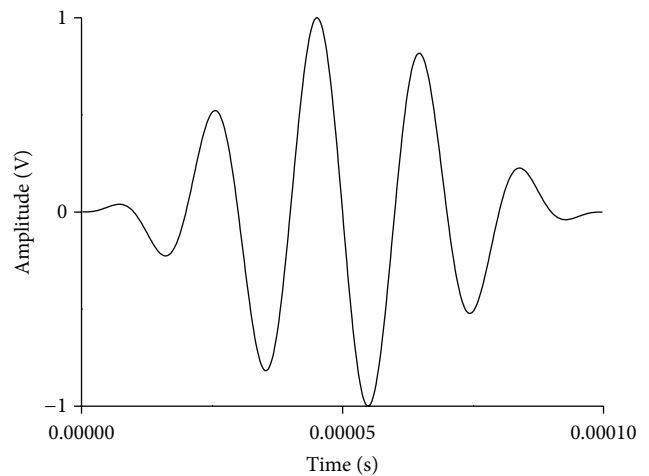


FIGURE 9: Input wave.

In fact, the values of group C should be zero. However, the wave transmission cannot ensure to be totally linear due to different concrete interfaces, resulting in the nonzero values of the group C. Based on the above reasons, the result is reasonable. While the SYM index values of these test groups are 0.432, 0.491, and 0.098, the same conclusion can be obtained.

So far, we know that this method used for compactness detection of CFSTC is feasible and effective. Next, a lot of tests will be conducted for the purpose of the comprehensive analysis of common defects in the CFSTC. Meanwhile this technology provides a new way for active monitoring and damage detection online for defects of concrete structures.

4.2. Application of Time Reversal Method

4.2.1. *Description of Experiments.* For further analysis of common defects of CFSTC, other five specimens are designed and produced. The differences among these specimens are types of defects and the size of defects, such as holes and deboning between steel and concrete. In order to find out the main influencing factors for concrete compactness, the diameters of partitions are 150 mm and 180 mm, respectively. Parameters of specimens are shown in Table 1.

The artificial defects and the location of SAs are shown in Figure 13.

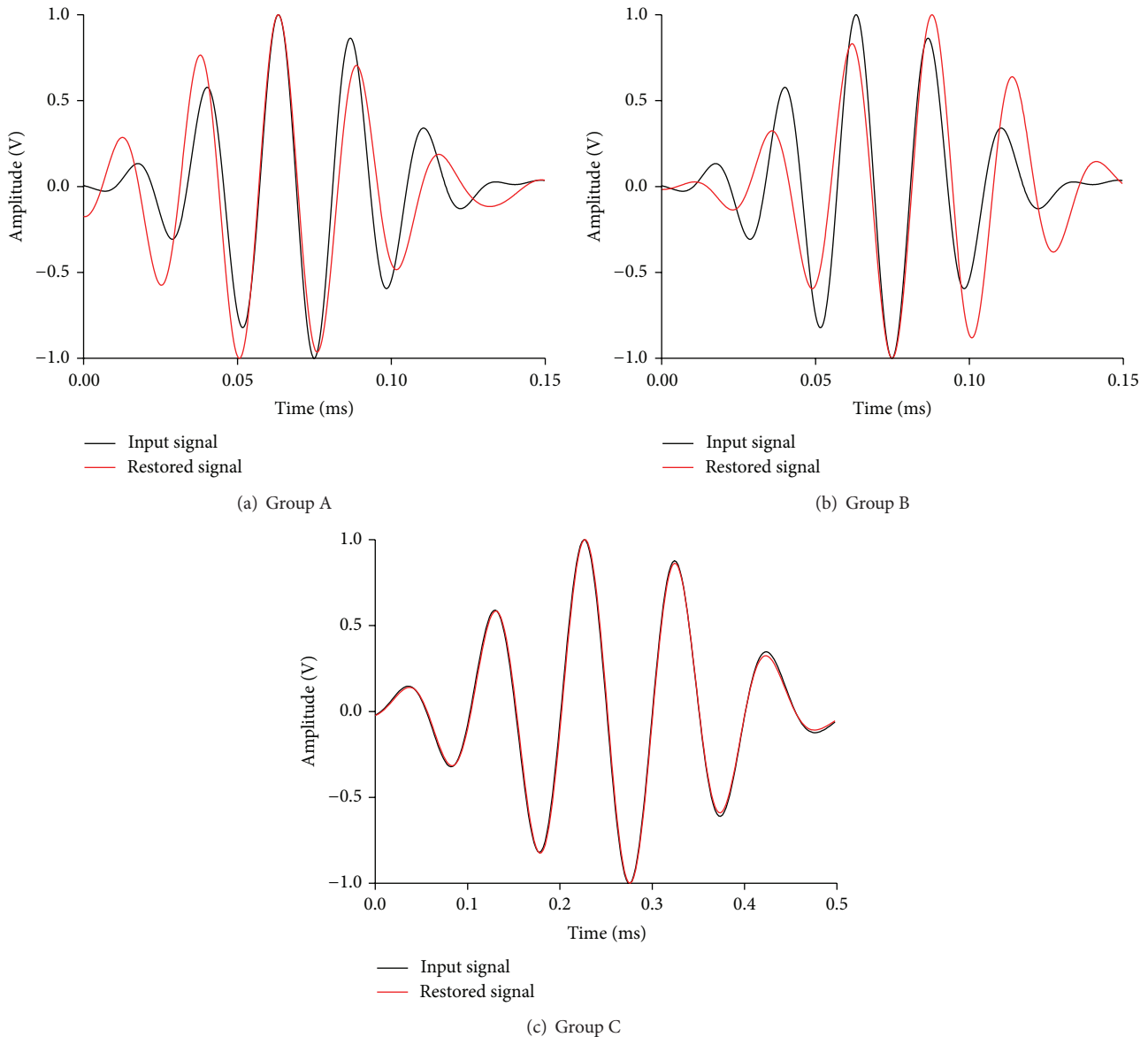


FIGURE 10: Comparison of input signal and restored signal.

4.2.2. Process of the Experiment. The apparatus and process of experiment are the same as the verification experiment. The signal is still a five-peak pulse signal of 10 kHz. The signal processing method is the same as the verification experiment. The time history plots of the signal and time-reversed signal are shown in Figure 14.

4.3. Experimental Results

4.3.1. Compactness of Concrete under Different Diameter of Partition. This part aimed to fully understand whether the change of the diameter of partition has an influence on the compactness of concrete below the partition by comparison between specimens number 1 and number 5. This part of specimen number 1 consists of six test groups, which

are PZT1-PZT2(A), PZT2-PZT3(B), PZT4-PZT5(C), PZT5-PZT6(D), PZT1-PZT3(E), and PZT4-PZT6(F). Corresponding to specimen number 1, test groups of number 5 are PZT2-PZT4(A), PZT4-PZT6(B), PZT3-PZT5(C), PZT5-PZT7(D), PZT2-PZT6(E), and PZT3-PZT7(F), respectively. Two SAs of these groups are used for sensor and actuator. Based on the process of verification experiment, the input signal is excited, received, time-reversed, and restored. Comparing the difference between the input signal and the restored signal, the compactness of the concrete can be identified. The compactness indices TR and SYM are shown in Figures 15 and 16, respectively.

The TR values of these groups are greater than zero, and it means that the compactness of concrete in the area below the partition is not good. It can be seen that even the diameter of the partition is relatively large and the void area still exists.

TABLE 1: Parameters of specimens.

Number	Size $b \times h \times l/mm$	Diameter d/mm	Strength grade	Contents		
				Artificial defects	PZT patches	Detection type of compactness
Number 1	$300 \times 300 \times 3000$	150	C30	NO	NO	Compactness below partition
Number 2	$300 \times 300 \times 3000$	150	C30	YES	NO	Artificial defects
Number 3	$300 \times 300 \times 3000$	150	C30	YES	YES	Compactness below partition
Number 4	$300 \times 300 \times 3000$	180	C30	NO	NO	Compactness of concrete in the tube
Number 5	$300 \times 300 \times 3000$	180	C30	NO	YES	Contrast to Number 1

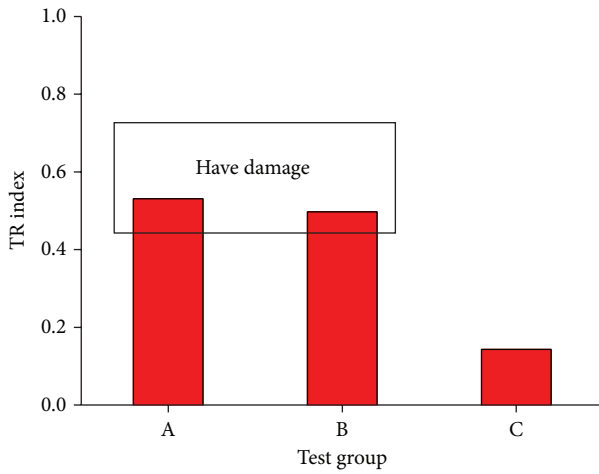


FIGURE 11: The TR index of these test groups.

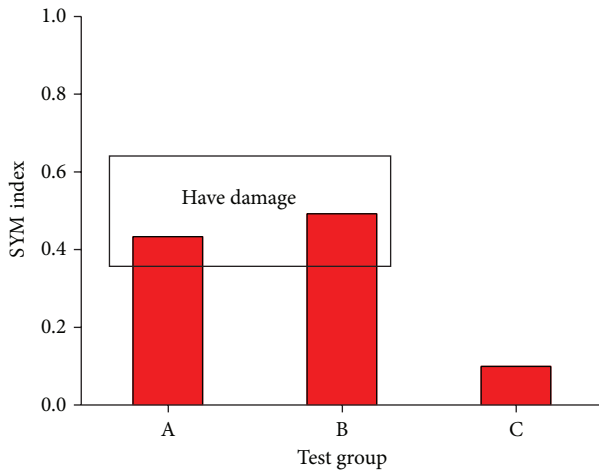


FIGURE 12: The SYM index of these test groups.

But the TR value of number 5 is smaller than that of number 1; it shows that the exchange for the diameter of the partition is effective for improvement of compactness of concrete below the partition. On this condition, the concrete can pass the partition smoothly and become denser. Otherwise, the TR values of test groups (E) and (F) are larger than the remaining ones because the void area of groups (E) and (F) is stacked with the one that is in the test groups (A) and (B), (C) and (D).

The same conclusion can be got from the SYM values of these test groups for specimens number 1 and number 5.

4.3.2. *Poor Cementation between Steel and Concrete.* The purpose of this part is to detect the poor cementation between steel and concrete that exists or is simulated by artificial defects in specimens number 3 and number 5. Test groups of specimen number 3 consist of PZT2-PZT7(H) and PZT5-PZT8(J). Corresponding to specimen number 3, test groups of number 5 are PZT1-PZT9(H) and PZT8-PZT10(J). The experimental process and signal processing are the same as the former. The compactness indices TR and SYM are shown in Figures 17 and 18, respectively.

Figures 17 and 18 show the comparison of groups number 3 and number 5, and the TR value of test group (J) is bigger than (H). This is because the thickness of the artificial defect in test group (J) is greatly larger than group (H). However, the differences of TR value between two groups are not like that of artificial defect thickness, having nonlinear relationship between them. The same conclusion is suitable for specimen number 5. Namely, the poor cementation between steel and concrete existing in the whole specimen and the upper of the specimen is more serious. Therefore, the symmetry of the restored signal is violated and SYM values are bigger than zero. Poor cementation between steel and concrete can be verified similarly and much clearly by SYM values.

4.3.3. *Compactness of Concrete for Different Sections.* This part is to detect compactness of concrete for different sections in specimens number 3 and number 4. The difference between them is the diameter of the partition. Test groups of specimen number 3 consist of PZT1-PZT3(A) and PZT4-PZT6(B). Corresponding to specimen number 4, test groups of number 5 are PZT1-PZT3(A) and PZT4-PZT6(B). The experimental process and signal processing are the same as the former. The compactness indices TR and SYM are shown in Figures 19 and 20, respectively.

It is known that the TR value of test group (A) is smaller than test group (B) for specimens number 3 and number 4, which means that the compactness of concrete under the section is better than that above it. Under the action of gravity, concrete is compressed and filled constantly. Strict casting process is also an important guarantee for the compactness of concrete. Less moisture, better curing, and sealing also do a good favor for the better compactness of concrete.

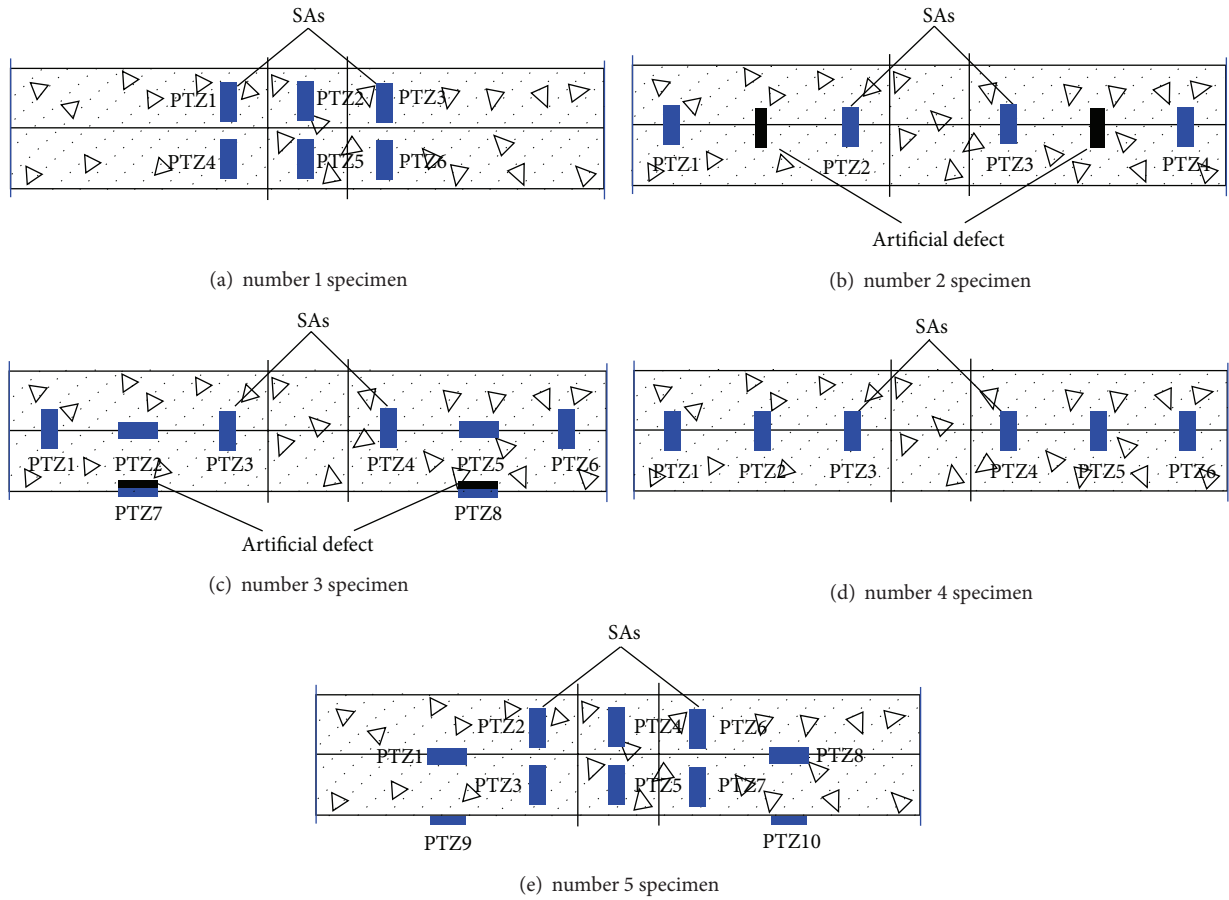


FIGURE 13: The artificial defects and the location of SAs.

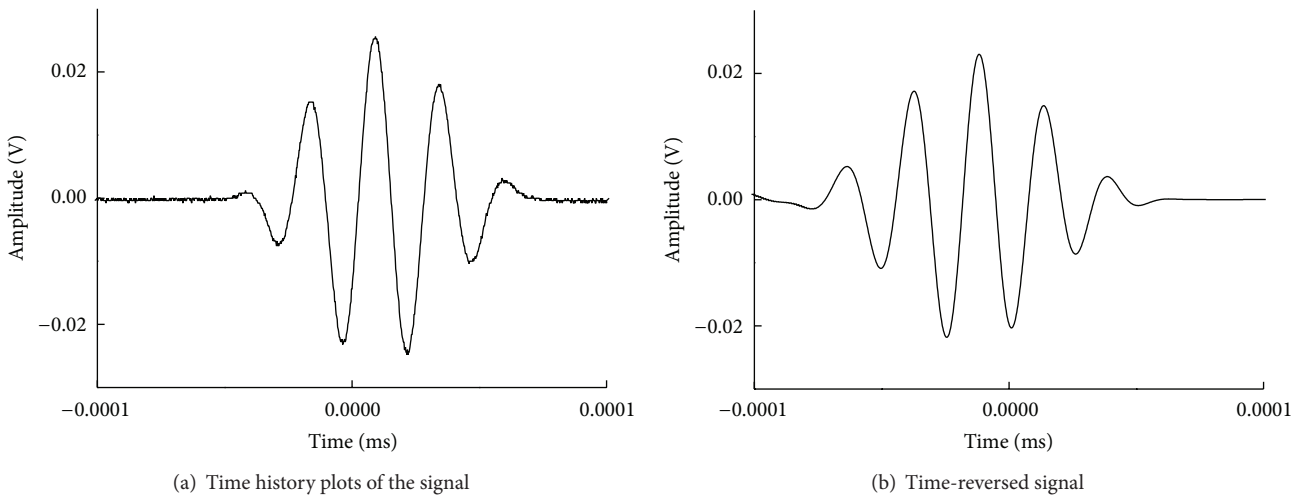


FIGURE 14: The history and time-reversed signal.

The TR value of test group (A) for specimen number 3 is slightly bigger than specimen number 4, and the TR value of test group (B) is nearly as the same as each other, which means that the change of diameter of partition has something to do with the compactness of concrete below the section and has

nothing to do with the up section. The same conclusion can be identified by SYM.

4.3.4. *Compactness of Different Artificial Defects.* In order to detect the compactness of concrete under different damage,

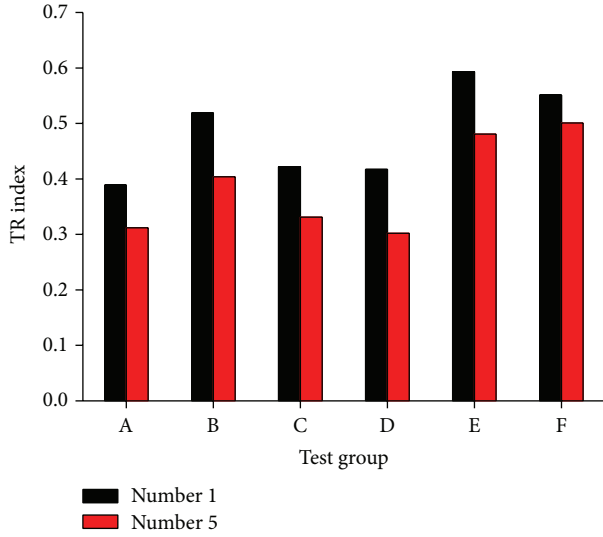


FIGURE 15: The TR index for specimens number 1 and number 5.

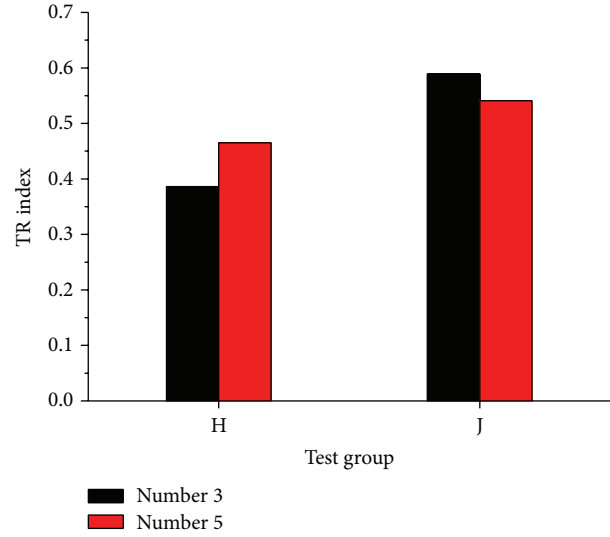


FIGURE 17: The TR index for specimens number 3 and number 5.

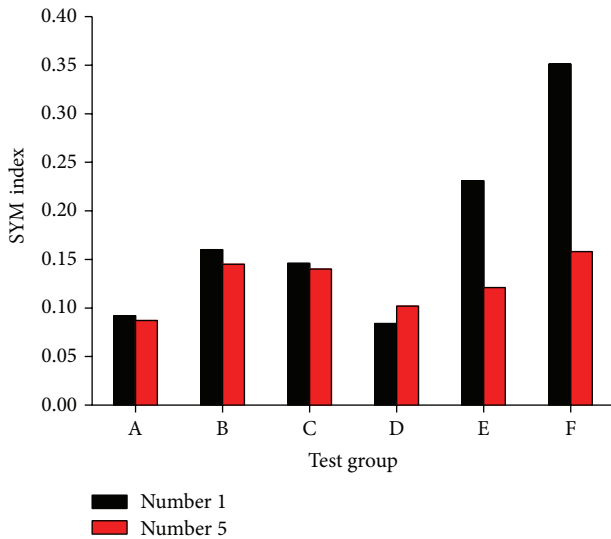


FIGURE 16: The SYM index for specimens number 1 and number 5.

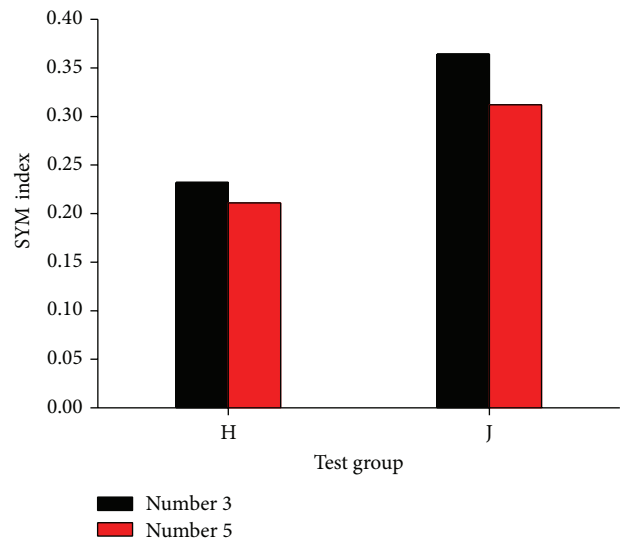


FIGURE 18: The SYM index for specimens number 3 and number 5.

specimen number 2 with two kinds of artificial defects of different thickness is designed. Test groups of specimen number 2 consist of PZT1-PZT2(A) and PZT3-PZT4(B). The experimental process and signal processing are the same as the former. The compactness indices TR and SYM are shown in Figures 21 and 22, respectively.

It can be seen that the TR index of test group (B) is nearly two times that of test group (A). The difference between each other is the thickness of artificial defects. The TR values of them are nearly the same as the thickness. It is clear that the artificial defects can be detected successfully and the detected area is consistent with the actual condition when any of the test groups is employed as actuator and sensor. It can be found that the damage areas can be successfully detected. The experimental results show that the proposed approach can effectively evaluate the damage existence and location.

5. Conclusions

In this paper, a detection approach for the compactness of concrete using two damage indices which are defined with the time reversal theory on the measurements of SAs installed in the CFST column and excited by smart aggregates in the concrete was developed. The effectiveness of the proposed approach was experimentally verified with a CFST model column. A five-peak pulse signal of 10 kHz was employed to excite smart aggregates which act as actuators in concrete. The two proposed damage indices were employed to identify the existence and location of the artificially mimicked damage areas and real one. The results showed that the detected areas are satisfactorily in agreement with the predesigned damage conditions.

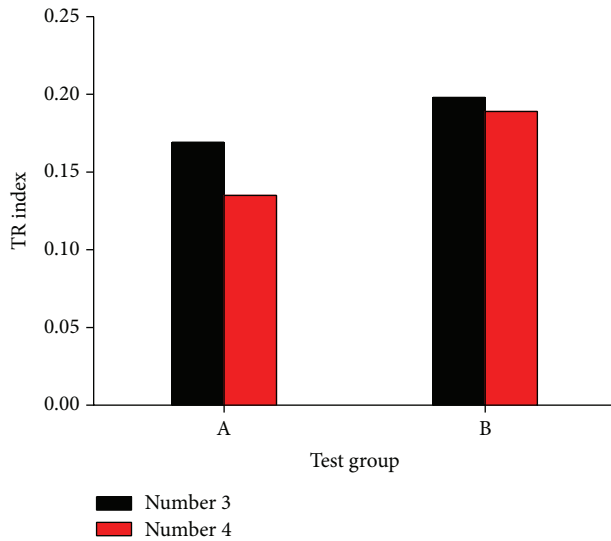


FIGURE 19: The TR index for specimens number 3 and number 4.

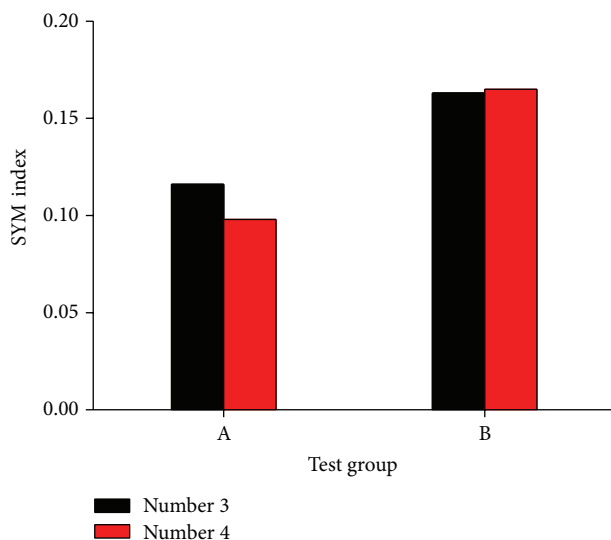


FIGURE 20: The SYM index for specimens number 3 and number 4.

The conclusion is as follows.

- (1) The void of concrete below the partition and poor cementation between steel and concrete are inevitable in the concrete in filled steel tube columns. The only difference is the degree of the damage.
- (2) The compactness of concrete below the section is better than that above it.
- (3) For double partition, the compactness of concrete below the lower one is worse than the high one. Increasing the diameter of the partition does a good favor for the compactness of concrete below the partition. Therefore, it is a better way to improve the compactness of concrete by increasing the diameter

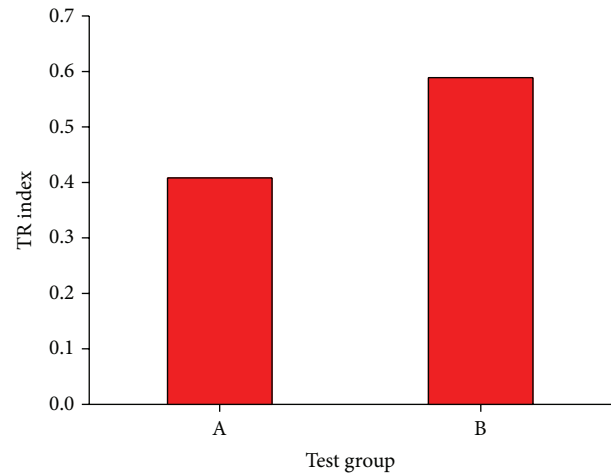


FIGURE 21: The TR index for specimen number 2.

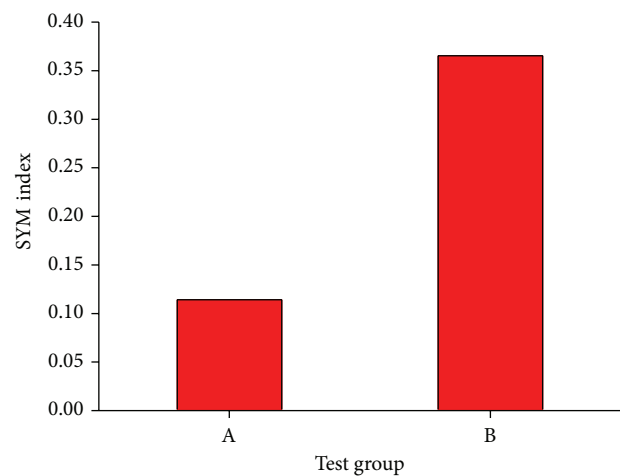


FIGURE 22: The SYM index for specimen number 2.

of the column. Therefore, it can be an important guarantee for load-carrying capacity and in the ductility of the CFSTC.

Moreover, the damage index defined with the TR and SYM is sensitive to the damage. The proposed PZT-based SAs and sensing techniques and the corresponding analysis approach have great potential to be applied in practice for the inaccessible damage detection of CFST engineering structures.

Conflict of Interests

The authors declare that there is no conflict of interests regarding the publication of this paper.

Acknowledgments

This work was financially supported in part by the National Natural Science Foundation of China (51278313 and 51308357), the Natural Science Foundation of Liaoning

Province (201202180), the Science Foundation of Liaoning Education Department (L2012214), and Key Laboratory Foundation of Liaoning Province (JG2009-18), as well as Angang Construction Group 2011 Foundation.

References

- [1] M. Saafi and T. Sayyah, "Health monitoring of concrete structures strengthened with advanced composite materials using piezoelectric transducers," *Composites B*, vol. 32, no. 4, pp. 333–342, 2001.
- [2] C. S. Wang, F. Wu, and F.-K. Chang, "Structural health monitoring from fiber-reinforced composites to steel-reinforced concrete," *Smart Materials and Structures*, vol. 10, no. 3, pp. 548–552, 2001.
- [3] F. Wu and F.-K. Chang, "Debond detection using embedded piezoelectric elements in reinforced concrete structures. Part I: experiment," *Structural Health Monitoring*, vol. 5, no. 1, pp. 5–15, 2006.
- [4] S. Yan and W. Sun, "Experimental research on crack damage detection of concrete beam based on PZT wave method," *Concrete*, vol. 234, no. 4, pp. 20–23, 2010 (Chinese).
- [5] B. H. Qi, S. Yan, F. Liu, B. He, and J. Fu, "Diagnostic test about density of concrete filled steel tube column with smart aggregates," *Journal of Shenyang Jianzhu University*, vol. 28, no. 3, pp. 491–496, 2012 (Chinese).
- [6] M. Fink, "Time-reversed acoustics," *Scientific American*, vol. 281, no. 5, pp. 91–97, 1999.
- [7] G. Song, H. Gu, Y. L. Mo, T. T. C. Hsu, and H. Dhonde, "Concrete structural health monitoring using embedded piezoceramic transducers," *Smart Materials and Structures*, vol. 16, no. 4, article 003, pp. 959–968, 2007.
- [8] S. Yan, W. Sun, G. Song et al., "Health monitoring of reinforced concrete shear walls using smart aggregates," *Smart Materials and Structures*, vol. 18, no. 4, Article ID 047001, pp. 1–6, 2009.
- [9] T. H. Yi and H. N. Li, "Methodology developments in sensor placement for health monitoring of civil infrastructures," *International Journal of Distributed Sensor Networks*, vol. 2012, Article ID 612726, 11 pages, 2012.
- [10] V. Bottega, A. Molter, O. A. A. da Silveira, and J. S. O. Fonseca, "Simultaneous piezoelectric actuator and sensor placement optimization and control design of manipulators with flexible links using SDRE method," *Mathematical Problems in Engineering*, vol. 2010, Article ID 362437, 23 pages, 2010.
- [11] H. S. Shang, T. H. Yi, and L. S. Yang, "Experimental study on the compressive strength of big mobility concrete with nondestructive testing method," *Advances in Materials Science and Engineering*, vol. 2012, Article ID 345214, 6 pages, 2012.
- [12] T. H. Yi, H. N. Li, and H. M. Sun, "Multi-stage structural damage diagnosis method based on "energy-damage" theory," *Smart Structures and Systems*, vol. 12, no. 3-4, pp. 345–361, 2013.
- [13] B. Xu, T. Zhang, G. Song, and H. Gu, "Active interface debonding detection of a concrete-filled steel tube with piezoelectric technologies using wavelet packet analysis," *Mechanical Systems and Signal Processing*, vol. 36, pp. 7–17, 2013.
- [14] Q. Huang, B. Xu, B. Li, G. Song, and J. Teng, "Monitoring for large cross-section CFSTs of a super high-rise building with piezoceramic actuators and sensors," *Advanced Materials Research*, vol. 163–167, pp. 2553–2559, 2011.
- [15] H. W. Park, H. Sohn, K. H. Law, and C. R. Farrar, "Time reversal active sensing for health monitoring of a composite plate," *Journal of Sound and Vibration*, vol. 302, no. 3, pp. 50–66, 2004.
- [16] S. D. Kim, C. W. In, K. E. Cronin, H. Sohn, and K. Harries, "Reference-free NDT technique for debonding detection in CFRP-strengthened RC structures," *Journal of Structural Engineering*, vol. 133, no. 8, pp. 1080–1091, 2007.

Research Article

Intelligent Platform for Model Updating in a Structural Health Monitoring System

Danhui Dan,¹ Tong Yang,² and Jiongxin Gong¹

¹ Department of Bridge Engineering, Tongji University, Room 711, Bridge Building, 1239 Siping Road, Shanghai 200092, China

² Lin Tung-Yen & Li Guo-Hao Consultants Shanghai Ltd., Shanghai 200092, China

Correspondence should be addressed to Danhui Dan; dandanhui@tongji.edu.cn

Received 10 October 2013; Accepted 12 December 2013; Published 20 January 2014

Academic Editor: Ting-Hua Yi

Copyright © 2014 Danhui Dan et al. This is an open access article distributed under the Creative Commons Attribution License, which permits unrestricted use, distribution, and reproduction in any medium, provided the original work is properly cited.

The main aim of this study is to develop an automated smart software platform to improve the time-consuming and laborious process of model updating. We investigate the key techniques of model updating based on intelligent optimization algorithms, that is, accuracy judgment methods for basic finite element model, parameter choice theory based on sensitivity analysis, commonly used objective functions and their construction methods, particle swarm optimization, and other intelligent optimization algorithms. An intelligent model updating prototype software framework is developed using the commercial software systems ANSYS and MATLAB. A parameterized finite element modeling technique is proposed to suit different bridge types and different model updating requirements. An objective function library is built to fit different updating targets. Finally, two case studies are conducted to verify the feasibility of the techniques used by the proposed software platform.

1. Introduction

The use of monitoring information from structural health monitoring systems facilitates the updating of finite element models with real-time and online structures. By doing so, we can not only update the structural benchmark analyses model but also continuously track the changes in the target physical parameters and the characteristic index in any location [1–3]. The automation and intelligence of the model updating process is the key problem that hinders the achievement of these goals in structural health monitoring system [4, 5]. After 20 years of research, existing structural health monitoring systems at home and abroad have entered the third stage, where the emphasis is on the processing and utilization of data to implement data-based online early warnings and assessments of individual health status [5, 6]. During this stage, the model-based assessment method is simply regarded as a supplementary approach that is used in an offline manner and it has not become the main focus of the online algorithm. Model updating has been studied only to provide a benchmark model for this method [1, 6].

In recent years, the theory and technology of model updating have continued to progress, especially in computational model updating (CMU) and model validation [7, 8] research, some of the techniques used when updating parameter selection [9, 10], uncertainty processing techniques for updating results from continuous monitoring information [11, 12], and alternative technologies that employ small numbers of calculations of complex finite element calculation during a modified iteration step [13–16]. Model updating software has also made rapid progress, while some commercial finite element software systems have expanded their functions to model updating, such as DDS's FEMtools [17], the Balmes' structural dynamics toolbox SDTools [18], and Schedlinski's SysVal [19]. All of these software systems have model updating functions, but these software updating methods are isolated, with poor universality and weak poor optimization abilities. It is difficult to ensure the optimization of the updated results, which need to be programmed completely and automated to reduce human intervention. However, technological progress constantly stimulates structural health monitoring system researchers

to include model updating in the development of the next generation of structural health monitoring systems, thereby making the systems more intelligent with online and real-time updating processes. This will allow the use of physical and mechanical field information to address the monitoring target, thereby expanding the evaluation of sources and the scope of information, as well as overcoming the shortcomings caused by limited measurement points [19].

Thus, we studied online intelligent model update techniques based on monitoring to develop a model updating prototype software framework based on the commercial finite element software system, ANSYS, and the scientific computing software system, MATLAB. We also developed an intelligent algorithms library, which includes particle swarm optimization (PSO), to drive most of the updating tasks. The use of this platform to combine updating tasks, objective functions, and intelligent algorithms facilitates efficient and flexible automatic model updating without manual intervention, thereby bridging the functions of the structural finite element modeling and updating both in the structure and in component level with the present structural health monitoring system. Finally, we consider the key components of the technique developed in this study by discussing the results of a vibration test with a continuous beam and a monitoring system implementation of a cable-stayed bridge, which demonstrated the feasibility of the proposed technique.

2. Descriptions of the Generality of Parametric Model Updates

Based on the differences between the objects updated, model updating methods can be divided into two categories: matrix updating and parametric updating, the essence of which is an optimization algorithm that minimizes the residuals. Matrix updating methods modify the system matrix of structure or submatrices directly. However, the relations among elements may disappear because of the massive volumes of data in the matrix elements that need updating and the drastic manipulations required before and after matrix updating. There may be imaginary elements and negative stiffness values, which means that the elements lose their definite physical meaning, so these methods are not suitable for large structures. Starting in the late 1980s, the research focus shifted gradually to parametric updating methods, which regard the structural design parameters (such as the boundary conditions, physical properties, and geometric features) that constitute system matrixes or the abstract parameters as updating objects, thereby ensuring that the model has a definite physical meaning after updating. Although there are many parametric model updating methods with different characteristics, the core process can be described using the same model.

The number of design parameters in structure finite element models is n , where the first m is the parameters that need to be updated, so the design parameters can be expressed as

$$\mathbf{p} = [p_1, p_2, p_3, \dots, p_m, \dots, p_n]. \quad (1)$$

The system matrix of the structure (global stiffness matrix, mass matrix, and damping matrix) can be expressed as a function of the design parameters:

$$\begin{aligned} \mathbf{K} &= f_K(\mathbf{p}), \\ \mathbf{M} &= f_M(\mathbf{p}), \\ \mathbf{C} &= f_C(\mathbf{p}). \end{aligned} \quad (2)$$

In the corresponding finite element model, the experimental model also has the following relationship between the system matrix and design parameter values:

$$\begin{aligned} \mathbf{K}^* &= f_K^*(\mathbf{p}^*), \\ \mathbf{M}^* &= f_M^*(\mathbf{p}^*), \\ \mathbf{C}^* &= f_C^*(\mathbf{p}^*). \end{aligned} \quad (3)$$

The aim of updating is to ensure that the finite element model ($\mathbf{K}, \mathbf{M}, \mathbf{C}$) approximates the experimental model ($\mathbf{K}^*, \mathbf{M}^*, \mathbf{C}^*$), so it can take advantage of the former to perform inversions or predictions of the mechanical field, or to perform system identification, as well as other tasks. The sources of updating are the differences between the two models, where the magnitude of the differences can be described comprehensively by an objective function

$$\begin{aligned} f &= F(\mathbf{K}, \mathbf{M}, \mathbf{C}, \mathbf{K}^*, \mathbf{M}^*, \mathbf{C}^*) \\ &= F(f_K(\mathbf{p}), f_M(\mathbf{p}), f_C(\mathbf{p}), f_K^*(\mathbf{p}^*), f_M^*(\mathbf{p}^*), f_C^*(\mathbf{p}^*)) \\ &= F_{f,p}(f_K, f_M, f_C, f_K^*, f_M^*, f_C^*, \mathbf{p}, \mathbf{p}^*). \end{aligned} \quad (4)$$

Therefore, model updating can be considered to be an optimization problem:

$$\begin{aligned} & (f_K, f_M, f_C, \mathbf{p})^{\text{opt}} \\ &= \arg \min_{\substack{f_K, f_M, f_C \rightarrow f_K^*, f_M^*, f_C^* \\ \mathbf{p} \rightarrow \mathbf{p}^*}} (F_{f,p}(f_K, f_M, f_C, f_K^*, f_M^*, f_C^*, \mathbf{p}, \mathbf{p}^*)). \end{aligned} \quad (5)$$

As mentioned above, the precondition of design parameter model updating is ensuring the rationality of the finite element analyses model, that is, ensuring a suitable approximation of (f_K, f_M, f_C) using (f_K^*, f_M^*, f_C^*) . Otherwise, the results cannot be correct if a wrong finite element model is used for parameter updating. When modeling a finite element, the assumptions and approximations of structural geometry, materials, and boundary conditions have the main effects on rationality and the model structural error. The structural rationality of the finite element model can be guaranteed by ensuring the reasonable modeling of stiffness, mass, and damping and the rational processing of boundary conditions, rational modeling of loads, structural damage, and deterioration of performance. Thus, the objective functions and the optimization updating problem, respectively, can be simplified as

$$\begin{aligned} f &= F_p(\mathbf{p}, \mathbf{p}^*), \\ (f_K, f_M, f_C, \mathbf{p})^{\text{opt}} &= \arg \min_{\mathbf{p} \rightarrow \mathbf{p}^*} (F_p(\mathbf{p}, \mathbf{p}^*)). \end{aligned} \quad (6)$$

As a result, the problem of design parametric model updating can be described by (6). The general process can be summarized as follows.

- (i) We regard the experimental model as the reference to model the finite element model reasonably, thereby ensuring the approximation of (f_K, f_M, f_C) as (f_K^*, f_M^*, f_C^*) .
- (ii) Depending on the aim of updating and the updating object's characteristics, the design objective function describe the differences in performance (static effect, dynamic response, or structural characteristics) between the finite element model and the experimental model.
- (iii) An appropriate optimization algorithm is selected to find the optimal model.

Thus, it is clear that finite element model, the objective function, and the optimization algorithm are three main factors that affected design parameter model updating. Therefore, these three main factors must be standardized first before automating the updating process to ensure their seamless integration and data exchange, which is also the main focus of the present study.

3. Key Techniques for Intelligent Model Updating in an Online Environment

Finite element model updating research has made great progress and has been applied in some fields of engineering, but many problems still need to be solved when model updating is applied to large structures. The major constraints on online model updating are as follows: (1) model updating with large structures entails many degrees of freedom, intensive and complex calculations, and many iterative steps; (2) the limits of the iterative optimization algorithm and the difficulty of appropriate algorithm design, which mean that the optimization process has problems converging on an ideal solution; (3) the improper selection of the design variables or design space often leads to the optimization results losing their physical meaning; (4) single step iteration calculations are large and difficult to perform online and in real time; (5) some optimization steps are not completely programmed and may need manual intervention. These difficulties form a bottleneck that hinders model updating in an online environment. Therefore, we used the following techniques to overcome these difficulties.

3.1. Selection of Model Updating Parameters and Design of the Space Boundary Value. The selection of model parameters has a huge effect on model updating, because the number of parameters selected will affect the scale and speed of the optimization calculations directly, while the parameters selected will affect the physical meaning of the updating results and the pathological degree of the equation governing updating. After updating the parameter selection, the choice of the upper and lower bounds of the design space also needs to be reasonable. The choice should not vary greatly

within the definition domain, which is only mathematically reasonable; otherwise the value may be unreasonable from a physical perspective and abnormal in the usual sense of the structure.

Therefore, the design parameters should be selected before the parameter sensitivity analyses based on the actual conditions of the updating object. A sensitivity analyses that considers the statistical properties of updating parameters can then be performed. Given that the updating target function is f and the updating parameter is p , the initial value of the updating parameter is p_0 and δ_p is the statistical variation coefficient of parameter p , so the sensitivity after considering parameter's statistical features can be defined as follows:

$$s = \delta_p \cdot \left. \frac{\partial f}{\partial p} \right|_{p=p_0}. \quad (7)$$

After comparing and selecting various parameters using (7), the parameters with high sensitivity but low dispersion can be ranked at the end of the optional parameter sequence, or even excluded, to ensure the correct physical meaning and the structural rationality of the results. The Monte Carlo method or bootstrap method can be used to make the same choices. Updating the boundaries of the parameters can be achieved using the initial value and the coefficient of variation, that is, $p_0(1 \pm \delta_p)$.

3.2. Hybrid Objective Function. In recent years, research progress in model updating techniques means that dynamic fingerprints have been used increasingly to reflect the dynamic characteristics of the structure, such as the flexibility matrix, strain mode, modal curvature, and frequency response function. These have been applied widely to model updating techniques with good results. However, there are numerous dynamic fingerprints and many different cases, which have created problems when deciding the success or failure of model updating, because it is difficult to choose an appropriate dynamic fingerprint as an objective function. During dynamic model updating, there may be various choices of objective functions, such as frequencies, mode shapes, modal flexibility, modal strain energy, frequency response function, and static displacement, which can all be used as the independent variables of objective functions. Various objective functions perform differently in diverse updating environment, but in hybrid objective functions generally perform better. In the present study, the key objective functions were as follows.

A type of objective function that usually combines natural frequencies and mode shapes is

$$f = \sum_{i=1}^n \alpha_i \left(\frac{\omega_i - \omega_i^*}{\omega_i^*} \right)^2 + \sum_{i=1}^n \beta_i \left(\frac{1 - \sqrt{\text{MAC}_i}}{\text{MAC}_i} \right)^2. \quad (8)$$

In (8), ω_i and ω_i^* are the i th order of the modal frequencies and the measured modal frequencies of the finite element, respectively, α_i and β_i are the weight coefficients of the i th order, and MAC_i is the i th order modal assurance criterion of the measured model and the finite element model.

Another objective function used in previous study [14] is the cross-model cross-mode (CMCM) model updating method:

$$f = \|\delta_\lambda - [C \ E]\|. \quad (9)$$

In (9), δ_j is the fluctuation ratio of the eigenvalue:

$$\delta_j = \frac{\lambda_j^* - \lambda_j}{\lambda_j} \quad (10)$$

λ_j^* and λ are the i th order eigenvalues of the measured mode and the finite element mode, respectively, and C and E are the values of the cross-correlation coefficient of stiffness (COK) and cross-correlation coefficient of mass (COM), which are defined as follows:

$$C = \begin{bmatrix} C_{1,1} & \cdots & C_{1,N_e} \\ \vdots & C_{k,n} & \vdots \\ C_{nf \times nt, N_e} & \cdots & C_{nf \times nt, N_e} \end{bmatrix},$$

$$E = \begin{bmatrix} E_{1,1} & \cdots & E_{1,N_e} \\ \vdots & E_{k,n} & \vdots \\ E_{nf \times nt, N_e} & \cdots & E_{nf \times nt, N_e} \end{bmatrix}, \quad (11)$$

$$C_{k,n} = \frac{\text{COK}_{i,j^*}^{(n)}}{\text{COK}_{i,j^*}} = \frac{(\varphi_i)^T \mathbf{K}_n \varphi_i^*}{(\varphi_i)^T \mathbf{K} \varphi_i^*},$$

$$E_{k,n} = (1 + \delta_j) \frac{\text{COM}_{i,j^*}^{(n)}}{\text{COM}_{i,j^*}} = (1 + \delta_j) \frac{(\varphi_i)^T \mathbf{M}_n \varphi_i^*}{(\varphi_i)^T \mathbf{M} \varphi_i^*}.$$

In the equations, $k = i \times j = 1, 2, \dots, nf \times nt$, $n = 1, 2, \dots, N_e$.

The two objective functions are the representation of the directly designed parametric updating method and the indirectly designed parametric updating method based on phenomenological theory, respectively.

3.3. Alternative Technique for Complex Finite Element Calculation Using Small Amount of Computation Methods in a Single Updating Iteration Step. The model updating process can be transformed into an optimization problem, which generally requires an iterative technique that calculates an objective function many times according to certain rules. For large complex structures, each iterative step requires one (linear) or more (nonlinear) finite element analyses to obtain the independent variables of the objective function, which can include static effects, dynamic responses, the modal parameters and their relevant derived quantities, and frequency response functions. Thus, each calculation has a huge computational load, which means that model updating is not suitable for performing online. To achieve real-time online updating, alternative techniques use small amount of calculations approaches to replace complex finite element calculation. The main methods include the response surface method, influence matrix method, neural network method, support vector machine (SVM) method, and model reduced method.

The response surface method and the influence matrix method determine the relationship between an explicit function formulated as a transformation of the linear matrix and between the structural response and the updating parameter, by simulating the calculations in advance, which replaces the finite element calculation using a function or the product of a matrix. The neural network and SVM methods simulate the complex functional relationship using intelligent algorithms. A common feature of all of these methods is that a large number of finite element calculation rounds are needed in advance, and then an alternative technique of small amounts of calculations is induced in the process of updating by self-learning algorithm or fitting methods mathematically.

The model reduced method does not require a large number of calculations because it replaces the finite element system with many degrees of freedom in the original calculation with the finite element analyses of a reduced model with few degrees of freedom. The transform matrix of the reduced model, T , is a function of the correction parameters, which is concerned with the iterative calculations. Additionally, the process to generate T is also a complex calculation process which needs large amount of calculations. In the present study, therefore, a dynamic reduced method based on Neumann series is proposed to overcome above mentioned troublesome.

3.4. Automation of the Optimization Algorithm. After constructing the objective function, the model updating problem is transformed into a constrained optimization problem. There are three main categories of methods for solving optimization problems: analytical methods, traditional numerical methods, and intelligent optimization algorithms. In general, if an analytical method is used to solve complex optimization problems, it is almost impossible to achieve the solution because the conditions of the problems cannot meet the requirements of the assumed conditions for the analytical solution. Therefore, numerical methods have many advantages when dealing with complex optimization problems. Some traditional numerical iteration algorithms include Newton's method, the conjugate gradient method, linear programming method, and nonlinear programming method. With multiobjective combinatorial optimization problems, however, the traditional numerical optimization algorithms also have difficulties. The intelligent optimization algorithms that have emerged since the 1980s, such as genetic algorithm, simulated annealing algorithm, ant colony algorithm, PSO, artificial immune algorithms, and hybrid optimization strategies, have been developed by simulating certain natural phenomena or processes to provide feasible solutions for combinatorial optimization problems that are difficult to solve using traditional optimization techniques. From the beginning of the intelligent optimization algorithms are presented, the applications cover all the field of civil engineering are done by researchers, Yi et al. used generalized genetic algorithm and modified monkey algorithm to treat the problem of optimal sensor placement for structural health monitoring [20, 21]. Xu et al. used neural networks method to treat the real-time computing problem in the semiactive control of structures [22, 23]. The PSO is also investigated and

applied on the automation FEM model updating problem by our team [24–26].

We compared most of the optimization algorithms for model updating and found that most algorithms were useful in specific conditions [21–23]. Building an intelligent platform for model updating to make full use of the optimization results can be helpful when selecting a traditional optimization algorithm (such as sequential quadratic programming method) or a modern intelligent optimization algorithm (such as particle swarm intelligent algorithm and evolutionary algorithm) to address different issues, which can make the model updating process more flexible and efficient, so it can be applied to engineering applications.

4. Components of an Intelligent Platform for Structural Health Monitoring System Model Updating

At present, most of the large finite element software systems that are used widely in engineering lack support for model updating, while some finite element software systems that have been developed specifically for model updating do not perform well with conventional finite element analyses, which makes it difficult for them to handle complex engineering structures and they have insufficient optimization ability. Based on the sensitivity analyses theory of model parameter updating and by combining the numerical calculation software MATLAB with the finite element modeling ability ANSYS, we developed an intelligent platform for model updating in a structural health monitoring system. Our system facilitates automated model updating for actual engineering structures because there is an urgent need for health monitoring systems at present. By extracting the general steps of the dynamic-based parametric bridge model updating process, we developed a common software architecture and implemented some key techniques, which should allow the subsequent production of large online bridge updating software.

The commonality of our proposed framework is mainly reflected in the following: the optimization algorithm and target function are modular, so different optimization algorithms and target functions can be selected for different problems; the system is extensible, so the optimization algorithm and target function can be added independently depending on needs, according to certain standards.

4.1. Data Exchange Interface and the Process Control between MATLAB and ANSYS. The ANSYS parametric design language (APDL), which is shipped with ANSYS, can be used for general process control, but it may be more difficult and very slow when implementing specific complex physical models. In the proposed framework, therefore, MATLAB is responsible for the optimization and control process, whereas ANSYS is responsible for finite element calculation. The data generated by MATLAB's optimization module are passed to ANSYS for structure analyses and ANSYS then returns the updating data to MATLAB's optimization module. This cycle is repeated until the results converge. During this process,

to ensure the collaboration between MATLAB and ANSYS, there needs to be smooth transmissions among three types of information: call instructions, data interactions, and the interactions among running state.

There is no ready-made interface between MATLAB and ANSYS, but MATLAB provides some universal methods for calling external programs, such as "!", the DOS function, and the system function. "!" and the DOS function can call a shell program to execute a command required by the Windows system, while the system function can perform operating system commands and return the results.

There is also no direct data exchange system between MATLAB and ANSYS, so the exchange of data must occur via files. We used text files as the medium of data exchange. Text files are simple but they have a high data storage capacity. Both software systems provide suitable functions for reading and writing text files.

Implementing the transfer of status information between two types of software is the key to process control. We achieved the mutual notification of status information by setting up a state variables identification function (flag M). This function judges whether ANSYS is operating by reading the status value in the MATLAB program. Thus, if ANSYS stops running, the flag will be zero and it notifies MATLAB that the current run is over so the next step of the calculation can be run; otherwise MATLAB will wait. The format uses the system or DOS functions to call ANSYS as follows:

```
[status,result]
=system ("D:\Ansys\v110\ANSYS\bin\intel
\anss110 -b -i ansys/ansysconcle
-o output.out")
```

After the ANSYS performs the calculation, the status returns a value of 0. Thus, the returned value of the status can be used to write a flag file, as follows:

```
function flag(status)
if status==0
    out=objfunt4;
    %objfunt4 is the objective function
end
```

4.2. Parametric Finite Element Modeling Solution. The parametric finite element technique refers to the definition of the finite element model structure using a group of undetermined parameters, where the parameters can be the structural geometry size and physical and mechanical properties. During parametric model updating design, the parameters that need to be updated constitute the undetermined parameters of the parameterized finite element model. ANSYS provides a parameter design language (APDL), which is used to complete the finite element analyses automatically. APDL's command is a type of script command, which can provide users with parameters, vectors, cycles, and a series of functions, while a batched analyses technique is also provided by ANSYS.

The basic steps of the parametric finite element analyses method are as follows. First, abstract the characteristic parameters of the described model according to the geometrical structure of the model and simplify them as appropriate. Second, establish the finite element analyses process, including entity modeling, analyses, and results treatment processes, using the command stream file in ANSYS. Third, replace the parameters in the model with abstracted characteristic parameters by APDL, which constitutes the finite element analyses process with variable parameters. Finally, depending on the requirements of the design and analyses, provide specific characteristic values to the parameters and conduct the finite element analyses to obtain the results. The main difference between parametric finite element analyses and general finite element analyses is that the preprocessing geometry model, material property, loading, and boundary conditions are parametric and the parameters must be assigned values before the calculations.

Depending on the basic flow of the parametric finite element analyses, we divide the general finite element model into the corresponding modules shown in Figure 1. Ansysconsole is the main control module of the model, which is responsible for the finite element analyses process control. Text file Inf and Para are the initial parameter files of parametric model, where Inf records the model's calculation type, basic parameters, and so forth and Para records the trial data generated by the optimization algorithm. MCF and MCS are the result files for the finite element analyses, where the former records the modal frequency and the latter records the modal shape. These four files comprise the data module of the model and they are the key components of the interaction with MATLAB, that is, Model, Loading, D&D, and BC form the basic model file, where Model is the initial model, Loading simulates the load conditions, D&D can simulate the damage and performance degradation of the structure, and BC is the model boundary condition. Specific modules can also be added to the fixed format. Finally, Cal_m is the computing core of the model that handles the model analyses.

4.3. Objective Function Library Design. An objective function is a metric used to describe the level of difference between theoretical and experimental model features, which comprised the geometrical and mechanical parameters of the structure. Optimization processes are error-minimizing processes that are applied to the experimental model and the theoretical model. The objective functions used for model updating include static-based objective functions, dynamic-based objective functions, and static and dynamic combined objective functions.

Method for Calling an Objective Function. Because the data generated by the intelligent algorithms are the initial parameters that need to be updated and the data needed by the objective function are the corresponding responses of the structure, an interface function, called parafinder, must be established between the intelligent algorithm and objective function. Its main functions are passing the parameters provided by master program, passing the parameters provided by the optimization algorithm, preliminary processing of the parameters provided by the optimization algorithm, selecting

an objective function, and returning objective function values to the optimization algorithm. The method used to call an objective function is shown in Figure 2.

Objective Function Library. Different objective functions are calculated depending on the parameters transferred from parafinder. Each objective function has its own name and the main functions include obtaining the parameters passed by the master program, obtaining the data produced by the optimization algorithm, and calculating the objective function value. Based on the commonly used objective functions for bridge model updating to produce an objective function library with a standard interface, we developed the objective function library table shown in Table 1. The standard input and output of each objective function are shown in Table 2. In the table, f_{ai} and f_{ti} represent the calculated frequency and test frequency, respectively, ϕ_{ai} and ϕ_{ti} represent the calculated modal vector and test modal vector, respectively, and u_{ai} and u_{ti} represent the calculated static displacement and the measured displacement, respectively.

4.4. Intelligent Algorithm Library Design. After establishing the objective function, the model updating problem is transformed into a constrained optimization problem with multiobjective functions. In this section, the main problem that needs to be solved is developing a method that addresses the model updating problem, that is, the optimization algorithm. MATLAB provides intelligent algorithm libraries, which can be used as tools by the model updating software. We used PSO as a possible method for the intelligent optimization algorithm class library.

The PSO Intelligent Algorithm. The PSO algorithm was inspired by population behavior and has been used to solve optimization problems. In the algorithm, each case represents a potential solution to the problem, where each particle has a corresponding fitness value that is determined by a fitness function. The velocity of a particle determines the direction and distance of the particle's movement, where the velocity is adjusted dynamically based on the particle's experience, thereby allowing individual optimization in the solution space. The calling format for the PSO algorithm is as follows:

```
d_shown=[]; %PSO drawing parameters.
D=; % The dimension of the input.
mv=60; % The largest particle velocity.
VR=[];% Hunting zone.
PSO = [10 300 20 3 3 0.9 0.9 100 1e-25
        2000 1e-5 1 1 1e-5 10 10.0];
% Basic parameters of PSO.
seed=;%Original value.
[optOUT,tr,te,bestpos]
=pso.Trelea.vectorized
('parafinder",D,d_shown,mv,VR,0,PSO,
 "goplotps0",seed);
```

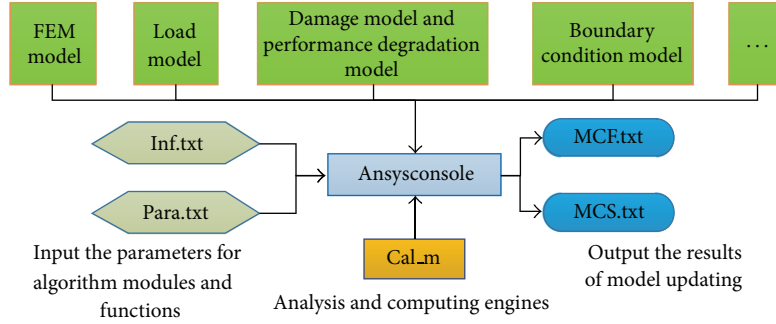


FIGURE 1: Schematic of the parameterized FE model.

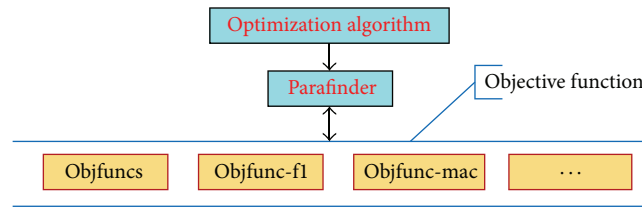


FIGURE 2: Invoking a routine using the target functions library.

TABLE 1: Library of target functions.

Objective function type	Features	Name	Function name
Static-based		Static objective function	Objfuncs
Static and dynamic based		Static and dynamic objective function	Objfunsd
		Frequency	Objfund-f1 Objfund-f2
	Transmission characteristics	Mode of vibration	Objfund-mac1 Objfund-mac2
		Strain mode	Objfund-strain
		Frequency-response function	Objfund-response
	Transmission curvature	Modal curvature	Objfund-mcurvature
		Flexibility curvature	Objfund-fcurvature
Dynamic-based	Characteristic parameter	Frequency band energy spectrum	Objfund-spectrum
		Subband energy spectrum	Objfund-subspectrum
		Joint frequency and mode shape	Objfund-fmac
	Complex function	Flexibility matrix	Objfund-fmatrix
		Modal strain energy	Objfund-starinenergy

TABLE 2: Input-output target functions library.

Objective function	Remarks	Input	Output
Objfun-df1	Frequency change square ratio	f_{ai}, f_{ti}	Depends on its definition [20]
Objfun-df2	Frequency change square ratio	f_{ai}, f_{ti}	Ditto
Objfun-mac1	Modal assurance criterion	ϕ_{ai}, ϕ_{ti}	Ditto
Objfun-mac2	Modal assurance criterion	ϕ_{ai}, ϕ_{ti}	Ditto
Objfun-fmac	Joint frequency and mode shape	$f_{ai}, f_{ti}, \phi_{ai}, \phi_{ti}$	Ditto
Objfuncs	Static objective function	u_{ai}, u_{ti}	Ditto
Objfunsd	Static and dynamic based	$u_{ai}, u_{ti}, f_{ai}, f_{ti}, \phi_{ai}, \phi_{ti}$	Ditto

TABLE 3: Library of intelligent optimization algorithms.

Type	Name	Interface	Input	Output
Traditional algorithm	Sequential quadratic programming	byfmincon	a, b	X_N
Intelligent algorithm	Particle swarm optimization	Bypso	a, b, c, d, e	$A_{M \times N}$
	Genetic algorithm	Byga	a, c, f, g, h, i	$A_{M \times N}$
	Artificial fish-swarm algorithm	Byaf	a, c, j, k, l, m	$A_{M \times N}$
	Ant colony algorithm	Byaca	a, s, n, o, p	$A_{M \times N}$
	Immune algorithms	Byia	a, c, h, i, q, r, s	$A_{M \times N}$
	Annealing algorithm	Bysa	t, u, v, w	$A_{M \times N}$

Parafinder is an interface function between the PSO algorithm and the objective function library.

Intelligent Optimization Algorithm Library. Based on the calling method and the method used to establish the interface function with the PSO algorithm, the standard programming library including other commonly used intelligent optimization algorithms is shown in Table 3.

In Table 3, the parameters of the output X_N , which is an N -dimensional trial vector where N is the number of parameters, are as follows: $A_{M \times N}$ represents an $M * N$ trial matrix, M represents the size of the population, and N represents the number of parameters. The input parameters are as follows: a represents the maximum number of iterations, b represents the convergence error, c represents the size of the population, d represents the algorithm type, e represents the disturbed value, f represents the individual length, g represents the generation gap, h is the crossover probability, i is the mutation probability, j represents the largest feed testing number, k represents perception distance, l represents the crowding degree factor, m represents the moving step, n represents the importance factor of a pheromone, o represents the importance factor of an inspiration function, p represents the pheromone volatilization factor, q represents the volume of a memory database, r represents the evaluation parameters of diversity, s represents the number of distribution centers, t represents the cooling rate, u represents the initial temperature, v represents the termination temperature, and w represents the chain length.

4.5. Technical Proposal and Prototype Software for the Model Updating Platform. After choosing appropriate updating parameters, it is necessary to enter the updating module, where the parameters produced by the optimization algorithm are subjected to finite element analyses to determine the physical quantities that correspond to the measured values. The objective function value is calculated to determine whether the model error has been minimized and to determine whether the iterations should continue; otherwise the updating process is over. The basic flowchart of this process is shown in Figure 3.

Based on processes, the prototype of the overall software framework was implemented using MATLAB in a prototype program. ANSYS was readily implemented in the MATLAB environment to combine the model, objective function, and optimization algorithm, thereby implementing the overall process of automated model updating.

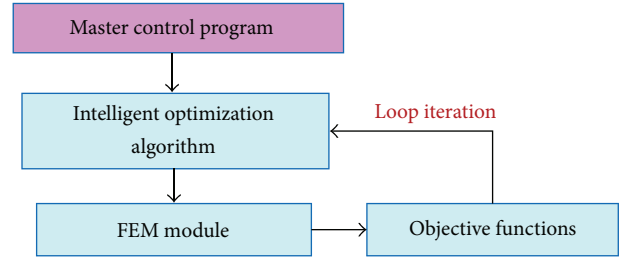


FIGURE 3: Flowchart of the software system for intelligent model updating.

TABLE 4: Parameters to be updated.

Num.	Parameter	Initial value	Upper limit	Lower limit
1	(E) Mpa	3.2×10^4	3.6×10^4	2×10^4
2	(D) kg/m^3	2.5×10^3	2.6×10^3	2.2×10^3
3	(K_1) N-m/rad	1000	1×10^6	0
4	(K_2) N-m/rad	1000	1×10^6	0
5	(K_3) N-m/rad	1000	1×10^6	0
6	(K_4) N-m/rad	1000	1×10^6	0

5. Verification of the Validity of the Prototype Software

5.1. Offline Verification of the Prototype Software Intelligent Updating Platform: Continuous Beam Experiments. The test model was a three-span reinforced concrete continuous beam structure, where the three spans were 1000, 1700, and 1700 mm, respectively, as shown in Figure 4. At the bottom of the continuous beam, there were five positions, that is, A, B, C, D, and E, which were installed with acceleration sensors. The test was a single-point excitation method and the sampling frequency was 512 Hz.

Before model updating, the parameters with greater sensitivity should be selected as the parameters for updating. Based on the structure, the parameters selected are shown in Table 4.

In Table 4, E is the elastic modulus, D is the density, and K_i is the rotational stiffness of the i th bearing.

Based on a model test where the physical quantities were measured, the objective function given in (8) was selected as the m function, Objfund-fmac , from the objective function library. After selecting the PSO algorithm from the intelligent optimization algorithms library and configuring

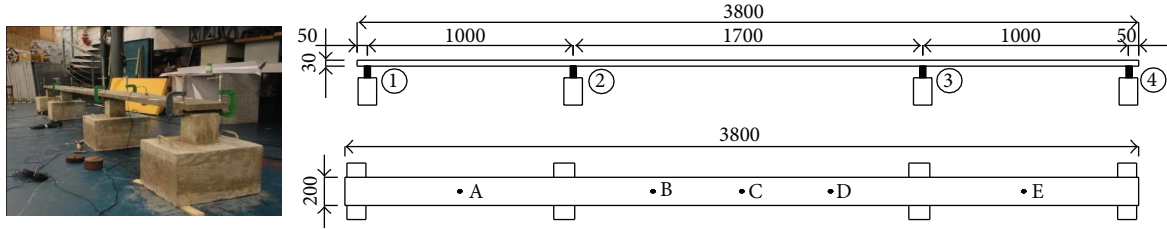


FIGURE 4: Three-span continuous beam test.

TABLE 5: Parameters for updating.

Num.	Parameter	Original values	Updating values
1	(E) Mpa	$3.2e4$	$2.67e4$
2	(D) kg/m^3	$2.5e3$	$2.53e3$
3	(K_1) N-m/rad	1000	48320.33
4	(K_2) N-m/rad	1000	2448.81
5	(K_3) N-m/rad	1000	87109.14
6	(K_4) N-m/rad	1000	233.8

the appropriate operating parameters, the m script automatically performed the task successfully. The objective function approximately reached convergence and the convergence process is shown in Figure 5. The parameters searched are shown in Table 5. A comparison of the model parameters before and after updating is shown in Table 6.

Table 6 shows that the updated frequency was very close to the measured frequency and the testing frequency error was below 1%, with the exception of the third degree. All four MAC values were above 0.9, which shows that the updated model correlated well with the measured model, and this also demonstrated the effectiveness of the updating results. The updating process was simple to write in the MATLAB script where the main contents of the script were model selection, the objective function and optimization algorithm, configuring the input parameters of the calling functions, calling ANSYS, monitoring ANSYS performance, and finally outputting the calculated results file. After launching, the whole process ran automatically and there were no requirements for manual intervention. This example demonstrates the feasibility of our proposed automatic model updating software framework.

5.2. Online Verification of the Prototype Software Intelligent Updating Platform: Cable Force Monitoring. In the previous example, the feasibility of automated model updating was verified offline with measured data. However, it is more challenging and useful to update the structure online using ongoing experimental data. Therefore, we considered the selection of real-time cable monitoring devices on a cable-stayed bridge, which was equipped with structure monitoring system. We connected the prototype software to the monitoring system using a MATLAB program that we developed, which read the data from the remote web-based bridge monitoring system [27], established a web connection to a specific cable acceleration channel, captured the cable

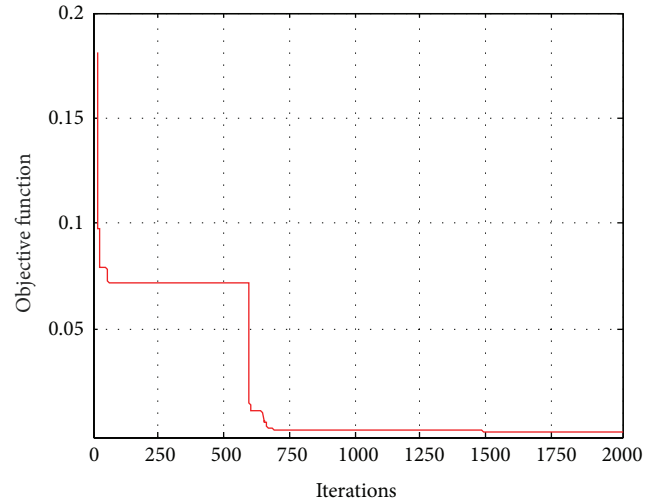


FIGURE 5: Convergence curve of the objective function.

acceleration records automatically using a compiled m script, identified the cable vibration frequency automatically, called the ANSYS program automatically for model analyses by building a finite element model, inputted the measured frequency and the calculated frequency into the objective function automatically, selected the PSO algorithm from the intelligent optimization algorithm library, automatically updated the cable model online, selected the cable force and bending stiffness as the updating parameters, and finally provided the updated results.

Based on the parameters of the cable obtained from the design data, these parameters were given corresponding input variables when calling the parameterized finite element model. The PSO algorithm was selected for updating and the objective function approximately converged after 20 iteration steps. The results for the cable force and bending stiffness are shown in Table 7, where the reference value of the cable force was obtained using the frequency formula and the error between the identified cable force and the calculated cable force was 3.3%. EI_0 represents the identified bending stiffness, while EI_1 and EI_2 represent the bending stiffness when the steel cable was treated as a fully bonding model and as a no binding model, respectively. A comparison of the frequencies derived from model updating and the identified frequencies is shown in Table 8. The curve of the updating process objective function is shown in Figure 6.

As shown in Table 8, the frequency sequences calculated by the automatic model updating prototype software and

TABLE 6: Frequencies and modal shape parameters after updating.

Degree	Test frequency (Hz)	Original frequency (Hz)	Updating frequency (Hz)	Error before updating (%)	Error after updating (%)	MAC before updating	MAC after updating
1	26.38	25.02	26.26	4.76	0.5	0.995	0.98
2	57.68	54.75	58.37	5.06	1.2	0.937	0.989
3	65.22	64.54	65.15	1.05	0.1	0.955	0.979
4	88.49	93.11	87.89	5.22	0.7	0.817	0.901

TABLE 7: Identified cable forces and flexible stiffness.

/	Cable forces (kN)	/	Flexible stiffness (kN·m ²)
Updated value	2900	EI ₀	486
Reference value	3000	EI ₁	511
Error (%)	3.3	EI ₂	3.4

TABLE 8: Frequencies after updating.

Order	Measured frequencies (Hz)	Updated frequency (Hz)	Error (%)
1	1.27	1.304	2.61
2	2.637	2.609	1.07
3	3.906	3.915	0.23
4	5.273	5.223	0.96
5	6.543	6.533	0.15
6	7.91	7.848	0.79
7	9.18	9.166	0.15

the measured frequency sequences were approximately the same; that is, maximum error was 2.61% and the bending stiffness estimate was also reasonable. These results indicate that the proposed model updating prototype software also performs well and reliably in an online environment, which is important for its further development.

6. Conclusions and Prospects

In this study, we developed an intelligent model updating prototype software framework platform, which is based on the commercial finite element software, ANSYS, and the scientific computing software, MATLAB. The proposed parameterized ANSYS finite element modeling scheme is suitable for updating different bridge structure models. We built a standard objective function library for different updating targets. To automate the overall updating process, we constructed an intelligent algorithms library, which included PSO, for different types of updating tasks. The intelligent algorithms library is the driving force of the automated updating process. After careful planning, it can allow the combination of bridge and component models, objective functions, and intelligent algorithms to provide a flexible, efficient, and universal bridge structure model updating platform for online monitoring environments. To illustrate the technical feasibility of our proposed scheme, we implemented the main technical links, which we tested using data from a continuous beam vibrations test and a cable-stayed bridge

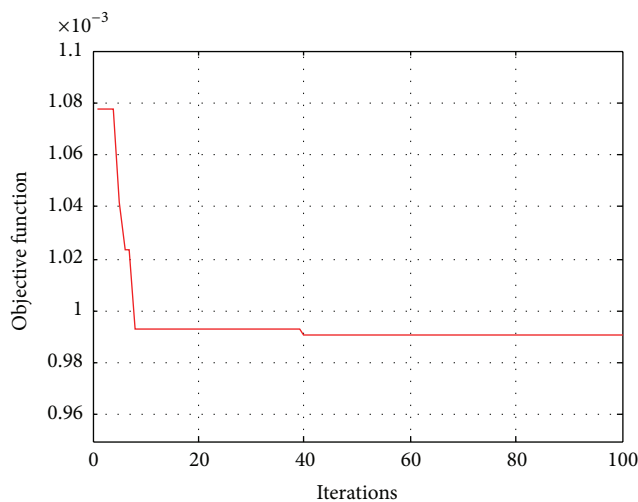


FIGURE 6: Convergence curve for the target function.

monitoring system. The results demonstrated the feasibility of our method for monitoring-based online intelligent model updating.

Conflict of Interests

The authors declare that there is no conflict of interests regarding the publication of this paper.

Acknowledgment

This project was supported by The Project of National Key Technology R&D Program in the 12th Five Year Plan of China (Grant no. 2012BAJ11B01).

References

- [1] C. R. Farrar, F. M. Hemez, D. D. Shunk, D. W. Stinemat, B. R. Nadler, and J. J. Czarnecki, *A Review of Structural Health Monitoring Literature: 1996–2001*, Los Alamos National Laboratory, Los Alamos, NM, USA, 2004.
- [2] K. H. Hsieh, M. W. Halling, and P. J. Barr, “Overview of vibrational structural health monitoring with representative case studies,” *Journal of Bridge Engineering*, vol. 11, no. 6, pp. 707–715, 2006.
- [3] J. Ou, “Research and practice of intelligent sensing technologies in civil structural health monitoring in The Mainland of China,” in *Nondestructive Evaluation for Health Monitoring and*

- Diagnostics*, p. 61761D, International Society for Optics and Photonics, 2006.
- [4] L. Sun, D. Dan, Z. Sun, and Q. Yue, "Health monitoring system for a cross-sea bridge in Shanghai," *IABSE Symposium Report*, vol. 92, no. 28, pp. 9–16, 2006.
 - [5] Z.-D. Xu, M. Liu, Z. Wu, and X. Zeng, "Energy damage detection strategy based on strain responses for long-span bridge structures," *Journal of Bridge Engineering*, vol. 16, no. 5, pp. 644–652, 2011.
 - [6] T.-H. Yi, H.-N. Li, and M. Gu, "Recent research and applications of GPS-based monitoring technology for high-rise structures," *Structural Control and Health Monitoring*, vol. 20, no. 5, pp. 649–670, 2012.
 - [7] J. E. Mottershead and M. I. Friswell, "Model updating in structural dynamics: a survey," *Journal of Sound and Vibration*, vol. 167, no. 2, pp. 347–375, 1993.
 - [8] B. A. Zárate and J. M. Caicedo, "Finite element model updating: multiple alternatives," *Engineering Structures*, vol. 30, no. 12, pp. 3724–3730, 2008.
 - [9] G.-H. Kim and Y.-S. Park, "An improved updating parameter selection method and finite element model update using multiobjective optimisation technique," *Mechanical Systems and Signal Processing*, vol. 18, no. 1, pp. 59–78, 2004.
 - [10] N. Abu Husain, H. Haddad Khodaparast, and H. Ouyang, "Parameter selection and stochastic model updating using perturbation methods with parameter weighting matrix assignment," *Mechanical Systems and Signal Processing*, vol. 32, pp. 135–152, 2012.
 - [11] A. Deraemaeker, P. Ladevèze, and P. Leconte, "Reduced bases for model updating in structural dynamics based on constitutive relation error," *Computer Methods in Applied Mechanics and Engineering*, vol. 191, no. 21–22, pp. 2427–2444, 2002.
 - [12] D. Göge and M. Link, "Assessment of computational model updating procedures with regard to model validation," *Aerospace Science and Technology*, vol. 7, no. 1, pp. 47–61, 2003.
 - [13] J. Carvalho, B. N. Datta, A. Gupta, and M. Lagadapati, "A direct method for model updating with incomplete measured data and without spurious modes," *Mechanical Systems and Signal Processing*, vol. 21, no. 7, pp. 2715–2731, 2007.
 - [14] W.-M. Li and J.-Z. Hong, "New iterative method for model updating based on model reduction," *Mechanical Systems and Signal Processing*, vol. 25, no. 1, pp. 180–192, 2011.
 - [15] W.-X. Ren and H.-B. Chen, "Finite element model updating in structural dynamics by using the response surface method," *Engineering Structures*, vol. 32, no. 8, pp. 2455–2465, 2010.
 - [16] Y. Lu and Z. Tu, "A two-level neural network approach for dynamic FE model updating including damping," *Journal of Sound and Vibration*, vol. 275, no. 3–5, pp. 931–952, 2004.
 - [17] <http://www.femtools.com/courses/updating.htm>.
 - [18] <http://www.sdtools.com/sdt/index.html>.
 - [19] W. Song and S. Dyke, "Development of a cyber-physical experimental platform for real-time dynamic model updating," *Mechanical Systems and Signal Processing*, vol. 37, no. 1–2, pp. 388–402, 2013.
 - [20] T.-H. Yi, H.-N. Li, and M. Gu, "Optimal sensor placement for structural health monitoring based on multiple optimization strategies," *Structural Design of Tall and Special Buildings*, vol. 20, no. 7, pp. 881–900, 2011.
 - [21] T. H. Yi, H. N. Li, and X. D. Zhang, "A modified monkey algorithm for optimal sensor placement in structural health monitoring," *Smart Materials and Structures*, vol. 21, no. 10, Article ID 105033, 2012.
 - [22] Z.-D. Xu, Y.-P. Shen, and Y.-Q. Guo, "Semi-active control of structures incorporated with magnetorheological dampers using neural networks," *Smart Materials and Structures*, vol. 12, article 80, 2003.
 - [23] Z.-D. Xu, "Earthquake mitigation study on viscoelastic dampers for reinforced concrete structures," *Journal of Vibration and Control*, vol. 13, no. 1, pp. 29–43, 2007.
 - [24] T. Yang, *A study on the model updating techniques under the health monitoring environment. [Dissertation for master degree]*, Tongji University, 2012, (Chinese).
 - [25] P. Zhang, *PSO based model updating on cables and its tension identification. [Dissertation for master degree]*, Tongji University, 2010, (Chinese).
 - [26] Y. Chen, *PSO based cable damper system parameter identification. [Dissertation for master degree]*, Tongji University, 2012, (Chinese).
 - [27] D. Dan, L. Sun, and Y. Wang, "Applying online identification on Donghai Bridge anywhere, anytime, and anyway," in *Proceedings of the 6th World Forum on Smart Materials and Smart Structures Technology (SMSST '07)*, vol. 1, pp. 677–684, May 2007.

Research Article

A Method of Data Recovery Based on Compressive Sensing in Wireless Structural Health Monitoring

Sai Ji,^{1,2} Yajie Sun,^{2,3} and Jian Shen¹

¹ Jiangsu Engineering Center of Network Monitoring, Nanjing University of Information Science & Technology, Nanjing 210044, China

² State Key Laboratory of Mechanics and Control of Mechanical Structures, Nanjing University of Aeronautics and Astronautics, Nanjing 210016, China

³ School of Information and Control, Nanjing University of Information Science & Technology, Nanjing 210044, China

Correspondence should be addressed to Sai Ji; jisai@nuist.edu.cn

Received 8 October 2013; Revised 11 December 2013; Accepted 13 December 2013; Published 12 January 2014

Academic Editor: Jun Li

Copyright © 2014 Sai Ji et al. This is an open access article distributed under the Creative Commons Attribution License, which permits unrestricted use, distribution, and reproduction in any medium, provided the original work is properly cited.

In practical structural health monitoring (SHM) process based on wireless sensor network (WSN), data loss often occurs during the data transmission between sensor nodes and the base station, which will affect the structural data analysis and subsequent decision making. In this paper, a method of recovering lost data in WSN based on compressive sensing (CS) is proposed. Compared with the existing methods, it is a simple and stable data recovery method and can obtain lower recovery data error for one-dimensional SHM's data loss. First, response signal x is measured onto the measurement data vector y through inner products with random vectors. Note that y is the linear projection of x and y is permitted to be lost in part during the transmission. Next, when the base station receives the incomplete data, the response signal x can be reconstructed from the data vector y using the CS method. Finally, the test of active structural damage identification on LF-21M aviation antirust aluminum plate is proposed. The response signal gathered from the aluminum plate is used to verify the data recovery ability of the proposed method.

1. Introduction

In wireless sensor networks for structural health monitoring [1–3], a large number of sensor nodes are deployed in the monitoring area [4] to implement data sensing and data acquisition in real time. Such information of structural health status is sent to the base station for users to make decisions. However, data loss in wireless sensor networks is common and it is heavily affected by hardware (such as faulty sensors), network communication interference (such as noise, collision and unreliable link during the communication), wireless conditions (such as WSN's scale), and so on. In particular, in SHM, complex structures and harsh environments often lead to continuous data loss or random data loss during the data transmission. Such imperfect data will affect the accuracy of identification of structural damage and thus will lead to wrong decisions. For the influence of lost data on structural analysis, Nagayama et al. [5] carried out an experimental study on the imote2 based SHM_A platform. Their experimental results show that the loss of 0.5 percent

of data affects the coherence function in a similar way as 5 to 10 percent measurement noise addition. They also explain that a loss of 0.5 percent data might be acceptable, considering that corresponding 5 to 10 percent observation noise is unexceptional in SHM. However, due to limited resources and geographical location, data loss rate during transmission is up to 20% even reaches and 86%. Now, data loss is a critical problem in wireless sensor network based structural health monitoring.

To solve the problem, some data recovery methods [6–8] were proposed. Aktan et al. [6] used linear regression method and average method to realize the lost data recovery. These methods have a large data recovery error, as well as impractical. Hu et al. [7] presented a method of radical basis function (RBF) neural networks to restore the bridge deflection data loss. Zhao et al. [8] proposed the data restoring method by using back propagation (BP) neural networks to solve the problem of strain monitoring data loss in performance monitoring of large-span steel sky bridge. Although RBF or

BP neural networks can predict unknown lost data, it is difficult to choose the appropriate neural network model. Even for the same monitoring area, the approach to establish a neural network model is not the same from different angles. To overcome the disadvantages of the above methods, a powerful and generic technique for estimating missing data based on compressive sensing is proposed. The existing methods based on CS [9–11] can recover an entire dataset from only a small fraction of data. Kadhe et al. [9] integrated the emerging framework of CS with real expander codes for reliably transmitting image data in multimedia sensor networks. Pudlewski et al. [10] presented a system which uses CS to encode, compress, and protect an image from channel errors and packet losses. Although they can realize the reliable data transmission for two-dimensional image data, the two methods can not be directly applied to SHM's data loss. Since the collected data from SHM is real-time one-dimensional data by high-frequency sampling and is different from image data, a new method for estimating one-dimensional lost data should be studied in SHM. Charbiwala et al. [11] explored the application of CS to handle data loss from erasure channels by viewing it as a low encoding-cost, proactive, and erasure correction scheme. But the method has a relatively large recovery data error and can not satisfy the requirements of SHM. In this paper, we proposed a simple and stable data recovery approach based on CS which can obtain lower recovery data error for one-dimensional SHM's data loss. Instead of transmitting response signal, the CS method transfers the linear measurement data between sensor nodes and base station in WSN. The linear measurement data, which is allowed to be lost in part during the transmission, can be reconstructed into response signal in the base station.

The rest of this paper is organized as follows. In Section 2, related works of the CS and introduction of the sparse representation in data recovery method are presented. In Section 3, the procedure of lost data recovery is introduced. Experiments on perforated LF-21M aluminum plate are provided in Section 4 to verify the effectiveness of the proposed method. Summaries are covered in Section 5.

2. Related Work

2.1. A Summary for CS. Compressive sensing (CS) provides an alternative to Shannon/Nyquist sampling when signal under acquisition is known to be sparse or compressible [12, 13]. Mainly, CS theory includes three parts: the sparse representation of the signal, the sensing matrix ensuring the data minimal information loss, and the reconstruction algorithm using the no-distortion observed value to reconstruct signals.

In the process of sparse representation, signals are measured through inner products with random vectors and thus fewer measurements than periodic samples are needed. Suppose that x is original signal, y is measurement signal, and \hat{x} is reconstructed signal from y . In particular, x in SHM is also called response signal. For any N -dimensional response signal x , its measurements y is taken as follows:

$$y = \Phi x, \quad (1)$$

where $x \in R^N$ is N -dimensional response signal, $y \in R^M$ is M -dimensional linear measurement data, and $\Phi \in R^{M \times N}$ ($M \ll N$) is the sensing matrix. Usually, the response signal is not absolutely sparse. If it can be an approximate sparse signal in some transform domains such as Fourier domain or wavelet domain, we considered that it is compressible signal. So, through one of the orthogonal transformations Ψ , let $x = \Psi\alpha$; we can achieve sparse representation as follows:

$$y = \Phi x = \Phi\Psi\alpha = \Theta\alpha, \quad (2)$$

where $\Psi \in R^{N \times N}$ is the orthogonal transformations matrix and α is the K -sparse decomposition coefficients in the Ψ transform domain. Note that K is the number of nonzero values in α and K should be a small value. Without loss of generality, we denote the matrix multiplication $\Phi\Psi$ as a single sensing matrix Θ . So, formula (2) can be regarded as the linear projection of original signal x with Φ , and it could be also viewed as the linear projection of transform decomposition coefficients α in Θ . If y and $\Theta = \Phi\Psi$ meet with the restricted isometry property (RIP) [14], K -sparse decomposition coefficients α can be reconstructed by solving the l_0 norm [15] from y as follows:

$$\hat{\alpha} = \arg \min \|\alpha\|_0 \quad \text{s.t. } \Theta\alpha = y, \quad (3)$$

where $\hat{\alpha}$ is the only exact solution of decomposition coefficients α . Then, the exact solution \hat{x} can be obtained by reconstructing $\hat{\alpha}$ under the orthogonal transform basis Ψ shown as follows:

$$\hat{x} = \Psi\hat{\alpha}. \quad (4)$$

To further demonstrate the intrinsic relationship between Ψ and Φ , while $\Theta = \Phi\Psi$ met with the RIP, Baraniuk [16] proposed that the equivalence condition of the RIP which is Φ irrelevant with Ψ ; that is, the Θ row vector cannot be represented by Ψ column vector, and the Ψ row vector cannot be represented by Θ column vector. Therefore, we select tectonic Φ sensing matrix, such as Gaussian random matrix, in the orthogonal base matrix Ψ which is fixed to make $\Theta = \Phi\Psi$ satisfy with RIP in this paper.

In the process of signal reconstruction, the algorithm is mainly divided into three categories which are greedy algorithm [17], convex optimization algorithms [18, 19], and the sparse Bayesian statistical optimization algorithm [20]. The most typical algorithm is matching pursuit (MP) algorithm [18] and orthogonal matching pursuit (OMP) algorithm [19]. Among them, OMP is an efficient reconstruction algorithm in CS for recovering sparse signals despite its high computational cost for solving large scale problems. It is a simple, stable, and fast reconstruction algorithm. In this paper, we used OMP algorithm as the stabled reconstruction method.

2.2. Lost Data Recovery Method Based on CS. On the basis of the above CS theory, the lost data recovery method based on CS also contains three parts. The last two parts of the sensing matrix selection and the reconstruction algorithm selection

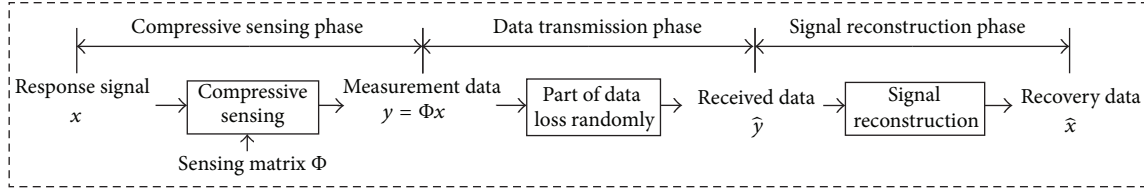


FIGURE 1: Procedure of the data recovery method.

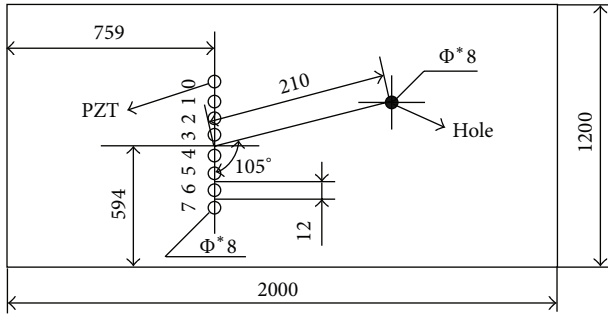


FIGURE 2: Structure diagram (unit: mm).

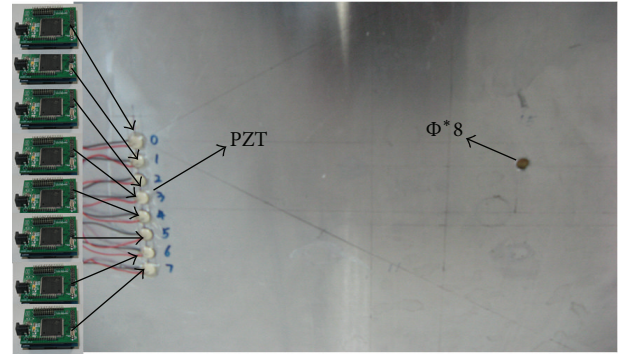


FIGURE 3: Perforated aluminum specimen.

are similar to those of the above method in lost data recovery method. But the first part of signal's sparse representation is different from the common CS theory.

In the process of sparse representation, suppose that we acquire an $M (= N)$ length linear measurement data vector $y \in R^M$ by the linear projection of $x \in R^N: y = \Phi x$. Considering the randomly data loss of the M length linear measurement data y during transmission, the received data on base station is $y \in R^{M-M_L}$, where $y \in R^{M-M_L}$ is an $\widehat{M} = M - M_L$ -dimensional linear measurement data vector and M_L is the number of lost data of y . Then, the measurement data with lost data can be shown as

$$\widehat{y} = \widehat{\Phi}x = \widehat{\Phi}\Psi\alpha = \widehat{\Theta}\alpha, \quad (5)$$

where $\widehat{\Phi}$ and $\widehat{\Theta}$ are corresponding sensing matrix with $\widehat{M} = M - M_L$ rows vectors lost. If \widehat{y} and $\widehat{\Theta} = \widehat{\Phi}\Psi$ meet with the RIP, K -sparse decomposition coefficients α can be reconstructed by solving the l_0 norm from \widehat{y} as follows:

$$\widehat{\alpha} = \arg \min \|\alpha\|_0 \quad \text{s.t.} \quad \widehat{\Theta}\alpha = \widehat{y}. \quad (6)$$

When the base station receives the incomplete data \widehat{y} , the response signal x can also be reconstructed from the decomposition coefficients $\widehat{\alpha}$ under the orthogonal transform basis Ψ . The formula is same as the formula (2).

3. The Procedure of Proposed Data Recovery Method

The procedure of the lost data recovery method based on CS can be presented as three phases, which is shown in Figure 1. First, in the compressive sensing phase, the response signal x is transformed into linear measurement data y through

inner products with random sensing matrix Φ . The obtained measurement data $y = \Phi x$ will be transmitted between nodes and base station. Next, in the data transmission phase, measurement data y may be randomly lost part of data in wireless transmission. The received data in the base station will be changed to \widehat{y} . Finally, in the signal reconstruction phase, the original response signal \widehat{x} is reconstructed from the received \widehat{y} based on the formula (5), formula (6), and formula (2).

4. Investigation Results for the Proposed Method in SHM

4.1. Introduction of Data Acquisition System Based on CS. In order to get the effective and real data of the experiments, we designed a data acquisition experimental system. Figure 2 is the schematic diagram of the aluminum plate pasted piezoelectric patch which basic dimension is $1200 \times 2000 \times 1.5$ (mm). The diameter of the eight piezoelectric patches is Φ^*8 mm and the thickness is 0.2 mm. Center spacing of two adjacent piezoelectric patches is 12 mm. Moreover, the eight piezoelectric patches labels are 0~7 from the bottom up orderly. The circle marked Φ^*8 mm on the figure is a borehole on aluminum plate for the simulation of structural damage location.

Figure 3 is the perforated LF-21M aluminum specimen. The sensor node on the figure is a kind of self-developed high speed wireless piezoelectric sensor nodes, which has the active excitation function. The stimulus signal frequency of sensor node is up to 100 kHz and can meet the needs of active health monitoring. In the data acquisition process, a narrowband modulated sinusoidal signal is used for stimulus signal, whose center frequency is 40 KHZ, amplitude is

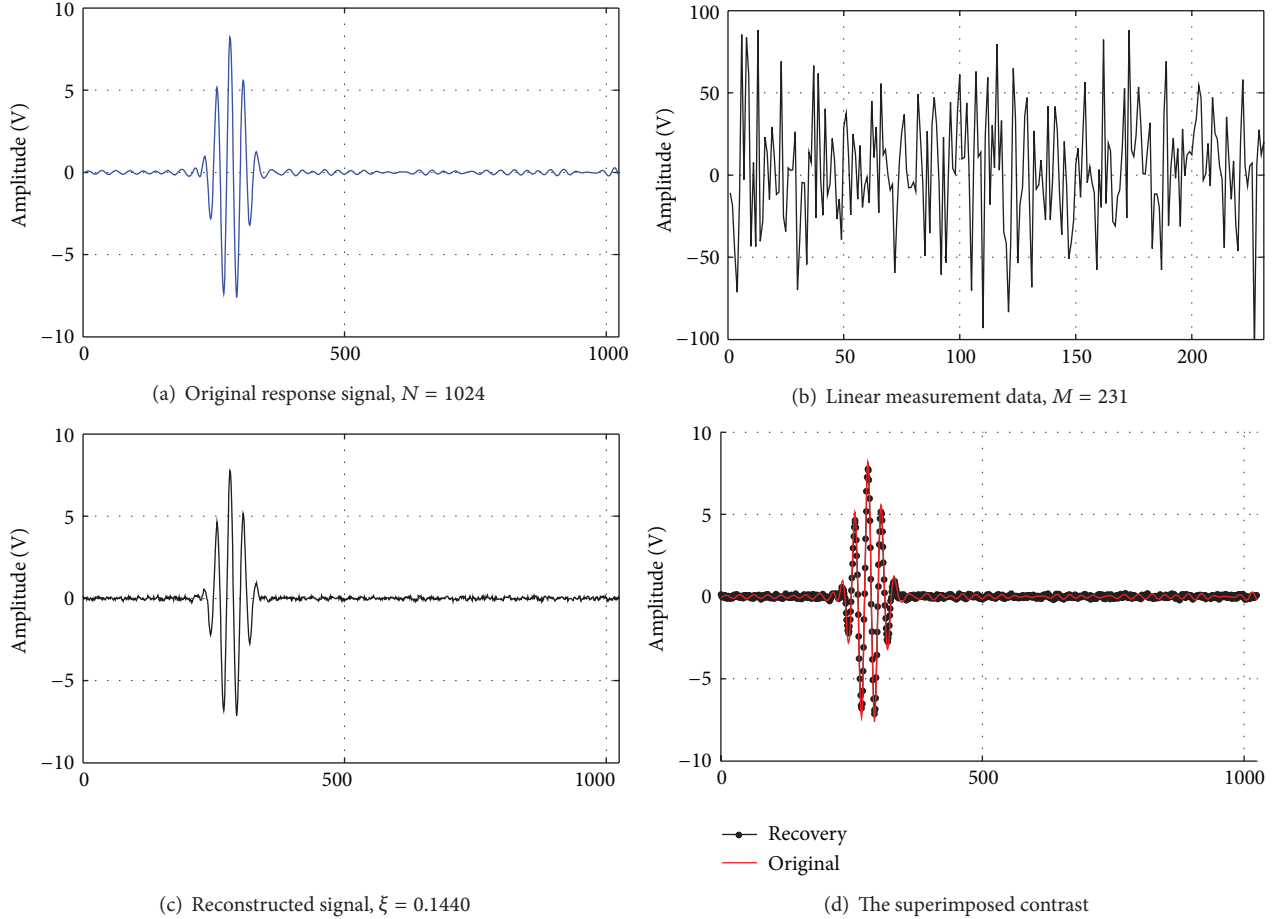


FIGURE 4: The analysis for signal reconstruction based on CS.

± 10 V and the peak number is five. We used the polling method for data collection. Each of the eight piezoelectric patches is selected as the driver in turn, while the rest of the piezoelectric patches are used as the receiver. Each receiver should collect the data of reflection wave on the direction of $0^\circ \sim 180^\circ$. Note that the data of reflection wave is also called original response signal.

A typical original response signal gathered from aluminum plate by sensors is shown in Figure 4(a). The sampling frequency is 1 MHz and collected 1024 points. It can be seen that the response signals are nearly sparse because part of the point is near to zero. Using Gaussian random matrix as sensing matrix, Figure 4(b) is the linear measurement data from original response signal. The reconstructed signal by OMP algorithm is shown in Figure 4(c), and the relative error of the reconstructed signal is $\xi = 0.1440$. The superimposed contrast between reconstructed signal and the original one is in Figure 4(d), and the result shows the well reconstruction.

4.2. The Analysis of Lost Data Recovery Results

4.2.1. Reconstruction Error Definition. In order to evaluate the performance of data recovery method, we define the parameter of the reconstruction error. Reconstruction error (ξ) is

on behalf of the similarity degree of the reconstructed signal and the original one. It is an important indicator to measure the effects of data decompression which is written as formula (7), where \hat{x} , x separately indicated the reconstructed signal and the original one. The smaller the reconstruction error is, the higher the data recovery accuracy of the compressed sensing reconstruction algorithm is.

Consider

$$\xi = \frac{\|\hat{x} - x\|_2}{\|x\|_2}. \quad (7)$$

4.2.2. Loss Data Set and Packet Loss Probability Definition. In this example, an original response data sequence is defined as $x(n)$, $n = 1, 2, 3, \dots, N$. In the practical application of SHM, the performance of structural damage identification may be affected when the length of the collected data is less than 1024. So, the acquisition data in SHM is usually more than 1024; that is, $N \geq 1024$. With the increase of the length of N (such as $N = 2048$), the number of signal's zero value increases and the performance of the proposed method based on CS is getting better. Therefore, in order to satisfy the requirements of SHM, we take the lower limit of the length $N = 1024$. Keep

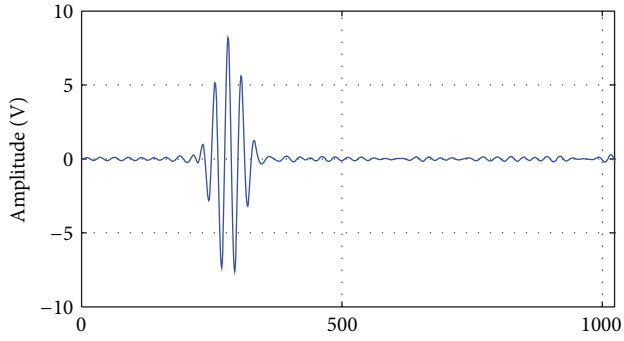
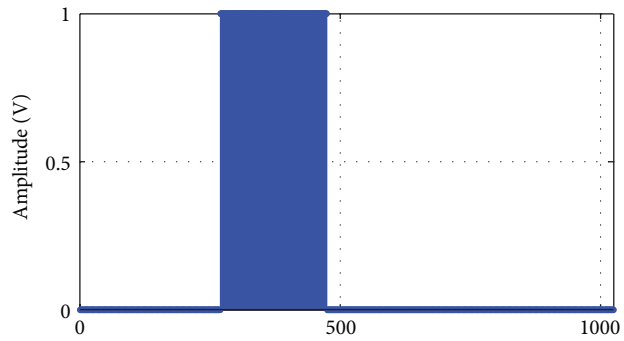
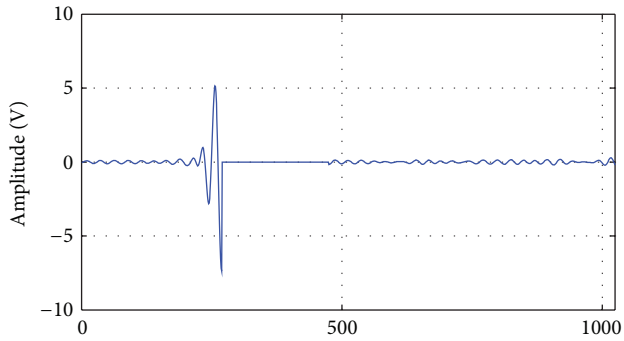

 (a) Original response signal, $N = 1024$

 (b) Simulated loss data sets, $p = 20\%$

 (c) Received data, $p = 20\%$, $M = 1024$

FIGURE 5: Response data with 20% continuous data loss in transmission.

the length of linear measurement data same as the original data; that is, $M = N = 1024$. Therefore, there is no any increasing data acquisition cost for the proposed loss data recovery method.

In the actual transmission, the packet loss probability of data can not be accurately controlled. Therefore, a simulation data loss is proposed to verify the feasibility of the data recovery method. To simulate the data loss process in data transmission, including continuous data loss and random data loss, we design a loss data set $q(n)$, $n = 1, 2, \dots, N$, which is shown in Figures 5(b) and 6(b). Among them, Figure 5(b) is a continuous loss data set and Figure 6(b) is a random one. The value of $q(n)$ is always equal to zero or one. Replacing the original response signal with zero value in the data loss position, then the received data $x_L(n)$ on base

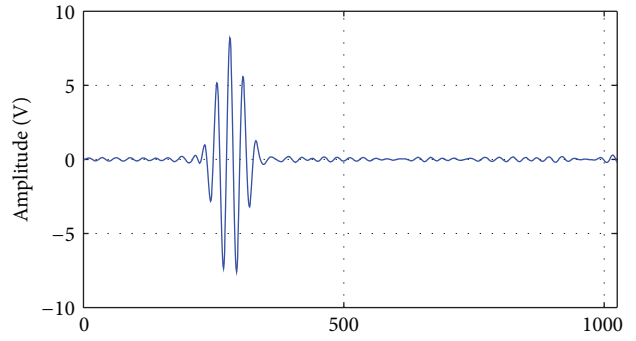
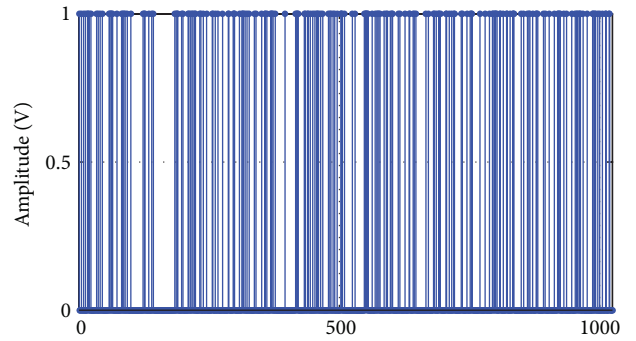
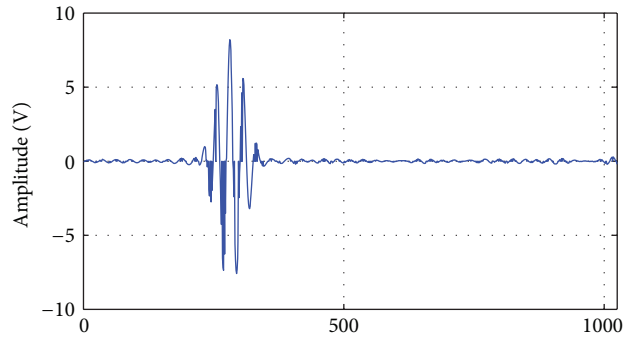

 (a) Original response signal, $N = 1024$

 (b) Simulated loss data sets, $p = 20\%$

 (c) Received data, $p = 20\%$, $M = 1024$

FIGURE 6: Response data with 20% random data loss in transmission.

station are shown in Figures 5(c) and 6(c). Such process of simulation data loss can be presented as formula (8), where $x(n)$ is the original response signal and $x_L(n)$ is the received data with data loss in part during transmission:

$$x_L(n) = x(n) \times (1 - q(n)), \quad n = 1, 2, 3, \dots, N. \quad (8)$$

According to the loss data set $q(n)$, the packet loss probability p can be defined as the ratio of loss data number and response data length, which is written as formula (8), where N is the length of original response data sequence, and here, $N = 1024$. The formula $\sum_{n=1}^N q(n)$ is the number of sequence points whose value is equal to one in loss data set. To investigate the loss data recovery ability, the packet loss probability is $p = (0.05, 0.1, 0.15, 0.2, \dots, 0.4)$ in the simulation.

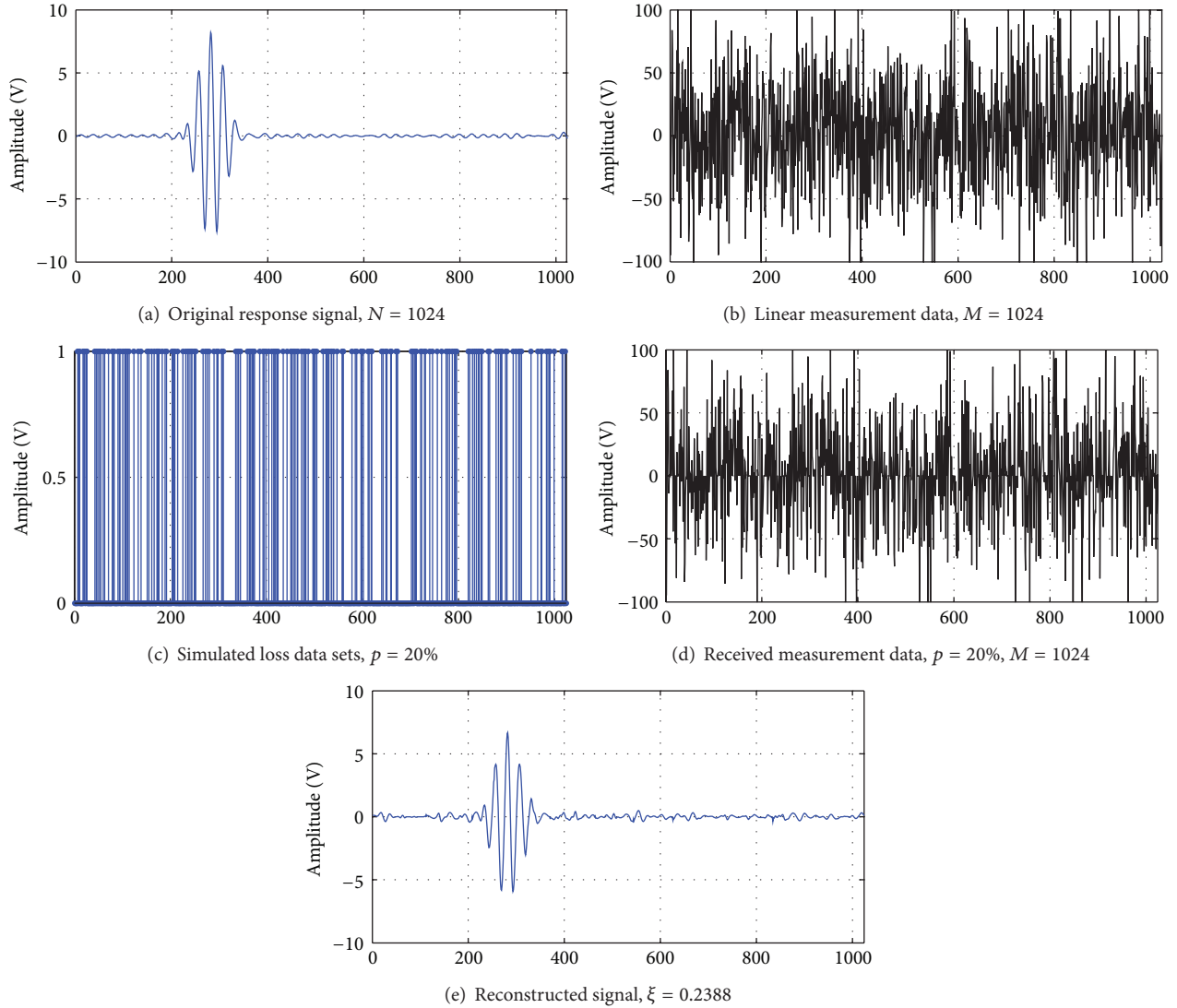


FIGURE 7: Data recovery with 20% random data loss.

Consider

$$p = \frac{\sum_{n=1}^N q(n)}{N}. \quad (9)$$

The simulated data loss process is shown in Figures 5 and 6. Figure 5 describes the process of response signal continuous loss 20% data in data transmission, where Figure 5(a) is the original response signal and its length is 1024. When there is a response signal with 1024 length continuous loss 20% data, the length of loss data is $M_L = \lceil 1024 \times 20\% \rceil = 205$, where the $\lceil \cdot \rceil$ is the function that can round up the value to integer. Figure 5(b) is the location of 20% selected lost data in loss data set; the data sequence number from 270 to 475 is lost. Figure 5(c) is the received data with 20% continuous data loss on base station. Figure 6 is the process of response data with 20% random data loss and its process is similar as in Figure 5. Without loss of generality,

we will choose the random data loss in the next experiment analysis.

4.2.3. Random Data Loss in Part with Fixed $p = 0.20$. To illustrate the procedure of the loss data recovery, an example of data recovery based on CS with 20% data random loss is shown in Figure 7. Figure 7(a) shows the original response data x with 1024 sequence points. The linear measurement data y is calculated by $y = \Phi x$ and will be sent to base station, as shown in Figure 7(b), where the sensing matrix Φ is a Gaussian random matrix with zero mean and unit variance. Figure 7(c) is a loss data set of location $q(n)$ with 20% randomly data loss of y . After the base station received the data \hat{y} with random data loss in part, as shown in Figure 7(d), it can reconstruct and recover the response signal. The reconstructed data \hat{x} can be calculated by formula

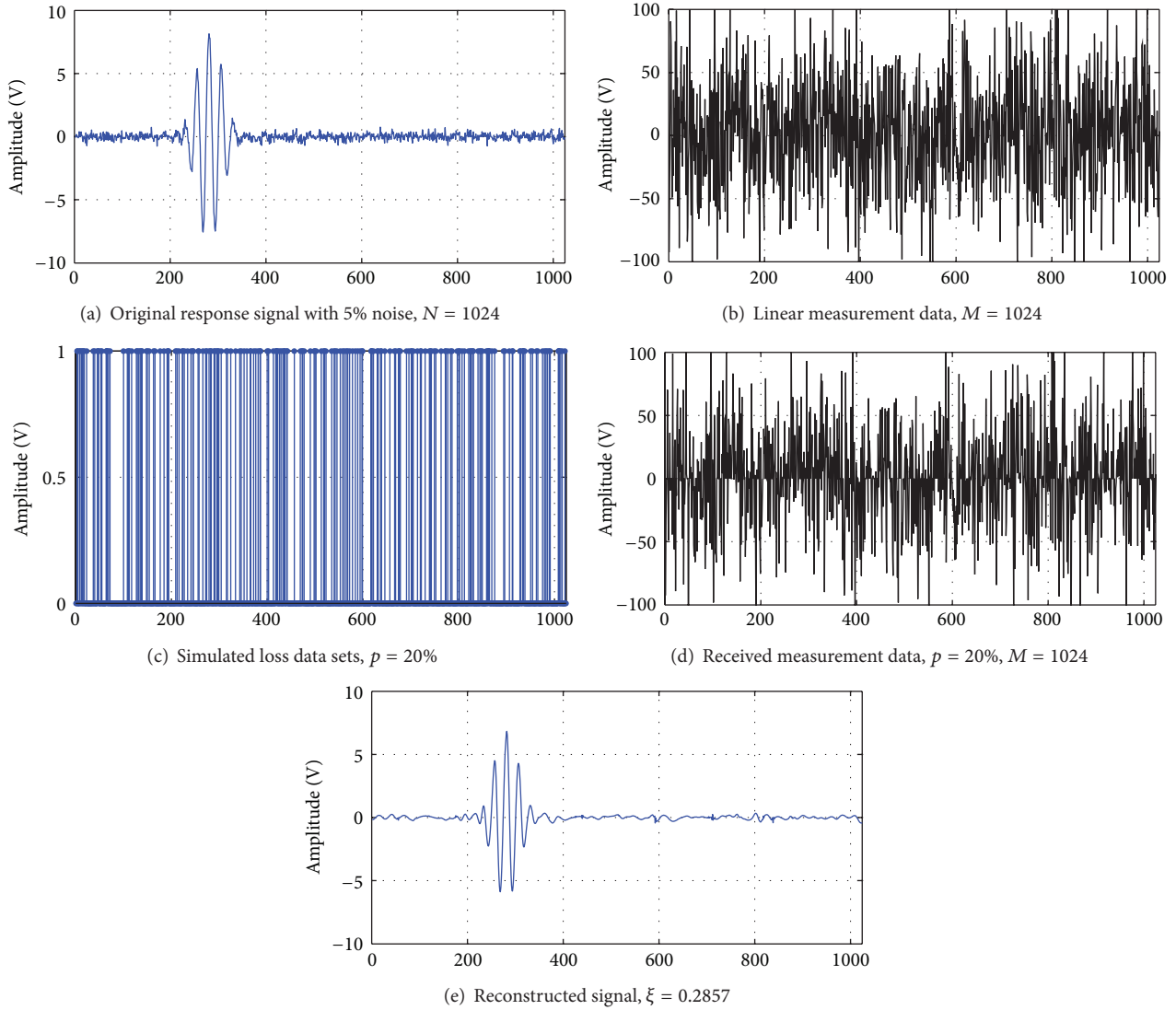


FIGURE 8: Data recovery with 20% random data loss and with 5% noise.

(4) and the result with reconstruction error $\xi = 0.2388$ is shown in Figure 7(e).

During the experiment of our SHM, 5% or less than 5% noise corruption may be found. To verify immunity and robustness of the proposed method to noise, the noise corruption on the transform data y also be considered besides considering the data random loss. Considering the additional 5% noise corruption on the original response data, the result is shown in Figure 8 and the reconstruction error ξ is 0.2857.

The results of the two experiments show that when the packet loss probability is fixed at 20%, the proposed method has good effect in random lost data recovery.

4.2.4. Random Data Loss in Part with Different p . The investigation of data recovery above is in the fixed packet loss probability, but different parameter of p will produce different

effect on the recovery. To further analyze the performance of the proposed method, we change the range of p value from 0.05 to 0.4 and verify the ability of data recovery method at different p .

The results of two experiments, including with 5% noise method and without noise method, are shown in Figure 9. The trend lines of reconstruction error in Figure 9 show that with the increase of p , the reconstruction errors are rising steadily. Overall, the error values of with 5% noise method are higher than the method without noise. Within a range of $p \in [0.05, 0.4]$, the former method has an error value range between 0.1893 and 0.4859, while the latter method has a minimum error value of 0.1185 and a maximum of 0.4999. The experimental results show that the proposed method has good recovery performance on random data loss at different packet loss probability. In the practical application of SHM, the reconstruction errors ξ should be less than 0.3 so as to satisfy the engineering requirement. Therefore, the p must be

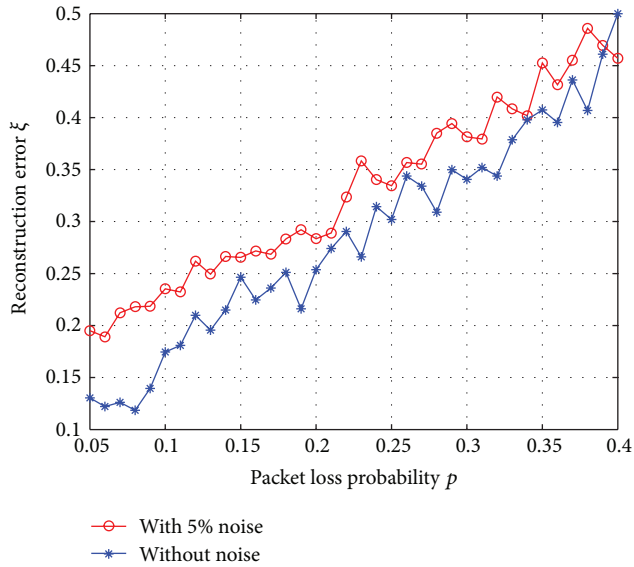


FIGURE 9: Reconstruction error at different packet loss probability in random data loss in part.

less than 0.23 in the method without noise and must be less than 0.21 in the method with 5% noise, which is shown in Figure 9.

5. Conclusions

This paper proposed a novel method based on CS for loss data recovery in wireless structural health monitoring. First, the original response signal was measured by a random Gaussian sensing matrix so as to generate a linear measurement data vector, where data loss in part is allowed in wireless data transmission. Secondly, the response signal is reconstructed by linear measurement data with part loss by OMP reconstruction algorithm. Finally, an example of the wireless sensor data measured from a real LF-21M aluminum plate is collected so as to illustrate the data recovery ability of the proposed method. Experiments results show that the proposed data recovery method can recover signals with data loss in part and resist to the additional noise corruption during the data transmission.

Conflict of Interests

The authors declare that there is no conflict of interests regarding the publication of this paper.

Acknowledgments

This work was a project supported by the Natural Science Foundation of the Jiangsu Higher Education Institutions of China (Grant no. 11KJB520011), the Natural Science Foundation of China (Grant no. 51305211 and Grant no. 61300237), and the PAPD.

References

- [1] T.-H. Yi, H.-N. Li, and M. Gu, "Experimental assessment of high-rate GPS receivers for deformation monitoring of bridge," *Measurement*, vol. 46, no. 1, pp. 420–432, 2013.
- [2] J. Wu, S. Yuan, X. Zhao, Y. Yin, and W. Ye, "A wireless sensor network node designed for exploring a structural health monitoring application," *Smart Materials and Structures*, vol. 16, no. 5, pp. 1898–1906, 2007.
- [3] L. Qiu and S.-F. Yuan, "A phase synthesis time reversal impact imaging method for on-line composite structure monitoring," *Smart Structures and Systems*, vol. 8, no. 3, pp. 303–320, 2011.
- [4] T.-H. Yi, H.-N. Li, and M. Gu, "Sensor placement for structural health monitoring of Canton Tower," *Smart Structures and Systems*, vol. 10, no. 4, pp. 313–329, 2012.
- [5] T. Nagayama, S. H. Sim, Y. Miyamori, and B. F. Spencer Jr., "Issues in structural health monitoring employing smart sensors," *Smart Structures and Systems*, vol. 3, no. 3, pp. 299–329, 2007.
- [6] E. Aktan, S. Chase, D. Inman, and D. Pines, "Monitoring and managing the health of infrastructure systems," in *Health Monitoring of Highway Transportation Infrastructure*, vol. 3 of *Proceedings of the SPIE*, pp. 6–8, 2001.
- [7] S.-R. Hu, W.-M. Chen, P. Zhang et al., "Research of bridge deflection restoring based on RBF neural networks," *Chinese Journal of Scientific Instrument*, vol. 27, no. 12, pp. 1605–1608, 2006.
- [8] X. Zhao, J. Jia, and Y.-M. Zheng, "Strain monitoring data restoring of large-span steel skybridge based on BP neural network," *Chinese Journal of Architecture and Civil Engineering*, vol. 27, no. 1, pp. 101–106, 2006.
- [9] S. Kadhe, S. Thaskani, M. G. Chandra, and B. S. Adiga, "Reliable data transmission in sensor networks using compressive sensing and real expander codes," in *Proceedings of the National Conference on Communications (NCC '12)*, vol. 1, pp. 1–5, Kharagpur, India, 2012.
- [10] S. Pudlewski, A. Prasanna, and T. Melodia, "Resilient image sensor networks in lossy channels using compressed sensing," in *Proceedings of the 8th IEEE International Conference on Pervasive Computing and Communications Workshops (PERCOM '01)*, pp. 62–67, Mannheim, Germany, 2010.
- [11] Z. Charbiwala, S. Chakraborty, S. Zahedi et al., "Compressive oversampling for robust data transmission in sensor networks," in *Proceedings of the IEEE International Conference on Computer Communications (INFOCOM '10)*, San Diego, Calif, USA, 2010.
- [12] D. L. Donoho, "Compressed sensing," *IEEE Transactions on Information Theory*, vol. 52, no. 4, pp. 1289–1306, 2006.
- [13] E. Candes, "Compressive sampling," in *Proceedings of the International Congress of Mathematicians*, pp. 1433–1452, European Mathematical Society Publishing House, Madrid, Spain, 2006.
- [14] E. J. Candes and T. Tao, "Decoding by linear programming," *IEEE Transactions on Information Theory*, vol. 51, no. 12, pp. 4203–4215, 2005.
- [15] E. J. Candes, J. Romberg, and T. Tao, "Robust uncertainty principles: exact signal reconstruction from highly incomplete frequency information," *IEEE Transactions on Information Theory*, vol. 52, no. 2, pp. 489–509, 2006.
- [16] R. G. Baraniuk, "Compressive sensing," *IEEE Signal Processing Magazine*, vol. 24, no. 4, pp. 118–124, 2007.
- [17] J. A. Tropp and A. C. Gilbert, "Signal recovery from random measurement via orthogonal matching pursuit," *IEEE Transactions on Information Theory*, vol. 53, no. 12, pp. 4655–4666, 2007.

- [18] S. S. Chen, D. L. Donoho, and M. A. Saunders, "Atomic decomposition by basis pursuit," *SIAM Journal on Scientific Computing*, vol. 43, no. 1, pp. 129–159, 2001.
- [19] S. J. Kim, K. Koh, M. Lustig et al., "Gorinevsky: a method for large scale regularized least squares," *IEEE Journal on Selected Topics in Signal Processing*, vol. 4, no. 1, pp. 606–617, 2007.
- [20] S. Ji, Y. Xue, and L. Carin, "Bayesian compressive sensing," *IEEE Transactions on Signal Processing*, vol. 56, no. 6, pp. 2346–2356, 2008.

Research Article

Structural Damage Identification Based on the Minimum System Realization and Sensitivity Analysis

W. R. Li,^{1,2} Y. F. Du,^{1,2} S. Y. Tang,¹ and L. J. Zhao¹

¹ Key Laboratory of Disaster Prevention and Mitigation in Civil Engineering of Gansu Province, Lanzhou University of Technology, Lanzhou 730050, China

² Western Engineering Research Center of Disaster Mitigation in Civil Engineering of Ministry of Education, Lanzhou University of Technology, Lanzhou 730050, China

Correspondence should be addressed to Y. F. Du; dooyf@lut.cn

Received 16 October 2013; Revised 28 November 2013; Accepted 5 December 2013; Published 8 January 2014

Academic Editor: Jun Li

Copyright © 2014 W. R. Li et al. This is an open access article distributed under the Creative Commons Attribution License, which permits unrestricted use, distribution, and reproduction in any medium, provided the original work is properly cited.

On the basis of the thought that the minimum system realization plays the role as a coagulator of structural information and contains abundant information on the structure, this paper proposes a new method, which combines minimum system realization and sensitivity analysis, for structural damage detection. The structural damage detection procedure consists of three steps: (1) identifying the minimum system realization matrixes A, B, and R using the structural response data; (2) defining the mode vector, which is based on minimum system realization matrix, by introducing the concept of the measurement; (3) identifying the location and severity of the damage step by step by continuously rotating the mode vector. The proposed method was verified through a five-floor frame model. As demonstrated by numerical simulation, the proposed method based on the combination of the minimum realization system and sensitivity analysis is effective for the damage detection of frame structure. This method not only can detect the damage and quantify the damage severity, but also is not sensitive to the noise.

1. Introduction

As our economy enjoys a rapid growth and engineering construction technologies become mature increasingly, the number of high-rise buildings and long-span structures has been increasing. Because all of these structures are landmark of the city where they are located, the damage or collapse will cause great losses of properties and lives. So the performance of these structures under complex environmental factors has attracted extensive attentions. As an effective way of evaluating the safety of a structure, structural health monitoring is employed to track and evaluate damage and deterioration during regular operation and after extreme events for structure [1–5]. Although structural health monitoring can be considered as synonymous to damage detection, it actually refers to a much broader research and application area that can be employed for different purposes, such as validation of the properties of new structure, life cycle performance of structure, and structural control. However, damage

detection is a very critical component of structural health monitoring. Damage detection in the context of SHM can employ a collection of robust and practical damage detection methodologies to locate and quantify damage of changes in observable behaviors. Over the recent twenty years, a large number of scholars have proposed many methods of damage detection [6–10], for example, damage detection based on the structural dynamic characteristic [11, 12]. However, in essence, a large part of these methods extract structural damage features from the transformation of the structural dynamic parameters. Mathematically speaking, all of these methods select a mathematical model that can precisely and concisely describe the structure and then achieve the structural dynamic characteristics parameters through specific transformations, so as to detect structural damage. However, this process which gradually condenses extracts and purifies information shows certain disadvantages. On the one hand, repeated mathematical transformation is slightly tedious and would cause many errors in truncation and calculation; on

the other hand, the achieved structural mode parameters, for example, frequency, which reflect the whole structural properties, are not sensitive enough to microdamage, early damage, and local damage of the structure; the results of identification based on which the final decision was made will cause many misjudgments. Therefore, it is necessary to explore a more concise method that is easy to operate and sensitive to damages after the relations between structural excitation and response were successfully described by a mathematical model. Therefore, this paper proposes a new method, which combines minimum system realization and sensitivity analysis, for structural damage detection. First, the theoretical background and basis of the minimum system realization are briefly discussed and the minimum structural system realization matrixes \mathbf{A} , \mathbf{B} , and \mathbf{R} of the structure were obtained. Then, the concept of measurement is introduced and the mode vector which characterizes structural information based on the minimum system realization matrix was defined, and then the sensitivity theory was applied to detect structural damage step by step by continuously rotating the mode vector. Finally, the proposed method was verified by a five-floor frame model.

2. Minimum System Realization

The so-called realization is to determine state space description which described internal structural characteristics system through the transfer function matrix which described external causal relationship of system [13]. Given transfer function matrix $\mathbf{G}(s)$ of linear time-invariant system, if $[\mathbf{A}, \mathbf{B}, \mathbf{R}]$ can be obtained to make $\mathbf{G}(s) = \mathbf{R}(s\mathbf{I} - \mathbf{A})^{-1}\mathbf{B}$ tenable, $[\mathbf{A}, \mathbf{B}, \mathbf{R}]$ can be regarded as a realization of the given transfer function matrix $\mathbf{G}(s)$, namely, a realization of the system. There are various forms of realizing the same system, and transfer function matrix can only reflect the part of the system that can be controlled and observed, and $\mathbf{G}(s)$ can derive the realization of different dimensionalities. These different equations demonstrate different physical structures of the system, among which the minimum dimensionality realization can obtain equivalent external transfer characteristics with the simplest system model. And that is the so-called minimum system realization [14].

A finite dimensional, discrete-time, linear, time-invariant dynamical system has the state variable equations [15]:

$$\begin{aligned} \mathbf{x}(k+1) &= \mathbf{A}\mathbf{x}(k) + \mathbf{B}\mathbf{u}(k), \\ \mathbf{y}(k+1) &= \mathbf{R}\mathbf{x}(k+1), \end{aligned} \quad (1)$$

where $\mathbf{x}(k)$ is an n -dimensional state vector; $\mathbf{y}(k)$ is response vector of actual measurement; \mathbf{A} , \mathbf{B} , and \mathbf{R} are system matrix, control matrix, and measurement matrix, respectively; $\mathbf{u}(k)$ is input vector; k is sample indicator.

It is assumed that $\mathbf{u}(k)$ is impulse excitation; namely, $u_i(0) = 1$ ($i = 1, 2, \dots, n; k = 0$), $u_i(k) = 0$ ($i = 1, 2, \dots, n; k =$

$1, 2, \dots$), and $\mathbf{x}(0) = \mathbf{0}$; substitute all of these equations into (1):

$$\begin{aligned} \mathbf{y}(1) &= \mathbf{R}\mathbf{x}(1) \\ &= \mathbf{R}[\mathbf{A}\mathbf{x}(0) + \mathbf{B}\mathbf{u}(0)] = \mathbf{R}\mathbf{B}\mathbf{u}(0); \\ \mathbf{y}(2) &= \mathbf{R}\mathbf{x}(2) \\ &= \mathbf{R}[\mathbf{A}\mathbf{x}(1) + \mathbf{B}\mathbf{u}(1)] = \mathbf{R}\mathbf{A}\mathbf{x}(1) \\ &= \mathbf{R}\mathbf{A}[\mathbf{A}\mathbf{x}(0) + \mathbf{B}\mathbf{u}(0)] = \mathbf{R}\mathbf{A}\mathbf{B}\mathbf{u}(0); \\ &\vdots \\ \mathbf{y}(k) &= \mathbf{R}\mathbf{x}(k) \\ &= \mathbf{R}\mathbf{A}^{k-1}\mathbf{x}(1) \\ &= \mathbf{R}\mathbf{A}^{k-1}[\mathbf{A}\mathbf{x}(0) + \mathbf{B}\mathbf{u}(0)] = \mathbf{R}\mathbf{A}^{k-1}\mathbf{B}\mathbf{u}(0); \end{aligned} \quad (2)$$

then the discrete time impulse response function matrix of the structure can be achieved:

$$\mathbf{h}(1) = \mathbf{R}\mathbf{B}, \quad (3)$$

$$\mathbf{h}(2) = \mathbf{R}\mathbf{A}\mathbf{B}, \dots, \mathbf{h}(k) = \mathbf{R}\mathbf{A}^{k-1}\mathbf{B},$$

where

$$\mathbf{h}(k) = \begin{bmatrix} h_{11}(k) & h_{12}(k) & \cdots & h_{1n}(k) \\ h_{21}(k) & h_{22}(k) & \cdots & h_{2n}(k) \\ \vdots & \vdots & & \vdots \\ h_{m1}(k) & h_{m2}(k) & \cdots & h_{mn}(k) \end{bmatrix}, \quad (4)$$

where $h_{ij}(k)$ is impulse response function between excitation point j and response point i at time k .

Thus, the general Hankel matrix can be constructed through the impulse response function matrix $\mathbf{h}(k)$:

$$\mathbf{H}(k) = \begin{bmatrix} \mathbf{h}(k) & \mathbf{h}(k+1) & \cdots & \mathbf{h}(k+s) \\ \mathbf{h}(k+1) & \mathbf{h}(k+2) & \cdots & \mathbf{h}(k+s+1) \\ \vdots & \vdots & & \vdots \\ \mathbf{h}(k+r) & \mathbf{h}(k+r+1) & \cdots & \mathbf{h}(k+r+s) \end{bmatrix}, \quad (5)$$

where r and s are random positive integers.

When $k = 0$, conduct singular value decomposition (SVD) on $\mathbf{H}(k)$, namely, $\mathbf{H}(0)$; then the following is tenable:

$$\mathbf{H}(0) = \mathbf{P}\Sigma\mathbf{Q}^T, \quad (6)$$

where \mathbf{P} and \mathbf{Q} are vector matrixes of the right and the left singular value and Σ is diagonal matrix shown below:

$$\Sigma = \begin{bmatrix} \Sigma_r & \mathbf{0} \\ \mathbf{0} & \mathbf{0} \end{bmatrix}, \quad (7)$$

$$\Sigma_r = \text{diag}[\sigma_1, \sigma_2, \dots, \sigma_r], \quad r = \text{rank}(\mathbf{H}(k)).$$

Set $\mathbf{P}_r, \mathbf{Q}_r$ as the first r rows of \mathbf{P}, \mathbf{Q} orthogonal matrixes, $\mathbf{E}_m^T = [\mathbf{I}_m, \mathbf{0}_m, \dots, \mathbf{0}_m]$, and $\mathbf{E}_l^T = [\mathbf{I}_l, \mathbf{0}_l, \dots, \mathbf{0}_l]$. Finally, the minimum system realization matrixes \mathbf{A}, \mathbf{B} , and \mathbf{R} are shown as follows:

$$\begin{aligned}\mathbf{A} &= \Sigma_r^{-1/2} \mathbf{P}_r^T \mathbf{H} (1) \mathbf{Q}_r \Sigma_r^{-1/2}, \\ \mathbf{B} &= \Sigma_r^{1/2} \mathbf{Q}_r^T \mathbf{E}_l, \\ \mathbf{R} &= \mathbf{E}_m^T \mathbf{P}_r \Sigma_r^{1/2}.\end{aligned}\quad (8)$$

3. Measurement

In mathematics, measurement (or distance function) is a function defining the distance between elements in the set. A set with measurement is called metric space. At the beginning of the 20th century, Fréchet, a French mathematician, found out that many analysis achievements involve the distance relations among functions from a more abstract view, through which the concept of metric space can be abstracted [16].

After achieving the minimum system realization, \mathbf{Z} can be defined by \mathbf{A}, \mathbf{B} , and \mathbf{R} :

$$\mathbf{Z} = \mathbf{RAB}. \quad (9)$$

With regard to the health structure and structure which is to be identified, \mathbf{Z} can be expressed by

$$\mathbf{Z}_0 = \mathbf{R}_0 \mathbf{A}_0 \mathbf{B}_0, \quad \mathbf{Z}_r = \mathbf{R}_r \mathbf{A}_r \mathbf{B}_r. \quad (10)$$

In fact, it can be seen that $\mathbf{Z}_0, \mathbf{Z}_r$ can be rewritten as $\mathbf{Z}_0 = \mathbf{Z}_0 \mathbf{I}, \mathbf{Z}_r = \mathbf{Z}_r \mathbf{I}$, where \mathbf{I} is unit matrix. Since any matrix can be seen as a coordination system, \mathbf{Z}_0 and \mathbf{Z}_r were described by \mathbf{Z}_0 and \mathbf{Z}_r in the coordinate system \mathbf{I} . According to this, the coordinate system \mathbf{Z}_0 is employed to describe \mathbf{Z}_0 and \mathbf{Z}_r , so as to obtain \mathbf{D}_0 and \mathbf{D}_r :

$$\mathbf{D}_0 = \mathbf{Z}_0 \mathbf{Z}_0, \quad \mathbf{D}_r = \mathbf{Z}_r \mathbf{Z}_0. \quad (11)$$

\mathbf{D}_0 and \mathbf{D}_r are a kind of measurement of \mathbf{Z}_0 and \mathbf{Z}_r in the coordinate system \mathbf{Z}_0 . The physical mean of this description in the structure damage detection is to use the coordinate system (\mathbf{Z}_0) which represents the health states to measure the states to be identified (\mathbf{Z}_r); in other words, it explores and quantizes the differences between the states to be identified (\mathbf{Z}_r) and the health states (\mathbf{Z}_0), so as to identify structural damages.

In the theory of matrix, any matrix can be regarded as a linear space, and any row vector of the matrix can be regarded as a linear transformation; a linear transformation in mathematics is also N -dimension array [17]. With the purpose of describing the array more concisely, a measurement method called 2-norm is brought in. Norm is the function with the concept of "length," while the norm of vector is used to measure the length of vector. Therefore, norms can be used to describe each row vector of matrix. Then, 2-norms of every row vector in matrixes \mathbf{D}_0 and \mathbf{D}_r are achieved,

respectively, and the corresponding mode vectors \mathbf{u}_0 and \mathbf{u}_r are also obtained as follows:

$$\begin{aligned}\mathbf{u}_0 &= [u_{10}, u_{20}, \dots, u_{n0}]^T, \\ \mathbf{u}_r &= [u_{1r}, u_{2r}, \dots, u_{nr}]^T.\end{aligned}\quad (12)$$

Vector \mathbf{u}_0 represents essential information of health structure, and vector \mathbf{u}_r represents essential information of damaged structure. Thereby, after bringing in the concept of measurement, the minimum realization matrix can be successively transformed into mode vector that can basically represent structural information, which can be used for our follow-up damage identification.

4. Sensitivity Theory

Sensitivity theory is mainly used to quantitatively describe the variances of structural behavior with structural parameters. In other words, structural parameter p shows a slight variance δp , how the structural behavior (mode vector \mathbf{u}) will vary and in which degree it will vary [18, 19].

Since mode vector \mathbf{u} is the function of structural parameter p , variance δp of the structural parameters is also reflected in vector $\delta \mathbf{u}$ correspondingly. First-order variation of the structural parameter p with vector $\delta \mathbf{u}$ was calculated, and then (13) is tenable:

$$\delta \mathbf{u} = \sum_{i=1}^n \frac{\partial \mathbf{u}}{\partial p_i} \delta p_i, \quad (13)$$

where $\delta \mathbf{u}$ is variance of mode vector, δp_i is variance of structural parameter in floor i , $\partial \mathbf{u} / \partial p_i$ is the sensitivity coefficient of mode vector \mathbf{u} of structural parameter p_i , and n is the number of structural parameters.

An n -floor structure was taken as an example, and the structural parameter p_k in floor k was assumed to be Δp_k variance; the variance $\Delta \mathbf{u}$ of mode vector \mathbf{u} after comparing with the health structure is shown below:

$$\Delta \mathbf{u} = \begin{Bmatrix} \Delta u_1 \\ \Delta u_2 \\ \vdots \\ \Delta u_n \end{Bmatrix} = \mathbf{u}_k - \mathbf{u}_0 = \begin{Bmatrix} u_{1k} - u_{10} \\ u_{2k} - u_{20} \\ \vdots \\ u_{nk} - u_{n0} \end{Bmatrix}, \quad (14)$$

where vector $\mathbf{u}_k = [u_{1k}, u_{2k}, \dots, u_{nk}]^T$.

The left and the right ends of (14) were divided by the structural damage degree Δp_k , and then we can obtain the variance of structural unit damage information in the floor k . Consider the following:

$$\frac{\Delta \mathbf{u}}{\Delta p_k} = \left[\frac{\Delta u_1}{\Delta p_k}, \frac{\Delta u_2}{\Delta p_k}, \dots, \frac{\Delta u_n}{\Delta p_k} \right]^T. \quad (15)$$

As a matter of convenience, \mathbf{s}_k and s_{ik} are used to represent $\Delta \mathbf{u} / \Delta p_k$ and $\Delta u_i / \Delta p_k$ ($i = 1, 2, \dots, n$), respectively, and

then the sensitivity vector \mathbf{s}_k of mode vector \mathbf{u} of structural parameter p in floor k can be achieved:

$$\mathbf{s}_k = [s_{1k}, s_{2k}, \dots, s_{nk}]^T. \quad (16)$$

Similarly, we can obtain the sensitivity vectors $\mathbf{s}_1, \mathbf{s}_2, \dots, \mathbf{s}_n$ of mode vector \mathbf{u} to structural parameter p of each floor, respectively. By combining the n vectors, we can get the sensitivity matrix \mathbf{S} :

$$\mathbf{S} = [\mathbf{s}_1, \mathbf{s}_2, \dots, \mathbf{s}_n] = \begin{bmatrix} s_{11} & s_{12} & \cdots & s_{1n} \\ s_{21} & s_{22} & \cdots & s_{2n} \\ \vdots & \vdots & & \vdots \\ s_{n1} & s_{n2} & \cdots & s_{nm} \end{bmatrix}. \quad (17)$$

A slight variance $\delta \mathbf{p}$ of the structural parameter p represents structural damage. Thereby, mode vector \mathbf{u}_r of damage structure contains the damage information of the structure, and, compared with that of the health structure, the following is tenable:

$$\delta \mathbf{u} = \mathbf{u}_r - \mathbf{u}_0 = \begin{Bmatrix} u_1 - u_{10} \\ u_2 - u_{20} \\ \vdots \\ u_n - u_{n0} \end{Bmatrix}. \quad (18)$$

Combining (13), the following is tenable:

$$\begin{bmatrix} s_{11} & s_{12} & \cdots & s_{1n} \\ s_{21} & s_{22} & \cdots & s_{2n} \\ \vdots & \vdots & & \vdots \\ s_{n1} & s_{n2} & \cdots & s_{nm} \end{bmatrix} \begin{Bmatrix} \delta p_1 \\ \delta p_2 \\ \vdots \\ \delta p_n \end{Bmatrix} = \begin{Bmatrix} \delta u_1 \\ \delta u_2 \\ \vdots \\ \delta u_n \end{Bmatrix}. \quad (19)$$

Namely,

$$\mathbf{S} \delta \mathbf{p} = \delta \mathbf{u}. \quad (20)$$

In other words, as long as the variance $\delta \mathbf{u}$ of sensitivity matrix \mathbf{S} and vector \mathbf{u} is known, the variance of structural parameter can be obtained through (20):

$$\delta \mathbf{p} = \mathbf{S}^{-1} \delta \mathbf{u}. \quad (21)$$

5. Damage Identification

General sensitivity analysis is shown in (20). The accuracy of the identification result mainly relies on the accuracy of sensitivity matrix. However, the accuracy of sensitivity matrix is not always guaranteed under the influence of various complex factors. Therefore, the accuracy of such identification that ‘‘set the tune with one beat of the gong’’ cannot always be guaranteed. This paper proposes an identification method which continuously modifies the sensitivity matrix to approach actual damage by keeping rotation of the mode vector. The identification process is showed in Figure 1.

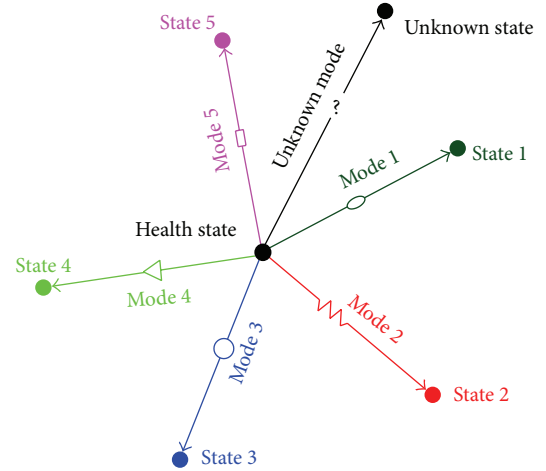


FIGURE 1: Process of structural damage identification.

In order to illustrate the process of the identification, a five-floor frame structure is taken as an example. State 1–State 5 represent the states when a certain severity of damage happens in different locations of the structure. The vectors which were described by Mode 1–Mode 5 represent the process from health state to State 1–State 5, respectively. The direction and characteristics of these vectors represent the location of damage, and the length of vector represents the severity of damage. When an unknown mode vector which points from the health state to an unknown state completely coincides with a known mode (the same in characteristics, direction, and size), single damage of the structure can be identified. If the unknown mode vector is always between two known modes, multiple damages of the structure can be identified by projecting the unknown mode vector to the two modes.

The damage is simulated by reducing the stiffness of the structure; it is assumed that damage α happens to different locations of the structure, respectively (define α as the standard damage value which was adopted to construct sensitivity matrix); five corresponding mode vectors were obtained using the above mentioned method and employed to construct the sensitivity matrix and then to identify unknown damage. Firstly, the similarity between the unknown and known modes can be basically confirmed by comparing the characteristics of unknown and known modes. Higher similarity demonstrates higher possibility that the unknown damage is similar to this standard damage. Thus, the location of structural damage can be judged. Secondly, project the unknown mode vector to the known mode vector after confirming the possible location of damage. The size of projection is the severity of possible damage. Define the damage severity as α' which has been located with the maximum possibility. Considering that α' is closer to the actual damage severity than α , so α' is utilized to reconstruct a sensitivity matrix to identify the unknown damage, and α'' is achieved; similarly, α'' was utilized to identify again; the iterations stop until the result of N and $N + 1$ iteration no longer varies. Thus, the final damage is identified. Therefore, it is possible

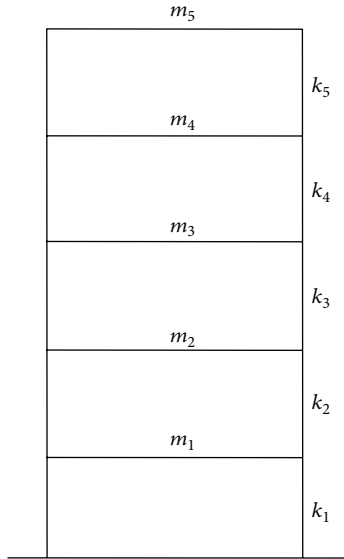


FIGURE 2: Five-floor frame model.

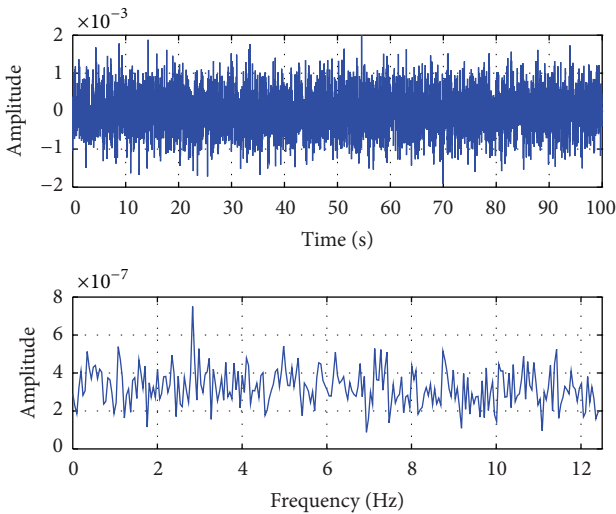


FIGURE 3: Time history and frequency spectrum curve of white noise excitation.

to identify the location and severity of structural damage accurately by updating the standard damage which was used to continuously modify the sensitivity matrix and rotating the mode vector.

6. Numerical Example

In order to verify the feasibility and effectiveness of the proposed method in identifying structural damage, a five-floor frame is used in the numerical study. The frame model is showed in Figure 2. The mass of each floor is $m_1 = m_2 = m_3 = m_4 = m_5 = 1.60 \times 10^7$ kg, and the stiffness of each floor is $k_1 = k_2 = k_3 = k_4 = k_5 = 3.363 \times 10^8$ N/m. The structure is subjected to white noise on the bottom. The time history

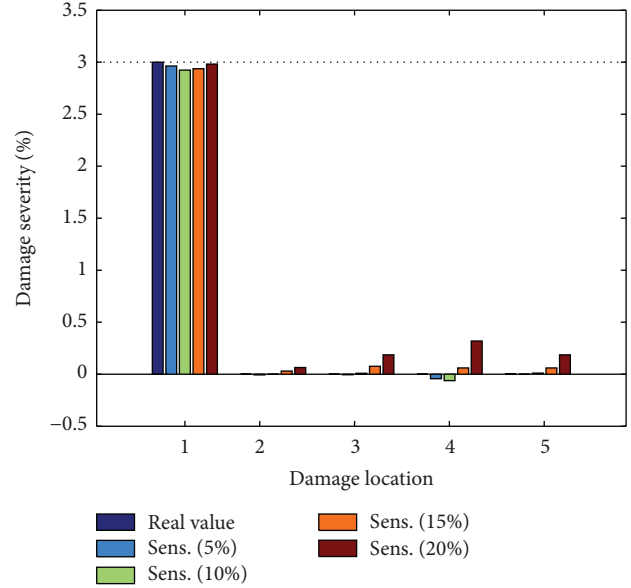


FIGURE 4: First-floor damage of 3%.

and frequency spectrum curve were showed in Figure 3. On the basis of sampling theorem, the responses are recorded at a sampling rate of 50 Hz and lasting for 100 s. A total of 5,000 time points of structural responses are obtained from each floor for the undamaged structure as well as for the structure in damage case. Six damage cases in numerical simulation were given in the Table 1. The damage was simulated by the reduction of the stiffness of the structure, for example, “damage of 20%” represents the stiffness of the structure reduce by 20%.

6.1. Selection of Standard Damage. In order to discuss the influence of the sensitivity matrix constructed by different standard damage on the result of identification, standard damage severities at 5%, 10%, 15%, and 20% were adopted to construct the sensitivity matrix, and the damage cases mentioned above were analyzed. The results can be seen in Figures 4 to 9.

It can be found that this method can locate the damage when the different severity of damage happened in a different floor accurately (floor 1, floor 3 damage) using different sensitivity matrix by comparing Figures 4 and 6, Figures 5 and 7. Comparing Figures 4 and 5, Figures 6 and 7, it can be found that this method can quantify the severity of the damage accurately. As these six figures are further analyzed, it is suggested by Figures 4 and 6 that the standard damage of 5% shows the optimal performance in identifying 3% damage. From Figures 5 and 7 it is suggested that the sensitivity matrix which was constructed by standard damage of 20% shows the optimal performance in identifying 20% damage; it also can be found by Figure 8, Figure 9 that the sensitivity matrix which constructed by standard damage of 10% shows the optimal performance in identifying 12% damage and the sensitivity matrix which was constructed by standard damage

TABLE 1: Single damage case of five-floor frame model.

	Case 1	Case 2	Case 3	Case 4	Case 5	Case 6
Damage location	1	1	3	3	2	4
Damage severity	3%	21%	3%	21%	12%	25%

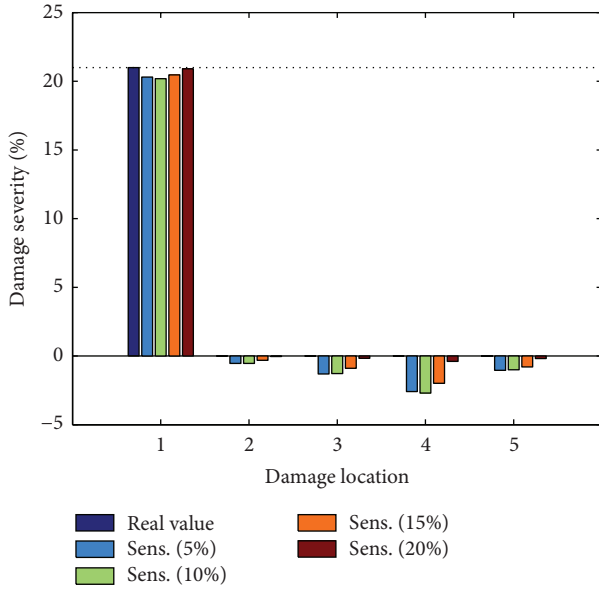


FIGURE 5: First-floor damage of 21%.

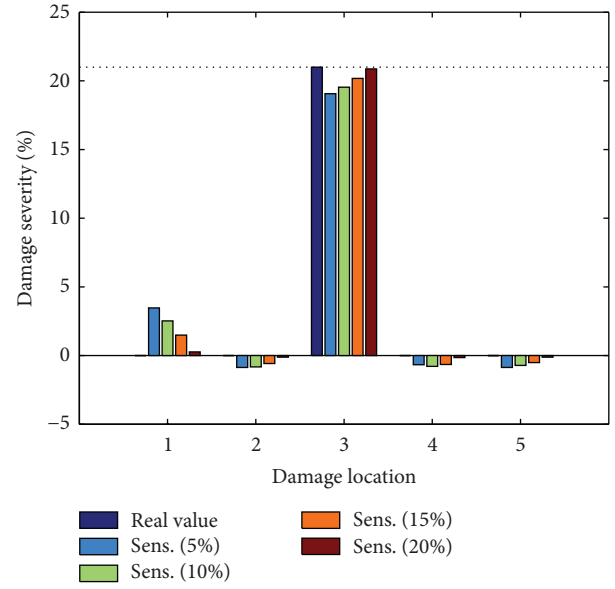


FIGURE 7: Third-floor damage of 21%.

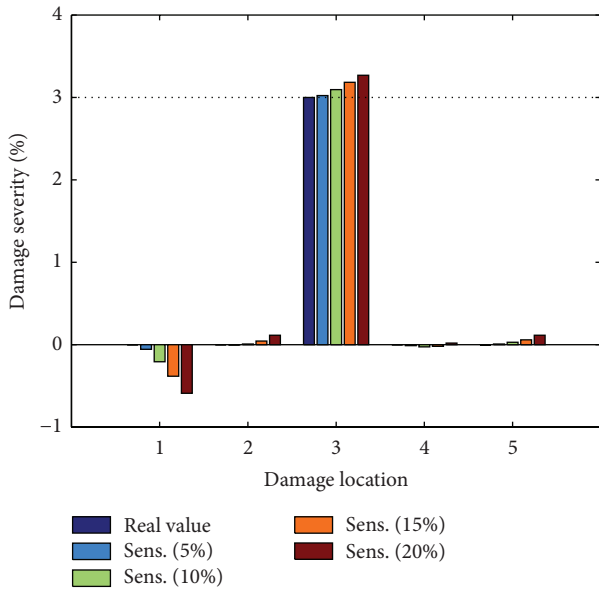


FIGURE 6: Third-floor damage of 3%.

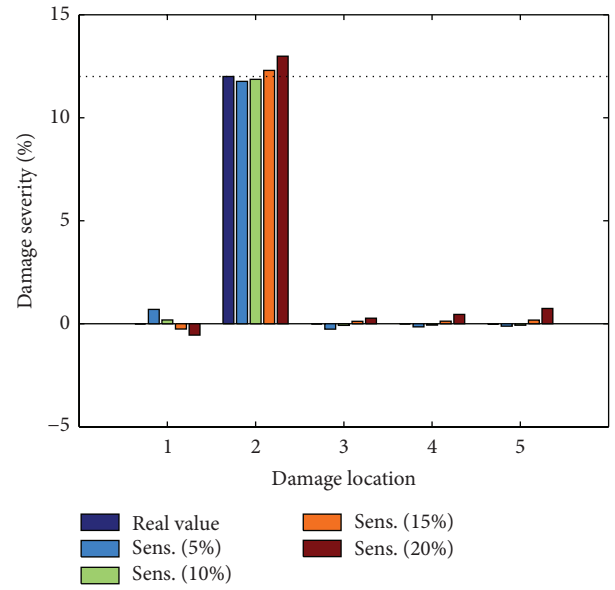


FIGURE 8: Second-floor damage of 12%.

of 20% shows the optimal performance in identifying 25% damage. Thus, it is not difficult to find out that the closer the standard damage value adopted to construct the sensitivity matrix is, the better the identified results are obtained. However, in general, it can be seen from Figures 4 to 9 that the standard damages values selected to construct the sensitivity

matrix are quite different, but they can identify damages in different locations and severity very well. This demonstrates that the selection of standard damage value does not affect the result of damage identification. That is to say that this method has no special requirements to standard damage value. Therefore, it is feasible to approach the actual damage

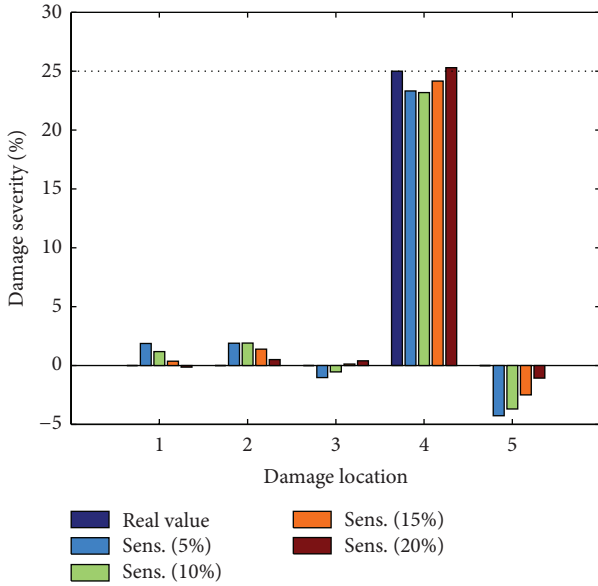


FIGURE 9: Fourth-floor damage of 25%.

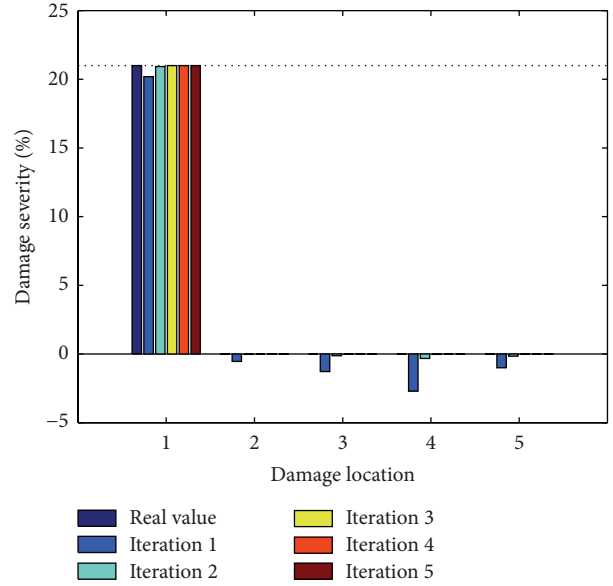


FIGURE 11: First-floor damage of 21%.

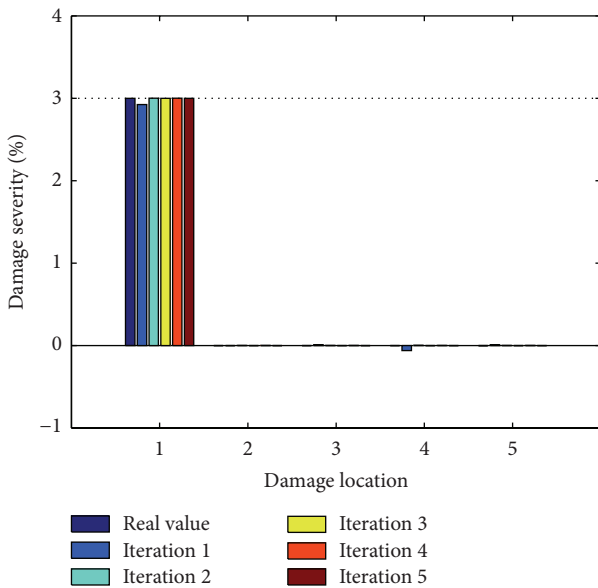


FIGURE 10: First-floor damage of 3%.

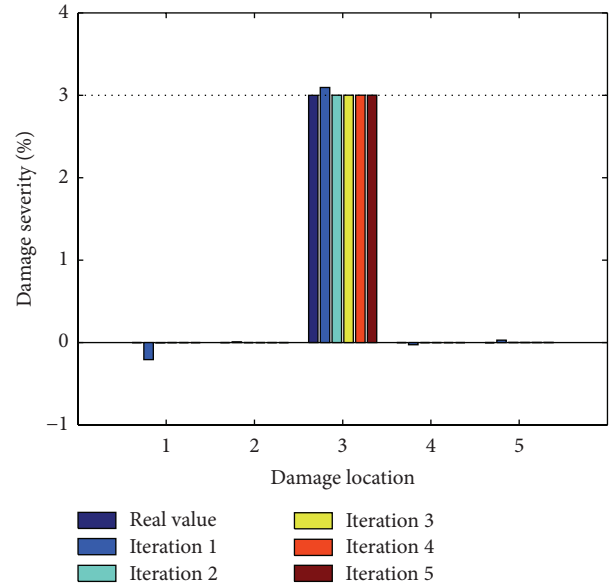


FIGURE 12: Third-floor damage of 3%.

by continuously updating the standard damage value which was used to construct the sensitivity matrix and rotating the mode vectors.

6.2. *Single Damage Analysis.* Based on the above discussions, the standard damage of 10% was employed to construct the sensitivity matrix. Given that there is no noise in the response data, five iterations are adopted to identify the above mentioned cases. The results were showed in Figures 10–15.

It can be seen from Figures 10–15 that this method can locate the damage and quantify the damage severity under different damage cases accurately. Misjudgments might occur

in the first iteration but they will disappear after several iterations. In these figures, Figures 12 and 13 are typical “step approaching,” which approaches the actual damage by increasing or decreasing step by step. Figure 15 is typical “pendulum approaching,” which approaches the actual damage by oscillating near the actual damage. It can be seen from Figures 10 and 12 that this method can identify slight damage, for example, damage of 3%, through two iterations; it can be seen from Figures 11, 13, and 15 that despite the serious damages like 21% and 25%, this method can satisfy the requirement of accuracy by three or four iterations. If the selected standard damage value happens to be very close to the actual damage (shown in Figure 14), the result of one iteration is already

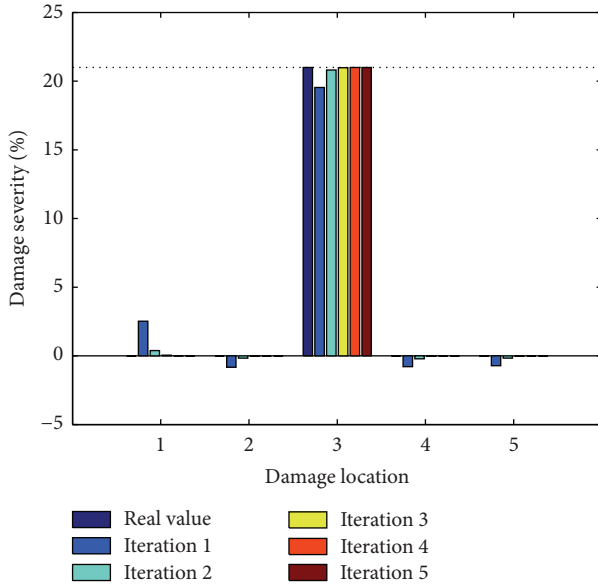


FIGURE 13: Third-floor damage of 21%.

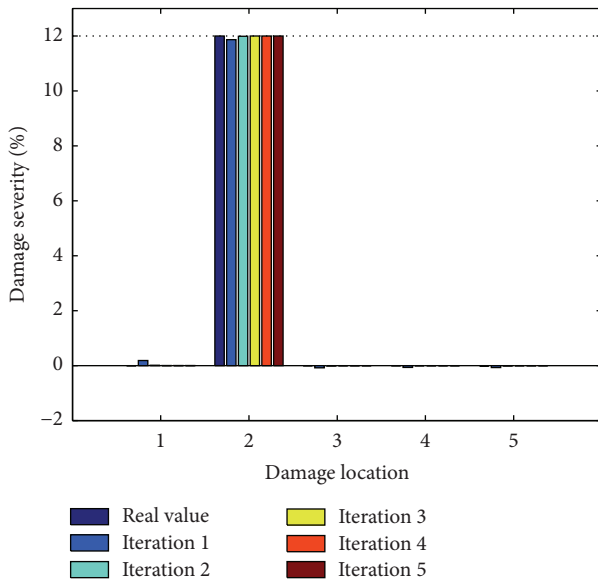


FIGURE 14: Second-floor damage of 12%.

quite accurate. It is worth noting that there is no misjudgment in several iterations when identifying slight damages. This means that this method shows great advantages in identifying slight damages. Overall, this method takes only a few iterations to identify structural damages, which substantially shortens the time needed to identify the damage.

6.3. Antinoise Performance Analysis. In order to discuss the antinoise performance of this method, white Gaussian noise was added to the response data at the noise-to-signal ratio of 0%, 1%, 3%, and 5%, respectively. The standard damage of

TABLE 2: Multiple-damage case of five-floor frame model.

	Case 1		Case 2	
Damage location	2	3	4	5
Damage severity	10%	5%	12%	18%

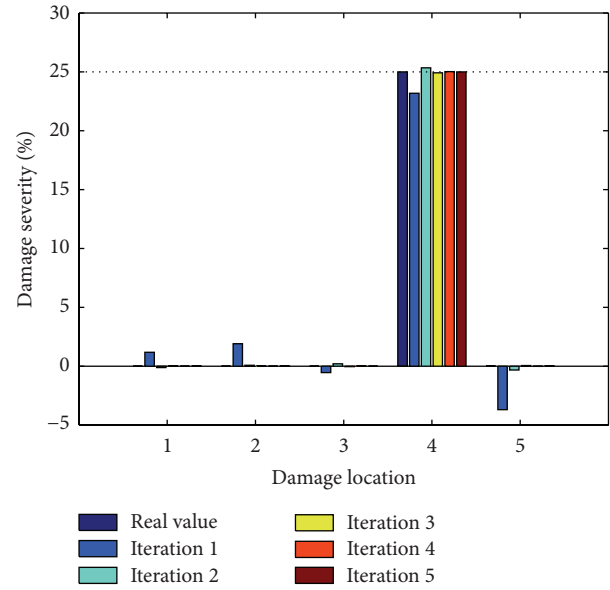


FIGURE 15: Fourth-floor damage of 25%.

10% in each floor of the structure was employed to construct the sensitivity matrix and the above mentioned cases were analyzed. The results were showed in Figures 16, 17, 18, 19, 20, and 21.

It is suggested from Figures 16 to 21 that this method shows certain antinoise performance. The location and severity of structural damage can still be identified very well when 5% noise was added to the response of the damage of 21% to 25%; but the noise produces greater influence on slight damage of 3%. Taking case 1 and case 3 as an example, the location and severity of damage can be identified well when 1% and 3% noises were added to the response of the damage structure. When 5% noise was added, misjudgments show up, but they can also locate structural damage. As to case 5, it is indicated by Figure 20 that, when the standard damage and actual damage selected to construct the sensitivity matrix are very close, the influence of noise can be weakened and dramatic fluctuations can be avoided.

6.4. Multiple-Damage Analysis. In practical engineering, multiple structural damages might occur in different locations. This paper also discusses the method in the identification of multiple damages. The five-floor frame shown in Figure 2 is simulated. The standard damages of 8% and 15% were used to construct sensitivity matrix. Given that there is no noise pollution in the response data, five iterations were adopted to identify the different damage cases showed in Table 2. The results were showed in Figures 22 to 25.

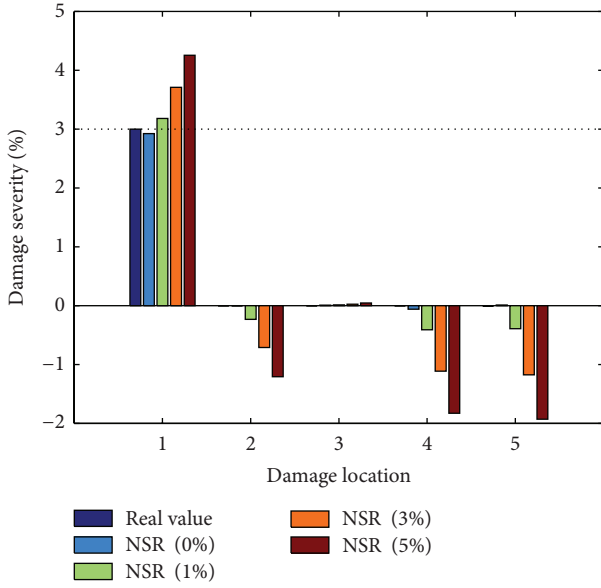


FIGURE 16: First-floor damage of 3%.

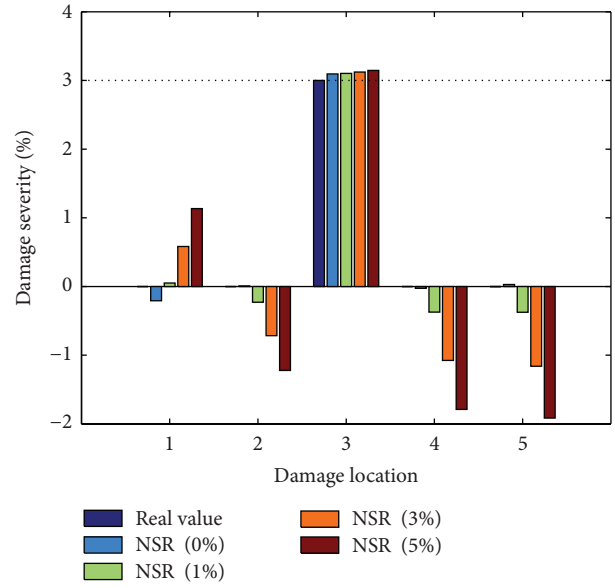


FIGURE 18: Third-floor damage of 3%.

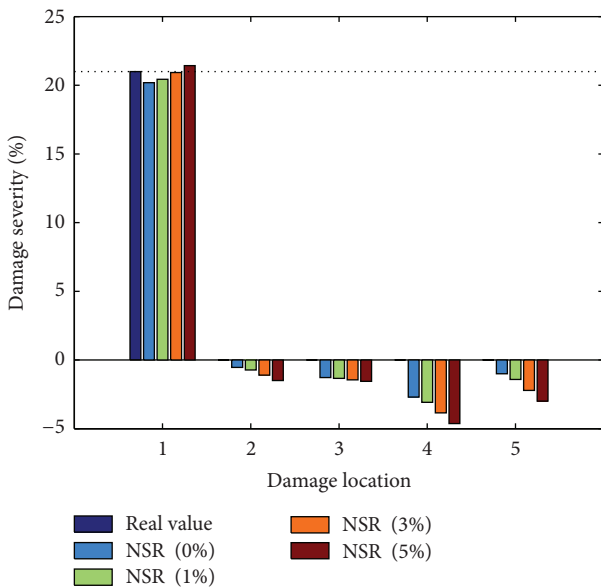


FIGURE 17: First-floor damage of 21%.

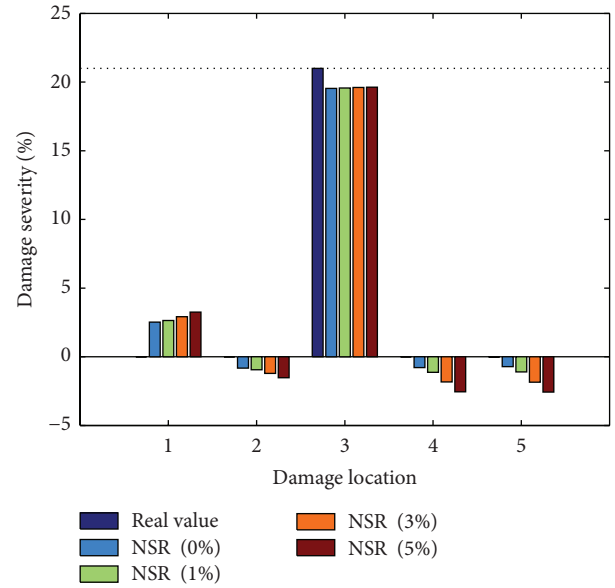


FIGURE 19: Third-floor damage of 21%.

It is suggested by Figures 22 to 25 that this method can locate structural damage very accurately even with multiple damages, but the severity of damage is not very ideal. It is not difficult to find out by comparing Figures 22 and 23, Figures 24 and 25 that the standard damage selected to construct the sensitivity matrix barely has any influence on the results of multiple damages. It is also found out by Figures 22 to 25 that this method shows satisfying effect when identifying multiple damages consisting of middle and slight damages, but it seems to be helpless in front of multiple damages consisting of middle and large damages because the corresponding mode vector under multiple structural damages is not just a simple

superposition of the corresponding mode vector in case of single damages and the coupling among multiple damages has greater influence on the mode vector needed in the identification process.

7. Conclusion

Based on the minimum system realization and sensitivity analysis, this paper proposed a new method of identifying structural damages. The feasibility and effectiveness of this method was verified by numerical simulation analysis. The main conclusions are as follows.

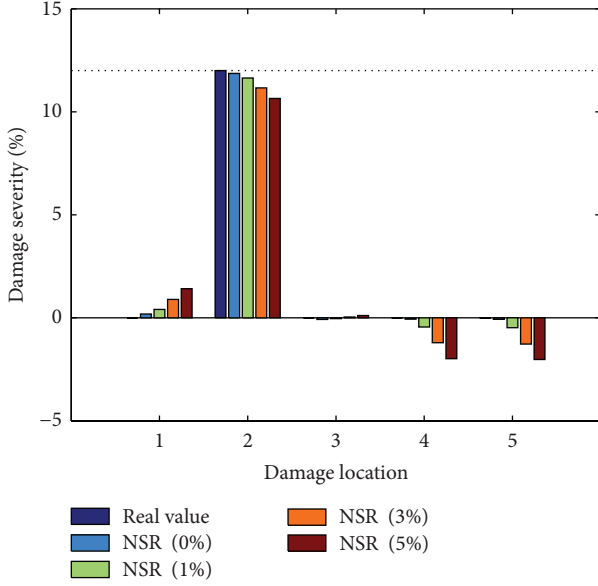


FIGURE 20: Second-floor damage of 12%.

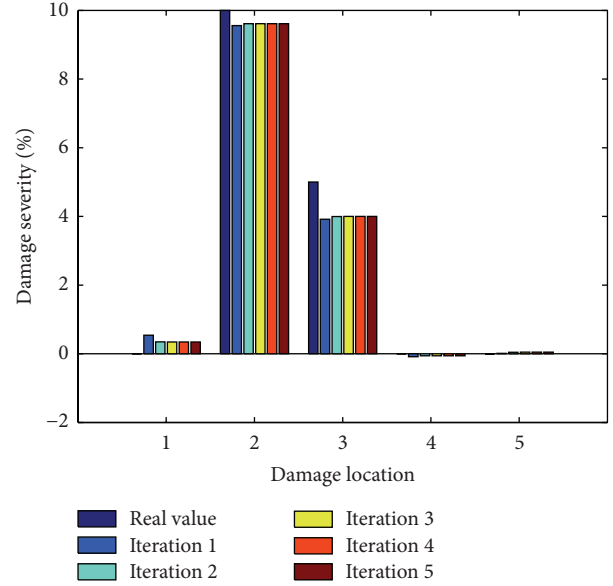


FIGURE 22: Identification result of case 1 (8%).

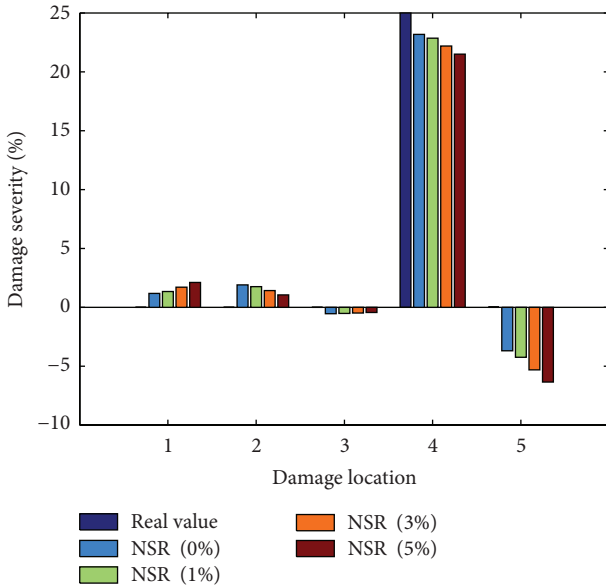


FIGURE 21: Fourth-floor damage of 25%.

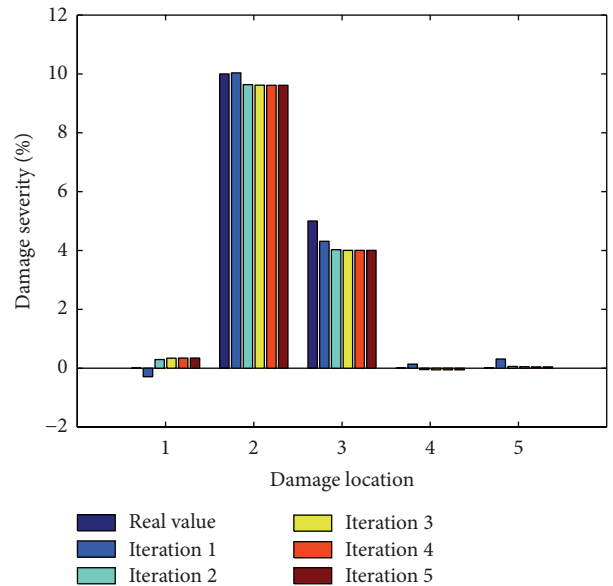


FIGURE 23: Identification result of case 1 (15%).

- (1) This method has no special requirement to the standard damage selected to construct sensitivity matrix, and this offers great convenience to identify the damage.
- (2) This method needs only a few iterations to identify structural damages very accurately through “step approaching” or “pendulum approaching.” This greatly shortens the time needed to identify damages. What is more important is that this method shows more remarkable performance in the identification of slight damages.
- (3) This method shows certain antinoise performance. Even with stronger noise, it can still identify the location and severity of large structural damages; as to slight damages, the influence of noise is large, but this method can still locate the structural damages.
- (4) Although this method shows satisfying effect in identifying multiple damages consisting of middle and slight damages, it can only locate middle and large damages because of the coupling among multiple damages. Therefore, further study needs to be conducted in this aspect.

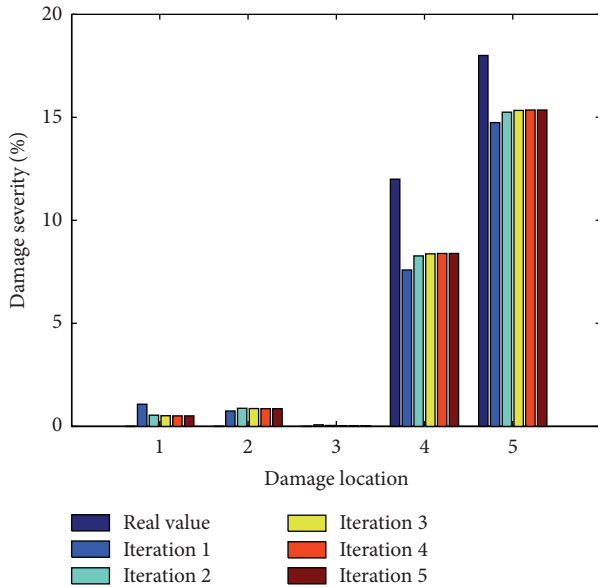


FIGURE 24: Identification result of case 2 (8%).

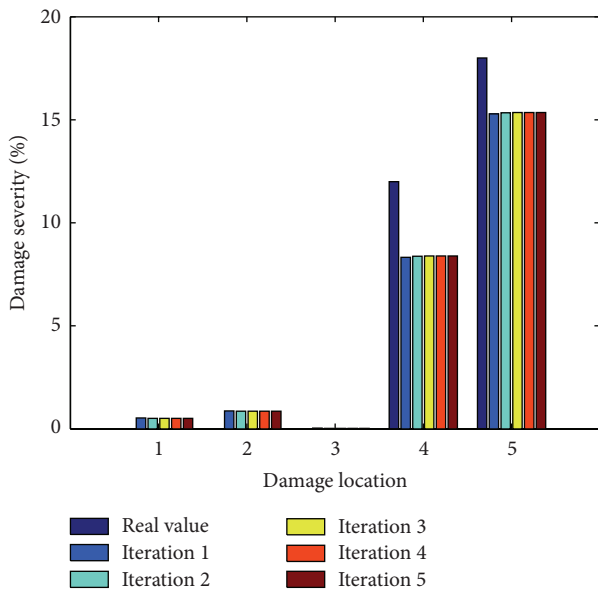


FIGURE 25: Identification result of case 2 (15%).

(5) Although the proposed damage identification methodology has shown promise in the numerical investigation, issues to be addressed still exist to make it applicable in practice. Therefore, experimental study is needed in further work to investigate the feasibility of the methodology in practical applications.

Conflict of Interests

The authors declare that they have no conflict of interests regarding the publication of this article.

Acknowledgment

This research was supported in part by a Grant from National Science Foundation of China under Project no. 51178211. This support is gratefully acknowledged.

References

- [1] J. Ou and H. Li, "Structural health monitoring in mainland China: review and future trends," *Structural Health Monitoring*, vol. 9, no. 3, pp. 219–231, 2010.
- [2] Y. Q. Ni, X. W. Ye, and J. M. Ko, "Monitoring-based fatigue reliability assessment of steel bridges: analytical model and application," *Journal of Structural Engineering*, vol. 136, no. 12, pp. 1563–1573, 2010.
- [3] D. Balageas, *Introduction to Structural Health Monitoring*, ISTE, 2006.
- [4] Y. Q. Ni, X. W. Ye, and J. M. Ko, "Modeling of stress spectrum using long-term monitoring data and finite mixture distributions," *Journal of Engineering Mechanics*, vol. 138, no. 2, pp. 175–183, 2012.
- [5] C. R. Farrar and K. Worden, "An introduction to structural health monitoring," *Philosophical Transactions of the Royal Society A*, vol. 365, no. 1851, pp. 303–315, 2007.
- [6] S. D. Fassois and F. P. Kopsaftopoulos, "Statistical time series methods for vibration based structural health monitoring," in *New Trends in Structural Health Monitoring*, pp. 209–264, Springer, Vienna, Austria, 2013.
- [7] A. A. Mosavi, D. Dickey, R. Seracino, and S. Rizkalla, "Identifying damage locations under ambient vibrations utilizing vector autoregressive models and Mahalanobis distances," *Mechanical Systems and Signal Processing*, vol. 26, no. 1, pp. 254–267, 2012.
- [8] T. H. Yi, H. N. Li, and H. M. Sun, "Multi-stage structural damage diagnosis method based on energy-damage theory," *Smart Structures and Systems*, vol. 12, no. 3-4, pp. 345–361, 2013.
- [9] V. Srinivas, K. Ramanjaneyulu, and C. A. Jeyasehar, "Multi-stage approach for structural damage identification using modal strain energy and evolutionary optimization techniques," *Structural Health Monitoring*, vol. 10, no. 2, pp. 219–230, 2011.
- [10] H. N. Li, T. H. Yi, M. Gu, and L. S. Huo, "Evaluation of earthquake-induced structural damages by wavelet transform," *Progress in Natural Science*, vol. 19, no. 4, pp. 461–470, 2009.
- [11] S. W. Doebling, C. R. Farrar, M. B. Prime et al., *Damage Identification and Health Monitoring of Structural and Mechanical Systems from Changes in Their Vibration Characteristics: A Literature Review*, Los Alamos National Lab, Los Alamos, NM, USA, 1996.
- [12] W. Fan and P. Qiao, "Vibration-based damage identification methods: a review and comparative study," *Structural Health Monitoring*, vol. 10, no. 1, pp. 83–111, 2011.
- [13] S. Y. Zhang and L. Q. Gao, *Modern Control Theory*, Tsinghua University Press, 2010.
- [14] C. T. Chen, *Linear System Theory and Design*, Oxford University Press, 2009.
- [15] W. Heylen, S. Lammens, and P. Sas, *Modal Analysis Theory and Testing*, Department Werktuigkunde, Katholieke University Leuven, Heverlee, Belgium, 1997.
- [16] M. M. Fréchet, "Sur quelques points du calcul fonctionnel," *Rendiconti del Circolo Matematico di Palermo*, vol. 22, no. 1, pp. 1–72, 1906.
- [17] A. S. Householder, *The Theory of Matrices in Numerical Analysis*, Courier Dover Publications, 2013.

- [18] A. Saltelli, K. Chan, and E. M. Scott, Eds., *Sensitivity Analysis*, vol. 134, Wiley, New York, NY, USA, 2000.
- [19] G. G. Bordonaro, M. R. Hajj, A. H. Nayfeh, and J. C. Duke, "Parameter sensitivities to damage progression," *Structural Control and Health Monitoring*, vol. 18, no. 5, pp. 481–491, 2011.

Research Article

A Three-Dimensional Model of the Effective Electromechanical Impedance for an Embedded PZT Transducer

Chunyuan Zuo, Xin Feng, and Jing Zhou

Faculty of Infrastructure Engineering, Dalian University of Technology, Dalian 116024, China

Correspondence should be addressed to Xin Feng; fengxin@dlut.edu.cn

Received 15 October 2013; Accepted 4 December 2013

Academic Editor: Ting-Hua Yi

Copyright © 2013 Chunyuan Zuo et al. This is an open access article distributed under the Creative Commons Attribution License, which permits unrestricted use, distribution, and reproduction in any medium, provided the original work is properly cited.

A three-dimensional model of the effective electromechanical impedance for an embedded PZT transducer is proposed by considering the interaction between a PZT patch and a host structure. By introducing an effective mechanical impedance, the coupled electromechanical admittance formulations are derived using the piezoelectric constitutive equations. Then, a modified methodology for monitoring structure changes using an electromechanical impedance (EMI) technique is proposed. In the proposed method, the changes in the host structure are monitored by using the “active” part associated with the structural mechanical impedance, which is extracted from the measured raw admittance signatures. The strength gain of a concrete beam with embedded PZT transducers during the curing age was monitored with the proposed methodology. The experimental results demonstrate that the use of the “active” part is more sensitive as opposed to the raw admittance signatures for structural health monitoring (SHM).

1. Introduction

In general, a typical structural health monitoring (SHM) system includes three major components: a sensor system, a data processing system (including data acquisition, transmission, and storage), and a health evaluation system. The sensor system is the key component in the SHM system [1, 2]. The advent of commercially available smart piezoelectric materials has provided new opportunities for SHM. The key characteristic of PZT materials is the utilization of the converse piezoelectric effect to actuate the structure in addition to the direct piezoelectric effect to sense structural deformation [3, 4]. By the direct and converse piezoelectric effects of PZT materials, the electromechanical impedance (EMI) technique simultaneously employs piezoelectric ceramic (PZT) patches as both sensors and actuators.

In recent years, the EMI technique has gained wide attention and emerged as a favorable tool for structural damage detection. This technique can diagnose several types of structures, including bolted connections [5, 6], cable-stayed bridges [7], aerospace structures [8], reinforced concrete structures [9, 10], and pipeline structures [11]. The basic

concept of this approach is to use high-frequency excitations to monitor the local area of the host structure for changes in the structural mechanical impedance caused by damage [12]. In the EMI technique, a small-size PZT patch is bonded to or embedded into the monitored structure and excited by an alternating voltage sweep signal. The PZT patch transfers the vibrations to the host structure, which is deformed and produces a local dynamic response. Simultaneously, the response of the host structure is transferred back to the PZT patch. Because of the electromechanical coupling property of PZT materials, the structural mechanical impedance of the host structure can be determined by the electrical impedance of the PZT patch. By monitoring the variations of the measured electrical impedance, the change in the structural mechanical impedance induced by structural damage can be detected. The advantages of EMI-based approaches include but are not limited to a lightweight and inexpensive sensor, high sensitivity to incipient damage for high-frequency actuating, and immunity to ambient or far-field loads.

The interaction between the PZT patch and the host structure is the key issue for sensor design and data interpretation in EMI-based methods. During the last two decades,

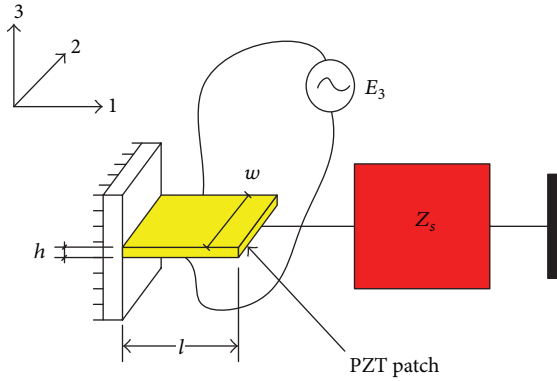


FIGURE 1: Liang's 1D impedance model [13].

several modeling approaches have been proposed for describing the PZT-structure interaction. Among them, two well-known approaches are the static approach and the impedance approach. The former one developed by Crawley and de Luis [16] uses a statically determined equivalent force and moment as the amplitude of the forcing function. It is assumed that the mechanical interaction between the bonded actuator and the host structure occurs at the ends of the actuator in the form of concentrated forces. This approach is simple and easy to use but it often leads to misleading results. More importantly, the static approach does not correctly capture the physical essence of the PZT-structure interaction. In order to improve the accuracy, Liang et al. [13] presented the impedance approach instead of the static approach. This approach modeled the PZT patch connected to the host structure represented by the mechanical impedance Z_s , as shown in Figure 1. The multidimensional effects associated with PZT vibrations are ignored in Liang's model. Zhou et al. [14] extended the one-dimensional (1D) model to a generic two-dimensional (2D) PZT-structure model by considering the coupled vibration in the plane. This model replaced the structural impedance with a matrix consisting of the direct impedances Z_{xx} and Z_{yy} and the cross-impedances Z_{xy} and Z_{yx} , as shown in Figure 2. Experimental difficulties prevent the direct application of Zhou's model for extraction of the structural mechanical impedance. To overcome this shortcoming, a new concept of "effective impedance" was introduced in the effective impedance model of Bhalla and Soh [15]. In this model, the PZT-structure mechanical interaction extends all over the finite-sized PZT patch, as shown in Figure 3. This model condenses the two-directional physical coupling between the PZT patch and the host structure into a single impedance term, which can be determined from the measured admittance signatures. Hence, the model bridges the gap between Liang's 1D model and Zhou's 2D model.

Conventionally, the impedance models are usually considered as 1D or 2D, and the coupling between the extensional and longitudinal vibrations is neglected. To satisfy the requirements of the 1D model, the thickness of the PZT patch must be much smaller than its radius (length and width). However, the PZT patch has finite dimensions of thickness and radius (length and width) in practical applications,

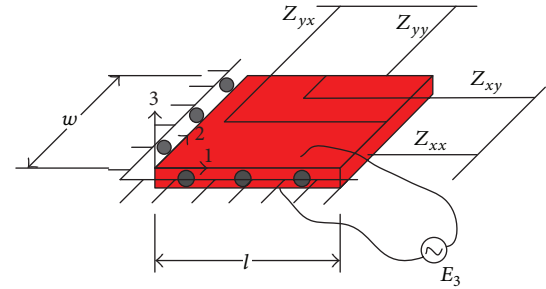


FIGURE 2: Zhou's 2D impedance model [14].

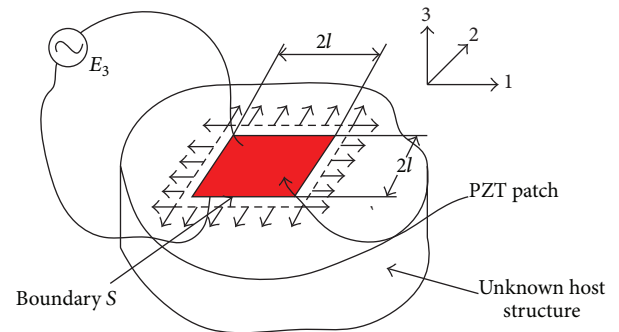


FIGURE 3: 2D effective impedance model of Bhalla and Soh [15].

and both the extensional and longitudinal vibrations are important [17]. Hence, there is a need for the development of a three-dimensional (3D) PZT-structure interaction model, which considers the coupling between the extensional and longitudinal vibrations. The study presented here aims to model the PZT-structure interaction considering the 3D coupled vibration effect. In this paper, a 3D effective electromechanical impedance model for an embedded PZT plate is proposed by adopting the "effective impedance" concept. The new model describes the extensional actuations along the radial direction and longitudinal actuation along the thickness direction of the PZT patch. The advantage of the 3D effective impedance model is that it can only capture the "active part" associated with the structural mechanical impedance by filtering the PZT contribution. Then, the inherent properties of the monitored structure can be detected with a higher accuracy than with the raw admittance signal only. To validate the effectiveness of the proposed method, a concrete beam with embedded PZT transducers during the curing age was measured to monitor the strength gain.

2. Theoretical Background

In a linear vibration system, the steady-state response $x(t)$, that is, displacement, velocity, or acceleration, is caused by the harmonic force $F(t)$. $x(t)$ and $F(t)$ have the same frequency, and $x(t)$ lags behind $F(t)$ by a phase angle ϕ . The structural mechanical impedance Z is defined as the ratio of the harmonic excitation to its steady-state response. Conventionally, the velocity impedance is regarded as the

mechanical impedance. Therefore, the structural mechanical impedance is expressed as

$$Z = \frac{F}{\dot{u}} = \frac{F_o e^{j\omega t}}{\dot{u}_o e^{j(\omega t - \phi)}} = \frac{F_o}{\dot{u}_o} e^{j\phi}, \quad (1)$$

where F_o is the amplitude of the excitation force, ω is the circular frequency of the excitation force, \dot{u}_o is the amplitude of the velocity, and ϕ is the phase angle of the velocity response.

The existing models are based on the definition that the structural mechanical impedance refers to a particular point, and the point considered is the PZT end point. However, the PZT-structure interaction is not restricted at the PZT end point, and it extends all over the PZT patch. The force transmission between the PZT patch and the host structure occurs along the entire boundary of the PZT patch [15]. Ignoring the effect of the PZT vibrations in the thickness direction and assuming the frequency range of interest to be much lower than the dominant modes of thickness vibration, a new concept of “effective mechanical impedance” was defined by Bhalla and Soh [15]. However, the embedded PZT patch has both the extensional and longitudinal vibrations in practical applications. Hence, the formulations of the “effective mechanical impedance” of 3D model need to be established.

We consider a circular PZT patch embedded into an unknown host structure, as shown in Figure 4, subjected to an electric field. The interaction of the PZT patch with the host structure is represented in the form of the boundary traction f , and the PZT-structure interaction force is assumed along the entire boundary of the PZT patch. Further, the PZT patch is assumed to be extremely small as compared to the host structure, and it has negligible mass and stiffness. Hence, the PZT patch can be regarded as an effective drive point. In addition, the impedance of the effective drive point is defined as the effective mechanical impedance.

The “effective mechanical impedance” of the PZT patch is defined as

$$Z_{a,\text{eff}} = \frac{\oint_S f \cdot \hat{n} dS}{\dot{u}_{\text{eff}}} = \frac{F_{\text{eff}}}{\dot{u}_{\text{eff}}}, \quad (2)$$

where F_{eff} is the effective force; \hat{n} is the unit vector normal to the boundary; $u_{\text{eff}} = \delta V / A_o$ is defined as effective displacement of the PZT patch, where δV is the change in volume of the PZT patch; and A_o is the surface area of the PZT patch. Differentiation of the effective displacement with respect to time yields the effective velocity \dot{u}_{eff} . The “effective mechanical impedance” of the host structure can be defined based on applying the force on the surface of the host structure, along the boundary of the location of the embedded PZT patch.

3. Three-Dimensional Electromechanical Impedance Models

The existing impedance models are usually considered to be 1D or 2D models, and they neglect the longitudinal vibration

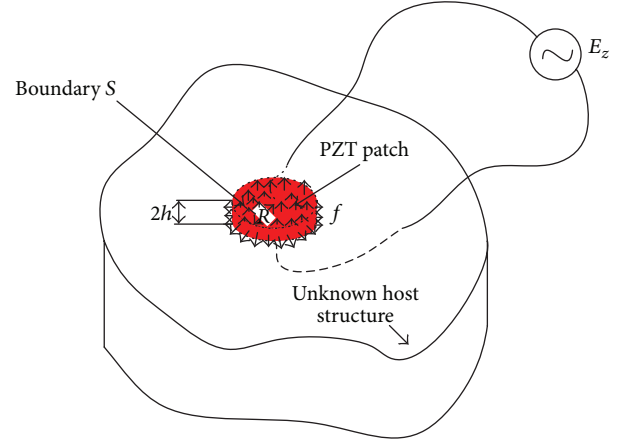


FIGURE 4: 3D effective impedance model.

of the PZT patch. Hence, there is a need for the development of a 3D PZT-structure interaction model that considers both the extensional and longitudinal vibrations of the PZT patch. By applying the concept of “effective mechanical impedance,” a 3D effective impedance model is proposed. The features of the proposed impedance model are that there are no restrictions of the PZT dimensions, and the model more accurately represents the actual situation.

3.1. 3D Electromechanical Admittance Formulation by the Effective Impedance. A circular PZT patch of radius R and thickness $2h$ is shown in Figure 5. The polarization direction is along the Z axis, and the external exciting electric field E_z is also applied along the Z -direction and parallel to the polarization direction. Then, the vibration of the PZT patch can be regarded as a symmetrical vibration, and the shearing effect can be ignored. Owing to the symmetrical vibration, it is sufficient to use 1/8 of the PZT patch and host structure. Because of the mechanical and piezoelectric anisotropy of the PZT patch, the formulations $S_{11}^E = 1/\bar{Y}^E$, $S_{12}^E = -\nu_{12}S_{11}^E = -\nu_{12}/\bar{Y}^E$, $S_{13}^E = -\nu_{13}S_{11}^E = -\nu_{13}/\bar{Y}^E$, and $S_{33}^E = \nu_{33}S_{11}^E = \nu_{33}/\bar{Y}^E$ are obtained. In cylindrical coordinates, the constitutive relations of the PZT patch are expressed as [18]

$$\begin{aligned} D_z &= \bar{\epsilon}_{33}^T E_z + d_{31} (T_{rr} + T_{\theta\theta}) + d_{33} T_{zz}, \\ S_{rr} &= \frac{T_{rr}}{\bar{Y}^E} - \frac{\nu_{12} T_{\theta\theta}}{\bar{Y}^E} - \frac{\nu_{13} T_{zz}}{\bar{Y}^E} + d_{31} E_z, \\ S_{\theta\theta} &= -\frac{\nu_{12} T_{rr}}{\bar{Y}^E} + \frac{T_{\theta\theta}}{\bar{Y}^E} - \frac{\nu_{13} T_{zz}}{\bar{Y}^E} + d_{31} E_z, \\ S_{zz} &= -\frac{\nu_{13} T_{rr}}{\bar{Y}^E} - \frac{\nu_{13} T_{\theta\theta}}{\bar{Y}^E} + \frac{\nu_{33} T_{zz}}{\bar{Y}^E} + d_{33} E_z, \end{aligned} \quad (3)$$

where T_{rr} , $T_{\theta\theta}$, and T_{zz} are, respectively, the radial, tangential, and axial stress; S_{rr} , $S_{\theta\theta}$, and S_{zz} are, respectively, the radial, tangential, and axial strain; S_{ij}^E is the elastic compliance constant in the short-circuited condition; \bar{Y}^E is the complex Young's modulus of elasticity at a constant electric field;

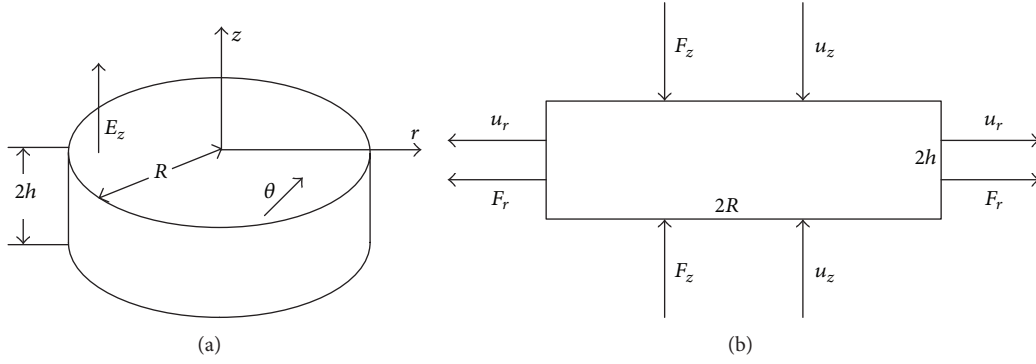


FIGURE 5: (a) Geometry of the circular PZT patch and (b) stresses and displacements on the PZT patch.

ν_{12} , ν_{13} , and ν_{33} are Poisson's ratios; d_{31} and d_{33} are the piezoelectric strain coefficients; E_z is the electric field; D_z is the electric displacement; and ϵ_{33}^T is the complex electric permittivity at a constant stress.

We let $n = T_{zz}/(T_{rr} + T_{\theta\theta})$. n is defined as the mechanical coupling coefficient between different vibrational modes [17]. By algebraic manipulation, we obtain

$$T_{rr} + T_{\theta\theta} = \frac{\overline{Y^E}}{\lambda} [S_{rr} + S_{\theta\theta} + S_{zz} - (2d_{31} + d_{33}) E_z], \quad (4)$$

$$T_{zz} = \frac{n\overline{Y^E}}{\lambda} [S_{rr} + S_{\theta\theta} + S_{zz} - (2d_{31} + d_{33}) E_z],$$

where $\lambda = 1 - \nu_{12} - \nu_{13} + n(\nu_{33} - 2\nu_{13})$. Then, the effective force of the PZT-structure interaction is given by

$$\begin{aligned} F &= \oint_S \mathbf{f} \cdot \hat{\mathbf{n}} dS = (T_{rr} + T_{\theta\theta}) \cdot \frac{2\pi R h}{4} + T_{zz} \cdot \frac{\pi R^2}{4} \\ &= \frac{\pi R (2h + nR)}{4\lambda} [S_{rr} + S_{\theta\theta} + S_{zz} - (2d_{31} + d_{33}) E_z]. \end{aligned} \quad (5)$$

In the short-circuited condition, the effective force is expressed as

$$F_{\text{short-circuited}} = \frac{\pi R (2h + nR) \overline{Y^E}}{4\lambda} (S_{rr} + S_{\theta\theta} + S_{zz}). \quad (6)$$

As derived in [18, 19], the displacements of the PZT patch in cylindrical coordinates are provided by

$$\begin{aligned} u_r &= A_1 J_1(\kappa_1 r) e^{j\omega t}, \\ u_\theta &= 0, \\ u_z &= A_2 \sin(\kappa_2 z) e^{j\omega t}, \end{aligned} \quad (7)$$

where the wave number of the radial direction $\kappa_1 = \omega \sqrt{(2\rho\lambda(1 + \nu_{12}))/((1 + \nu_{12} + \lambda)\overline{Y^E})}$ and the wave number of the longitudinal direction $\kappa_2 = \omega \sqrt{\rho\lambda/n\overline{Y^E}}$. A_1 and A_2 are constants determined by the boundary conditions. $J_1(x)$ is the Bessel function of the first kind and first order, and $J_1'(x) =$

$J_0(x) - (1/x)J_1(x)$. By differentiating (7) with respect to time, the velocities are obtained as follows:

$$\begin{aligned} \dot{u}_r &= \frac{\partial u_r}{\partial t} = A_1 j\omega J_1(\kappa_1 x) e^{j\omega t}, \\ \dot{u}_\theta &= \frac{\partial u_\theta}{\partial t} = 0, \\ \dot{u}_z &= \frac{\partial u_z}{\partial t} = A_2 j\omega \sin(\kappa_2 z) e^{j\omega t}. \end{aligned} \quad (8)$$

The strains are obtained by differentiating (7) with respect to the coordinate axes:

$$\begin{aligned} S_{rr} &= \frac{\partial u_r}{\partial r} = A_1 \left[\kappa_1 J_0(\kappa_1 r) - \frac{1}{r} J_1(\kappa_1 r) \right] e^{j\omega t}, \\ S_{\theta\theta} &= \frac{u_r}{r} = \frac{A_1}{r} J_1(\kappa_1 r) e^{j\omega t}, \\ S_{zz} &= \frac{\partial u_z}{\partial z} = A_2 \kappa_2 \cos(\kappa_2 z) e^{j\omega t}. \end{aligned} \quad (9)$$

Under the multimode vibration and free boundary conditions, the frequency equations for the PZT patch in a coupled vibration are obtained as follows:

$$\begin{aligned} \cot \kappa_2 \cdot 2h &= 0 \\ \kappa_1 R J_0(\kappa_1 R) &= (1 - \nu_{12}) J_1(\kappa_1 R). \end{aligned} \quad (10)$$

Then, the following relations are obtained by solving (8) and (9):

$$\begin{aligned} \kappa_2 \cdot 2h &= (2m - 1) \frac{\pi}{2}, \quad (m = 1, 2, 3, \dots), \\ \kappa_1 R &= R(n), \quad (n = 1, 2, 3, \dots), \end{aligned} \quad (11)$$

where $R(n)$ is the root for (9), and it is a function of ν_{12} . By substituting $\kappa_1 = \omega \sqrt{(2\rho\lambda(1 + \nu_{12}))/((1 + \nu_{12} + \lambda)\overline{Y^E})}$, $\kappa_2 = \omega \sqrt{\rho\lambda/n\overline{Y^E}}$, and $\lambda = 1 - \nu_{12} - \nu_{13} + n(\nu_{33} - 2\nu_{13})$ and solving, n is obtained as follows:

$$n = \frac{2 - \nu_{13}}{(1 + \nu_{12})C' - (\nu_{33} - 2\nu_{13})}, \quad (12)$$

where $C' = ((2i - 1)^2 \pi^2)/(8R^2(j)) \cdot (R^2/h^2)$.

Based on the definition of the effective displacement in (1), the displacement at the boundaries of 1/8 of the PZT patch is expressed as

$$u_{\text{eff}} = \frac{\delta V}{A_o} \approx \frac{2hu_{r_o} - Ru_{z_o}}{2h + R}. \quad (13)$$

Differentiating with respect to time, the effective velocity is obtained:

$$\dot{u}_{\text{eff}} \approx \frac{2h\dot{u}_{r_o} - R\dot{u}_{z_o}}{2h + R}. \quad (14)$$

To simplify the calculation, we assume that

$$\frac{u_{z_o}}{h} = -\nu_{13} \cdot \frac{u_{r_o}}{R}. \quad (15)$$

Substituting (7), the following formulations are derived:

$$\frac{A_1}{A_2} = -\frac{R \sin(\kappa_2 h)}{\nu_{13} h J_1(\kappa_1 R)}, \quad \frac{A_2}{A_1} = -\frac{\nu_{13} h J_1(\kappa_1 R)}{R \sin(\kappa_2 h)}. \quad (16)$$

Substituting (6), (8), (9), and (14) into (2), the effective impedance of the PZT patch is expressed as

$$Z_{a,\text{eff}} = \frac{\pi(2h + R)(2h + nR)\overline{Y}^E}{4\lambda(2 + \nu_{13})hj\omega} \cdot \left[\frac{\kappa_1 R J_0(\kappa_1 R)}{J_1(\kappa_1 R)} - \nu_{13} \frac{\kappa_2 h}{\tan(\kappa_2 h)} \right]. \quad (17)$$

The effective force F is related to the effective impedance of the host structure by

$$F = \oint_S f \cdot \hat{n} dS = -Z_{s,\text{eff}} \cdot \dot{u}_{\text{eff}}. \quad (18)$$

By substituting (8), (9), and (18) into (2), with $E_z = (V_o/2h)e^{j\omega t}$, the constants A_1 and A_2 are obtained:

$$\begin{aligned} A_1 &= (\alpha R V_o Z_{a,\text{eff}}) \\ &\times \left(2h \cdot J_1(\kappa_1 R) \left[\frac{\kappa_1 R J_0(\kappa_1 R)}{J_1(\kappa_1 R)} - \nu_{13} \right. \right. \\ &\quad \left. \left. \cdot \frac{\kappa_2 h}{\tan(\kappa_2 h)} \right] (Z_{s,\text{eff}} + Z_{a,\text{eff}}) \right)^{-1}, \\ A_2 &= (-\nu_{13} \alpha V_o Z_{a,\text{eff}}) \\ &\times \left(2 \sin(\kappa_2 h) \left[\frac{\kappa_1 R J_0(\kappa_1 R)}{J_1(\kappa_1 R)} - \nu_{13} \right. \right. \\ &\quad \left. \left. \cdot \frac{\kappa_2 h}{\tan(\kappa_2 h)} \right] (Z_{s,\text{eff}} + Z_{a,\text{eff}}) \right)^{-1}. \end{aligned} \quad (19)$$

The instantaneous electric current is expressed as

$$\bar{I} = \frac{dQ(t)}{dt} = \iint_A \dot{D}_Z dA = j\omega \iint_A D_{Z(Z=h)} dA. \quad (20)$$

Substituting (4), (9), and (19) into (3), the electromechanical admittance of the 3D effective electromechanical impedance model is derived as

$$\begin{aligned} \bar{Y} &= \frac{\bar{I}}{\bar{V}} = G + Bj \\ &= \frac{\pi R^2 j\omega}{2h} \\ &\times \left[\frac{\overline{\epsilon}_{33}^T}{\lambda} - \frac{\alpha\beta\overline{Y}^E}{\lambda} \right. \\ &\quad \left. + \left(\left(\frac{\alpha\beta\overline{Y}^E}{\lambda} \cdot \left(2 - \nu_{13} \cdot \frac{\kappa_2 h}{\tan(\kappa_2 h)} \right) \cdot Z_{a,\text{eff}} \right) \right. \right. \\ &\quad \left. \left. \times \left(\left[\frac{\kappa_1 R J_0(\kappa_1 R)}{J_1(\kappa_1 R)} - \nu_{13} \cdot \frac{\kappa_2 h}{\tan(\kappa_2 h)} \right] \right. \right. \right. \\ &\quad \left. \left. \left. \times (Z_{s,\text{eff}} + Z_{a,\text{eff}}) \right)^{-1} \right) \right], \end{aligned} \quad (21)$$

where $\alpha = 2d_{31} + d_{33}$ and $\beta = d_{31} + nd_{33}$; $\bar{V} = V_o e^{j\omega t}$ is the instantaneous voltage across the PZT patch.

This formulation contains $Z_{a,\text{eff}}$ and the effective structural mechanical impedance $Z_{s,\text{eff}}$. $Z_{a,\text{eff}}$ is constant for certain material parameters. The variations in $Z_{s,\text{eff}}$ caused by a change in the inherent properties of the host structure directly influence the electromechanical impedance. Hence, the variations in the inherent properties can be monitored by the measured electromechanical impedance.

3.2. Decomposition of the Coupled Electromechanical Admittance Signatures. In Section 3.1, the complex electromechanical admittance of the proposed impedance model has been derived. By rearranging the various terms in (21), it can be separated into two parts as

$$\begin{aligned} \bar{Y} &= \underbrace{\frac{\pi R^2 j\omega}{2h} \cdot \left[\frac{\overline{\epsilon}_{33}^T}{\lambda} - \frac{\alpha\beta\overline{Y}^E}{\lambda} \right]}_{\text{Part I}} \\ &\quad + \underbrace{\frac{\pi R^2 j\omega}{2h} \cdot \frac{\alpha\beta\overline{Y}^E}{\lambda} \cdot \left(\frac{Z_{a,\text{eff}}}{Z_{s,\text{eff}} + Z_{a,\text{eff}}} \right)}_{\text{Part II}} \cdot \bar{T}, \end{aligned} \quad (22)$$

where $\bar{T} = (2 - \nu_{13} \cdot (C_2 \kappa_2 h / \tan(C_2 \kappa_2 h))) / [(C_1 \kappa_1 R J_0(C_1 \kappa_1 R) / J_1(C_1 \kappa_1 R)) - \nu_{13} \cdot (C_2 \kappa_2 h / \tan(C_2 \kappa_2 h))]$. Part I only relates to the parameters of the PZT patch and is independent of the host structure. Part II represents the coupling between the PZT patch and the host structure. Hence, (22) is written as

$$\bar{Y} = \bar{Y}_P + \bar{Y}_A, \quad (23)$$

where \bar{Y}_P describes the PZT contribution that is insensitive to any structural changes; it is the ‘‘passive’’ part; \bar{Y}_A represents the contribution of the PZT-structure interaction and is

sensitive to any structural changes near the PZT patch; it is the “active” part [20]. By substituting $\overline{Y^E} = Y^E(1 + \eta j)$ and $\overline{\varepsilon_{33}^T} = \varepsilon_{33}^T(1 - \delta j)$, $\overline{Y_P}$ is expressed as

$$\overline{Y_P} = G_P + B_P j, \quad (24)$$

where

$$G_P = \frac{(\pi R)^2 f}{h} \left(\delta \varepsilon_{33}^T + \frac{\alpha \beta Y^E}{\lambda} \cdot \eta \right), \quad (25)$$

$$B_P = \frac{(\pi R)^2 f}{h} \left(\varepsilon_{33}^T - \frac{\alpha \beta Y^E}{\lambda} \right).$$

The measured electrical admittance signals contain the “passive” and “active” parts. The existence of the “passive” part influences the sensitivity of the raw electrical admittance signals for SHM. Hence, if the PZT parameters are predicted, the “passive” part can be filtered out, and the “active” part can be derived from the raw electrical admittance signals:

$$G_a = G - G_P, \quad (26)$$

$$B_a = B - B_P.$$

Substituting (25) and (26) into (22), the complex form of the “active” part is expressed as

$$\overline{Y_A} = G_a + B_a j = \frac{\pi R^2 j \omega}{2h} \cdot \frac{\alpha \beta \overline{Y^E}}{\lambda} \cdot \frac{Z_{a,\text{eff}}}{(Z_{s,\text{eff}} + Z_{a,\text{eff}})} \cdot \overline{T}. \quad (27)$$

4. Experimental Investigations

In this study, a concrete beam with an embedded PZT patch during the curing age was monitored to measure the strength gain. First, an Agilent4294A precision impedance analyzer was used for collecting the electric admittance signals. By a series of computational procedures, the “active” part associated with the mechanical impedance was derived from the raw electrical admittance signal. Finally, the “active” part was utilized to monitor the strength gain of the concrete beam during the curing age. The objective of this experiment was to demonstrate the feasibility and sensitivity of utilizing the “active” part by filtering out the PZT contribution for SHM.

4.1. Experimental Setup. In the experiment, a concrete beam with dimensions of 10 mm × 10 mm × 50 mm was used for the strength gain monitoring of concrete in the early age by the proposed approach. To measure the EMI signatures during the curing age, a PZT patch having a thin epoxy adhesive that can be regarded as a waterproof layer was embedded into the concrete structure. The diameter of the PZT patch was 20 mm, and the thickness was approximately 2 mm. The properties of the PZT patch are listed in Table 1. The experimental setup for collecting the electrical admittance signals is shown in Figure 6. The patch was wired to the Agilent4294A precision impedance analyzer. Then, the

TABLE 1: Properties of the PZT patch.

Physical parameter	Value
Density, ρ (kg/m ³)	7600
Young's modulus, Y^E (N/m ²)	7.75×10^{10}
Piezoelectric strain coefficient, d_{31} (m/V)	120×10^{-12}
Piezoelectric strain coefficient, d_{33} (m/V)	280×10^{-12}

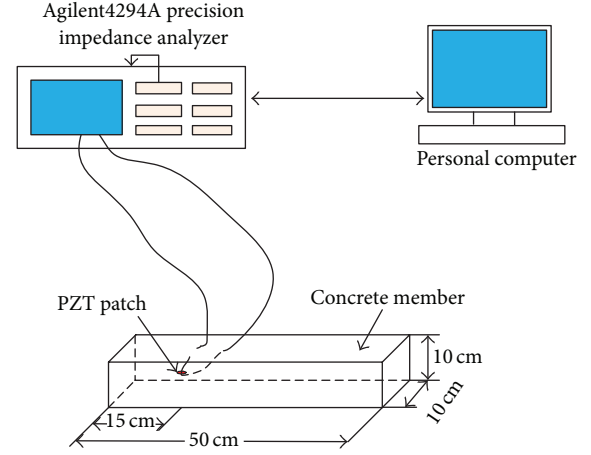


FIGURE 6: Experimental setup.

Agilent4294A precision impedance analyzer was connected to a computer via a GPIB interface.

By applying a high-frequency excitation voltage to the PZT patch with the Agilent4294A analyzer, the electromechanical admittance signature produced by the coupling vibration between the PZT patch and the host structure was measured in the frequency range of 20–200 kHz, including the real part (conductance G) and the imaginary part (susceptance B). In the monitored frequency range, 801 data points were taken with a 1-V sweeping sine wave for the excitation. However, the measured signals are often contaminated by noise originating from the measurement system [21, 22]. To minimize the influence of noise, eight averages of the signatures were calculated per frequency point. The impedance signature at the age of 1 day was measured and defined as the baseline, and then subsequent tests were taken at the ages of 2, 3, 4, and 7 days. By analyzing the measured electrical admittance signatures, the strength gain of the concrete beam during the curing age can be monitored by the proposed approach.

4.2. Determination of the PZT Parameters. Owing to the influence of the production process and the high temperature in the welding process between the PZT and the wires, the properties of the PZT patches provided by the manufacturer are unreliable. In the EMI technique, the “active” part of the electrical admittance signals is predicted based on the PZT parameters. Hence, more accurate PZT parameters need to be derived before extracting the “active” part from the measured raw admittance signatures.

For a PZT patch in the free-free condition prior to its embedding into the host structure, the complex electromechanical admittance is derived as ($Z_{s,\text{eff}} = 0$)

$$\overline{Y}_{\text{free}} = G_f + B_f j = \frac{\pi R^2 j \omega}{2h} \left[\overline{\epsilon}_{33}^T + \frac{\alpha \beta \overline{Y}^E}{\lambda} \cdot (T - 1) \right]. \quad (28)$$

By substituting $\overline{Y}^E = Y^E(1 + \eta j)$, $\overline{\epsilon}_{33}^T = \epsilon_{33}^T(1 - \delta j)$, $T = M + N \cdot j$, $[\kappa_1 R \cdot J_0(\kappa_1 R)]/J_1(\kappa_1 R) = r + t \cdot j$, $(\kappa_2 h)/\tan(\kappa_2 h) = r' + t' \cdot j$, and $\omega = 2\pi f$, we obtain

$$G_f = \frac{(\pi R)^2 f}{h} \left[\delta \epsilon_{33}^T - \frac{\alpha \beta Y^E}{\lambda} \{ \eta (M - 1) + N \} \right], \quad (29)$$

$$B_f = \frac{(\pi R)^2 f}{h} \left[\epsilon_{33}^T + \frac{\alpha \beta Y^E}{\lambda} \{ (M - 1) - \eta N \} \right],$$

where

$$M = \frac{(2 - \nu_{13} r') (r - \nu_{13} r') - \nu_{13} t' (t - \nu_{13} t')}{(r - \nu_{13} r')^2 + (t - \nu_{13} t')^2}, \quad (30)$$

$$N = -\frac{(2 - \nu_{13} r') (t - \nu_{13} t') + \nu_{13} t' (r - \nu_{13} r')}{(r - \nu_{13} r')^2 + (t - \nu_{13} t')^2}.$$

Further, for low frequencies (typically $<1/5$ of the first resonance frequency of the PZT), $[\kappa_1 R \cdot J_0(\kappa_1 R)]/J_1(\kappa_1 R) = r + t \cdot j \rightarrow 2$ and $(\kappa_2 h)/\tan(\kappa_2 h) = r' + t' \cdot j \rightarrow 1$ (i.e., $r \rightarrow 2$, $t \rightarrow 0$, $r' \rightarrow 1$, and $t' \rightarrow 0$); therefore, $M \rightarrow 1$, $N \rightarrow 0$ [13], and the quasistatic sensor approximation is expressed as [23]

$$G_{f,\text{qs}} = \frac{(\pi R)^2 f}{h} \cdot \delta \epsilon_{33}^T, \quad (31)$$

$$B_{f,\text{qs}} = \frac{(\pi R)^2 f}{h} \cdot \epsilon_{33}^T.$$

Hence, the electrical constants ϵ_{33}^T and δ can be determined by the measured electric admittance signals $G_{f,\text{qs}}$ and $B_{f,\text{qs}}$ for low frequencies (typically <10 kHz). From this analysis, ϵ_{33}^T and δ were determined to be 1.4×10^{-8} F/m and 0.0096, respectively.

By using (29) with these PZT parameters, the electrical admittance signals of the PZT patch in the free-free condition in the frequency range of 20–220 kHz were obtained and compared with the measured free PZT signals (G, B) in Figure 7. Although the experimental and analytical free PZT signals have the good agreement in the figures, there are fundamental differences that warrant closer examination. For instance, the analytical resonance frequency is slightly higher than the experimental frequency.

In order to achieve much better agreement between the analytical and experimental signatures, the correction factors C_1 and C_2 are introduced in the terms $[\kappa_1 R \cdot J_0(\kappa_1 R)]/J_1(\kappa_1 R)$ and $(\kappa_2 h)/\tan(\kappa_2 h)$, and these terms may be replaced by $[C_1 \kappa_1 R \cdot J_0(C_1 \kappa_1 R)]/J_1(C_1 \kappa_1 R)$ and $(C_2 \kappa_2 h)/\tan(C_2 \kappa_2 h)$, respectively. By trial and error, the values of the correction

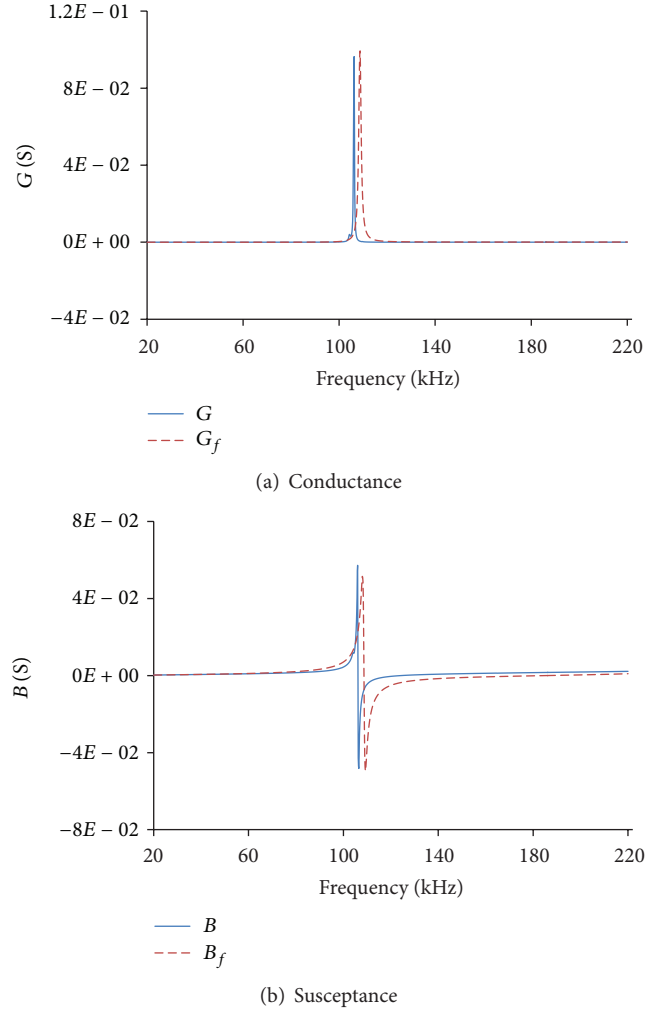


FIGURE 7: Comparison between the experimental and theoretical signals of the PZT patch in the free condition.

factor were $C_1 = 1.023$ and $C_2 = 0.98$. Hence, very good agreement is observed between the analytical and experimental signatures. Using curve-fitting techniques, it was found that $\eta = 0.021$ and $K = (\alpha \beta Y^E)/\lambda = 7.63 \times 10^{-9} \text{NV}^{-2}$. From these PZT parameters, the “active” part associated with the structural mechanical impedance by filtering the PZT contribution can be extracted from the measured raw admittance signatures.

4.3. Results and Analysis. As mentioned above, the PZT parameters can be accurately predicted by the measured admittance signatures of the PZT patches in the “free-free” condition. Hence, the “passive” part (PZT contribution) is filtered out, and the “active” part associated with the structural mechanical impedance can be extracted from the measured raw admittance signatures. The spectra are shown in Figure 7. With an increase in the curing time for the concrete specimen, the amplitudes of the G_a and B_a curves gradually diminished, and the curves shifted to the right. This indicates that the “active” part is sensitive to changes in the

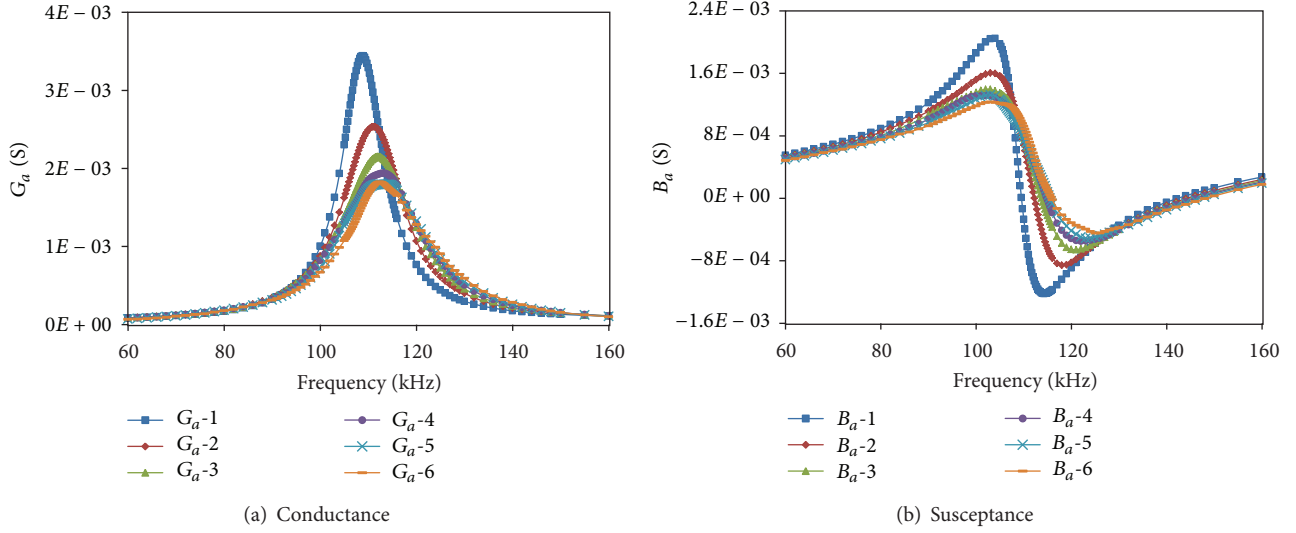


FIGURE 8: “Active” part extracted from the measured raw admittance signatures.

inherent properties of a concrete beam with embedded PZT transducers during the curing age.

Figure 8 depicts the variations of the “active” part curve, but the extent of the changes in the inherent properties cannot be directly determined. In other words, the spectra of the “active” part only qualitatively represent the strength gain of the concrete beam during the curing age. Although the spectra are qualitatively useful, they lack any quantitative accuracy. Traditionally, statistical pattern recognition techniques have been employed to quantify the changes in the admittance signatures, such as relative deviation, root-mean-square deviation, and mean-absolute-percentage deviation [24]. In order to quantitatively analyze the strength gain for the concrete beam during the curing age, two statistical indices are defined as follows.

- (1) Root-mean-square deviation (RMSD)

$$\text{RMSD} (\%) = \sqrt{\frac{\sum_{i=1}^N (y_i - \bar{y}_i)^2}{\sum_{i=1}^N \bar{y}_i^2}} \times 100. \quad (32)$$

- (2) Correlation coefficient (CC)

$$\text{CC} = \frac{(y_i^T \cdot \bar{y}_i)^2}{|y_i^T \cdot y_i| \cdot |\bar{y}_i^T \cdot \bar{y}_i|}, \quad (33)$$

where y_i and y_i^T separately denote the vector and its transpose for the “active” part of the electrical admittance (G_a and B_a) for curing times of 2, 3, 4, 5, and 7 days; and \bar{y}_i and \bar{y}_i^T separately denote the vector and its transpose for the “active” part of the electrical admittance for a curing time of 1 day.

Figure 9 shows the plots of the RMSD and CC indices for the “active” part and the measured raw admittance signatures, which are calculated at various stages during the curing age with respect to the baseline signature. From Figure 8, we find that the RMSD index increased and the

CC index decreased during the curing age for the concrete beam. These indexes qualitatively represent the variations in the inherent properties of the interior of the concrete beam.

The existing EMI techniques only depend on the real part of the measured electrical signatures, but the information in the imaginary part is lost. By eliminating the “passive” part, the admittance signatures are more sensitive to any structural changes than the raw signatures. By comparing the “active” part and the measured raw admittance signatures, the indices of the real part are similar, whereas the indices of the imaginary part have a large difference. Further, the indices of the imaginary component are similar to the indices of the real component in the “active” admittance signatures. This indicates that utilization of the imaginary component for damage identification is feasible. The experimental results demonstrate that the “active” part of the admittance signatures is more sensitive than the raw admittance signatures for SHM. Furthermore, the imaginary component can also be used for SHM.

5. Conclusions

In this paper, a three-dimensional effective electromechanical impedance model for an embedded PZT transducer is proposed. Based on the concept of effective impedance, the 3D coupled electromechanical admittance equation is derived. By rearranging the various terms, the admittance equation is separated into an “active” part and a “passive” part. Because the “active” part is sensitive to any structural changes near the PZT patch, it is feasible to use the “active” part for SHM. Then, the proposed method is used to monitor the strength gain of a concrete beam with embedded PZT transducers during the curing age. The results show that the “active” part of the admittance signatures is more sensitive to any structural damage than the raw admittance signatures, which demonstrates the validity of the proposed method.

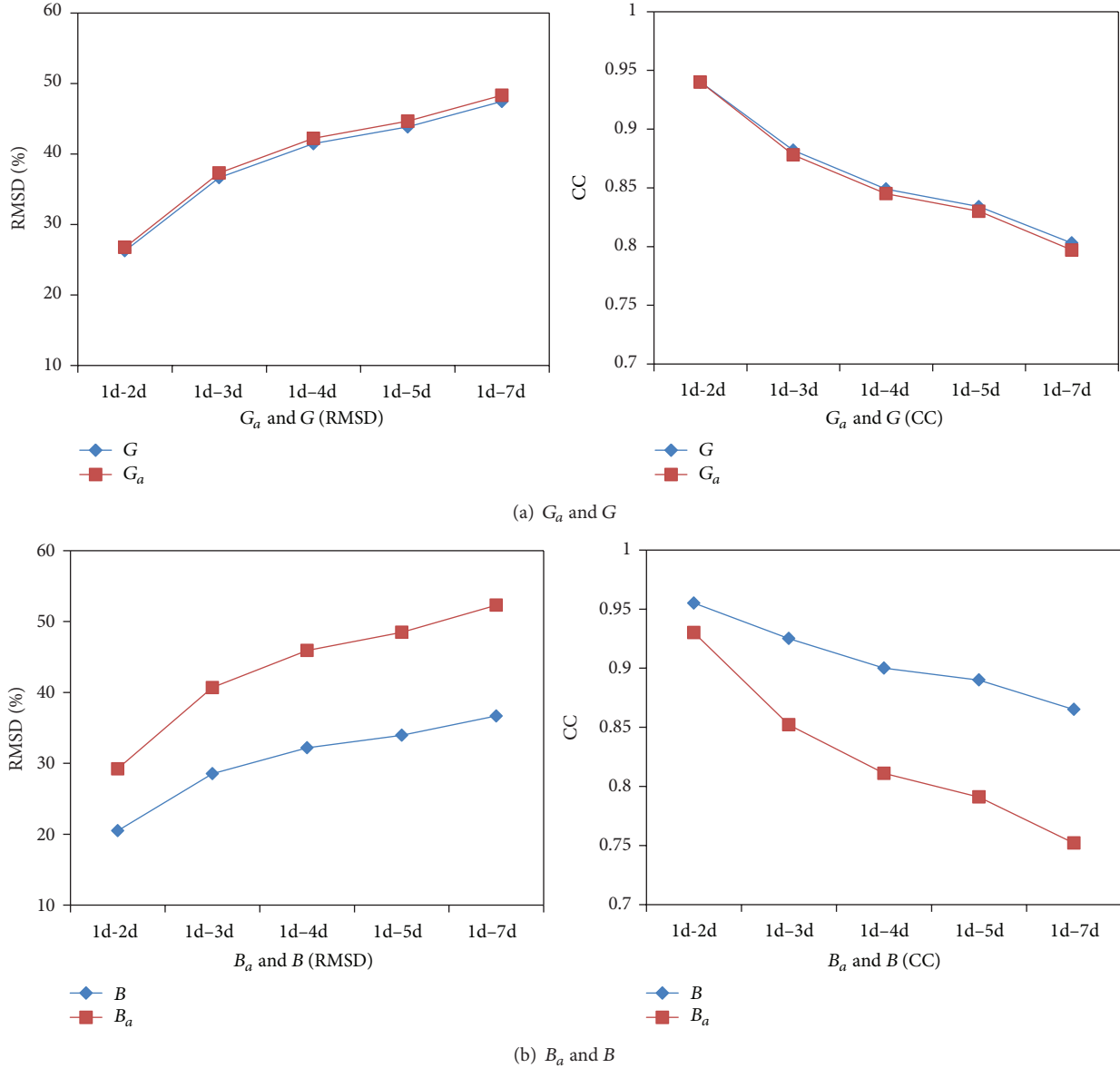


FIGURE 9: Comparison between the “active” part and the measured raw admittance signatures.

Acknowledgments

This work was supported by the Sate Key Development Program for Basic Research of China with Grant no. 2013CB0-35906 and Grants from the National Natural Science Foundation of China (51121005, 51078060). The authors gratefully acknowledge the support from the Education Department of Liaoning Province with Grant no. L2012010.

References

[1] T. Yi, H. Li, and M. Gu, “Optimal sensor placement for health monitoring of high-rise structure based on genetic algorithm,” *Mathematical Problems in Engineering*, vol. 2011, Article ID 395101, 12 pages, 2011.

[2] T. H. Yi and H. N. Li, “Methodology development in sensor placement for health monitoring of civil infrastructures,” *International Journal of Distributed Sensor Networks*, vol. 2012, Article ID 612726, 11 pages, 2012.

[3] I. Chopra, “Review of state of art of smart structures and integrated systems,” *AIAA Journal*, vol. 20, no. 11, pp. 2145–2187, 2002.

[4] S. Yan, N. Z. Zhao, Q. J. Wang, and G. B. Song, “Dynamic mechanical model of surface-bonded PZT actuator: theory and experiment,” *Applied Mechanics and Materials*, vol. 303–306, pp. 1732–1735, 2013.

[5] K. Nguyen, J. Park, and J. Kim, “Imote2-based multi-channel wireless impedance sensor nodes for local SHM of structural connections,” in *Sensors and Smart Structures Technologies for Civil, Mechanical, and Aerospace Systems*, vol. 7981 of *Proceedings of SPIE*, pp. 79811P–79811P-11, San Diego, Calif, USA, March 2011.

- [6] J. T. Kim, K. D. Nguyen, and J. H. Park, "Wireless impedance sensor node and interface washer for damage monitoring in structural connections," *Advances in Structural Engineering*, vol. 15, no. 6, pp. 871–885, 2012.
- [7] K. D. Nguyen, P. Y. Lee, and J. T. Kim, "Smart PZT-interface for SHM in tendon-anchorage of cable-stayed bridge," in *Sensors and Smart Structures Technologies for Civil, Mechanical and Aerospace System*, vol. 8345 of *Proceedings of SPIE*, pp. 834519–834519-11, San Diego, Calif, USA, March 2012.
- [8] Z. A. Chaudhry, T. Joseph, F. P. Sun, and C. A. Rogers, "Local-area health monitoring of aircraft via piezoelectric actuator/sensor patches," in *Smart Structures and Materials 1995: Smart Structures and Integrated Systems*, vol. 2443 of *Proceedings of SPIE*, pp. 268–276, San Diego, Calif, USA, March 1995.
- [9] J. W. Ayres, F. Lalande, Z. Chaudhry, and C. A. Rogers, "Qualitative impedance-based health monitoring of civil infrastructures," *Smart Materials and Structures*, vol. 7, no. 5, pp. 599–605, 1998.
- [10] G. Song, H. Gu, Y. L. Mo, T. T. C. Hsu, and H. Dhonde, "Concrete structural health monitoring using embedded piezoceramic transducers," *Smart Materials and Structures*, vol. 16, no. 4, pp. 959–968, 2007.
- [11] G. Park, H. H. Cudney, and D. J. Inman, "Feasibility of using impedance-based damage assessment for pipeline structures," *Earthquake Engineering and Structural Dynamics*, vol. 30, no. 10, pp. 1463–1474, 2001.
- [12] G. Park, H. Sohn, C. R. Farrar, and D. J. Inman, "Overview of piezoelectric impedance-based health monitoring and path forward," *Shock and Vibration Digest*, vol. 35, no. 6, pp. 451–463, 2003.
- [13] C. Liang, F. P. Sun, and C. A. Rogers, "Coupled electro-mechanical analysis of adaptive material systems—determination of the actuator power consumption and system energy transfer," *Journal of Intelligent Material Systems and Structures*, vol. 5, no. 1, pp. 12–20, 1994.
- [14] S. Zhou, C. Liang, and C. A. Rogers, "An impedance-based system modeling approach for induced strain actuator-driven structures," *Journal of Vibration and Acoustics*, vol. 118, no. 3, pp. 323–331, 1996.
- [15] S. Bhalla and C. K. Soh, "Structural health monitoring by piezo-impedance transducers. I: modeling," *Journal of Aerospace Engineering*, vol. 17, no. 4, pp. 154–165, 2004.
- [16] E. F. Crawley and J. de Luis, "Use of piezoelectric actuators as elements of intelligent structures," *AIAA Journal*, vol. 25, no. 10, pp. 1373–1385, 1987.
- [17] S. Y. Lin, "Coupled vibration analysis of piezoelectric ceramic disk resonators," *Journal of Sound and Vibration*, vol. 218, no. 2, pp. 205–217, 1998.
- [18] IEEE, "IEEE standard on piezoelectricity," IEEE 176-1987, 1988.
- [19] A. H. Meitzler, H. M. O'Bryan, and H. F. Tiersten, "Definition and measurement of radial mode coupling factors in piezoelectric ceramic materials with large variations in Poisson's ratio," *IEEE Transactions on Sonics and Ultrasonics*, vol. 20, no. 3, pp. 233–239, 1973.
- [20] S. Bhalla and C. K. Soh, "Structural health monitoring by piezo-impedance transducers. II: applications," *Journal of Aerospace Engineering*, vol. 17, no. 4, pp. 166–175, 2004.
- [21] T. H. Yi, H. N. Li, and X. Y. Zhao, "Noise smoothing for structural vibration test signals using an improved wavelet thresholding technique," *Sensors*, vol. 12, no. 8, pp. 11205–11220, 2012.
- [22] T. H. Yi, H. N. Li, and H. M. Sun, "Multi-stage structural damage diagnosis method based on "energy-damage" theory," *Smart Structures and Systems*, vol. 12, no. 3-4, pp. 345–361, 2013.
- [23] V. Giurgiutiu and A. N. Zagrai, "Embedded self-sensing piezoelectric active sensors for on-line structural identification," *Journal of Vibration and Acoustics*, vol. 124, no. 1, pp. 116–125, 2001.
- [24] K. K.-H. Tseng and A. S. K. Naidu, "Non-parametric damage detection and characterization using smart piezoceramic material," *Smart Materials and Structures*, vol. 11, no. 3, pp. 317–329, 2002.

Review Article

Review of Physical Based Monitoring Techniques for Condition Assessment of Corrosion in Reinforced Concrete

Ying Lei¹ and Zhu-Peng Zheng^{1,2}

¹ Department of Civil Engineering, Xiamen University, Xiamen 361005, China

² Department of Mechanical & Electrical Engineering, Xiamen University, Xiamen 361005, China

Correspondence should be addressed to Ying Lei; ylei@xmu.edu.cn

Received 30 October 2013; Revised 6 December 2013; Accepted 7 December 2013

Academic Editor: Ting-Hua Yi

Copyright © 2013 Y. Lei and Z.-P. Zheng. This is an open access article distributed under the Creative Commons Attribution License, which permits unrestricted use, distribution, and reproduction in any medium, provided the original work is properly cited.

Monitoring the condition of steel corrosion in reinforced concrete (RC) is imperative for structural durability. In the past decades, many electrochemistry based techniques have been developed for monitoring steel corrosion. However, these electrochemistry techniques can only assess steel corrosion through monitoring the surrounding concrete medium. As alternative tools, some physical based techniques have been proposed for accurate condition assessment of steel corrosion through direct measurements on embedded steels. In this paper, some physical based monitoring techniques developed in the last decade for condition assessment of steel corrosion in RC are reviewed. In particular, techniques based on ultrasonic guided wave (UGW) and Fiber Bragg grating (FBG) are emphasized. UGW based technique is first reviewed, including important characters of UGW, corrosion monitoring mechanism and feature extraction, monitoring corrosion induced debonding, pitting, interface roughness, and influence factors. Subsequently, FBG for monitoring corrosion in RC is reviewed. The studies and application of the FBG based corrosion sensor developed by the authors are presented. Other physical techniques for monitoring corrosion in RC are also introduced. Finally, the challenges and future trends in the development of physical based monitoring techniques for condition assessment of steel corrosion in RC are put forward.

1. Introduction

Reinforced concrete (RC) makes up a large part of the civil infrastructures. For instance, over half of the building and bridge inventories in China are reinforced concrete. Normally, concrete reinforced with steel is a rather splendid combination in which concrete also provides a high alkaline environment for the steel, helping to protect it from corrosion. However, corrosion of steel is inevitable, especially when RC structures are exposed to harsh environments with high carbon dioxide or chloride concentrations. The resulting corrosion products occupy volumes 6–10 times that of the steel [1]. The increased volume induces tensile stresses in the concrete which result in cracking, delamination, and spalling. As a result, the reinforcements get exposed to direct environmental attack and the corrosion is accelerated. Corrosion, if undiscovered can cause catastrophic failure of the structure, is currently one of the primary durability concerns for RC

structures. Corrosion causes billions of US dollars to be spent annually in repair, rehabilitation, and reconstruction efforts of RC structures, which makes it arguably the single largest infrastructural problem facing the industrialized countries [2]. It is imperative to develop effective monitoring techniques for condition assessment of corrosion in reinforced concrete.

A wide range of techniques have been reported in the literature that may be suitably employed for the monitoring of corrosion of steel in concrete structures for the purpose of diagnosing the cause and extent of the reinforcement corrosion [1–3]. Most of the existing techniques are electrochemical techniques such as half cell potential mapping and linear polarization which relate corrosion rate and extent through assessment on surrounding concrete medium. While many electrochemical techniques have been well-established, none of these techniques concentrate on corrosion monitoring through direct condition assessment or measurements

on embedded steel. As alternative tools for monitoring steel corrosion, some physical based techniques have been proposed [4, 5]. Compared with the electrochemistry based approaches, these physical approaches can not only provide supplemented tools for monitoring steel corrosion, but also conduct more accurate condition assessment of steel corrosion. However, there are still many challenges and difficulties of these physical based monitoring techniques for practical application of condition assessment of corrosion in reinforced concrete because the reinforcements are typically embedded inside concrete. Therefore, it is still imperative to investigate effective monitoring techniques for early detection of corrosion in steel embedded in concrete. Among the proposed physical based monitoring techniques, techniques based on ultrasonic guided wave (UGW) and fiber Bragg grating (FBG) have many advantages for monitoring corrosion-related damage in reinforcing bars, so they gained popularity among researchers in the past decades. This paper reviews some physical based monitoring techniques with emphases on the UGW and FBG based monitoring techniques for the condition assessment of steel corrosion in reinforced concrete in the last decade. The challenges and future trends in the development of physical based monitoring techniques for condition assessment of corrosion in reinforced concrete are also put forward. The structure of the rest of the paper is as follows. Section 2 reviews the UGW based techniques for corrosion monitoring of RC, which contains some important characters of UGW, mechanism of monitoring corrosion and feature extraction based on UGW, monitoring corrosion induced deboning, pitting, and interface roughness, respectively, and monitoring combined effects in actual corrosion and so forth; Section 3 reviews FBG for monitoring corrosion in RC, which contains mechanism of the FBG based corrosion sensor, design of FBG corrosion sensor proposed by the authors, and application of the designed FBG corrosion sensors in Xiamen Xiang'an Subsea Tunnel in China; Section 4 introduces some of other physical techniques for monitoring corrosion in RC. Finally, the challenges and future trends in the development of physical based monitoring techniques for condition assessment of corrosion in reinforced concrete are summarized in the conclusions.

2. UGW Based Techniques for Corrosion Monitoring of RC

2.1. Some Important Characters of Guided Waves. In an infinite isotropic solid medium only two types of independent wave propagation exist, that is, compression and shear waves. When geometry constraints are introduced and the dimensions are close to the wavelength, the wave becomes dispersive and is called a guided wave. The propagation of guided waves is in accordance with the elastic theory in elastic media, whereas they follow the viscoelastic theory in nonelastic media. Pipes, anchor molts, rails, and steel rebar are typical waveguides.

There are three types of propagating waves in a cylindrical waveguide: longitudinal, torsional, and flexural waves due to complex effect of boundaries and they have frequency-dependent properties with notations of $L(m, n)$, $T(m, n)$, and

$F(m, n)$, respectively [6]. The characters “ m ” and “ n ” represent the circumferential displacement and the sequential order of the mode, respectively.

The displacement is symmetrical corresponding to $m = 0$, where as $m = 1, 2, 3, \dots$ refers to asymmetrical displacements. Longitudinal modes that propagate in the steel rebar only have two types of displacement, namely, radial displacement μ_r and axial displacement μ_z . Considering the boundary condition $\sigma_{rr} = \sigma_{rz} = 0$ ($r = a$), the Pochhammer frequency equation can be achieved by solving the following wave equation [6]:

$$\frac{2\alpha}{a} (\beta^2 + k^2) J_1(\alpha a) J_1(\beta a) - (\beta^2 - k^2) J_0(\alpha a) J_1(\beta a) - 4k^2 \alpha \beta J_1(\alpha a) J_0(\beta a) = 0, \quad (1)$$

where $\alpha^2 = (\omega^2/c_L^2) - k^2$, $\beta^2 = (\omega^2/c_T^2) - k^2$, ω is the angular velocity, k is real wave number, c_L and c_T are the velocity of longitudinal and transverse waves in media, a is the radius of the cylinder, and J is Bessel function, respectively. Equation (1) is a transcendental equation with independent variables ω and k . Thus, a single frequency ω has more than one solution. This phenomenon corresponds well to the fact that many modes exist at a single frequency, indicating the multiple modes property of UGWs.

Phase and group velocities are two fundamental parameters that describe the characteristics of wave propagation. Phase velocity is defined as the speed of the phase of the wave propagation in the waveguide, whereas group velocity corresponds to the speed of the wave packet propagation. The curves that depict the relationships between frequency and phase velocity and group velocity are called dispersion curves. All waveguides, both symmetrical and asymmetrical, have special dispersion curves, which can be obtained via numerical calculation [7, 8]. Other characters of guided wave propagation can be obtained in many textbooks, for example, [9–15].

For a typical steel bar in air, in which the diameter of the bar is 22 mm, density is 7932 kg/m³, compression longitudinal velocities is 5960 m/s, and transverse velocity is 3260 m/s [7, 16]; the dispersive curves of phase and group velocity are shown in Figures 1 and 2, respectively.

Based on Figures 1 and 2, the following characters of UGW are drawn.

- (1) More than two modes exist corresponding to a single frequency. The number of modes increases with the increasing of the frequency.
- (2) Dispersion occurs in all modes, indicating that phase velocity or group velocity changes with frequency.
- (3) Cut-off frequency is common in all the modes except for $L(0, 1)$ and $F(1, 1)$. In other words, only $L(0, 1)$ and $F(1, 1)$ modes can be excited when the frequency is lower than 87 kHz. This feature is very important to select the excitation frequency of the guided wave signal.

Therefore, guided waves have some important characters, such as, the capability of testing over long distances with

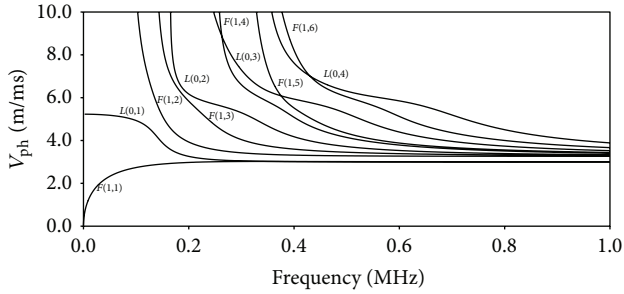


FIGURE 1: Phase velocity dispersion curves.

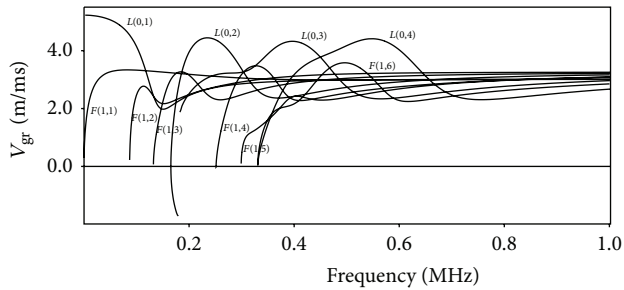


FIGURE 2: Group velocity dispersion curves.

a greater sensitivity, the ability to test multilayered structures, and being relatively inexpensive due to simplicity and sensor cost [17]. Furthermore, frequency and mode tuning can be utilized for evaluation of different types of deterioration or damage because UGWs have many different modes at a single frequency that are sensitive to different defects.

Due to the above characters, the guided wave based techniques have been found to be very efficient for damage detection and condition assessments of various aerospace, civil structures, and other nondestructive testing (NDT) areas, for example, Ajay and Carlos presented a review of guided wave for structural health monitoring; Sohn et al. [18] investigated delamination detection in composites through guided wave imaging; Song et al., [19, 20] developed smart piezoceramic transducers for concrete structural health monitoring; Schöpfer et al. [21] proposed a mathematical analysis of the strip-element method for the computation of dispersion curves of guided waves in anisotropic layered media including a thorough analysis of the corresponding infinite-dimensional eigenvalue problem as well as a proof of the existence of eigenvalues; De Marchi et al. [22] studied an approach based on a Warped Frequency Transform (WFT) to compensate the dispersive behavior of ultrasonic guided waves, followed by a Wigner-Ville time-frequency analysis and the Hough Transform to further improve localization accuracy. Giurgiutiu [23] studied lamb wave generation with piezoelectric wafer active sensors for structural health monitoring (SHM); Zhu et al. [24] carried out studies on two concrete slabs with different debonding between the rebars and concrete. Three proposed indices were used to identify the bond loss. They are the attenuation factor, the damage index (DI) value which is based on the comparison between the original waveform and the response signal, and the damage index based on wavelet

component energy (WDI) value which is based on the wavelet component energy. The experimental results show that the technique is effective to detect the single bond loss. The DI value increases when the debond length increases but the damage location has no obvious effect on DI values. The WDI value increases with the debond length and changes with the damage location; Wang et al. [25] investigated the effects of a defect's geometric parameter on the two reflection signals in pipe using guided waves and proposed a new strategy for accurate and quantitative pipeline defect characterization; Iyer et al. [26] proposed an ultrasound acoustics-based methodology that acquires depth perception and complement 2-D crack features available from the Sewer Scanner and Evaluation Technology camera for inspection of concrete pipes; Cobb et al. [27] studied the torsional guided wave attenuation in piping from coating, temperature, and large-area corrosion and obtained the experimental results that wave attenuation is a good indicator of general corrosion level with some limitation regarding coating type; Salzburger et al. [28] studied the pipe inspection with guided waves by Electromagnetic Acoustic Transducers (EMATs) which can contribute new solutions for ultrasonic testing (UT) of pipes using guided waves; Ahmad and Kundu [29] studied the influence of water flow through pipe networks for damage detection using guided waves; Beard et al. [30] used guided waves to inspect concrete reinforcing tendons and evaluated the effect of factors such as leakage and defect geometry; Zhu et al. [31] used ultrasonic guided waves for nondestructive evaluation/structural health monitoring of trusses. Other recent developments of guided waves for SHM were also discussed in a review prepared by Huang et al. [32].

This paper concentrates on the review of the studies and progress of monitoring corrosion in reinforced concrete in the last decade based on the above characters of ultrasonic guided waves

2.2. Mechanism and Feature Extraction of Monitoring Corrosion in RC Based on UGW. Concrete is alkaline due to the presence of hydroxides of calcium, potassium, and sodium ($\text{Ca}(\text{OH})_2$, KOH , and NaOH). Due to the high alkalinity of concrete, the steel reinforcing bars are passivated by an iron oxide film that protects the bar. However, in the presence of oxygen, water, and aggressive ions such as chlorides steel bars are depassivated and corrosion is initiated. For the above corrosion mechanism, reinforcement corrosion can occur in a localized manner, that is, pitting, or over a larger area, that is, general corrosion, and it is dependent on a number of different parameters. As a general rule, low to medium amounts of chloride lead to more uniform attacks, whereas medium to high amounts of chloride and concrete carbonation lead to more localized attacks.

Most of current guided wave based techniques for monitoring corrosion in steel bars are based on the following three mechanisms and feature extraction.

- (1) Corrosion causes the increase in bond between the reinforcing steel bars and concrete, makes the surface of steel bars rough, and therefore affects the guided wave propagation characters.

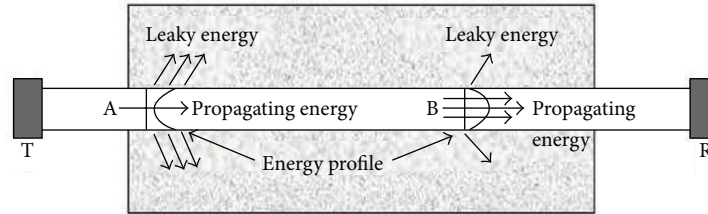


FIGURE 3: Two types of guided wave modes A and B can propagate from the transmitter T to the receiver R. From Miller et al. [33].

- (2) Severe pitting is caused by corrosion and the discontinuity in steel bar affects the guided wave propagation characters.
- (3) Corrosion eventually causes delamination or separation of steel rebar from the concrete affecting the strength of the propagating wave due to delamination.

Based on the above mechanism and feature extraction, most of the proposed UGW based techniques for monitoring corrosion can be categorized into four groups as: (1) monitoring corrosion induced debonding, (2) monitoring pitting corrosion, (3) monitoring corrosion induced interface roughness, and (4) monitoring combined effects in actual corrosion. The following sections review the above four groups of UGW based monitoring techniques for monitoring corrosion reinforced concrete including numerical simulation and signal processing. The influence effects such as loading condition and surface geometry of steel bar are also discussed.

2.3. Monitoring Corrosion Induced Debonding. It has been reported by Miller et al. [33] that there are two possible types of energy profiles inside the bar that can be observed in propagating guided wave modes as the wave energy travels through a steel bar from transmitter T to receiver R and these two types are denoted as modes A and B shown in Figure 3. For mode A, the energy profile is such that most of the energy propagates near the circumference of the rod; it is a surface-seeking mode and is chosen to assess the interfacial changes. For mode B, the energy is confined near the core or central axis of the rod, it is a core-seeking mode and is suitable for detecting pitting corrosion for its low attenuation and large range of detection. Once the interface condition between steel bar and concrete changes, the energy propagation may change as well.

Na et al. [34] used both high (1 MHz) and low frequencies (150 KHz) to study the effect of various bond levels by surrounding the rebar with a PVC pipe in RC beams and the effect of debonding location on the received waveforms. They in the same way conducted a comparison of steel concrete interfaces and glass fiber polymer-concrete interfaces using the guided waves [35, 36].

Reis et al. [37] used the fundamental flexural mode below 250 kHz for estimation of corrosion damage in steel reinforced mortar. Debonding defects were simulated by wrapping a tape around the rebar. Waveform energy that is indicative of attenuation was used to relate to corrosion damage.

Loss of bond between steel and surrounding concrete could be detected and evaluated by this method.

Wu and Chang [38, 39] used the piezoelectric discs as sensors and actuators to detect debonding in reinforced concrete structures. A set of reinforced concrete square beam specimens with various bond levels were built and tested using guided mechanical waves at lower frequencies. The concrete specimen was 508 mm long with a 19 mm diameter bar. A PVC pipe was wrapped in the middle portion of the bar to simulate debonding damage.

He et al. [40] used frequencies between 1 and 2 MHz to relate the effect of debonding on signals in cylindrical specimens. Specimens simulating 0%, 25%, 33%, 50%, 75%, and 100% debonding were created. Bond was inhibited between the steel and concrete by surrounding the rebar with high-density polyethylene for the necessary length prior to embedment.

Li et al. [41] used five-cycle sinusoidal signals with 120 kHz central frequency to investigated the UGW energy attenuation on the different debonding levels between steel bar and concrete in both time-domain and frequency-domain analyses. Delamination was simulated by using PVC pipes.

All the above test results indicated that both in time domain and frequency domain, the received waveform is less attenuated with the increase in debonding for both low and high frequencies. However, the lower frequencies showed more sensitivity to the change in bond. There was no significant change in the waveform arrival time reported. The location of debonding is not discernible through pulse transmission as reported by Evin et al. [42, 43].

Wang et al. [44] conducted the debonding damage assessment in RC structures by numerical simulations. They developed a concrete-steel spectral element in the frequency domain to analyze wave propagation along a steel rebar in concrete. Scalar damage parameters characterizing changes in the interface (i.e., debonding damage) were incorporated into the formulation of the spectral finite element that is used for damage detection of reinforced concrete structures. A reinforced concrete beam with embedded piezoelectric elements was carried out to verify the developed spectral element method (SEM) for modeling wave propagations. Effects of the debonding damage and material properties were also studied to evaluate the effect of different damage scenarios on wave propagation in the reinforced concrete structures. The results showed that the modeling can be used to predict the wave propagation along the steel bar in

concrete with complex interaction between the steel rebar and concrete.

Lu et al. [45] evaluated simulated corrosion in a form of partial removal of material from the rebar embedded in the concrete by attaching rectangular piezoelectric zirconate-titanate transducer (PZT) patches at the exposed ends of the rebar. In consideration of the inevitable discrepancies in different concrete beams due to specimen preparation and sensor installation, principal component analysis (PCA) based on statistical parameters extracted from wave signals was applied to highlight the difference between benchmark and damaged rebar. The results showed that PCA is capable of reducing the dimension of a complex set of original data, whose characteristics can be represented and highlighted by the first few mapped principal components. The different rebar conditions can be classified with the assistance of PCA, in terms of the existence of damage and its corresponding severity.

2.4. Monitoring Pitting Corrosion. Valor et al. [46] presented two Markov chain models to simulate pitting corrosion. The first model describes the time evolution of pit depths. The second Markov chain pitting corrosion model gives account for the maximum pit depths. Both models have been developed and validated using experimental pitting corrosion data.

In the technique of pulse echo, when there is an interface such as a crack, void, or flaw in the wave path, part of the energy is reflected back from the interface and received by the same transmitting transducer. From the display, the time of flight between the excitation and reflected pulse is measured. Knowing the group velocity of the excited longitudinal wave mode in the steel bar, the location of the defect can be calculated as follows [47]:

$$D = \frac{Vt}{2}, \quad (2)$$

where D is the distance of defect from transducer end, V is the group velocity of excited mode, and t is time of flight.

Pavlakovic et al. [48] conducted the monitoring of localized corrosion in the reinforcement by creating 2 mm and 4 mm deep saw cuts (perpendicular to the bar axis) in a solid bar 8 mm in diameter and then casting in grout. A pulse-echo arrangement was used for the saw cut reinforcement specimens, with the discontinuity located 450 mm away from the transmission site. A longitudinal guided wave at 3.75 MHz was transmitted, with the results showing that wave reflections are clearly detectable from both saw cuts.

Di Scalea et al. [49] created a 2 mm saw cut in a seven-wire steel strand specimen located in an anchored region undergoing tensile loading. By using a through transmission test setup, it was found that the attenuation of the waveform increased for the saw cut specimen as compared to an undamaged specimen.

Sharma and Mukherjee [47] used $L(0,7)$ mode at 1 MHz frequency to monitor notch defect in steel bars in concrete simulating pitting phenomena caused by corrosion. Both pulse echo and pulse transmission techniques were used to monitor corrosion. Appearance of notch echo indicated presence of notch in the embedded bar. By knowing the time

of flight of this echo, the location of the damage can be computed by (2). It was observed that the amplitude of notch echo increased with the increase in the notch dimensions. However, the notch echo peak did not rise perceptibly even at 20% damage. Thus, its discernibility to small notches is not very high due to the nature of the mode $L(0,7)$ used for testing. As the energy of the mode is concentrated at the centre of the bar, the mode is not sensitive to surface irregularities. However, the notch location is not discernible through pulse transmission, but as the percent of damage increased from 0% to 60%, the magnitude of the transmitted peak reduces. This is because as the notch dimensions increased, more energy is reflected back and less of it travels through the bar to reach the other end. Hence, relative signal attenuation of the transmitted pulse can relate to the extent of the damage in the bar.

Precise measurement of time of the flight (TOF) of the propagating signal plays a pivotal role in structure damage localization. Dai and He [50] applied a time-frequency analysis method, Wigner-Ville Distribution (WVD), to calculate the TOF of signal based on its excellent time-frequency energy distribution property. Experiments for damage localization of one-dimensional and two-dimensional structures have been studied. The results showed that the WVD-based method has better performance on the accuracy and the stability of damage localization in one-dimensional structure in comparison with traditional Hilbert envelope and Gabor wavelet transform methods.

As an incident guided wave is hitting an obstacle such as pitting in the steel bar due to corrosion, not only the same type of wave is reflected and transmitted but also mode conversion occurs at discontinuities. This mode conversion is quantified in terms of reflection and transmission, or, scattering coefficients. Gaul et al. [51] analyzed reflection and transmission of guided waves at arbitrarily shaped discontinuities in the cylinders using finite element and boundary element methods. The numerical results were confirmed with a series of laser-based ultrasound measurements. There was a good agreement between numerical and experimental results.

2.5. Monitoring Corrosion Induced Interface Roughness. Miller et al. [52] corroded rebar specimens to different levels to simulate the general corrosion, which were conducted by impressed current, removed some of the corrosion using sandpaper or wire brush, and then embedded into concrete. The diameter of the steel rebar was 22.23 mm and the specimen size was 12.7 cm \times 12.7 cm \times 60.96 cm. Two corroded steel rebars removed some of the corrosion by 100-grid sandpaper to simulate the "medium corroded sample". Another two rebars were simulated as "least corroded sample" by using the wire brush to further remove the corrosion. Tone-burst pulses were invoked at 1 MHz. The results indicate that the wave is more attenuated as the corrosion level increases. This was attributed to better bonding between the corroded steel surface and concrete, allowing more energy leakage.

Gaydeck et al. [53] embedded a 7 mm steel wire into a concrete mix with a 4% calcium chloride solution added to induce corrosion. The reinforced concrete specimen was

cylindrical, with an outer diameter of 150 mm and a length of 1 m. The steel wire was exposed on either end of the concrete to allow for transducer coupling. After the concrete had initially cured, a transducer with a 200 kHz resonance was used to invoke a longitudinal wave (single-cycle pulse). Six months later, after slight corrosion occurred, another wave was sent into the specimen. The higher frequency content was most affected (i.e., loss in signal strength) by the corrosion product accumulation. This was attributed to the corrosion pressure creating better acoustic coupling at the interface between the steel and concrete, thereby allowing more energy leakage.

2.6. Monitoring Combined Effects in Actual Corrosion. Sharma and Mukherjee [54] studied the different modes of guided wave in the steel bar embedded in concrete. The dispersion curves show that the $L(0, 1)$ mode at a low frequency of 100 KHz is of the significant amount of axial displacement at the steel/concrete interface, so it is a surface-seeking mode and is chosen to assess the interfacial changes. It also shows that the energy of $L(0, 7)$ mode at a high frequency of 1 MHz is concentrated in the central core of the bar. Hence it is a core-seeking mode and is suitable for detecting pitting corrosion for its low attenuation and large range of detection, as shown in Figure 2.

Furthermore, the different progressions of rebar corrosion in concrete in chloride and oxide environments were conducted respectively by the surface- and core-seeking guided wave modes [2, 54]. The above two modes were used to monitor beams undergoing accelerated impressed current corrosion. The results showed that pitting and nonuniform area loss were highlighted by severe signal attenuation in chloride corrosion with core-seeking mode. With surface-seeking mode, the signal strength of chloride corrosion initially rises followed by the drop. This indicates that chloride corrosion starts with delamination followed by local loss of material. In oxide corrosion, the rate of corrosion is slow and localized marked by initial drop in signal due to pressure buildup by formation of corrosion products and then slow bond deterioration as depicted by gradual rise in signal strength in surface-seeking mode. Thus effective combination of surface-seeking and core-seeking of guided wave modes can relate to the differences in corrosion mechanisms and rates in the two environments in RC structures; however, the simulation of chloride corrosion as delamination is not realistic. A judicious combination of notching and delamination would be more effective for simulating chloride corrosion.

Ervin and Reis [42] and Ervin et al. [55] used both low (<200 KHz, $L(0, 1)$ mode) and high [2–9 MHz, $L(0, 9)$ mode] guided longitudinal modes for monitoring corrosion in reinforced mortar by the accelerated corrosion experiments. It was found that surface-seeking modes were sensitive to the combined effect of bond deterioration and mortar stiffness reduction while core-seeking modes related well to change in cross-sectional area of the reinforcement.

During the corrosion progression, both phenomena of increasing surface roughness and increasing separation between steel and concrete can occur simultaneously or at different stages of corrosion. Their contribution to energy propagation of guided waves is opposite to each other, so the net signal strength may either increase or decrease depending on

which effect is stronger at that time, therefore a change in the signal strength does not necessarily always imply increasing corrosion. To avoid the perplex problem, Miller et al. [33] proposed a new guided wave-based technique to monitor corrosion in reinforced concrete by studying the change in the time of flight (TOF) of propagating wave in loaded reinforced concrete structures at various levels of corrosion. RC beam specimen was conducted by accelerated corrosion and subjected to bending loads at different corrosion levels. The results showed that the degree of corrosion is related to the change in the TOF of propagating waves as the RC beam is loaded laterally. The main advantage of the proposed approach is that the test result is independent of energy propagation of guided waves. In addition, it is not affected by the bonding condition between the sensors and structure.

2.7. Influence Factors of UGW Based Monitoring for Corrosion in RC. Effect of loading conditions, temperature, concrete strength, reinforcing ribs, and anchorages on the guided waves has been reported.

Wu and Chang [38, 39] investigated tension test on the rebar to determine whether loading would have any effect on the guided wave characteristics. The results showed that the applied load does not affect the wave amplitude for the frequency range and mode tested. However, the time of arrival of the waveforms did change once yielding occurred due to the rapid increase in length. They also investigated how guided wave characteristics are affected by bending. Longitudinal modes were invoked using 5-cycle tone bursts, primarily around 90 kHz. As the load was increased during a four-point bending test, a crack, perpendicular to the axis of the reinforced concrete specimen, formed in the tension zone and extended up towards the neutral axis. The results showed that as the applied loads and cracking of the surrounding concrete matrix increased, the amplitude of the waveform increased.

Li et al. [41] used Ansys software to simulate the propagation of guided waves in the rebar and explore the characteristics of ultrasonic guided wave in the steel rebar waveguide. Then two-dimensional fast Fourier transform was used to process the numerical results and to evaluate the debonding damage. The results showed that both the group velocity and the amplitude of longitudinal modes were not very sensitive to stress and temperature variations. However, the received UGW signal energy decreased with the increasing concrete strength.

For the effects of reinforcing ribs and anchorages, it was concluded that [56] (1) wave propagation is largely unaffected by the presence of surface features when the ratio of the wavelength to the surface feature dimensions is large, and there was particular sensitivity to diagonal rib patterns compared to an orthogonal axisymmetric rib pattern; (2) specimens without stirrups had stronger waveform amplitudes than specimens with stirrups.

3. Fiber Bragg Grating (FBG) for Monitoring Corrosion in RC

Fiber optic sensors have a number of advantages over conventional sensors, such as high sensitivity, immunity to electromagnetic interference, corrosion resistance, small-volume,

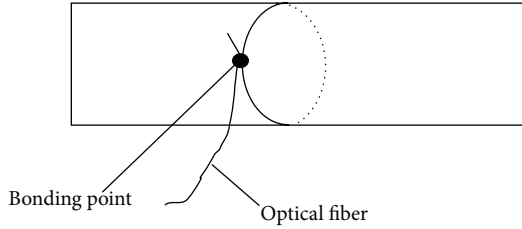


FIGURE 4: Optical fiber grating bound on surface of steel cylinder.

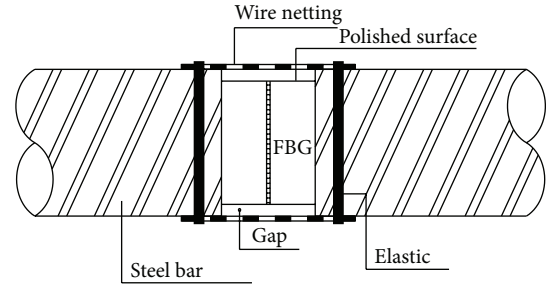


FIGURE 5: The scheme of package.

negligible weight, variable form, and one-line multipoint monitoring. Thus, they are valuable in structural health monitoring. Kundu et al. [57] proposed a general review of their applications in structural health monitoring. Hou et al. [58] proposed an improved negative pressure wave method based on FBG based strain sensors and wavelet analysis. Compared to conventional pressure sensors, FBG based strain sensors have favorable properties, such as high sensitivity, cheap cost, and ease of installation. Furthermore, a wavelet transform based method for identifying the pressure drop points within the FBG signals was proposed to calculate the leak position.

Many studies on FBG for monitoring corrosion are emerging in recent years. Majumder et al. [59] proposed a structural corrosion-monitoring sensor based on a pair of prestrained fiber Bragg gratings which will cause the prestrain to gradually relax when the target structure becomes corroded. Lee et al. [60] proposed a fiber optic corrosion sensor to detect rebar corrosion which was made of one fiber Bragg grating (FBG) sensor and twin steel rebar elements packaged up with concrete. Gao et al. [61] used an 80% etched-cladding fiber Bragg grating sensor to monitor the production of corrosion waste in a localized region of the rebar. Abu Hassan et al. [62] modification of the wavelength-strain coefficient of FBG for the more accurate prediction of steel bar corrosion embedded in concrete. Cheng and Dong [63] presented a new methodology to corrosion detection in reinforced concrete structures, by combining fiber Bragg grating (FBG) sensors with the electrochemical and physical properties of rebar in a simplified assembly. Ali-Alvarez et al. [64] proposed and built a simple noncontact force sensor based on an optical fiber Bragg grating attached to a small magnet for corrosion measurement. Pacheco and Bruno [65] proposed a novel long-period fiber grating (LPFG) sensor coated with a thin film of nano iron and silica particles for corrosion monitoring.

Some researches on monitoring corrosion in RC by FBG have been done by the authors of this paper. After continuous improvement a new corrosion sensor based on FBG is ultimately used in civil infrastructures. The following section reviews the studies and application by the authors [66, 67].

3.1. Mechanism of the FBG Based Corrosion Sensor. FBG is obtained by producing a periodic variation in the index of refraction along the short sections (about 10–20 mm) in the core of an optical fiber. If it is fixed on the surface of a steel bar, the variation in the volume due to corrosion can be measured by monitoring the wavelength shift of the FBG.

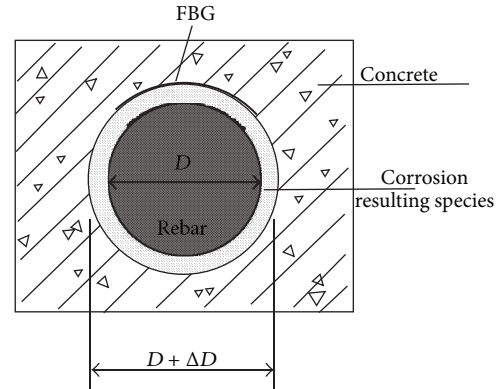


FIGURE 6: FBG strain.

The corrosion intensity can be described by the wavelength shift of FBG as follows [67]:

$$\begin{aligned} \rho &= \frac{\Delta V}{V} = \frac{(D + \Delta D)^2 - D^2}{D^2} \\ &= \left(1 + \frac{\Delta D}{D}\right)^2 - 1 = (1 + \epsilon)^2 - 1 \\ &= \left(1 + \frac{\Delta \lambda_b}{\kappa_\epsilon}\right)^2 - 1, \end{aligned} \quad (3)$$

where D is the original diameter of steel rebar, ΔD is the diameter increment, $\Delta \lambda_b$ is the wavelength shift of FBG, κ_ϵ is the strain sensitivity of FBG, and ρ is the increase rate of the steel volume.

3.2. Design of FBG Corrosion Sensor. The corrosion sensor using FBG is designed in the following procedures: (1) Mechanically polish the surface of a 20 mm part of reinforcement made of hot rolled steel; (2) enwind FBG one coil on the polished surface of the reinforcement tightly and then bind it through the epoxy binder at the junction as shown in Figure 4; (3) put one piece of wire netting above the polished area to prevent FBG from being destroyed during concrete pouring which is fixed by the elastic on two ends as shown in Figure 5.

The FBG can expand freely without constraint from the protective layer because there is 2 mm gap between them. Water and air can reach the steel rebar at the packaged region through the holes on the wire netting, so it is in the same corrosion condition as others. As shown in Figure 6, when



FIGURE 7: Cracking of concrete block.

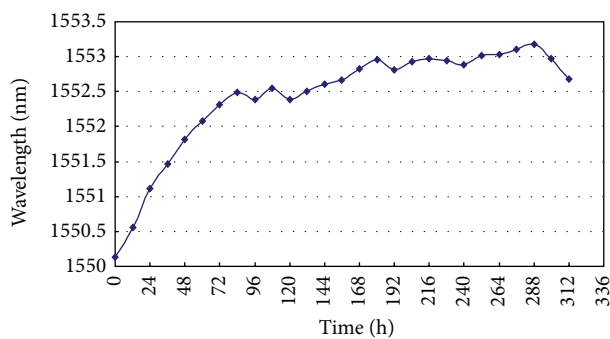


FIGURE 8: Wavelength of FBG versus elapsed time.

the reinforcement is corroded within the concrete structure, the resulting species deposits continuously on the surface of the rebar because the loss of mass is hindered by concrete, the volume of the steel rebar increases during corrosion, and the coverage concrete is finally cracked. During the corrosion, the tensile strain in the FBG is increased with the increasing diameter of steel reinforcement. Finally, the tensile stress in the FBG can reach the level to break FBG; the corrosion sensor then becomes invalid.

Experimental tests on the designed FBG corrosion sensor were carried out by accelerated corrosion condition and some vessels were embedded from outer side of the specimen to the polished area to make the position where sensor was attached easier to be corroded. As shown in Figure 7, substantial cracks occurred in the specimen. The results obtained from the sensor were analyzed. It can be observed from Figure 8 that the wavelength shift increases gradually with time, and even the curve is fluctuated in some parts, the overall trend is increased. Evidently, the curve can be divided into three parts. In the first part, that is, from point A to B, the wavelength shift is increased rapidly with time due to the voluminous rust product accumulation, which is a consequence of the concrete pores adjacent to the rebar. In the second part, that is, from point B to C, there is only relatively small increase in the curve with some fluctuations, which is due to the fact that concrete is further compacted and micro cracks are occurring. In the last part, the wavelength shift is declined at turning point C because of the appearance of large cracks, and



FIGURE 9: Corroded bar from FBG sample.

the resulting species dissolved into the solution, and the volume of the steel reinforcement decreased during corrosion.

To confirm the results, a commercial device named CANIN (type: EN-0503) which was based on half-cell corrosion potential method was used to monitor the corrosion. It was noted from the test that when the wavelength changed from 1550 nm to 1554 nm, the potential read from the CANIN was between 500 and 400 mv, which verifies the appearance of light corrosion. It can be observed from Figure 9, that there is a significant difference between the polished region and the other region of the bar, which indicates the occurrence of corrosion in the area where FBG is attached (marked by the dashed line in the figure).

The lab experimental results indicated that the FBG has a clear difference in reading precorrosion and postcorrosion data, and the monitoring data are reliable to evaluate the corrosion. Thus, the designed FBG based corrosion sensors can be used for monitoring corrosion of steel reinforcements in concrete structures.

3.3. Application of the Designed FBG Corrosion Sensors in Xiamen Xiang'an Subsea Tunnel in China. Xiamen Xiang'an Subsea Tunnel in China is located in eastern part of Xiamen island and is connecting Xiamen island and the Xiang'an mainland as shown in Figure 10. It is the largest cross-section subsea tunnel in China with a total length of 8.695 km. The deepest part of the tunnel is 70 meter below the sea level. The construction of the tunnel was started in September 2005 and finished in April 2010.

The FBG based corrosion sensors developed by the authors were made of the same steel as the practical engineering and applied in the Xiamen Xiang'an Subsea Tunnel. Corrosion sensors were installed at the apex and haunches of dangerous section as shown in Figure 11.

Additionally, to compensate effects of temperature variations on the shift of wavelength, another FBG sensor encapsulated in a polyvinyl chloride (PVC) pipe was arranged in parallel nearby freely to monitor the wavelength shift resulted from temperature variation, as shown in Figures 12, 13, 14 and 15.

Other embedded corrosion sensors were installed to compare the accuracy of data, including the commercial multiprobe CorroWatch sensor and ERE20 reference electrode produced by Force company in Denmark.



FIGURE 10: General plan and profile view of Xiang'an Subsea-tunnel.

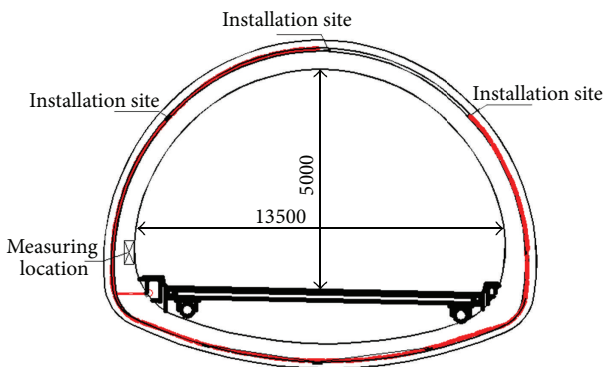


FIGURE 11: Section view and installation site in Xiang'an Sub-sea Tunnel.

Twenty FBG sensors were installed in different positions of the tunnel. After concreting, sixteen sensors survived. Monitoring data have been collected since April 2010. So far, the results obtained from the sensors are shown in Figure 16. It can be observed that all surviving sensors are still in work and there is no obvious corrosion in monitoring areas of the tunnel. The data from other electrochemical sensors at the same position also demonstrated that corrosion has not started yet. Data from all the sensors will be collected for the next several years and will be analyzed to develop a detailed knowledge-based corrosive behavior of the rebars.

4. Introduction of Some Other Physical Techniques for Monitoring Corrosion in RC

There are some other physical techniques for monitoring steel corrosion. These techniques are briefly reviewed as follows.

4.1. Electrical Resistance Probe. Electrical resistance (ER) probe is one specific type of embedded sensor which is simple to be used for monitoring corrosion. In the technique, resistance probes made of the same material with steel bar are first embedded in concrete, and then the resistance of probes can be measured by balancing bridge which is inversely proportional to its cross-sectional area. Therefore, the thickness reduction due to corrosion can be estimated from

the change in resistance of probes so as to achieve the test purpose [68, 69]. Although applications of these probes in concrete are relatively rare, the results have proved that they can accurately determine the cumulative corrosion damage of steel in cementitious materials [70]. Consequently, reliable assessment of the average general corrosion rate over defined time intervals is possible [70]. On the other hand, the response of these probes to localized corrosion types and transient events is limited. ER probes are based on physical response to corrosion and are therefore not directly susceptible to variations in the electrochemical parameters. For this reason they are particularly suited for the long-term verification of the suitability of electrochemical sensors for corrosion measurements in concrete [71].

4.2. X-Ray Diffraction. X-Ray technique is based on the principle that intensity of X-Ray beams reduces while passing through a corroded material. Analysis of material composition and relative amounts of corrosion products can be achieved by the technique. It is simple but hazardous [72–75].

4.3. Vortex and Magnetic Flux Leakage. Steel bar reaches magnetic saturation with the electromagnetic devices placed on the surface of concrete. Abnormal phenomenon in magnetic field will appear due to loss in cross-sectional area of steel bar caused by corrosion. Loss rate of the cross-sectional area of reinforcement can be determined with analysis of these exceptions. It is an effective method to quantitatively detect the loss of reinforcement with accuracy and it is non-destructive [76–80].

4.4. Acoustic Emission. Yuma et al. studied corrosion mechanisms in reinforced concrete by acoustic emission (AE) [81]. During corrosion in reinforcement concrete, the surrounding concrete will crack due to the expansion stress resulted from the corrosion products. When it is cracking, part of energy will release in the form of sound waves. Therefore position and strength of the emission source can be detected by acoustic emission sensors. It is hard to avoid interference with other waves, so it is difficult to establish the relationship between the level of reinforcement corrosion activity and the intensity of acoustic emission [82]. Calabres et al. [83, 84] recently

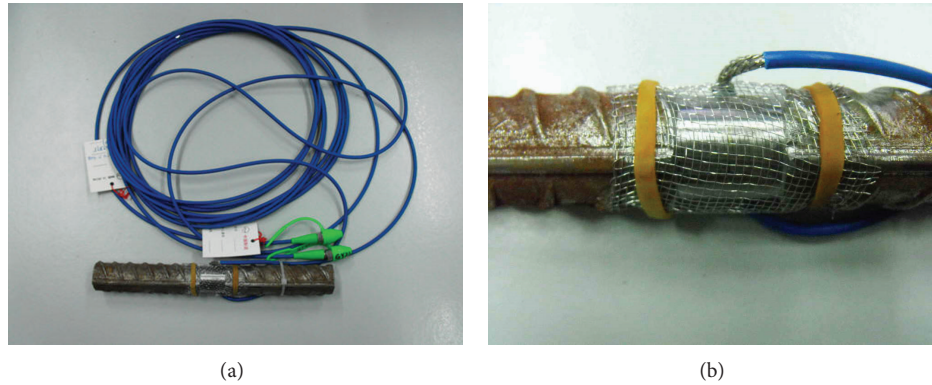


FIGURE 12: Fiber optic corrosion sensor.



FIGURE 13: Reference FBG sensor for temperature compensation.

studied noise removal and univariate and multivariate statistical analysis in AE corrosion monitoring of steel reinforcement in concrete. Kundu et al. [57] used a combination of a PZT and an electromagnetic acoustic transducer (EMAT) to inspect the interface between steel bar and concrete, such that arrangement was made to overcome the major shortcoming of PZT and EMAT. Elfergani et al. [85] reported on using the acoustic emission (AE) technique to detect and locate the early stages of corrosion and macrocracks and furthermore classify different crack types to aid maintenance priorities. Benedetti et al. [86] presented an accelerated corrosion and continuous AE monitoring test. The effectiveness of AE in detecting and characterizing the initiation of the corrosion process is discussed on the basis of results from small-scale, precracked RC specimens that are representative of areas near the clear cover in typical RC members. They proposed a new approach of AE data interpretation based on time-driven parameters.

5. Conclusions

In this paper, some physical based monitoring techniques for condition assessment of steel corrosion in reinforced concrete in the last decade are reviewed. Especially, techniques based on ultrasonic guided wave (UGW) and Fiber Bragg grating (FBG) are emphasized as these two important techniques have many advantages for monitoring corrosion in reinforced

concrete. Also, FBG corrosion sensors developed by the authors with its application are presented.

From the review, it can be seen that physical based monitoring techniques can conduct accurate condition assessment of steel corrosion through direct measurements on embedded steels. Compared with the conventional monitoring techniques based on electrochemistry, physical based monitoring techniques not only provide alternative tools for monitoring steel corrosion in concrete but also have the distinguished superiority as electrochemistry techniques can only assess corrosion through monitoring the surrounding concrete medium.

It is addressed in this review that UGW based monitoring techniques are promising for the accurate condition assessment of steel corrosion in reinforced concrete over a larger inspection range compared with other techniques. However, there are still difficulties in the practical application of UGW based techniques for the condition assessment of corrosion in reinforced concrete. The main challenges and future development trends of UGW based techniques are as follows.

- (1) Most of the current researches are concentrated on monitoring individual phenomenon of interface roughness, debonding, and steel pitting induced by corrosion in reinforced concrete. Although much progress has been made, accurate detection the range of interface roughness and debonding and the location of steel pitting is still challenging. Moreover, it is imperative to develop the efficient techniques for monitoring the combined effects induced by the actual steel corrosion concrete.
- (2) One more difficulty of UGW based technique for monitoring corrosion in reinforced concrete is the limitation of monitoring range for certain modes and frequencies. Unlike guided wave propagation in other multilayered systems, such as a metal pipeline in air, wave energy in steel bars embedded in mortar or concrete is lost (i.e., attenuated) at high rates due to leakage into the surrounding concrete. Generally, modes exist that have attenuation minima, or dips, with minimal amounts of wave energy lost due to leakage



FIGURE 14: Photographs of field application.

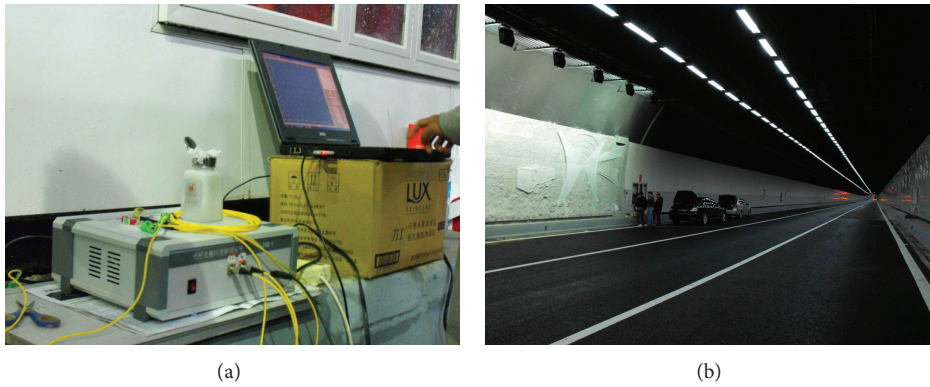


FIGURE 15: Photographs of testing in situ.

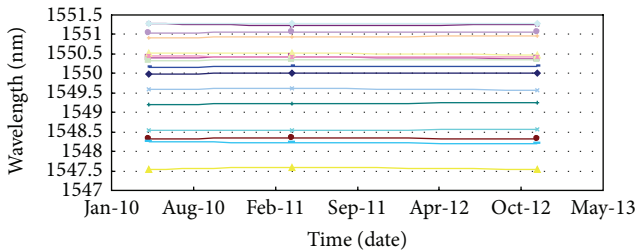


FIGURE 16: Wavelength of FBG versus elapsed time in the tunnel.

and material absorption. So the successful development of UGW monitoring techniques require careful model studies to be performed based on properly understanding the nature of the waves and knowledge of the attenuation.

- (3) The increase of steel corrosion level in an RC structure can either increase the recorded wave strength because of increasing separation between steel and concrete or decrease the strength of the recorded guided waves due to increasing surface roughness. During the corrosion progression, both phenomena can occur simultaneously or at different stages of corrosion, the net signal strength may either increase or decrease depending on which effect is stronger at that time or may remain unchanged if the two opposing effects cancel each other. This is another difficulty

associated with the current guided wave-based techniques. To study which effect dominates, propagation mechanism, factors, and regular pattern of attenuation of guided waves along steel bar embedded in concrete are very important. These are future research trends.

It is also noted that monitoring techniques based on Fiber Bragg grating (FBG) are also useful tools for condition assessment of steel corrosion in reinforced concrete. Some relevant techniques have been applied in the monitoring of RC structures. However, current techniques can only conduct localized inspection of corrosion. It is expected to develop distributed and long-gauge fiber Bragg grating technique for solution of this problem.

While other physical based monitoring techniques have been proposed, corrosion process can occur in multiple stages, and the mechanism of corrosion is sophistic; there is no single evaluation method to accurately detect and monitor in situ the entire corrosion process to date. It is the future development trend to combine with a variety of methods simultaneously for the accurate condition assessment of steel corrosion reinforced concrete infrastructures.

Acknowledgments

This research is supported by the National Natural Science Foundation of China (NSFC) through the Grant no. 51178406,

the research funding SLDRCE10-MB-01 from the State Key Laboratory for Disaster Reduction in Civil Engineering at Tongji University, China, and the Key Project of Fujian province of China (no. 2013Y0079). The authors also greatly appreciate the collaboration work from Professor X. P. Dong at the school of information science and engineering of Xiamen University for the field testing of proposed FBG corrosion.

References

- [1] J. P. Broomfield, *Corrosion of Steel in Concrete: Understanding, Investigation and Repair*, Taylor & Francis, New York, NY, USA, 2nd edition, 2007.
- [2] S. Sharma and A. Mukherjee, "Nondestructive evaluation of corrosion in varying environments using guided waves," *Research in Nondestructive Evaluation*, vol. 24, no. 2, pp. 63–88, 2013.
- [3] H. S. Shang, T. H. Yi, and Y. P. Song, "Behavior of plain concrete of a high water-cement ratio after freeze-thaw cycles," *Materials*, vol. 5, no. 9, pp. 1698–1707, 2012.
- [4] H.-S. Shang, T.-H. Yi, and L.-S. Yang, "Experimental study on the compressive strength of big mobility concrete with non-destructive testing method," *Advances in Materials Science and Engineering*, vol. 2012, Article ID 345214, 6 pages, 2012.
- [5] P. Matt, "Non-destructive evaluation and monitoring of post-tensioning tendons," *fib Bull.* 15: Durability of post-tensioning tendon, pp. 100–108, 2001.
- [6] R. W. Griffiths and G. W. Nelson, "Recent and current developments in distributed fiber optic sensing for structural monitoring," in *Fiber Optic and Laser Sensors VI*, vol. 985 of *Proceedings of SPIE*, pp. 69–76, San Diego, Calif, USA, 1989.
- [7] J. L. Rose, *Ultrasonic Waves in Solid Media*, Cambridge University Press, Cambridge, UK, 1999.
- [8] J. L. Rose, "Dispersion curves in guided wave testing," *Materials Evaluation*, vol. 61, no. 1, pp. 20–22, 2003.
- [9] J. D. Achenbach, *Wave Propagation in Elastic Solids*, vol. 16 of *North-Holland Series in Applied Mathematics and Mechanics*, North-Holland, New York, NY, USA, 1984.
- [10] J. Miklowitz, *The Theory of Elastic Waves and Waveguides*, vol. 22 of *North-Holland Series in Applied Mathematics and Mechanics*, North-Holland, New York, NY, USA, 1978.
- [11] C. S. Kino, *Acoustic Waves: Devices, Imaging and Digital Signal Processing*, Prentice Hall, Upper Saddle River, NJ, USA, 1987.
- [12] B. A. Auld, *Acoustic Fields and Waves in Solids*, vol. 2, Kreiger Publishing, Malabar, Fla, USA, 2nd edition, 1990.
- [13] K. F. Graff, *Wave Motion in Elastic Solids*, Dover Publications, New York, NY, USA, 1991.
- [14] A. H. Nayfeh, *Wave Propagation in Layered Anisotropic Media with Applications to Composites*, vol. 39 of *North-Holland Series in Applied Mathematics and Mechanics*, North-Holland, Amsterdam, The Netherlands, 1995.
- [15] J. L. Rose, "A baseline and vision of ultrasonic guided wave inspection potential," *Journal of Pressure Vessel Technology*, vol. 124, no. 3, pp. 273–282, 2002.
- [16] Z. P. Zheng, Y. Lei, X. P. Cui, and Y. Song, "Non-destructive test of the steel bar by using piezoceramics sheets," in *Proceedings of the 3rd International Conference on Advanced Measurement and Test*, Xiamen, China, March 2013.
- [17] T. R. Hay and J. L. Rose, "Interfacing guided-wave ultrasound with wireless technology," in *Smart Structures and Materials—Sensors and Smart Structures Technologies for Civil, Mechanical, and Aerospace Systems*, vol. 5391 of *Proceedings of SPIE*, pp. 314–320, San Diego, Calif, USA, March 2004.
- [18] H. Sohn, D. Dutta, J. Y. Yang et al., "Delamination detection in composites through guided wave field image processing," *Composites Science and Technology*, vol. 71, no. 9, pp. 1250–1256, 2011.
- [19] G. Song, Y. L. Mo, K. Otero, and H. Gu, "Health monitoring and rehabilitation of a concrete structure using intelligent materials," *Smart Materials and Structures*, vol. 15, no. 2, pp. 309–314, 2006.
- [20] R. L. Wang, H. Gu, Y. L. Mo, and G. Song, "Proof-of-concept experimental study of damage detection of concrete piles using embedded piezoceramic transducers," *Smart Materials and Structures*, vol. 22, no. 4, Article ID 042001, 2013.
- [21] F. Schöpfer, F. Binder, A. Wöstehoff, and T. Schuster, "A mathematical analysis of the strip-element method for the computation of dispersion curves of guided waves in anisotropic layered media," *Mathematical Problems in Engineering*, vol. 2010, Article ID 924504, 17 pages, 2010.
- [22] L. De Marchi, E. Baravelli, G. Cera, N. Speciale, and A. Marzani, "Warped Wigner-Hough transform for defect reflection enhancement in ultrasonic guided wave monitoring," *Mathematical Problems in Engineering*, vol. 2012, Article ID 358128, 15 pages, 2012.
- [23] V. Giurgiutiu, "Lamb wave generation with piezoelectric wafer active sensors for structural health monitoring," in *Smart Structures and Materials: Smart Structures and Integrated Systems*, vol. 5056 of *Proceedings of SPIE*, pp. 111–122, San Diego, Calif, USA, March 2003.
- [24] X. Q. Zhu, H. Hao, and K. Q. Fan, "Detection of delamination between steel bars and concrete using embedded piezoelectric actuators/sensors," *Journal of Civil Structural Health Monitoring*, vol. 3, no. 2, pp. 105–115, 2013.
- [25] X. Wang, P. W. Tse, C. K. Mechefske, and M. Hua, "Experimental investigation of reflection in guided wave-based inspection for the characterization of pipeline defects," *NDT & E International*, vol. 43, no. 4, pp. 365–374, 2010.
- [26] S. Iyer, S. K. Sinha, M. K. Pedrick, and B. R. Tittmann, "Evaluation of ultrasonic inspection and imaging systems for concrete pipes," *Automation in Construction*, vol. 22, pp. 149–164, 2012.
- [27] A. C. Cobb, H. Kwun, L. Caseres, and G. Janega, "Torsional guided wave attenuation in piping from coating, temperature, and large-area corrosion," *NDT & E International*, vol. 47, pp. 163–170, 2012.
- [28] H.-J. Salzburger, F. Niese, and G. Dobmann, "Emat pipe inspection with guided waves," *Welding in the World*, vol. 56, no. 5–6, pp. 35–43, 2012.
- [29] R. Ahmad and T. Kundu, "Influence of water flow through pipe networks for damage detection using guided waves," in *Nondestructive Testing of Materials and Structures*, vol. 6 of *RILEM Bookseries*, pp. 681–687, Springer, Amsterdam, The Netherlands, 2013.
- [30] M. D. Beard, M. J. S. Lowe, and P. Cawley, "Inspection of steel tendons in concrete using guided waves," in *AIP Conference Proceedings*, vol. 22 of *Review of Quantitative Nondestructive Evaluation*, pp. 1139–1147, Bellingham, Wash, USA, July 2003.
- [31] X. Zhu, P. Rizzo, A. Marzani, and J. Bruck, "Ultrasonic guided waves for nondestructive evaluation/structural health monitoring of trusses," *Measurement Science and Technology*, vol. 21, no. 4, Article ID 045701, 2010.

- [32] G. Huang, F. Song, and X. Wang, "Quantitative modeling of coupled piezo-elastodynamic behavior of piezoelectric actuators bonded to an elastic medium for structural health monitoring: a review," *Sensors*, vol. 10, no. 4, pp. 3681–3702, 2010.
- [33] T. H. Miller, T. Kundu, J. Huang, and J. Y. Grill, "A new guided wave—based technique for corrosion monitoring in reinforced concrete," *Structural Health Monitoring*, vol. 12, no. 1, pp. 35–47, 2013.
- [34] W.-B. Na, T. Kundu, and M. R. Ehsani, "Ultrasonic guided waves for steel bar concrete interface testing," *Materials Evaluation*, vol. 60, no. 3, pp. 437–444, 2002.
- [35] W.-B. Na, T. Kundu, and M. R. Ehsani, "Lamb waves for detecting delamination between steel bars and concrete," *Computer-Aided Civil and Infrastructure Engineering*, vol. 18, no. 1, pp. 58–63, 2003.
- [36] W.-B. Na, T. Kundu, and M. R. Ehsani, "A comparison of steel/concrete and glass fiber reinforced polymers/concrete interface testing by guided waves," *Materials Evaluation*, vol. 61, no. 2, pp. 155–161, 2003.
- [37] H. Reis, B. L. Ervin, D. A. Kuchma, and J. T. Bernhard, "Estimation of corrosion damage in steel reinforced mortar using guided waves," *Journal of Pressure Vessel Technology*, vol. 127, no. 3, pp. 255–261, 2005.
- [38] F. Wu and F.-K. Chang, "Debond detection using embedded piezoelectric elements in reinforced concrete structures—part I: experiment," *Structural Health Monitoring*, vol. 5, no. 1, pp. 5–15, 2006.
- [39] F. Wu and F.-K. Chang, "Debond detection using embedded piezoelectric elements for reinforced concrete structures—part II: analysis and algorithm," *Structural Health Monitoring*, vol. 5, no. 1, pp. 17–28, 2006.
- [40] C. He, J. K. van Velsor, C. M. Lee, and J. L. Rose, "Health monitoring of rock bolts using ultrasonic guided waves," in *AIP Conference Proceedings*, Quantitative Nondestructive Evaluation, pp. 195–201, Reston, Va, USA, 2006.
- [41] D. Li, T. Ruan, and J. Yuan, "Inspection of reinforced concrete interface delamination using ultrasonic guided wave non-destructive test technique," *Science China Technological Sciences*, vol. 55, no. 10, pp. 2893–2901, 2012.
- [42] B. L. Ervin and H. Reis, "Longitudinal guided waves for monitoring corrosion in reinforced mortar," *Measurement Science and Technology*, vol. 19, no. 5, Article ID 055702, 2008.
- [43] B. L. Ervin, D. A. Kuchma, J. T. Bernhard, and H. Reis, "Monitoring corrosion of rebar embedded in mortar using high-frequency guided ultrasonic waves," *Journal of Engineering Mechanics*, vol. 135, no. 1, pp. 9–19, 2009.
- [44] Y. Wang, X. Zhu, H. Hao, and J. Ou, "Guided wave propagation and spectral element method for debonding damage assessment in RC structures," *Journal of Sound and Vibration*, vol. 324, no. 3–5, pp. 751–772, 2009.
- [45] Y. Lu, J. C. Li, L. Ye, and D. Wang, "Guided waves for damage detection in rebar-reinforced concrete beams," *Construction and Building Materials*, vol. 47, pp. 370–378, 2013.
- [46] A. Valor, F. Caleyo, L. Alfonso, J. C. Velázquez, and J. M. Hallen, "Markov chain models for the stochastic modeling of pitting corrosion," *Mathematical Problems in Engineering*, vol. 2013, Article ID 108386, 13 pages, 2013.
- [47] S. Sharma and A. Mukherjee, "Longitudinal guided waves for monitoring chloride corrosion in reinforcing bars in concrete," *Structural Health Monitoring*, vol. 9, no. 6, pp. 555–567, 2010.
- [48] B. N. Pavlakovic, M. J. S. Lowe, and P. Cawley, "High-frequency low-loss ultrasonic modes in imbedded bars," *Journal of Applied Mechanics*, vol. 68, no. 1, pp. 67–75, 2001.
- [49] F. L. di Scalea, P. Rizzo, and F. Seible, "Stress measurement and defect detection in steel strands by guided stress waves," *Journal of Materials in Civil Engineering*, vol. 15, no. 3, pp. 219–227, 2003.
- [50] D. Dai and Q. He, "Structure damage localization with ultrasonic guided waves based on a time-frequency method," *Signal Processing*, vol. 96, pp. 21–28, 2014.
- [51] L. Gaul, H. Sprenger, C. Schaal, and S. Bischoff, "Structural health monitoring of cylindrical structures using guided ultrasonic waves," *Acta Mechanica*, vol. 223, no. 8, pp. 1669–1680, 2012.
- [52] T. Miller, C. J. Hauser, and T. Kundu, "Nondestructive inspection of corrosion and delamination at the concrete-steel reinforcement interface," in *Proceedings of the ASME International Mechanical Engineering Congress and Exposition*, pp. 121–128, New Orleans, La, USA, November 2002.
- [53] P. A. Gaydeck, F. M. Burdekin, W. Damaj, D. G. John, and P. A. Payne, "Digital deconvolution analysis of ultrasonic signals influenced by the presence of longitudinally aligned steel cables in pre-stressed concrete," *Measurement Science and Technology*, vol. 3, no. 9, article 909, pp. 909–917, 1992.
- [54] S. Sharma and A. Mukherjee, "Monitoring corrosion in oxide and chloride environments using ultrasonic guided waves," *Journal of Materials in Civil Engineering*, vol. 23, no. 2, pp. 207–211, 2011.
- [55] B. L. Ervin, J. T. Bernhard, D. A. Kuchma, and H. Reis, "Estimation of corrosion damage to steel reinforced mortar using frequency sweeps of guided mechanical waves," in *Smart Structures and Materials—Sensors and Smart Structures Technologies for Civil, Mechanical, and Aerospace Systems*, vol. 6174 of *Proceedings of SPIE*, pp. 1–12, San Diego, Calif, USA, 2006.
- [56] B. L. Ervin, J. T. Bernhard, D. A. Kuchma, and H. Reis, "Estimation of general corrosion damage to steel reinforced mortar using frequency sweeps of guided mechanical waves," *Insight*, vol. 48, no. 11, pp. 682–692, 2006.
- [57] T. Kundu, S. Banerjee, and K. V. Jata, "An experimental investigation of guided wave propagation in corrugated plates showing stop bands and pass bands," *Journal of the Acoustical Society of America*, vol. 120, no. 3, pp. 1217–1226, 2006.
- [58] Q. M. Hou, L. Ren, W. Jiao, P. H. Zou, and G. B. Song, "An improved negative pressure wave method for natural gas pipeline leak location using FBG based strain sensor and wavelet transform," *Mathematical Problems in Engineering*, vol. 2013, Article ID 278794, 8 pages, 2013.
- [59] M. Majumder, T. K. Gangopadhyay, A. K. Chakraborty, K. Dasgupta, and D. K. Bhattacharya, "Fibre Bragg gratings in structural health monitoring—present status and applications," *Sensors and Actuators A*, vol. 147, no. 1, pp. 150–164, 2008.
- [60] J.-R. Lee, C.-Y. Yun, and D.-J. Yoon, "A structural corrosion-monitoring sensor based on a pair of prestained fiber Bragg gratings," *Measurement Science and Technology*, vol. 21, no. 1, Article ID 017002, 2010.
- [61] J. Gao, J. Wu, J. Li, and X. Zhao, "Monitoring of corrosion in reinforced concrete structure using Bragg grating sensing," *NDT & E International*, vol. 44, no. 2, pp. 202–205, 2011.
- [62] M. R. Abu Hassan, M. H. Abu Bakar, K. Dambul, and F. R. Adikan, "Optical-based sensors for monitoring corrosion of reinforcement rebar via an etched cladding Bragg grating," *Sensors*, vol. 12, no. 11, pp. 15820–15826, 2012.

- [63] W. Chen and X. Dong, "Modification of the wavelength-strain coefficient of FBG for the prediction of steel bar corrosion embedded in concrete," *Optical Fiber Technology*, vol. 18, no. 1, pp. 47–50, 2012.
- [64] S. Ali-Alvarez, P. Ferdinand, S. Magne, and R. P. Nogueira, "Corrosion detection and evolution monitoring in reinforced concrete structures by the use of fiber Bragg grating sensor," in *Sensors and Smart Structures Technologies for Civil, Mechanical, and Aerospace Systems*, vol. 8692 of *Proceedings of SPIE*, San Diego, Calif, USA, April 2013.
- [65] C. J. Pacheco and A. C. Bruno, "A noncontact force sensor based on a fiber Bragg grating and its application for corrosion measurement," *Sensors*, vol. 13, no. 9, pp. 11476–11489, 2013.
- [66] Y. Huang, Z. Gao, G. Chen, and H. Xiao, "Long period fiber grating sensors coated with nano iron/silica particles for corrosion monitoring," *Smart Materials and Structures*, vol. 22, no. 7, Article ID 075018, 2013.
- [67] Z. Zheng, X. Sun, and Y. Lei, "Monitoring corrosion of reinforcement in concrete structures via fiber Bragg grating sensors," *Frontiers of Mechanical Engineering in China*, vol. 4, no. 3, pp. 316–319, 2009.
- [68] Z. Zheng, Y. Lei, and X. Sun, "Measuring corrosion of steels in concrete via fiber Bragg grating sensors—lab experimental test and in-field application," in *Proceedings of the Earth and Space Conference*, pp. 2422–2430, Honolulu, Hawaii, USA, March 2010.
- [69] J.-P. Cai and S. B. Lyon, "A mechanistic study of initial atmospheric corrosion kinetics using electrical resistance sensors," *Corrosion Science*, vol. 47, no. 12, pp. 2956–2973, 2005.
- [70] A. A. Sagüés and M. T. Walsh, "Kelvin Probe electrode for contactless potential measurement on concrete—properties and corrosion profiling application," *Corrosion Science*, vol. 56, pp. 26–35, 2012.
- [71] A. Legat, M. Leban, and Ž. Bajt, "Corrosion processes of steel in concrete characterized by means of electrochemical noise," *Electrochimica Acta*, vol. 49, no. 17-18, pp. 2741–2751, 2004.
- [72] A. Česen, T. Kosec, and A. Legat, "Characterization of steel corrosion in mortar by various electrochemical and physical techniques," *Corrosion Science*, vol. 75, pp. 47–57, 2013.
- [73] A. Michel, B. J. Pease, M. R. Geiker, H. Stang, and J. F. Olesen, "Monitoring reinforcement corrosion and corrosion-induced cracking using non-destructive X-ray attenuation measurements," *Cement and Concrete Research*, vol. 41, no. 11, pp. 1085–1094, 2011.
- [74] B. Ingham, M. Ko, N. Laycock et al., "In situ synchrotron X-ray diffraction study of scale formation during CO₂ corrosion of carbon steel in sodium and magnesium chloride solutions," *Corrosion Science*, vol. 56, pp. 96–104, 2012.
- [75] J. Wei, X. X. Fu, J. H. Dong, and W. Ke, "Corrosion evolution of reinforcing steel in concrete under dry/wet cyclic conditions contaminated with chloride," *Journal of Materials Science & Technology*, vol. 28, no. 10, pp. 905–912, 2012.
- [76] M. Outirite, M. Lagrenée, M. Lebrini et al., "Ac impedance, X-ray photoelectron spectroscopy and density functional theory studies of 3,5-bis(*n*-pyridyl)-1,2,4-oxadiazoles as efficient corrosion inhibitors for carbon steel surface in hydrochloric acid solution," *Electrochimica Acta*, vol. 55, no. 5, pp. 1670–1681, 2010.
- [77] B. Fernandes, M. Titus, D. K. Nims, A. Ghorbanpoor, and V. K. Devabhaktunia, "Practical assessment of magnetic methods for corrosion detection in an adjacent precast, prestressed concrete box-beam bridge," *Nondestructive Testing and Evaluation*, vol. 28, no. 2, pp. 99–118, 2012.
- [78] Y. Dost, N. Apaydın, E. Dedeoğlu, D. K. MacKenzie, and O. Z. Akkol, "Non-destructive testing of Bosphorus bridges," in *Non-destructive Testing of Materials and Structures*, vol. 6 of *RILEM Bookseries*, pp. 819–825, 2013.
- [79] L. Jones, S. Pessiki, C. Naito, and I. Hodgson, "Inspection methods & techniques to determine non visible corrosion of prestressing strands in concrete bridge components task 2—assessment of candidate NDT methods," *Transportation Research Board of the National Academies*, 2010, <http://trid.trb.org/>.
- [80] B. Fernandes, M. Titus, D. K. Nims, A. Ghorbanpoor, and V. Devabhaktuni, "Field test of magnetic methods for corrosion detection in prestressing strands in adjacent box-beam bridges," *Journal of Bridge Engineering*, vol. 17, no. 6, pp. 984–988, 2012.
- [81] K. Yuma, W. Tomoyo, K. Tomoe, and O. Masayasu, "Corrosion mechanisms in reinforced concrete by acoustic emission," *Construction and Building Materials*, vol. 48, pp. 1240–1247, 2013.
- [82] M. Ohtsu, K. Mori, and Y. Kawasaki, "Corrosion process and mechanisms of corrosion-induced cracks in reinforced concrete identified by AE analysis," *Strain*, vol. 47, no. 2, pp. 179–186, 2011.
- [83] L. Calabrese, G. Campanella, and E. Proverbio, "Noise removal by cluster analysis after long time AE corrosion monitoring of steel reinforcement in concrete," *Construction and Building Materials*, vol. 34, pp. 362–371, 2012.
- [84] L. Calabrese, G. Campanella, and E. Proverbio, "Identification of corrosion mechanisms by univariate and multivariate statistical analysis during long term acoustic emission monitoring on a pre-stressed concrete beam," *Corrosion Science*, vol. 73, pp. 161–171, 2013.
- [85] H. A. Elfergani, R. Pullin, and K. M. Holford, "Damage assessment of corrosion in prestressed concrete by acoustic emission," *Construction and Building Materials*, vol. 40, pp. 925–933, 2013.
- [86] M. di Benedetti, G. Loreto, F. Matta, and A. Nanni, "Acoustic emission monitoring of reinforced concrete under accelerated corrosion," *Journal of Materials in Civil Engineering*, vol. 25, no. 8, pp. 1022–1029, 2013.

Research Article

GPS and InSAR Time Series Analysis: Deformation Monitoring Application in a Hydraulic Engineering Resettlement Zone, Southwest China

Ruya Xiao and Xiufeng He

Institute of Satellite Navigation & Spatial Information System, Hohai University, Nanjing 210098, China

Correspondence should be addressed to Xiufeng He; xfhe@hhu.edu.cn

Received 10 October 2013; Accepted 25 November 2013

Academic Editor: Ting-Hua Yi

Copyright © 2013 R. Xiao and X. He. This is an open access article distributed under the Creative Commons Attribution License, which permits unrestricted use, distribution, and reproduction in any medium, provided the original work is properly cited.

Booming development of hydropower in China has resulted in increasing concerns about the related resettlement issues. Both global positioning system (GPS) and persistent scatterer interferometric synthetic aperture radar (InSAR) time series analysis are applied to measuring the magnitude and monitoring the spatial and temporal variations of land surface displacement in Hanyuan, a hydraulic engineering resettlement zone, southwest China. The results from the GPS monitoring system established in Hanyuan match well the digital inclinometer results, suggesting that the GPS monitoring system can be employed as a complement to the traditional ground movement monitoring methods. The InSAR time series witness various patterns and magnitudes of deformation in the resettlement zone. Combining the two complementary techniques will overcome the limitations of the single method.

1. Introduction

Pubugou Hydropower Station with a 186 m high core wall rock-fill dam located in the middle reaches of Dadu River, southwest China, is built for power generation, flood control, and sediment retaining retention. Several towns have been inundated by the backwater, and the population in the whole area needs to relocate, involving more than 100,000 residents, which in resettlement scale is next only to the Three Gorges and Xiaolangdi water control project among modern hydraulic engineering projects in China.

The resettlement zone, new Hanyuan County, located on Luobogang hillock, consists of unstable broken limestone, weathered shale, and schist shone with laminated loess. In 2009 and 2010, two landslide failures occurred in Hanyuan, resulting in great loss of lives and properties. Thus, to detect early indications of catastrophic movements, monitoring is essential to predict landslides.

However, the current conventional deformation monitoring techniques are always time-consuming and costly. In addition, even if taken regularly, the monitoring points are not usually dense enough to assist in understanding the mechanisms of the landslide. Therefore, in this paper, we

address deformation monitoring applications through several geodetic techniques, that is, global positioning system (GPS) and interferometric synthetic aperture radar (InSAR) in the reservoir resettlement county.

The remainder of the paper is organized as follows. Section 2 briefly introduces the principles of GPS and InSAR time series analysis. Site conditions and SAR data used are described in Section 3. In Section 4, we present the GPS monitoring system established in the study area and comparison between GPS and digital inclinometers in a landslide case. Then, time series results obtained by both GPS and InSAR are also displayed. Finally, conclusions of the paper are drawn in Section 5.

2. Method

Two modern geodetic techniques developed since the late 1980s, global positioning system (GPS) and interferometric synthetic aperture radar (InSAR), have revolutionized the way we observe the Earth surface. GPS can provide 3D information at each GPS observation points while InSAR can image the line of sight (LOS) component of deformation

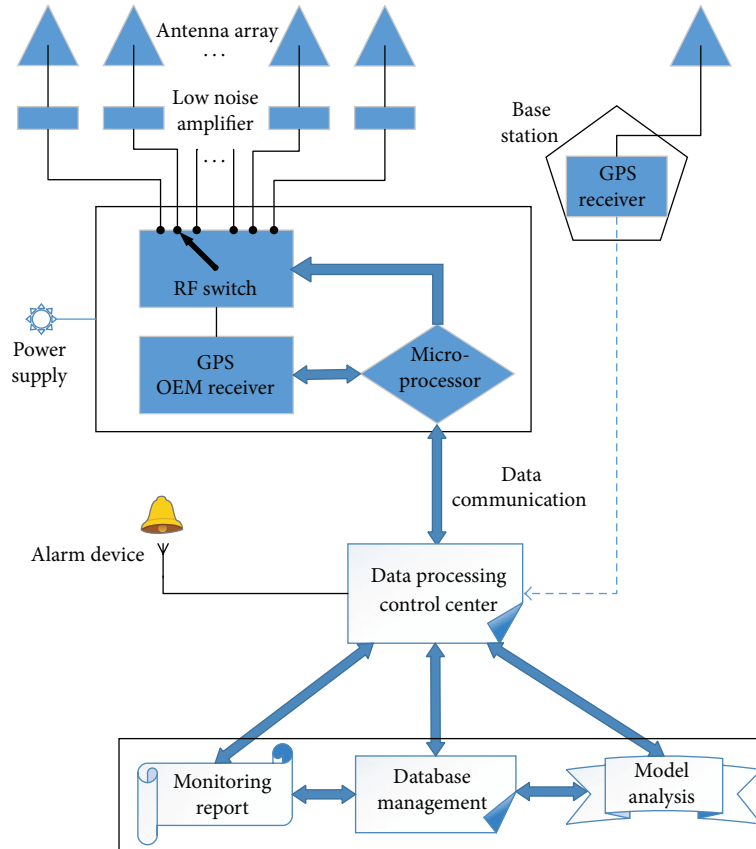


FIGURE 1: Outline of multiantenna GPS system for deformation monitoring.

over a large area at spatial resolution of tens of meters [1–4]. The technology using GPS to monitor deformation is mature; thus, we just briefly introduce the multiantenna monitoring system, aiming at decreasing the device investment.

2.1. GPS Multiantenna Monitoring System. GPS is considered as one of the best techniques for deformation monitoring thanks to its higher automation and lower labor consuming than that of traditional geodetic survey techniques [5–8]. Depending on density of the GPS antenna, the spatial resolution is low. Therefore, GPS does have disadvantages, with the major drawback being the high cost associated with placing a permanent GPS receiver at each monitoring point.

The approach of linking a single GPS receiver with multiple antennas mounted at several monitoring points has been implemented. We use a dedicated electronic timed switching device, the GPS multiantenna switch (GMAS), to connect one receiver with individual antennas. This significantly reduces the number of receivers required, thus decreasing hardware investment. GMAS has been patented in China (Patent no: 00219891.6, Owners: Xiufeng He, Xiaoli Ding, Yongrong Sun, Yongqi Chen et al.). The receiver conducts standard pseudo-range and carrier-phase observations for each antenna [9–12]. It takes efficient advantage of the characteristics of deformation survey, such as the position of a surveyed point, which changes relatively little between two consecutive

survey epochs. Figure 1 shows the outline of multiantenna GPS system.

2.2. Persistent Scatterers InSAR Time Series. InSAR can provide measurements of surface movements at a considerably improved spatial resolution with quite high accuracy, that is, centimeter or even millimeter level, over the whole area. Thus, repeat-pass satellite InSAR is a rapidly evolving remote sensing technology for observing the Earth surface and now well developed with many applications [13–18].

Due to the slow surface displacements rate, phase ambiguity problems related to temporal and geometrical decorrelations, and strong tropospheric effects, it is difficult to obtain reliable measurements of subsidence in densely vegetated areas using conventional InSAR techniques. In the late 1990s it is noticed that some radar targets maintain stable backscattering characteristics for a period of month or years, and the phase information from these stable targets (hereafter called Persistent Scatterers, PS) can be used, even over a long time period. This led to the development of PS InSAR methodologies, adopting both amplitude stability and coherence stability (i.e., correlation) as pixel selection criteria [19–21]. The persistent scatterers technique is a powerful tool that overcomes the above-said limitation of routine InSAR by simultaneously exploiting all the available SAR images gathered during repeated satellite passes.

The deformation was modeled in time and a temporal model of evolution was fitted to the double difference phase during the process as the phase is unwrapped. By taking the phase difference between nearby persistent scatterer candidates, atmospheric and orbit errors are mainly reduced. Besides, signals lacking in consistency in both space and time dimension are always considered as the atmospheric error rather than the deformation signal. By high-pass filtering the unwrapped phase in time and low-pass filtering in space we estimate the spatially correlated errors. Deformation and DEM error contributing to the double difference phase are later modeled for the whole time series. The residuals between the model and the double phase signal were considered as the noise level. Then for each persistent scatterer candidates, network adjustment is applied to estimating the noise.

Stanford method for persistent scatterers (StaMPS) is used for analyzing crustal deformation in nonurban environments in this paper. Unlike Ferretti method, StaMPS produces a time series of deformation, with no prior assumptions about the temporal nature of deformation. Therefore, it can get better performance and be more reliable under the circumstances of unknown or not readily parameterized deformation. Here only PS identification and selection steps of the innovative PS processing method are discussed; more detailed information about the algorithm, such as the phase unwrapping and spatially correlated terms removal, can be found in [22].

2.2.1. Amplitude Analysis. Ferretti et al. [19] defined the amplitude dispersion index as

$$D_A \equiv \frac{\sigma_A}{m_A}, \quad (1)$$

where σ_A and m_A are, respectively, the standard deviation and the mean of the amplitude values. For a constant signal and high signal to noise ratio (SNR), $D_A \approx \sigma_\Phi$, where σ_Φ is the phase standard deviation. As lower D_A indicates higher phase stability, consideration of amplitude is useful both to reduce the number of pixels for phase analysis and to better estimate the probability of a pixel being a PS. The pixels selected as PS candidates have $D_A \leq 0.4$ [23].

2.2.2. Phase Analysis. The residual phase (with flat earth and DEM reference phase removal), $\Phi_{\text{int},i}$, of the x th pixel in the i th interferogram can be written as

$$\Phi_{\text{int},x,i} = \Phi_{\text{def},x,i} + \Delta\Phi_{\epsilon,x,i} + \Phi_{\text{atm},x,i} + \Delta\Phi_{\text{orb},x,i} + \Phi_{n,x,i}, \quad (2)$$

where Φ_{def} is the phase change due to the deformation of the pixel in the satellite line-of-sight (LOS) direction, $\Delta\Phi_\epsilon$ is the residual topographic phase due to DEM error, Φ_{atm} is the phase equivalent of the difference in atmospheric retardation between passes, $\Delta\Phi_{\text{orb}}$ is the residual phase due to orbit inaccuracies, and Φ_n is the noise term due to variability in scattering from the pixel, thermal noise, and coregistration errors.

The spatially correlated phase is estimated through low-pass adaptive filtering. A 5th order Butterworth filter, $L(x, y)$,

with a typical cutoff wavelength of 800 m was used as a narrow low-pass filter response. The adaptive part of the combined filter determines the pass band based on the dominant frequencies present in the phase of the pixels themselves [20]. The response is calculated as

$$H(x, y) = |Z(x, y)|, \quad (3)$$

where Z is the smoothed intensity of the 2D FFT. Combine $H(x, y)$ with $L(x, y)$ to form the new filter response,

$$G(x, y) = L(x, y) + \beta \left(\frac{H(x, y)}{\bar{H}(x, y)} - 1 \right)^\alpha, \quad (4)$$

where $\bar{H}(x, y)$ is the median value of $H(x, y)$. α (typically 1) and β (typically 0.3) are adjustable weighting parameters.

Subtracting the filtered phase value $\bar{\Phi}_{\text{int},x,i}$ from $\Phi_{\text{int},x,i}$ leaves

$$\Phi_{\text{int},x,i} - \bar{\Phi}_{\text{int},x,i} = \Delta\Phi_{\epsilon,x,i} + \Phi_{n,x,i} - \bar{\Phi}'_{n,x,i}. \quad (5)$$

The phase error caused by DEM inaccuracies is proportional to the perpendicular baseline, B_\perp , so

$$\Delta\Phi_{\epsilon,x,i} = B_{\perp,x,i} K_{\epsilon,x}, \quad (6)$$

where K_ϵ is a proportionality constant. Substituting this expression into (6) gives

$$\Phi_{\text{int},x,i} - \bar{\Phi}_{\text{int},x,i} = B_{\perp,x,i} K_{\epsilon,x} + \Phi_{n,x,i} - \bar{\Phi}'_{n,x,i}. \quad (7)$$

Using all the available interferograms we can estimate K_ϵ for pixel x in a least square sense, as this is the only term that correlates with baseline.

A measure based on the temporal coherence of pixel x is defined as

$$\gamma_x = \frac{1}{N} \left| \sum_{i=1}^N \exp \left\{ j \left(\Phi_{\text{int},x,i} - \bar{\Phi}_{\text{int},x,i} - \Delta\widehat{\Phi}_{\epsilon,x,i} \right) \right\} \right|, \quad (8)$$

where N is the number of available interferograms and $\Delta\widehat{\Phi}_{\epsilon,x,i}$ is the estimate of $\bar{\Phi}'_{n,x,i}$. Assuming that $\bar{\Phi}'_{n,x,i}$ values are small, γ_x is a measure of the phase stability of the pixel and hence an indicator of whether the pixel is a PS.

2.2.3. PS Probability. The γ_x values are binned and normalized to get a probability density. All pixels are divided into two sets: PS pixels and non-PS pixels. $p(\gamma_x)$ is, then, a weighted sum of the probability density for the PS pixels, $p_{\text{PS}}(\gamma_x)$, and the probability density for the non-PS pixels, $p_R(\gamma_x)$; that is,

$$p(\gamma_x) = \alpha p_{\text{PS}}(\gamma_x) + (1 - \alpha) p_R(\gamma_x), \quad (9)$$

where $0 \leq \alpha \leq 1$. To derive $p_R(\gamma_x)$, 10^6 pseudo-pixels with random phase are simulated; that is, $W\{\psi_{x,i} - \tilde{\psi}_{x,i}\} = \exp(jR)$, where R is a random variable in the interval $[-\pi, \pi]$, and follow the steps described above to arrive at a value of γ_x for each pseudo-pixel. We bin these values and normalize



FIGURE 2: Cracks found on the retaining walls in Hanyuan.

the distribution to obtain an estimate for $p_R(\gamma_x)$. For low values of γ_x , that is, <0.3 , $p_{PS}(\gamma_x) \approx 0$ which implies that

$$\int_0^{0.3} p(\gamma_x) d\gamma_x = (1 - \alpha) \int_0^{0.3} p_R(\gamma_x) d\gamma_x. \quad (10)$$

We use the data to evaluate the integral on the left and the simulation to evaluate the integral on the right. Thus, we are able to estimate a conservative value of α . For pixel x , the probability that it is a PS is

$$P(x \in \text{PS}) = 1 - \frac{(1 - \alpha) p_R(\gamma_x)}{p(\gamma_x)}. \quad (11)$$

2.2.4. PS Selection. After every iteration, the new γ_x is compared to the old value to see the changes of γ_x . The root-mean-square of the change are calculated. Once the RMS falls below the RMS threshold, for example, 0.005, the solution should have converged. The selection of PS pixels is based on the PS probability [21]. The probability can be calculated more accurately by considering the amplitude dispersion of the pixels, $\widehat{D}_{A,x}$, as well as γ_x . Pixels are binned by $\widehat{D}_{A,x}$, ensuring that there are at least 10^4 pixels in every bin, resulting in a number of data probability distributions, $p(\gamma_x, \widehat{D}_{A,x})$. For each distribution, $p(\gamma_x, \widehat{D}_{A,x})$, we estimate $\alpha(\widehat{D}_{A,x})$. If only pixels with γ_x above a threshold value, $\gamma^{\text{thresh}}(\widehat{D}_{A,x})$, are selected, the number of those pixels that are non-PS pixels is given by

$$(1 - \alpha(\widehat{D}_{A,x})) \int_{\gamma^{\text{thresh}}}^1 p_R(\gamma_x) d\gamma_x. \quad (12)$$

We choose $\gamma^{\text{thresh}}(\widehat{D}_{A,x})$ such that the fraction of non-PS pixels to the total number of chosen pixels is acceptable for our particular application; that is,

$$\frac{(1 - \alpha(\widehat{D}_{A,x})) \int_{\gamma^{\text{thresh}}}^1 p_R(\gamma_x) d\gamma_x}{\int_{\gamma^{\text{thresh}}}^1 p(\gamma_x, \widehat{D}_{A,x}) d\gamma_x} = q, \quad (13)$$

where q is the maximum fraction of all the selected pixels that we will accept to be non-PS pixels (false positives).

We expect γ_x to decrease with increasing $\widehat{D}_{A,x}$. This implies that as $\widehat{D}_{A,x}$ increases, $P(\gamma_x, \widehat{D}_{A,x})$ will skew more to lower values of γ_x . The net effect on $\gamma^{\text{thresh}}(\widehat{D}_{A,x})$ is to increase with increasing \widehat{D}_A . Empirically, we find that the relationship is approximately linear; that is, $\gamma^{\text{thresh}} = \kappa \widehat{D}_A$, where κ is a constant. We find the best-fitting κ by least-squares inversion and select pixels for which $\gamma_x > \kappa \widehat{D}_{A,x}$ as PS.

3. Study Area

3.1. Site Conditions. Three ancient landslides, namely, Luan-shigang, Futang, and Kangjiaping were identified by geologists on Luobogang hillock. The stability of the hill slopes is adversely affected by the water surface rising and fluctuation in the reservoir. Large-scale catastrophic movements may be triggered when the shear stress exceeds the shear resistance of the material.

Hundreds of retaining walls were built to minimize large movement of the landslides. But cracks were soon observed on the retaining walls (Figure 2). The displacements of landslides cause continuous damage to buildings and infrastructures.

3.2. SAR Data Set. The present study used a data set composed of 34 images produced by ENVISAT/ASAR systems spanning the time from September 20, 2003 to August 14, 2010. The ENVISAT ASAR data (descending orbits track 61) were provided under the European Space Agency (ESA)-National Remote Sensing Center of China (NRSCC) Dragon cooperation project, collected with a nominal radar look angle of 23° . DORIS precise orbits data provided by the ESRIN help desk of ESA were applied to calculating ENVISAT interferometric baselines. The 3 arcsecond (~ 90 m) shuttle radar topography mission (SRTM) DEM data were used to correct the interferometric phase for topography at the first step and then for geocoding the C-band SAR data (transforming Range-Doppler coordinates into Universal Transverse Mercator map geometry system).

The size of the test area is about $12 * 12$ km, covering about 29.26° to 29.40° N and 102.53° to 102.72° E (Figure 3). The scene acquired on May 31, 2008 is selected as the “master” image.

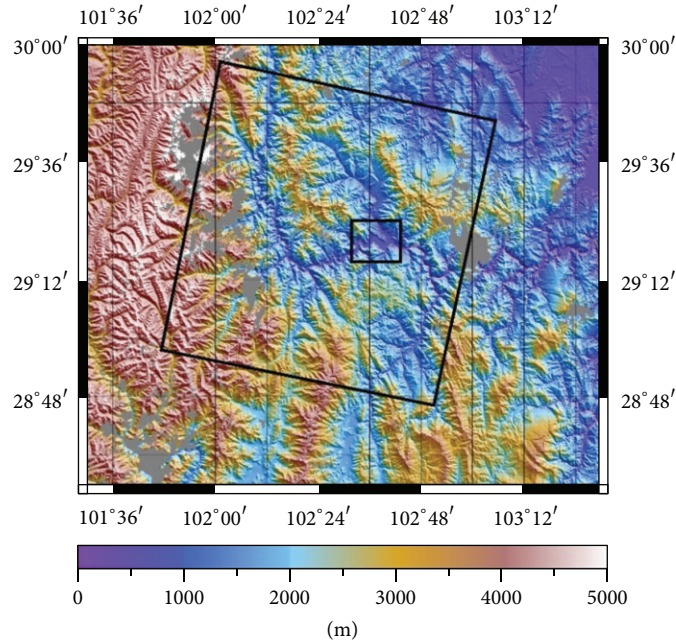


FIGURE 3: Location map of Hanyuan County, Sichuan. The bigger black rectangle indicates the ENVISAT scene footprint (descending orbits track 61) used in the PS analysis and the smaller one represents the region of interest in this paper.

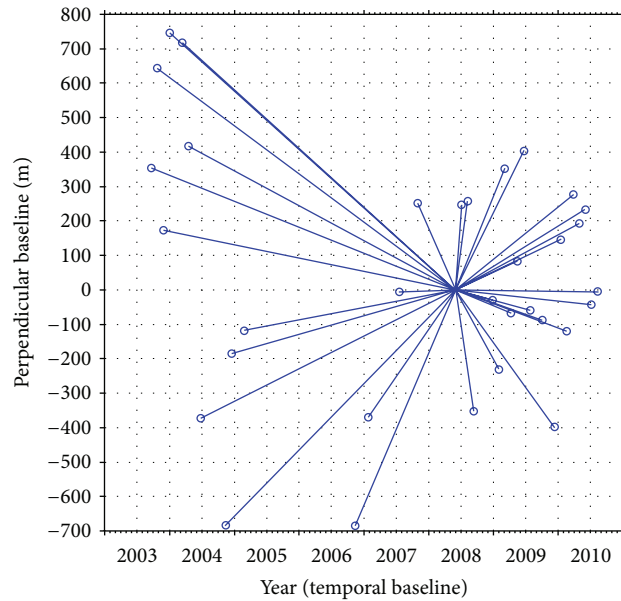


FIGURE 4: Perpendicular baseline relative to the “master” scene plot for the interferometric stack.

The maximum temporal baseline is 1715 days, and the maximum normal baseline is about 746 m. Figure 4 and Table 1 show more details about the temporal and perpendicular baselines.

4. Results and Analysis

4.1. GPS Monitoring System. More than 100 monitoring stations are installed in the whole county. The 28 continuous

monitoring stations operate 7 * 24 hours per week and engineers will periodically check the other 90 stations. In key areas with more buildings, the density of GPS monitoring stations is also higher. Detailed information about the GPS monitoring network can be found in [24].

The power to the GPS receivers and data transmission devices is supplied by the uninterruptible power system (UPS) at the monitoring sites. Although solar panels are all employed at each site, power from the city electricity grid is always the preferred option when it is available.

TABLE 1: ENVISAT ASAR data set used in the PS time series analysis.

Date	Temporal baseline (day)	Perp. baseline (m)	Date	Temporal baseline (day)	Perp. baseline (m)
20-Sep-2003	-1715	354.5	13-Sep-2008	105	351.5
25-Oct-2003	-1680	644.8	27-Dec-2008	210	-28.4
29-Nov-2003	-1645	172.3	31-Jan-2009	245	230.4
3-Jan-2004	-1610	745.9	7-Mar-2009	280	351.8
13-Mar-2004	-1540	716.9	11-Apr-2009	315	-66.6
17-Apr-2004	-1505	416.8	16-May-2009	350	84.2
26-Jun-2004	-1435	373.2	20-Jun-2009	385	403.7
13-Nov-2004	-1295	682.7	25-Jul-2009	420	-58.7
18-Dec-2004	-1260	184.3	3-Oct-2009	490	-88.5
26-Feb-2005	-1190	118.1	12-Dec-2009	560	398.7
18-Nov-2006	-560	682.8	16-Jan-2010	595	145.8
27-Jan-2007	-490	369.7	20-Feb-2010	630	118.6
21-Jul-2007	-315	-5.6	27-Mar-2010	665	277.2
3-Nov-2007	-210	251.4	1-May-2010	700	193.3
31-May-2008	0	0	5-Jun-2010	735	232.5
5-Jul-2008	35	246.8	10-Jul-2010	770	-43
9-Aug-2008	70	257.4	14-Aug-2010	805	-5.3

Each site needs to transfer massive amount of data to the control center which is located within a town area. A public wireless phone network or other media may be used. In this case, we chose the wireless transmission and 3rd generation telecommunication technologies.

The central servers housed inside the control center are connected with a local area network (LAN). The control center serves two main functions. Firstly, it receives the monitoring data, verifies the integrity of the data, assesses the status of all the devices, and issues control commands to the field stations. Secondly, the control center is responsible for data analysis, storage of processed data, deformation modeling, forecast, and transmission of information.

4.2. GPS versus Digital Inclinometer in a Landslide Case. The GPS monitoring system is designed to detect mm level movements. Figure 5 illustrates the movements on the three components captured by the system in August 2011. The result for site TP6-1 showed a significant displacement which occurred in August, and it became stable again in September. The site moves by almost 15 mm to the north as well as 5 mm to the west within 20 days.

The engineers periodically collect subsurface deformation data using RST MEMS digital inclinometer system at GPS monitoring stations. Measurements were taken along two perpendicular directions, both *A* and *B* axes, from the depth of 0.5 m to 28.5 m at 0.5 m intervals. Figure 6 shows the comparison between the GPS and digital inclinometer results on TP6-1 during the unstable period. The total displacements at the depth of 0.5 m from inclinometer (which is the measurement point closest to the ground surface) were compared with the results obtained from GPS. Generally, the displacement amplitude on the ground surface will be larger than that in subsurface. Therefore, the magnitude from digital inclinometer is smaller than that from GPS monitoring. The

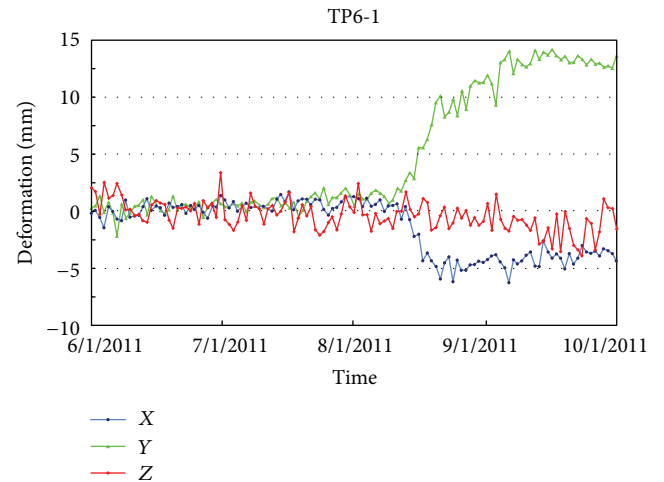


FIGURE 5: The movements captured by the landslide monitoring system during August 2011.

displacement trend and time of occurrence captured by both methods match well.

Field investigations were conducted shortly after the displacement was discovered. Construction activities near site TP6-1 influenced the stability of the local ground. A mound of soil heaped in the south results in much more load and pressure to the retaining wall. We believe that this is the main reason for the monitoring site moving north.

Due to page limit, detailed information about the GPS monitoring system established in Hanyuan and the result time series is omitted here in this paper. The exhaustive report and analysis can be found in [24].

4.3. Time Series InSAR Results. Pubugou Hydropower Station started to impound water for the first time on November

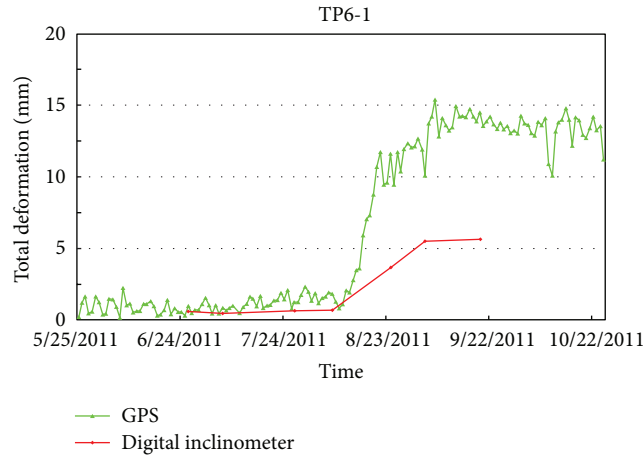


FIGURE 6: GPS versus digital inclinometer results for the displacement on TP6-1 in August 2011.

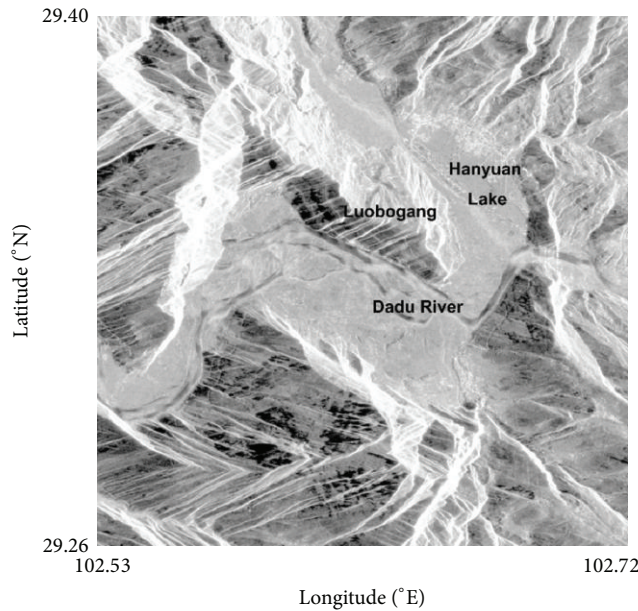


FIGURE 7: The new resettlement county, Luobogang hillock, in the SAR image. After completing the hydropower project and water storage, a reservoir was formed and the old Hanyuan County is now under water.

1, 2009. The old county no longer existed from then on. In the mean SAR amplitude image (Figure 7), we can clearly see the Dadu River and the Luobogang resettlement zone. A reservoir, named Hanyuan Lake, was formed at the location of the old Hanyuan County.

With StaMPS, the density of PS identified over most of the region was about 20 per km² (1794 PSs in total, excluding the water area). No PSs were identified in the densely vegetated area due to the seasonal cultivation, flood irrigation, and crop growth. Even in some parts of urban area (on Luobogang), relatively rare PSs were identified because of the construction activities in the resettlement zone which lead to local interferometric phase decorrelation. In addition, due to the side-looking radar signals, the slope and aspect in the mountain areas also have considerable influence on PS detection.

Unlike other PS algorithms, StaMPS extracts the LOS deformation via phase unwrapping rather than assuming a model for how displacement rates vary with time. Figure 8 demonstrates the LOS deformation time series at Hanyuan during the period from 2003 to 2010. For the scene predating the “master” image, positive phase implies movement towards the satellite, and vice versa.

Based on the unwrapped phase time series, mean LOS velocity of PSs was calculated. As shown in Figure 9, the density of PS in the southern part of the new county reached more than 40 per km². Due to the construction activities, rare PSs were detected in downtown. Scatterers appearing on all the images were accepted as PS and the ones existed in only a subset of the data stack were rejected. Therefore, no scatterers were identified in the old county which disappeared



FIGURE 8: Time series of LOS deformation at Hanyuan spanning from September 2003 to August 2010, referenced temporally to the “master” scene (May 31, 2008) and superimposed on the mean amplitude image.

after the water storage. Standard deviation of the mean LOS velocity shows the precision of the linear regression.

Overall, the mean LOS velocity of the PSs is relatively slow. Several PSs in two typical regions, displayed in Figure 10, are selected for further analysis.

The deformation histories of the PSs (4 PSs in Figure 10 upper case and 5 PSs in the lower case) in such a small region match well. This, to a certain degree, verified the reliability of the phase unwrapping. The average velocities of the adjacent PSs in the two cases are about 3 mm/year and -4 mm/year, respectively. It should be noted that the sign of the deformation and the velocity implies the movement towards or away from the satellite on the LOS direction.

Without the information of the look angle and aspects of the slope, we cannot determine the movement direction (uplift or subsidence) only from the InSAR results. This is also the main limitation of the InSAR technique, which can be improved by integrating ascending/descending orbits data from multiplatform satellite sensors.

The real-time GPS landslide monitoring system of new Hanyuan county began trial operation in May 2011. The ENVISAT satellite was brought to a new lower orbit in October 2010. The orbital change ends the PS time series analysis using ASAR data. Unfortunately, no synchronous data can be collected from the two sources; thus, verification between GPS and InSAR is impossible.

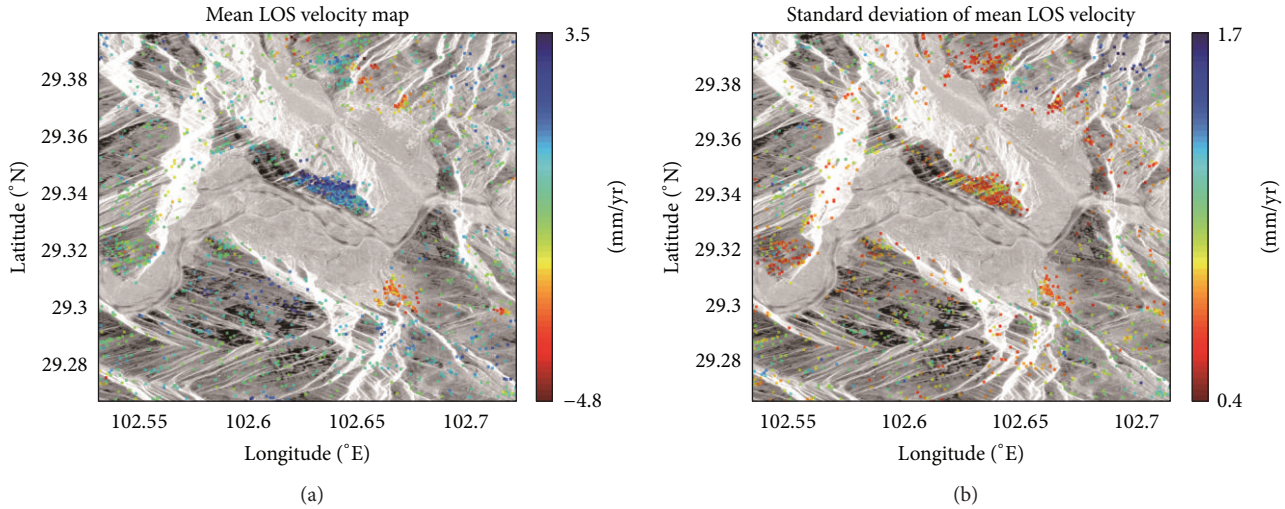


FIGURE 9: Mean LOS deformation velocity map of the PSs and the standard deviation of mean LOS velocity. The units are mm/year with positive values being towards the satellite along the LOS direction.

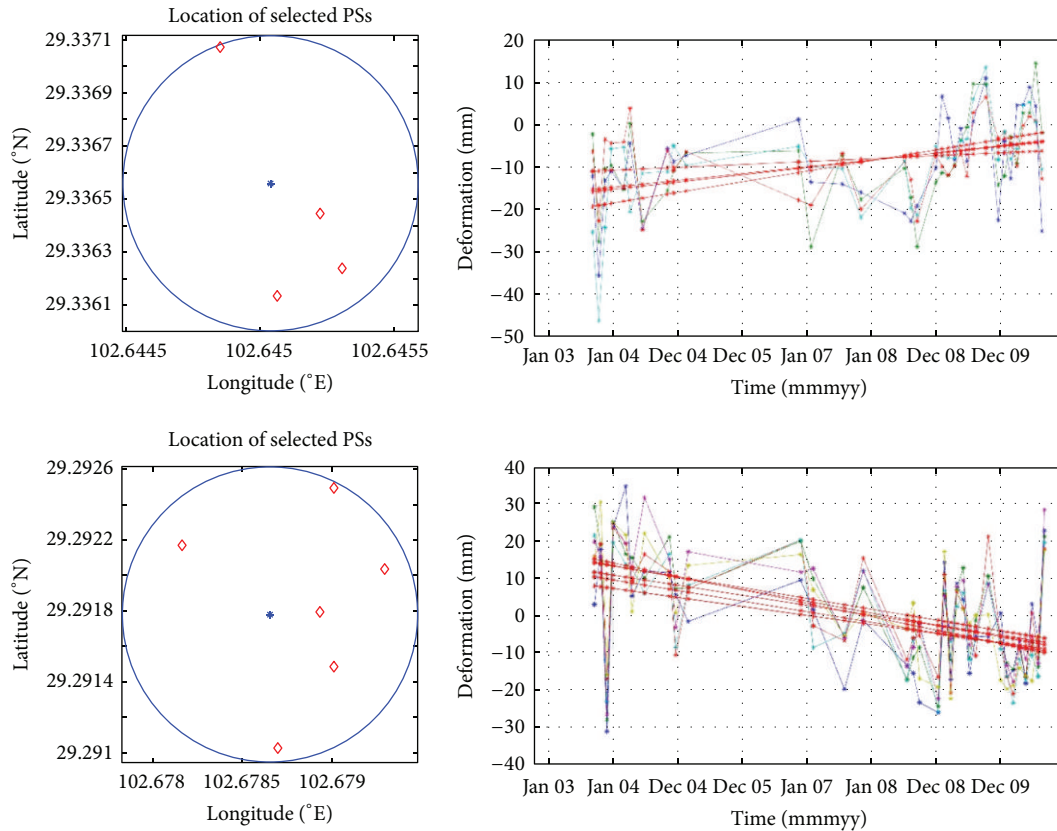


FIGURE 10: LOS deformation time series of the selected PSs. The red lines indicate linear trends.

5. Concluding Remarks

The measurement of ground surface movements over Hanyuan is one of the important field monitoring activities which would provide advance warning against sudden failures. A real-time landslide monitoring system using GPS in

new Hanyuan County is now in normal operation. The comparison between GPS and digital inclinometer results shows a high consistency in respect of the displacement trend. This suggests that the GPS monitoring system can be employed as a complement to the traditional ground movement monitoring methods.

New Hanyuan County is not an ideal environment for the application of conventional InSAR technique because of its dense vegetation cover, high soil moisture content and humidity, and the active constructions over the past years. However, the persistent scatterer InSAR approach can overcome the problems, and the time series of surface displacements show various patterns and magnitudes of deformation in the resettlement zone.

GPS provides 3D information at relatively sparse observation points while InSAR captures LOS deformation on a surface (in effect, as for PS approach, the “surface” refers to denser points) with wide coverage. Therefore, it is obvious that the two techniques are complementary. Unfortunately, neither ENVISAT ASAR nor ALOS PALSAR satellite data can be synchronous with the ground GPS monitoring results. Nevertheless, the historical information obtained via InSAR technique using archived scenes cannot be replicated.

Acknowledgments

This work is supported by the National Natural Science Foundation of China (Grant nos. 41274017, 41204002, 41301449, 40974001, and 50579013), the Key Technology R&D Program of Jiangsu Province (Grant no. BE2010316), Fundamental Research Funds for the Central Universities (Grant no. 2010B14714), Jiangsu Graduate Student Research Innovative Projects (Grant no. CXZZ11.0451), and Open Research Fund of Key Laboratory of Disaster Reduction and Emergency Response Engineering of the Ministry of Civil Affairs (Grant no. LDRERE20120102). The ENVISAT scenes are obtained from the European Space Agency (ESA) under a Category-1 Proposal no. 2774. Ms. Zhu Jialu’s help in polishing the language is highly appreciated; meanwhile, the authors would like to thank the anonymous reviewers for their constructive comments that helped in improving the quality of this paper.

References

- [1] X. He, H. Luo, Q. Huang, and M. He, “Integration of InSAR and GPS for hydraulic engineering,” *Science in China E*, vol. 50, no. 1, pp. 111–124, 2007.
- [2] M. Peyret, Y. Djamour, M. Rizza et al., “Monitoring of the large slow Kahrod landslide in Alborz mountain range (Iran) by GPS and SAR interferometry,” *Engineering Geology*, vol. 100, no. 3–4, pp. 131–141, 2008.
- [3] Y. Yin, W. Zheng, Y. Liu, J. Zhang, and X. Li, “Integration of GPS with InSAR to monitoring of the Jiaju landslide in Sichuan, China,” *Landslides*, vol. 7, no. 3, pp. 359–365, 2010.
- [4] T.-H. Yi, H.-N. Li, and M. Gu, “Recent research and applications of GPS-based monitoring technology for high-rise structures,” *Structural Control and Health Monitoring*, vol. 20, no. 5, pp. 649–670, 2013.
- [5] P. Psimoulis, M. Ghilardi, E. Fouache, and S. Stiros, “Subsidence and evolution of the Thessaloniki plain, Greece, based on historical leveling and GPS data,” *Engineering Geology*, vol. 90, no. 1–2, pp. 55–70, 2007.
- [6] E. M. D. Souza, J. F. G. Monico, and A. Pagamisse, “GPS satellite kinematic relative positioning: analyzing and improving the functional mathematical model using wavelets,” *Mathematical Problems in Engineering*, vol. 2009, Article ID 934524, 18 pages, 2009.
- [7] T. H. Yi, H. N. Li, and M. Gu, “Experimental assessment of high-rate GPS receivers for deformation monitoring of bridge,” *Measurement*, vol. 46, no. 1, pp. 420–432, 2013.
- [8] T. Yi, H. Li, and M. Gu, “Full-scale measurements of dynamic response of suspension bridge subjected to environmental loads using GPS technology,” *Science China Technological Sciences*, vol. 53, no. 2, pp. 469–479, 2010.
- [9] Y. Chen, X. Ding, D. Huang, and J. Zhu, “A multi-antenna GPS system for local area deformation monitoring,” *Earth, Planets and Space*, vol. 52, no. 10, pp. 873–876, 2000.
- [10] X. L. Ding, Development a et al., “Field testing of a multi-antenna GPS system for deformation monitoring,” *Wuhan University Journal of Natural Sciences*, vol. 8, no. 2, pp. 671–676, 2003.
- [11] X. He, G. Yang, X. Ding, and Y. Chen, “Application and evaluation of a GPS multi-antenna system for dam deformation monitoring,” *Earth, Planets and Space*, vol. 56, no. 11, pp. 1035–1039, 2004.
- [12] X. He, D. Jia, and W. Sang, “Monitoring steep slope movement at Xiaowan dam with GPS multi-antenna method,” *Survey Review*, vol. 43, no. 323, pp. 462–471, 2011.
- [13] P. Lu, N. Casagli, F. Catani, and V. Tofani, “Persistent scatterers interferometry hotspot and cluster analysis (PSI-HCA) for detection of extremely slow-moving landslides,” *International Journal of Remote Sensing*, vol. 33, no. 2, pp. 466–489, 2012.
- [14] A. M. Lubis, N. Isezaki, and T. Sato, “Two-dimensional coseismic deformation field of the Sumatra-Andaman earthquake 2004 Mw 9.2 derived from synthetic aperture radar observation,” *Remote Sensing Letters*, vol. 2, no. 2, pp. 107–116, 2011.
- [15] X. Ding and W. Huang, “D-InSAR monitoring of crustal deformation in the eastern segment of the Altyn Tagh Fault,” *International Journal of Remote Sensing*, vol. 32, no. 7, pp. 1797–1806, 2011.
- [16] W. Fu, H. Guo, Q. Tian, and X. Guo, “Landslide monitoring by corner reflectors differential interferometry SAR,” *International Journal of Remote Sensing*, vol. 31, no. 24, pp. 6387–6400, 2010.
- [17] Z. Li, E. J. Fielding, P. Cross, and R. Preusker, “Advanced InSAR atmospheric correction: MERIS/MODIS combination and stacked water vapour models,” *International Journal of Remote Sensing*, vol. 30, no. 13, pp. 3343–3363, 2009.
- [18] Z. Li, E. J. Fielding, and P. Cross, “Integration of InSAR time-series analysis and water-vapor correction for mapping postseismic motion after the 2003 Bam (Iran) earthquake,” *IEEE Transactions on Geoscience and Remote Sensing*, vol. 47, no. 9, pp. 3220–3230, 2009.
- [19] A. Ferretti, C. Prati, and F. Rocca, “Permanent scatterers in SAR interferometry,” *IEEE Transactions on Geoscience and Remote Sensing*, vol. 39, no. 1, pp. 8–20, 2001.
- [20] A. Hooper, H. Zebker, P. Segall, and B. Kampes, “A new method for measuring deformation on volcanoes and other natural terrains using InSAR persistent scatterers,” *Geophysical Research Letters*, vol. 31, no. 23, pp. 1–5, 2004.
- [21] A. Hooper, P. Segall, and H. Zebker, “Persistent scatterer interferometric synthetic aperture radar for crustal deformation analysis, with application to Volcán Alcedo, Galápagos,” *Journal of Geophysical Research B*, vol. 112, no. 7, Article ID B07407, 2007.
- [22] A. J. Hooper, *Persistent Scatterer Radar Interferometry for Crustal Deformation Studies and Modeling of Volcanic Deformation*, Stanford University, 2006.

- [23] A. J. Hooper, "A multi-temporal InSAR method incorporating both persistent scatterer and small baseline approaches," *Geophysical Research Letters*, vol. 35, no. 16, Article ID L16302, 2008.
- [24] R. Xiao and X. He, "Real-time landslide monitoring of Pubugou hydropower resettlement zone using continuous GPS," *Natural Hazards*, vol. 69, no. 3, pp. 1647–1660, 2013.

Research Article

FBG-Based Creep Analysis of GFRP Materials Embedded in Concrete

Guo-Wei Li,^{1,2} Cheng-Yu Hong,^{3,4} Jian Dai,^{1,5} Liang Yu,^{1,5} and Wan-Huan Zhou⁶

¹ Key Laboratory of Ministry of Education for Geotechnique and Embankment Engineering, Hohai University, Nanjing, Jiangsu, China

² Highway and Railway Engineering Institute, Hohai University, Nanjing, Jiangsu, China

³ Department of Civil Engineering, Shantou University, Shantou, Guangdong, China

⁴ State Key Laboratory of Earthquake Dynamics, Institute of Geology, China Earthquake Administration, China

⁵ Geotechnical Research Institute, Hohai University, Nanjing, Jiangsu, China

⁶ Department of Civil and Environmental Engineering, Faculty of Science and Technology, University of Macau, Macau

Correspondence should be addressed to Cheng-Yu Hong; joeyhcy@gmail.com

Received 14 October 2013; Accepted 29 November 2013

Academic Editor: Jun Li

Copyright © 2013 Guo-Wei Li et al. This is an open access article distributed under the Creative Commons Attribution License, which permits unrestricted use, distribution, and reproduction in any medium, provided the original work is properly cited.

This paper presents a typical study regarding the creep interaction behavior between prestressed glass fiber reinforced polymer (GFRP) bar and concrete when this GFRP bar is subjected to a constant external pullout force. A number of optical fiber Bragg grating (FBG) sensors were mounted on GFRP bar surface by using an innovative installation method to measure strain distributions. Test results indicate that the complicated interaction at GFRP bar-concrete interface can be evaluated using a transitional factor. Variation trends of this transitional factor indicate three typical zones characterized by different strain/stress variation trends of the GFRP bar when prestress values are sustained at specific levels. These three typical zones include stress release zone, stress transition zone, and continuous tension zone. Test results also suggest that the instant stress loss at the interaction interface between concrete and GFRP bar was quite limited (less than 5%) in present test. Contributed proportion of each GFRP bar section was obtained to represent the creep behavior of the GFRP bar embedded in concrete. This investigation improved the understanding of the short-term interaction behavior between prestressed GFRP bar and concrete.

1. Introduction

Fiber reinforced polymer (FRP), as a newly developed composite material, has been widely used for temporary and long-term reinforcement of slopes, excavations, and retaining walls in recent years. The behavior of FRP bar, particularly glass fiber reinforced polymer (GFRP) bar composite material, is quite different from steel bars particularly in the stiffness and strength properties. In several engineering projects, GFRP bar has been accepted for the replacement of common steel bars due to the advantages of high resistance to corrosion under severe environmental conditions, high tensile strength, light weight, and ease of handling during production process. Bond strength at the interface between concrete and FRP bar material is a major concern to researchers and engineers accounted for safety analysis and engineering design. The most common measure to examine the interface strength is

pullout (or compression) test, where the stress transferring mechanism can be comprehensively understood by the measurement of force-displacement relationships [1–5]. Some typical sensors such as fiber Bragg grating sensors were found to be very effective for the measurement of particularly small structural deformation [6].

Creep behavior of GFRP bar embedded in concrete is normally investigated in terms of the frictional resistance mobilized at the interaction interface. Typical analytical studies show that the use of a proper mathematical model (or different stress-displacement relationships) to simulate the interface behavior between GFRP bar and concrete is possible [7–9], while the practical interaction behavior is normally complex, depending upon a number of uncertain factors, such as bar types, surface treatment methods, surface degradation, and external temperature changes, [8, 10–13]. Researchers have made substantial contributions to the safety

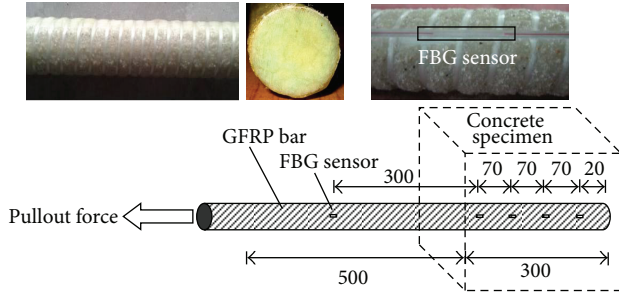


FIGURE 1: Photos of the GFRP bar used in present test and a schematic view of dimensions of test specimens and locations of FBG strain sensors.

analysis of engineering structures reinforced by GFRP bars using mathematical models or from the analysis of practical measurement results [14, 15].

Creep behavior between GFRP composite material and concrete is critical and normally examined using pullout tests or compression tests. This interaction process normally requires a time-dependent process [16, 17]. Long-term or short-time creep behavior is mostly realized by deformation (strain) measurement of FRP reinforced specimens under different loading tests (applied on concrete or FRP material). Sá et al. [7] examined the time-stress relationships of GFRP element subjected to sustained external loads using empirical methods. The effective stiffness reduced nearly 25% after a measurement period of more than one year. A good agreement between analytical predictions and measurement results is obtained. Sá et al. [18] also found that creep-creepity measured on fiber reinforced polymer (FRP) materials and pultruded glass fibre reinforced polymers (GFRPs) was quite significant after the first hour in experiment.

Other experimental studies indicate that the behavior of FRP material embedded in concrete is complicated. Ferrier et al. [19] carried out a systematic study on eight concrete specimens which were confined using FRP composite materials, with a new analytical approach proposed to predict the concrete behavior under compression. Major test results from Soong et al. [8] suggest that the maximum pullout force of the GFRP bar consists of debond load, bearing load, and frictional load. The quantified calculation of each force component was derived. Seracino et al. [20] adopted rheological model to predict the strain variation associated with time. The whole test lasted for one year. Creep strain shows significant rise in the first ten days when the concrete specimen was subjected to axial compression. Zhang et al. [21] performed a creep test study on four specimens, which were loaded for 312 days, and then all external loads were released to evaluate the deformation recovery behavior. A modified model was also adopted and the calculated results were used to verify the measurement data. The creep compression tests which lasted for about one year presented by Wang and Zhang [22] show that the creep behavior of the concrete confined by FRP has substantial effect on the elastic modulus and deformation capability. Other experimental studies indicate that the interaction behavior

TABLE 1: Parameter values of test materials.

Parameter	Unit	Value
Elastic modulus of GFRP bar	GPa	50
Ultimate tensile strength of GFRP bar	MPa	853
GFRP bar diameter	mm	26
Anchorage length of GFRP bar in concrete	mm	300
Anchorage length of steel tube	mm	400
Length of free part of GFRP bar	mm	500
Ratio of water over soundless breaking	—	0.3 : 1
Curing time of concrete	day	28
Ultimate compressive strength of concrete	MPa	34.5

between concrete and FRP composite material is complex and depends on many uncertain factors, such as temperature level, creep behavior, water condition (tap-water or sea-water), and moisture condition (wet or dry) [13, 23, 24]. This paper presents a typical experimental investigation regarding the creep interaction behavior of GFRP bars embedded in concrete and the related stress transfer mechanism during loading process. Basic test setup, an innovative installation method of optical fiber sensors, typical measurement results, and the related test findings are summarized and analyzed for better understanding of the creep interaction behavior at the interface between concrete and GFRP bar.

2. Materials Properties and Experimental Equipment

Glass fiber reinforced polymer (GFRP) material was adopted as reinforcement in concrete in present experiment. This composition material consisted of 17.3% epoxy resin, 75.7% glass fiber, and 7% silica. The concrete used in present study consisted of 14.3% cement, 28.6% medium sand, 50% gravel, and 7.1% water. Figure 1 shows a schematic view of dimensions of test specimen. The GFRP bar was 26 mm in diameter, 500 mm in free part length, and 300 mm in anchorage length in concrete. This dimension is similar to the most common GFRP bars used in practical field. Table 1 summarizes all parameter values of materials used in the present study.

For the measurement of occurred strain along the GFRP bar during loading process, a total of five fiber Bragg grating (FBG) sensors were mounted on the GFRP bar surface with an innovative installation method. Locations of these five FBG sensors (in the anchorage part) were 0, 40, 110, 180, and 250 mm away from the GFRP bar head. In comparison with traditional strain sensors (e.g., strain gauge), FBG sensor is more sensitive to the occurred small deformation (the minimum resolution of FBG sensor is less than $10 \mu\epsilon$). This employed installation method of FBG sensors is a key procedure to reflect the real deformation of GFRP bar structures under external load. In this test, a 2 mm wide, 2 mm deep, and 15 mm long slot was created on the GFRP bar surface using an electric saw. The FBG strain sensor part was embedded in this slot carefully and fixed inside at the two ends with instant glue. Epoxy resin was then used to cover the whole sensor part. Normally after 2-3 hours, the FBG sensor could

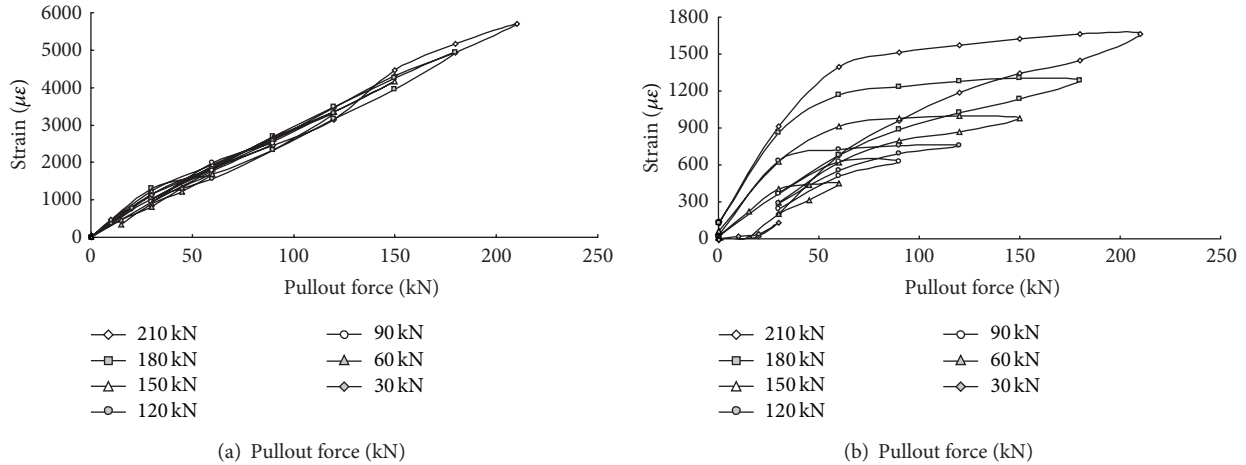


FIGURE 2: Typical relationships of GFRP bar strain against pullout force for the GFRP locations, (a) 40 mm and (b) 250 mm.

be encapsulated in this slot and used to measure the real strain change. Since FBG sensor is a flexible material and not sensitive to compression, all FBG sensors were maintained in slightly tension effect before placing into slots of GFRP bar surface. Figure 1 (upper part) presents a FBG sensor fully covered with epoxy resin in a slot of the GFRP bar surface. Typical photos of cross-sectional area and length of the GFRP bar are also shown in this figure indicating the exact location of a FBG sensor which reflects the magnitude of optical wavelength shift associated with external deformation and temperature change. The basic linear relationship between FBG sensor and the occurred strain can be found in Hong et al. [2]. Basic setup of pullout test of the GFRP bar embedded in concrete is also presented in Figure 1. For the application of pullout force on the GFRP anchorage bar, a reaction frame was designed and installed on the bar head. A hydraulic jack was used between concrete specimen and stainless steel tube to apply pullout force on the anchorage part, with a load cell in between to measure the applied external load.

3. Pullout Test

After the concrete specimen was cured 28 days after grouting, a step loading method was employed on the GFRP bar head to examine the pullout resistance of the GFRP bar and the occurred strain distribution along this GFRP bar. Loading increment was 30 kN and was maintained 10 minutes for each loading step. The ultimate pullout force applied at the GFRP bar head was 210 kN. The pullout force was then reduced in a corresponding step by step form (load reduction for each unloading step = 30 kN). During the whole pullout test process, all load values and strain data were collected by load cell and optical fiber sensors, respectively. The frequency of strain data collection was 10 Hz.

4. Monitoring Strain Results and Analysis

As introduced in the previous section, the pullout force was applied step by step. Figures 2(a) and 2(b) show typical measured strain curves against pullout force measured by

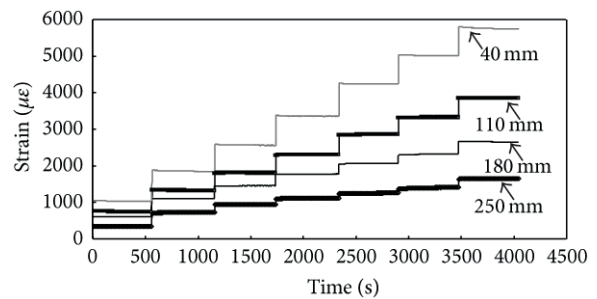


FIGURE 3: Relationships of measured strain of GFRP bar against time at different locations of the GFRP bar.

the optical fiber sensors at the locations 40 and 250 mm to GFRP bar tip. The maximum tension strain values measured in present test were about 5500 $\mu\epsilon$ at the bar head and about 1600 $\mu\epsilon$ at the location 250 mm to the GFRP bar head. This indicates that the FBG sensor is capable of identifying very large tension deformation. Figure 3 shows the measured strain distribution against pullout time. All the measured strain values increase in a step by step form, and the measured strain values decrease from GFRP bar head (40 mm) to the location close to the GFRP bar tip (250 mm) at different loading levels.

To better understand the transitional interaction behavior between GFRP bar and concrete, all measured strain data after pullout force was maintained at a specified level are summarized in present study. Figures 4(a), 4(b), 4(c), 4(d), and 4(e) show the typical strain variation trends against time after a specified pullout force (210 kN) was sustained at the GFRP bar head. All strain data were collected immediately after the pullout force is applied and maintained at the GFRP bar head. It is clear that the strain values show different variation trends against time in all these figures. At the location close to the GFRP bar head, strain values show continuous reductions; for example, reductions of strain values at the locations of 0, 40, and 110 mm are around 76, 82, and 13 $\mu\epsilon$, respectively as shown in Figures 4(a), 4(b), and 4(c).

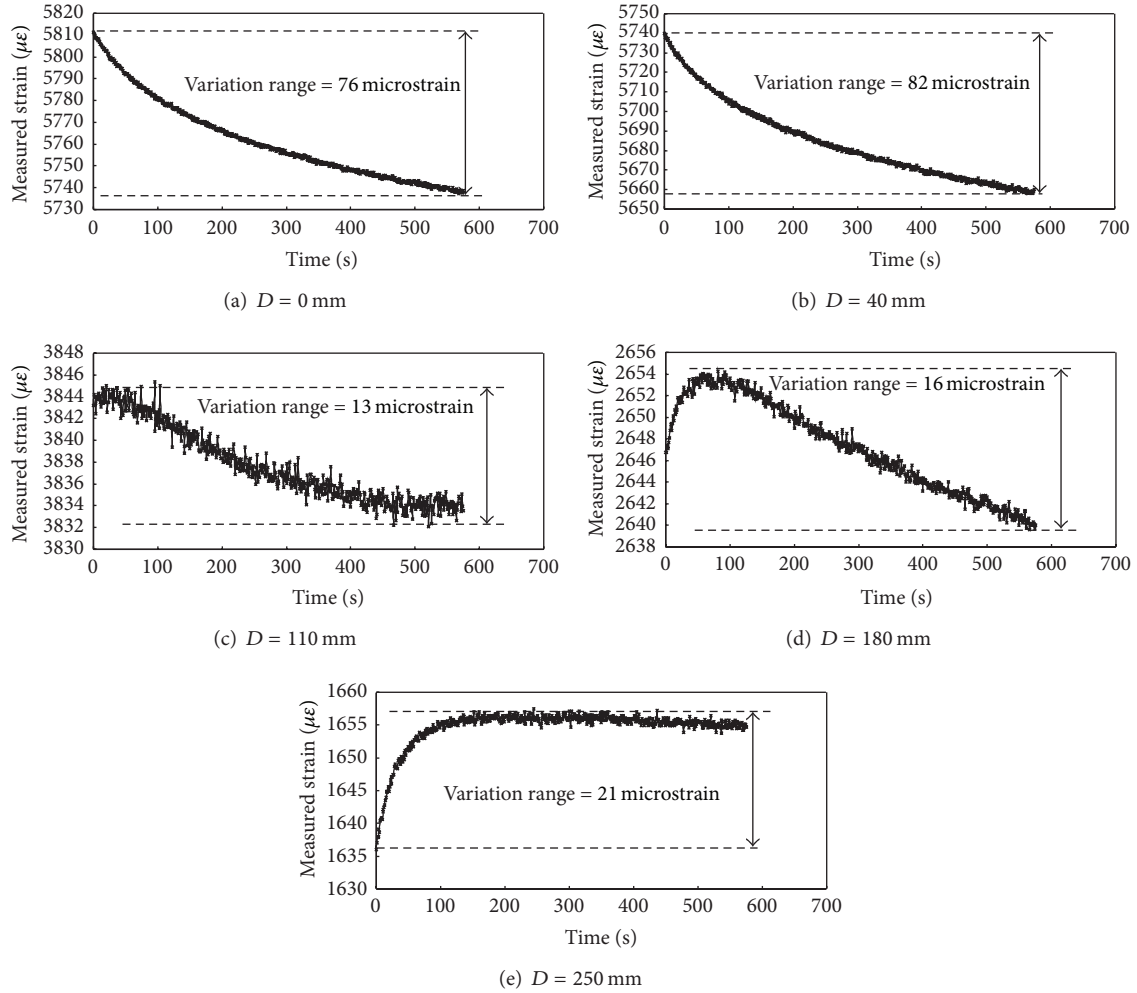


FIGURE 4: Typical measured strain variations against time after the application of 210 kN pullout force at the different distances from the GFRP bar head—(a) 0 mm, (b) 40 mm, (c) 110 mm, (d) 180 mm, and (e) 250 mm.

This suggests that the tension deformation of the GFRP bar relaxes slightly after the pullout force is immediately sustained. This GFRP bar deformation at the location of 180 mm shows slightly different variation trend compared with the locations near the GFRP bar head as shown in Figure 4(d), where the measured strain values increase first then decrease substantially (maximum reduction is $16 \mu\epsilon$). Why? Immediately after the application of pullout force, the GFRP bar head would react first; then, a relevant tension deformation takes place at the bar head and starts to transfer along the longitudinal direction. At the deeper location like 180 mm in Figure 4(d), pullout force requires a process to transfer and achieve this location, so that the measured strain increases first (due to the reaction of the GFRP bar to pullout force) and deformation relaxes progressively (strain release). Figure 4(e) also verifies this observation; that is, the initial strain values increase substantially but show slight reductions afterwards. The optical fiber sensors used in present test show a relative high resolution and successfully identify very small strain values (less than $10 \mu\epsilon$).

5. Transitional Interaction Behavior between GFRP Bar and Concrete

Significant pullout force may result in debonding condition and damage the initial bonding state between GFRP bar and concrete. It is therefore crucial to understand the real strain/stress transfer process during and after the application of pullout force. From the measured strain results shown in Figures 4(a)–4(e), three typical interaction states can be obtained including consistent rise, obvious rise followed by a reduction, and continuous reduction of tension strain values. To better identify these three typical variation trends, a normalized parameter, namely, transitional factor λ_T , is proposed to represent these strain/stress development states of the GFRP bar as follows:

$$\lambda_T = \frac{\epsilon_i - \epsilon_{\min}}{\epsilon_{\max} - \epsilon_{\min}}, \quad (1)$$

where ϵ_i , ϵ_{\max} , and ϵ_{\min} are present, maximum, and minimum strain values during the sustaining process of pullout force

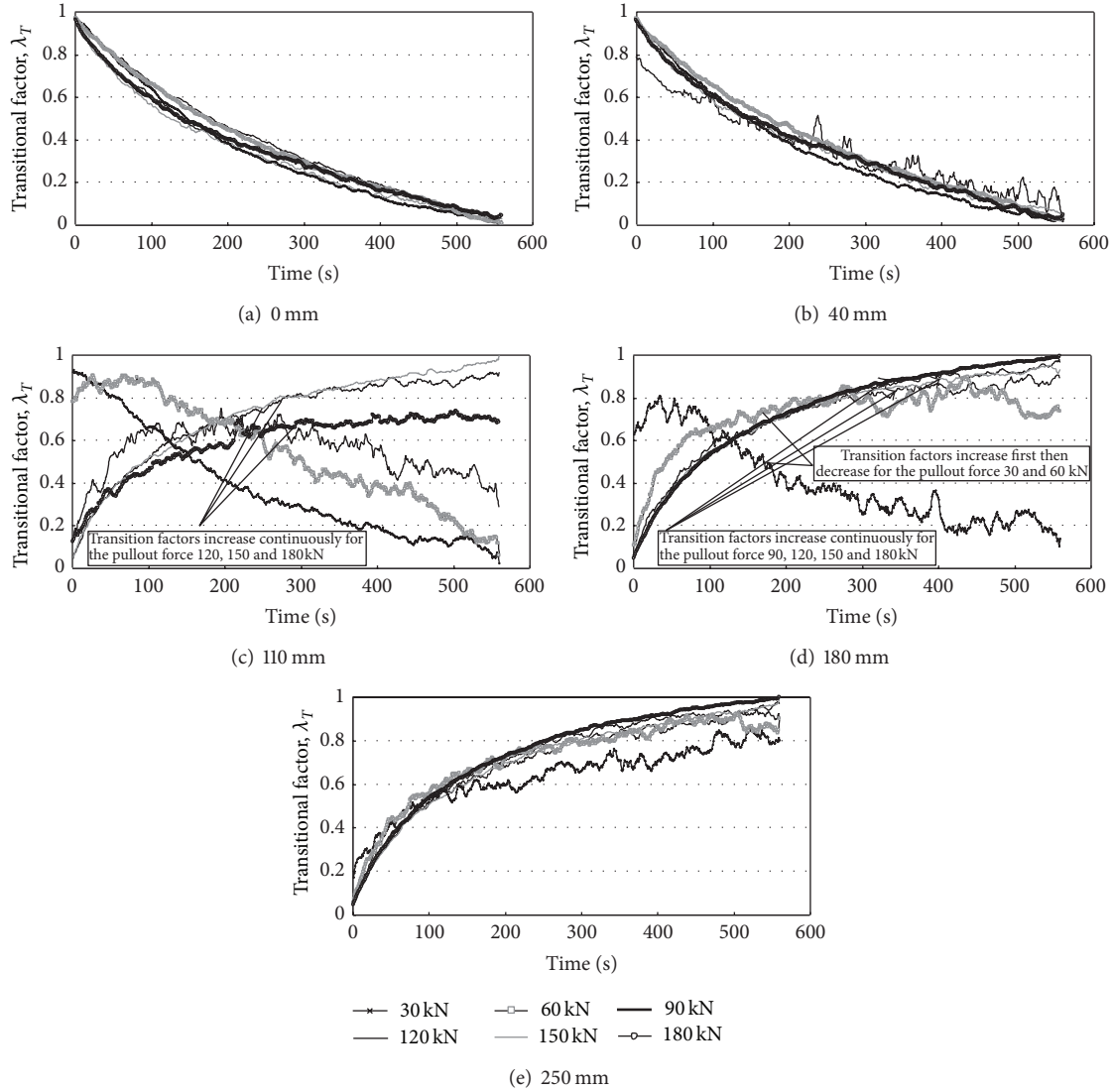


FIGURE 5: Relationships of transitional factor variations against time at different sensor distances from bar head, (a) 0 mm, (b) 40 mm, (c) 110 mm, (d) 180 mm, and (e) 250 mm.

at the GFRP bar head. As $(\epsilon_{\max} - \epsilon_{\min})$ is a constant value for a specified pullout process, and $(\epsilon_{\max} \geq \epsilon_i \geq \epsilon_{\min})$ always hold, so that $0 \leq \lambda_T \leq 1$. This proposed transitional factor λ_T is a normalized factor, providing a basic evaluation of stress transition behavior (stress release or concentration) at various loading processes. A continuous increase (decrease) of λ_T value indicates a continuous development (release) of tension strain. It is noted that the normalized transitional factor λ_T is time-dependent and may vary substantially as time elapses.

Figures 5(a)–5(e) summarize changes of all λ_T values at different GFRP bar locations (bar head, 40, 110, 180, and 250 mm to bar head) against time under different pullout force values. To clearly identify variation trends of this parameter, average values of λ_T are obtained in these figures (calculated by averaging every ten strain values). For the strain sensors at the GFRP bar head and 40 mm to the bar

head (0 mm and 40 mm as marked in Figures 5(a) and 5(b)), the λ_T values show continuous reductions. This indicates an immediate and consistent strain release effect occurred at both the two locations. In addition, the change of pullout force seems to have limited effect on the variation trends of λ_T values against time at bar head (Figures 5(a) and 5(b)). This may be interpreted as that, as a result of the pullout force at the bar head, the external load can be easily transferred into deeper locations close to GFRP bar head, leading to an substantial stress release effect immediately after the pullout load is maintained at the bar head.

In comparison with Figures 5(a) and 5(b), variation trends of transitional factors against time are totally different as shown in Figures 5(c), 5(d), and 5(e). A number of consistent increasing curves (e.g., at 120, 150 and 180 kN in Figure 5(c); at 90, 120, 150, and 180 kN in Figure 5(d)), or increasing trends followed by an immediate decreasing

trends (e.g., at 30, 60, and 90 kN in Figure 5(c), 30 and 60 kN in Figure 5(d)), and consistent increasing trends are found (e.g., at all loading levels in Figure 5(e)). These continuous increasing trends of λ_T values suggest that, though pullout force values no longer increase at the bar head, the related mobilized tension effect still exists at certain depth of the GFRP bar. This tension effect along GFRP bar is transitional and normally requires a time consuming process (though the required time of this process may be quite limited). Continuous increasing trends of transitional factor normally present at high pullout force values (120, 150, and 180 kN in Figure 5(c); 90, 120, 150, and 180 kN in Figure 5(d)). The calculated transitional factor λ_T becomes weaker and weaker and finally decreases with time at low pullout force values (30 kN and 60 kN in Figure 5(c) and 30 kN in Figure 5(d)). Main reason of this finding is that the high pullout force (e.g., 180 kN) leads to significant tension effect, and this tension effect is relatively strong and results in a corresponding highly transferring effect of strain/stress into deeper locations. All λ_T variation curves in Figure 5(e) show continuous and substantial rise at 250 mm from GFRP bar head, which is also the deepest location among all sensors. The pullout effect at this location is the weakest, but the transferring effect requires a long time to approach the maximum tension strain, so that the tension strain values remain increase.

To summarize, from all observations in Figures 4(a)–4(e) and Figures 5(a)–5(e), the interaction interface during pullout can be divided into three typical zones. Zone (a) is the location where tension deformation relaxes after the application of pullout force (corresponds to Figures 4(a)–4(c) and Figures 5(a) and 5(b)). This is mainly due to the stress release process at the GFRP bar head or stress redistribution along the GFRP bar. Zone (b) is the GFRP bar location where transition part (between the process of strain release and the mobilization of tension effect) presents and passes (Figures 4(d), 5(c), and 5(d)); that is, the occurred strain values increase first then decrease after the maximum tension strain is approached. Zone (c) is the location where the interface between concrete and GFRP bar is still subjected to tension effect. This is the case that the pullout effect at the GFRP bar head requires a process to transfer and achieve the bar tip (Figures 4(e) and 5(e)). All these three zones are time-dependent and can be transferred to each other after pullout force is sustained at the GFRP bar head.

As found from the previous section, the pullout deformation requires a process to approach the location close to the GFRP bar tip. The evaluation of this transitional process is critical for the understanding of the mechanical behavior of structures reinforced by GFRP composite materials. In the present study, a new factor, namely, normalized transitional time factor N_T , is defined to quantify the transitional behavior of the GFRP bar in concrete as follows:

$$N_T = \frac{T_{\max}}{\Delta T}, \quad (2)$$

where T_{\max} refers to the time interval required for a specified GFRP bar location to approach the maximum tension strain. ΔT is the total measurement time which may vary significantly for different measurement tests and depends on

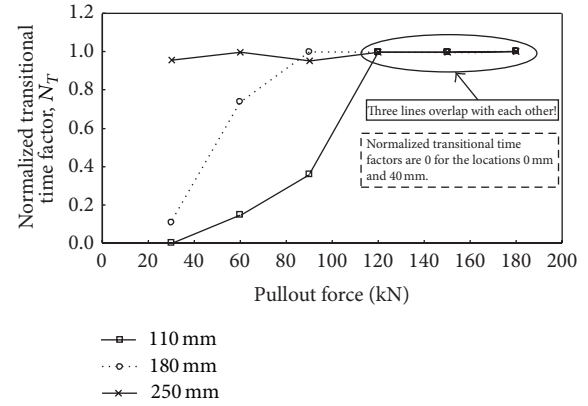


FIGURE 6: Relationships of normalized transitional time factor against pullout force at different locations of the GFRP bar.

the exact measurement time in different tests. For example, the measurement time for long-term and short-term tests varies significantly. In addition, this factor N_T can be extended for assessing the transitional behavior of different structures, for example, soil nails, anchor bars, and so forth. A high N_T value indicates a related long time required mobilizing the maximum tension strain, and this may be suitable for the case where long GFRP bars are used in concrete structures.

The calculated results of normalized transitional time factor are summarized against time in Figure 6. Only three typical cases are considered, that is, the locations of 110, 180, and 250 mm to the GFRP bar tip, and as for other two locations (0 and 40 mm), the related N_T values are all zero. That is, the maximum tension strain is approached immediately after pullout force is sustained at the GFRP bar head. It is clear from Figure 6 that N_T value increases from 0 at pullout force of 30 kN to almost 1.0 at the pullout force 120 kN and remains a constant value as pullout force further develops (from 120 to 180 kN). While for the sensor location 180 mm, N_T value increases initially as well but approaches a constant value at the pullout force of 90 kN, which is lower than that at the location of 110 mm. All N_T values almost approach a constant value at sensor location 250 mm, indicating that the maximum tension effect remains to develop during the whole testing process. The initial low N_T value indicates that the smaller the sensor distance to GFRP bar head, the lower the N_T value, as well as the slower the mobilization of the maximum tension strain particularly at high pullout force levels. The increase of pullout force or the reduction of the sensor distance to the GFRP bar head contributes to a high N_T value (or a relatively long time to mobilize the maximum tension strain).

6. Stress Redistribution of GFRP Bar Subjected to Pullout Force

Stress loss would occur after the application of pullout force. Two typical processes of stress loss may be involved, such as instantaneous loss and long-term time-dependent loss.

The instantaneous loss of stress may be due to elastic shortening and stress release of the reaction frame, and so forth, while the long-term time-dependent loss of stress may be a result of creep, shrinkage, and release problems associated with the interaction behavior between concrete and GFRP materials. In order to simulate the process of instant stress loss, only the strain data ten minutes after the sustaining process of pullout force at the GFRP bar head were selected in analysis. It is noted that the selection of ten minutes may not be long enough for assessing initial stress loss, but the present consideration is only an example, which may be a typical reference for practical consideration and also a comparison with more data to be collected in further tests. The stress loss coefficient μ is obtained by dividing the minimum axial stress/strain by the maximum axial stress/strain as follows:

$$\mu = \frac{\varepsilon_{\min}}{\varepsilon_{\max}}, \quad (3)$$

where ε_{\min} and ε_{\max} are minimum and maximum axial strain values that resulted from pullout force, respectively. It is noted that bending effect of GFRP bar in pullout test is ignored in this study.

Figure 7 shows relationships of average stress loss against pullout force at different GFRP bar locations. It is clear the proportion of stress loss decreases as the increase of pullout force, and all percentages of stress loss are extremely limited (lower than 4%). As the increase of pullout force, the mobilized axial force (or strain) increases as well, but the proportion of axial stress loss at high pullout force levels shows relatively minor reductions; that is, the pullout force increases much faster than the increasing rate of the corresponding stress loss, though the stress loss that occurred at low loading levels is not as significant as that at high loading levels. Variation trend of average percentage of stress loss shows a similar variation trend, with an average percentage loss of stress which reduces from 2.2% (bar head) to about 1.5% (bar tip). All percentages of stress loss are very limited in the short-term period after the pullout force is sustained.

7. Contribution of Pullout Resistance of Each GFRP Bar Section

The interface between GFRP bar and concrete contributes frictional resistance which is equal to the pullout force applied at the GFRP bar head. The investigation of the pullout resistance contribution from different GFRP bar sections is useful for understanding the interaction mechanism (particularly the transitional interaction behavior) between GFRP bar and concrete. In this study, the GFRP bar is divided into four sections by optical fiber strain sensors. Each bar section contributes certain frictional resistance. From obtained strain results, the corresponding axial force distribution along the GFRP bar can be determined using the following relationship:

$$p_i = AE\varepsilon_i, \quad (4)$$

where p_i is the axial force ($i = 1, 2, 3, 4$), A and E are the cross-sectional area and the GFRP bar modulus, and ε_i denotes

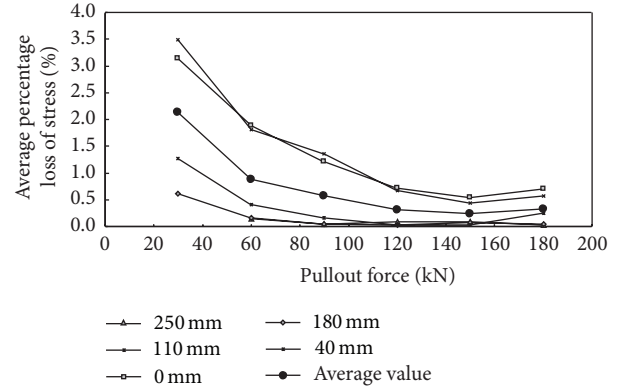


FIGURE 7: Relationships of percentage loss of prestress against pullout force at different sensor locations.

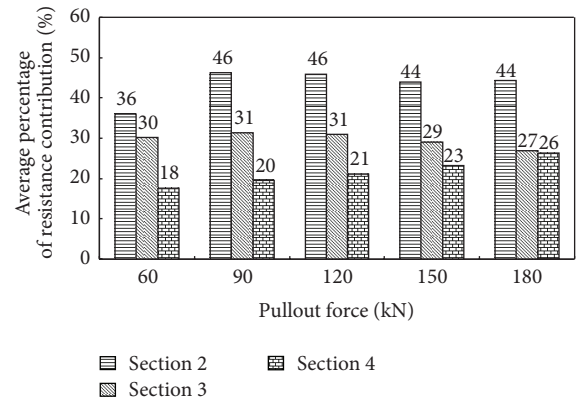


FIGURE 8: Average contribution of pullout resistance of different GFRP bar sections.

the measured strain. The axial force difference at the two ends of each bar section is also the frictional resistance and can be calculated as follows if the measured two point strain values ε_i and ε_{i-1} are known:

$$p_i - p_{i-1} = AE\varepsilon_i - AE\varepsilon_{i-1}. \quad (5)$$

The total (or applied) pullout force of the GFRP bar head is p_1 , which can be obtained using the strain ε_1 measured at the GFRP bar head, so that the contributed percentage of each GFRP bar section is written as follows:

$$\delta_i = \frac{p_i - p_{i-1}}{p_1 - p_4} = \frac{AE(\varepsilon_i - \varepsilon_{i-1})}{AE(\varepsilon_1 - \varepsilon_4)} = \frac{\varepsilon_i - \varepsilon_{i-1}}{\varepsilon_1 - \varepsilon_4}, \quad (6)$$

where δ_i is the contributed proportion of pullout resistance of each GFRP bar section i ($i = 1, 2, 3, 4$). p_4 is the calculated axial force (50 mm) close to the GFRP bar tip. Equation (6) indicates that the contributed percentage of all GFRP bar sections can be examined using all strain sensor readings.

The contribution of frictional resistance from different GFRP bar sections is calculated and summarized in Figure 8, where the average percentage of frictional resistance contributions of different sections (Section 2 to Section 4 from GFRP bar head to tip divided by four FBG sensors inside

concrete) is obtained by using (6). Section 2 is the bar part close to the loading position. At relatively low loading levels, for example, 60 kN, the contributed percentage of frictional resistance of Section 2 (closest to the GFRP bar head) is 36%, which is higher than that of Section 3 (30%) and Section 4 (18%). Because of the increase of the pullout load, the contributed proportion of frictional resistance of Section 2 is around 44%, while the contributions of the last two sections (Sections 3 and 4) become closer and closer. The contributed percentage of frictional resistance changes from 30% for Section 3 and 18% for Section 4 at the load of 60 kN to 27% for Section 3 and 26% for Section 4 at the load of 180 kN. This is also a result of the load transferring effect from GFRP bar head to the bar tip.

8. Conclusions

A typical study regarding the creep analysis of GFRP bar embedded in concrete is presented with the focus on the GFRP bar behavior after the pullout force is sustained at a specific level. Based on a comprehensive and quantified analysis, transitional stress transfer state at the interface between GFRP bar and concrete and stress contributions of different GFRP bar sections are presented and analyzed to better understand the interaction characteristics of GFRP bar. Conclusions and typical findings are summarized as follows.

- (1) The measured strain values after the pullout force is sustained at a specific level show continuous increase, or increase first then decrease, or decrease continuously as time elapses. The interface between concrete and GFRP bar may be divided into three typical zones characterized by the above different strain variation trends, including the stress release part, the stress transferring part, and the part subjected to continuous tension effect.
- (2) A normalized transitional factor λ_T is proposed to identify the strain/stress development state of the GFRP bar. The three typical variation trends of λ_T value, continuous rise or reduction, or rise first followed by typical reduction indicate three corresponding stress transferring states, that is, a continuous development of tension deformation, a continuous release of tension stress, and a presence of stress transitional zone.
- (3) The proportion of stress loss decreases as the increase of pullout force, and all percentages of stress loss are extremely limited (lower than 4%). As the mobilized axial force (or strain) increases, the proportion of axial stress loss at high pullout force levels shows relative reductions. All percentages of stress loss are very limited in the short-term period after the pullout force is sustained at a constant level.
- (4) Contributed percentage of frictional resistance of GFRP bar decreases from bar head to bar tip at constant pullout load. As the pullout load becomes higher and higher, the contribution proportions of frictional resistance for the two bar sections in the deeper

locations become closer and closer. This is due to the load transferring effect along the GFRP bar.

Acknowledgments

The authors wish to thank the financial supports from the government of Guangdong Province and Ministry of education of China (Project no. 2009B09060011), STU Scientific Research Foundation for Talents (SRFT) (Project no. NTF12015), and State Key Laboratory of Earthquake Dynamics Institute of Geology, China Earthquake Administration (Project, no. LED2013B01). This work is also supported by the Macau Science and Technology Development Fund (Grant no. FDCT/011/2013/A1) and the University of Macau Research Fund (Grant nos. MYRG189(Y2-L3)-FST11-ZWH and MYRG067(Y2-L2)-FST12-ZWH). The help and support from the technical staff of the Rock and Soil Mechanics Laboratory in the College of Civil and Transportation Engineering of Hohai University are also acknowledged.

References

- [1] L. Chu and J. Yin, "Comparison of interface shear strength of soil nails measured by both direct shear box tests and pullout tests," *Journal of Geotechnical and Geoenvironmental Engineering*, vol. 131, no. 9, pp. 1097–1107, 2005.
- [2] C. Hong, J. Yin, W. Jin, C. Wang, W. Zhou, and H. Zhu, "Comparative study on the elongation measurement of a soil nail using optical lower coherence interferometry method and FBG method," *Advances in Structural Engineering*, vol. 13, no. 2, pp. 309–319, 2010.
- [3] W. Zhou, J. Yin, and C. Hong, "Finite element modelling of pullout testing on a soil nail in a pullout box under different overburden and grouting pressures," *Canadian Geotechnical Journal*, vol. 48, no. 4, pp. 557–567, 2011.
- [4] N. Gurung, "A theoretical model for anchored geosynthetics in pull-out tests," *Geosynthetics International*, vol. 7, no. 3, pp. 269–284, 2000.
- [5] K. C. Yeo and S. K. Leung, "Soil nail design with respect to Hong Kong conditions," *Landmarks in Earth Reinforcement*, vol. 1, pp. 759–764, 2001.
- [6] H. F. Pei, J. H. Yin, H. H. Zhu, and C. Y. Hong, "Performance monitoring of a glass fiber-reinforced polymer bar soil nail during laboratory pullout test using fbg sensing technology," *International Journal of Geomechanics*, vol. 13, no. 4, pp. 467–472, 2013.
- [7] M. F. Sá, A. M. Gomes, J. R. Correia, and N. Silvestre, "Creep behavior of pultruded GFRP elements, part 2: analytical study," *Composite Structures*, vol. 93, no. 9, pp. 2409–2418, 2011.
- [8] W. H. Soong, J. Raghavan, and S. H. Rizkalla, "Fundamental mechanisms of bonding of glass fiber reinforced polymer reinforcement to concrete," *Construction and Building Materials*, vol. 25, no. 6, pp. 2813–2821, 2011.
- [9] L. Vasseur, S. Matthys, and L. Taerwe, "An analytical study on the bond behaviour between an externally bonded FRP and concrete in the case of continuous beams," *Mechanics of Composite Materials*, vol. 44, no. 3, pp. 269–278, 2008.
- [10] M. Esfandeh, A. R. Sabet, A. M. Rezadoust, and M. B. Alavi, "Bond performance of FRP rebars with various surface deformations in reinforced concrete," *Polymer Composites*, vol. 30, no. 5, pp. 576–582, 2009.

- [11] H. Ko and Y. Sato, "Bond stress-slip relationship between FRP sheet and concrete under cyclic load," *Journal of Composites for Construction*, vol. 11, no. 4, pp. 419–426, 2007.
- [12] H. Toutanji, P. Saxena, L. Zhao, and T. Ooi, "Prediction of interfacial bond failure of FRP-concrete surface," *Journal of Composites for Construction*, vol. 11, no. 4, pp. 427–436, 2007.
- [13] J.-F. Berthet, E. Ferrier, P. Hamelin, G. Al Chami, M. Thériault, and K. W. Neale, "Modelling of the creep behavior of FRP-confined short concrete columns under compressive loading," *Materials and Structures/Materiaux et Constructions*, vol. 39, no. 285, pp. 53–62, 2006.
- [14] Y. Q. Ni, X. W. Ye, and J. M. Ko, "Monitoring-based fatigue reliability assessment of steel bridges: analytical model and application," *Journal of Structural Engineering*, vol. 136, no. 12, pp. 1563–1573, 2010.
- [15] Y. Q. Ni, X. W. Ye, and J. M. Ko, "Modeling of stress spectrum using long-term monitoring data and finite mixture distributions," *Journal of Engineering Mechanics*, vol. 138, no. 2, pp. 175–183, 2011.
- [16] C. Hong, J. Yin, W. Zhou, and H. Pei, "Analytical study on progressive pullout behavior of a soil nail," *Journal of Geotechnical and Geoenvironmental Engineering*, vol. 138, no. 4, pp. 500–507, 2012.
- [17] W. H. Zhou and J. H. Yin, "A simple mathematical model for soil nail and soil interaction analysis," *Computers and Geotechnics*, vol. 35, no. 3, pp. 479–488, 2008.
- [18] M. F. Sá, A. M. Gomes, J. R. Correia, and N. Silvestre, "Creep behavior of pultruded GFRP elements, part I: literature review and experimental study," *Composite Structures*, vol. 93, no. 10, pp. 2450–2459, 2011.
- [19] E. Ferrier, L. Michel, B. Jurkiewicz, and P. Hamelin, "Creep behavior of adhesives used for external FRP strengthening of RC structures," *Construction and Building Materials*, vol. 25, no. 2, pp. 461–467, 2011.
- [20] R. Seracino, N. M. Jones, M. S. M. Ali, M. W. Page, and D. J. Oehlers, "Bond strength of near-surface mounted FRP strip-to-concrete joints," *Journal of Composites for Construction*, vol. 11, no. 4, pp. 401–409, 2007.
- [21] D. J. Zhang, Y. F. Wang, and Y. S. Ma, "Compressive behaviour of FRP-confined square concrete columns after creep," *Engineering Structures*, vol. 32, no. 8, pp. 1957–1963, 2010.
- [22] Y. Wang and D. Zhang, "Creep-effect on mechanical behavior of concrete confined by FRP under axial compression," *Journal of Engineering Mechanics*, vol. 135, no. 11, pp. 1315–1322, 2009.
- [23] C. M. L. Tavares, M. C. S. Ribeiro, A. J. M. Ferreira, and R. M. Guedes, "Creep behaviour of FRP-reinforced polymer concrete," *Composite Structures*, vol. 57, no. 1–4, pp. 47–51, 2002.
- [24] J. Dai, H. Yokota, M. Iwanami, and E. Kato, "Experimental investigation of the influence of moisture on the bond behavior of FRP to concrete interfaces," *Journal of Composites for Construction*, vol. 14, no. 6, pp. 834–844, 2010.

Research Article

Condition Assessment on Thermal Effects of a Suspension Bridge Based on SHM Oriented Model and Data

Bo Chen,¹ Zhi-wei Chen,² Yu-zhou Sun,³ and Sheng-lin Zhao¹

¹ Key Laboratory of Roadway Bridge and Structural Engineering, Wuhan University of Technology, Wuhan 430070, China

² School of Architecture and Civil Engineering, Xiamen University, Xiamen 361005, China

³ School of Civil Engineering and Architecture, Zhongyuan University of Technology, Zhengzhou 450007, China

Correspondence should be addressed to Bo Chen; cbsteven@163.com

Received 9 October 2013; Accepted 6 November 2013

Academic Editor: Ting-Hua Yi

Copyright © 2013 Bo Chen et al. This is an open access article distributed under the Creative Commons Attribution License, which permits unrestricted use, distribution, and reproduction in any medium, provided the original work is properly cited.

This paper aims to carry out the condition assessment on temperature distribution and thermal effects of a long span suspension bridge. The structural health monitoring (SHM) oriented data analysis is first performed and several indices are developed to process the time-varying temperature, displacement, and strain responses. An analytical procedure based on heat transfer theory is presented to determine the temperature distributions within the bridge. The fine finite element models of the deck plate, the cross frame, and the bridge tower are constructed for thermal analysis. A new approach to the thermal-structural coupling analysis of long span bridges is proposed to examine the structural thermal effects. The feasibility and validity of the proposed data process method and the new approach for thermal-structural coupling analysis are examined through detailed numerical simulation. The numerical results are compared with the field measurement data obtained from the long-term monitoring system of the bridge and they show a very good agreement, in terms of temperature distribution in different time and in different seasons. This exercise verifies the accuracy of the heat transfer analysis employed and the effectiveness and validity of the proposed approaches for data processing and thermal-structural coupling analysis.

1. Introduction

Long span bridges are subjected to thermal effects due to the interaction with the environmental conditions. The interaction with air temperature and solar radiation leads to seasonal and daily temperature changes in the bridges. Temperature variations in bridges may induce the structural movement and thermal stresses due to the indeterminacy, which may cause the damage events of the structural components, even the entire bridge [1–3]. Thermal effects on long span bridges have been investigated across the world to simulate the temperature distribution of bridges and predict the structural responses by establishing one-dimensional to three-dimensional finite element (FE) models. Zuk [4] investigated the thermal behaviour of several highway bridges and found that the temperature distribution was affected by many factors such as air temperature, wind, humidity, intensity of solar radiation, and material type. Capps [5] measured temperature and longitudinal movements of a steel box bridge in

the UK. Churchward and Sokal [6] instrumented a section of prestressed concrete bridge for recording temperature profiles at different instants of time. The structural temperature distribution and thermal variations have also been examined based on computer models with the aid of FE model since 1970s [7]. The effects of solar radiation, convection, heat of hydration, member size, and geometry have been taken into consideration. Elbadry and Ghali [8] examined the temperature distribution and estimated stresses of a concrete bridge by developing a two-dimensional FE model. Branco and Mendes [9] proposed an approach to define temperature design values for concrete bridges. Based on a numerical technique, the results of a parametric study were developed for the evaluation of design values for temperature differences in small and medium span bridges located in Portugal.

The field measurement and monitoring of temperature distribution and thermal effects of bridges have been widely carried out in recent years due to the rapid development and application of structural health monitoring (SHM)

technology. Shahawy and Arockiasamy [10] compared the measured time-dependent strains of the Sunshine Skyway Bridge with the analytical predictions. Roberts-Wollman et al. [11] compared the calculated and measured deflections of a box girder bridge. Fu and DeWolf [12] carried out field measurement and numerical simulation on a curved concrete bridge concerning the temperature effects on the tilt and natural frequencies. Desjardins et al. [13] studied modal data and average girder temperature collected over a six-month period in the Confederation Bridge. Tong et al. [14, 15] and Au et al. [16] carried out similar investigations for both composite bridges and steel bridges. They also carried out a laboratory study and a field study on the Tsing Ma Bridge to verify the heat conduction models. Wong et al. [17, 18] introduced a 3-year thermal monitoring and response monitoring of the Ting Kau Bridge. Xu et al. [19] investigated the temperature-induced displacement responses of Tsing Ma Bridge based on field monitoring data from 1997 to 2005.

The configurations and performance of long span bridges such as suspension bridges are quite different from those of common concrete bridges. For long span bridges, the current research focuses on field monitoring of the temperature and bridge displacement only. There have been few studies on the evaluation of thermal effects of long span bridges based on SHM oriented bridge model. The feature extraction and data mining on the thermal monitoring information of bridges are very rare. Consequently, the SHM oriented feature extraction and condition assessment on the thermal effects of long span bridges are very limited [20].

To this end, the condition assessment on temperature distribution and thermal effects of a long span suspension bridge are carried out by taking the Tsing Ma Suspension Bridge as an example structure. The SHM oriented data analysis is first performed by proposing a data processing technique based on empirical mode decomposition (EMD). Several indices are developed to process the time-varying temperature, displacement, and strain responses collected by SHM system. An analytical procedure based on heat transfer theory is presented to determine the temperature distributions within the bridge. Several FE models are constructed for deck plates and bridge sections to compute the temperature distribution, which are used to calculate the bridge thermal displacement and thermal stress. A new approach for the thermal-structural coupling analysis of long span bridges is proposed to examine the structural thermal effects. The feasibility and validity of the proposed data process approach and the new approach for thermal-structural coupling analysis are examined through detailed simulation. The made observation indicates that the simulated temperature distribution and effects of the bridge are in good agreement with those from field measurement.

2. Bridge Configuration and Health Monitoring System

2.1. Bridge Configuration. Located at latitude N22.2° and longitude E114.1°, Tsing Ma Suspension Bridge has a total span of 2132 m and carries a dual three-lane highway on the

upper level of the bridge deck and two railway tracks and two protected carriageways at the lowest level within the bridge deck. The main span across the Tsing Yi island and the Ma Wan island has 1377 m long, as shown in Figure 1. The angle between the bridge longitudinal axis and the south is 73°. The height of the two reinforced concrete bridge towers, the Tsing Yi tower and the Ma Wan tower, is about 206 m, measured from the base level to the tower saddle. The two main cables of 36 m apart in the north and south are accommodated by the four saddles located at the top of the tower legs. The diameter of the main cables is 1.0 m. The lengths of the Tsing Yi side span and the Ma Wan side span are 300 m and 455 m, respectively. The structural translational movements at the Ma Wan abutment are restrained in three translational directions. At the Tsing Yi abutment, the vertical (z -axis) and lateral (y -axis) movements of the bridge deck are restrained while the deck can move freely along the longitudinal direction (x -axis).

The bridge deck at the main span is a suspended deck type. Figure 2 illustrates the configuration of an 18 m long typical suspended deck module, which includes a main cross frame and four neighbouring intermediate cross frames. The five cross frames of 4.5 m apart from each other are connected by two outer longitudinal trusses. Two symmetrical bays of top orthotropic deck plates are connected to the top chords of the cross frames, and the decks are constructed with a row of the central cross bracing. Regarding the bottom deck, there are two railway tracks laid on the central bay of the deck in addition to two bays of orthotropic deck plates on the two outer sides that are all supported on the bottom chords of the cross frames. There are two rows of outer cross bracings added to brace the bottom chords of the cross frames and separate the orthotropic deck plate and railway track. Another kind of bracing, namely, sway bracing, is used to brace the main cross frame from the two adjacent intermediate cross frames.

2.2. Health Monitoring System. A wind and structural health monitoring system (WASHMS) for the Tsing Ma Bridge has been devised, installed, and operated by the HighWays Department of the Government of Hong Kong Special Administrative Region (HKSAR) since 1997. The WASHMS is composed of five subsystems, namely, sensory system, data acquisition system, data processing and analysis system, computer for system operation and control, and fiber optic cabling network system [17]. About 280 sensors, including anemometers, temperature sensors, accelerometers, strain gauges, level sensing stations, displacement transducers, weigh-in-motion stations, and GPS receivers, were installed at different locations on the bridge for collecting various types of structural and environmental information.

The position of the temperature sensors on the Tsing Ma Bridge is shown in Figure 1. The collected temperature data from WASHMS can be grouped into three categories: (1) ambient temperature (T_1 and T_2); (2) section temperature (T_3 and T_4); and (3) cable temperature (T_5 , T_6 , and T_7). One air temperature sensor (Ch. 81, T_1) is approximately at the middle section of the main span and attached to a sign gantry which stands on the upper deck. The other five

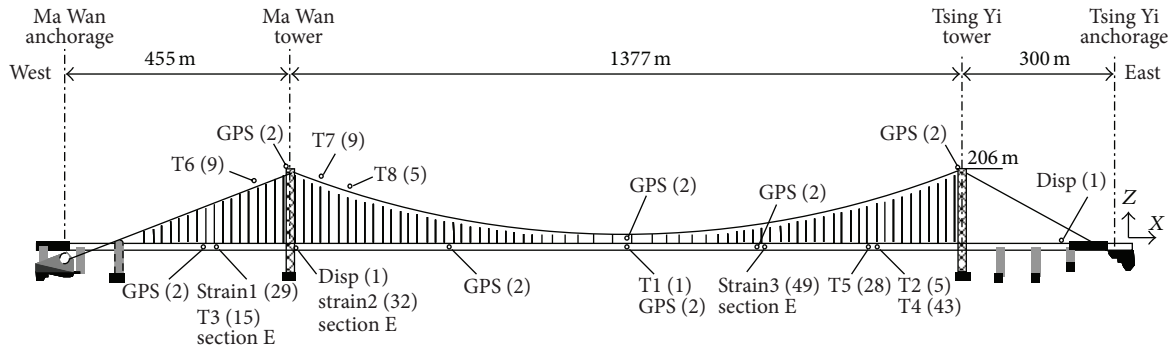


FIGURE 1: Configuration and sensor layout of the Tsing Ma Suspension Bridge.

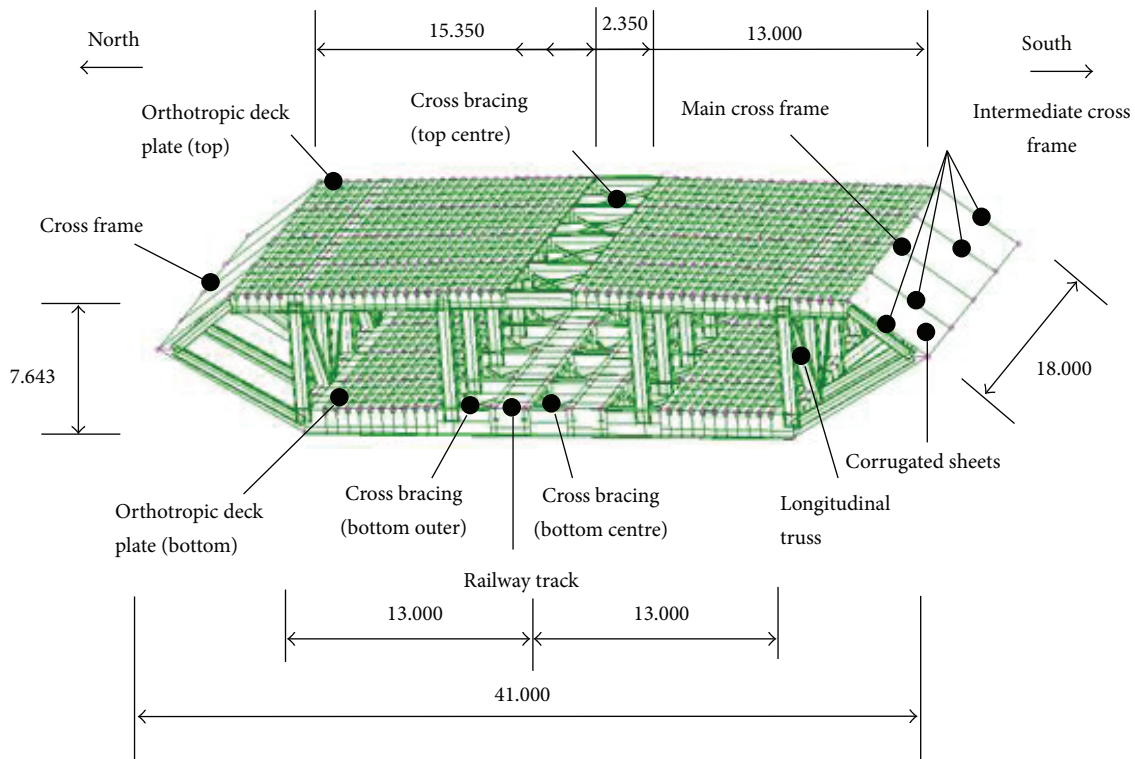


FIGURE 2: Configuration of a suspended deck module (unit: m).

air temperature sensors (Ch. 82 to Ch. 86, T_2) measure the ambient temperature inside the bridge deck section of the main span near the Tsing Yi tower. 23 thermocouples (T_5 , T_6 , and T_7) were embedded inside the main cables at three different locations to measure the cable temperature.

The deck section in the Ma Wan side span is equipped with 15 sensors (T_3) and another deck section close to the Tsing Yi tower is equipped with 71 sensors (T_4). Figure 3 illustrates seven groups of temperature sensors (details 10 to 16, 28 sensors in total) mounted on the orthotropic deck plates 2.25 m away from the section. At each detail, one sensor measures the temperature of steel plate and the other three sensors measure the temperature distribution over the deck trough. In addition, there are four temperature sensors mounted on diagonal bracing members between adjacent

cross frames and two temperature sensors installed on the corrugated sheets on south side of the bridge section, which are not shown here for brevity. The sampling frequency of all of the temperature sensors is 0.07 Hz.

The displacements of the bridge in the three orthogonal directions: (1) longitudinal (x -direction); (2) lateral (y -direction); and (3) vertical (z -direction), are recorded by using displacement transducers and GPS stations. As shown in Figure 1, one displacement transducer is installed in the north side of a bearing frame which sits on the lowest portal beam of the Ma Wan tower with bearing connection. The longitudinal movement of the bridge deck at the Tsing Yi abutment is recorded by another displacement transducer, which is underneath the expansion joint bearing and attached between the Tsing Yi abutment and the bottom chord of

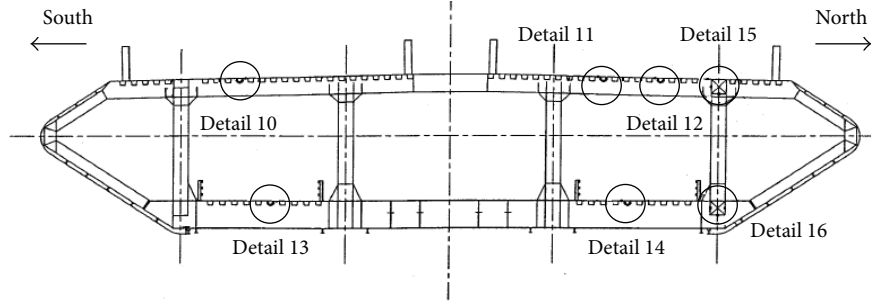


FIGURE 3: Position of temperature sensors on the deck plate (T_4).

a cross frame next to the abutment to measure the displacement of the deck section. The components of the bridge implemented with the GPS receivers include bridge towers, main cables, and bridge deck. Two base reference stations sit at a storage building adjacent to the bridge monitoring room. The Ma Wan tower and Tsing Yi tower are, respectively, installed with a pair of GPS receivers, and they are mounted at the top of saddles on each of the tower legs. The displacement of the main cables is monitored through a pair of GPS receivers at the midspan. The midspan of the Ma Wan side span is equipped with a pair of receivers. Three pairs of GPS receivers are located at one quarter, one half, and three quarters of the main span of the bridge deck. It is seen from Figure 1 that 110 strain gauges have been installed at three deck sections of the Tsing Ma Bridge. Taking Section E as an example, 32 strain gauges were installed at the longitudinal truss near the Ma Wan tower. The outer and inner trusses were equipped with four pairs of gauges (denoted as SP) and two single gauges (denoted as SS).

3. SHM Oriented Data Analysis

3.1. Signal Processing Based on EMD. The response signals can be processed by using empirical mode decomposition (EMD) [21]. As a new signal processing method, the EMD can decompose any data set into several intrinsic mode functions (IMFs) by a procedure called sifting process. Suppose $x(t)$ is a time history to be decomposed. The sifting process is conducted by first constructing the upper and lower envelopes of $x(t)$ by connecting its local maxima and local minima through a cubic spline. Designate the mean value of the two envelopes as $m_1(t)$ and compute the difference between the original time history and the mean value

$$h_1(t) = x(t) - m_1(t). \quad (1)$$

The component $h_1(t)$ is then examined to see if it satisfies the requirements to be an IMF. If not, the sifting process is to be repeated by treating $h_1(t)$ as a new time history until $h_1(t)$ is an IMF, designated as $c_1(t)$. Then, the first IMF is separated from the original time history, giving a residue $r_1(t)$ as

$$r_1(t) = x(t) - c_1(t). \quad (2)$$

The sifting process is applied successively to each subsequent residue to obtain the subsequent IMFs until either the residue

$r_n(t)$ is smaller than a predetermined value or it becomes a monotonic function. The original time history is finally expressed as the sum of the IMF components plus the final residue

$$x(t) = \sum_{j=1}^n c_j(t) + r_n(t), \quad (3)$$

where $c_j(t)$ is the j th IMF component; n is the total number of IMF components; and $r_n(t)$ is the final residue. After the decomposition, the first IMF component obtained has the highest frequency content of the original time history while the final residue represents the component of the lowest frequency in the time history.

3.2. Feature Extraction and Analysis on Strain Data. Figure 4 illustrates the position of six strain gauges (four SP types and two SS types) at the north inner truss. Displaced in Figure 5 are the time histories of axial strain between 12:00 AM to 13:00 PM for strain gauge SPTEN04. It is seen that there exist several spikes with large amplitude which are induced by running trains. The measured time histories may include the effects of vehicles. In addition, it can be seen that the time histories at other time durations are quite similar to that at the noon. Thus, this signal $x^s(t)$ is decomposed by using EMD and 13 IMFs can be obtained as shown in Figure 6

$$x^s(t) = \sum_{j=1}^{ns} c_j^s(t) + r_{ns}^s(t), \quad (4)$$

where $c_j^s(t)$ is the j th IMF component of the strain response; ns is the total number of IMF components of strain response; and $r_{ns}^s(t)$ is the final residue.

The signal is decomposed with EMD without using intermittency check and thereby the cut-off frequency is not required in the sifting process. It is known from the principles of the EMD that the IMF with the highest frequency components will be extracted first from the original signal and the IMF with the lowest frequency components is extracted finally. Figure 6 displays the time histories of IMFs and residue, and the Fourier spectrum of each component is displayed in Figure 7. The statistical values of all the IMFs and residue are listed in Table 1. It can be found from Figure 6 that the magnitude of the first four IMFs is quite small in

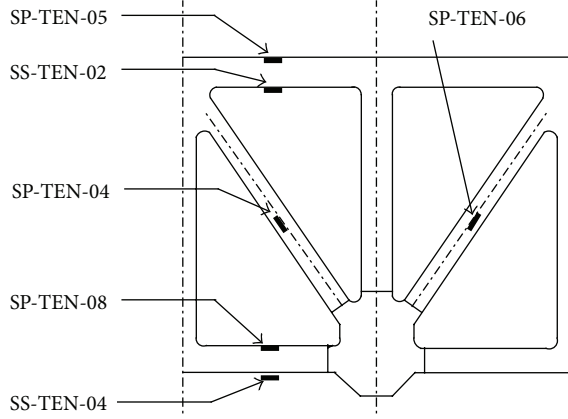


FIGURE 4: Strain gauges at north inner longitudinal truss.

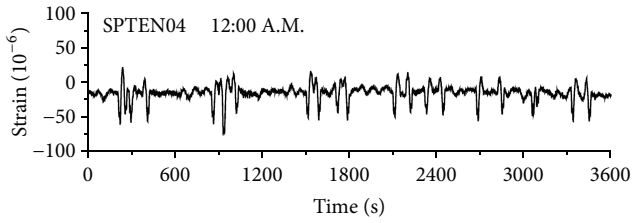


FIGURE 5: Time histories of axial strain between 12:00 AM and 13:00 PM.

comparison with that of the other IMFs. Similar observations can be made from the spectrum amplitude of the first four IMFs as shown in Figure 7. In addition, it is seen that the frequency range of the first four IMFs is much wider than that of other signal components. The data in Table 1 indicate that the mean values of the first four IMFs are close to zero and their amplitudes are very small. Therefore, it is clear that the first four IMFs are the noise components in the original strain time histories.

The middle eight IMFs (IMF5 to IMF12) have very small mean value while their time histories exist obvious signal fluctuation. Many spikes with large amplitudes can also be observed in the time histories of these IMFs as shown in Figure 6. Because the varying ambient temperature in the Tsing Ma Bridge in an hour is small, therefore the thermal-induced structural responses may change very slowly and the corresponding responses mainly include low frequency components. Therefore, the middle eight IMFs are the signal components induced by traffics and other dynamic excitations such as wind. The Fourier spectrum of the eight IMFs displayed in Figure 7 demonstrates that the dynamic loading dominates the frequency range of 0.001~0.08 Hz. The frequency component higher than 0.08 Hz can be regarded as noise, and the low frequency component with little variation is regarded as the static displacement because of the dead load. The sum of last IMF and residue can be taken as the effects of gravity and thermal loading. Because the gravity loading of the bridge is not changed commonly, the hourly variation of thermal effects can be computed. Therefore, the strain responses of the bridge can

TABLE 1: Statistical values of IMFs and residue.

Number	Mean	Maximum absolute value	Standard deviation
IMF 1	$-7.5424E-4$	1.31275	0.24134
IMF 2	$-7.09953E-5$	1.73038	0.20125
IMF 3	$1.90728E-4$	1.17978	0.19486
IMF 4	$-3.32764E-4$	0.90878	0.15156
IMF 5	-0.01426	9.93309	0.68445
IMF 6	-0.02884	8.74782	1.78688
IMF 7	0.11534	30.5291	5.68814
IMF 8	-0.08829	36.2402	6.90871
IMF 9	0.36278	17.0608	4.76462
IMF 10	0.06263	7.10906	2.6422
IMF 11	-0.04511	2.57784	1.3094
IMF 12	-0.12939	1.29054	0.77235
IMF 13	-0.21269	1.95364	1.31424
Residue	-16.0510	16.0519	0

be decomposed firstly to reconstruct the noise component $x_{\text{noise}}^s(t)$, dynamic component $x_{\text{dyn}}^s(t)$, and static component $x_{\text{static}}^s(t)$, respectively, with the aid of spectrum analysis

$$x_{\text{noise}}^s(t) = \sum_{j=1}^{ms} c_j^s(t),$$

$$x_{\text{dyn}}^s(t) = \sum_{j=ms+1}^{ms-1} c_j^s(t), \quad (5)$$

$$x_{\text{static}}^s(t) = c_{ms}^s(t) + r_{ns}^s(t),$$

where ms is the total number of noise IMF components. If the absolute mean value of a particular IMF is quite small, this IMF can be regarded as noise component

$$\text{abs}(\text{mean}(c_j^s(t))) < \varepsilon_{ms}, \quad (6)$$

where $\text{abs}()$ means to take the absolute value; ε_{ms} is the threshold value of absolute mean value of a particular IMF component and can be set as 1×10^{-3} for the strain responses of the example bridge (see Table 1).

Figures 8(a) and 8(b) display the strain responses induced by dynamic excitations $x_{\text{dyn}}^s(t)$ and static loading $x_{\text{static}}^s(t)$, respectively. It is also observed that some measurement data are associated with zero standard deviation. A zero standard deviation physically indicates that a steady value of measurement without any signal fluctuation is recorded within the statistical period considered. As a result, the statistical values of mean, maximum, and minimum having the same magnitude are correspondingly noted in this case. Having a perfectly flat signal is considered as an abnormal measurement. Correspondingly, the index to eliminate the abnormal data is set in terms of the zero standard deviation of any IMF component and is given by

$$\text{std}(c_j^s(t)) = 0. \quad (7)$$

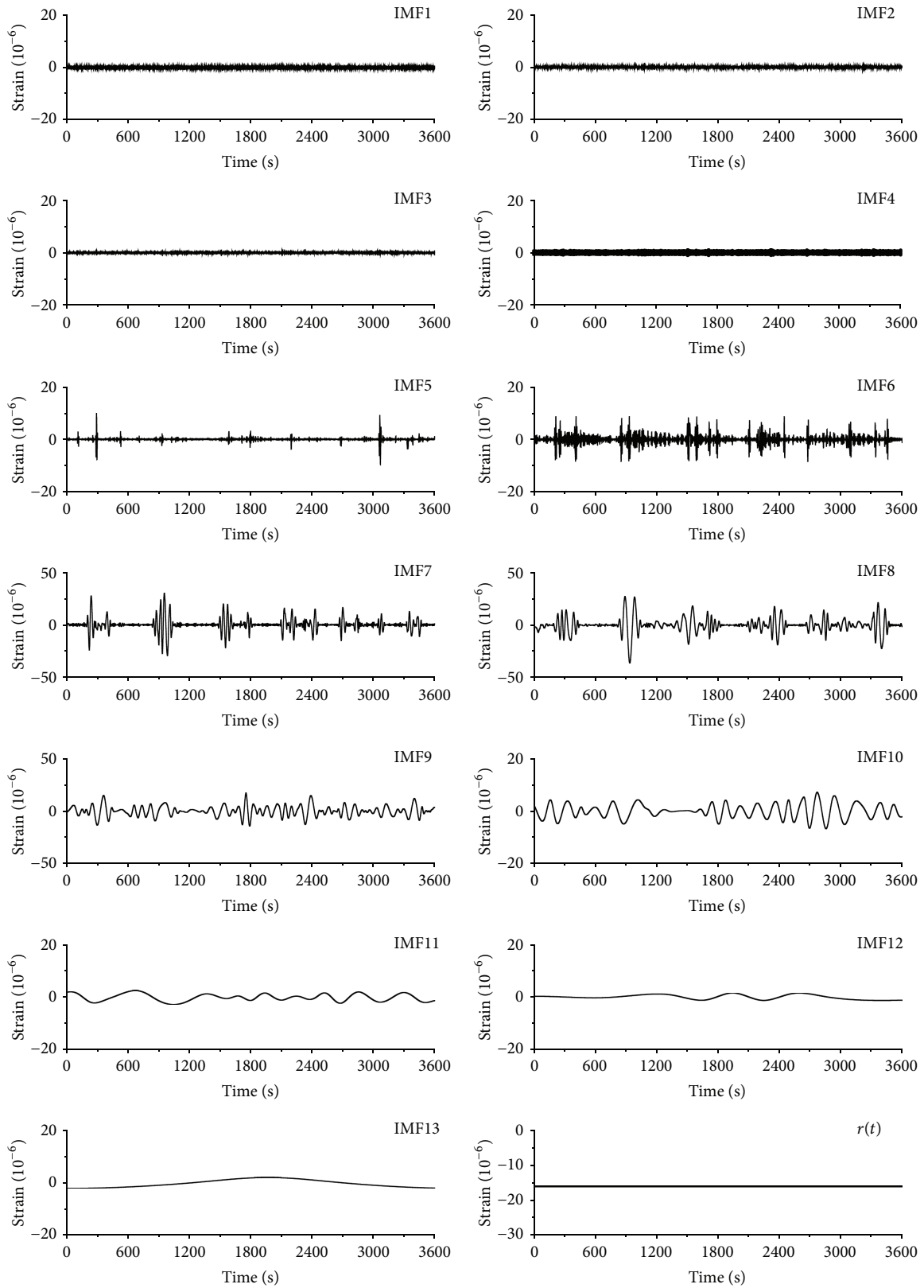


FIGURE 6: Time histories of IMFs and residue.

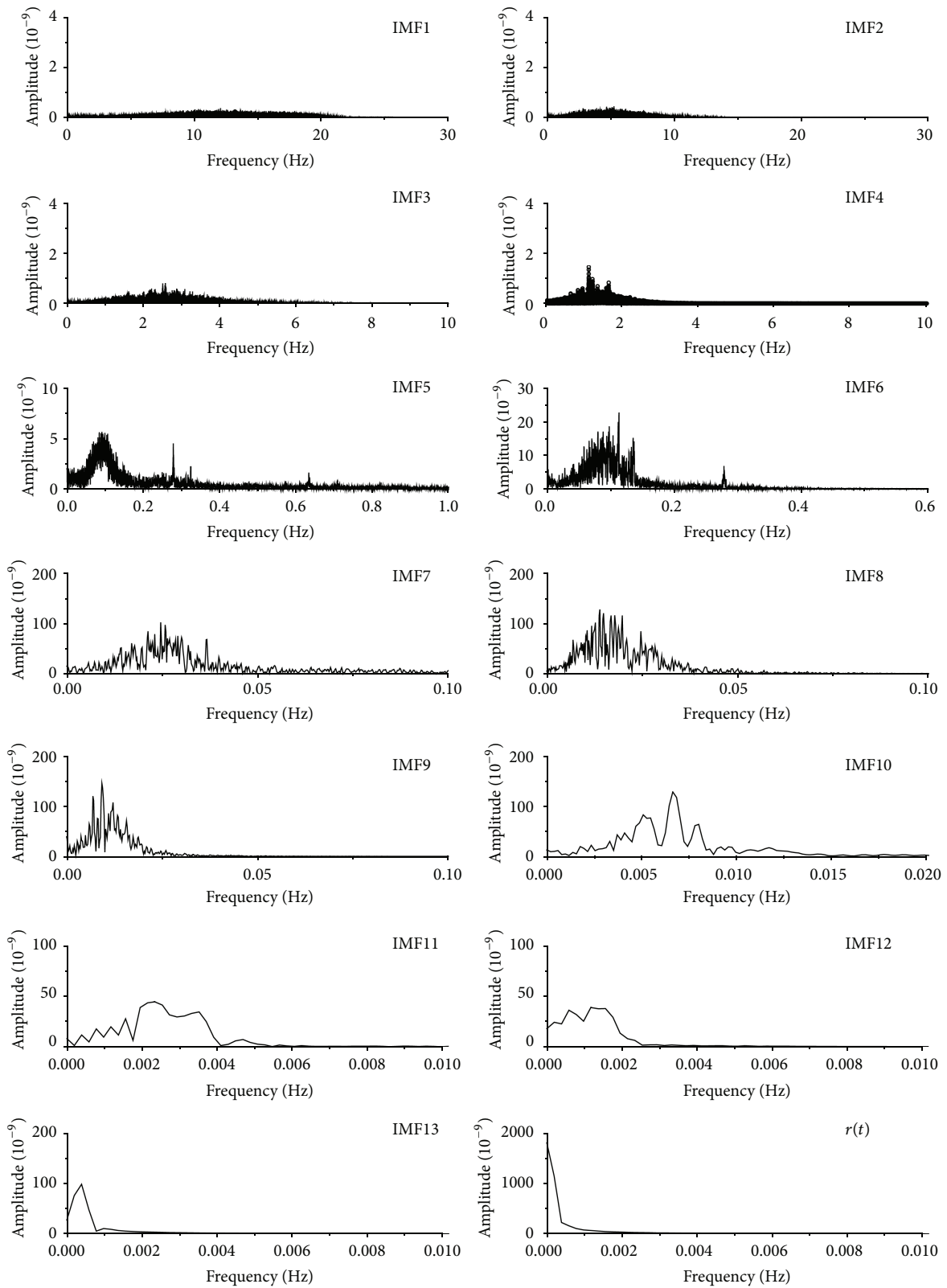


FIGURE 7: Fourier spectrum of IMFs.

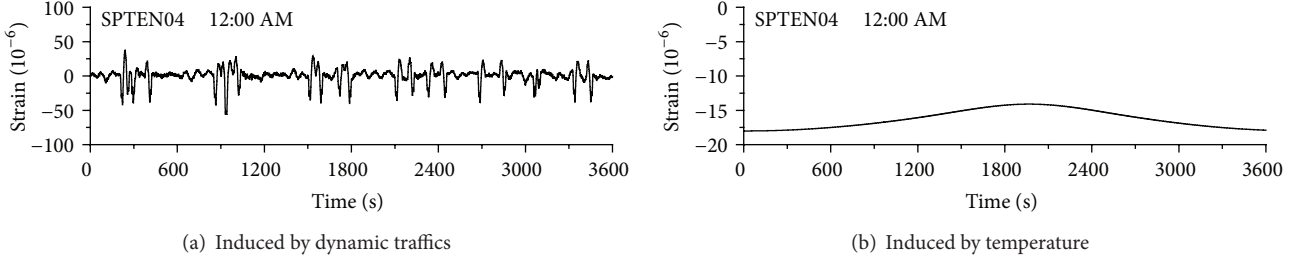


FIGURE 8: Time histories of axial strain.

As far as the responses without demonstrating abnormal magnitude, there still is a possibility that the bridge responses with reasonable magnitude are induced by dynamic excitations such as traffics and strong winds instead of the temperature variation. Because the temperature variation would commonly induce static effects on the bridge responses, the structural dynamic responses affected by the temperature should be insignificant intuitively. Therefore, the standard deviation of measurement data is an effective indicator of dynamic effect and it would be very small for temperature induced bridge responses on an hourly basis in comparison with those induced by traffics and winds. Thus, a criterion based on the standard deviation of hourly measurement data can be selected as the indicating index and is expressed as

$$\text{std}(x_{\text{dyn}}^s(t)) > \xi_s, \quad (8)$$

where ξ_s is the threshold value of standard deviation of a particular hourly strain response.

3.3. Feature Extraction and Analysis on Temperature Data.

Similar to the signal processing of strain responses, the time history of the measured temperature can be decomposed by EMD

$$x^T(t) = \sum_{j=1}^{nt} c_j^T(t) + r_{nt}^T(t), \quad (9)$$

where $c_j^T(t)$ is the j th IMF component of the temperature response; nt is the total number of IMF components of temperature response; and $r_{nt}^T(t)$ is the final residue.

Because the dynamic loading cannot substantially affect the temperature responses of the bridge, the temperature responses of the bridge can be decomposed firstly to reconstruct noise component $x_{\text{noise}}^T(t)$ and nonnoise component $x_t^T(t)$, respectively, with the aid of spectrum analysis

$$\begin{aligned} x_{\text{noise}}^T(t) &= \sum_{j=1}^{mt} c_j^T(t), \\ x_t^T(t) &= \sum_{j=mt+1}^{nt} c_j^T(t) + r_{nt}^T(t), \end{aligned} \quad (10)$$

where mt is the total number of IMF components of noise contamination.

The instrument malfunction may induce the abnormal information in the measurement data sets. In the collected statistical data, data with extremely large or small magnitude are a typical case considered to be the abnormal data. The observed extreme values are usually unrealistic, and this case can be checked from the hourly maximum and/or minimum values which are largely different from the normal data. Thus, the first index to eliminate the abnormal data is set in terms of difference between the hourly maximum and minimum values and is expressed as

$$\text{abs}(x_{t,\text{max}}^T - x_{t,\text{min}}^T) > \varepsilon_T, \quad (11)$$

where $\text{abs}()$ means to take the absolute value; $x_{t,\text{max}}^T$ and $x_{t,\text{min}}^T$ denote the hourly maximum and minimum temperature value, respectively; ε_T is a real number defining the limit of the difference between the maximum and minimum values under the normal temperature loading environment and is selected as 5°C for the example bridge.

In reality, the temperature of Hong Kong is within a certain range and an extremely low temperature recorded by the temperature sensor does not have any physical meaning. Having a temperature signal with extremely low value is considered as an abnormal measurement. Therefore, the second index is set in order to eliminate the extreme low data from temperature information [19]

$$x_t^T(t) < T_{\text{min}}, \quad (12)$$

where T denotes the hourly mean value of temperature; T_{min} is a real number, which defines the threshold value of minimum temperature which is selected as -5°C in this study for Hong Kong situation. Similar to that for strain responses, the standard deviation can be utilized to eliminate the abnormal measurement data having a perfectly flat signal

$$\text{std}(c_j^T(t)) = 0. \quad (13)$$

As discussed above, temperature variation in an hour would not be intensive and the standard deviations of measured temperature would be very small. Thus, an index based on the standard deviation of hourly temperature responses can be selected to eliminate the abnormal temperature data induced by instrument malfunction

$$\text{std}(x_t^T(t)) > \xi_T, \quad (14)$$

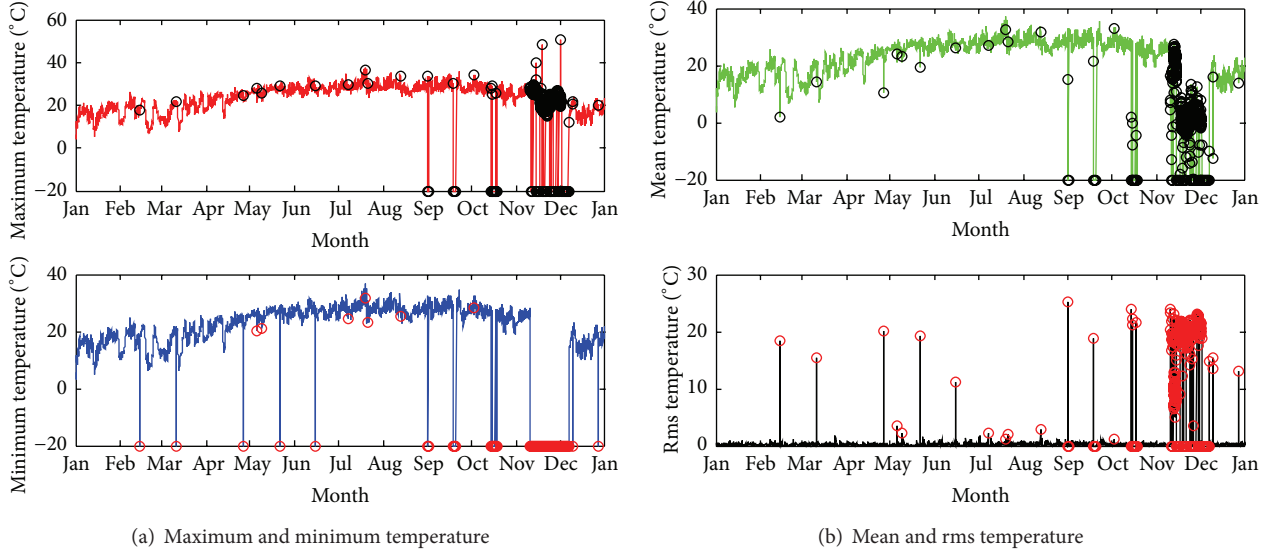


FIGURE 9: Hourly ambient temperature in 2005 from the sensor with channel number 81.

where ξ_T is the threshold value of standard deviation of a particular hourly temperature response and is set as 2°C for the example bridge.

Evaluation of the elimination performance for temperature data from the sensor with channel number 81, which is installed on a sign gantry for ambient temperature measurement in the middle of the main span, can be seen in Figures 9(a) and 9(b). The temperature time histories in terms of the four statistical values maximum, minimum, mean, and root mean square (rms) in the year of 2005 are displayed. The circle marks locate those data that meet the elimination criteria. It is noted that the data with unreasonable extreme values and larger dynamic fluctuations are identified for removal.

3.4. Feature Extraction and Analysis on Displacement Data. The time history of the measured displacement responses can be decomposed by EMD

$$x^d(t) = \sum_{j=1}^{nd} c_j^d(t) + r_{nd}^d(t), \quad (15)$$

where $c_j^d(t)$ is the j th IMF component of the displacement response; nd is the total number of IMF components of displacement response; and $r_{nd}^d(t)$ is the final residue. The displacement responses of the bridge can be decomposed into noise component $x_{\text{noise}}^d(t)$, dynamic component $x_{\text{dyn}}^d(t)$, and static component $x_{\text{static}}^d(t)$, respectively, with the aid of spectrum analysis

$$x_{\text{noise}}^d(t) = \sum_{j=1}^{md} c_j^d(t),$$

$$x_{\text{dyn}}^d(t) = \sum_{j=md+1}^{nd-1} c_j^d(t),$$

$$x_{\text{static}}^d(t) = c_{nd}^d(t) + r_{nd}^d(t),$$

$$x_t^d(t) = x_{\text{dyn}}^d(t) + x_{\text{static}}^d(t), \quad (16)$$

where md is the total number of displacement IMF components of noise contamination. If the absolute mean value of a particular IMF is quite small, this IMF can be regarded as noise component. $x_t^d(t)$ denotes the nonnoise component of the displacement responses. Similar to the signal analysis of strain and temperature data, the standard deviation and the difference between the hourly maximum and minimum values are utilized to eliminate the abnormal data

$$\text{std}(c_j^d(t)) = 0, \quad (17)$$

$$\text{abs}(x_{t,\text{max}}^d - x_{t,\text{min}}^d) > \varepsilon_d,$$

where $x_{t,\text{max}}^d$ and $x_{t,\text{min}}^d$ denote the hourly maximum and minimum displacement value, respectively; ε_d is a real number defining the limit of the difference between the maximum and minimum values of displacement responses. An index based on the standard deviation of hourly measurement data is selected to eliminate the data substantially induced by dynamic excitation

$$\text{std}(x_{\text{dyn}}^d(t)) > \xi_d, \quad (18)$$

where ξ_d is the threshold value of standard deviation of a particular hourly displacement response set. Regarding selection of threshold values (ε_d and ξ_d) for the data elimination criteria, different values are individually selected for the displacement responses because they possess different measurement features and variation ranges. The threshold values obtained by trial and error are summarized in Table 2.

TABLE 2: Summary of threshold values for elimination criteria.

Type of sensor	Channel number/location	Direction of measurement	Threshold value	
			ε_d	ξ_d
Displacement transducer	Ch. 5	Lateral	3 mm	1 mm
	Ch. 6	Longitudinal	100 mm	20 mm
		Longitudinal	150 mm	15 mm
	GPS station	Tower	Lateral	150 mm
Vertical			300 mm	50 mm
Cable		Longitudinal	250 mm	25 mm
		Lateral	250 mm	25 mm
Deck	Vertical	1000 mm	100 mm	
	Longitudinal	150 mm	15 mm	
		Lateral	150 mm	15 mm
		Vertical	1000 mm	100 mm

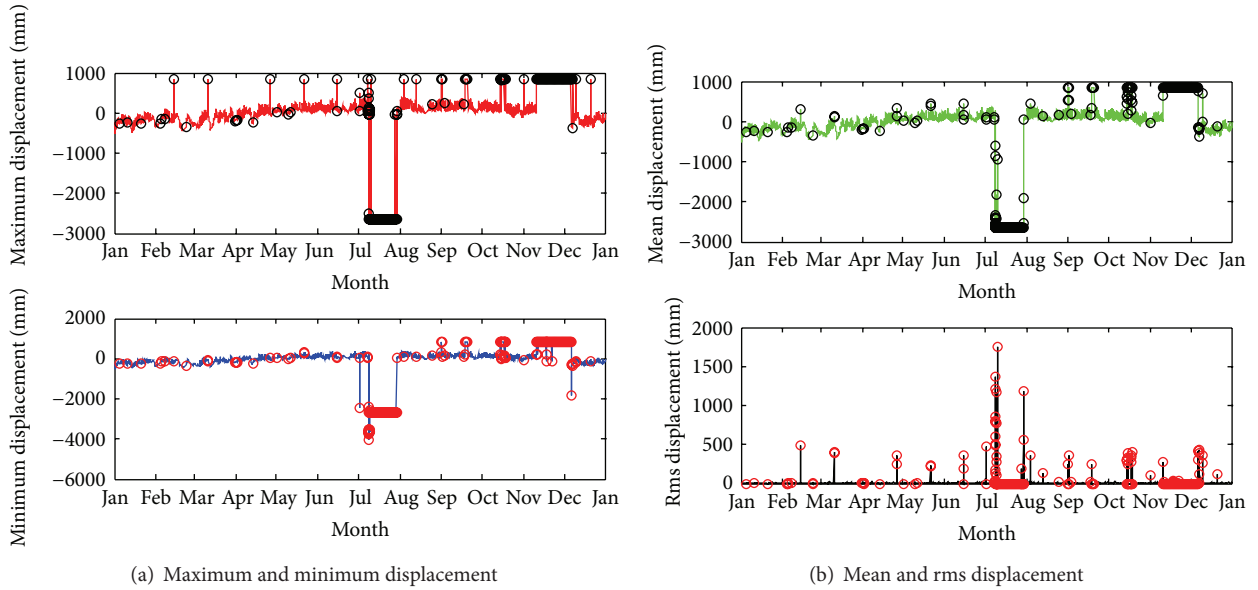


FIGURE 10: Annual time histories of bridge longitudinal displacement in 2005 from transducer with channel number 6.

A satisfactory performance of data removal is also noted for the bridge motion measured by displacement transducers of which the time histories of the four statistical values in 2005 are shown in Figures 10(a) and 10(b). The considered displacement transducer for illustration is assigned with channel number 6 and this sensor measures the longitudinal movement of the bridge deck at the Tsing Yi abutment. It can be seen that the elimination scheme is capable of detecting all the unreasonable and undesirable data. Those measurements with zero magnitude in standard deviation, as observed in the time history in rms value, are also identified. The annual time histories of bridge vertical displacement recorded by GPS in the same period as considered in the preceding three signals are displayed in Figures 11(a) and 11(b). It is observed that the jumping of signal is the most detected abnormality in the displayed time histories compared with the measurement errors associated with the zero magnitude of standard deviation. Again, the effectiveness of the

proposed indices for removal of the erroneous statistical data is clearly demonstrated. The quality of the GPS measurement can be appreciated from seldom identification of the data with error in zero standard deviation. However, overshooting of the signal is still the signal defects detected sometimes. The GPS data with standard deviation of larger value than the normal value is also commonly observed and removed. The occurrence of this case is more often than overshooting of the signal. It can be seen that the proposed several indices are capable of detecting all the unreasonable and undesirable data from the collected strain, temperature, and displacement responses. It is found that different structural responses may have different number of IMFs after being processed by using EMD. The made observations indicate that the first several IMFs are the signal components of noise contamination. Then, the following several IMFs are the signal induced by various dynamic excitations, and the last IMF and the residue are the signal mainly induced by temperature variation.

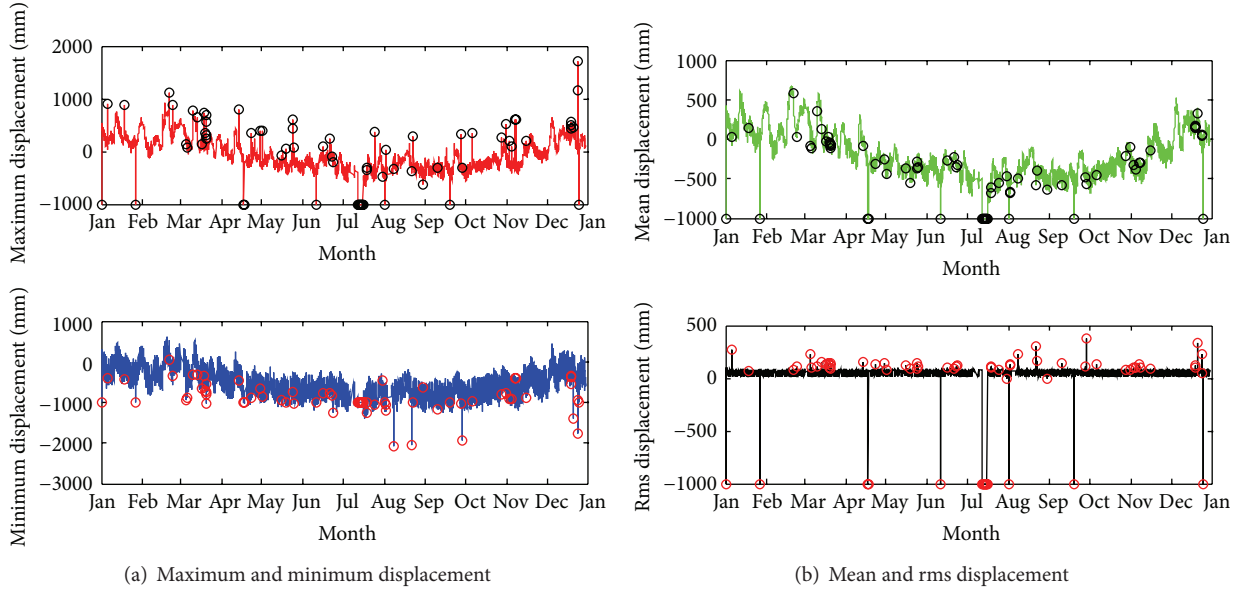


FIGURE 11: Annual time histories of bridge vertical displacement in 2005 from GPS.

4. Temperature Distribution

4.1. Heat Transfer Analysis. As far as a bridge subjected to solar radiation is concerned, it is commonly assumed that thermal variation in the direction of the longitudinal axis is not significant [8, 22]. Therefore, the temperature field T of a bridge cross section can be expressed by a two-dimensional heat flow equation as

$$k \left(\frac{\partial^2 T}{\partial x^2} + \frac{\partial^2 T}{\partial y^2} \right) = \rho c \frac{\partial T}{\partial t}, \quad (19)$$

in which x and y are Cartesian coordinates, k is the isotropic thermal conductivity coefficient, ρ is the density of material, and c is the specific heat of the material. For a bridge subjected to solar radiation, the thermal energy transferred between the bridge surface and environment consists of convection q_c , thermal irradiation q_r , and solar radiation q_s [9]. The heat flow effects induced by convection and thermal irradiation for the bridge component can be expressed as

$$q_c + q_r = h(T_a - T_s), \quad (20)$$

$$h = h_c + h_r, \quad (21)$$

where T_a and T_s denote the air temperature and the structural surface temperature, respectively; h_c and h_r denote the convection heat transfer coefficient and the radiation heat transfer coefficient, respectively.

The convection heat transfer coefficient h_c is a function of many variables such as wind speed, surface roughness, and the geometric configuration of the exposed structure. The h_r is a function of the emissivity coefficient of the bridge surface and the ambient temperature [9]. The rate of heat absorbed by the bridge surface due to solar radiation q_s is [23, 24]

$$q_s = \alpha I, \quad (22)$$

where α ($0 < \alpha < 1$) is absorptivity coefficient of the surface material; I is solar radiation including direct solar radiation, diffuse solar radiation, and reflected solar radiation on a surface, respectively. The energy transferred between the surface elements and the environment is

$$q = q_c + q_r + q_s. \quad (23)$$

Based on (20) and (25), the heat flow of a bridge surface considering solar radiation is

$$q = h(T_a - T_s) + \alpha I \quad (24)$$

or a more convenient form

$$q = h(T^* - T_s), \quad (25)$$

$$T^* = T_a + \frac{\alpha I}{h},$$

where T^* is usually termed as “equivalent air temperature” because it includes both the air temperature and solar radiation. In the computer analysis of a structural temperature field, the air temperature can be measured continuously as a function of time.

4.2. Temperature Distribution of Bridge. It is very difficult to establish a global model for the entire bridge and carry out the transient thermal analysis on the entire bridge due to the complicated structural configuration. Thermal variation of the bridge deck in the longitudinal direction of the bridge can be assumed insignificant and thus one typical segment is studied. Consequently, FE models of a typical deck plate, a cross frame, and a segment of the bridge tower are established using three-dimensional solid elements with the aid of commercial FE packages ANSYS (2010). The orthotropic bridge deck plate consists of steel deck plates, asphalt concrete cover,

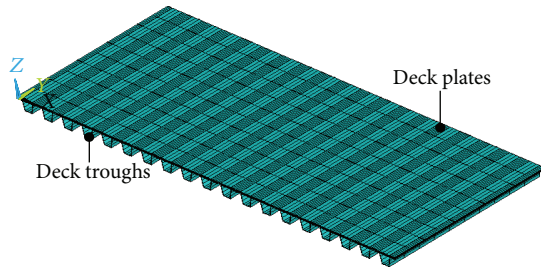


FIGURE 12: Configuration of deck plate.

and deck troughs as shown in Figure 12. The thickness of the upper and lower deck plates is 13 mm, while the counterparts for upper deck trough and lower deck trough are 8 mm and 10 mm thick, respectively. The steel deck plates are covered by 40 mm asphalt concrete. The deck plates, troughs, and deck covers are modelled using thermal type solid elements. The FE model around detail 12 for heat transfer analysis consists of 24244 nodes and 18211 three-dimensional SOLID90 elements.

The transient heat transfer analysis is carried out to determine the temperature distribution of the deck plate based on the actual thermal boundary conditions. The thermal conductivity of asphalt, concrete, and steel is 2.50, 1.54, and 55 W/(m·C), respectively. The density of asphalt, concrete, and steel is 2100, 2400, and 7800 kg/m³, respectively. The heat capacity of asphalt, concrete, and steel is 960, 950, and 460 J/(kg·C), respectively. The absorptivity coefficient of asphalt, concrete, and steel is 0.9, 0.65, and 0.685, respectively. The convection heat transfer coefficient h_c can be computed in line with the wind speed and geometric configuration of deck plate by using an empirical formula [25].

The calculated temperature of the deck plate of detail 12 on summer and spring is compared with the measurement counterparts and shown in Figure 13. It is observed that the predicted temperature agrees with the measurement very well at all time points, which validates the effectiveness of the numerical model and the heat transfer analysis. The temperature of the deck plate in other two seasons is also calculated and the parameters are the same as those adopted in summer calculations except that the radiation intensity varies in different seasons. The temperature variation in autumn and winter agrees with the measurement and the results are not shown here for brevity. Similar to deck plates, the heat transfer analysis of other bridge components such as cross frame and bridge tower is also carried out. A detailed three-dimensional FE model of one cross frame is constructed consisting of 29090 nodes and 3910 three-dimensional SOLID90 elements, as shown in Figure 14(a). The cross frame is modelled based on the design with minor simplification due to the omission of accessory components. The cross frame is enclosed by the deck plates and corrugate sheets, and the heat exchange occurs between the plates and the section frame. Therefore, the temperature measured at the interface between the cross frame and enclosed plates (sheets) is used as a thermal boundary condition for heat transfer computation. Other surfaces of the frame that are exposed to air do not receive solar radiation directly. Figure 14(b)

indicates the detailed FE model of one tower segment with 28762 nodes and 24000 three-dimensional solid elements. The tower segment is enclosed by two semicircles and one rectangular with two rectangular holes in the middle. The depth of the tower section is 6.0 m. Because the outer surface of the tower segment is a curve, the solar radiation on the tower surface changes with the varying node location. To facilitate the application of solar intensity, the surface of the tower is divided into 18 segments and each segment receives the same solar radiation that is calculated according to their orientation. The made observations indicate that the numerical results agree with the measurement counterparts very well at different time for the upper left chord, lower chord, and vertical truss members. Similar observations can be made from the results of tower segment, whose results are not shown here for brevity.

5. Thermal-Structural Coupling Analysis

5.1. Traditional Thermal-Structural Coupling Analysis. A global FE model of the entire bridge is constructed as shown in Figure 15(a) for structural analysis to compute the temperature-induced responses. Components are simplified appropriately and modelled with relatively coarse meshes in the structural analysis as compared with the heat transfer analysis. Regarding the FE model of the entire Tsing Ma Bridge, all the frame components and longitudinal trusses are modelled as beam elements that are appropriately meshed for connections with highway decks and railway tracks. The configuration of a typical bridge section in the concerned FE model of the entire bridge is displayed in Figure 15(b). It is seen that there are sixteen nodes in the section and nineteen beam elements are adopted to construct a single bridge section. Shell elements are utilized to simulate the upper and lower orthotropic deck plates. The bracing, railway beam, and other longitudinal members are also constructed with beam or bar elements. Since the highway decks and railway tracks are vertical at different levels with the cross frames and longitudinal trusses, multipoint constraints (MPCs) are used to connect them to simulate the master-slave relationship. The bridge towers, piers are simulated by using three-dimensional solid elements. The suspensors and main cables are also model by using bar elements. The entire model has 23960 nodes and 28856 elements. Totally 4788 MPCs are also used for connections between the orthotropic deck plates and the chords of cross frames.

The computation of bridge thermal effects is a typical thermal-structural coupling analysis because the temperature distribution is calculated firstly and then taken as the loading on the bridge model to determine the temperature-induced responses such as displacement and strain. In the FE computation, the thermal-structural coupling analysis is carried out by using the sequential coupling method [26]. In the application of this approach, the heat transfer analysis is conducted firstly to determine the structural temperature fields, and all the thermal information is stored in thermal database. Then, the nodal temperature loading is taken as body loading of the model to compute the structural

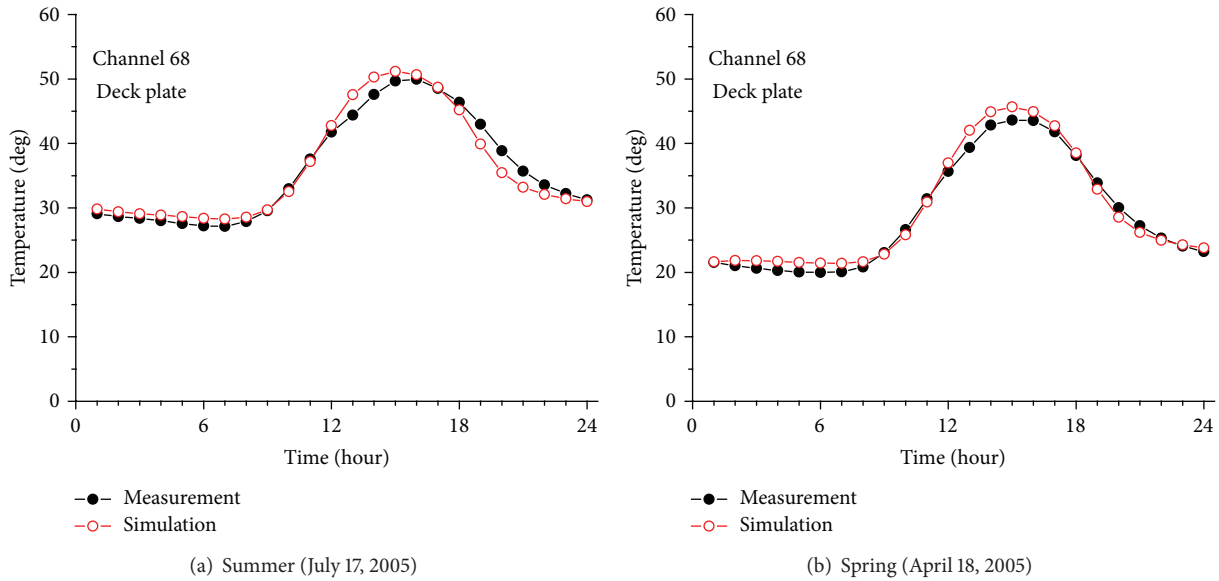


FIGURE 13: Comparison of the measured and simulated temperature at detail 12 in spring.

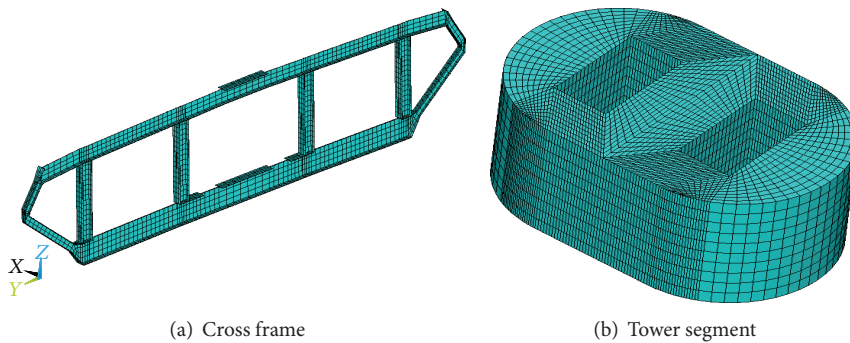


FIGURE 14: Finite element models of bridge components.

responses. It is clear that the heat transfer analysis and structural analysis are performed based on thermal FE model with thermal element and structural FE model with structural elements, respectively. However, the number of nodes and elements of the two models should be the same to transfer the nodal temperature to nodal thermal loading one by one. This is a very important precondition for the sequential coupling method in the thermal-structural coupling analysis [26]. In reality, the sequential coupling method only can be successfully applied to the structural model with small scales instead of large-scale structures such as the Tsing Ma Bridge.

The detailed FE models of a deck plate, a cross frame, and a tower segment for heat transfer analysis are described and plotted in Figures 12 and 14, respectively. Fine meshes are required for these models to compute the exact temperature fields and thus the large number of nodes and elements can be expected. Therefore, the models of a deck plate, a cross frame, and a tower segment for thermal effect analysis should have the same scales by using the sequential coupling method. The Tsing Ma Bridge has hundreds of cross frames and thousands of deck plates. Therefore, there may exist about two million

nodes and elements in the entire bridge model constructed by the heat transfer model and solved by the sequential coupling method. In reality, the FE model of the entire bridge with a remarkably large scale is unreasonable and time consuming for the current structural analytical technique. To this end, a new approach for thermal-structural coupling analysis of long span bridge is proposed and applied to the Tsing Ma Suspension Bridge.

5.2. A New Approach for Thermal-Structural Coupling Analysis. As discussed above, pretty complicated FEM models are not necessary when examining the global temperature-induced structural responses of the entire bridge. Therefore, a simplified analytical model with an appropriate dimension is expected for balancing satisfactory accuracy and analytical expense. Thus, the three-dimensional FE model of the Tsing Ma bridge as shown in Figure 15 is utilized for thermal effect analysis. Because the sizes of the FE model for heat transfer analysis are much larger than those for response analysis, the size of the temperature loading from the heat transfer analysis is very large and cannot be applied directly to

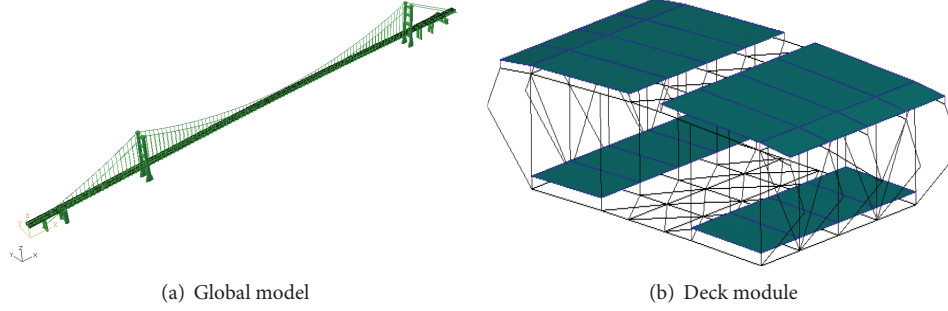


FIGURE 15: Finite element model of the Tsing Ma bridge.

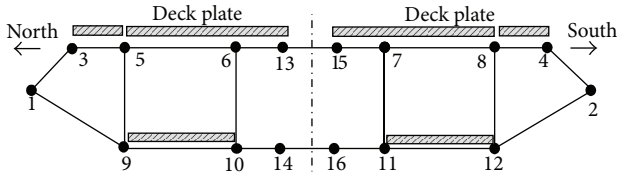


FIGURE 16: Configuration of a cross frame in the global model.

the global model due to its small node dimension. To analyze the thermal responses of the entire bridge, the temperature loading should be applied to the global bridge model. It is found that the node number of single cross frame based on the thermal solid model (Figure 15) is 23960, while the node number of the same frame for structural analysis is only 19 as shown in Figure 16. Therefore, the equivalent temperature loading can be constructed for thermal response assessment by using the concept of effective temperature.

The effective temperature is proposed to study the measured temperatures of the bridge deck section and the main cable section [19]. The effective temperature is considered instead of the temperature measured from any single sensor in the cross section concerned. The effective temperature is a theoretical temperature calculated by weighting and adding temperatures measured at various locations within the cross section. The weighting is the ratio of the area of cross section for a particular sensor to the total area of cross section

$$T_E = \frac{\int T dA}{A}. \quad (26)$$

The effective deck temperature and effective cable temperature are indices to depict the integral temperature effects of bridge decks and bridge cables. Thus, an index named effective nodal temperature is proposed in this study to construct the nodal temperature loadings for the thermal effect analysis. The effective nodal temperature for a node i in bridge deck T_i^{deck} is a temperature calculated by weighting and adding temperatures obtained at various locations within the volume affiliated to node i . The weighting is the ratio of the volume of the section for a particular node i to the total volume of the cross frame section

$$T_i^{\text{deck}} = \frac{\sum_{j=1}^{nf} T_j^f V_j^f + \sum_{j=1}^{np} T_j^p V_j^p + \sum_{j=1}^{nb} T_j^b V_j^b}{\sum_{j=1}^{nf} V_j^f + \sum_{j=1}^{np} V_j^p + \sum_{j=1}^{nb} V_j^b}, \quad (27)$$

where nf , np , and nb denote the numbers of volume elements of cross frame, deck plate, and truss brace affiliated to node i ; V_j^f , V_j^p , and V_j^b denote the volume of the j th element of cross frame, deck plate, and brace affiliated to node i ; T_j^f , T_j^p , and T_j^b denote the temperature of the j th element of cross frame, deck plate, and brace affiliated to node i . Similarly, the effective nodal temperature for a node i in bridge tower T_i^{tower} and bridge cable T_i^{cable} can be expressed as

$$T_i^{\text{tower}} = \frac{\sum_{j=1}^{nt} T_j^t V_j^t}{\sum_{j=1}^{nt} V_j^t}, \quad (28)$$

$$T_i^{\text{cable}} = \frac{\sum_{j=1}^{nc} T_j^c V_j^c}{\sum_{j=1}^{nc} V_j^c},$$

where nt and nc denote the numbers of volume elements of tower segment and cable affiliated to node i ; V_j^t and V_j^c denote the volume of the j th element of tower segment and cable affiliated to node i ; T_j^t and T_j^c denote the temperature of the j th element of tower segment and cable affiliated to node i .

The element affiliation to a certain node i can be evenly divided according to geometric position as shown in Figure 16 for simplification. Thus, the effective temperature loading of the bridge at different time instant $\mathbf{T}^E(t)$ is computed and expressed as

$$\mathbf{T}^E(t) = [\mathbf{T}^{\text{deck}}(t), \mathbf{T}^{\text{tower}}(t), \mathbf{T}^{\text{cable}}(t)]. \quad (29)$$

The thermal expansion coefficients of concrete and steel can be adopted based on material properties in the thermal analysis. It is reported above that the orthotropic plate of the Tsing Ma Bridge is constructed with steel plate, steel trough, and asphalt concrete cover. The bridge plates, however, are simulated by using shell elements in the global FE model; therefore, an equivalent thermal expansion coefficient for the deck plate with the trough and cover is proposed. To assume that the thermal expansion of the real plate is equal to that of the simulated shell element subjected to same effective plate temperature, one can obtain that

$$\alpha_E^{P, \text{cP}} (A_c + A_s) = \alpha_c T_E^{\text{cP}} A_c + \alpha_s T_E^{\text{cP}} A_s, \quad (30)$$

in which α_c and α_s are the thermal expansion coefficients of concrete and steel, respectively; α_E^P is the equivalent thermal

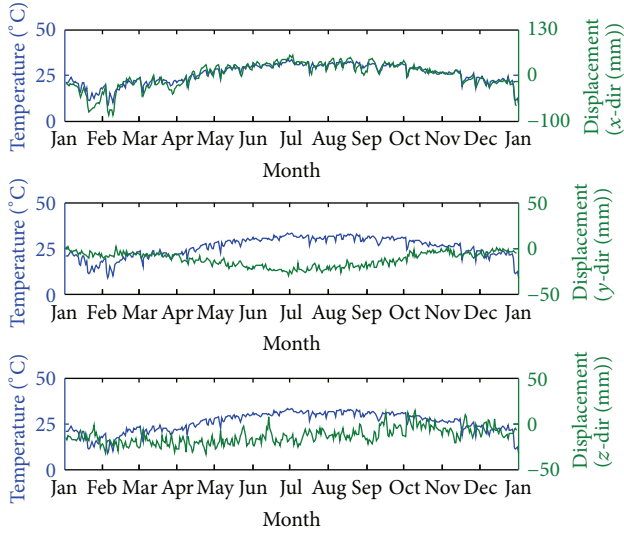


FIGURE 17: Comparison of effective cable temperature and displacement of the Ma Wan tower in 2004.

expansion coefficient of shell elements; T_E^{cP} is the effective temperature of the orthotropic deck plate; A_c and A_s are the concrete area and steel area in cross section, respectively. Then, the equivalent thermal expansion coefficient is given by

$$\alpha_E^P = \frac{\alpha_c A_c + \alpha_s A_s}{(A_c + A_s)}. \quad (31)$$

6. Temperature Effects of the Bridge

6.1. Displacement of the Bridge. To gain a better understanding towards different parts of the bridge movement in the three orthogonal directions, the variation ranges and patterns of bridge displacement responses are investigated. In this regard, the extent of temperature effects on the bridge displacement in the three different directions is unveiled in this section. The displacement of the Ma Wan tower in the three directions in comparison with the effective cable temperature is carried out and displayed in Figure 17. The displacement is the average value, which is performed by WASHMS and provided in the original records, based on the measurements from the two stations. It can be seen that only the displacement in the x -direction (longitudinal) shows a good agreement with the effective deck temperature. The lateral (y -dir.) and vertical (z -dir.) displacements are small and seem to be not well correlated with the effective cable temperature and are thus not dominantly affected by the temperature. Moreover, the displacements of the Tsing Yi tower in the three directions are also analyzed and similar conclusions to those of the Ma Wan tower can be drawn out. The longitudinal displacement of the bridge deck recorded by displacement transducers from 2003 to 2005 is displayed in Figure 18 in comparison with the effective deck temperature. It is observed that the longitudinal displacement at the Tsing Yi abutment shows a good agreement with the effective deck temperature.

The displacements of the bridge deck in the 1/4 span of the main span from the Ma Wan tower (MWMS) on July 17, 2005, are computed and compared with measurement as shown in Figure 19. The curves indicate that the displacements in the x - (longitudinal) and z - (vertical) directions show a good agreement with the measurement. The lateral (y -dir.) displacement is noted to be independent of the temperature and is thus not affected by the temperature. Similar observations can be made from the results at main span, side span, and the bridge tower which are not displayed for brevity. It is observed that only the simulated hourly displacement variations in the longitudinal direction at Ma Wan side span MWSS show a good agreement with the measured hourly displacement variations. The lateral (y -dir.) and vertical (z -dir.) hourly displacement variations seem to be not well correlated with the temperature and are thus not dominantly affected by the temperature. The results from wind excited dynamic analysis indicate that the lateral responses are mainly induced by wind, in particular dynamic wind loadings.

6.2. Stress of the Bridge. The variation in stresses on bridge members is investigated in this section. Considering that temperature tends to cause static strain of the bridge whereas traffic loadings cause dynamic strain, hourly mean strain is calculated and regarded due to temperature variation. For the axial loaded members, the stress is calculated from the strain by multiplying Young's modulus of steel, 2.01×10^{11} Pa. Take the north inner longitudinal truss at Figure 4 as an example. The strains at the upper chord, diagonal brace, and bottom chord are measured by strain gauges. Their hourly mean stresses from the measurement data on July 17, 2005, are shown in Figure 20 in comparison with the numerical counterparts. It is noted that the strain induced by moving train loadings has been removed from the original time histories by using the proposed data process approach. The figure shows that the calculated stresses agree well with the field measurements, indicating that the stress variation is mainly caused by the temperature changes. The temperature-induced stresses are about 10 MPa in maximum, much smaller than the design strength of steel. Therefore, the proposed new approach can successfully conduct the thermal-structural coupling analysis of the long span bridge.

7. Concluding Remarks

The condition assessment on temperature distribution and thermal effects of the Tsing Ma Suspension Bridge is carried out in this study. The data collected from the SHM system are processed with the aid of empirical mode decomposition (EMD). The signal components induced by dynamic excitations and noise are extracted from the original data time histories. Several indices are proposed to process the time-varying temperature, displacement, and strain responses obtained by SHM system. The heat transfer analysis of the bridge is conducted to calculate the temperature distributions within the bridge. By assuming that the temperature along the bridge longitudinal direction is constant, one typical bridge segment is specially studied. A similar assumption is applied to the towers. Fine FE models of various components such

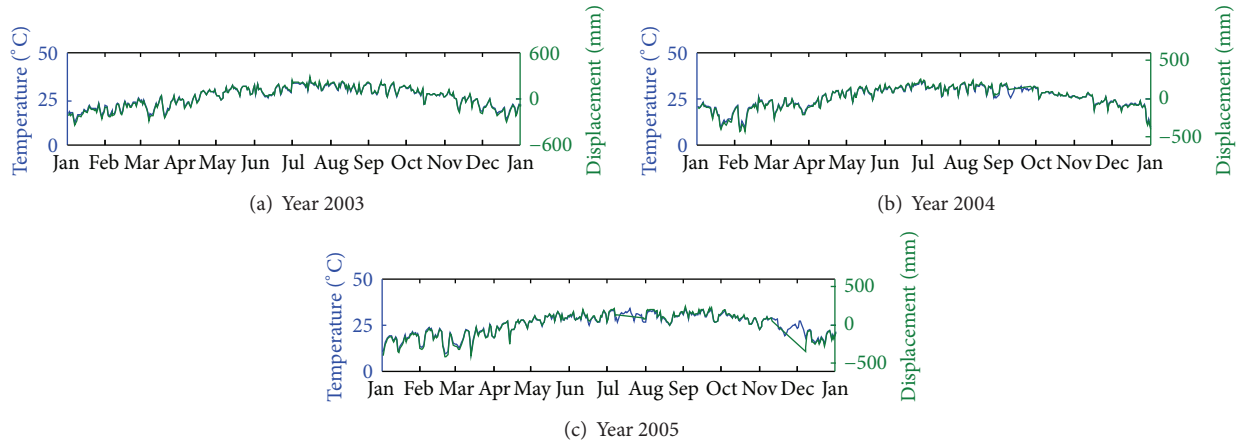


FIGURE 18: Comparison of effective deck temperature and longitudinal displacement at the Tsing Yi abutment.

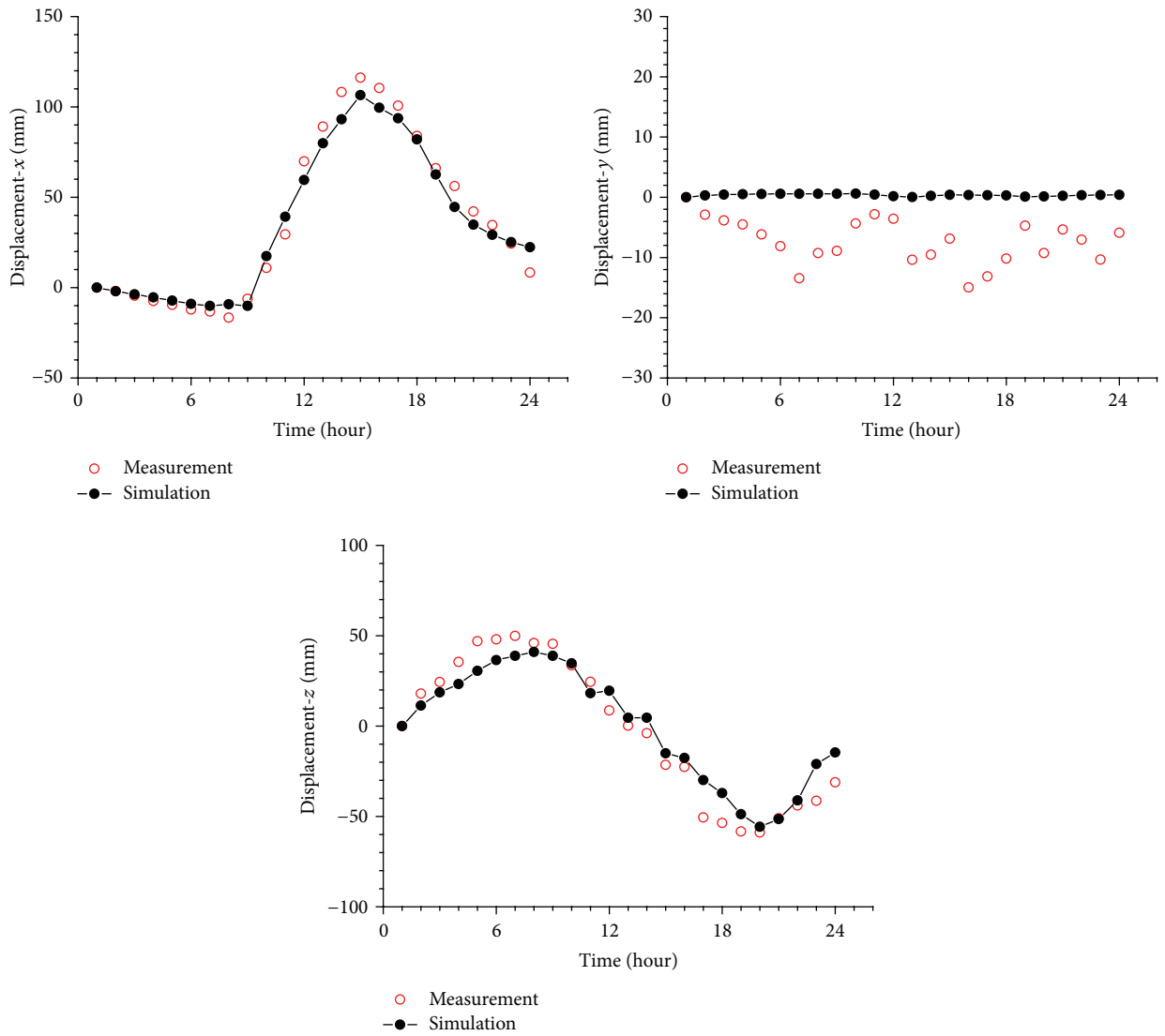


FIGURE 19: Displacement of the bridge deck (MWMS) with respect to time tower in 2004.

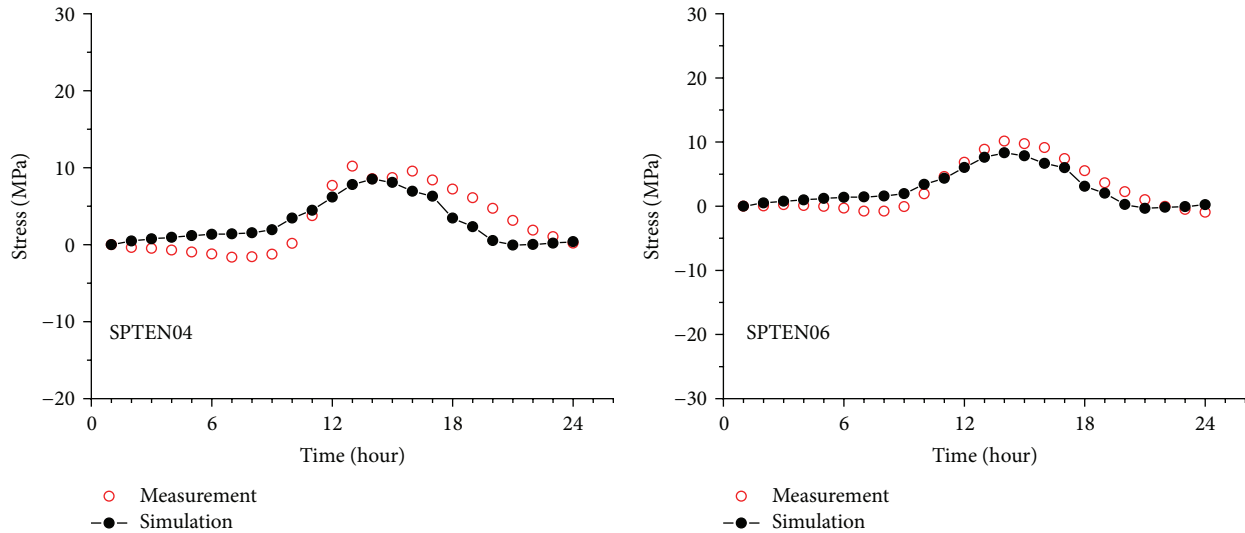


FIGURE 20: Variations of member stresses with respect to time.

as the deck plate, the frame section, and the tower section are constructed. A new approach for the thermal-structural coupling analysis of long span bridges is proposed to examine the structural thermal effects. The feasibility and validity of the proposed data process approach and the new approach for thermal-structural coupling analysis are examined through detailed simulation and comparison.

The made observation indicates that the proposed data processing approach can successfully eliminate the noise components from the original data sets. It can be seen that the proposed several indices are capable of detecting all the unreasonable and undesirable data from the collected strain, temperature, and displacement responses. The proposed analytical model and approach can successfully predict the structural temperature of various components at different time. The approach for thermal-structural coupling analysis established in this study can be successfully applied in the assessment of the thermal effects of the Tsing Ma Suspension Bridge. It should be pointed out that the parameters and results are valid only for the example building examined in this study. For other bridges with different parameters, the methodology for the signal processing and thermal effect assessment demonstrated in this study is still valid.

Acknowledgments

The writers are grateful for the financial support from the National Natural Science Foundation of China (51178366), the Fundamental Research Funds for the Central Universities (WUT, 2013-II-015), and the Technological Project of the Chinese Southern Power Grid Co. Ltd (K-GD2013-0222).

References

- [1] O. S. Salawu, "Detection of structural damage through changes in frequency: a review," *Engineering Structures*, vol. 19, no. 9, pp. 718–723, 1997.
- [2] T. Yi, H. Li, and M. Gu, "Full-scale measurements of dynamic response of suspension bridge subjected to environmental loads using GPS technology," *Science China Technological Sciences*, vol. 53, no. 2, pp. 469–479, 2010.
- [3] T. H. Yi, H. N. Li, and M. Gu, "Experimental assessment of high-rate GPS receivers for deformation monitoring of bridge," *Measurement*, vol. 46, no. 1, pp. 420–432, 2013.
- [4] W. Zuk, "Thermal behaviour of composite bridges-insulated and uninsulated," *Highway Research Record*, vol. 76, pp. 231–253, 1965.
- [5] M. W. R. Capps, "The thermal behavior of the Beachley Viaduct/Wye Bridge," Tech. Rep. TRRL Report LR 234, Ministry of Transport, Road Research Laboratory, 1968.
- [6] A. Churchward and Y. J. Sokal, "Prediction of temperatures in concrete bridges," *Journal of Structural Division*, vol. 107, no. 11, pp. 2163–2176, 1981.
- [7] M. J. N. Priestley, "Design of concrete bridges for thermal gradients," *ACI Journal*, vol. 75, no. 5, pp. 209–217, 1978.
- [8] M. M. Elbadry and A. Ghali, "Temperature variation in concrete bridges," *Journal of Structural Engineering*, vol. 109, no. 10, pp. 2355–2374, 1983.
- [9] F. A. Branco and P. A. Mendes, "Thermal actions for concrete bridge design," *Journal of Structural Engineering*, vol. 119, no. 8, pp. 2313–2231, 1993.
- [10] M. A. Shahawy and M. Arockiasamy, "Analytical and measured strains in sunshine skyway bridge. II," *Journal of Bridge Engineering*, vol. 1, no. 2, pp. 87–97, 1996.
- [11] C. L. Roberts-Wollman, J. E. Breen, and J. Cawrse, "Measurements of thermal gradients and their effects on segmental concrete bridge," *Journal of Bridge Engineering*, vol. 7, no. 3, pp. 166–174, 2002.
- [12] Y. Fu and J. T. DeWolf, "Effect of differential temperature on a curved post-tensioned concrete bridge," *Advances in Structural Engineering*, vol. 7, no. 5, pp. 385–397, 2004.
- [13] S. L. Desjardins, N. A. Londoño, D. T. Lau, and H. Khoo, "Real-time data processing, analysis and visualization for structural monitoring of the confederation bridge," *Advances in Structural Engineering*, vol. 9, no. 1, pp. 141–157, 2006.

- [14] M. Tong, F. T. K. Au, L. G. Tham, and K. Y. Wong, "A study of temperature measurement in long span steel bridge," in *Proceedings of the Workshop on Research and Monitoring of long Span Bridges*, pp. 188–195, Hong Kong, 2000.
- [15] M. Tong, L. G. Tham, F. T. K. Au, and P. K. K. Lee, "Numerical modelling for temperature distribution in steel bridges," *Computers and Structures*, vol. 79, no. 6, pp. 583–593, 2001.
- [16] F. T. K. Au, L. G. Tham, M. Tong, and P. K. K. Lee, "Temperature monitoring of steel bridges," in *Health Monitoring and Management of Civil Infrastructure Systems*, vol. 4337 of *Proceedings of SPIE*, pp. 282–291, Newport Beach, Calif, USA, March 2001.
- [17] K. Y. Wong, C. K. Lau, and A. R. Flint, "Planning and implementation of the structural health monitoring system for cable-supported bridges in Hong Kong," in *Nondestructive Evaluation of Highways, Utilities, and Pipelines IV*, vol. 3995 of *Proceedings of SPIE*, pp. 266–275, Newport Beach, Calif, USA, March 2000.
- [18] K. Y. Wong, D. K. L. Man, and K. W. Y. Chan, "Thermal load and response monitoring of Ting Kau (Cable-Stayed) bridge," in *Proceedings of the International Conference on Innovation and Sustainable Development of Civil Engineering in the 21st Century*, pp. 249–252, Beijing, China, August 2002.
- [19] Y. L. Xu, B. Chen, C. L. Ng, K. Y. Wong, and W. Y. Chan, "Monitoring temperature effect on a long suspension bridge," *Structural Control and Health Monitoring*, vol. 17, no. 6, pp. 632–653, 2010.
- [20] T. H. Yi, H. N. Li, and M. Gu, "Wavelet based multi-step filtering method for bridge health monitoring using GPS and accelerometer," *Smart Structures and Systems*, vol. 11, no. 4, pp. 331–348, 2013.
- [21] B. Chen and Y. L. Xu, "A new damage index for detecting sudden change of structural stiffness," *Structural Engineering and Mechanics*, vol. 26, no. 3, pp. 315–341, 2007.
- [22] H. C. Fu, S. F. Ng, and M. S. Cheung, "Thermal behavior of composite bridges," *Journal of Structural Engineering*, vol. 116, no. 12, pp. 3302–3323, 1989.
- [23] W. M. Rohsenow, *Handbook of Heat Transfer Applications*, McGraw-Hill, New York, NY, USA, 1988.
- [24] F. Kehlbeck, *Einfluss der Sonnenstrahlung bei Brückenbauwerken*, Werner, Dusseldorf, Germany, 1975.
- [25] M. Froli, N. Hariga, G. Nati, and M. Orlandini, "Longitudinal thermal behaviour of a concrete box girder bridge," *Structural Engineering International*, vol. 6, no. 4, pp. 237–242, 1996.
- [26] ANSYS 11.0, ANSYS, Southpointe, Pa, USA, 2010.

Research Article

Slope Stability Analysis Based on Measured Strains along Soil Nails Using FBG Sensing Technology

Hua-Fu Pei,¹ Chao Li,¹ Hong-Hu Zhu,² and Yu-Jie Wang³

¹ Department of Civil and Environmental Engineering, Harbin Institute of Technology, Shenzhen Graduate School, Shenzhen 518055, China

² School of Earth Sciences and Engineering, Nanjing University, Nanjing 210046, China

³ Department of Geotechnical Engineering, China Institute of Water Resources and Hydropower Research, Beijing 100038, China

Correspondence should be addressed to Chao Li; lichaosz@hit.edu.cn

Received 18 October 2013; Accepted 21 November 2013

Academic Editor: Xiao-Wei Ye

Copyright © 2013 Hua-Fu Pei et al. This is an open access article distributed under the Creative Commons Attribution License, which permits unrestricted use, distribution, and reproduction in any medium, provided the original work is properly cited.

In the past few decades, slope stability analysis using numerical methods is becoming a hot issue, but it is based on extremely ideal assumptions. Soil nailing technique, as one of the most cost-effective reinforcing methods, has already been widely used for reinforcing slopes. In this study, to evaluate the safety factor of a slope, the strains on soil nails were measured by fiber Bragg grating (FBG) sensor. Strains along soil nails in the same cross section of a slope can be computed using the measured wavelength shifts of FBG sensors. In order to evaluate the stability of a slope, an optimal model was proposed to search the potential slip surfaces based on measured strain values. Maximum sum of strains on soil nails at different elevations of the same cross section was taken as the objective. Positions of soil nails, circular slip surface, and boundary conditions of the soil nails were summarized and taken as constraints. Finally, safety factors can be computed using the searched slip surface regarding the axial stress of soil nails. This method combines the limit equilibrium methods with measured axial strains on site which can reflect the actual condition of field slopes.

1. Introduction

Soil nailing technique firstly appeared in France [1, 2]. For ease of construction and some other potential benefits, soil nailing has been proven to be a practical technique for slope reinforcement [3, 4]. It is currently one of the predominant methods for slope reinforcement in Hong Kong. However, it is difficult to evaluate the working state of an in-service soil nail in a slope. In this case, measurement of the strain and stress is becoming essential in order to investigate the performance of in-service soil nails in the process of stress redistribution in slopes.

Structural health monitoring is becoming a hot issue for supplying prosperous parameters to evaluate the safety of in-service structures [5–9]. However, there are several inherent disadvantages of conventional strain sensors in monitoring strains along soil nails [10–12] including poor long-term stability, low accuracy, too many cables needed for multipoint measurement, and electromagnetic interference. In general,

the soil nail diameter is relatively small ranging from 100 mm to 250 mm. If we use conventional strain sensors to monitor a number of locations along the nail, say, 10 to 20, then many electrical cables are needed which will fill most of the hole space and thus affect the integrity of the soil nail. Fiber Bragg grating (FBG) is a relatively new optical fiber sensing technology [13, 14]. Wavelength shifts of FBG sensors vary linearly with both environmental temperature and strain changes. FBG sensors have a number of advantages, such as [15, 16]

- (i) immunity to electromagnetic interference (EMI) which guarantees quality signals and data;
- (ii) long-term stability (since measurement is based on the light wavelength changes) which makes the sensors suitable for long-term monitoring, say, 50 to 100 years in principle;
- (iii) excellent accuracy (up to 1×10^{-6} strain) which makes our measurement more accurate;

- (iv) high resistance to corrosion (since the core fiber is silica) which makes the sensors last for a long time in corrosive environments;
- (v) multiplexing for FBG sensors which can measure strains and temperatures (or other parameters specially designed transducers based on the technologies) at multipoints or full distribution along one fiber line;
- (vi) tiny size of the sensors which can be used to measure the parameters of a very small region (local strains, cracks, displacements, etc.);
- (vii) long-distance sensing which can measure over a large area or from a far distance.

For slope stability analysis, two-dimensional (2D) plane strain method is generally employed for simplicity. Based on the simplified method, the limit equilibrium method (LEM) is proposed as the most popular calculation method, which is well known to be a statically indeterminate problem and assumptions on the internal force distribution on each slice are required for the solution of the factor of safety (FOS) [17–19]. The calculus of variational approach by Baker and Garber [20] does not require the assumption on the internal force distribution, but it is quite difficult to get a solution. Besides, limit analysis methods based on the upper-bound and lower-bound theorems have also been developed but used to solve simplified problems [21–24]. However, its applications in complicated site conditions are still limited and are not widely adopted by design engineers.

In this paper, the authors developed an innovative soil nail monitoring system based on FBG sensing technique. From the strains measured by FBG sensors, the authors proposed an optimal model to evaluate the stability of the soil-nailed slopes.

2. Principle of FBG Sensor

Hill et al. [25] discovered photosensitivity in optical fiber and fabricated the FBG with a visible laser beam propagating along the fiber core. Since then, FBG sensors are widely used in military, aerospace engineering, mechanical engineering, and civil engineering. One reason for this popularity is that FBGs can measure multiple parameters at multiple points, such as temperature and strain, at a series of points along one fiber line and have a number of advantages over the conventional sensors as explained before. According to Bragg's law, when a broadband source of light has been injected into the fiber, FBG reflects a narrow spectral part of light at a certain wavelength, which is dependent on the grating period and the refractive index of fiber [26]. In the reflected spectrum of an FBG sensor, the wavelength at which the reflectivity peaks is called the Bragg wavelength λ_B and can be expressed by

$$\lambda_B = 2n_{\text{eff}}\Lambda, \quad (1)$$

where n_{eff} is the effective core index of refraction and Λ is the periodicity of the index modulation.

For a standard single mode silica fiber, the relationship between the Bragg wavelength change $\Delta\lambda_B$, strain change $\Delta\varepsilon$, and temperature change ΔT can be simplified as [27]

$$\frac{\Delta\lambda_B}{\lambda_B} = c_\varepsilon\Delta\varepsilon + c_T\Delta T, \quad (2)$$

where λ_B is the original Bragg wavelength under strain free and 0°C condition, typically between 1510 and 1520 nm (10^{-9} m), and c_ε and c_T are the calibration coefficients for strain and temperature, respectively. In order to measure actual strains due to force, temperature compensation of FBG sensors is required. This can be easily achieved by adding an additional FBG into an empty copper tube and placed in the same temperature field. Once the temperature is measured, the mechanical strain can be corrected to be

$$\Delta\varepsilon = \frac{1}{c_\varepsilon} \left(\frac{\Delta\lambda_B}{\lambda_B} - c_T\Delta T \right). \quad (3)$$

A fiber with a series of FBGs with different original wavelengths is normally fixed along a soil nail by using methods of cement grouting, clamps, and so forth. Using (3), the mechanical strains along the fiber fixed along the soil nail can be obtained.

3. An Optimal Method to Search a Critical Slip Surface of a Soil-Nailed Slope

For ease of construction, a typical soil nail consists of steel rebar (from 20 mm to 45 mm) in the middle of a drillhole and grouted by cement slurry with different diameters ranging from 100 mm to 250 mm, surrounded by soil mass. As shown in Figure 1, the soil nails in the vertical cross section of a slope are constructed uniformly with a specified vertical distance and a certain inclination angle. The lengths of these soil nails at different elevations are generally designed to be different according to the preliminary numerical simulation results conducted by designers. In this condition, the stability requirements can be satisfied by the mobilization of shear resistance on the soil-cement interface.

The averaged Young's modulus of a soil nail can be simplified as

$$E = \frac{E_s A_s + E_c A_c}{A_s + A_c}, \quad (4)$$

where E is the averaged Young's modulus of the steel rebar and surrounding cement slurry; E_s and E_c are the elastic moduli of steel rebar and cement grout, respectively; and A_s and A_c are the areas of the cross sections of steel rebar and concrete, respectively.

In this study, a series of bare FBG strain sensors with different peak wavelengths were multiplexed and mounted in a pregrooved surface of a soil nail. The axial force on the i th cross section of the soil nail can be expressed by

$$N_i = E \cdot (A_s + A_c) \cdot \varepsilon_i, \quad (5)$$

where N_i is the axial force at the measurement point and ε_i is the strain value measured by the i th FBG strain sensor.

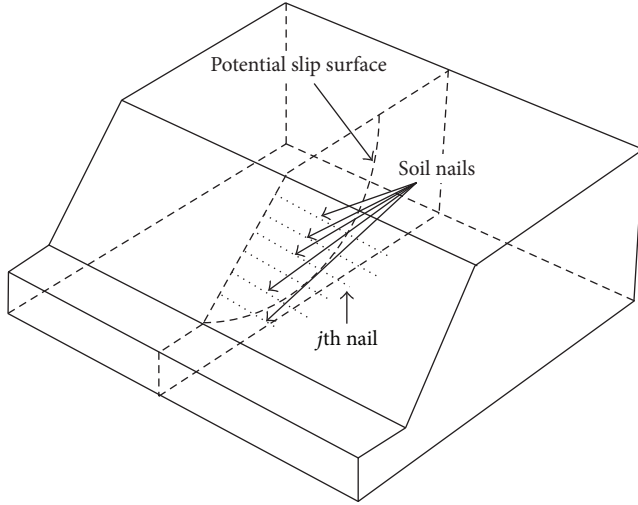


FIGURE 1: Schematic illustration of soil nails and potential slip surface in a soil-nailed slope.

In this study, the following assumptions are used.

- The potential slip surface goes through the soil nails at different elevations in the same section.
- The slip surface is assumed to be circular.
- The bending strains are neglected along the soil nails.

The objective of the optimal model is to search for the maximum sum of strains along these soil nails in the same cross section. In this optimal model, relative positions of soil nails and circular shape of potential slip surface can be taken as constraints. Thus, intersecting points between soil nails and circular potential slip surface can be specified using the optimal model.

The governing equation can be expressed by

$$\begin{aligned}
 & \text{Max} \quad \sum_{i=1}^n \varepsilon_i \\
 & \text{s.t.} \quad 0 \leq x_i \leq a_i \\
 & \quad \quad x_i < 0.5(x_{i-1} + x_{i+1}) \\
 & \quad \quad x_0^2 + y_0^2 = r^2 \\
 & \quad \quad (x_i - x_0)^2 + (y_i - y_0)^2 = r^2,
 \end{aligned} \tag{6}$$

where ε_i is the strain value measured on i th soil nail; x_0 and y_0 are the horizontal and the vertical coordinates of the centre of circular landslide, respectively; r is the radius of the potential circular slip surface; x_i and y_i are the vertical and horizontal coordinates of the interacting point between the potential slip surface and the i th soil nail, respectively; a_i and b_i are the horizontal and vertical coordinates of i th soil nail tip, respectively.

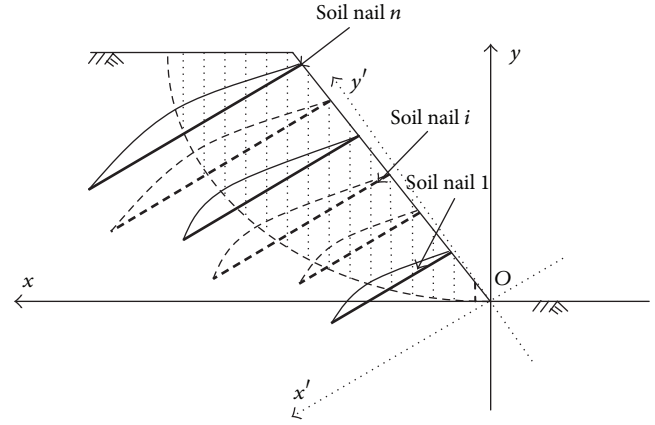


FIGURE 2: Cross section of a slope reinforced with soil nails.

4. Slope Stability Analysis Using Limit Equilibrium Method

To conduct slope stability analysis, the slope as shown in Figure 2 can be divided into slices. The coordinates of center of the potential slip surface and intersections between slip surface and soil nails can be transmitted into Cartesian coordinates by the Helmert transformation; that is,

$$\begin{aligned}
 x' &= x \cos \alpha + y \sin \alpha, \\
 y' &= x \sin \alpha + y \cos \alpha.
 \end{aligned} \tag{7}$$

Stress analysis of the slices is shown in Figure 3. In this figure, N_j is the gravitational force of the j th slice; N_i is the axial force of the i th soil nail at the j th slice; X_{j+1} is the friction force between the j th slice and the $(j+1)$ th slice; X_j is the friction force between the j th slice and the $(j-1)$ th slice; Y_j is the friction force between the slice and the bottom part.

In this paper, FBG sensors with sequent initial wavelengths were mounted along a precut groove surface of soil nails. Based on the measured strains along the soil nails, the axial force distribution of soil nails can be calculated. In a slope reinforcement project, soil nails were employed to reinforce these cut slopes according to the complex geological condition. In this study, three vertical sections were chosen. One cross section was chosen to calculate the factor of stability in this paper. Soil nails from the top to the bottom were signed as 1–6 in this section which are shown in Figure 4.

The monitored slope (220 m long and 42 m high) consists of heavily weathered granite. In the reinforcement engineering, the drillholes for soil nails are 110 mm in diameter. The composition of the steel-mortar body is designed as 110 mm in diameter. The steel rebar (32 mm or 28 mm in diameter) is HRB335, while the mortar is of Grade 30. The authors chose three cross sections, including 18 soil nails at three stages. Among them, the soil nails at the first stage (near to the slope toe) are 9 m in length. At the second and third stages, the soil nails and anchors are 12 m and 15 m in length, respectively. Three-strain and one-temperature sensors were installed onto the soil nails. Six soil nails were instrumented with FBG strain

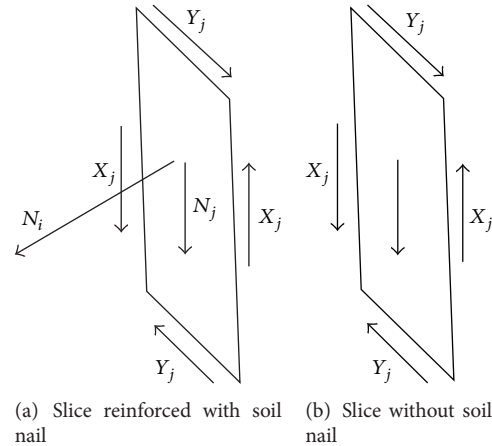


FIGURE 3: Slices with and without soil nail.

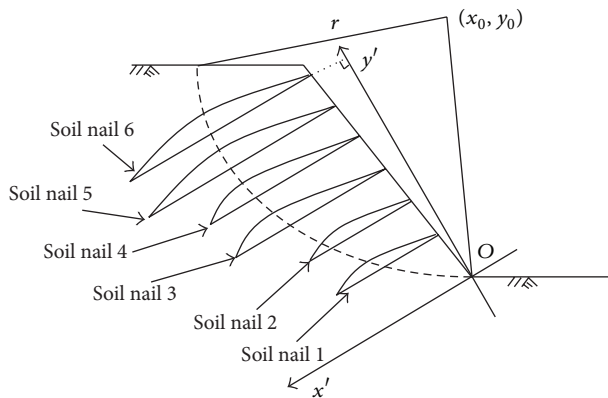


FIGURE 4: Schematic illustration of strain distributions on soil nails in a cross section of slope.

and temperature sensors which were used for temperature compensation.

The wavelengths of all FBG sensors have been collected for three times, from which the strain can be calculated compared with the recorded initial wavelengths. Temperature compensation can be achieved using the wavelength shifts measured by FBG temperature sensors. To fulfill the requirement of the optimal model, the strains along soil nails were fitted by polynomial functions at different collection times. Substituting these fitting polynomial equations into the optimal model, the radius of slip surface and coordinates of center of circular slip surface are simultaneously acquired. Once these landslide surfaces were searched, the calculated passive region can be divided into vertical slices as other classical theoretical methods. The axial forces are also applied on slices reinforced with soil nails which can be computed from the measured strains by the corresponding FBG strain sensors.

5. Conclusions and Suggestions

In this study, the optimal model combines limit equilibrium method with field monitoring results. The shape of slip

surface was assumed as an arc. FBG sensors were used to measure the strain along soil nails which was used to calculate the axial force of soil nails. This method can be used to evaluate a slope reinforced with soil nails. Compared to simulation results using other limit equilibrium methods, the calculated results based on the field monitoring data are more reliable. However, this newly proposed optimal method is a modified limit equilibrium method based on the assumptions including circular slip surface, maximum sum of strains and strain distribution fitting method. Further research is required to investigate the relationship between the measured strain values and the safety factor of the slope.

Acknowledgments

The work described in this paper was supported by grants from Shenzhen Science and Technology Innovation Committee (Project no. JCYJ20130329154442496), the National Natural Science Foundation of China (Project no. 41302217), and the National Basic Research Program of China (973 Program) (Project no. 2011CB710605), which are gratefully acknowledged.

References

- [1] C. Plumelle, F. Schlosser, P. Delage, and G. Knochenmus, "French national research project on soil nailing. Clouterre," in *Proceedings of the International Reinforced Soil Conference*, pp. 660–675, Glasgow, Scotland, June 1990.
- [2] F. Schlosser, C. Plumelle, P. Unterreiner, and J. Benoit, "Failure of full scale experimental soil nailed wall by reducing the nails lengths (French Research Project CLOUTEERE)," in *Proceedings of the International Conference on Earth Reinforcement Practice*, pp. 531–535, Fukuoka, Japan, 1992.
- [3] D. A. Bruce and R. A. Jewell, "Soil nailing: application and practice—part 1," *Ground Engineering*, vol. 19, no. 8, pp. 10–15, 1986.
- [4] D. A. Bruce and R. A. Jewell, "Soil nailing: application and practice—part 2," *Ground Engineering*, vol. 20, no. 1, pp. 21–33, 1987.

- [5] T.-H. Yi, H.-N. Li, and M. Gu, "Optimal sensor placement for structural health monitoring based on multiple optimization strategies," *The Structural Design of Tall and Special Buildings*, vol. 20, no. 7, pp. 881–900, 2011.
- [6] T. H. Yi, H. N. Li, and X. Y. Zhao, "Noise smoothing for structural vibration test signals using an improved wavelet thresholding technique," *Sensors*, vol. 12, no. 8, pp. 11205–11220, 2012.
- [7] H. F. Bai, T. H. Yi, H. N. Li, and L. Ren, "Multisensors on-site monitoring and characteristic analysis of UHV transmission tower," *International Journal of Distributed Sensor Networks*, vol. 2012, Article ID 545148, 10 pages, 2012.
- [8] Y. Q. Ni, X. W. Ye, and J. M. Ko, "Monitoring-based fatigue reliability assessment of steel bridges: analytical model and application," *Journal of Structural Engineering*, vol. 136, no. 12, pp. 1563–1573, 2010.
- [9] Y. Q. Ni, X. W. Ye, and J. M. Ko, "Modeling of stress spectrum using long-term monitoring data and finite mixture distributions," *Journal of Engineering Mechanics*, vol. 138, no. 2, pp. 175–183, 2012.
- [10] F. Schlosser, "Behaviour and design of soil nailing," in *Proceedings of the International Symposium on Recent Developments in Ground Improvement Techniques*, pp. 399–413, Bangkok, Thailand, 1982.
- [11] G. Franzen, *Soil nailing: a laboratory and field study of pull-out capacity [Doctoral thesis]*, Department of Geotechnical Engineering, Chalmers University of Technology, Göteborg, Sweden, 1998.
- [12] J. H. Yin, H. H. Zhu, W. Jin, A. T. Yeung, and L. M. Mak, "Performance evaluation of electrical strain gauges and optical fiber sensors in field soil nail pullout tests," in *Proceedings of the 27th HKIE Geotechnical Division Annual Seminar on Geotechnical Advancements in Hong Kong Since 1970s*, pp. 249–254, Hong Kong, 2007.
- [13] H. F. Pei, J. H. Yin, H. H. Zhu, and C. Y. Hong, "Monitoring performance of a glass fiber reinforced polymer soil nail during laboratory pullout test using FBG sensing technique," *International Journal of Geomechanics*, vol. 13, no. 4, pp. 467–472, 2013.
- [14] H. F. Pei, J. H. Yin, H. H. Zhu, C. Y. Hong, W. Jin, and D. S. Xu, "Monitoring of lateral displacements of a slope using a series of special FBG based in-place inclinometers," *Measurement Science and Technology*, vol. 23, no. 2, Article ID 025007, 2012.
- [15] H.-H. Zhu, J.-H. Yin, A. T. Yeung, and W. Jin, "Field pullout testing and performance evaluation of GFRP soil nails," *Journal of Geotechnical and Geoenvironmental Engineering*, vol. 137, no. 7, pp. 633–642, 2011.
- [16] H. H. Zhu, A. N. L. Ho, J. H. Yin, H. W. Sun, H. F. Pei, and C. Y. Hong, "An optical fibre monitoring system for evaluating the performance of a soil nailed slope," *Smart Structures and Systems*, vol. 9, no. 5, pp. 393–410, 2012.
- [17] A. W. Bishop, "The use of the slope circle in the stability analysis of slopes," *Geotechnique*, vol. 5, no. 1, pp. 7–17, 1955.
- [18] N. R. Morgenstern and V. E. Price, "The analysis of the stability of general slip surfaces," *Geotechnique*, vol. 15, pp. 79–93, 1965.
- [19] N. Janbu, *Slope Stability Computations*, Soil Mechanics and Foundations Engineering Report, The Technical University of Norway, Trondheim, Norway, 1968.
- [20] R. Baker and M. Garber, "Theoretical analysis of the stability of slopes," *Geotechnique*, vol. 28, no. 4, pp. 395–411, 1978.
- [21] W. F. Chen, *Limit Analysis and Soil Plasticity*, Elsevier, New York, NY, USA, 1975.
- [22] Y.-J. Wang, J.-H. Yin, and C. F. Lee, "The influence of a non-associated flow rule on the calculation of the factor of safety of soil slopes," *International Journal for Numerical and Analytical Methods in Geomechanics*, vol. 25, no. 13, pp. 1351–1359, 2001.
- [23] J. Chen, J.-H. Yin, and C. F. Lee, "Upper bound limit analysis of slope stability using rigid finite elements and nonlinear programming," *Canadian Geotechnical Journal*, vol. 40, no. 4, pp. 742–752, 2003.
- [24] J. Chen, J.-H. Yin, and C. F. Lee, "A three-dimensional upper bound approach to slope stability analysis using rigid finite elements: improvement, verification and application," *Geotechnique*, vol. 55, no. 7, pp. 547–556, 2005.
- [25] K. O. Hill, Y. Fujii, D. C. Johnson, and B. S. Kawasaki, "Photosensitivity in optical fiber waveguides: application to reflection filter fabrication," *Applied Physics Letters*, vol. 32, no. 10, pp. 647–649, 1978.
- [26] G. Meltz, W. W. Morey, and W. H. Glenn, "Formation of Bragg gratings in optical fibers by a transverse holographic method," *Optics Letter*, vol. 14, no. 15, pp. 823–825, 1989.
- [27] A. Othonos and K. Kalli, *Fiber Bragg Gratings: Fundamentals and Applications in Telecommunications and Sensing*, Artech House, Boston, Mass, USA, 1999.

Research Article

Field Measurement of Wind Speeds and Wind-Induced Responses atop the Shanghai World Financial Center under Normal Climate Conditions

Yong Quan, Shuai Wang, Ming Gu, and Jun Kuang

State Key Laboratory of Disaster Reduction in Civil Engineering, Tongji University, Shanghai 200092, China

Correspondence should be addressed to Ming Gu; minggu@tongji.edu.cn

Received 8 September 2013; Revised 15 November 2013; Accepted 15 November 2013

Academic Editor: Ting-Hua Yi

Copyright © 2013 Yong Quan et al. This is an open access article distributed under the Creative Commons Attribution License, which permits unrestricted use, distribution, and reproduction in any medium, provided the original work is properly cited.

Field measurement data on wind velocities and wind-induced acceleration responses at the top of the 492 m high Shanghai World Financial Center (SWFC) under normal climate conditions are studied. Characteristics of the mean wind speeds and turbulence intensities, gust factors, power spectral densities, and turbulence integral scales of the fluctuating wind speed are analyzed in different observation time intervals. Power spectral densities of wind-induced acceleration are also investigated. The basic natural frequencies and structural damping ratios of the building are identified based on Hilbert-Huang transform method and random decrement method. The field measurement results of wind-induced responses of the SWFC are finally compared with those from the corresponding high-frequency force balance wind tunnel test study.

1. Introduction

Field measurement of wind velocities and wind-induced responses is an essential aspect of wind engineering. In 1960, a field measurement study on mean wind speed at different heights and time intervals was conducted by Durst [1], who also proposed an empirical formula for different terrain categories. A long-term observation of wind speeds and wind directions with ultrasonic anemometers in Tokyo and Yokohama was performed by Choi [2] and Kato et al. [3]. Several databases on local wind characteristics, for example, the offshore observation databases in Canada and the United Kingdom [4, 5] and the Froya database in Norway [6, 7], were established successively with field measurement data. The characteristics of the mean and fluctuating wind velocity of typhoon Muifa were analyzed by An et al. [8] through field measurement at the top of the Shanghai World Financial Center. The field measurement data of the wind-induced responses at the top of a 254 m high bridge tower was researched by Larose et al. [9] and compared with the corresponding wind tunnel test study results in frequency domain. The dynamic characteristics of a 200 m high building were identified from its field measured wind-induced vibration data by Li et al. [10], and then the correlation between

structural damping and acceleration responses was discussed. Field measurements of the strong wind characteristics and wind-induced responses at the 384 m high Shenzhen Diwang Mansion and the 420.5 m high Shanghai Jin Mao Tower were conducted by Xu and Zhan [11] and Li et al. [12], respectively, and relevant empirical formulas were fitted. Field measured acceleration responses under strong winds at the 391 m high Guangzhou Citic Tower and the 450 m high Guangzhou West Tower were shown by Fu et al. [13, 14] and compared with the corresponding wind tunnel test. Bai et al. [15] studied the wind velocity, acceleration responses, and base bending strains on parts of a transmission tower. Yi et al. [16] and Li et al. [17] applied GPS technology to field measurement of high-rise structures and studied the displacement responses.

The previous studies on the field measured wind speeds and wind-induced responses were mainly focused on typhoon climate conditions, while those under normal climate conditions were barely found. Based on the wind speed and wind-induced acceleration responses measured by the structural health monitoring system (SHMS) installed on the SWFC, the mean and fluctuating wind speeds at a level near 500 m under normal climate conditions are thus analyzed in the present study. The maximum wind speeds



FIGURE 1: Panorama of SWFC.

and the turbulence characteristics for different observation time intervals are discussed. Frequency domain and time-frequency domain analysis of the field measured acceleration responses at the topmost part of the SWFC are also conducted. The dynamics of the building are identified with random decrement method (RDM). The wind-induced acceleration responses from the field measurement are compared with those from the corresponding high-frequency force balance (HFFB) wind tunnel test study. Some conclusions are drawn based on the results.

2. Field Measurement Profile

Figure 1 presents the structural health monitoring system installed in the SWFC, which mainly consists of a wind velocity monitoring system and a structural vibration monitoring system. The wind velocity monitoring system is installed on the northeast and southwest end of the top of the building at a level of 495 m high from the ground (Figure 2). As shown in Figure 3, each side has a Windmaster Pro triaxial ultrasonic anemometer (Gill Co. Ltd, UK). The distance between the two sites of instruments is 72 m. The x -, y -, and z -axes of the anemometer face the north, west, and upward direction, respectively (Figure 4). The wind angle increases along the counterclockwise direction; thus, the measured wind velocity is 0° for the south wind and 90° for the east wind. Since they are exposed outdoors, the anemometers might be influenced by the climate like rainfall and temperature. The equipment used here has a permissible rainfall less than 300 mm/hr, and the operating temperature is between -40 and 70° . Thus, the data collection is reliable under normal climate conditions. The measuring range of the anemometer is from 0.01 m/s to 65 m/s. The maximum dynamic response frequency is 40 Hz and the actual sampling frequency is 10 Hz. All the data are collected in real time and stored by using the CR1000 data collection system (Campbell Co. Ltd, USA). In order to prevent the anemometers from being struck by lightning,

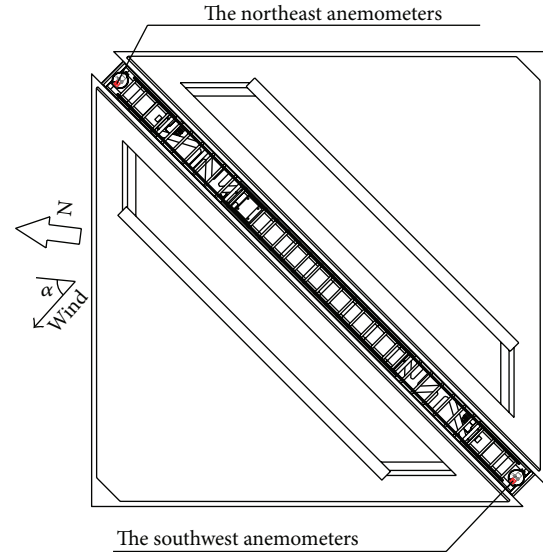


FIGURE 2: Sketch of location of the anemometers.



FIGURE 3: Windmaster Pro ultrasonic anemometer.

the anemometers are installed on the beam and fixed on the lightning rod with a flange on each side of the topmost part of the building. Meanwhile, the anemometers are several meters higher than the top of the building to reduce the effects of the building itself, and CFD method was used to identify its effective angles.

Computational fluid dynamics simulation of the wind field around the target building shows that the mean and fluctuating wind speeds approaching the building are influenced by the building itself. However, the influences are negligible when the included angle between the approaching wind and the y -axis of the building is smaller than 15° (Figure 5), and those angles are defined as the effective wind angle. Effective wind angle ranges at the northeast and southwest ends are 120° to 150° and 300° to 330° , respectively. The following analyzed samples are those whose 10 min mean wind speeds

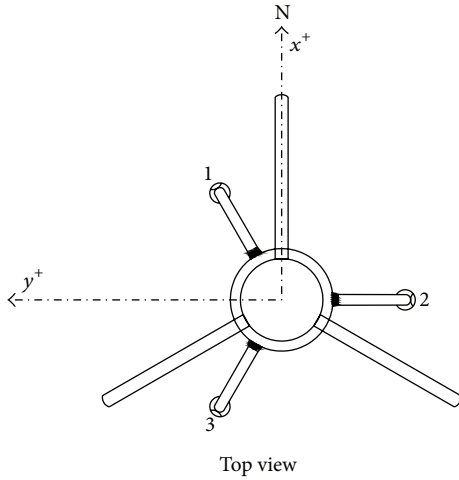


FIGURE 4: Definition of x - and y -axes of the anemometer.

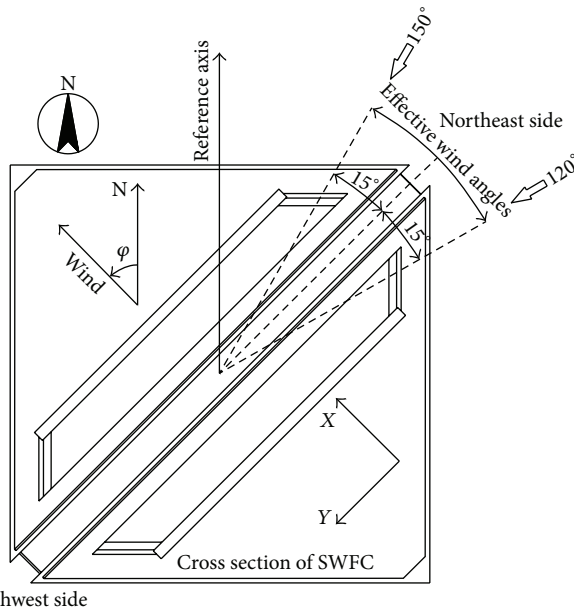


FIGURE 5: Sketch of axes directions of the building, effective range of wind angles, and definition of wind angles.

are relatively large (over 8 m/s) and wind angles are in the effective wind angle ranges.

The acceleration data are measured by the acceleration sensors installed on the 98th floor of the building (475 m). The acceleration sensors are SLJ-100 balance accelerometer produced by China Earthquake Administration. The basic frequency of the accelerometer is 100 Hz, the measurement range is $\pm 2g$, and the frequency band is 0–100 Hz. The two horizontal normal axes of the sensors are parallel to the body axes of the building (Figure 5). Vibration signals are simultaneously measured from the three orthogonal directions by the sensors. Two different groups of wind-induced responses data with a length of 10 min are selected for further analysis. In those two data groups, the mean wind

speed and the corresponding mean wind angle are 16.33 m/s, 139° and 9.48 m/s, 123° , respectively. Apparently, the mean wind angles fall in the effective wind angle range at the northeast end.

3. Characteristics of Wind Speed

The characteristics of the measured mean and fluctuating wind speeds are analyzed in this section. The wind velocity samples are shown at first. Then, the mean wind speeds under different average time intervals are analyzed. The turbulence intensity, gust factors, and turbulence scales of the fluctuating wind speeds are also discussed.

3.1. Mean Wind Speed. Three orthogonal components of wind speed, $u_x(t)$, $u_y(t)$, and $u_z(t)$, are measured simultaneously with the ultrasonic anemometers from the three directions of the x -, y -, and z -axes, respectively. Ignoring the vertical component, $u_z(t)$, the mean wind speeds, U , and directions, ϕ , are calculated through the vector splitting method as follows:

$$U = \sqrt{\overline{u_x(t)^2} + \overline{u_y(t)^2}}, \tag{1}$$

$$\cos(\phi) = \frac{\overline{u_x(t)}}{U}, \quad \sin(\phi) = \frac{\overline{u_y(t)}}{U}.$$

The longitudinal and lateral fluctuating components, $u(t)$ and $v(t)$, are calculated with the following formula, respectively:

$$u(t) = u_x(t) \cos \phi + u_y(t) \sin \phi - U, \tag{2}$$

$$v(t) = -u_x(t) \sin \phi + u_y(t) \cos \phi.$$

The analyzed samples are collected from the anemometers at the southwest and northeast ends of the SWFC rooftop (Table 1).

Figure 6 shows the maximum values of mean wind speeds in 1 hr with the durations of 3 s, 10 min, and 1 hr, respectively, and the mean wind angles with a duration of 1 hr. The mean wind angle has no apparent change within the analytical time intervals. The maximum values of mean wind speeds within 1 hr decrease with the increase of the durations, but the maximum 10 min wind speeds within 1 hr are close to the mean wind speed of 1 hr.

Figures 7 and 8 show the relationship between the maximum 10 min mean wind speeds within 1 hr and the 1 hr mean wind speed, as well as that between the maximum 3 s mean wind speeds within 10 min and the 10 min mean wind speeds, respectively. The figures also show a linear fitting in which the length of the error bar in Figure 7 represents the standard deviation, and the fitting demonstrates a good result. As shown in Figure 7, the ratio of the maximum 10 min mean wind speeds within 1 hr and the 1 hr mean speed is approximately 1.04. In most cases, the standard deviation of the maximum 10 min mean wind speeds within 1 hr does not exceed 1 m/s. In Figure 8, the correlation between the

TABLE 1: Record of measured samples.

Location	Date	Recording time	Recording duration (min)	The maximum 10 min mean wind speed (m/s)
Southwest side	February 13, 2009	4:50:00 to 10:49:59	360	21.78
	December 9, 2008	0:00:00 to 9:59:59	600	14.37
Northeast side	February 15, 2009	14:00:00 to 23:59:59	600	15.17
	November 16, 2009	14:00:00 to 17:59:59	240	16.36
	November 9 and 10, 2009	22:20:00 (November 9) to 6:19:59 (November 10)	480	16.97

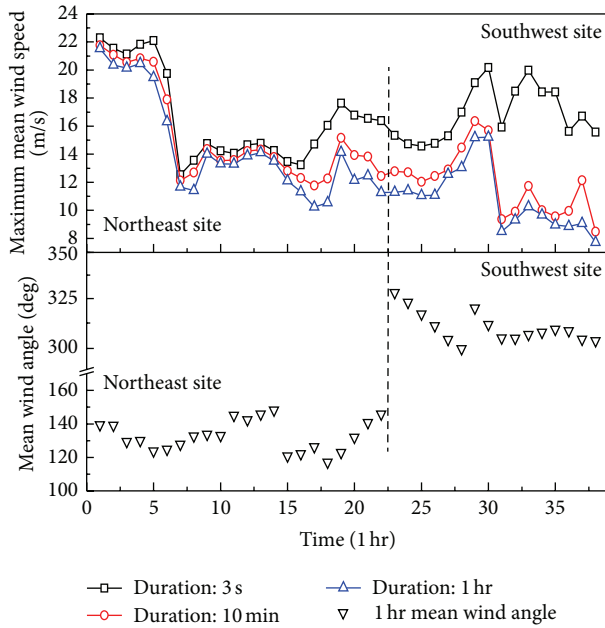


FIGURE 6: Maximum mean wind speeds in 1 hr for different durations and 1 hr mean wind directions.

maximum 3 s mean wind speeds within 10 min (instant maximum wind speed) and the 10 min mean wind speeds can be expressed as $y = 0.85x + 4.5$.

3.2. Fluctuating Wind Speeds

3.2.1. Turbulence Intensity and Gust Factor. Turbulence intensity is defined as the ratio of the standard deviation and the mean values of the approaching wind speeds. The analyzed time interval is 10 min (all average time intervals mentioned subsequently are 10 min, unless specified otherwise). The turbulence intensity is calculated as follows:

$$I_i = \frac{\sigma_i}{U} \quad (i = u, v), \quad (3)$$

where σ_i is the standard deviation of the fluctuating wind speeds; u and v represent the longitudinal and lateral components of the fluctuating wind speeds, respectively.

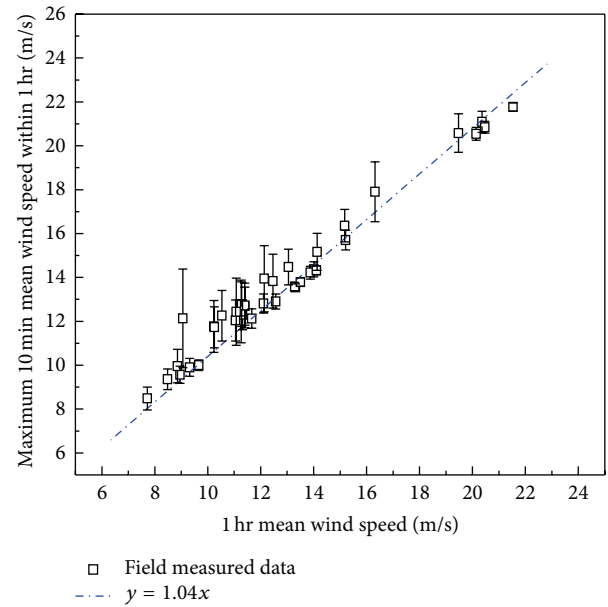


FIGURE 7: Maximum 10 min mean wind speeds versus 1 hr mean wind speeds.

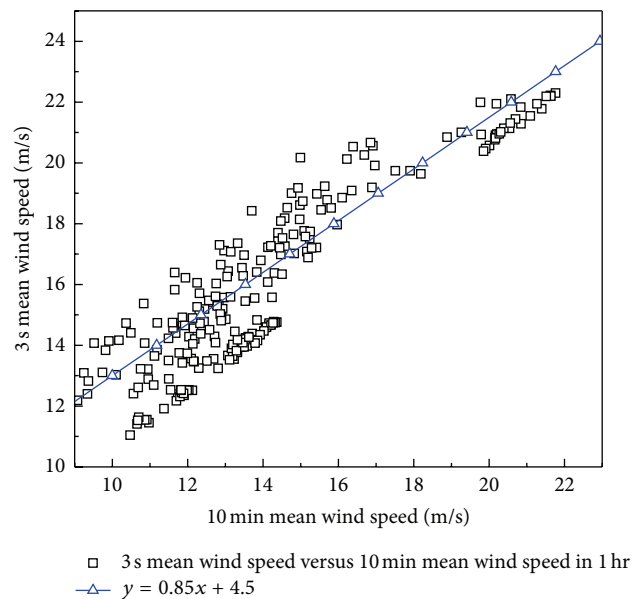


FIGURE 8: Maximum 3 s mean wind speeds versus 10 min mean wind speeds.

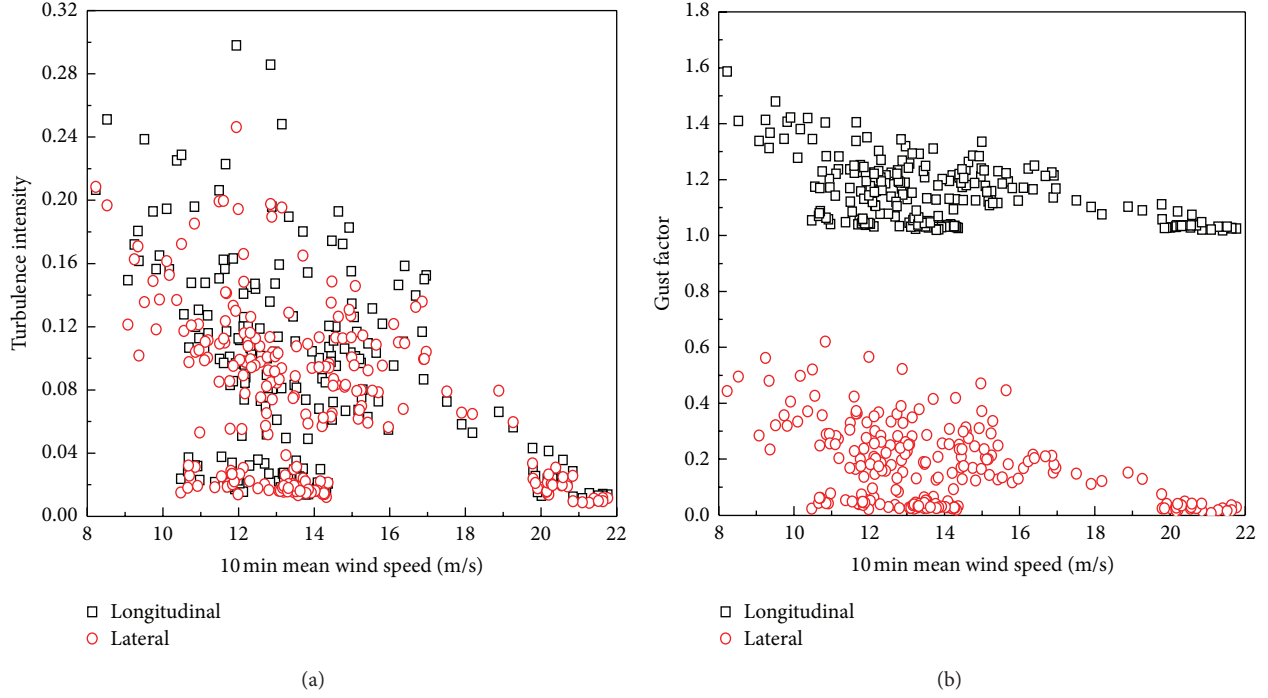


FIGURE 9: Relationships among turbulence intensities, gust factors, and 10 min mean wind speeds. (a) Turbulence intensities versus mean wind speeds and (b) gust factors versus mean wind speeds.

Gust factor is defined as the ratio of the maximum wind speed within the gust duration, t_g , and the 10 min mean wind speeds U , which can be expressed as

$$G_u(t_g) = 1 + \frac{\max(\overline{u(t_g)})}{U}, \quad G_v(t_g) = \frac{\max(\overline{v(t_g)})}{U}, \quad (4)$$

where $\max(\overline{u(t_g)})$ and $\max(\overline{v(t_g)})$ represent the maximum mean wind speeds of the longitudinal and lateral fluctuating wind speeds, respectively, within the gust duration time t_g (s) during the observation time interval.

Figures 9(a) and 9(b) illustrate the relationships between turbulence intensities and the 10 min mean wind speeds as well as between the gust factors and the 10 min mean wind speeds, respectively. The longitudinal and lateral turbulence intensities both decrease as the mean wind speeds increase (Figure 9(a)). The longitudinal turbulence intensity is in $[0.01, 0.30]$ and the mean value is 0.085. The lateral turbulence intensity is in $[0.01, 0.25]$ and the mean value is 0.075. The ratio of those two values is $\bar{I}_u : \bar{I}_v = 1 : 0.88$. The longitudinal turbulence intensity recommended by AIJ [18] for the same terrain category (V type) and the same height (495 m) is 0.11 and that based on the Chinese load code [19] is 0.12. As shown in Figure 9(b), the longitudinal and lateral gust factors both decrease as the 10 min mean wind speeds increase. Regulations of turbulence intensity and gust factors were also found by Fu et al. [13] through field measurement of a 391 m high-rise building in south China under typhoon condition. Then, the gust factors remain almost the same after

the mean wind speed reaches approximately 20 m/s. When the gust duration time t_g is equal to 3 s, the longitudinal gust factor \bar{G}_u is in $[1.02, 1.59]$ and the mean value is 1.15; the lateral gust factor \bar{G}_v is in $[0.01, 0.62]$ and the mean value is 0.17, $\bar{G}_u : \bar{G}_v = 1 : 0.15$.

Figure 10 shows the correlation between the longitudinal gust factor and the turbulence intensity as well as between the lateral gust factor and the turbulence intensity for a gust duration time of $t_g = 3$ s. The longitudinal and lateral gust factors both increase as the turbulence intensity increases. A linear fitting is shown for the relationship between the turbulence intensity and the gust factor. Then, based on a previous study [20], a nonlinear fitting is used in accordance with the following formula:

$$G_u(t_g) = 1 + k_1 \times I_u^{k_2} \ln\left(\frac{T}{t_g}\right), \quad (5)$$

where T represents the mean time interval. Choi [21] defined T as 1 hr and suggested that $k_1 = 0.62$ and $k_2 = 1.27$. As shown in Figure 10, the linear fitting relations between the longitudinal gust factors and turbulence intensity as well as between the lateral gust factors, and turbulence intensity are $G_u = 1 + 1.6 I_u$ and $G_v = 2.4 I_v$, respectively. The results of the linear and nonlinear fitting are almost similar, which implies that the gust factor and turbulence intensity have a linear relationship. By comparing the measurement results, the empirical formula proposed by Choi [21], as well as the linear and nonlinear fitting, the measured results of the gust factors and the results from the said empirical formula are relatively close when the turbulence intensity is smaller than

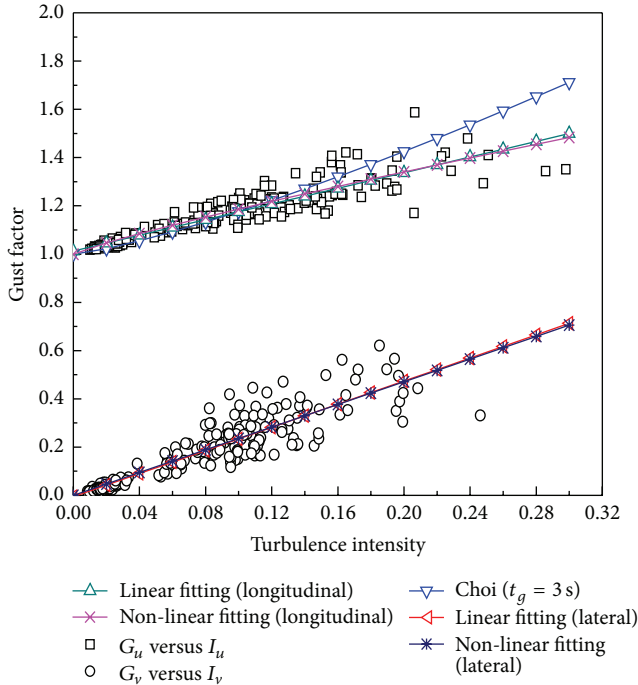


FIGURE 10: Turbulence intensities versus gust factors.

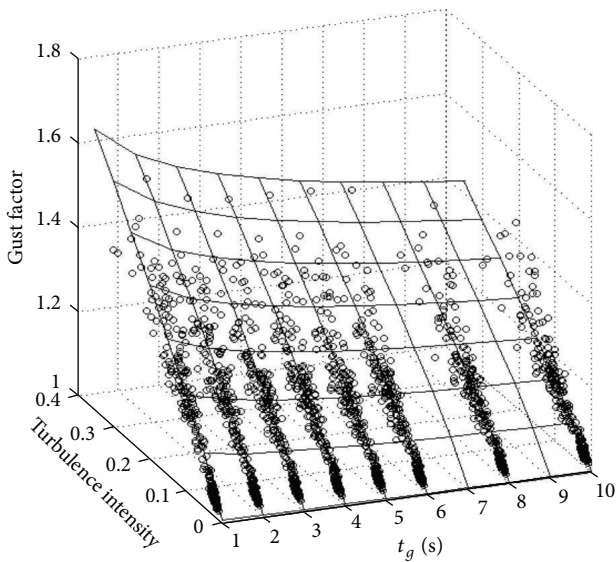


FIGURE 11: Correlations between longitudinal gust factors and turbulence intensities in various durations.

0.16. When the turbulence intensity is over 0.16, the measured gust factors are smaller than the calculated ones.

Figures 11 and 12 show the correlation between gust factors and turbulence intensities in various duration times for longitudinal and lateral components of the approaching wind, respectively. Both figures adopt three-dimensional coordinates to show the longitudinal and lateral measured results with hollow round dots. The nonlinear fitting results of formula (5) are also shown in those figures with solid lines. The fitting result of the relationship between the longitudinal

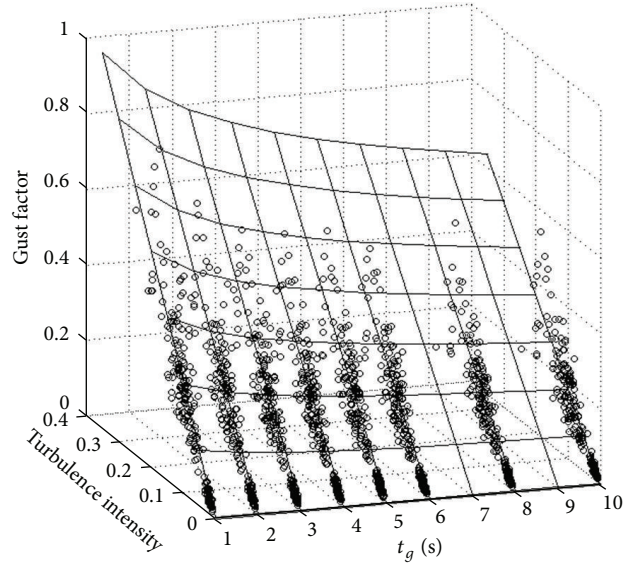


FIGURE 12: Correlations between lateral gust factors and turbulence intensities in various durations.

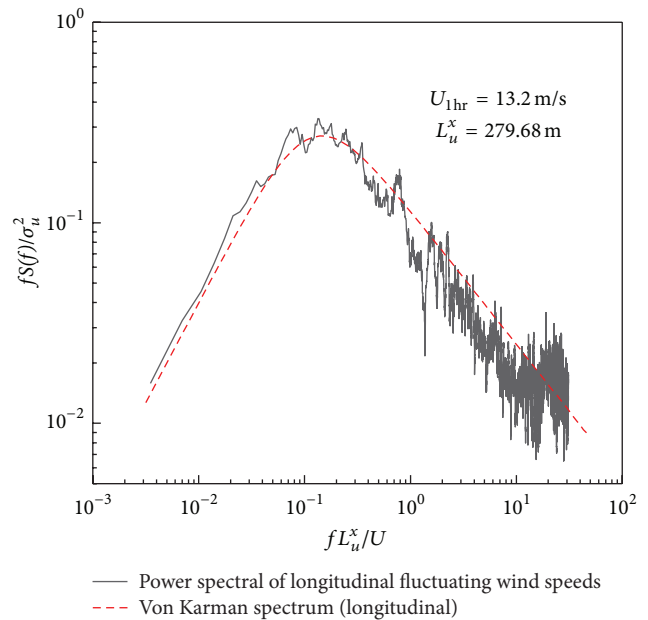


FIGURE 13: PSD of longitudinal fluctuating wind speeds.

gust factors and the turbulence intensities is $G_u = 1 + 0.26 I_u^{0.87} \ln(600/t_g)$. The fitting result of the relationship between the lateral gust factors and turbulence intensities is $G_v = 0.44 I_v \ln(600/t_g)$. When turbulence intensities remain constant, the gust factors decline as the gust duration time t_g increases.

3.2.2. *The Power Spectral Density of Fluctuating Wind Speeds.* Figures 13 and 14 show the power spectral densities of the longitudinal and lateral fluctuating wind speeds of the field measurement, which is almost matched with the von Karman spectra. However, not all power spectral densities

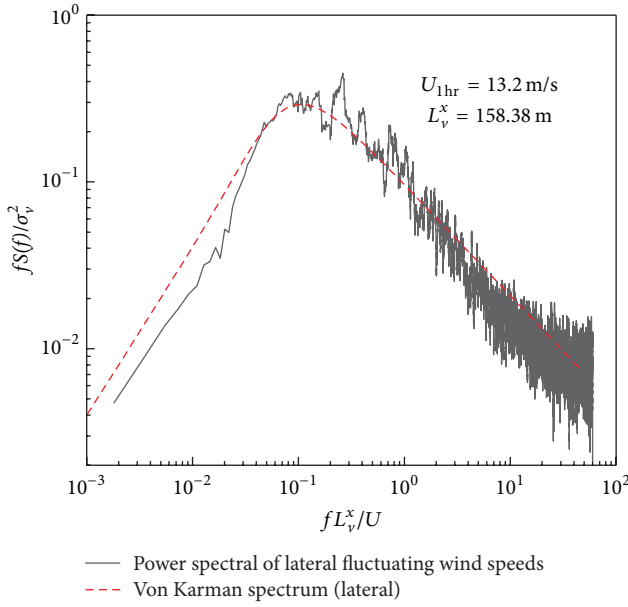


FIGURE 14: PSD of lateral fluctuating wind speeds.

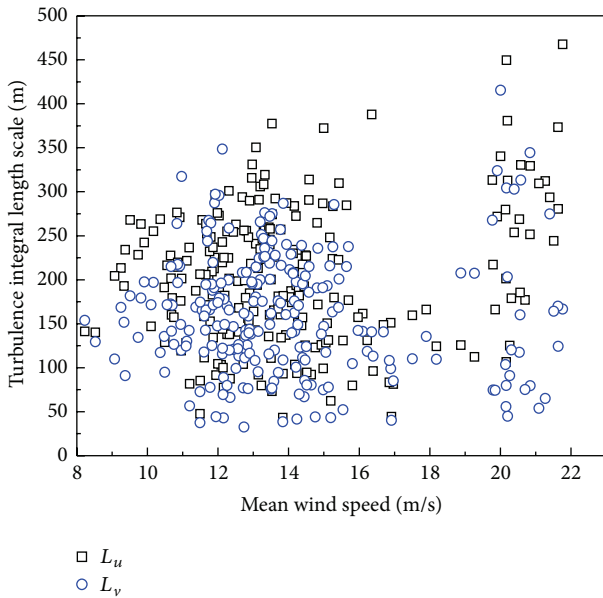


FIGURE 15: Turbulence integral scales versus 10 min mean wind speeds.

of measured fluctuating wind speeds are in accordance with the von Karman spectra, particularly if the mean wind speeds are over 20 m/s. In the power spectral densities of the fluctuating wind speed, both longitudinal and lateral components at high frequency severely deviate from the von Karman spectra and exhibit an uptrend characteristic. Similar phenomenon that power spectral densities match well with the von Karman spectrum at low wind speeds and are uptrend at high wind speeds was also found in the research of Fu et al. [14] at a 450 m high-rise building in south China. The deviation and uptrend characteristic may be caused by

the nonstationary original data. Since fast Fourier transform (FFT) is effective only for stationary data, the power spectral density determined through FFT method cannot reflect the overall characteristics of the original data.

3.2.3. *Turbulence Integral Scale.* The turbulence integral scale can be expressed as follows:

$$L_i^x = \frac{US_i(0)}{2\sigma_i^2} \quad (i = u, v, w), \quad (6)$$

where $S_i(0)$ is the value that corresponds to the power spectral density of the u , v , and w components of approaching wind speed for a frequency of 0.

Figure 15 shows the relationship between turbulence integral scales and the 10 min mean wind speeds for longitudinal and lateral components of approaching wind. Longitudinal and lateral turbulence integral scales have an increasing trend as the mean wind speeds increase. This trend was also found by Li et al. [10] in the typhoon measurement on the top of Jin Mao building, which is close to SWFC. The mean values of the longitudinal and lateral turbulence integral scales are $\bar{L}_u^x \approx 200$ m and $\bar{L}_v^x \approx 160$ m, respectively. Thus, $\bar{L}_u^x : \bar{L}_v^x = 1 : 0.8$.

4. Acceleration Response of the Building in Normal Climate Wind and Identification of Dynamic Parameters

The time histories and the power spectral densities of the acceleration responses for strong wind in normal climate are discussed at first in this section. Then, time-frequency analysis is conducted with the Hilbert-Huang transform (HHT) method. The dynamic characteristics of the building, that is, basic mode frequency and structural damping ratio, are identified by using the random decrement method. The dynamic characteristics identified from various methods are compared with one another and with the finite element analysis results. Finally, the acceleration responses from the field measurement are analyzed and compared with those from the corresponding wind tunnel test.

4.1. *Time History of Acceleration Response.* Figures 16 and 17 show the time histories of acceleration responses with particular wind speeds. The lateral wind-induced accelerations (X direction) are significantly larger than the longitudinal ones (Y direction). As shown in Figure 16, both lateral and longitudinal acceleration responses are relatively slight during the first 5 min, but the lateral responses increase sharply in the last 5 min. According to wind velocity records, the increase may be caused by the difference of the wind directions between the first and last 5 min. During the first 5 min, the included angle between the approaching wind and the y -axis of the building is 7° . However, it is 0° in the last 5 min when the vibration in the X direction (lateral direction) is stronger.

In another record of wind-induced acceleration responses as shown in Figure 17, there is no apparent difference between

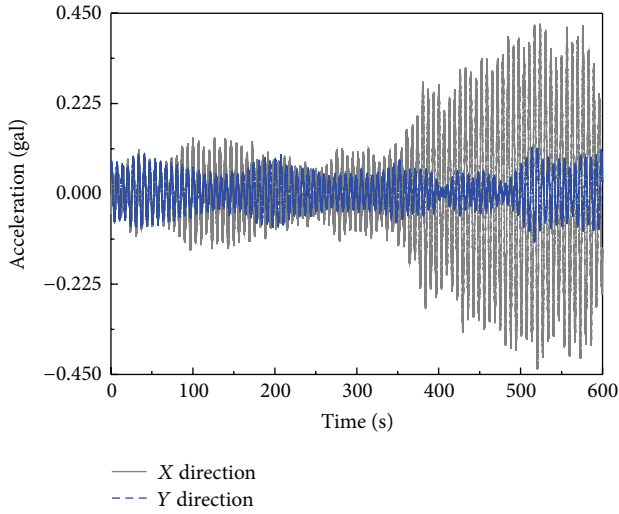


FIGURE 16: Time histories of acceleration responses with a 9.48 m/s wind speed.

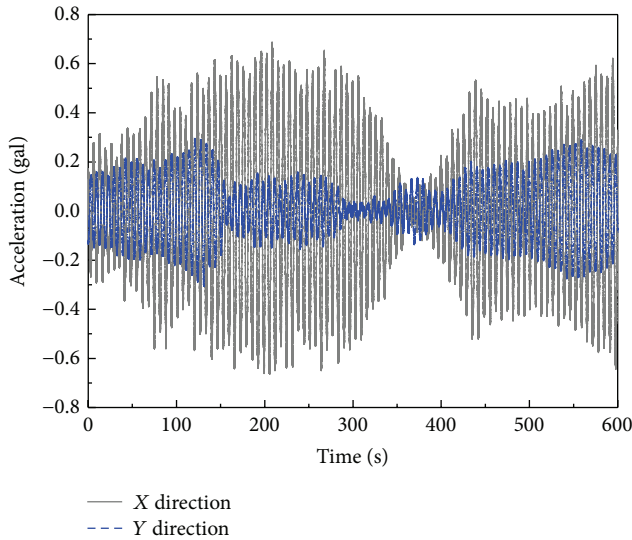


FIGURE 17: Time histories of acceleration responses with 16.33 m/s wind speed.

the first and last 5 min. Both mean wind speeds and wind directions during the two time intervals have no obvious change.

4.2. Power Spectral Density of Acceleration Response. Figures 18, 19, 20, and 21 present the power spectral densities of the measured acceleration responses in X and Y directions on the 98th floor of the building. The wind-induced vibrations are mainly contributed by the vibrations of the basic modes in structural X and Y directions. The natural vibration frequencies of those two basic modes are close to each other. For example, when the wind speed is 16.33 m/s, the natural vibration frequencies in X and Y directions identified from the power spectral densities are 0.154 Hz and 0.153 Hz, respectively. The responses of the several high-order modes

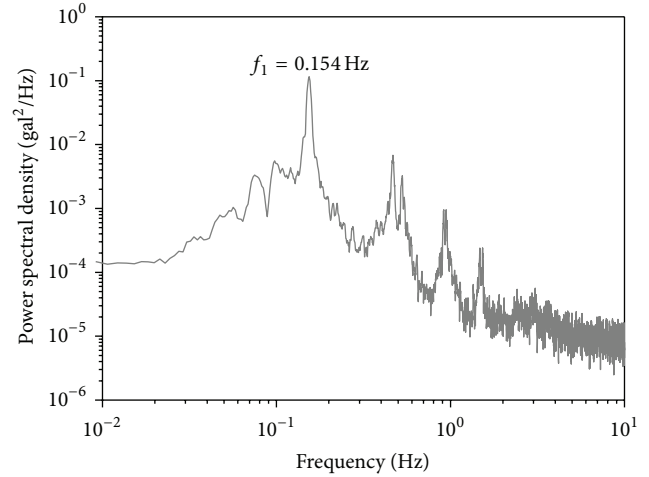


FIGURE 18: PSD of acceleration responses in X direction with 16.33 m/s wind speed.

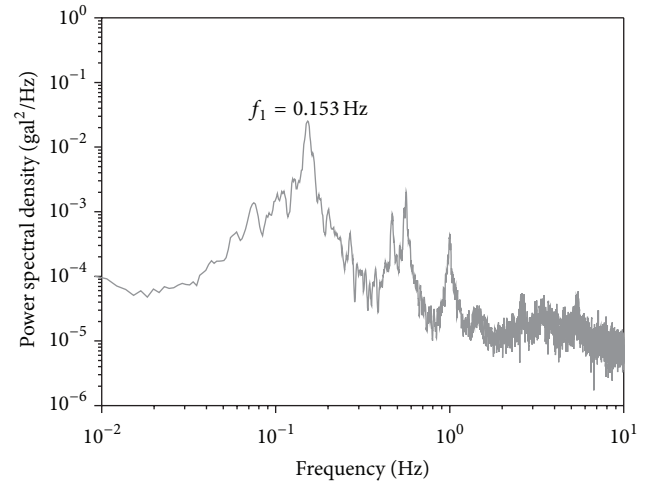


FIGURE 19: PSD of acceleration responses in Y direction with 16.33 m/s wind speed.

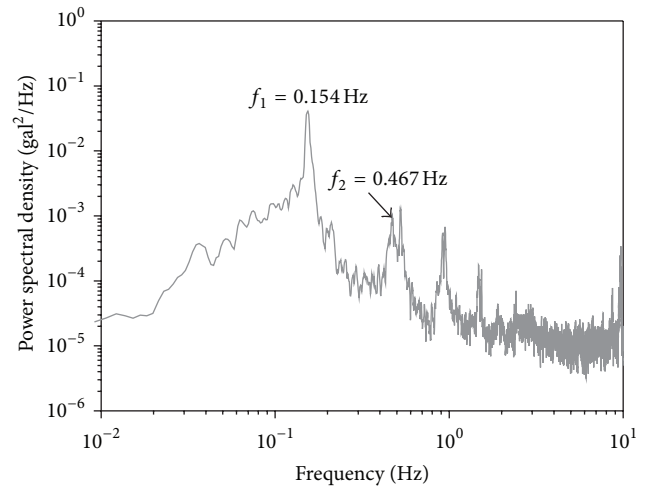


FIGURE 20: PSD of acceleration responses in X direction with 9.48 m/s wind speed.

TABLE 2: Natural vibration frequency of SWFC (Hz).

Mode	Finite element method	Measured results		
		FFT method	HHT method	RDM method
First-order bending in Y direction	0.146	0.153	0.152	0.153
First-order bending in X direction	0.153	0.154	0.152	0.155
Second-order bending in X direction	0.465	0.467	0.468	—
Second-order bending in Y direction	0.481	0.468	0.469	—

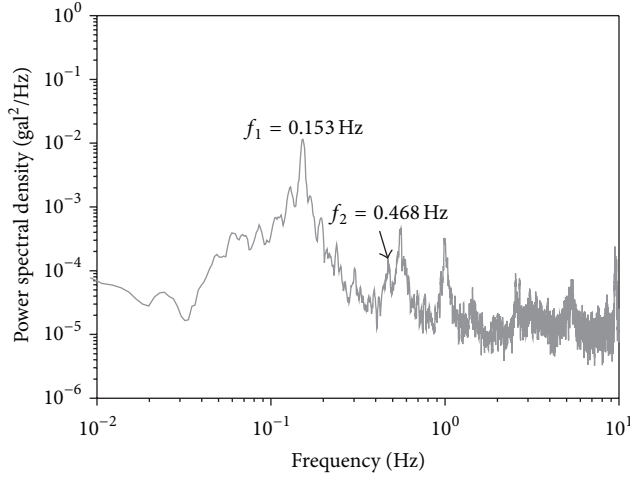


FIGURE 21: PSD of acceleration responses in Y direction with 9.48 m/s wind speed.

are perceptible in the power spectral densities, while they are negligible because of the significance of contributions from the basic modes.

4.3. Time-Frequency Analysis of Acceleration Response. Time-frequency analysis of the acceleration responses is conducted on several periods with the HHT method [22]. Based on the HHT analysis, the measured record of acceleration responses corresponding to the fastest 10 min mean wind speed (16.33 m/s) is picked out for the following analysis. Empirical mode decomposition (Figures 22 and 23) is conducted at first. The intrinsic mode functions (IMF) of the first six orders have narrow ranges and high-frequency components but have narrow ranges and low-frequency components in the eleventh to thirteenth orders. Figure 24 shows that the original signals match well with the superposition of IMF in the eighth to tenth orders. Figure 25 indicates that in the low-frequency domain, the power spectral densities of the superimposed IMF in the eighth to tenth orders almost match those of the original data. The matched power spectral densities can effectively reflect the frequency domain characteristics in the first five orders of the building. When the frequency is over 2 Hz, the difference is more apparent because the high-frequency component is filtrated by the IMFs of the eighth to tenth orders.

Figure 26 shows the time-frequency series of acceleration responses. The Hilbert-Huang marginal spectra of acceleration signal in the field measurement are presented in Figure 27. The basic mode frequency in the X direction is 0.152 Hz and 0.468 Hz for the second mode.

4.4. Identification of Dynamic Structural Characteristics in Time Domain. The random decrement method (RDM) [23], a time averaged method, is adopted to identify the natural frequencies and structural damping ratios of the basic mode in X and Y directions of the building.

Figures 28 and 29 show the identified results of the basic natural frequencies and damping ratios in X and Y directions versus the intercepting threshold values. The basic natural frequencies in X and Y directions are 0.155 Hz and 0.153 Hz, respectively, which change hardly with the increase of the intercepting threshold values. When the intercepting thresholds reach a certain value, the damping ratios are almost constant. The values in X and Y directions fluctuate at approximately 2.4% and 1.6%, respectively. The difference of those two values may be attributed to the dissimilar foundation in X and Y directions, which may be caused by the construction of the Shanghai Center Building located in the southwest side of the target building. Therefore, the soil-structure interaction changes the wind-induced responses of SWFC [24] and thus affects the identification of its damping ratios.

Finite element model was established in a former seismic review of SWFC. The profile and vibration mode in Y and X directions of that model are shown in Figure 30. The translational vibration modes of the first two orders according to finite element analysis are in the Y and X directions, and the corresponding basic mode frequencies are 0.146 Hz and 0.153 Hz [25]. Table 2 lists the results of the finite element analysis and this field measurement. The natural frequencies of the first two orders identified by the power spectral density, HHT marginal spectra, and RDM match the natural frequencies from the finite element analysis.

5. Comparison between Field Measured Wind-Induced Responses and Those from HFFB Wind Tunnel Test Study

The Boundary Layer Wind Tunnel Laboratory at the University of Western Ontario, Canada, once conducted a wind tunnel test on SWFC by using the HFFB technology [26]. The laboratory defined two test cases as the present one and the

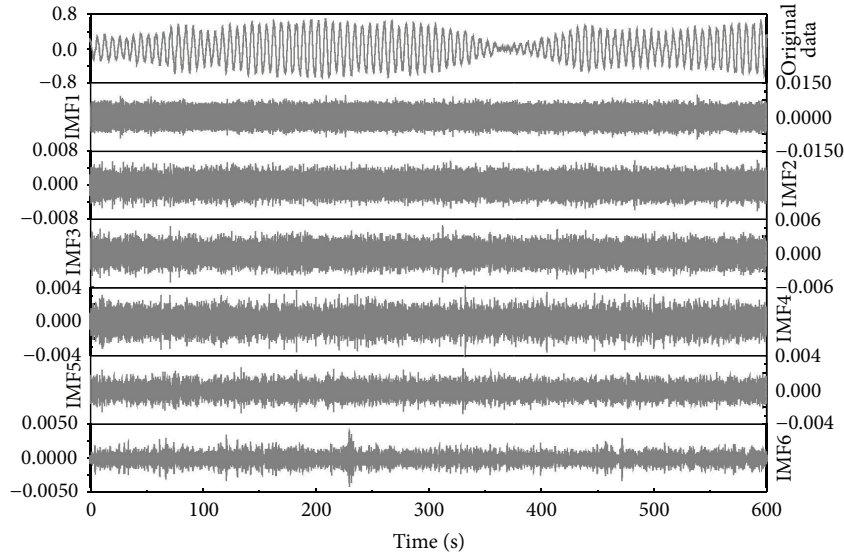


FIGURE 22: IMFs of the first to sixth orders.

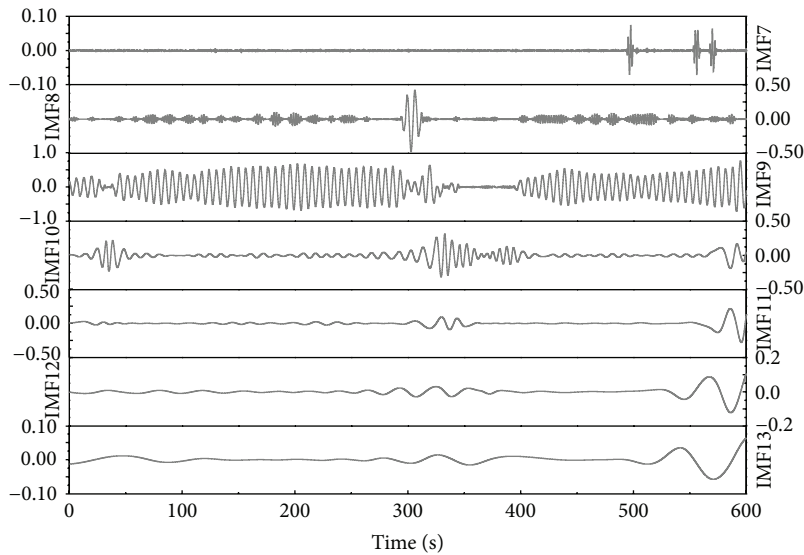


FIGURE 23: IMFs of the seventh to thirteenth orders.

future one, which are named the first and second environmental conditions, respectively. The first one simulated the environment when SWFC was being built, and the second one added some new high-rise buildings in plan at that time. Particularly, the main distinction between these two test cases is that the second one considered the “future” existence of the Shanghai Center Building, which was designed to be 400 m at that time.

The field measured data are the responses from the 98th floor of the building (approximately 475 m). However, the data from the wind tunnel test study are the responses at the top of the building (492 m). For comparison, the former ones are converted to the top of the building according to the mode and direction. The lengths of field measured acceleration data adopted for the comparison close to 10 min. The mean wind

speeds and wind angles are obtained as shown in Table 3. The wind angles for the wind-induced responses are mostly in the range of northeast effective wind angle range (120° to 150°); therefore, the interference from the target building itself on the mean wind speeds can be ignored. When the wind tunnel test data are used to calculate the wind-induced responses, the damping ratios for the basic modes in X and Y directions are assumed to be 2.4% and 1.6%, respectively. Since the vibration mode along the height is not strictly linear, hypothesis of a linear distribution and modification of the tested base moment are therefore conducted to calculate the response.

When the mean wind speeds are small, the wind-induced responses in X and Y directions (lateral and longitudinal directions) generally match the measured results

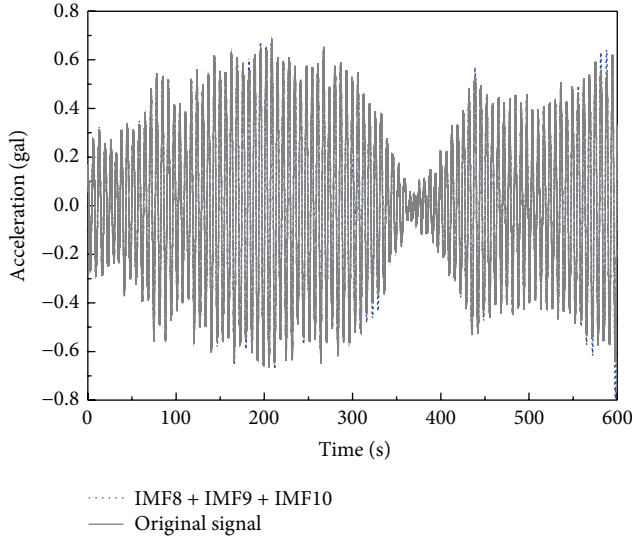


FIGURE 24: Comparison between the original signal and the superposition of IMFs in the eighth to tenth orders.

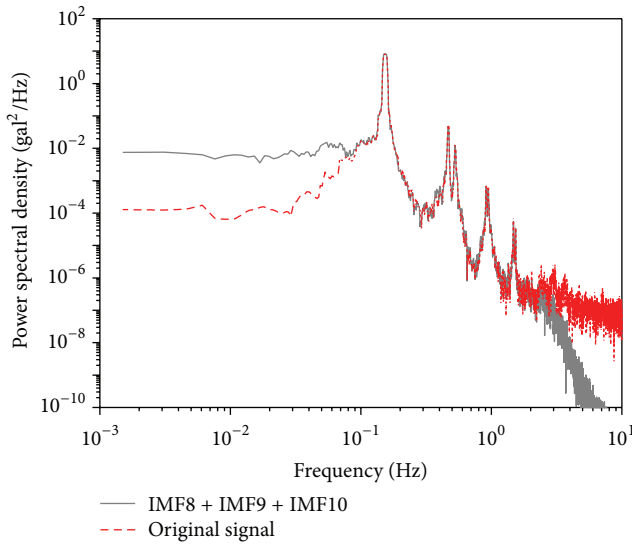


FIGURE 25: PSD of the original signal and superposition of IMFs in the eighth to tenth orders.

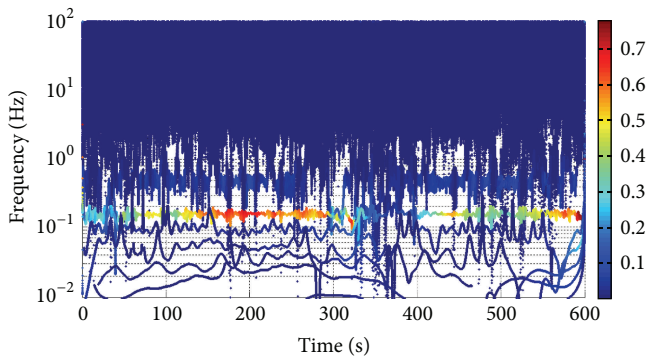


FIGURE 26: Time-frequency analysis of field measured accelerations.

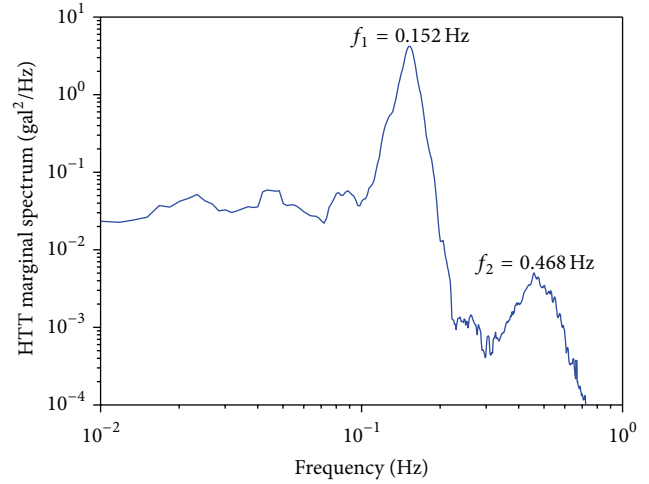


FIGURE 27: Hilbert-Huang marginal spectra of field measured accelerations.

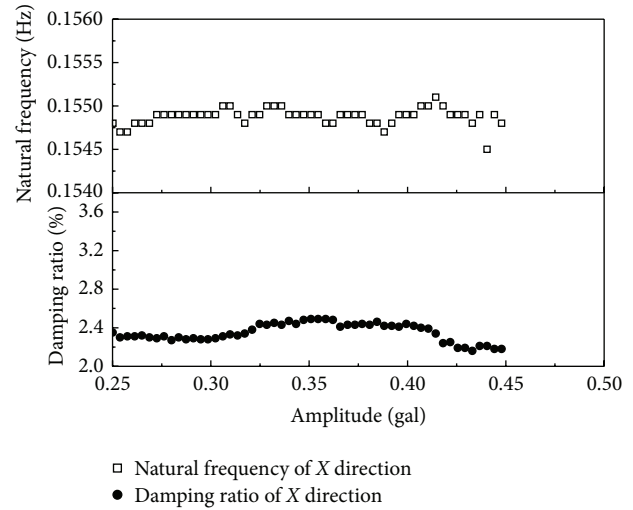


FIGURE 28: Natural frequencies and damping ratios versus amplitude in X direction.

(Figures 31 and 32). When the mean wind speeds are over 14.5 m/s, the field measured data in the Y direction (longitudinal direction) properly match the tested ones, while in the X direction (lateral direction) the field measured data are slightly larger than the tested ones. The differences between those two directions may be related to three issues: the difference of the wind directions, lateral aerodynamic damping, and the interference effects from surrounding buildings. Firstly, the wind angles corresponding to the measured data are variable within the interval of 107° to 170° , but the wind angle of the wind tunnel test is stable at 135° (Table 3). The wind-induced responses in the X direction (lateral direction) are sensitive to the wind direction changes; however, the longitudinal direction is a different case. Secondly, the calculation results of the wind tunnel are obtained by applying the aerodynamic force tested from the rigid model on the structural finite element model without

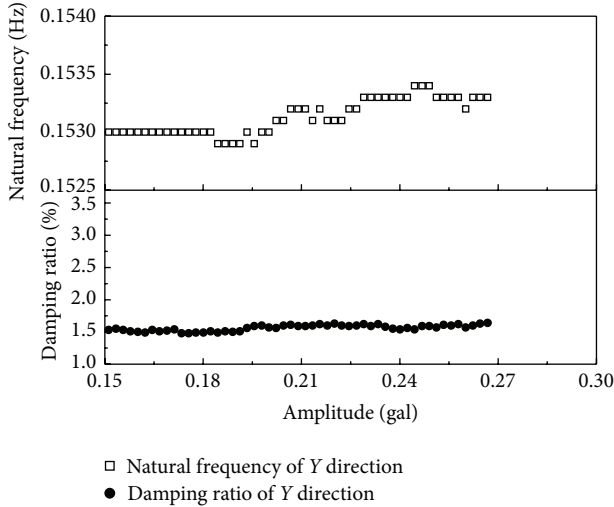


FIGURE 29: Natural frequencies and damping ratios versus amplitude in Y direction.

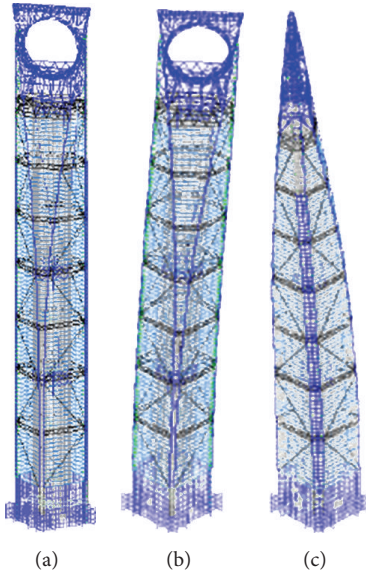


FIGURE 30: Finite element model and the first two bending modes: (a) finite element model, (b) basic bending mode in Y direction and (c) basic bending mode in X direction.

considering effects of the aerodynamic damping, whereas the lateral aerodynamic damping of this real super-tall building may be shown as a negative value [27]. Last, numerous differences also exist between the current surroundings and the wind tunnel test case.

6. Conclusions

Detailed analysis of the wind velocities at 500 m upper air in Shanghai and wind-induced responses of the SWFC under normal climate conditions is conducted by collecting data through the SHMS at the top of this building. The field measured results of the wind-induced responses are

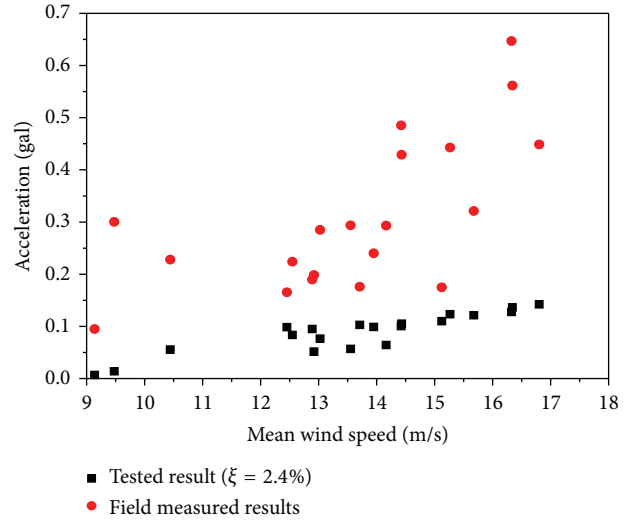


FIGURE 31: Tested wind-induced accelerations versus field measured ones in X direction.

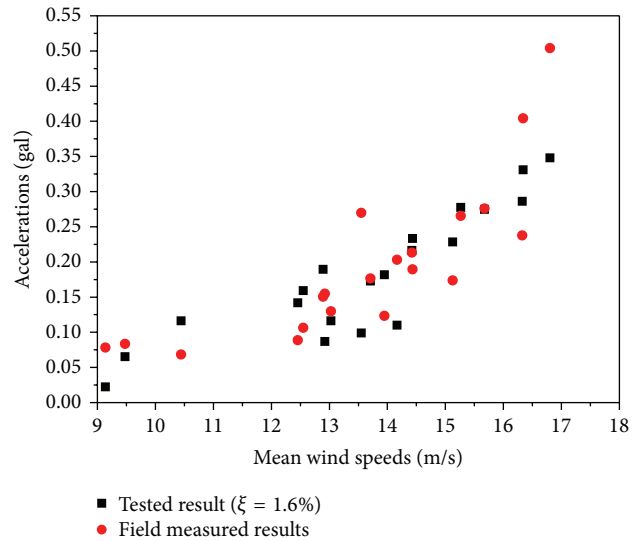


FIGURE 32: Tested wind-induced accelerations versus field measured ones in Y direction.

compared with the corresponding HFFB wind tunnel test results. The following conclusions are drawn.

- (1) Through linear fitting, the ratio of maximum 10 min mean wind speeds within 1 hr and the 1 hr mean speed is approximately 1:1.04. The relationship between the maximum 3 s mean wind speeds within 10 min and the 10 min mean wind speeds is expressed as $y = 0.85x + 4.5$.
- (2) When mean speed is small, both the turbulence intensity and the gust factor decrease with the increase of the mean wind speed. When the mean wind speed is over 20 m/s, the turbulence intensity and the gust factor are not sensitive to the changes of the mean

TABLE 3: 10 min mean wind speeds and mean wind angles for comparison during each period.

Date/time to record	10 min mean wind speed (m/s)	10 min mean wind angle ($^{\circ}$)
20101020/12:59:51	9.14	132.74
20101020/13:59:51	10.44	135.58
20101020/14:59:51	9.48	138.64
20101023/8:59:51	12.46	107.27
20101023/9:59:51	13.71	116.32
20101023/10:59:51	13.95	118.89
20101023/11:59:51	15.13	120.64
20101023/12:59:51	14.43	129.88
20101023/13:59:51	15.68	126.54
20101023/14:59:51	15.27	131.66
20101023/15:59:50	16.34	131.93
20101023/16:59:51	16.80	130.64
20101024/5:59:51	12.55	127.54
20101024/6:59:51	14.42	125.99
20101024/7:59:51	16.33	122.87
20101024/8:59:51	12.89	134.52
20101025/4:59:51	13.55	171.76
20101025/5:59:51	12.92	175.38
20101025/6:59:51	14.17	168.48
20101025/7:59:51	13.03	162.92

wind speed. The ratio of the lateral and longitudinal turbulence intensities is approximately 0.88.

- (3) The power spectral densities of the longitudinal and lateral fluctuating wind speeds match well with the von Karman spectra when the mean wind speed is small. However, when the mean wind speed is over 20 m/s, the power spectral densities are larger than the von Karman spectra.
- (4) The longitudinal and lateral turbulence integral scales have an increasing trend with the increase of mean wind speed. The ratio of the longitudinal and lateral turbulence integral scale is approximately 1 : 0.8.
- (5) The natural frequencies of the first two modes identified by using the power spectral density, HHT marginal spectra, and RDM match properly with the results from the finite element method. The damping ratio in X and Y directions is about 2.4% and 1.6%, respectively.
- (6) The measured longitudinal and lateral responses match properly with the results from the wind tunnel test when the mean wind speeds are small. When the mean wind speed is over 20 m/s, the longitudinal responses of measurement and test match each other well, while the measured lateral responses are slightly larger than the tested ones. This phenomenon may be related to the differences of the approaching wind directions, lateral aerodynamic damping, and the building surroundings.

Acknowledgment

The authors are grateful for the support provided by the National Natural Science Foundation of China (Grant nos. 51278367, 50878159, and 90715040).

References

- [1] C. S. Durst, "Wind speeds over short periods of time," *The Meteorological Magazine*, vol. 89, no. 1056, pp. 181–186, 1960.
- [2] E. C. C. Choi, "Field measurement and experimental study of wind speed profile during thunderstorms," *Journal of Wind Engineering and Industrial Aerodynamics*, vol. 92, no. 3-4, pp. 275–290, 2004.
- [3] N. Kato, T. Ohkuma, J. R. Kim, H. Marukawa, and Y. Niihori, "Full scale measurements of wind velocity in two urban areas using an ultrasonic anemometer," *Journal of Wind Engineering and Industrial Aerodynamics*, vol. 41, no. 1-3, pp. 67–78, 1992.
- [4] J. D. McClintock, G. S. Pond, L. W. Davidson, Offshore Wind Gust Climatologies, and Sea Consult Limited, "Report prepared for atmospheric environment," Tech. Rep., Service Canadian Climate Center Marine Applied Unit, 1987.
- [5] J. A. Wills, A. Grant, C. F. Boyack, Offshore Mean Wind Profile, and Department of Energy, "Offshore technical report," Tech. Rep. OTH86226, 1986.
- [6] O. J. Andersen and J. Løvseth, "Gale force maritime wind. the Frøya data base. Part 1: sites and instrumentation. review of the data base," *Journal of Wind Engineering and Industrial Aerodynamics*, vol. 57, no. 1, pp. 97–109, 1995.
- [7] O. J. Andersen and J. Løvseth, "Stability modifications of the Frøya wind spectrum," *Journal of Wind Engineering and Industrial Aerodynamics*, vol. 98, no. 4-5, pp. 236–242, 2010.
- [8] Y. An, Y. Quan, and M. Gu, "Field measurement of wind characteristics of Typhoon Muifa on the Shanghai world financial center," *International Journal of Distributed Sensor Networks*, vol. 2012, Article ID 893739, 11 pages, 2012.
- [9] G. L. Larose, A. Zasso, S. Melelli, and D. Casanova, "Field measurements of the wind-induced response of a 254 m high free-standing bridge pylon," *Journal of Wind Engineering and Industrial Aerodynamics*, vol. 74–76, pp. 891–902, 1998.
- [10] Q. S. Li, J. R. Wu, S. G. Liang, Y. Q. Xiao, and C. K. Wong, "Full-scale measurements and numerical evaluation of wind-induced vibration of a 63-story reinforced concrete tall building," *Engineering Structures*, vol. 26, no. 12, pp. 1779–1794, 2004.
- [11] Y. L. Xu and S. Zhan, "Field measurements of Di Wang Tower during Typhoon York," *Journal of Wind Engineering and Industrial Aerodynamics*, vol. 89, no. 1, pp. 73–93, 2001.
- [12] Q. S. Li, Y. Q. Xiao, J. Y. Fu, and Z. N. Li, "Full-scale measurements of wind effects on the Jin Mao building," *Journal of Wind Engineering and Industrial Aerodynamics*, vol. 95, no. 6, pp. 445–466, 2007.
- [13] J. Y. Fu, Q. S. Li, J. R. Wu, Y. Q. Xiao, and L. L. Song, "Field measurements of boundary layer wind characteristics and wind-induced responses of super-tall buildings," *Journal of Wind Engineering and Industrial Aerodynamics*, vol. 96, no. 8-9, pp. 1332–1358, 2008.
- [14] J. Y. Fu, J. R. Wu, A. Xu, Q. S. Li, and Y. Q. Xiao, "Full-scale measurements of wind effects on Guangzhou West Tower," *Engineering Structures*, vol. 35, pp. 120–139, 2012.

- [15] H. F. Bai, T. H. Yi, H. N. Li, and L. Ren, "Multisensors on-site monitoring and characteristic analysis of UHV transmission tower," *International Journal of Distributed Sensor Networks*, vol. 2012, Article ID 545148, 10 pages, 2012.
- [16] T.-H. Yi, H.-N. Li, and M. Gu, "Recent research and applications of GPS-based monitoring technology for high-rise structures," *Structural Control and Health Monitoring*, vol. 20, no. 5, pp. 649–670, 2013.
- [17] H.-N. Li, T.-H. Yi, X.-D. Yi, and G.-X. Wang, "Measurement and analysis of wind-induced response of tall building based on GPS technology," *Advances in Structural Engineering*, vol. 10, no. 1, pp. 83–93, 2007.
- [18] "AIJ-RLB-2004 Recommendations for loads on buildings," Architecture Institute of Japan, Tokyo, Japan, 2004.
- [19] "GB 50009-2012 Load code for the design of building structures," Architecture & Building Press, Beijing, China, 2012.
- [20] S. Cao, Y. Tamura, N. Kikuchi, M. Saito, I. Nakayama, and Y. Matsuzaki, "Wind characteristics of a strong typhoon," *Journal of Wind Engineering and Industrial Aerodynamics*, vol. 97, no. 1, pp. 11–21, 2009.
- [21] E. C. C. Choi, *Wind Loading in Hong Kong: Commentary on the Code of Practice on Wind Effects Hong Kong*, Hong Kong Institute of Engineers, Hong Kong, China, 1983.
- [22] N. E. Huang, Z. Shen, R. L. Steven et al., "The empirical mode decomposition and the Hubert spectrum for nonlinear and non-stationary time series analysis," *Proceedings of the Royal Society A*, vol. 454, no. 1971, pp. 903–995, 1998.
- [23] Y. Tamura, H. Yasui, and H. Marukawa, "Non-elastic responses of tall steel buildings subjected to across-wind forces," *Wind and Structures*, vol. 4, no. 2, pp. 147–162, 2001.
- [24] X.-J. Hong and M. Gu, "Probability model and solution on earthquake effects combination in along wind resistant design of tall-flexible buildings," *Applied Mathematics and Mechanics*, vol. 27, no. 5, pp. 627–636, 2006.
- [25] Report of SWFC Seismic Review, Mori Building Architects & Engineers (MORI), Tokyo, Japan, 2003.
- [26] Wind Engineering Studies for the Shanghai World Financial Center, PRC, (*Part 1 Studies Accelerations and Torsion Velocities From Force Balance Studies Using Standard BLWTL Statistical Methodology*), The University of Western Ontario, Ontario, Canada, 2002, BLWT-SS41-2002.
- [27] A. G. Davenport, "The influence of turbulence on the aeroelastic responses of tall structures to wind," in *Practical Experiences with Flow-Induced Vibrations*, pp. 681–695, Springer, Karlsruhe, Germany, 1979.

Research Article

Analysis on Factors Affecting the Self-Repair Capability of SMA Wire Concrete Beam

Li Sun, Dezhi Liang, Qianqian Gao, and Jianhong Zhou

School of Civil Engineering, Shenyang Jianzhu University, Shenyang 110168, China

Correspondence should be addressed to Li Sun; sunli2009@163.com

Received 24 September 2013; Accepted 21 November 2013

Academic Editor: Xiao-Wei Ye

Copyright © 2013 Li Sun et al. This is an open access article distributed under the Creative Commons Attribution License, which permits unrestricted use, distribution, and reproduction in any medium, provided the original work is properly cited.

Crack expansion of concrete is the initial damage stage of structures, which may cause greater damage to structures subject to long-term loads or under extreme conditions. In recent years, the application of intelligent materials to crack self-repair has become a hotspot among researchers. In order to study the influence of factors on the self-repair capability of shape memory alloy (SMA) wire concrete beam, both theoretical and experimental methods were employed for analysis. For the convenience of experiment, composite materials (epoxy cement mortar and silicone polymer clay) instead of concrete were used. The SMA wires were externally installed on and internally embedded in epoxy resin cement mortar beams and silicone polymer clay beams. Comparison of crack repair situation between two installation methods turns out that both methods possess their own advantages and disadvantages and should be employed according to the actual situation. The influence of unbonded length on the self-repair capability of embedded type SMA wire beams and the necessary minimum unbonded length to achieve self-repair function were studied. The results state clearly that the longer the unbonded length is, the better the crack repair situation is.

1. Introduction

SMA [1] is a kind of material with shape memory function realized by phase transition which is induced by stress and temperature. Plastic deformation will be generated when SMA which is shaped under a high temperature is placed in a low or room temperature environment. When the ambient temperature rises to the critical temperature, that is, phase transition temperature, the deformation disappears and SMA can be recovered to the initial design state. In this process, the displacement or stress in SMA is the function of temperature. The phenomenon that deformation disappears with the increase of temperature and the shape recovers is called the shape memory effect.

For concrete structures which are prone to crack, the shape memory effect of SMA can be employed to reinforce or repair the cracked structures. One way is to fix SMA material on the structure, and the other is to embed SMA material as reinforcement in the structure, reserving a certain unbonded length.

Many researchers have done much work in this field. By fixing SMA wires on concrete beams, Luo [2] investigated

the driving performance and the repair performance of SMA wires. By embedding prestressed SMA wires in concrete beams, He et al. [3] studied the response of the beams under static loading and constant impact loading and the effects of the SMA wires on the repair of cracks. Embedding SMA wires in composite components, Tao [4] tested the repair function of restoring force induced by heating in SMA wires. Maji and Negret [5] embedded SMA stereopsis in mortar trabeculae and loaded used three-point bending test until visible cracks appeared. Then the SMA stereopsis was heated by electricity. After a period of time, the visible crack fully recovers, which turns out that the SMA stereopsis has a great driving function.

Shi Yan et al. [6] applied the shape memory effect of the SMA to make intelligent reinforced concrete continuous beams. The principle of self-repairing property and the factors affecting self-repairing property were experimentally studied. It turns out that deformation and crack width can be significantly decreased by the heated SMA bars. The driving effect can be enhanced by increasing the total cross-section area of the SMA bars or the reinforcement ration of the SMA bars. Li et al. [7–9] investigated SMA for intelligently

TABLE 1: Properties of tested beams.

Beam no.	Specimen dimension (mm)	Unbonded length of beams l_1 (mm)	Diameter of Ni-Ti alloy wire (mm)	Thickness of protective layer (mm)	Type of material
Al-1	20 × 30 × 200	0	0.5	5	Mixtures of epoxy resins and cement mortars
Al-2	20 × 30 × 200	10	0.5	5	Mixtures of epoxy resins and cement mortars
Al-3	20 × 30 × 200	40	0.5	5	Mixtures of epoxy resins and cement mortars
Al-4	20 × 30 × 200	—	—	—	Mixtures of epoxy resins and cement mortars
Bl-1	20 × 30 × 200	0	0.5	5	Mixtures of silicones and clays
Bl-2	20 × 30 × 200	10	0.5	5	Mixtures of silicones and clays
Bl-3	20 × 30 × 200	40	0.5	5	Mixtures of silicones and clays
Bl-4	20 × 30 × 200	—	—	—	Mixtures of silicones and clays

Note: “—” indicates that there is no SMA wire in the beam.

self-repairing of concrete structures. The results present that the heating method is an important influencing factor in the restoring force of SMA.

However, no further research has been done by scholars on comparison of the advantages and disadvantages between the two installation methods mentioned above and the influence of unbonded length on the repair capacity of internally embedded installation method. This is just the main subject which the paper focuses on.

2. Experiment Scheme

For the convenience of experiment, the tested beams are made from composite materials instead of concrete. Seven groups of beams numbered as Al-1, Al-2, Al-3, Al-4, Bl-1, Bl-2, and Bl-3 are made. Beams from Al-1 to Al-4 are made from epoxy resins and cement mortars and the rest are made from silicones and clays. The dimension of beams and SMA alloy wires and the unbonded length of SMA alloy wires are tabulated in Table 1.

The experiment was completed in the mechanical laboratory of Shenyang Jianzhu University and a universal testing machine was used as the loading device. Firstly, three-point bending test was employed to load each beam until visible cracks appeared. The cracked beams were repaired in two ways. One way was to internally embed SMA wires in the structure with reserving a certain unbonded length, as shown in Figure 1(a). The power was connected to the beam at both ends of the alloy wire for heating the alloy wire, so that the cracks were repaired by force generated by heated alloy wire. This method was applied to beams numbered as Al-1, Al-2, Al-3, Bl-1, Bl-2, and Bl-3, in which the unbonded lengths of SMA wires were different. The other way was to externally install Ni-Ti alloy wires on the surface of beam numbered as Al-4, as shown in Figure 1(b). The power was connected to the beam at both ends of the alloy wire for heating the alloy wire, so that the cracks were repaired by force generated by heated alloy wire. According to crack recovery situation, current strength, and power-on time, the advantages and

disadvantages of the two installation methods mentioned above were compared and the influence of unbonded length of the internally embedded installation repair method was analysed.

3. Factors Affecting the Self-Repair Capability of Polymer Beams

3.1. Influence of Installation Method. As can be seen from Figure 1, different bending moment results from different acting location of the restoring force generated by the alloy wire using the two methods. Assume that the central axis is in the middle of the beam, and mechanics is analyzed based on the theory of the concrete structure.

(1) Force analysis of internal embedded repair method:

$$M_m = F \left(\frac{h}{2} - c \right), \quad (1)$$

$$F = \sigma S, \quad (2)$$

where M_m indicates the restoring bending moment, F is the restoring force, h is the height of beam, c is the thickness of the protective layer, σ is restoring stress in the SMA wire, and S is the cross sectional area of the SMA wire.

(2) Force analysis of external installation repair method:

$$M_f = F \left(\frac{h}{2} + x \right), \quad (3)$$

where x indicates the distance from the SMA wire to the bottom of the beam.

Comparing (1) with (3), $M_m < M_f$ if the restoring force F is the same. In view of this, external installed SMA wire is more favorable in beam crack closure.

Experiment configurations of beam crack closure using different installation methods of SMA wires are shown in Figures 2 and 3. Bending moments in two cases are different due to different acting points of the restoring forces F generated

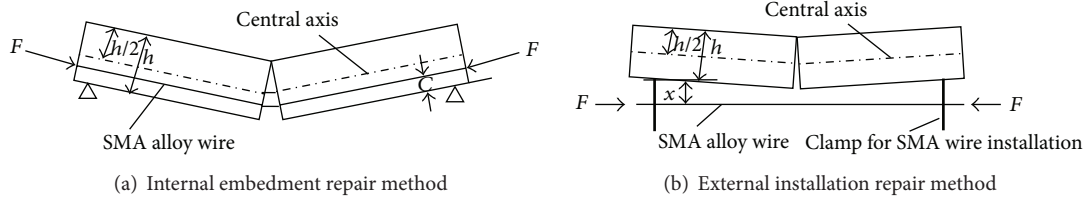


FIGURE 1: Methods of repairing beam cracks.

TABLE 2: The basic situations in beam crack closure processes.

Beam no.	Crack width before power-on w (mm)	Crack recovery value Δw (mm)	Crack recovery degree η (%)	Current intensity I (A)	Power-on time t (s)
Al-1	3.075	1.11	36.1	3	30
Al-4	2.212	2.186	98.8	2.8	20

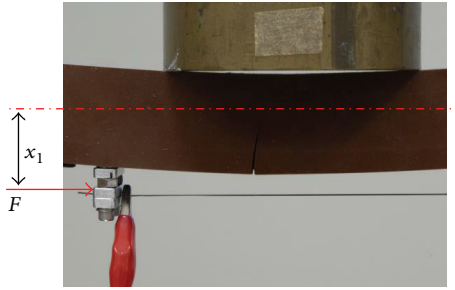


FIGURE 2: External installed SMA wires.

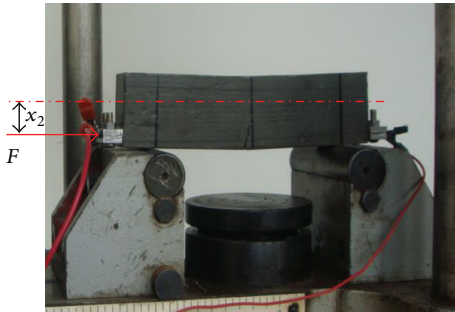


FIGURE 3: Internal embedded SMA wires.

by the alloy wires. If restoring forces F are the same, we have $x_1 > x_2$ according to (1) and (3). Therefore, the bending moment in Figure 2 is larger than that in Figure 3. The crack can be more easily recovered using external installed SMA wire (as shown in Figure 2), and less energy is consumed. Without regard to any other factor except for installation method, comparison between two installation methods is tabulated in Table 2.

As can be seen from Table 2, external installed SMA wire not only needs smaller current intensity and less power-on time, but also recovers much more than internal embedded SMA wire does.

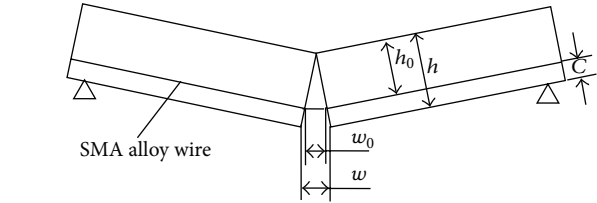


FIGURE 4: Schematic diagram of internally embedded SMA wires for crack closure.

However, the installation process of external installation method is more complicated. There are not only pre-embedded parts in the structure, but also installation devices externally erected outside the structure. The cost of external installation method is much higher than that of internally embedded method. But SMA wires which are used in external installation method are reusable and have lower cost and higher activation force. Therefore, both methods have their own advantages and disadvantages. We should select the necessary installation method according to a specific situation.

3.2. Influence of Unbounded Length in the Embedded SMA Beam. In order to study more accurately the influence of unbounded length of internal embedded SMA wires on the self-repairing capacity of beam, the analysis method of controlling crack width in reinforced concrete structures is referred to. According to the bond slip theory, the actual operative length of SMA alloy wires can be expressed as

$$l = w_0 + 2 \times 20D + l_1, \quad (4)$$

where D is the diameter of SMA wire, l_1 is the unbounded length of SMA wire, and w_0 is the length of SMA wire between the surfaces of the crack, as shown in Figure 4. $20D$ is the slip length of the SMA wire at both ends of the crack, which is estimated according to the reinforcement anchorage length ranges from concrete code [10]. where, the effective height of the cross-section of the beam is given by

$$h_0 = h - c. \quad (5)$$

TABLE 3: Theoretical recovered length of internally embedded SMA alloy wires.

Beam no.	w (mm)	w_0 (mm)	D (mm)	l_1 (mm)	l (mm)	ε (%)	δ (mm)
Al-1	3.075	2.561	0.05	0	22.561	5	1.128
Al-2	2.842	2.367	0.05	10	32.367	5	1.618
Al-3	2.975	2.478	0.05	40	62.478	5	3.124
Bl-1	2.865	2.387	0.05	0	22.387	5	1.119
Bl-2	4.514	3.760	0.05	10	33.760	5	1.688
Bl-3	2.681	2.233	0.05	40	62.233	5	3.112

TABLE 4: Experimental and theoretical values of crack recovery.

Beam no.	Crack width w (mm)	Experimental value		Theoretical value	
		Values of crack recovery	Degree of crack recovery	Values of crack recovery	Degree of crack recovery
		Δw (mm)	η (%)	$\Delta w'$ (mm)	η' (%)
Al-1	3.075	1.11	36.1	1.354	55.0
Al-2	2.842	1.828	64.3	1.943	31.6
Al-3	2.975	2.879	96.8	2.975	100
Bl-1	2.865	1.123	39.2	1.344	53.1
Bl-2	4.514	3.25	72.0	2.026	55.1
Bl-3	2.681	2.617	97.6	2.681	100

According to the proportional relationship in Figure 4,

$$w_0 = \frac{h_0}{h} w. \quad (6)$$

By introducing (5) into (6), the following equation can be obtained:

$$w_0 = \frac{h-c}{h} w, \quad (7)$$

where h is the height of beam, c is the thickness of the protective layer, and w is the crack width. By introducing (7) into (4), the actual operative length of alloy wire can be obtained when the unbonded length of SMA wire is l_1 :

$$l = \frac{h-c}{h} w + 2 \times 20D + l_1. \quad (8)$$

If the strain of SMA wire is ε and the SMA wire completely recovers its initial shape, the recovery strain is also ε . When the unbonded length of SMA wire is l_1 and the cracks are completely repaired, the recovered length of alloy wire can be obtained as

$$\delta = l\varepsilon = \left(\frac{h-c}{h} w + 2 \times 20D + l_1 \right) \varepsilon. \quad (9)$$

By substituting the parameters of internally embedded SMA wires beam into (9), we can obtain the value of the theoretically recovered length of SMA wires, as shown in Table 3.

Based on the unbonded length of SMA wires tabulated in Table 3, the experiment study on the self-repair ability of beam cracks was conducted. Figure 5 shows the influence of unbonded length of SMA wires on recovery degree of cracks.

Beams numbered as Al-1, Al-2, and Al-3 are made of the same materials. As can be seen from Figure 5 and Table 3, the longer the unbonded length is, the better the cracks recover. Cracks on beam Al-3 are almost nonvisible. Therefore, the unbonded length of SMA wires in beam Al-3 meets the required length. Similar situations for beams Bl-1, Bl-2, and Bl-3 can be observed, as shown in Figure 5.

However, further study is necessary to verify non-theoretical unbonded length of SMA wires in the beam that meets the required length for repairing cracks. The experimental and theoretical variations of crack width during recovery process are tabulated in Table 4, where the unbonded length in beams Al-1, Al-2 and Al-3 are respectively, 0 mm, 10 mm, and 40 mm and the same in beams Bl-1, Bl-2, Bl-3.

As can be seen from Table 4, the experimental and theoretical values of crack recovery in beams with internally embedded SMA wires are in good agreement. Therefore, in order to achieve the self-repair ability, the unbonded length l_m in embedded SMA polymer beams must satisfy the relationship $l_m \geq l_1$. The minimum unbonded length achieving self-repair is given by

$$l_m \geq l_1 = \frac{\delta}{\varepsilon} - \frac{h-c}{h} w - 2 \times 20D, \quad (10)$$

where δ represents the recovered length of SMA wire, ε is the recovery strain of SMA wire, h is the height of beam, c is the thickness of the protective layer, and D is the diameter of SMA wire.

3.3. Other Factors Affecting Self-Repairing Capability. The material characteristics of the beams also affect the self-repairing capability. The stiffness of beam Bl-3 made from pouring clays and silicones is small. More energy is needed

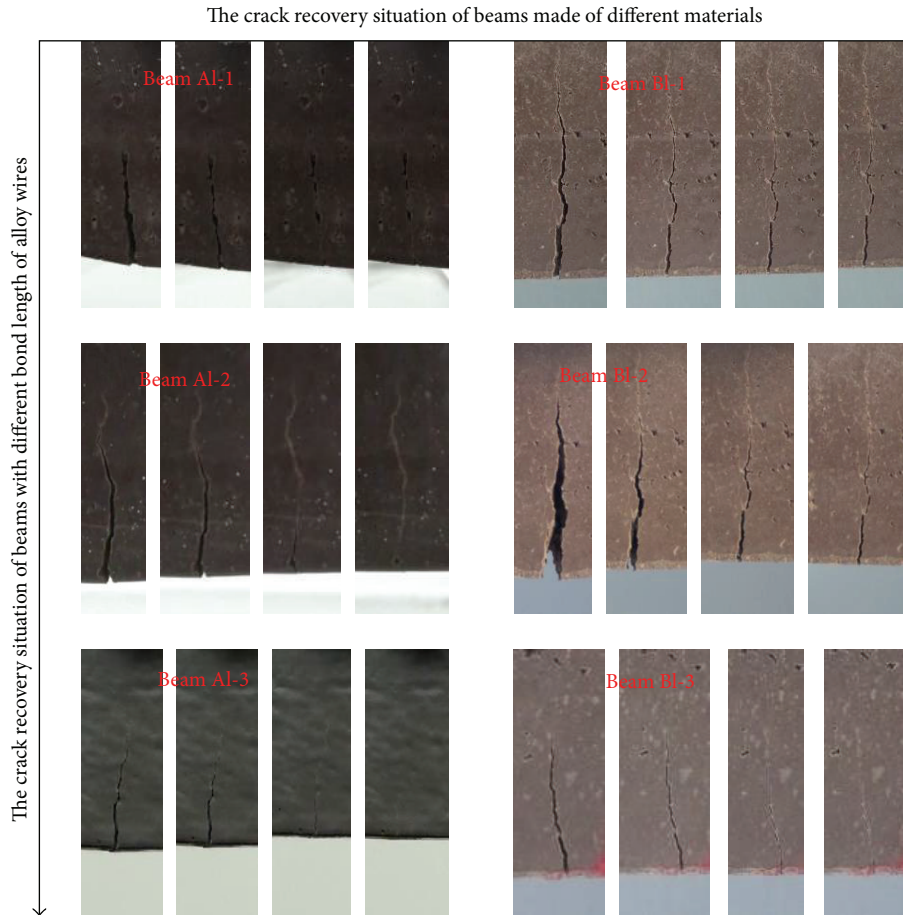


FIGURE 5: Crack recovery situation of beams with internally embedded SMA wires.

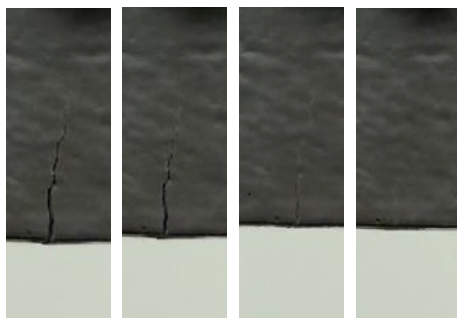


FIGURE 6: Crack closure of beam A1-3.

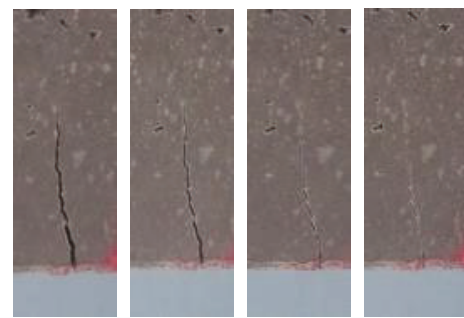


FIGURE 7: Crack closure of beam B1-3.

to recover the deformation. The stiffness of beam A1-3 made from pouring epoxy cements and mortars is large and the energy required for repairing is relatively less. Under the condition of very nearly the same recovery degree in beams B1-3 and A1-3, as shown in Figure 6 and Figure 7, and the same power-on time, the required current intensity for beam A1-3 is 40 percent less than that for beam B1-3.

The current intensity and the crack closure situation are tabulated in Table 5. As can be seen, the required current intensity for the beam made from silicones and clays is larger

than that for the beam made from epoxy resins and cement mortars. Therefore, the material characteristics do not play a decisive role in crack closure of beams, but they have certain influence on it. Repairing efficiency of the beam made from flexible materials is low, and the current intensity must be large enough to achieve full recovery.

The shape memory effect and superelastic characteristics of SMA materials of different types are different, and the bond between bars and sterepsinema with aggregate in the beam is also different. Therefore, the properties of SMA alloy also affect the self-repair ability. In addition, the beam crack slags

TABLE 5: Current intensity and crack closure degree.

Beam no.	Crack width w (mm)	Values of crack recovery Δw (mm)	Degree of crack recovery η (%)	Current intensity I (A)
Al-1	3.075	1.11	36.1	3
Al-2	2.842	1.828	64.3	3
Al-3	2.975	2.879	96.8	3
Al-4	2.212	2.186	98.8	2.8
Bl-1	2.865	1.123	39.2	5
Bl-2	4.514	3.25	72.0	5
Bl-3	2.681	2.617	97.6	5
Bl-4	4.012	4.005	99.8	3.5

will be stuck in the cracks and will hinder crack closure, which also has influence on crack closure.

4. Conclusion

In this paper, based on the small stiffness of the composite materials and obvious crack closure phenomenon, the crack closure capacity of beams is theoretically and experimentally analyzed and it can be concluded as follows.

- (1) External installation method and internal embedment method are viable in crack closure, and both methods have their own advantages and disadvantages. We should select the appropriate method according to specific conditions.
- (2) The minimum unbonded length of the embedded SMA polymer beams that achieve repair is given by (10).
- (3) Properties of beam material and SMA affect crack closure. These factors should be avoided or excluded in the repairing process.

Conflict of Interests

The authors declare that there is no conflict of interests regarding the publication of this paper.

Acknowledgments

This work has been supported by the National Natural Science Foundation of China (51178277), Program for New Century Excellent Talents in University (NCET-12-1013), Program for Liaoning Excellent Talents in University (LR2012018), and the Shenyang City Science Foundation of China (F11-163-9-00).

References

- [1] Z.-P. Cao and S.-L. Wang, "Study on application of intelligent material systems and structures to civil engineering," *Journal of Chongqing Jianzhu University*, vol. 23, no. 1, pp. 1–4, 2001.
- [2] Z.-W. Luo, *Basic Theoretical Studies on Intelligent Concrete Beams Using Unbonded External SMA Wires*, Tongji University, Shanghai, China, 2006.
- [3] S.-L. He, X.-Y. Huang, and M.-S. Chen, "The research of shape memory alloy reinforced concrete with self-diagnosis and self-adaptation smart structures," in *Proceedings of the Chinese Materials Symposium*, pp. 622–625, Industry Press, Beijing, China, 1996.
- [4] B.-Q. Tao, *Smart Materials Structures*, Defense Industry Press, 1997.
- [5] A. K. Maji and I. Negret, "Smart prestressing with shape-memory alloy," *Journal of Engineering Mechanics*, vol. 124, no. 10, pp. 1121–1128, 1998.
- [6] S. Yan, J. Sun, and W. Wang, "Deformation property of smart concrete continuous beams reinforced with shape memory alloy rebars," *Concrete*, pp. 8–12, 2010.
- [7] H. Li, C. X. Mao, Z. Q. Liu, and J. P. Ou, "Shape memory alloy-based smart civil structures with self-sensing and repairing capabilities," in *Sensing Issues in Civil Structural Health Monitoring*, Chapter 4, pp. 259–268, 2005.
- [8] H. Li, Z.-Q. Liu, and J.-P. Ou, "Experimental study of a simple reinforced concrete beam temporarily strengthened by SMA wires followed by permanent strengthening with CFRP plates," *Engineering Structures*, vol. 30, no. 3, pp. 716–723, 2008.
- [9] H. Li, Z.-Q. Liu, and J.-P. Ou, "Study on reinforced concrete beams strengthened using shape memory alloy wires in combination with carbon-fiber-reinforced polymer plates," *Smart Materials and Structures*, vol. 16, no. 6, pp. 2550–2559, 2007.
- [10] D.-J. Ding, *Modern Concrete Structures*, China Architectural Press, 2000.

Research Article

Analysis of Precursors Prior to Rock Burst in Granite Tunnel Using Acoustic Emission and Far Infrared Monitoring

Zhengzhao Liang,^{1,2} Xiangxin Liu,³ Yanbo Zhang,³ and Chunan Tang¹

¹ School of Civil Engineering, Dalian University of Technology, Dalian 116024, China

² The Key Laboratory of Safety for Geotechnical and Structural Engineering of Hubei Province, Wuhan University, Wuhan 430072, China

³ College of Mining Engineering, Hebei United University, Tangshan, Hebei 063009, China

Correspondence should be addressed to Zhengzhao Liang; z.z.liang@163.com

Received 9 October 2013; Accepted 5 November 2013

Academic Editor: Xiao-Wei Ye

Copyright © 2013 Zhengzhao Liang et al. This is an open access article distributed under the Creative Commons Attribution License, which permits unrestricted use, distribution, and reproduction in any medium, provided the original work is properly cited.

To understand the physical mechanism of the anomalous behaviors observed prior to rock burst, the acoustic emission (AE) and far infrared (FIR) techniques were applied to monitor the progressive failure of a rock tunnel model subjected to biaxial stresses. Images of fracturing process, temperature changes of the tunnel, and spatiotemporal serials of acoustic emission were simultaneously recorded during deformation of the model. The b -value derived from the amplitude distribution data of AE was calculated to predict the tunnel rock burst. The results showed that the vertical stress enhanced the stability of the tunnel, and the tunnels with higher confining pressure demonstrated a more abrupt and strong rock burst. Abnormal temperature changes around the wall were observed prior to the rock burst of the tunnel. Analysis of the AE events showed that a sudden drop and then a quiet period could be considered as the precursors to forecast the rock burst hazard. Statistical analysis indicated that rock fragment spalling occurred earlier than the abnormal temperature changes, and the abnormal temperature occurred earlier than the descent of the AE b -value. The analysis indicated that the temperature changes were more sensitive than the AE b -value changes to predict the tunnel rock bursts.

1. Introduction

The study of rock failure under stress is a subject of widespread interest, with relevance to both rock engineering applications, such as tunneling design, oil recovery, safe design of nuclear waste repositories, and natural processes such as volcanism and seismology. As a typical failure style, a rock burst is a kind of sudden expulsion of rock occurring under high stress in deep underground engineering. The opening of a tunnel relieves neighboring rocks of tremendous pressure, which can literally cause the rock to explode as it attempts to reestablish stress and strain equilibrium. The released energy leads to the violent fracture of the surrounding rock around the excavation and reduces the potential energy of the rock, which makes the surrounding rock to reach another equilibrium state.

In the past few years, many methods of forecasting rock bursts have been proposed, including rock mechanics assessment, stress detection, and modern mathematical theories. However, a comprehensive understanding of rock bursts and associated damage mechanisms has remained elusive [1, 2]. Fairhurst and Cook considered stress-induced buckling of rock layers as a rock burst mechanism, but most researchers have limited this mechanism to fairly minor events [3]. White et al. described field examples of large rock bursts and other rib deformation that they inferred to have resulted from buckling [4]. The evidence for one large burst described as caused by buckling, the Craig drift rock burst (Strathcona Mine of Falconbridge, Ltd., ON, Canada) is suggestive but not compelling. Many studies simply sidestep consideration of damage mechanisms or ascribe damage to a seismic impulse or to crushing, with no specific damage mechanism specified.

For many reasons, it is important to be able to predict the time, location, and intensity of potential rock burst. Rock fracture and rock burst in stressed rock have been observed in the laboratory by a number of methods. One approach is the direct observation of samples by scanning electron microscopy (SEM) [5], optical camera, and microscopy [6]. These images provide direct and visual description of fracturing process in a straightforward way.

Far infrared (FIR) is a region in the infrared spectrum of electromagnetic radiation. When temperature changes, the related infrared energy is proportional to the fourth power of the absolute temperature. Small temperature change will cause large variations in infrared energy. Far infrared (FIR) technology is often applied to monitor temperature variations of stressed rocks [7, 8]. Based on a series of experimental studies, Geng and Cui pointed out that rock IR radiation energy increased with increasing stress on the rock and that some IR precursor information could predict rock fracturing [9, 10]. Based on the pioneering IR experimental studies on mine rocks, Wu and Wang suggested that there existed three kinds of IR radiation temperature features and three kinds of IR thermal features during the loading and failure process of coal and sandstone; they also found that the precursor indication through IR detection was comparable to that of acoustic emission detection and electrical resistance detection [11–13].

Far infrared monitoring can capture temperature distribution near the surface of the specimens. The far infrared results can reflect the amount of stress induced energy conducted from inside the specimens, but the deep energy and temperature condition cannot be obtained. These direct observations, including video monitoring and far infrared monitoring, are useful techniques for both brittle and ductile failure but is limited in that only the surface of the test specimen can be observed [14].

Another approach involves monitoring the hypocenter distribution, energy released, and hit counts of acoustic emission (AE) events caused by microcracking activity [14–16]. AE technique provides an analysis of the microcracking activity inside the rock volume and has an important advantage over other techniques in that tests can be performed under confining pressure, which is very important in the simulation of underground conditions. AE are considered very useful for understanding and explaining the various mechanisms of unstable failure of rock, that is, rock burst problems. Experiments aimed at investigating failure zone development and fault growth under loading conditions, that is, when failure is allowed to develop unstably, have become possible and also more significant in recent years. The disadvantage of the AE technique is that it is insensitive to ductile deformation, which does not produce appreciable AE. However, rock bursts in brittle failure can produce intensive AE activities and large amounts of energy, because almost all rock bursts occur in rocks with high stiffness and strength in high stress condition. The AE technique is applicable to locate the failure positions and determine the energy released in rock failure laboratory experiments and engineering applications related to slope failure and excavation problems in mines [17–20]. The recent development of high-speed

multichannel waveform recording technology has made it possible to monitor the hypocenters of AE associated with spontaneously/unstably fracturing processes in stressed rock samples with high precision.

Among various parameters analyzed from AE data, the most significant one is the b -value which is derived from the amplitude distribution data of AE following the methods used in rock burst prediction as well as seismology investigations. Variations in the seismic b -value have already been qualitatively linked to the state of stress, to changes in fracture mechanism in laboratory-scale rock fracture experiments, and to the heterogeneity of the material [7, 16, 20].

Rock bursts basically depend on the size and depth of the excavation. The likelihood of rock bursts occurring increases as depth increases. This study presents the rock burst investigation of a granite tunnel subjected to different confining pressures by using acoustic emission (AE) and far infrared (FIR) techniques to monitor the precursory information. The characteristics of the AE and FIR were analyzed to predict rock burst hazard.

2. Experiment Investigation

2.1. Specimen Preparation and Loading Condition. Totally, 12 granite rock specimens were prepared to model the rock burst of underground tunnels. The dimension of the specimens was approximately 150 mm × 150 mm × 75 mm, and an opening (30 mm diameter) was prepared in the center of the specimens (Figure 1). To reduce boundary effects, the side length of the specimens was 5 times that of the diameter of the opening. Biaxial loading was applied on the specimens to model the tunnel in different stress conditions. The horizontal force was increased to 30 KN, 60 KN, or 90 KN and then remained to be a constant. The vertical displacement loading was increased gradually until the collapse of the specimens with a rate of 0.3 mm per minute. All the experimental cases and the loading conditions were listed in Table 1.

The compression tests were carried out on a servo-controlled rock testing machine (RLW-3000), and the deformation and the vertical force applied were monitored. The acoustic emission activities were recorded by an AE detector with 8 channels. The multiparameter AE data, including AE hits, ring-down counts, and amplitudes, was obtained using a computer-based AE system (PAC). The thermal condition of the specimens was monitored by a far infrared radiation imager (ThermaCAM SC3000). A high speed video with high resolution was stationed in front of the rock testing machine to record the progressive failure process of the granite specimens.

To consider the influence of lateral stress on the deformation of the rocks, another group of specimens was subjected to uniaxial compression beforehand. Their force-time curves under uniaxial compression were shown in Figure 2. It was observed that all the specimens were in elastic deformation stage when the axial force was increased to 90 KN. Therefore, in the following tests, the maximal lateral force was limited to 90 KN.

TABLE 1: Specimens dimension and loading condition.

No.	Lateral force (kN)	Vertical displacement loading (mm/min)	Dimension (mm)
HSHG-30-1	30	0.3	149.22 × 72.06 × 150.94
HSHG-30-2			147.76 × 75.96 × 149.22
HSHG-30-3			151.68 × 72.84 × 153.12
HSHG-30-4			150.32 × 75.16 × 151.12
HSHG-60-1	60	0.3	149.12 × 74.58 × 148.76
HSHG-60-2			151.20 × 73.86 × 152.94
HSHG-60-3			149.92 × 74.94 × 151.66
HSHG-60-4			150.24 × 75.18 × 150.36
HSHG-90-1	90	0.3	149.40 × 74.52 × 148.92
HSHG-90-2			148.34 × 73.48 × 149.42
HSHG-90-3			148.40 × 75.32 × 149.16
HSHG-90-4			149.82 × 74.84 × 150.26

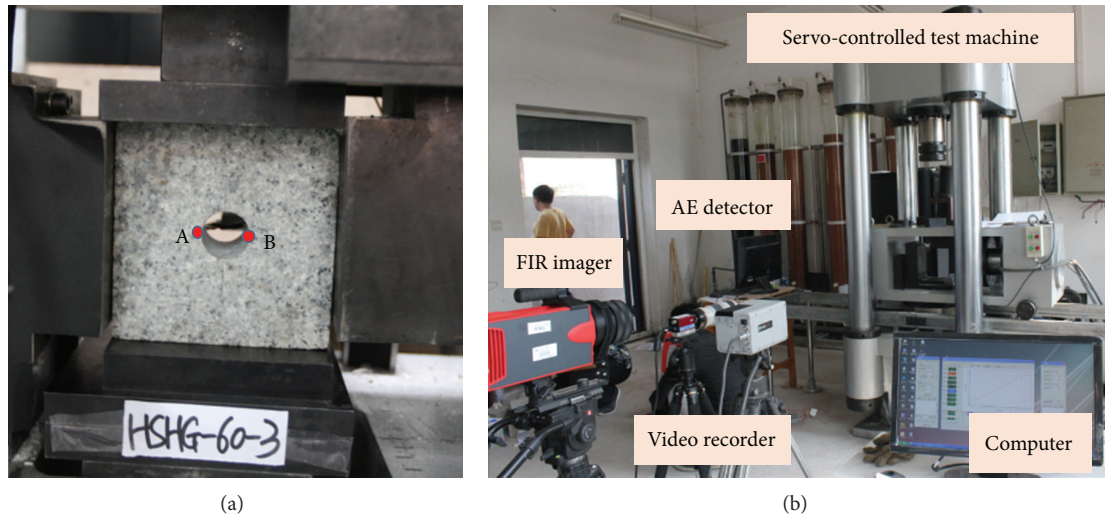


FIGURE 1: The servo-controlled rock test machine (RLW-3000).

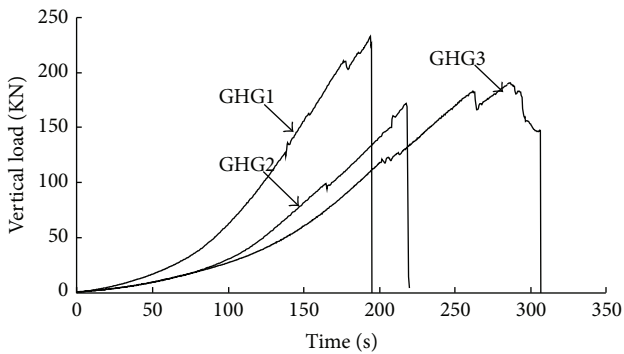


FIGURE 2: Vertical load-time curves of the granite specimens under uniaxial compression.

2.2. *Fracturing Images.* The macroscopic fracture pictures of the granite tunnel specimens under different lateral pressure

were shown in Figure 3. It is noted that the specimens were named HSHG-XX-Y, where XX indicated the lateral force, and Y was the number in that group.

For the specimens under the horizontal force of 30 KN, only a few small rock fragments were observed to fall down from the right side wall of the tunnel at 825 s, and larger flakes of rocks were spalled on the surface of the tunnel wall at 910 s. Macrofractures initiated from the two sides and then propagated to the boundary at 940 s, which resulted in the bulking of the rock tunnel (Figure 3(a)).

Figure 3(b) demonstrated the fracture patterns of the specimen HSHG-60-2. A few rock fragments appeared at 838 s, and some small fragments were observed to eject from the sides of the tunnel at 961 s. The specimen fractured in the same mode with HSHG-30-2 when the macrofractures appeared.

The intensive rock burst appeared in the specimen HSHG-90-2. When the horizontal force was increased to



FIGURE 3: The macroscopic fracture pictures of the granite specimens.

90 KN, rock spalling did not appear until 909 s. The specimen collapsed abruptly only in several seconds when the explosion of rock fragments was observed. Due to the high vertical stress and dilatation of the rock, the cross section of the tunnel was compressed to be an ellipse shape.

2.3. Far Infrared Thermal Results. The far infrared thermal imager can monitor high temperature or low temperature

on the surface of the specimens. Only the high temperature of Point A and Point B (Figure 1) was recorded to analyse the rock burst precursors. Because the compressive stress concentrating around the tunnel wall and the friction between the microcracks produced energy release, the high temperature was much useful to predict the hazard.

The vertical force versus time curves and the temperature of Point A and B on two sides of the wall versus time

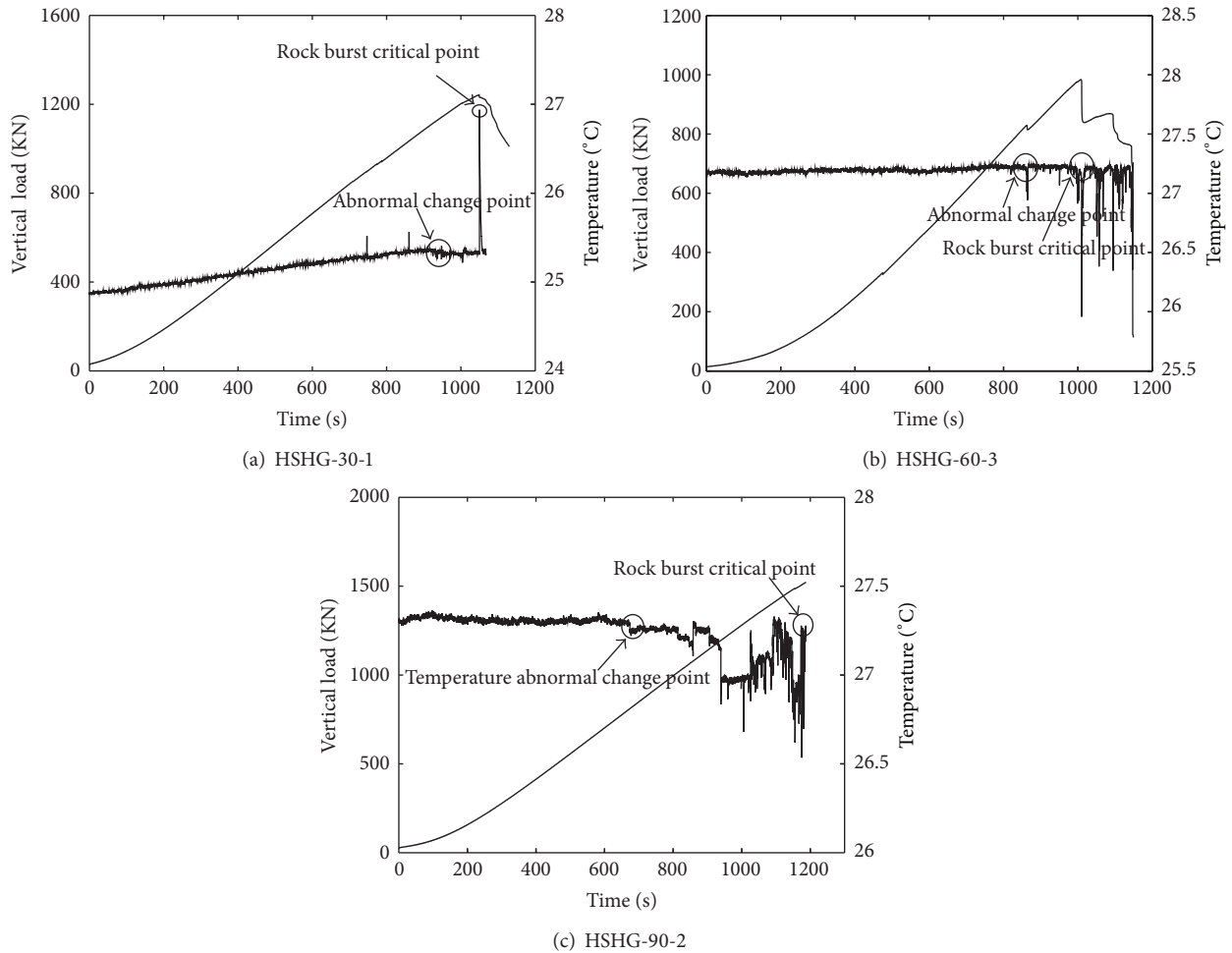


FIGURE 4: The relation of the temperature, vertical load, and loading time of the granite specimens under different lateral pressures.

curves were plotted in Figure 4. It was observed that the average temperature of Point A and Point B increased as the vertical stress increased. The drops of the force-time curves resulted in the temperature fluctuations. When the stress was increased gradually prior to the tunnel failure, the temperature had many sudden jumps and drops. The fluctuation of the temperature suggested the events of stress concentration or stress release. The tensile fracturing led to the temperature drops, whereas the compressive stress or the friction between the crack walls led to the temperature jumps.

The temperature had an obvious great jump prior to the rock burst point, which could be termed as rock burst critical point. How to capture this critical point becomes much significant for prediction of rock bursts in tunnel engineering.

It is interesting that the range of temperature variation for the specimen HSHG-30-1 was smaller than the specimens HSHG-60-3 and HSHG-90-2 due to the variation of the lateral stress. The compressive stress was much smaller in the specimen HSHG-30-1 than in the specimens HSHG-60-3 and HSHG-90-2. Similarly, compared with the specimen HSHG-60-3, the variation of the temperature was more violent for the specimen HSHG-90-2.

2.4. Acoustic Emission Results. Figure 5 shows the vertical force and AE rate versus the loading time curves for the granite tunnel specimens under different vertical stress. The AE activities during the whole loading process could be divided into four stages: the increasing stage, the active stage, the decreasing stage, and the burst stage. In the first stage, AE rate was increased gradually with the increasing of the vertical stress, resulting from the opening or closing of the microcracks existing in the rocks. Initiation, propagation, and coalescence of new cracks led to AE increasing in the active stage. The curves of all the specimens underwent a downward period. The AE rate was decreased gradually even though the vertical stress was increased continuously in this stage. Only a small number of AE events were observed at the end of the decreasing stage. The accumulated elastic energy in the placid period caused the rock burst finally. In the last period, the weakened rock tunnel could not contain such great amount of energy applied by the loading system, and the release of the potential energy made the surrounding rock to reach another equilibrium state, accompanied by a sharp vertical force drop.

Rocks undergoing brittle failure produce a large number of acoustic emissions of varying amplitudes due to the formation and growth of microcracks, tensile cracks, shear cracks,

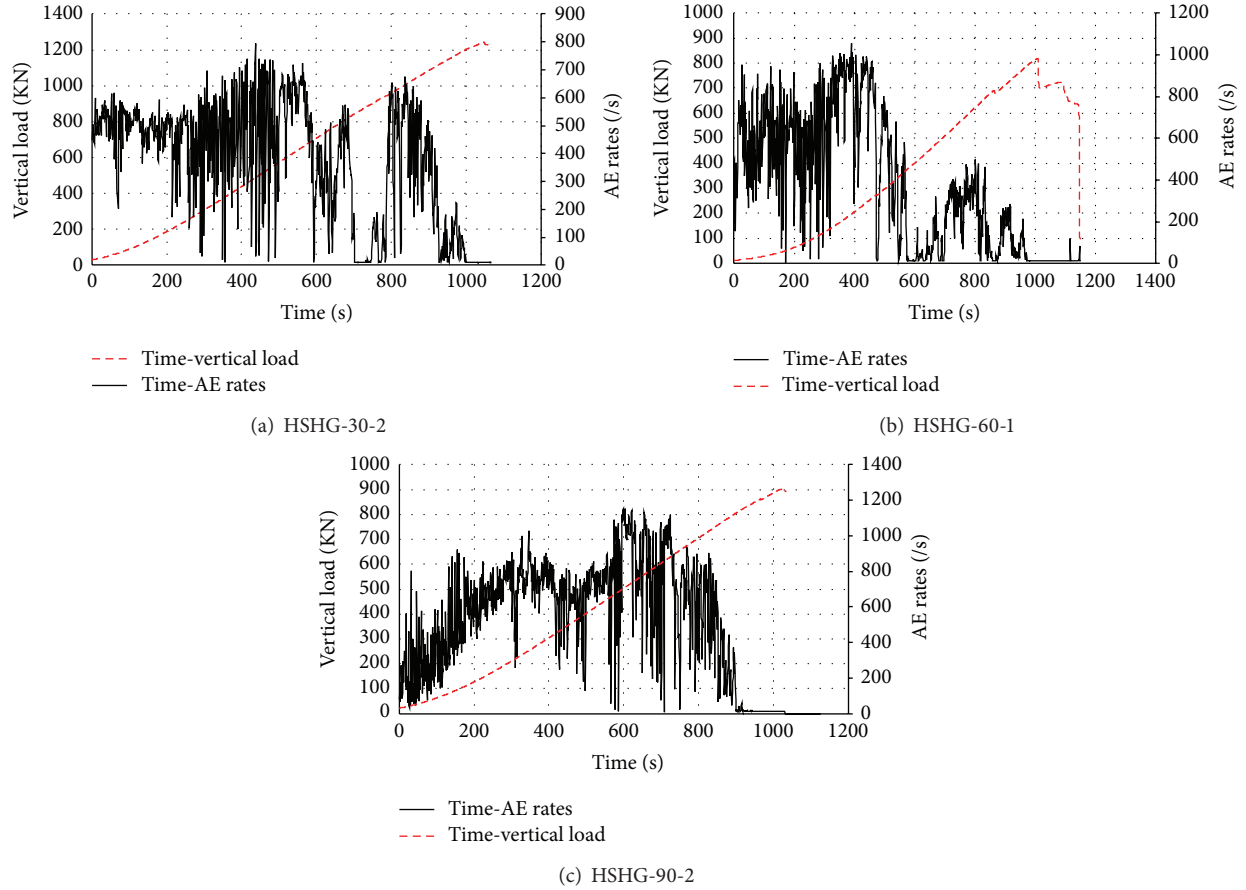


FIGURE 5: The curves of the vertical force and AE rate versus the loading time for the granite tunnel specimens.

and so forth. The cumulative as well as the discrete frequency-amplitude distribution of such AE shows a descending gradient and a major portion of it is linear. The amplitude data of that linear range is used to compute the b -value (slope of the log-linear frequency-magnitude distribution of AE) following the Gutenberg-Richter relationship for the cumulative frequency distribution data [21]. The Gutenberg-Richter Law in the most common form reads as follows:

$$\text{Log}[N(M)] = a - bM, \quad (1)$$

where N is the number of events with magnitude larger than M .

M and a and b are two constant coefficients.

Relation (1) has been widely researched and applied to study the effect of the magnitude uncertainty on the b -value and the effect of various regionalization on the b -value [22, 23]. In this investigation, the relation of accumulative frequency of AE events and the magnitude of AE energy was calculated to obtain the b -value by G-R law.

There are good prospects for making a quantitative diagnosis of the fracture development in the test rock structure under stress on the basis of AE amplitude information in terms of b -value. However, the method used for the determination of b -value is important, since selection of the

amplitude or magnitude limits of the “linear range” of the cumulative frequency distribution data of AE is critical. In the present study, the data of low amplitude or magnitude were included to calculate the b -value.

Figure 6 plots the curves of the vertical force and the b -value of AE events versus the loading time for the granite tunnel specimens. It was observed that the b -value fluctuated in a limited range at a high level in the beginning loading stage, indicating stress concentration, stress transfer, or stress release in the tunnel model, whereas the associated initiation and propagation of the microcracks in the specimens did not cause macrofracturing. The AE events generated due to the closure and rubbing of preexisting microcracks in the rock began to show a high b -value in this stage.

The b -value demonstrated a descendent gradient when the rock burst critical point was approaching. This phenomenon could be observed in all the rock specimens. The continuous descent of the b -value could be considered as the precursors to predict the tunnel rock bursts. Here the point where the b -value began to decrease was assumed to be the critical point.

The high b -value arose due to a large number of small AE hits (or events) representing new crack formation and slow crack growth, whereas the low b -value indicated faster or unstable crack growth accompanied by relatively high

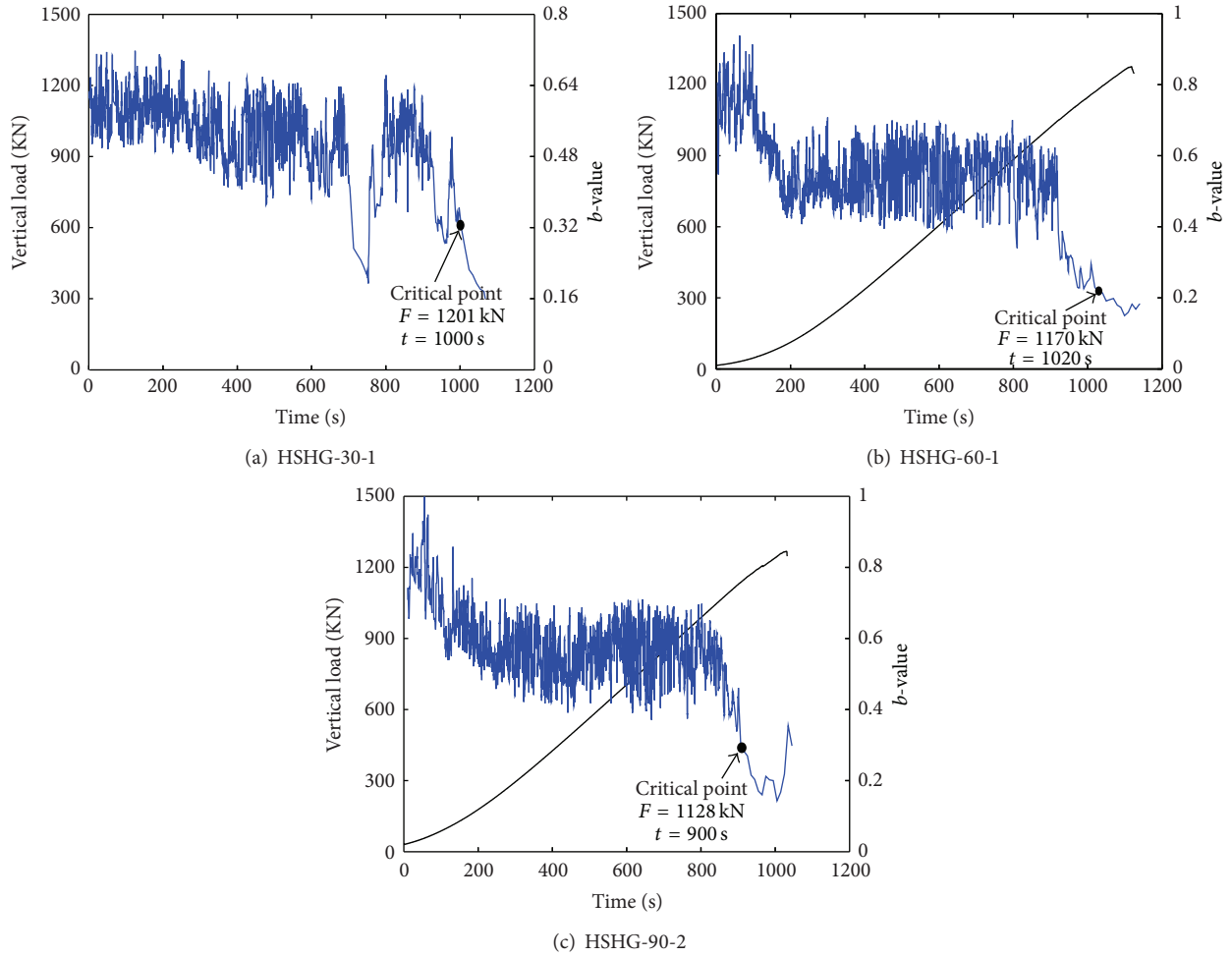


FIGURE 6: The curves of the vertical load and the b -value of AE energy versus the loading time for the granite tunnel specimens.

TABLE 2: Statistical analysis of the critical time and vertical peak load time.

F_H (kN)	Specimen no.	F_{max} (kN)	t_{max} (s)	F_b (kN)	t_b (s)	F_b/F_{max} (%)	Average F_b/F_{max} (%)	t_b/t_{max} (%)	Average t_b/t_{max} (%)
30	HSHG-30-1	1242	1048.7	1201	997.9	96.7	97.5	95.2	96.7
	HSHG-30-2	1241.5	947.5	1220	930.6	98.3		98.2	
60	HSHG-60-1	1275.8	1118.2	1170	1019.9	91.7	95.8	91.2	95.3
	HSHG-60-3	1287	1107.4	1285	1099.8	99.8		99.3	
90	HSHG-90-1	1521	1188	1415	1098.7	93	91.0	92.5	89.9
	HSHG-90-2	1267.2	1030.7	1128	900	89		87.3	

F_b : vertical load at the critical point of the b -value.
 t_b : time at the critical point of the b -value.
 F_{max} : vertical peak load.
 t_{max} : time at the peak load point.
 F_H : lateral load (horizontal load).

amplitude AE in large numbers, which resulted in the impending rock burst of the tunnel model.

Table 2 listed the peak vertical load, the load at the critical point on the b -value curves, and their times (HSHG-30-1, HSHG-30-2, HSHG-60-1, HSHG-60-3, HSHG-90-1, and HSHG-90-2). To make a comparison, the vertical peak load

and the peak time for all the specimens were listed. The average ratio of the vertical load at the critical point to the peak load (F_b/F_{max}) and the average ratio of the critical time to the peak load time (t_b/t_{max}) were calculated. It could be found that the average F_b/F_{max} was decreased from 97.5% to 91.0%, and the average t_b/t_{max} was decreased from 96.7% to

89.9% when the horizontal load was increased from 30 KN to 90 KN.

3. Discussion

3.1. The b -Value. The fluctuation of the b -value indicated the progressive fracture and damage process of the rock tunnel specimens under biaxial compression. The results show that, during the early loading stages, a large number of AE events generated from the closure and rubbing of the preexisting microcracks made a high b -value. Then the formation and propagation of new cracks on the eventual fracture plane produced a large amount of energy and AE hits, resulting in the high b -value. In the elastic deformation stage, the b -value curves showed a decreasing trend due to a small number of AE events. The b -value decreased sharply due to the crack coalescence and the accompanying stress relief under the further increased stress. The critical time of this decreasing phenomenon can be considered as most useful for prediction of rock burst time. These observations have some important applications for monitoring the stability and integrity of rock tunnels.

3.2. The Alarm Time of the Tunnel Rock Burst. The anomalies recorded by all kinds of sensors are often used to predict earthquakes, slope failure, or rock burst. The abnormal variation of seismic events are often analyzed to predict earthquakes, and anomalous microseismic changes often appear prior to slope failure or rock burst in rock engineering. The abnormal variation of the results monitored by AE and FIR can also provide the precursory information to predict the rock burst time of the tunnel model.

One of the most difficult problems of rock burst forecasting is time prediction. However, time prediction requires a better understanding of the processes which take place in rocks. Unlike earthquakes, the laboratory experiments can provide many monitoring techniques to capture the occurrence of abnormal behaviors of the small rock specimens.

The alarm time predicted by FIR technique was earlier than the time predicted by AE technique. The alarm time of the critical point monitored by FIR and AE techniques and the peak loading point were listed in Table 3. We used the critical time to alarm the rock burst hazards. In far infrared monitoring, the critical point was defined as the appearance of the abnormal temperature changes prior to the rock bursts. In acoustic emission monitoring, the critical point was defined as the point where the b -value of the frequency-magnitude distribution of AE began to descend sharply. As shown in Table 3, the alarm time predicted by far infrared radiation monitoring was earlier than that by acoustic emission monitoring for all the specimens. It indicated that the temperature changes were more sensitive than those of acoustic emission. The local temperature is increased when the stresses concentrated, whereas the acoustic emissions only can be located when the stresses are increased to failure occurrence subsequently. Therefore, the abnormal changes of the acoustic emission is later than those of the temperature.

TABLE 3: The alarm time of rock bursts analyzed from the AE and FIR results.

F_H	Specimen no.	Alarm time (s)	
		FIR	AE
30	HSHG-30-1	923	999
	HSHG-30-2	875	905
60	HSHG-60-1	879	1009
	HSHG-60-3	788	785
90	HSHG-90-1	674	924
	HSHG-90-2	878	856

The AE technique seems to be the most useful monitoring technique in rock tunnels. Due to rock's opaque feature, it is difficult to monitor the deformation and failure in rocks by using camera or video monitoring. What is more, compared with soil, rocks have less deformation before failure because of their high stiffness, which makes the deformation of rocks much smaller than soil. Similar to video monitoring, FIR technique only records the temperature variations of rock surfaces. Neither of them can detect the internal failure of analyzing the seismic sources, released energy, and associated amplitude and counts in rocks.

3.3. The Rock Burst Prediction Method. A combined prediction method based on multiparameters by multimonitoring techniques will provide a more useful and accurate early alarm [24, 25]. The video monitoring can capture some phenomena of rock fragment spalling, ejection, or rock explosion, the far infrared radiation technique can monitor the temperature variation on the surface of rocks, and the AE technique provides the seismic event counts, energy release, and failure location information. Each technique has its own advantages. The combined prediction method based on the high speed video, the far infrared and AE technique will provide a more accurate rock burst alarm. The block scheme of rock burst prediction algorithm is shown in Figure 7. The first criterion is whether the phenomenon of rock fragment fall down, ejection or rock explosion can be observed. The second criterion is the appearance of abnormal temperature changes monitored by the FIR technique. The last criterion is the descent of b -value based on AE data analysis. The alarm should be cancelled if all the criteria are not satisfied. Otherwise, these abnormal variations can be considered as precursors of a potential rock burst hazard in the rock tunnel, and some supporting measures should be carried out to strengthen the tunnels.

4. Conclusions

The acoustic emission and far infrared techniques and video monitoring were applied to monitor the failure precursors of a rock tunnel model subjected to biaxial compressive stress. The images of the fracturing process, temperature variation of the tunnel, and the spatiotemporal serials of the acoustic emission were obtained. The precursors of the monitored data by AE and FIR were analyzed. A combined

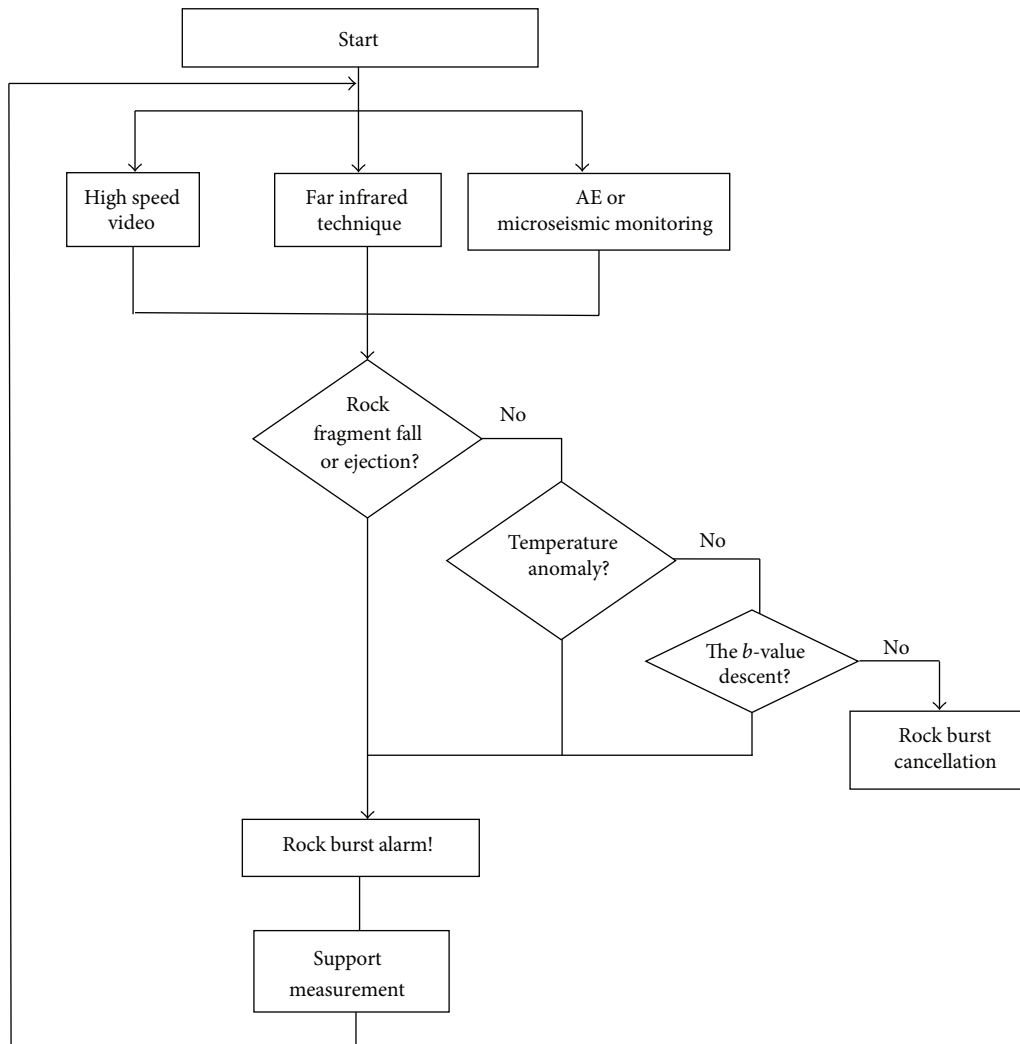


FIGURE 7: The block scheme of rock burst prediction algorithm.

rock burst prediction method based on acoustic emission and far infrared radiation was proposed to analyze rock burst hazards in tunneling engineering. The following conclusions can be drawn.

- (1) The vertical pressure can enhance the stability of the tunnel model and delay the approach of rock burst hazards. However, the tunnel with higher confining pressure demonstrated a more abrupt and stronger rock burst.
- (2) Rock fragment spalling and abnormal temperature around the wall were observed before the collapse of the tunnel.
- (3) The analysis of the AE events showed that a sudden drop and then a quiet period could be considered as the precursors of the rock burst hazard.
- (4) The abnormal temperature appeared earlier than the descent of the AE b -value. The analysis indicated that the temperature variations was more sensitive than the AE b -value variations to predict rock bursts.

Acknowledgments

This work was supported by the National Program on Key Basic Research Project of China (973 Program) (Grant no. 2014CB047100), the National Natural Science Foundation of China (Grant nos. 51121005, 51079017, and 51274053), the Foundation for the Author of National Excellent Doctoral Dissertation of China (no. 200960), the Open Research Fund Program of the Key Laboratory of Safety for Geotechnical and Structural Engineering of Hubei Province, and the Fundamental Research Funds for the Central Universities in China (DUT12ZD102).

References

- [1] C. A. Tang, "Preliminary engineering application of microseismic monitoring technique to rockburst prediction in tunneling of Jinping II project," *Journal of Rock Mechanics and Geotechnical Engineering*, vol. 2, no. 3, pp. 193–208, 2010.
- [2] N. W. Xu, C. A. Tang, L. C. Li et al., "Microseismic monitoring and stability analysis of the left bank slope in Jinping first

- stage hydropower station in southwestern China,” *International Journal of Rock Mechanics and Mining Sciences*, vol. 48, no. 6, pp. 950–963, 2011.
- [3] C. Fairhurst and N. G. W. Cook, “The phenomenon of rock splitting parallel to the direction of maximum compression in the neighborhood of a surface,” in *Proceedings of the 1st Congress on the International Society of Rock Mechanics*, vol. 1, pp. 687–692, National Laboratory of Civil Engineering, Lisbon, Portugal, 1966.
- [4] B. G. White, J. K. Whyatt, and D. F. Scott, “Geologic factors in rock bursts in the coeur d’alene mining district: structure,” in *Proceedings: Mechanics and Mitigation of Violent Failure in Coal and Hard-Rock Mines*, H. Maleki, P. F. Wopat, R. C. Repsher, and R. J. Tuchman, Eds., pp. 217–230, US Bureau of Mines Special Publication, 1995.
- [5] Y. Zhao, “Crack pattern evolution and a fractal damage constitutive model for rock,” *International Journal of Rock Mechanics and Mining Sciences*, vol. 35, no. 3, pp. 349–366, 1998.
- [6] S. J. D. Cox and C. H. Scholz, “Rupture initiation in shear fracture of rocks: an experimental study,” *Journal of Geophysical Research*, vol. 93, no. 4, pp. 3307–3320, 1988.
- [7] V. Frid, “Electromagnetic radiation method water-infusion control in rockburst-prone strata,” *Journal of Applied Geophysics*, vol. 43, no. 1, pp. 5–13, 2000.
- [8] V. Frid, “Calculation of electromagnetic radiation criterion for rockbursts hazard forecast in coal mines,” *Pure and Applied Geophysics*, vol. 158, no. 5–6, pp. 931–944, 2001.
- [9] N.-G. Geng, C.-Y. Cui, and M.-D. Deng, “The remote sensing observation in experiments of rock failure and the beginning of remote sensing rock mechanics,” *Acta Seismologica Sinica*, vol. 14, pp. 645–652, 1992.
- [10] C. Y. Cui, M. D. Deng, and N. G. Geng, “Rock spectral signatures under different pressures,” *Chinese Science Bulletin*, vol. 38, no. 16, pp. 1377–1382, 1993.
- [11] L. X. Wu and J. Z. Wang, “Study on the thermal infrared radiation temperature omen in coal-measure rock yielding underground pressure,” *China Mining Magazine*, vol. 6, no. 6, pp. 42–48, 1997.
- [12] L. X. Wu and J. Z. Wang, “Features of infrared thermal image and radiation temperature of coal rocks loaded,” *Science in China D*, vol. 41, no. 2, pp. 158–164, 1998.
- [13] L. X. Wu and J. Z. Wang, “Infrared radiation features of coal and rocks under loading,” *International Journal of Rock Mechanics and Mining Sciences*, vol. 35, no. 7, pp. 969–976, 1998.
- [14] X. Lei, K. Masuda, O. Nishizawa et al., “Detailed analysis of acoustic emission activity during catastrophic fracture of faults in rock,” *Journal of Structural Geology*, vol. 26, no. 2, pp. 247–258, 2004.
- [15] D. A. Lockner, J. D. Byerlee, V. Kuksenko, A. Ponomarev, and A. Sidorin, “Quasi-static fault growth and shear fracture energy in granite,” *Nature*, vol. 350, no. 6313, pp. 39–42, 1991.
- [16] K. Mogi, *Earthquake Prediction*, Academic Press, London, UK, 1985.
- [17] M. Cai and P. K. Kaiser, “Assessment of excavation damaged zone using a micromechanics model,” *Tunnelling and Underground Space Technology*, vol. 20, no. 4, pp. 301–310, 2005.
- [18] N. Dixon and M. Spriggs, “Quantification of slope displacement rates using acoustic emission monitoring,” *Canadian Geotechnical Journal*, vol. 44, no. 8, pp. 966–976, 2007.
- [19] D. Arosio, L. Longoni, M. Papini, M. Scaioni, L. Zanzi, and M. Alba, “Towards rockfall forecasting through observing deformations and listening to microseismic emissions,” *Natural Hazards and Earth System Science*, vol. 9, no. 4, pp. 1119–1131, 2009.
- [20] P. G. Meredith, I. G. Main, and C. Jones, “Temporal variations in seismicity during quasi-static and dynamic rock failure,” *Tectonophysics*, vol. 175, no. 1–3, pp. 249–268, 1990.
- [21] B. Gutenberg and C. F. Richter, *Seismicity of the Earth and Associated Phenomena*, Princeton University Press, Princeton, NJ, USA, 1954.
- [22] W. D. Smith, “The *b*-value as an earthquake precursor,” *Nature*, vol. 289, no. 5794, pp. 136–139, 1981.
- [23] M. V. M. S. Rao, D. S. N. Murthy, G. M. Nagaraja Rao, S. K. Mohanty, and S. Udayakumar, “Stress-induced micro-cracking and brittle failure of Godhra granite, Gujarat: a laboratory investigation using acoustic emission,” *Journal of the Geological Society of India*, vol. 64, no. 6, pp. 775–783, 2004.
- [24] T.-H. Yi, H.-N. Li, and M. Gu, “Recent research and applications of GPS-based monitoring technology for high-rise structures,” *Structural Control and Health Monitoring*, vol. 20, no. 5, pp. 649–670, 2013.
- [25] T.-H. Yi, H.-N. Li, and M. Gu, “Optimal sensor placement for structural health monitoring based on multiple optimization strategies,” *The Structural Design of Tall and Special Buildings*, vol. 20, no. 7, pp. 881–900, 2011.

Research Article

Statistical Estimation of Changes in the Dominant Frequencies of Structures in Long Noisy Series of Monitoring Data

Fanis Moschas¹ and Eva Steirou²

¹Laboratory of Geodesy and Geodetic Applications, Department of Civil Engineering, University of Patras, 26500 Patras, Greece

²GFZ German Research Centre for Geosciences, Section 5.4 Hydrology, Telegrafenberg, 14473 Potsdam, Germany

Correspondence should be addressed to Fanis Moschas; fmoschas@upatras.gr

Received 24 September 2013; Accepted 12 November 2013

Academic Editor: Ting-Hua Yi

Copyright © 2013 F. Moschas and E. Steirou. This is an open access article distributed under the Creative Commons Attribution License, which permits unrestricted use, distribution, and reproduction in any medium, provided the original work is properly cited.

Damage in structures is reflected in permanent changes of their natural frequencies and theoretically can be derived through measurements. Still, measurement-derived frequencies of structures usually reflect a superimposition of various effects, fluctuations due to environmental and loading conditions, noise, and possible permanent changes (damage or repair). The amplitude of the latter is usually of the same order of magnitude with the other effects; hence permanent shifts are masked by noise and cannot be identified, especially in long monitoring records. In order to overcome this problem, essential for the assessment of the structural health of various key structures, we adopt a statistical approach developed for the identification of shifts (inhomogeneities) in normally distributed climatological data, in particular the SNHT test. The efficiency of the SNHT was first tested on synthetic data and then on sets of estimates of dominant frequencies of a decaying pedestrian bridge. It was found that under certain conditions the SNHT can identify the location of shifts in dominant frequencies of structures; the amplitude of the shifts can then be easily computed. Since the efficiency of the test increases with the length of the time series, this test seems especially suitable for the analysis of long monitoring records.

1. Introduction

Structural damage in engineering structures is reflected in changes of their dominant frequencies, and there exist various techniques to infer damage from the analysis of measurements of the behaviour of the structures under various excitations and ambient conditions, usually accelerometer measurements [1–5]. However, in rare cases only observed changes in dominant frequencies are large (Figure 1(a)) and consistent with other compelling evidence (deterioration of the structure deduced from a visual inspection, highly reduced stiffness testified by increased deflections, correlation with a potentially destructive event, an earthquake, fire, etc.). In the majority of cases observed changes in dominant frequencies of structures are usually small (see Figure 1(b)) and of the same order of magnitude with transient changes, which may range up to 3–5% of the frequency value [3, 6, 7].

In particular, measurement-based determination of dominant frequencies of structures may reflect a combination

of several effects, including (1) measurement and computation bias, usually noise which lowers the accuracy of measurement-based results and calls for additional data-filtering [8, 9], (2) transient changes of the natural frequencies due to transient loading [3, 6, 7] or environmental effects (rain, snow, etc.), occasionally effects with seasonal persistence, for example, icing of bridge-supporting cables, see [10, 11], (3) excitation of different, neighbouring modes, and (4) permanent changes (shifts) of the natural frequencies due to damage and gradual deterioration (or even repairs) of the structures [1, 3, 5, 6, 12, 13]. For this reason, estimates of natural frequencies even before and after a certain potential damaging event (for instance an earthquake) tend to correspond to noisy data sets, that is, sets of fluctuating values, not giving clear evidence of a frequency shift.

In order to overcome this problem, a stochastic approach has been proposed in order to recognize whether two sets of data of measured frequency changes, before and after a critical event, indicate a real shift of frequencies and evidence

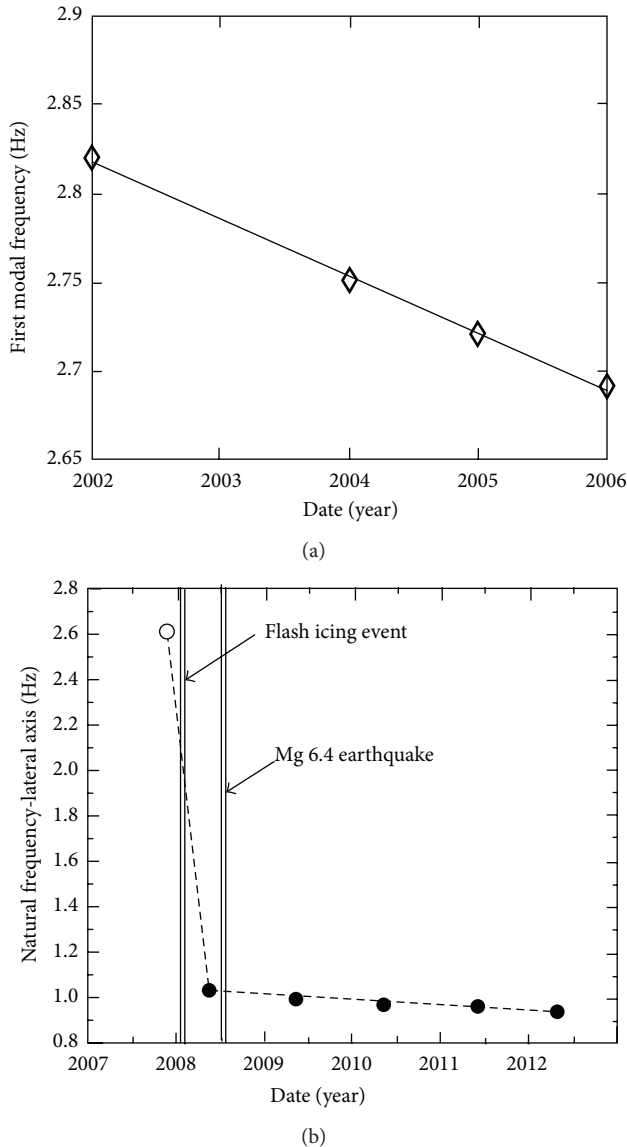


FIGURE 1: Examples of sudden and gradual drop of natural frequencies due to structural deterioration. (a) Natural frequencies of a concrete highway bridge derived from accelerometer measurements (modified after [3]) and (b) the extraordinary changes in the natural frequencies of the lateral axis of a timber pedestrian bridge derived from Robotic Total Station measurements (Stiros and Moschas, in review).

of damage (Moschas and Stiros, in review). This approach, based on a strict cross-correlation analysis, is especially suitable for cases of comparison of noisy spectral peaks corresponding to two different surveys and reflecting noise-contaminated data, mostly spectral leakage. However, this approach does not cover multi-epoch data, cases of a gradual decay (see Figure 1(b)), and so forth.

Another major problem is that permanent or periodic monitoring systems are currently available in several important structures (for instance, see [7]), leading to a large

volume of data, including measurement-based estimations of dominant frequencies of the structure as a function of time. The time series of measurement-derived modal frequencies are likely to reflect a combination of some or of all the effects stated above; they are noisy and long, and even if there is some indication of drop of dominant frequencies, the available techniques do not permit to identify whether and where a shift can be documented and use this result for the evaluation of the structural health of the monitored structures. This makes it necessary to introduce more sophisticated stochastic approaches for the analysis of multi-epoch data.

This situation is somewhat similar to a problem that has been faced in the past in the analysis of climatological data, like sea level, rainfall, or temperature records. The latter are usually affected by unrecorded changes in the measuring procedure, in the sensors or their caging, and of the environment around the measuring stations, leading to shifts of the segments of the time series after the unrecorded change(s) and biased estimations of the climatic signature of the station records. The need to detect such undocumented changes (inhomogeneities, mostly shifts) in the available records led to the development of various inhomogeneity tests (shift detectors) based on different types of methodologies like linear regression analysis [14] or decomposition in orthogonal functions [15] among which is the Standard Normal Homogeneity Test (SNHT; see [16]). This test (and its variations) remains the simplest and one of the most popular tests for the detection of inhomogeneities in climatological data sets.

The use of the SNHT test is usually confined to climatological studies and has not been adopted in other fields of science and engineering. In this paper we use this test to detect small changes (statistically significant, permanent shifts) of frequencies of structures derived from multisurvey field measurements. This test is first applied on synthetic data describing hypothetical frequency measurements and shifts, and then it is used to analyze multi-epoch measurements of the dominant frequency of a timber bridge in Patras, Greece.

Application of this test is successful if the examined time series are dominated by white noise [17]. Clearly, no data to confirm such hypothesis exist for natural frequency estimates but for the present preliminary approach it can be assumed that the combination of the four effects mentioned above tends to satisfy this condition.

2. Methodology

2.1. Overview. In our study we use the SNHT on data-series of measurement-based estimates of the dominant frequencies of a certain bridge, in order to detect possible shifts in its 1st (fundamental) natural frequency. We assume that measured peaks express the same modal frequency (or the same set or nearby modal frequencies) and that the two sets differ a little from each other and such differences indicate noise, transient effects, and in some cases small permanent changes to be identified. These data can in a first approach be considered to be dominated by white noise.

We focus on estimates of dominant frequencies in spectra derived from accelerometer recordings, but this method is

efficient for other types of measurements, such as frequencies derived from geodetic measurements of displacement, and so forth. Spectra are usually computed on the basis of FFT, but in our study we also use spectra based on the Least Squares Method [18] and the Normperiod Code [19]. A main advantage of this method is that it permits to estimate the level of statistical significance of the computed peaks and focus on the statistically significant peaks.

Then we apply the SNHT and try to identify at which point and at which level of significance a shift in frequencies can be documented. If the test is positive, the mean frequencies before and after the inhomogeneity are computed. The difference of the two values is a reliable estimate of the frequency change. Simple stochastic techniques permit to compute the variance of this estimate.

The SNHT is usually used for time series (e.g., monthly estimates of dominant frequencies), but under certain circumstances it can be used for sets of measurements corresponding to discrete epochs (surveys), each with several measurements (elements). In this last case, an equal number of frequency measurements should preferably be used for each survey. Additional limitations are imposed by the SNHT (see below). The overall process is summarized in the flowchart of Figure 2. Changes in the natural frequency of the studied bridge, due to gradual deterioration, were assumed to resemble abrupt shifts (inhomogeneities) between data sets from surveys carried out once per year. For this reason the simple SNHT, which is suitable for identifying a single shift in time series, was used for testing time series before and after a possible shift. As gradual deterioration of a structure may be expressed by multiple shifts of the natural frequency or by a gradual fall of the natural frequency during a certain period, different versions of the SNHT which permit to identify multiple shifts or changing trends [20] in the data set could be also used.

2.2. The Standard Normal Homogeneity Test (SNHT). The Standard Normal Homogeneity Test was introduced by Alexandersson [16] in order to identify inhomogeneities in time series of rainfall and temperature measurements, characterized by white noise. Inhomogeneities are defined as shifts in the mean value of the data before and after the inhomogeneity (shift). The same test and its variations are widely used in climatology [21].

The function of the test is to split a “suspect” time series in two segments and examine whether these two segments have different means. The process is repetitive, with the split point moving and covering all points of time series. For a point ν dividing a time series in two segments, a certain test variable T_ν is calculated for each pair of segments. A statistically significant inhomogeneity is identified if the value of T_ν corresponds to a peak exceeding a certain threshold value.

The main computational steps are the following.

(a) We examine a “suspect” time series q_i with length equal to n ($i = 1, 2, 3, \dots, n$) with a possible shift at

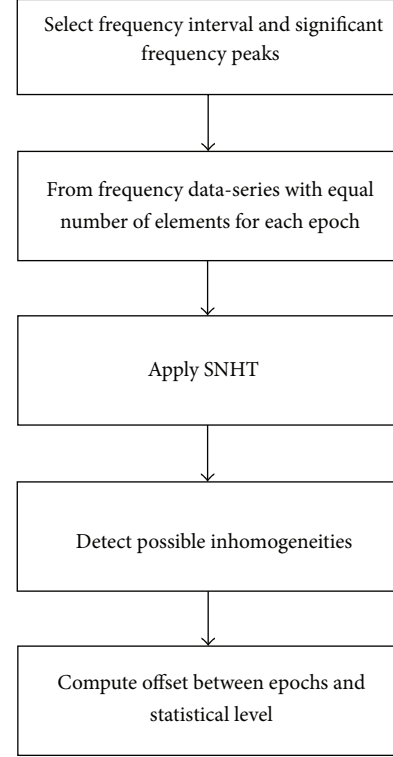


FIGURE 2: Flowchart summarizing the proposed methodology for detecting frequency shifts in spectra from structural vibration data sets using the SNHT.

point ν , $0 \leq \nu \leq n$ and we form a new normalized time series z_i using

$$z_i = \frac{(q_i - \bar{q})}{s_q} \quad (1)$$

with \bar{q} equal to the mean value and s_q to the standard deviation of q_i .

(b) Then we investigate whether all the elements z_i follow a normal distribution $N(0, 1)$ (null hypothesis H_0) or two different normal distributions $N(\mu_1, 1)$ and $N(\mu_2, 1)$ because of the shift (inhomogeneity, shift) at point ν (alternative hypothesis H_1). This is described by

$$H_0 : Z \in N(0, 1), \quad \forall i$$

$H_1 : \{\text{for } 1 \leq \nu \leq n, \mu_1 \neq \mu_2 \text{ we have}$

$$Z \in N(\mu_1, 1) \text{ for } i \leq \nu \text{ } Z \in N(\mu_2, 1) \text{ for } i > \nu\}. \quad (2)$$

(c) Hypotheses H_0 and H_1 are tested on the basis of a variable T_ν defined by

$$T_\nu = \nu \bar{z}_1^2 + (n - \nu) \bar{z}_2^2 \quad (3)$$

with (\bar{z}_1) and (\bar{z}_2) indicating the mean values of z before and after a point ν . This process is repeated for

the various values of ν , $0 < \nu < n$, and each time a variable T_ν is calculated. From the set of the various values of T_ν , the time series of T_ν , and the value defined by (4) is computed as follows:

$$T_0 = \max \{T_\nu\}. \quad (4)$$

If T_0 is larger than a critical value, an inhomogeneity at (or close to) point ν is documented. This critical value depends on the length of the compared time series and the chosen level of statistical significance and defines the statistical significance level of T_ν . Details are given by Alexandersson and Moberg [20] and Sahin and Cigizoglu [21].

Practically, the estimation of a shift is reliable for relatively long time series (with >5 elements) and for shifts somewhat distant from the first and last point of the time series [16]. Calculations are made with codes freely available by various investigators. In this study we used the code presented by Steirou [17].

2.3. Amplitude of the Shifts. If a statistically significant shift is documented in the examined time series, the latter is split in two segments; a mean value is computed for each of them, and from their difference the amplitude of the shift is estimated. Its variance (or typical error) can be also easily computed.

3. Detection of Shifts in Natural Frequencies Using the SNHT: Assessment Using Synthetic Data

In order to test the limits of application of the SNHT in spectral data, we first applied the SNHT on synthetic data series simulating measurements of a modal frequency, in an accuracy-oriented test. At first we assume “initial,” idealized time series presenting frequency estimates with no shifts or noise present. Then, in some of them, shifts were produced. Finally, white noise was added in these data series “dithering”. This noise accounts for measurement errors, for multiple nearby modal frequencies, and for the apparent/transient shifts (see Section 1).

Similar evaluation tests have been carried out for synthetic climatological data characterized as white noise but also for more complex synthetic climatological data (mostly generated by an AR(1) model). Results are encouraging for the case of white noise or data with short-term memory but false-alarm problems are still faced in the case of data with long-term persistence [17].

The synthetic data-series used in the present study included frequency shifts from an initial, idealized natural frequency of 1 Hz with values equal to 0.00, 0.02, 0.04, and 0.08 Hz. The selection of the particular frequency does not limit the generality because SNHT analyses normalized data (1). White noise added to the data had a standard deviation $\sigma = 0.04, 0.06, \text{ and } 0.08$ Hz. The selected standard deviations correspond to a 4%, 6%, and 8% deviation from the initial natural frequency of 1 Hz. These values are compatible with the values of transient changes in natural frequencies of structures reported by various investigators [3, 6, 7]. The

results from the application of the SNHT to the synthetic data are summarized in Figures 3–5.

From these figures, three main results were obtained.

First, shifts larger than the noise level (σ) can be clearly identified by a peak in the T_ν value. Still, shifts statistically insignificant can be detected if their level is approximately 2/3 of the noise level (data set 2, step 0.04 Hz in Figure 4).

Second, the location of the detected shift was close to the real location within a distance of maximum 3–4 point from the shift point (see dashed band in Figure 3) while on some cases the point of the shift, as identified by the SNHT, was on the same location with the real shift (see Figure 4).

Third, for the selected levels of data and uncertainties no false alarms (false identifications of frequency shifts) were detected.

These results encourage the application of SNHT in Structural Health Monitoring.

4. Case Study: Detection of Natural Frequency Shifts of a Timber Pedestrian Bridge

4.1. The Studied Bridge: Bearing System and Vibration Measurements. The tested timber footbridge is shown in Figure 6. It crosses the Kanellopoulos Avenue, at the northern entrance of Patras, Greece, and was constructed in 2000. The footbridge, with a maximum length of 29.5 and a central opening of 26.5 m, consists of timber members and certain steel elements, all connected with metal bolts. The bridge deck is supported by two timber arches and two timber pylons (see Figure 6). Hence in side view the bridge can be regarded as a continuous beam based on two joint columns and with intermediate support provided by the timber arches. Overall, the structure is very stiff in the vertical axis. On the other hand, due to misconstruction or omission of certain crucial elements necessary to offer stiffness, the bridge is flexible in the lateral axis. Since its construction, significant loosening of the connections between the bridge members occurred and can be observed, while several steel members offering stiffness are permanently deformed. Furthermore, the bridge presents large lateral deflections of its deck which create a feeling of insecurity to the crossing pedestrians who have almost abandoned the bridge mainly after 2008. These changes are reflected in a dramatic, extraordinary shifting of its main lateral frequency deduced from analysis of measurements using a Robotic Total Station (RTS, or Robotic Theodolite, Figure 1(b)). For this reason it is usually avoided by pedestrians.

Concerning the vertical sense, the bridge is somewhat stiff, although there is a clear feeling to pedestrians of an episodic deterioration in 2008 and of a subsequent gradual deterioration.

Seven annual surveys aiming to measure the bridge response and evaluate the variations of its structural health with time were carried out between 2007 and 2013. The methodology adopted in all annual surveys was to excite various modes of the bridge deck using different types of excitation by a group of pedestrians (heel drops, walk, coordinate walk, running, coordinated stationary jumps, and jumps on the two sides of the deck-torsional excitation); see [8, 22–24].

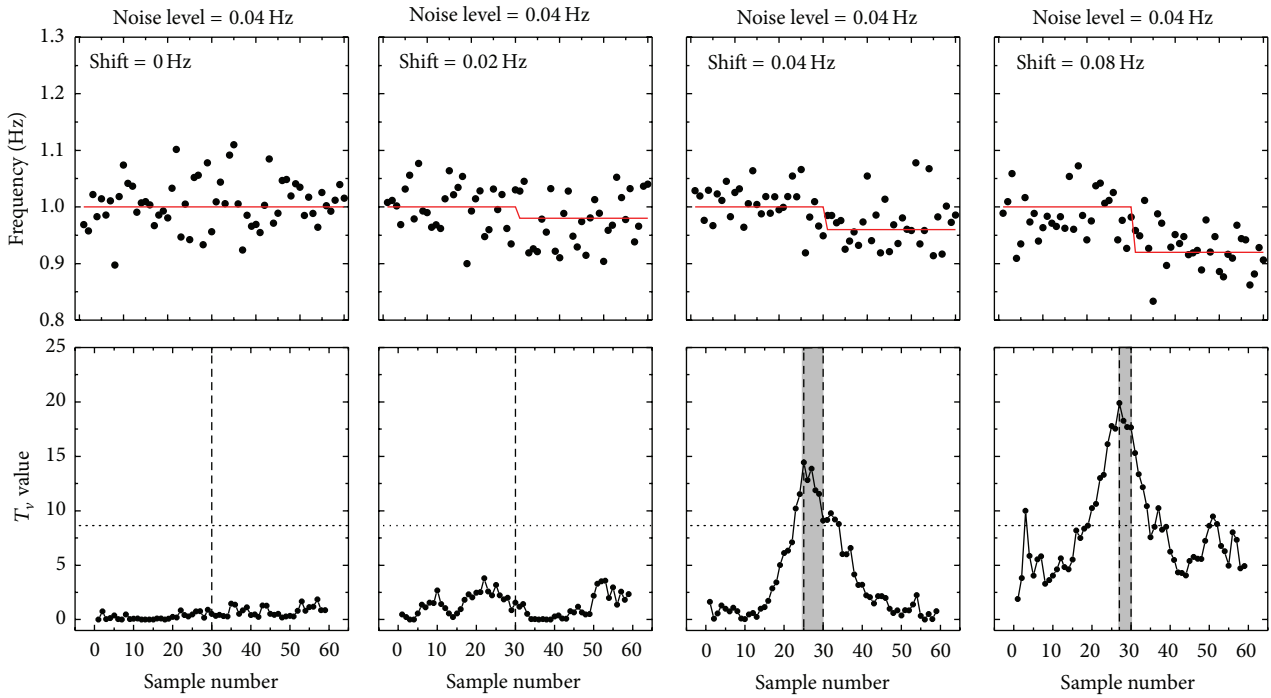


FIGURE 3: SNHT results for synthetic data set 1 with noise level $\sigma = 0.04$ Hz (4% of the frequency). Upper line: time series with no shift (shift = 0 Hz) and shifts equal to 0.02, 0.04, 0.08 Hz, that is, lower and higher of the noise standard deviation. A red line indicates the frequency shift. Lower line: the test variable T_v . A dotted horizontal line indicates the 95% level of statistical significance. Vertical dashed lines indicate the position of the real shift (always at point number 30) while a horizontal dashed line indicates the position of the maximum T_v . A gray area indicates the distance between the position of the maximum T_v and the position of the real shift.

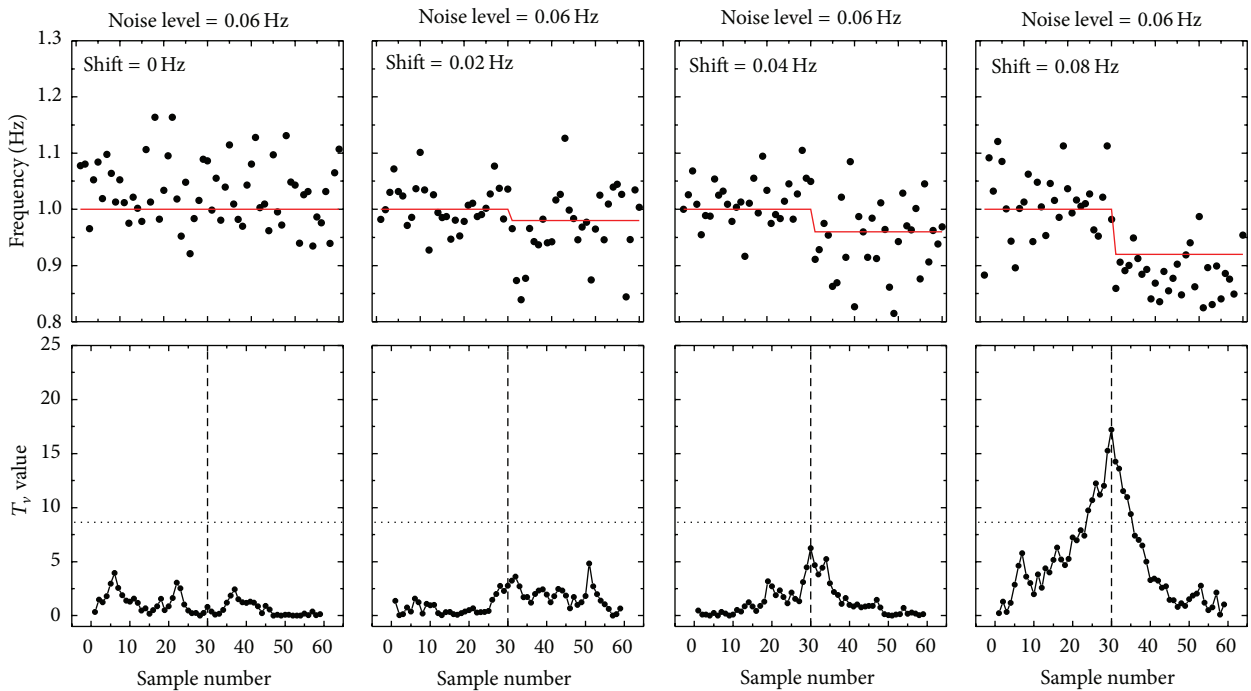


FIGURE 4: The same as Figure 2 for data set 2 with noise level $\sigma = 0.06$ Hz (6% of the frequency).

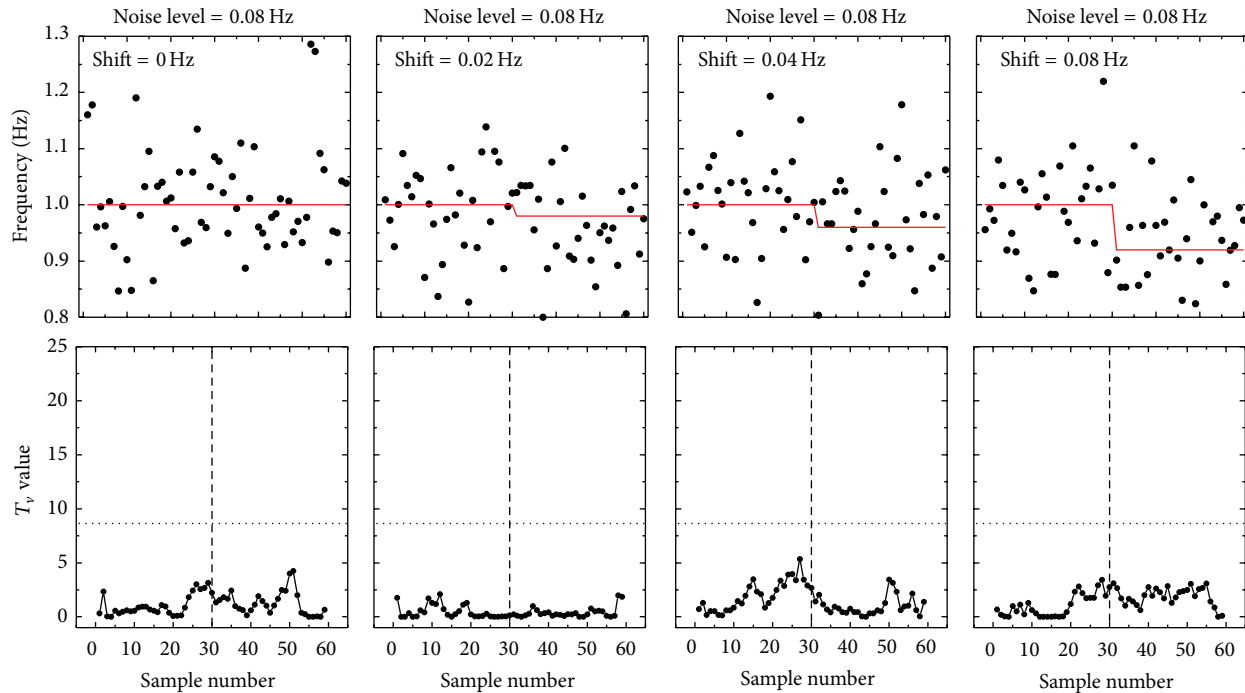


FIGURE 5: The same as Figure 2 for data set 3 with noise level $\sigma = 0.08$ Hz (8% of the frequency).

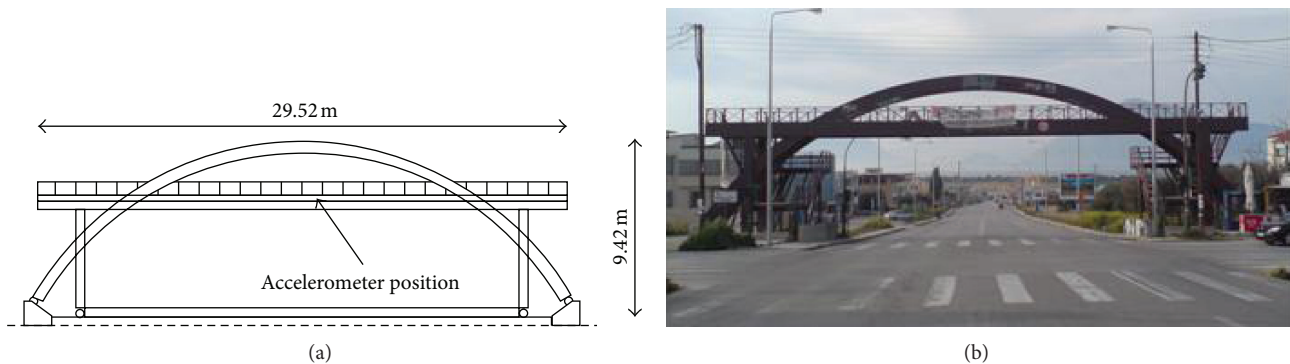


FIGURE 6: Structural concept (a) and side view (b) of the Kanellopoulos timber bridge in Patras, Greece. The bridge is relatively stiff along the vertical but flexible along the lateral axis, especially after episodic and gradual damage.

The bridge response was measured by several instruments including accelerometers, GPS, and Robotic Total Stations, occasionally by video recorders and a microwave interferometer (MA 200 Tellurometer).

This study is focused on measurements of the vertical response of the bridge using accelerometer records from the surveys of November 2007, May 2009, May 2010, May 2012, and April 2013. All surveys were carried out under nearly comparable loading and environmental conditions with the exception of 2012 when a larger number of pedestrians participated in the bridge excitation. Hence in this survey a higher dead load is expected to have led to slightly lower modal frequencies (see [6]).

During all surveys a set of Geo-Sig AC-23 acceleration sensor connected to a Geo-Sig GSR-24 recorder with GPS timing was used. In all surveys the accelerometer was

stiffly connected to the bridge handrail with the exception of May 2009 when the sensor was connected to the floor of the bridge deck. In all surveys the accelerometers were installed at the mid-span of the bridge deck (see Figure 6).

4.2. Spectral Analysis: Identification of the Bridge Natural Frequencies. Spectra of displacements during the excitation events of each survey were computed using the Normperiod code (details on the Normperiod code are given in Section 2). Spectra corresponding to the lateral accelerations are presented in Figure 7 where spectra from different events are marked with a different color. A different number of events, ranging from 9 to 28 events, were obtained during each survey. From the results it is obvious that the main frequency peaks during 2007 were concentrated around 2.6 Hz while

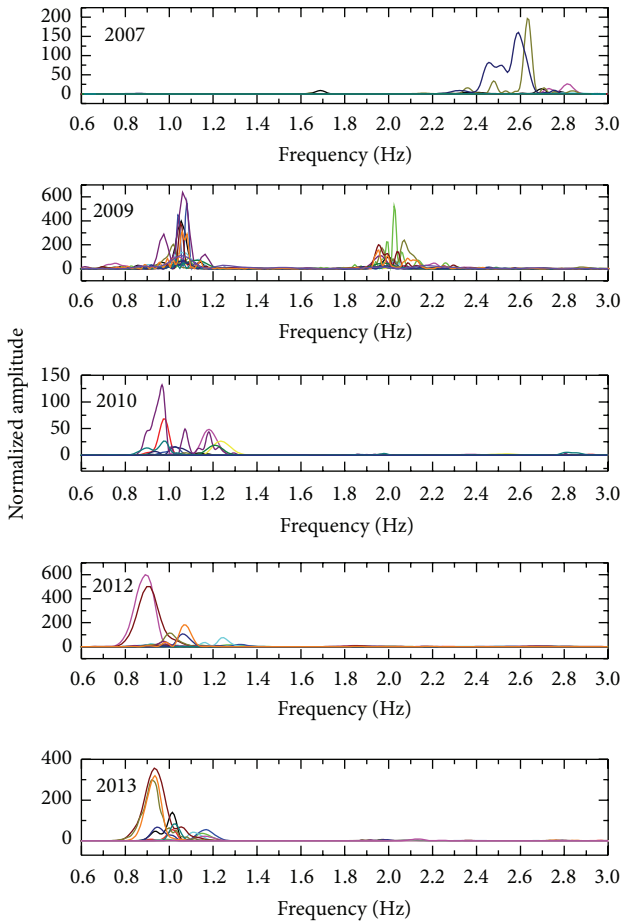


FIGURE 7: Spectra of the vertical response acceleration of the Kanellopoulos bridge during five annual surveys. Results were obtained after spectral analysis of the accelerometer recordings from different vibration events using the Normperiod code. Results from different events are marked with different colors. A dramatic shift of the dominating frequency peaks from 2.6 to 1 Hz can be identified between 2007 and 2009, followed by a gradual drop from 2009 to 2013. This shift is real and led to the abandonment of the bridge.

after 2009 the dominating frequency peaks are found around 1 Hz and 2.0 Hz and since 2010 at around 1 Hz. Observed peaks are statistically significant. The overall tendency of shifting frequencies is common in all instruments used and consistent with the feelings of pedestrians, avoiding this bridge in the last years. Similar results were obtained when spectral analysis was carried out using FFT (see Figure 8).

Two significant effects can be identified from the spectra of Figures 7 and 8.

- (a) A rapid fall of the first natural frequency in the lateral axis from 2.6 to 1 Hz between 2007 and 2009.
- (b) A gradual lowering of the first natural frequency in the lateral axis during the years 2009–2013.

The first effect indicates a major lowering of the stiffness of the bridge in the lateral axis that can only be attributed to loosening of the metal connections due to a rapid icing effect during the winter 2008, an extraordinary, regionally

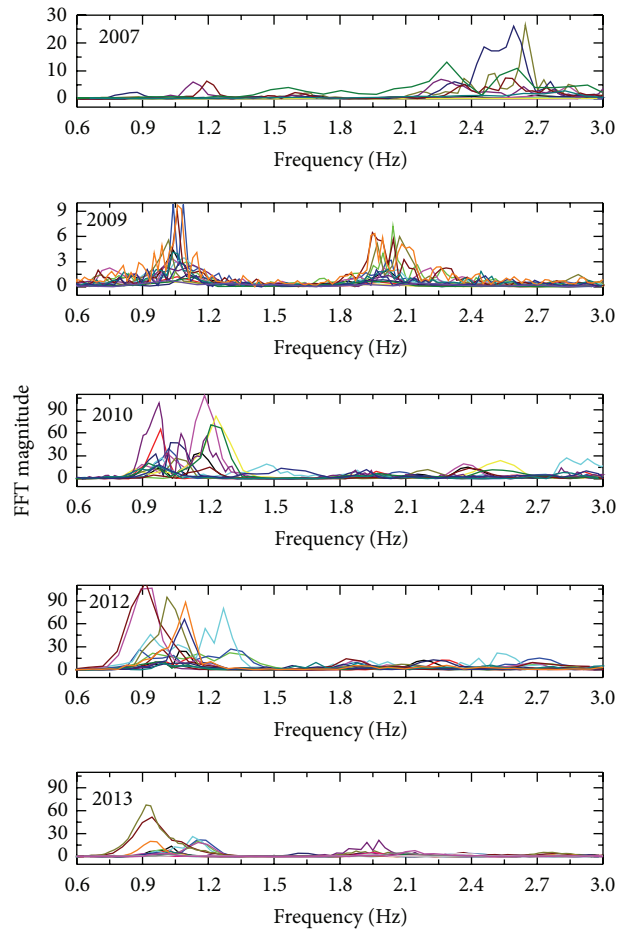


FIGURE 8: The same as Figure 7 but using FFT. Again different vibration events are marked with different colors.

catastrophic event. Another possibility is that the fall of the natural frequency is a measurement artifact, that the natural frequency close to 1 Hz was not excited during the first survey and the natural frequency close to 2.6 Hz was not excited during the last surveys (selective excitation). This is not, however, a likely explanation, for two reasons. First, because all surveys included different types of excitation, very similar in all surveys, and second, because a gradual loss of stiffness is observed in the vertical axis as well (see Moschas and Stiros (in review)), indicative of damage, obvious to pedestrians.

The shifting of the first natural frequency close to 1 Hz from 2009 to 2013 can be attributed to the gradual deterioration of the bridge bearing system, including the loosening of steel connections, permanent deformation of steel stiffening members, and decay of the timber members of the bridge that have been documented through the years.

From the spectra of Figure 7, the peaks above the 95% level of statistical significance were isolated and plotted in Figure 9(a). From this figure a concentration of peaks around two main frequencies, one slightly lower and one slightly higher than 1 Hz, can be identified. This distribution is identified after 2009 and may indicate two closely spaced natural frequencies.

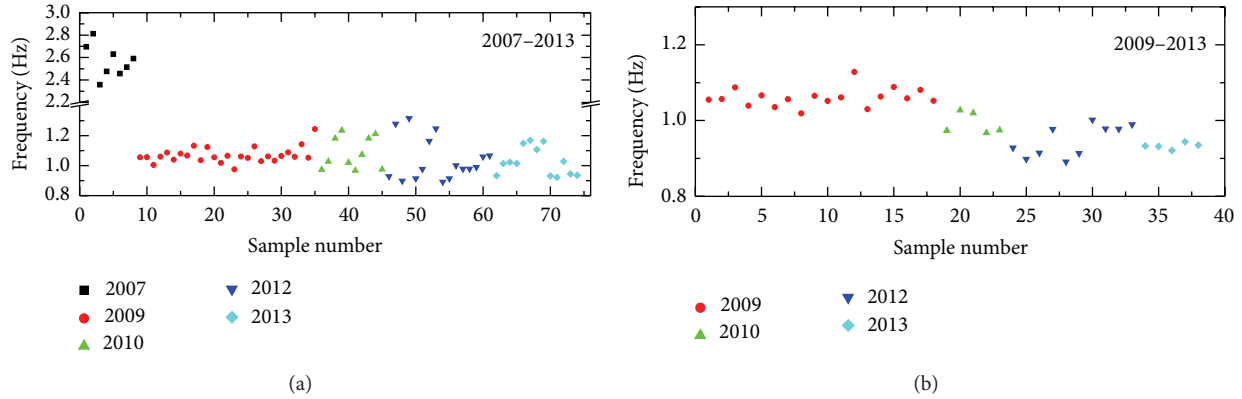


FIGURE 9: (a) All significant frequency peaks in the area between 0 and 3 Hz identified during the 5 annual surveys. A break is induced in the vertical axis for presentation reasons. A dramatic shift in frequencies is evident between 2007 and 2013. (b) Significant frequency peaks for the years after 2009 and further on. For the years 2010–2013 only the frequency peaks below 1 Hz were chosen and used in the analysis resulting in a smaller set of points compared with the set of (a). There is some evidence of lowering in the dominant frequency, but its location is not well defined.

The data set corresponding to the 2012 survey presents a pattern slightly different than that of the other years, with a larger separation between the two identified natural frequencies. Furthermore, the lower natural frequency lies at approximately 0.85 Hz and seems to increase towards 0.93 Hz in 2013. This difference can probably be attributed to the different loading conditions with a larger number of pedestrians (dead weight) during the 2012 survey. As discussed above results from the years 2010–2013 surveys contain two groups of significant frequency peaks: one lying slightly below and one slightly above 1 Hz, probably indicating the existence of two natural frequencies. Since the present study is focused on detecting changes in the first natural frequency of the bridge deck only the peaks below 1 Hz were taken into consideration as they correspond to the lower, hence fundamental, natural frequency. The results from the 2009 survey along with the peaks below 1 Hz from the 2010, 2012, and 2013 surveys are plotted in Figure 9(b).

4.3. Application of the SNHT on Natural Frequency Data from Different Annual Surveys. The frequencies appearing in Figure 9(b) were used during the application of the SNHT for the detection of frequency shifts between the annual surveys. The test was applied on the following data sets:

- on a data set covering years 2009–2013 (data of Figure 9(b)); the data of 2007 were ignored because the shift between 2007 and 2009 is obvious,
- on pairs of two yearly data sets from different years.

Application of the SNHT to the data set of years 2009–2013 (Figure 9(b)) led to the diagram of Figure 10. The test identified the dominant frequency drop between 2009 and 2010, very close to the real boundary of the two surveys.

At a next step the SNHT was applied for combinations of data sets from different surveys (2007–2009, 2009–2010, 2010–2012, 2010–2013 and 2009–2013). For combinations of data sets covering more than two years (for example 2010–2013) the comparison was made only between the first and the

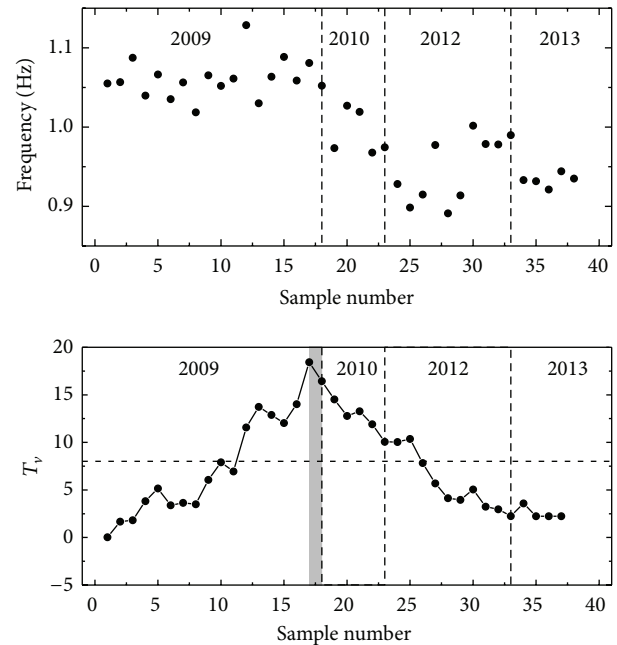


FIGURE 10: Results from application of the SNHT on the frequency estimates from the surveys covering the years 2009 to 2013. A clear frequency shift is detected between 2009 and 2010. A horizontal, dashed line in the bottom diagram indicates the 95% statistical significance level for the test, while vertical lines indicate the limits of the data sets corresponding to different annual surveys. A gray-shaded area marks the distance between the point of the real shift and the point of the shift identified by the SNHT.

last survey ignoring intermediate surveys. No test between 2012 and 2013 was made for the reasons explained above.

The test was made this time not for the original available yearly data sets, of variable length (Figures 9 and 10), but for modified data sets of equal length produced by padding of each set (i.e., repeat of the original data) so that both sets in each pair contain 18 points. A main reason is that certain

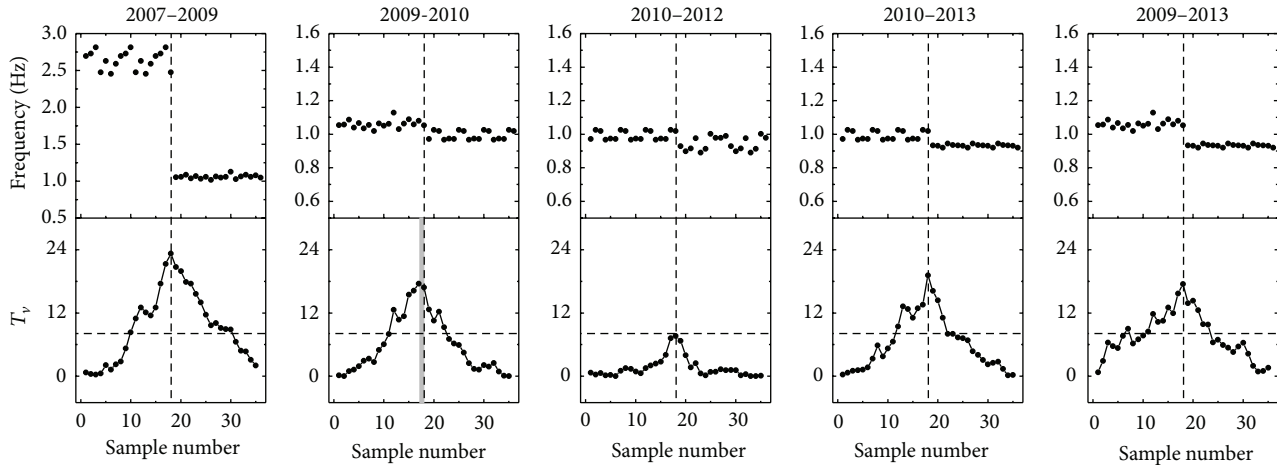


FIGURE 11: SNHT results for pairs of modified data sets from the annual surveys of the Kanellopoulos bridge. Top diagrams: time series of frequency peaks. Bottom diagrams: graph of the T_v function, with peaks indicating the location of possible shifts. A horizontal dashed line indicates the 95% level of statistical significance. The gray area in the diagram corresponding to the 2009-2010 test denotes the distance between the point of the shift identified by the SNHT and the point of the real shift.

surveys contain few data, while the test can identify shifts at some distance from the first and last point of the time series (see Section 2.2).

The results are shown in Figure 11. A frequency shift was identified at the boundary of the two surveys with the exception of the test between the 2009 and 2010 data sets.

5. Discussion

A large amount of monitoring data, spanning long period of time, can be collected from various bridges or other structures and can be exploited in order to estimate their dominant frequencies as a function of time. Frequency estimates are not idealized equal numbers, but fluctuating stochastic variables expressing measurement and computation errors, transient changes [6, 7, 9, 25] and damage-associated permanent changes [4, 26], as analysed in the Introduction. The amplitude of the permanent changes is usually of the order of the amplitude of the noise and of the transient changes usually up to a 3–5% value [3, 6, 7] and only in extraordinary cases can be much larger (Figure 1(b)). For this reason, damage-associated changes in the dominant frequencies cannot be readily identified from the available time series of measurement-derived dominant frequencies, that is, from long, apparently noisy data sets.

In order to solve this problem, we adopt a statistical approach developed for the identification of shifts in climatological, mostly temperature time series, especially the SNHT test. Various other tests, based on different types of methodologies, have been proposed in the past for the identification of inhomogeneities in data sets [14, 15]. The SNHT is one of the simplest and most popular tests used for this task in the field of climatology. Other more complicated tests for identification of shifts in natural frequencies and structural damage have been proposed in the field of Structural Health Monitoring [4, 13, 25]. The SNHT was applied in sets of observations of dominant frequencies which were assumed

to be dominated by white noise and suspect for a single small permanent shift.

At a first step the SNHT was applied on synthetic data simulating data sets with frequency shifts and added white noise with varying amplitude. The result of this assessment indicated that shifts with amplitude larger or equal to the standard deviation of the frequency estimates can be accurately detected by the SNHT, without false alarms, that is, identification of nonexisting shifts (see Figures 3–5).

At a next step the SNHT was applied on natural frequency data sets obtained from yearly repeated vibration measurements of a timber bridge in Patras Greece. A time series of statistically significant spectral peaks was formed from the spectral analysis of lateral displacements during events of forced excitation of the bridge (Figures 7 and 8). These data cover five surveys in 2007, 2009, 2010, 2012, and 2013. A major shift in the dominant lateral frequency is evident between 2007 and 2009, and for this reason the corresponding data sets were excluded from our analysis (Figure 9).

The analysis was made first for the series of yearly surveys between 2009 and 2013 and indicated a main shift between 2009 and 2010 (see Figure 10). Shifts between the other years were not detected, because of the structure of the particular test permitting to identify only single shifts in the time series. After a main shift is identified, the time series is split into two time series, and possible additional shifts are searched for each of them. When the test was applied between pairs of yearly data sets (Figure 11) a shift was identified between all surveys. The aim of the test is to identify statistically significant shifts in a time series. The results obtained are accurate, because the SNHT-identified shift is confirmed from independent evidence (measurement from various instruments, feeling of pedestrians, etc.).

SNHT is especially successful for long time series and for shifts at some distance from the first and last point of the time series [20]. Still the results previously presented are focusing on relatively small data sets; hence they indicate

the lower level of tolerance of this test-finer and more accurate results are expected for longer time series. This makes SNHT especially suitable for long time series deriving from permanent monitoring systems, such as those which have been installed in various important structures (bridges, high-rise buildings, etc.) [7, 27]. Application of the SNHT on data sets noisier than the one used in the present study will be very interesting and will possibly broaden the limits of applicability of the test.

Our approach was limited to the identification of the shift. This is the real problem and its amplitude can be computed as difference of the mean values of the two segments of the time series defined by the shift (inhomogeneity).

Another limitation is that estimates of dominant frequencies were assumed to be dominated by white noise. This is certainly a simplification [28], because seasonal effects (e.g., icing of cables of suspension bridges [10, 11]) may lead to data characterized by a different autocorrelation structure and transient effects may be misinterpreted as permanent shifts, especially in short time series. This can be avoided with a careful examination of the monitoring record, correlation of inferred shifts with meteorological effects, and so forth. In any case, any statistical test indicates only possible effects and should not be regarded as a black box.

Finally, in the present study frequency estimates were assumed to present abrupt shifts (inhomogeneities), due to the bridge deterioration through the years, between yearly surveys. For this reason the simple version of the SNHT which permits identification of single shifts in data sets was used. Different, more complicated versions of the SNHT permitting the identification of multiple shifts or of changes in the data set trend exist and could possibly be applied in data sets similar to the one studied in the present paper.

6. Conclusion

We have shown that a statistical test developed for climatological time series can be applied in time series of observed (better measurement derived) dominant frequencies of structures and hence detect possible damage (or ever repair or strengthening). The reason is that the amplitude of the permanent shifts is usually of the same order of magnitude with transient shifts and with measurement and computational noise, and hence it is difficult to identify permanent shifts without any specific statistical “tool.” This test can be applied of course in other types of monitoring data, for instance, deflections.

References

- [1] O. S. Salawu and C. Williams, “Bridge assessment using forced-vibration testing,” *Journal of Structural Engineering*, vol. 121, no. 2, pp. 161–173, 1995.
- [2] S. W. Doebling, C. R. Farrar, and M. B. Prime, “A summary review of vibration-based damage identification methods,” *Shock and Vibration Digest*, vol. 30, no. 2, pp. 91–105, 1998.
- [3] S. Soyoz and M. Q. Feng, “Long-term monitoring and identification of bridge structural parameters,” *Computer-Aided Civil and Infrastructure Engineering*, vol. 24, no. 2, pp. 82–92, 2009.
- [4] H. Li, T. Yi, M. Gu, and L. Huo, “Evaluation of earthquake-induced structural damages by wavelet transform,” *Progress in Natural Science*, vol. 19, no. 4, pp. 461–470, 2009.
- [5] T.-H. Yi, H.-N. Li, and H.-M. Sun, “Multi-stage structural damage diagnosis method based on “energy-damage” theory,” *Smart Structures and Systems*, vol. 12, no. 3, 2013.
- [6] J. H. G. Macdonald and W. E. Daniell, “Variation of modal parameters of a cable-stayed bridge identified from ambient vibration measurements and FE modelling,” *Engineering Structures*, vol. 27, no. 13, pp. 1916–1930, 2005.
- [7] E. J. Cross, K. Y. Koo, J. M. W. Brownjohn, and K. Worden, “Long-term monitoring and data analysis of the Tamar Bridge,” *Mechanical Systems and Signal Processing*, vol. 35, no. 1-2, pp. 16–34, 2013.
- [8] F. Moschas and S. Stiros, “Measurement of the dynamic displacements and of the modal frequencies of a short-span pedestrian bridge using GPS and an accelerometer,” *Engineering Structures*, vol. 33, no. 1, pp. 10–17, 2011.
- [9] T.-H. Yi, H.-N. Li, and X.-Y. Zhao, “Noise smoothing for structural vibration test signals using an improved wavelet thresholding technique,” *Sensors*, vol. 12, no. 12, pp. 11205–11220, 2012.
- [10] C. T. Georgakis, J. H. Macdonald, and C. A. Taylor, “Non-linear analysis of wind-induced cable-deck interaction,” in *Proceedings of IABSE Conference*, vol. 8, pp. 74–82, Cable-Supported Bridges—Challenging Technical Limits, Seoul, Korea, 2001.
- [11] E. T. Ingólfsson, C. T. Georgakis, F. Ricciardelli, and J. Jönsson, “Experimental identification of pedestrian-induced lateral forces on footbridges,” *Journal of Sound and Vibration*, vol. 330, no. 6, pp. 1265–1284, 2011.
- [12] J. M. W. Brownjohn, P. Moyo, P. Omenzetter, and Y. Lu, “Assessment of highway bridge upgrading by dynamic testing and finite-element model updating,” *Journal of Bridge Engineering*, vol. 8, no. 3, pp. 162–172, 2003.
- [13] E. P. Carden and J. M. W. Brownjohn, “Fuzzy clustering of stability diagrams for vibration-based structural health monitoring,” *Computer-Aided Civil and Infrastructure Engineering*, vol. 23, no. 5, pp. 360–372, 2008.
- [14] L. A. Vincent, “A technique for the identification of inhomogeneities in Canadian temperature series,” *Journal of Climate*, vol. 11, no. 5, pp. 1094–1104, 1998.
- [15] M. Becker, M. Karpytchev, M. Davy, and K. Doekes, “Impact of a shift in mean on the sea level rise: application to the tide gauges in the Southern Netherlands,” *Continental Shelf Research*, vol. 29, no. 4, pp. 741–749, 2009.
- [16] H. Alexandersson, “A homogeneity test applied to precipitation data,” *Journal of Climatology*, vol. 6, no. 6, pp. 661–675, 1986.
- [17] E. Steirou, *Investigation of Homogenization Errors in Hydro-Climatic Time Series with Long-Term Persistence*, National Technical University of Athens, Athens, Greece, 2013, (Greek).
- [18] N. R. Lomb, “Least-squares frequency analysis of unequally spaced data,” *Astrophysics and Space Science*, vol. 39, no. 2, pp. 447–462, 1976.
- [19] S. I. Pytharouli and S. C. Stiros, “Spectral analysis of unevenly spaced or discontinuous data using the “normperiod” code,” *Computers and Structures*, vol. 86, no. 1-2, pp. 190–196, 2008.
- [20] H. Alexandersson and A. Moberg, “Homogenization of Swedish temperature data. Part I: homogeneity test for linear trends,” *International Journal of Climatology*, vol. 17, no. 1, pp. 25–34, 1997.

- [21] S. Sahin and H. K. Cigizoglu, "Homogeneity analysis of Turkish meteorological data set," *Hydrological Processes*, vol. 24, no. 8, pp. 981–992, 2010.
- [22] J. M. W. Brownjohn and A. Pavic, "Experimental methods for estimating modal mass in footbridges using human-induced dynamic excitation," *Engineering Structures*, vol. 29, no. 11, pp. 2833–2843, 2007.
- [23] C. Gentile and N. Gallino, "Condition assessment and dynamic system identification of a historic suspension footbridge," *Structural Control and Health Monitoring*, vol. 15, no. 3, pp. 369–388, 2008.
- [24] A. Rönquist, E. Strømmen, and L. Wollebæk, "Dynamic properties from full scale recordings and FE-modelling of a slender footbridge with flexible connections," *Structural Engineering International*, vol. 18, no. 4, pp. 421–426, 2008.
- [25] B. Peeters and G. De Roeck, "One-year monitoring of the Z24-Bridge: environmental effects versus damage events," *Earthquake Engineering and Structural Dynamics*, vol. 30, pp. 149–171, 2001.
- [26] O. S. Salawu, "Detection of structural damage through changes in frequency: a review," *Engineering Structures*, vol. 19, no. 9, pp. 718–723, 1997.
- [27] K.-Y. Wong, "Instrumentation and health monitoring of cable-supported bridges," *Structural Control and Health Monitoring*, vol. 11, no. 2, pp. 91–124, 2004.
- [28] D. Koutsoyiannis, "The Hurst phenomenon and fractional Gaussian noise made easy," *Hydrological Sciences Journal*, vol. 47, no. 4, pp. 573–595, 2002.

Review Article

Recent Developments on Wireless Sensor Networks Technology for Bridge Health Monitoring

Guang-Dong Zhou¹ and Ting-Hua Yi^{2,3}

¹ College of Civil and Transportation Engineering, Hohai University, Nanjing 210098, China

² School of Civil Engineering, Dalian University of Technology, Dalian 116023, China

³ Key Laboratory of Concrete and Prestressed Concrete Structure, Ministry of Education, Southeast University, Nanjing 210096, China

Correspondence should be addressed to Guang-Dong Zhou; zhougd@hhu.edu.cn

Received 24 September 2013; Accepted 21 October 2013

Academic Editor: Stathis C. Stiros

Copyright © 2013 G.-D. Zhou and T.-H. Yi. This is an open access article distributed under the Creative Commons Attribution License, which permits unrestricted use, distribution, and reproduction in any medium, provided the original work is properly cited.

Structural health monitoring (SHM) systems have shown great potential to sense the responses of a bridge system, diagnose the current structural conditions, predict the expected future performance, provide information for maintenance, and validate design hypotheses. Wireless sensor networks (WSNs) that have the benefits of reducing implementation costs of SHM systems as well as improving data processing efficiency become an attractive alternative to traditional tethered sensor systems. This paper introduces recent technology developments in the field of bridge health monitoring using WSNs. As a special application of WSNs, the requirements and characteristics of WSNs when used for bridge health monitoring are firstly briefly discussed. Then, the state of the art in WSNs-based bridge health monitoring systems is reviewed including wireless sensor, network topology, data processing technology, power management, and time synchronization. Following that, the performance validations and applications of WSNs in bridge health monitoring through scale models and field deployment are presented. Finally, some existing problems and promising research efforts for promoting applications of WSNs technology in bridge health monitoring throughout the world are explored.

1. Introduction

A large number of bridges have been built to fulfill the requirement of advanced transportation all over the world and represent the key elements in terms of the safety and functionality of the entire highway system. As those bridges age, not only do structures deteriorate naturally, but also their utilization increases as populations grow in size and mobility. This structural degradation can pose major safety hazards, especially on long-span bridges. Between 1989 and 2000, more than 500 bridges are reported to have partially or totally collapsed in the United States due to triggering events (e.g., earthquake or vehicle collision), design and construction error, and undetected structural deterioration (e.g., scour or fatigue) [1, 2]. The I-35W Mississippi River bridge located in Minneapolis, Minnesota, USA, is one recent example: it failed on August 1, 2007, collapsing to the river and riverbanks

beneath, killing 13 people and injuring 145 [3]. As of 2009, an estimated 24% of the nation's over 600,000 bridges are currently classified as structurally deficient or functionally obsolete (12% structural deficient) by the Federal Highway Administration (FHWA) of the United States [4]. This suggests that accuracy and reliability of bridge inspections are imperative, and advanced quantitative methods to locate the damage are of pressing importance. Regular visual inspection, which is experiential dependence, traffic disturbance, and high cost, does not appear to be adequate to accurately reflect the true performance state of bridge components or the global condition of the entire bridge. In 2001, the FHWA conducted a study which found that 56% of medium-to-short-span bridges given an average condition rating by visual inspection were improperly assessed [5]. Structural health monitoring (SHM) that aims at monitoring structural behavior in real-time, evaluating structural performance

under various loads, and identifying structural damage or deterioration is an attractive alternative. It can be adopted for newly constructed bridges and existing bridges to understand structural health condition and prevent catastrophic failure by prior detection. Furthermore, it helps to verify structural design methodology and promote the development of structural analysis theory. Over the past decade, on-structure long-term monitoring systems have been implemented on bridges in Europe, the United States, Canada, Japan, Korea, China, and other countries [6].

A traditional wired SHM system includes three major components: a sensor system, a data processing system (including the data acquisition, transmission, and storage), and a health evaluation system [7]. The data of the sensor system are transmitted through coaxial wires and processed intensively by the data processing system. There are many disadvantages to the wired SHM system, as follows. (1) The first one is high cost. The extremely long communication cables and corresponding protection pipelines for the sensors require a lot of costs, which causes the investment of the SHM system to be prohibitively high. For example, the average installed cost per sensor of the monitoring system on the Bill Emerson Memorial Bridge is a little more than \$15,000 [8]; cable wiring used in the SHM system of the Yeongjong Bridge accounts for 50% of the total installation cost [9]. (2) The second disadvantage is low efficiency. The deployment of miles of cables is labor-intensive and time-consuming, with potentially over 75% of the installation time attributed to the installation of system wires and cables for long-span bridges [10, 11]. Centralized data processing makes the data processing system so busy that the efficiency of structural evaluation is low, which induces the real-time monitoring to become a challenge particularly for those sudden occurrences such as earthquakes and explosions. (3) The third one is susceptible disturbance. A wire-based system has more chances for disturbance or failure caused by nature and human beings since it has more independent components, such as data loggers, sensors, and flimsy cables. The long-distance transmission, changes in cable temperatures, and connections between sensors and cables cause sensor data to be hard-to-correct distortions [9]. (4) The fourth disadvantage is inflexibility. The sensor and cable are pier to pier, which means one coaxial cable only services one sensor generally. Adding or changing sensors implies deploying extra cables for data transmission and renewing data managing software. After the wired SHM system is completed, the modifying of the sensor system results in a lot of accessional work.

The new advances of microelectromechanical systems (MEMS) technology, wireless sensing technology, and integrated circuit technology have realized low-cost wireless sensors with onboard computation and wireless communication capabilities. In order to overcome the intrinsic faultiness of the traditional wired SHM system, the WSNs-based SHM system has recently emerged. The WSNs-based SHM system, which is defined by its use of wireless sensor networks (WSNs) to transfer data from sensor to sensor and from sensor to the central data repository, is considered a viable substitute for a wired monitoring system. The WSNs-based

SHM system, which employs the wireless sensors and WSNs, offers the potential for low-cost and reliable SHM. When compared to the traditional wired SHM system, the WSNs-based SHM system has the following advantages. (1) The first one is low cost. Using the WSNs, the wires are eliminated, and the work of cable installation and protection is released. Employing the onboard data conditioner on the wireless sensor makes the abandonment of the expensive independent demodulator possible. So the cost of the WSNs-based SHM system is reduced dramatically. The prototype wireless system proposed by Kim et al. costs about \$600 per node compared to thousands of dollars for a node with the same functionalities in a traditional wired network [12]. (2) The second advantage is high efficiency. Without deploying complicated cables, the installation of wireless sensors is very easy [13]. Whelan et al. [14] only spent approximately 2 h and 4 h, respectively, deploying 30 dual-axis wireless accelerometers and 30 wireless strain transducers on a highway bridge, which is impossible for the traditional wired SHM system. The onboard microprocessor of the wireless sensor can facilitate efficient distributed data processing and real-time damage detection [15, 16]. (3) The third one is reliability. The hardware of the wireless sensor is highly integrated and there are no additional supporting components, such as long cables, signal analyzer, and data memory. The WSNs-based SHM system is not easy to be disturbed by operation environment, and the reliability is improved. (4) The fourth advantage is flexibility. The sensors in the WSNs-based SHM system are organized by wireless transmission, which makes the updating, adding, moving, and replacing of sensors easy after the initial installation. The network can be reorganized quickly without disturbing the original data acquisition operation [9]. In addition, the rapid reduction in physical size and cost of MEMS-based wireless sensors and improvement of WSNs performance enable deployment of dense arrays of sensors to be feasible and economical, so that the quality of SHM can be dramatically improved with rich information which diagnosis algorithms can utilize to detect, locate, and assess structural damage, which is critical for SHM of complicated and large-scale bridges. Bridge health monitoring using a network of wireless sensors is one of the most promising emerging technologies and is seen as the next generation of SHM [17].

After the use of wireless communications in lieu of wires within a structural monitoring system by Straser and Kiremidjian [18] in 1998 as a means of reducing installation costs in large-scale structures, application of WSNs in bridge health monitoring has gained considerable attention. Now, WSNs technology for bridge health monitoring has seen substantial progress through interdisciplinary research efforts to address issues in sensors, networks, and application-specific algorithms. In this paper, the distinguished technology development of WSNs for bridge health monitoring is reviewed. Although the wireless sensors and sensor networks for SHM were summarized by Lynch and Loh in 2006 [19], the hardware of the wireless sensor node was emphasized in that paper. More importantly, most of the early attempts simply replaced wired communication with radio frequency (RF) links, which imply many flaws, such

as unreliable communication, sampling rate fluctuation, and inaccurate time synchronization. The rapid development of WSNs technology in recent years promotes the emergence of many novel and outstanding concepts in WSNs-based bridge health monitoring, which makes the performance of the system improve dramatically. The interest of this paper is the key issues related to the application of WSNs in bridge health monitoring. In Section 2, the requirements and characteristics of WSNs-based bridge health monitoring are discussed. In Section 3, the progress on the WSNs-based bridge health monitoring system involving wireless sensor, network topology, data processing technology, power management, and time synchronization is presented. In Section 4, performance validation and application of wireless sensors and WSNs in bridge health monitoring are given. Finally, some existing problems and promising research efforts in the WSNs-based bridge health monitoring are discussed. It should be noted that this review is not intended to be exhaustive listing but to provide representative examples as references for future researches.

2. Requirements and Characteristics of WSNs-Based Bridge Health Monitoring

The applications of WSNs include many fields, like wildlife habits, forest environments, agriculture, health, life rescue, and structural monitoring. When comparing with general applications of WSNs, the WSNs used for bridge health monitoring have some special requirements and characteristics, as follows.

(1) High resolution: the responses of bridges caused by ambient excitation and traffic are very weak generally. The sensor boards used for bridge health monitoring are required to detect such small-amplitude fluctuations of signals. Moreover, the sensor boards should have a low-noise design and should take noise-reducing measurements for weak signal sampling. Commonly, the resolutions of a wireless acceleration sensor and wireless strain sensor should be below 1 mg and $1 \mu\epsilon$, respectively.

(2) High frequency: most structural assessment methods are based on the dynamic responses of bridges. So, the dynamic test takes up the main part among different bridge monitoring subjects. Since the noise level is usually high in uncontrolled structural environments, oversampling is generally performed to improve the signal-to-noise ratio by reducing the relative noise energy. Therefore, the sampling rate of sensors used for the dynamic test in the bridge health monitoring system should be more than 50 Hz.

(3) High speed: WSN technology enables deployment of dense arrays of sensors, which is critical for increasing the potential of SHM. For the high sampling frequency and the hundreds or thousands of sensors, the tremendous volume of transportation data in WSN is generated and transmitted in each data sensing period. For example, 2-byte data samples collected at 100 Hz generate 12 kB of data every minute. High speed data transmission is attractive for bridge health monitoring, but the employed low-power radio transceivers now provide a limited bandwidth (e.g., a maximum of 250 kbps in the case of IEEE 802.15.4 networks) [20].

(4) High reliability: because of the noise effect, electromagnetic interference, packet collision, packet headers, and so forth, in a harsh environment like the practical bridge site, high communication reliability to transmit data and disseminate commands without loss of information is a key issue. Data loss would have the effect of increasing the noise, which would make modal identification more difficult and also affect the subsequent condition assessment [21]. Particularly for rare events, data loss is not acceptable.

(5) Long lifetime: bridge health monitoring is a work that runs throughout the whole lifetime of the structure. In general, the service life of a long-span bridge is more than 50 years. The sensors are expected to remain active during those years and have the ability to be interrogated at any time to acquire data. Now, most of the wireless sensors are powered by batteries with limited capacity. So, the implementation of careful power management is one of the most critical features of successful WSN deployment.

(6) Time synchronization: each wireless sensor in WSNs has its own clock, which is not synchronized initially with other sensor nodes. A time synchronization (TS) error of 1 ms results in an about 3.6-degree phase delay of a mode at 10 Hz, while the same time synchronization error causes a 36-degree phase delay at 100 Hz [21]. The time synchronization error is comparable or can even exceed the effect of sensor's noise [22]. Careful time synchronization is also required in the application of correlation analyses.

(7) Various signal formats: a bridge is a complicate system. To understand the performance of a bridge comprehensively, various parameters such as acceleration, strain, displacement, temperature, and crack need to be monitored. Collecting those parameters, the formats of the signals are heterogeneous. Some are dynamic and the others are static. Some are absolute values and the others are relative values. The WSNs for bridge health monitoring should be flexible to different types of signals.

(8) Long-distance transmission: the total lengths of bridges always exceed the broadcast domain of a node. For example, the main span of the Tsing Ma Bridge is 1377 m, the total length of the Runyang South Bridge is 2430 m, and the total length of the Hangzhou Bay Bridge is 36 miles. Single-hop communication in a large wireless network for bridge health monitoring is impractical. Therefore, multihop wireless communication is demanded [13].

(9) Fixed sensor locations: the aim of WSN deployment is structural condition evaluation. The locations of wireless sensors are selected to fulfill the requirement of structural analysis and damage diagnosis. Once the wireless sensors are arranged, their locations are not changed any more during a measurement period. Therefore, the mobility of wireless sensors is not an issue for bridge health monitoring and there is no need to consider the movement of wireless sensors when developing a WSNs route.

3. WSNs-Based Bridge Health Monitoring System

As a new concept in the field of SHM, the WSNs-based bridge health monitoring system, which eliminates the high

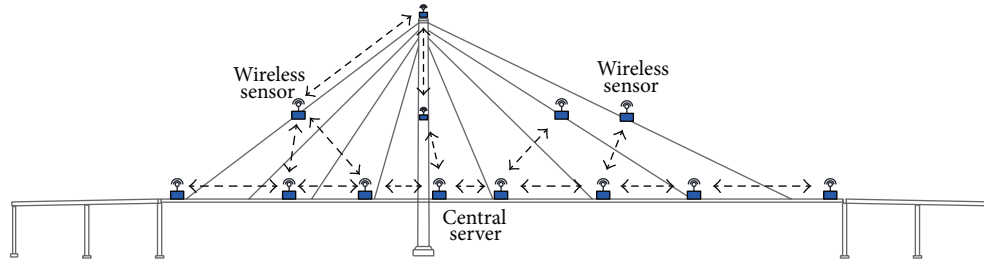


FIGURE 1: WSNs-based bridge health monitoring system.

cost cable, relies on the WSNs to transmit data. A typical WSN for bridge health monitoring is displayed in Figure 1. A lot of wireless sensors are deployed to key locations on a bridge. At first, the central server sends commands to activate wireless sensors, establish a WSN, and set the parameters of monitoring; then, the whole WSN executes TS; after that, the wireless sensors begin collecting data and transmitting raw data or processed results back to the central server; finally, the measured data can be used for advanced structural performance evaluation. Among them, handshake protocols are recommended to ensure the commands or data are sent to the appointed places.

The WSNs-based bridge health monitoring system is comprised of hardware and software. The hardware can be divided into a wireless sensor and central server. Wireless sensors are the cornerstone component of a WSNs-based bridge health monitoring system and are responsible for sensing structural responses and realizing in-network commands. The central server, which includes a gateway connecting to the data repository and the central control system for customized structural evaluation algorithms like that in the wired bridge health monitoring system, executes commands and data sending/receiving. And the software can be divided into different components: network operation, data collecting, data processing, power management, and so forth. The network operation is used for organizing network topology and controlling data stream. The data collecting performs strategies of data collecting such as TS, sampling rate, and sampling period. The data processing carries out onboard data processing, such as data compression, fast Fourier transform (FFT), and power spectrum density (PSD). The power management implements high efficiency power utilization like the sleeping model, triggering measurement, periodical test. Indeed, those components of software overlap, and the realization of an operation may involve different components. In addition, the software development requires an operation system. In this section, the technological development of key issues in the WSNs-based bridge health monitoring system is presented including wireless sensor, network topology, data processing technology, power management, and TS.

3.1. Wireless Sensor. Wireless sensors are not sensors defined by the conventional concept but rather are autonomous data acquisition nodes in which structural sensing elements (e.g., strain gauges, accelerometers, linear voltage displacement transducers, inclinometers, among others), the onboard

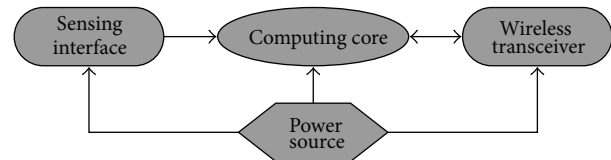


FIGURE 2: Subsystems of a wireless sensor.

microprocessor, and wireless communication elements are integrated. The greatest attribute of the wireless sensor is its collocation of computational resources with the sensor. Such resources can be used for data interrogating, digital signal processing, self-diagnosis, self-calibration, self-identification, and self-adaptation. This capability is particularly attractive within the context of SHM. So while cost has been an early motivator for considering the installation of wireless sensors in structures, the fact that wireless sensors are a new sensing paradigm offering autonomous data processing is fueling recent excitement. In general, a wireless sensor is composed by four functional subsystems: a sensing interface, a computing core, a wireless transceiver, and a power source, as shown in Figure 2 [2, 19]. For some of them, the actuation interface is also integrated, which is beyond the scope of this paper. The sensing interface includes an interface to which sensors can be connected and an analog-to-digital converter (ADC) to convert analog sensor signals to digital formats. The computing core generally consists of a microcontroller for the computational tasks, a random access memory (RAM) to stack the measured and processed data, and a flash memory with software programs for the system operation and data processing. The wireless transceiver is an integral component of the wireless system, which is composed of an RF radio modem and antenna to exchange information with other wireless sensors and to transfer data to the central server [23]. The power source, which is responsible for providing stable energy to the sensing interface, computing core, and wireless transceiver, commonly employs batteries.

The successful utilization of WSNs for bridge monitoring relies on their ability to capture data that provides a reasonable representation of the physical response. However, some of the inherent characteristics associated with wireless sensors have made high-fidelity data acquisition a challenging undertaking. Therefore, to date, a major effort in the field of wireless-based SHM is contributed to the development of high-performance wireless sensors. When designing an applicative wireless sensor for bridge health monitoring,

the performance and functionality of each subsystem must be carefully selected considering the structural type, quantities to monitor, sensor locations, and environment of the structure [23]. Although there are many commercially available wireless sensor nodes or sensor boards for measuring vibration, their performance cannot meet the requirement of bridge health monitoring mentioned in Section 2. For example, the Basic Sensor Board (ITS400) provided by MEMSIC lacks flexibility in selecting the cutoff frequency and sampling rate for data acquisition and has significant sampling rate errors [2, 24, 25]; the sensed data of the MTS310CA sensor board developed by Crossbow Technology, Inc., cannot well represent the physical response of the structure in the time domain and frequency domain [26].

Two methods are generally used for designing high-performance academic wireless sensors: the use of a commercially available platform interfaced with a customized sensor board and the use of a customized platform integrated with a customized sensor board. The first method uses commercial off-the-shelf motes, which is convenient and lends them to rapid development. However, the use of motes may restrict the performance and the operation of the platform. By contrast, the second method involves the development of a customized platform, which entails a complicated design and a long development cycle [13]. The main task of developing a wireless sensor is selecting appropriate components and connecting those components using the proper integrated circuit. At the same time, special control programs are configured to achieve presetting functions. In this section, academic wireless sensors explicitly proposed for use in bridge health monitoring are summarized.

In 1998, Straser and Kiremidjian [18] proposed a design of a low-cost wireless modular monitoring system (WiMMS) for civil structures by integrating a microcontroller with a wireless radio. This prototype represents the first major step by the structural engineering community towards decentralized data processing and wireless structural health monitoring [19]. The Motorola 68HC11 microprocessor is chosen to control the remote wireless sensing unit. To achieve reliable wireless communication, a Proxim Proxlink MSU2 wireless modem operating on the 902–928 MHz ISM band is used. In 2001, the WiMMS was improved by Lynch et al. [15, 27, 28] with emphasizing the power of the computational core. The 8-bit Atmel AVR AT90S8515 enhanced RISC (reduced instruction set computer) microcontroller is selected. Capable of eight million instructions per second, the microcontroller has high computational throughput without consuming large amounts of power. The Texas Instruments ADS7821 16-bit ADC with a maximum sample rate of 100 kHz and 80 mW power consumption is used to translate analog signals to a digital format for processing. In 2003, this wireless sensor was further improved with the goal of low power consumption but high computational performance [29–31]. A dual-processor computational core design was proposed. The low-power 8-bit Atmel AVR AT90S8515 microcontroller is utilized for overall unit operation and real-time data acquisition, and the 32-bit Motorola MPC555 PowerPC is integrated to execute intensive data processing algorithms at a clock rate of 20 MHz. When the two microcontrollers

are turned on, the AT90S8515 consumes 40 mW of power and the MPC555 (at 20 MHz) consumes 330 mW. In sleep mode, the two microcontrollers consume 12 mW, respectively. The modified wireless sensor is shown in Figure 3(a) [19]. And in 2005, the ADC was replaced with Texas Instrument ADS8341 16-bit ADC by Wang et al. [32–34]. An additional 128 kB of static random access memory (SRAM) is interfaced with the microcontroller for the storage of measurement data. The most attractive feature of the wireless sensing unit design is its wireless radio. The MaxStream 9XCite wireless modem with 900 MHz radio band and maximum transmission speed 38.4 kbps is used. The communication range of the radio is 300 m line-of-sight, yet the radio only consumes 250 mW when transmitting, 150 mW when receiving, and less than 5 mW when idle. With efforts to further reduce the size of the wireless sensor, the electrical circuit is redesigned and printed on a compact two-layer circuit board. When fully assembled, the wireless sensor is $10 \times 6.5 \times 4 \text{ cm}^3$ and is powered by five AA batteries, as shown in Figures 3(b) and 3(c). But the efforts have not stopped. First, the wireless communication system is renovated by the Chipcon CC2420, which is a single-chip IEEE 802.15.4 compliant radio capable of providing communication with ranges adequate for civil infrastructures [35]. The second significant improvement is the use of a four-layer circuit board, replacing the more limited two-layer boards. The four-layer boards allow for more compact designs, have the ability to devote the internal layers of the board to power and grounding planes, and provide a higher resolution for those channels. The latest version of the wireless sensor is named Narada, as plotted in Figure 3(d). Then, the Narada is used for executing many decentralized data processing algorithms proposed by Zimmerman et al. [36, 37].

Heo et al. [38] have designed a wireless MEMS-based accelerometer system, called SWMAS (Figure 4). This system consists of a sensor system module, a control and processing module, and a wireless modem module. The ADXL210 manufactured by Analog Devices is chosen for acceleration measurement because it could be used with the microcontroller directly without A/D converters. A low-power 8-bit microcontroller, Atmel AVR ATmega128 RISC, is selected for control of the data acquisition operation of the SWMAS. An external memory of 32 kbyte capacity is attached on the module to overcome the limit of SRAM. The CM-RS232 is integrated as the communication module. Based on calibration test results, performances of SWMAS were shown to agree fairly with values of the datasheet. In a free-vibration experiment using a cantilever beam, the response of SWMAS is in good agreement with the reference accelerometer. Subsequently, the SWMAS was improved to make it suitable to measure the response from structures such as very flexible bridges which have low amplitude and frequency of vibration signals [39]. First, the ADXL210 was replaced by the ADXL203. Secondly, the microcontroller was set at the noise reduction mode to get rid of the internal electric noise of the microcontroller occurring during A/D conversion. A sample test showed that the improved SWMAS could eliminate 70% of the noise.

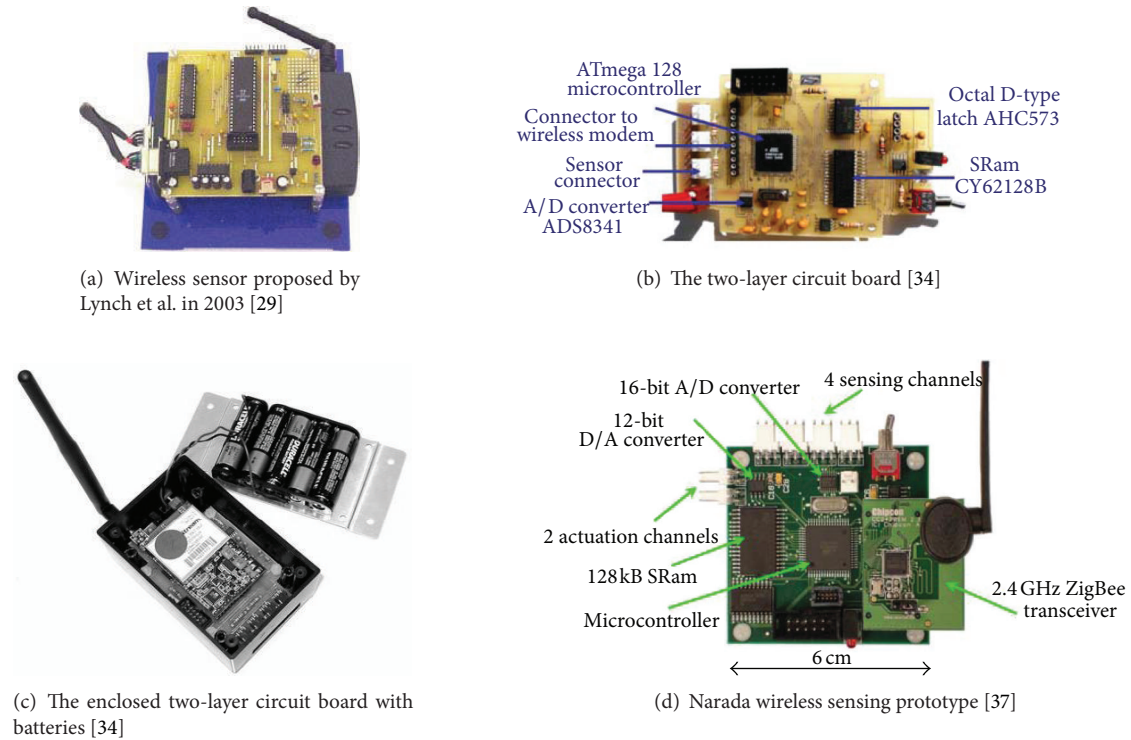


FIGURE 3: Prototypes of wireless sensor.

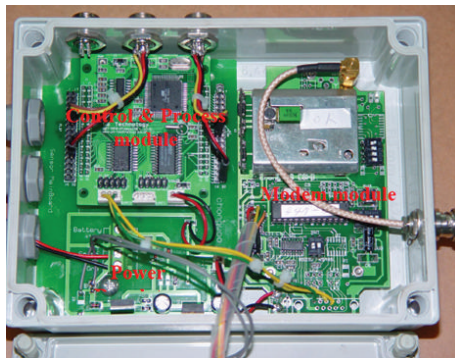


FIGURE 4: Prototype of SWMAS [38].

Park et al. [40] have described a wireless sensor, DuraNode, for structural monitoring. DuraNode has two low-power microcontrollers. One of the microcontrollers is dedicated to sampling the output of the accelerometers at a constant rate. The other microcontroller controls an 802.11b WLAN card and handles communication-related tasks such as forwarding incoming data packets to the next hop as well as sending out local data samples. These two microcontrollers communicate with each other using *Serial Peripheral Interface (SPI)*. Each one of the two microcontrollers is the PIC18F8720. It has 64 kbytes of flash program memory, 3328 bytes of on-chip SRAM, an EEPROM of 1 kbytes, and 8 channels of 10-bit ADCs. The sensor circuitry consists of MEMS-type sensors and signal conditioning circuitry. Three MEMS-type SD-1221 accelerometers are installed for sensing vibrations in

the x -, y -, and z -axes. The bandwidth and coverage of the 802.11b WLAN is up to 11 Mbps and 100 meters (outdoor, 1 Mbps), respectively.

Based on the commercial wireless sensor platform, Tmote Sky, Joshi et al. [41] have developed a sensor board with strain gauges. Tmote Sky developed by researchers at the University of California at Berkeley and marketed by MoteIV Corporation is a platform for extremely low power, high data-rate, sensor network applications designed with the dual goal of fault tolerance and development ease. Tmote Sky has on-chip RAM 10 kB, an IEEE 802.15.4 radio, and an integrated onboard antenna providing up to a 125-meter range. Tmote Sky offers a number of integrated peripherals including a 12-bit ADC and DAC, Timer, I2C, SPI, and UART bus. The microcontroller used in Tmote Sky is MSP430f1611, which has a 16-bit RISC processor, memory mapped analog peripherals, and memory mapped digital peripherals. The Chipcon CC2420 radio is included on the platform. The strain gauge used for this wireless sensor board has a nominal resistance of 1000Ω with a gauge factor of 2.105. A Wheatstone bridge is employed to convert the small resistance change in a strain gauge to voltage fluctuation. The PGA309, a programmable amplifier from Texas Instruments, is used in the signal conditioning circuit. PGA309 has basically two amplifiers: a front-end amplifier with gain selectable from 4 to 128 and an output amplifier with selectable gain of 2 to 9. It is also interfaced with an external EEPROM where some of the configuration data is stored and where the temperature compensation lookup table is also stored. Figure 5 displays the strain sensor board connected to a Tmote Sky.

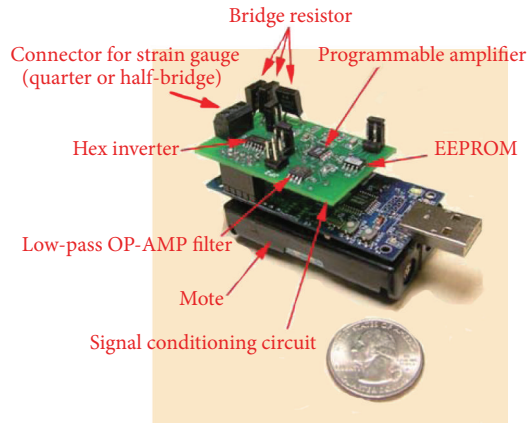


FIGURE 5: The strain sensor board connected to a Tmote Sky [41].

Using the MicaZ mote as the wireless sensor platform for control and communications, Kim et al. [12, 42] have designed an accelerometer sensor board for the application of bridge health monitoring. Figure 6(a) is a schematic of the major components of the board, and Figure 6(b) is the prototype of the accelerometer sensor board. The board has four independent accelerometer channels monitoring two directions (vertical and transverse) and a thermometer to measure temperature for compensation purposes. For the measurement of low-level and high-level accelerations, two commercially available MEMS accelerometer sensors are used each in two directions. Low-amplitude ambient vibrations, due to wind loading and traffic, are resolved by a two-dimensional Silicon Designs I221L accelerometer. A low-cost ADXL202E two-dimensional accelerometer was used to monitor stronger shaking as might be expected from earthquake excitation. Tests show that the Silicon Designs accelerometers have a hardware noise ceiling of $10 \mu\text{g}$, which is small enough to resolve signals with amplitude of a few hundreds of μg . Each channel from the MEMS accelerometers provides an analog voltage that is fed to a single-pole antialiasing low-pass filter with a cutoff frequency of 25 Hz for the reason that even very high vibration models of a long-span bridge application have frequencies well below the antialiasing filter. The filtered analog signal is fed to a 16-bit ADC for each of the four channels. A voltage regulator is contained on the sensor board to provide a constant 3 V output for the mote and a constant 5 V output for the ratiometric accelerometers. The MicaZ has a 512 kB flash memory, which can store up to 250,000 2-byte data samples and a 2.4 GHz radio frequency Chipcon CC2420 transceiver with a hardware interface that can support commercially available bidirectional antennas. This sensor is then applied to the SHM of the Golden Gate Bridge.

Employing the original design of wireless sensor node by Wang et al. [32, 33], Park et al. [43] have designed an acceleration-based sensor board (Acc-SSN) by modifying an antialiasing filter, MEMS accelerometer, and wireless radio capacity and an impedance-based wireless sensor board (Imp-SSN) based on the primary work of Mascarenas et al. [11], as shown in Figure 7. The Acc-SSN consists of eight

components: power supply, MEMS accelerometer, coupling capacitor, amplifier, antialiasing filter, ADC, microcontroller, and wireless radio. The MEMS accelerator SD1221 is selected in the Acc-SSN. The coupling capacitor was designed by using a high-pass filter with a cutoff frequency of 0.1 Hz. An operational amplifier is used to amplify low-level signals such as ambient vibration signals of civil structures. An 8th-order Butterworth low-pass filter with a cutoff frequency of 100 Hz is designed for SHM applications in civil structures. The four-channel 16-bit ADC ADS8341 (Texas Instruments, Inc.) is utilized as ADC, and the 8-bit microcontroller ATmega128 with low power consumption and low cost is selected as a microcontroller. The 2.4 GHz frequency XBee (Digi International, Inc.) is chosen as the wireless radio, of which the outdoor line-of-sight range is up to 100 m. The impedance chip of the Imp-SSN is the AD5933, which has the following embedded multifunctional circuits: function generator, digital-to-analog (D/A) converter, current-to-voltage amplifier, antialiasing filter, ADC, and discrete Fourier transform (DFT) analyzer. The AD5933 outputs real and imaginary values of impedance for a target frequency of interest and transfers the values into a microcontroller.

Adopting the commercial wireless sensor platform, Imote2, researchers at the University of Illinois at Urbana-Champaign (UIUC) [2] have developed a series of sensor boards or interface boards to meet the requirements of bridge health monitoring. The Imote2, developed by Intel, is well-suited to the demands of SHM applications. It has a low-power X-scale processor (PXA27x), whose speed can be selected based on application demands and power management, ranging from 13 MHz to 416 MHz. It incorporates a Chipcon 2420 802.15.4 radio with an onboard antenna. The onboard memory of the Imote2 is the feature that sets it apart from other wireless sensor platforms and enables the intense onboard calculation required for SHM applications, as well as storage of longer measurements. It has 256 kB of integrated RAM, 32 MB of external SDRAM, and 32 MB of flash memory. The Imote2 does not possess intrinsic sensing capabilities but rather provides a flexible platform for a range of sensing applications. The Structural Health Monitoring Accelerometer (SHM-A) board which uses a 3-axis analog accelerometer (LIS344ALH), a temperature and humidity sensor (Sensirion STH11), the light sensor (TAOS 2561), a gain difference amplifier (AD628), and a Quickfilter (QF4A512) has been designed, as shown in Figure 8 [44]. The board interfaces with the Imote2 via SPI I/O. The LIS344ALH, which has better performance than other comparably priced sensors [45], is a capacitive-type MEMS accelerometer with DC to 1500 Hz measurement range and offers an excellent price/performance ratio. The measurement range, resolution, and noise density of this accelerometer are $\pm 2 \text{ g}$, 0.66 V/g , and $50 \mu\text{g}/\sqrt{\text{Hz}}$, respectively. The QF4A512 employs a versatile 4-channel, 16-bit resolution ADC and a programmable signal conditional with a user-selectable sampling rate and programmable digital filters. A software driver for the SHM-A board was developed in TinyOS to control the functions of the QF4A512 such as loading the filter coefficients, allocating memory, timestamping, writing data, and onboard temperature compensation. The SHM-A

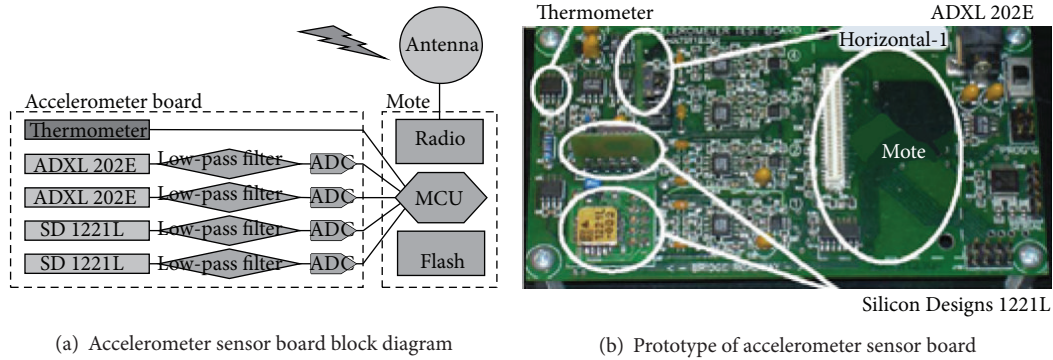


FIGURE 6: Accelerometer sensor board [12].

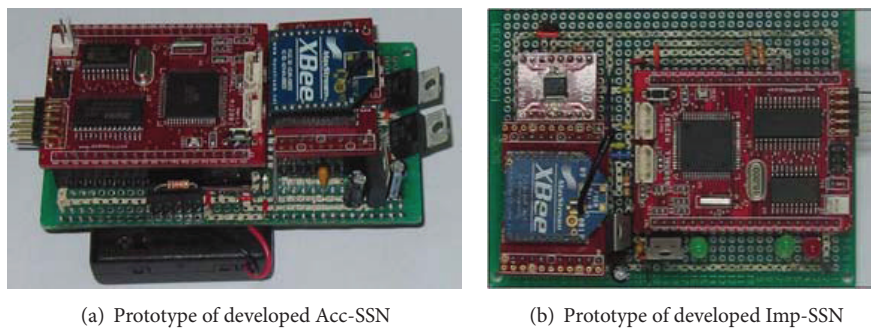


FIGURE 7: Wireless sensor proposed by Park et al. [43].

board provides excellent resolution for bridge health monitoring and is already commercialized by MEMSIC as the ISM400. Jo et al. [2, 46] have improved the resolution of the SHM-A board and developed a low-noise high-sensitivity accelerometer board (SHM-H) for the Imote2 platform to measure low-level ambient vibrations of structures, whose levels are typically on the order of 1 mg or less. Figure 9 shows the details of the SHM-H board. The z -axis of the SHM-A board is replaced with a low-noise and high-sensitivity sensor, the Silicon Designs SD1221L-002. To support the low-noise performance of the accelerometer, the resolution of the QF4A512 ADC was improved by reducing the span of the ADC from $\pm 2g$ to $\pm 1.2g$. The RMS noise of the SHM-H sensor board is 0.05 mg over 15 Hz bandwidth (0.08 mg over 70 Hz bandwidth), which is about 15% of the SHM-A board's noise level. Then, Spencer Jr. et al. [2, 47] designed a general purpose data acquisition board (SHM-DAQ board) for the Imote2 platform to interface with external analog sensors and digital sensors. Any type of analog sensor having DC voltage signals, whose ranges are 0~5 V or -5~5 V, and I2C digital sensors can be accommodated with Imote2 through the terminal block of this board. In 2010, Spencer Jr. et al. developed a strain sensor board (SHM-S board) for structural strain monitoring, as can be seen in Figure 10. This sensor board includes a signal amplification circuit and a Wheatstone bridge circuit to enhance the readability of the low level of strain gage signals. This sensor board is designed for stacked use with the SHM-DAQ board or SHM-A board,

which is also plotted in Figure 10. The resolution of SHM-S board is about $1 \mu\epsilon$ strain at 100 Hz. Besides, Spencer Jr. et al. have designed a pressure sensor board (SHM-P board) to provide wind pressure measurements using the AMSYS 5812 high-precision analog pressure sensor and a digital-to-analog converter (DAC) (SHM-D2A board) to support the output of signals using the TI-DAC8565.

The Laboratory for Intelligent Infrastructure and Transportation Technologies (LIITT) at Clarkson University has proposed a wireless sensor system (WSS) for concurrent measurement of both static and dynamic structural responses through strain transducers, accelerometers, and temperature sensors, as shown in Figure 11 [48]. The developed wireless sensor node incorporates the Imote Sky wireless sensor network platform. The onboard Chipcon CC2420 2.4 GHz transceiver offers an effective data rate of 250 kbps and low power consumption. An integrated 12-bit successive approximation register ADC provides eight external channels and a greater than 200 ksps maximum conversion rate. To facilitate high-resolution acquisition of distributed acceleration measurements for modal analysis of structures, a custom signal conditioning subcircuit provides analog low-pass filtering, digital offset correction, and digitally programmable gain for up to two single-ended analog signals. An independent signal conditioning interface is provided for the acquisition of differential sensor signals, such as Wheatstone bridge resistive sensors like strain transducers, load cells, pressure sensors, and displacement sensors.

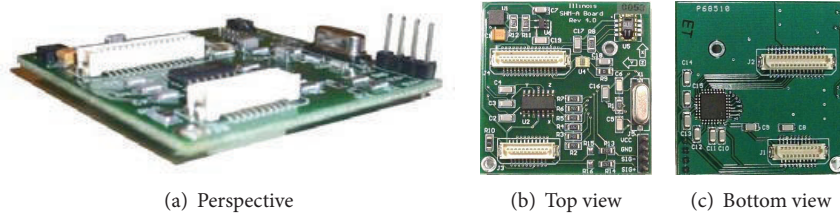


FIGURE 8: SHM-A board [2].

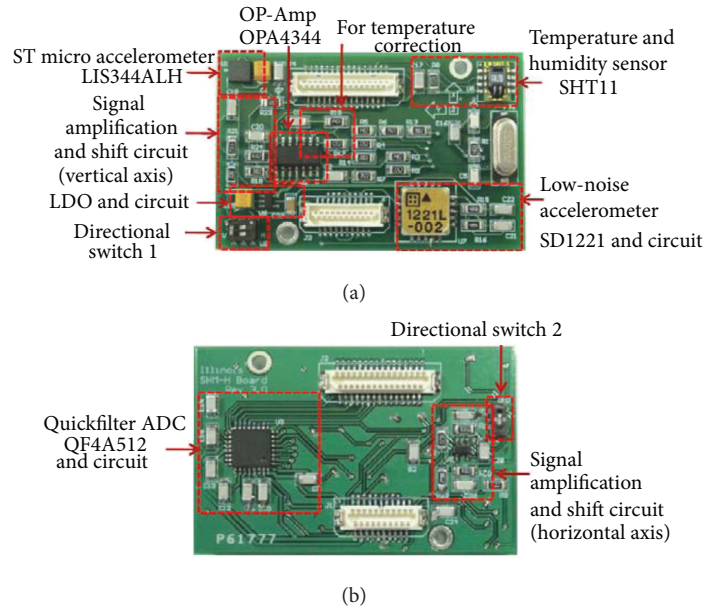


FIGURE 9: Top view (a) and bottom view (b) of SHM-H sensor board (revision 3) [46].

In 2010, Chen and Liu [49] developed a wireless sensor node. The sensor node consists of three circuit boards: the sensing board, the Gumstix board, and a wireless communication board. The Gumstix board communicates with the sensing board through I2C bus and connects to the wireless communication board through a parallel port. The Gumstix embedded computer is one of the world's smallest full function miniature computers with a size of 20 mm × 80 mm × 8 mm. The product is based on the Intel PXA-255 processor with X-scale technology and a Linux operating system. The Gumstix board has 64 MB RAM, 16 MB Flash, and 400 MHz CPU speed and also provides external memory spaces. Two server programs, a remote secure shell server and a web server, are provided for the users to remotely access the computer. The sensor board consists of an ATmega128L CPU for real-time data acquisition and communication with the Gumstix mother board, 16-bit ADCs and signal conditioning circuits for accelerometer and strain gage signal processing, an active sensing signal generator and response analyzer for active sensing with piezoelectric transducer (PZT) sensors/actuators, a ZigBee Module for low-power wireless communication, and an external SRAM for real-time data buffering.

Bocca et al. [20] have created a wireless sensor node, namely, ISMO-2 node, which originated from their previous ISMO node [3], as shown in Figure 12. The ISMO-2 node is based on the Sensinode U100 Micro.2420 sensor network platform. Its core is a TI MSP430F1611 MCU with 48 kB of program and 256 B of data flash memory and 10 kB of RAM. The platform also has an external 500 kB serial data flash memory (M25P40 by STMicroelectronics). The microcontroller unit (MCU) provides one 12-bit ADC (up to 8 channels available) and two 12-bit DACs. The clock of the MCU and the bus runs at 8 MHz. The radio module is an IEEE 802.15.4 compatible Chipcon CC2420 transceiver. The node is equipped with a dedicated sensor board, in which a 3-axis digital accelerometer (LIS3LV02DQ by STMicroelectronics, 7 × 7 × 1.5 mm³) is soldered. The Micro.2420 platform provides another 12-pin external connector to which a low-power temperature and humidity sensor (SHT71 by Sensirion) is connected.

Chae et al. [9] have proposed a sensor module that includes an A/D board and a ZigBee board (Figure 13) that was termed as u-Node. The u-Node is powered by a battery and a solar cell to operate and is hard-cased for water resistance. The distinguished feature of this node is that the 16-bit A/D

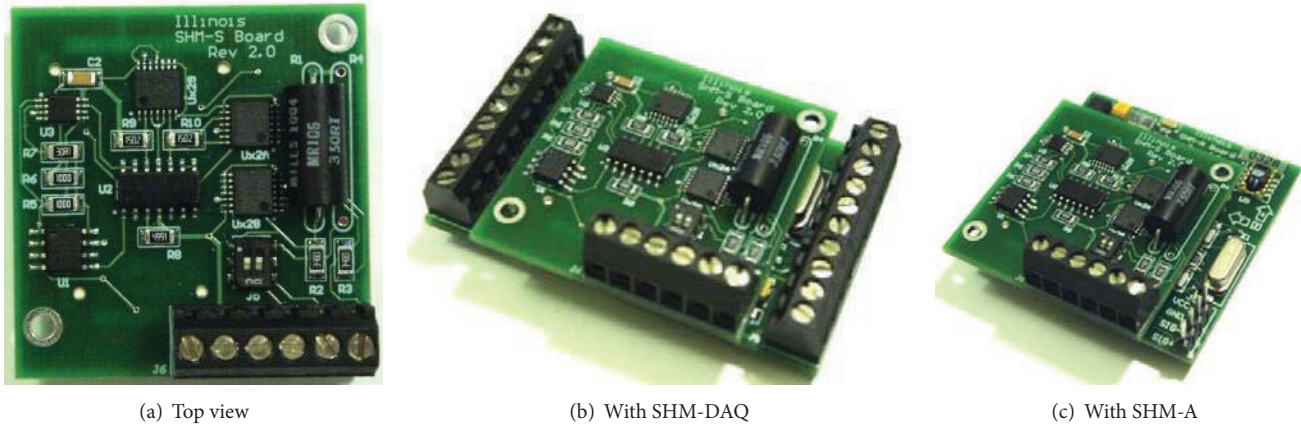


FIGURE 10: SHM-S board [2].

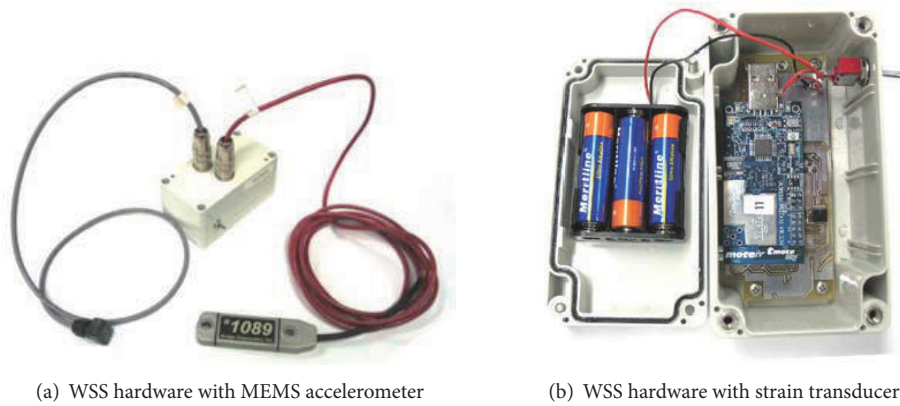


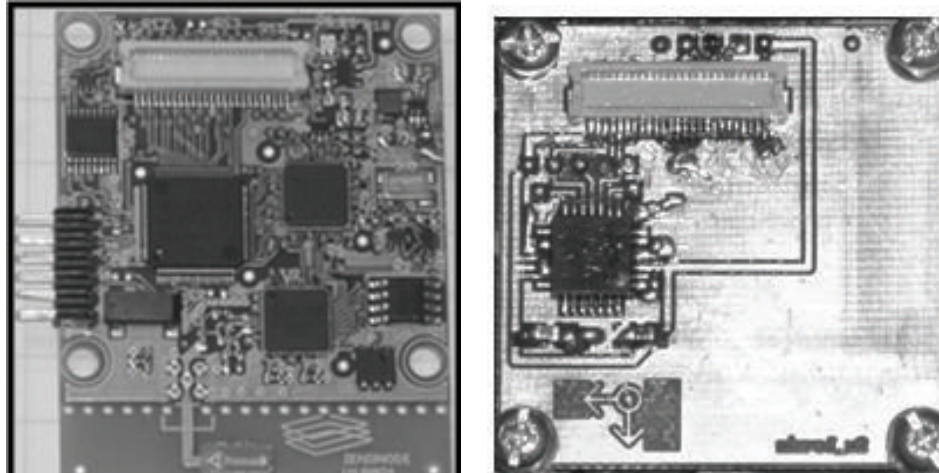
FIGURE 11: The WSS hardware [48].

board is compatible with the output of resistance, current, and voltage. Real-time clock (RTC) chips were used to ensure accurate monitoring times, with the Analog Devices AD7708 model for the ADC chip and an Atmel 128L for MCU. The A/D converting circuit is composed of a sensor interface, signal conditioning, A/D conversion, and power. Variety types of industrial sensors, such as accelerometer, strain gauge, thermometer, and wind gauge, can be used in this node. But the consistent and stable power supply to this node is a critical problem.

Hu et al. [13] have developed an S-Mote platform, an acceleration sensor board, and a strain sensor board to satisfy the requirements of bridge structural monitoring (Figure 14). The designed S-Mote improves the flexibility in connecting different sensor boards or in offering communication functions. The platform can collect different kinds of sensor signals, such as acceleration, temperature, and strain signals. S-Mote (Figure 14(a)), which is designed for SHM applications, is composed of four modules: microcontroller unit, RF module, power management unit, and sensor expansion pins. The ultralow-power microcontroller, MSP430F1611, was selected for S-Mote. The microcontroller runs on 1.8–3.6 V. When running at 1 MHz with a supply

voltage of 2.2 V, the microcontroller consumes $330 \mu\text{A}$ current in active mode; off-mode operation reduces consumption to $0.2 \mu\text{A}$. MSP430F1611 provides the largest on-chip (10 kB) RAM buffer, 48 kB of flash memory, an integrated 12-bit ADC, and a maximum conversion rate greater than 200 kbps. S-Mote has a 16-pin IDC expansion header for connecting sensor boards. Through exportation of I2C, UART, AD, and digital I/O over the expansion header, expanders can be used to attach different kinds of sensor boards. S-Mote uses the Chipcon CC2420 radio in a 2.4 GHz band. The two-dimensional Silicon Designs 1221L accelerometer is used in the acceleration sensor board, while multilevel amplifier technology is adopted to avoid the self-excited oscillation caused by excessive magnification. The foil strain gauge is chosen for the strain sensor board. An asymmetrical bridge circuit configuration is developed to compensate for temperature changes in the strain board.

Besides, other research groups have developed different wireless sensors to address the special demands of bridge health monitoring. Wang et al. [50] have designed a wireless sensor specifically for displacement and strain measurement using a polyvinylidene fluoride (PVDF) thin film sensor. Ruiz-Sandoval et al. [26] have developed an acceleration



(a) Micro.2420

(b) Acceleration board



(c) Temperature/humidity sensor

FIGURE 12: The ISMO-2 node [20].

board and a strain board using commercial Mica motes for communication and control, but the system relies on single-hop wireless communication, which is not scalable to large structures. Loh et al. [51] have presented a multifunctional carbon nanotube-polyelectrolyte-based nanocomposite passive wireless sensor for SHM applications. Harms et al. [52] have developed a wireless sensor named SmartBrick, which is equipped with a Quad-Band GSM/GPRS modem. Yang et al. [53] have presented a wireless sensor node which emphasizes monitoring the long-term continuous static behavior of a structure. Taylor et al. [54] have designed a wireless impedance sensor node (WID3) for use in high-frequency impedance-based SHM and low-frequency vibration data acquisition. Min et al. [55] have developed in-field adjustable impedance-based wireless sensor nodes in which an integrated impedance converter (AD5933) is equipped.

It is worth to say that many proposed wireless sensors mentioned previously are platforms on which a variety of sensors can be interfaced. If the output of a sensor can meet the demands of the input of the wireless sensor platform,

the sensor can be integrated with the wireless sensor platform. As a result, it is difficult to provide the exact structural parameters that can be measured by WSNs. Now, almost all structural parameters can be measured by WSNs, but the emphasis is placed on acceleration and strain.

3.2. Network Topology. The realization of operations in the WSNs-based bridge health monitoring system such as collecting data, transmitting data, and propagating orders relies completely on the WSNs. The network topology, which is used to organize wireless sensors in the network by routing and enable all sensors to cooperate with each other, is one of significant components in the WSN-based bridge health monitoring system. In general, according to the network topology, WSNs can be classified as a single-hop network and multihop network.

3.2.1. Single-Hop Network. Figure 15 shows the overview of the single-hop network, which is also called star topology.

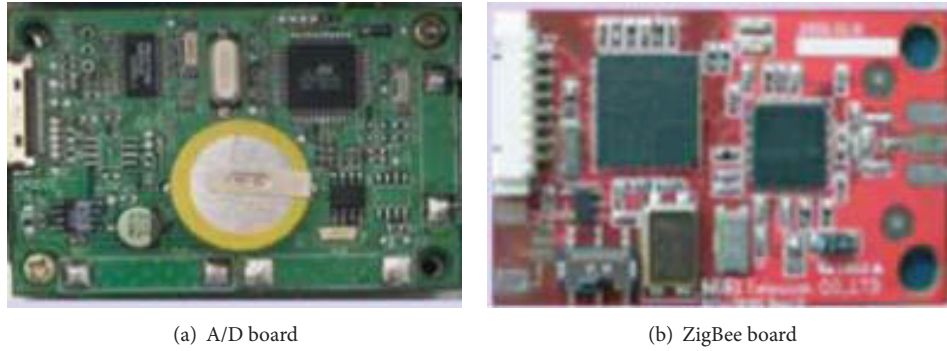


FIGURE 13: The u-Node [9].

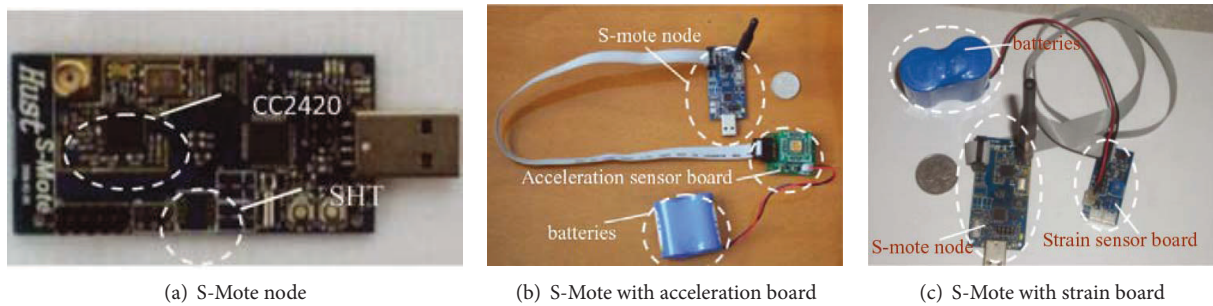


FIGURE 14: The prototype of the wireless sensor proposed by Hu et al. [13].

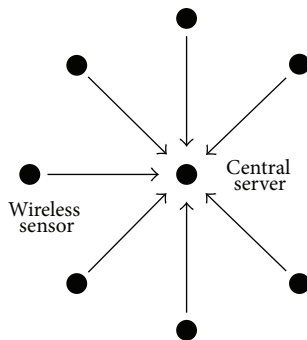


FIGURE 15: Single-hop network.

The central server is located in the center of the network. All wireless sensors are around the central server. Data are transmitted directly to the base station by a single hop. This network topology is very simple and robust. The failure of one node does not influence the operation of the whole network. But the data packets in a single-hop network are delivered one by one, the processing speed relied on the performance of the gateway and the central server. Furthermore, single-hop networks are spatially limited by the radio range and cannot span long distances without a large power supply. The single-hop network is fit for the monitoring of small-scale bridges like laboratory models [3, 9, 56, 57].

3.2.2. Multihop Network. The limited radio range of a general WSN using IEEE802.11 or IEEE802.15 wireless protocols,

combined with the impact of various environmental effects on the radio transmission, makes direct communication between all nodes impractical especially for long-span bridges. The multihop network, which transfers data between nodes or from sensor nodes to the central server by multihop communication, becomes an attractive alternative. Multihop communication transmits data and commands between two end nodes that are not in the direct radio range, using intermediary nodes. Multihop routing is more complex because each node has to determine how to find the most efficient routing to forward packets to the central server and coordinate transmission of packets received from other nodes. The routing needs to be reconfigured dynamically for robustness if a node fails and is no longer able to serve as an intermediary. Large-scale deployment of WSNs on long-span bridges gives rise to the need for multihop communication to provide adequate wireless coverage. The multihop network can be further classified into four categories: mesh-type network, tree network, linear multihop network, and random multihop network, as shown in Figure 16.

In a mesh-type network, there is no predetermined central server. Any node can be temporarily appointed as the central server according to the needs of data transmission and data processing. The node can transfer data to any other nodes within the transmission range. This type of network enables realizing completely auto damage diagnosis without external interference if a proper embedded software is designed. But the routing is very complex and is difficult to carry out, so it is rarely applied in the WSNs-based bridge health monitoring system.

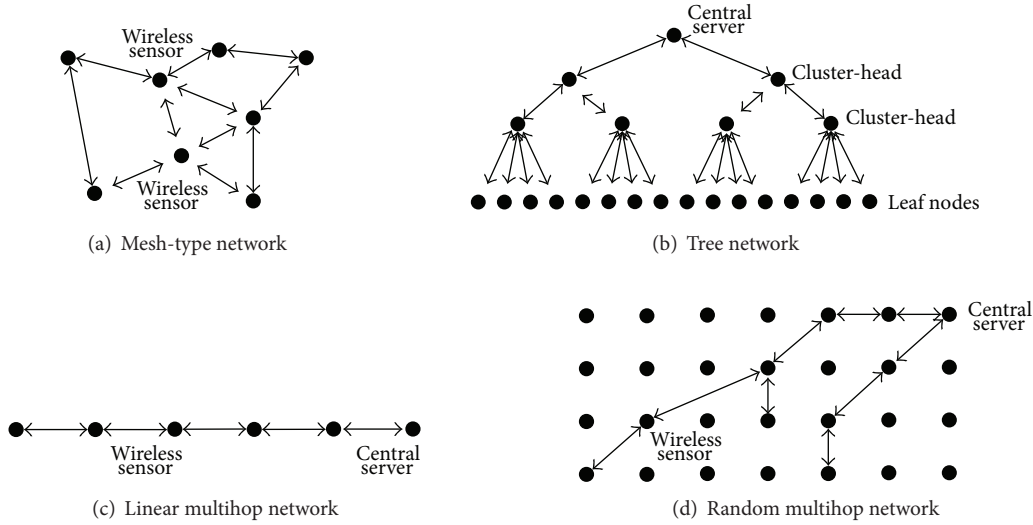


FIGURE 16: Multihop network.

The tree network is a type of multitiered network. The wireless sensors in the lowest level are named leaf nodes. The leaf nodes in WSN are assigned to different communities. In every community, there is a cluster-head, which is responsible for organizing communication and data processing within the community. And the communities can form a higher-level community until the cluster-head is able to communicate with the central server directly. The data packs are delivered from leaf nodes to the cluster-head, and to the higher-level cluster-head, to the base station finally. The communication among communities can be permitted or forbidden on different occasions. More power source and high computational ability are required for the cluster-head for heavy data transmission load and busy data processing. Gao et al. [58] proposed a distributed computing strategy (DCS) for SHM based on this network topology.

The data are transmitted one by one in a linear multihop network. All wireless sensors in the network form only one data link. Intermediary nodes have three functions: data sensing, data receiving, and data delivery. The geometrical diagram of a linear multihop network is very similar to that of a bridge span, so it is fit for long-span bridge monitoring. But the successful data transmission depends on every intermediary node in the data link. The death of any intermediary node may invalid the data link. In addition, packet loss recovery may be problematic in a long data link. The implement of the wireless health monitoring system on the Golden Gate Bridge is based on this type of network [12]. The speed of data collection is reduced dramatically with the increasing of the data link length.

And in a random multihop network, the data packs of wireless sensors are transmitted randomly until they arrive to the base station. Every data link from the wireless sensor to the central server can be regarded as a linear multihop network. But the wireless sensors have many choices of the next station. The random multihop network provides the maximum flexibility of wireless sensors configuration, which can fit the monitoring of a structure with complicate

geometry. Theoretically, this type of network can be scaled to an infinite area. But the nodes near the base station exhaust their power quickly for the large amount of transmitted data; “energy hole” is avoided uneasily [59].

3.3. Data Processing Technology. The bridge health monitoring assesses the safety and integrity of the structure based on the data measured by a variety of sensors. Since potentially problematic structural changes, such as corrosion, cracking, buckling, and fracture, all occur locally within a structure, responses from sensors close to the damaged site are expected to be more heavily influenced than those from sensors remote from the damage. As a result, to effectively detect arbitrary damage in a complicated structure, a dense array of sensors distributed over the entire structure will be required. Firstly, a tremendous amount of data is expected to be generated and managing this large amount of data is challenging. Secondly, data communication in WSNs is one of the most significant sources of power consumption and network failure, and reducing wireless communication becomes an important factor in prolonging the lifetime of WSNs. Thirdly, transferring a large amount of data will result in severe data congestion in the WSNs due to the limitation of wireless communication bandwidth. Because of the above three reasons, data processing technology, which assists in dealing with the large amount of data that is generated by a monitoring system, becomes an important issue in successfully implementing a large-scale WSN for evaluating the performance of bridges. Such an approach provides an adaptable sensor with self-diagnosis and self-calibration capabilities, thus reducing the amount of information that needs to be transmitted over the network.

In recent years, many data processing programs have been developed in the open-source environment of TinyOS, which is one of the most widely utilized operation systems (OSs) for deeply embedded wireless sensor networks. TinyOS is written in the high-level programming language nesC, which is based

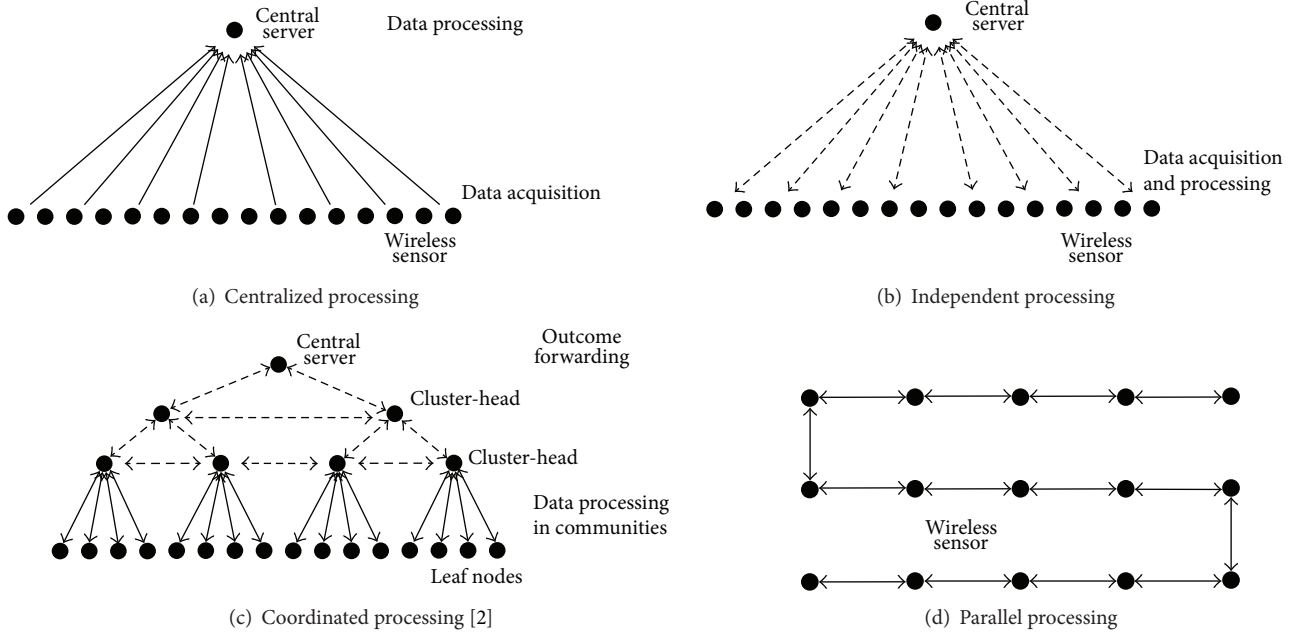


FIGURE 17: Data processing strategy.

upon the C programming language. Unfortunately, it is a very challenging environment for nonprogrammers to develop network control and application software. Extensive expertise is required to develop SHM applications in TinyOS [2, 19]. In general, data processing technology can be classified into four categories: centralized processing, independent processing, decentralized processing, and parallel processing. Figure 17 presents the data flow of different data processing algorithms. The latter three belong to the distributed processing strategy. In the distributed computing strategy, the sensing data are firstly processed locally by using the onboard microprocessor of the wireless sensor, and then unnecessary information is eliminated through data aggregation to efficiently utilize the network, reducing the information that needs to be transferred back to the central server. Indeed, the distributed processing strategy, which can utilize distributed computational capability efficiency, is regarded as another key motivation besides low cost that promotes the SHM from a traditional wired network to a wireless network and represents a new data management paradigm associated with SHM.

3.3.1. Centralized Processing. Centralized processing (Figure 17(a)), like the traditional wired bridge health monitoring system, requires that all data be sent back to a central server for further processing. Owing to the high-performance computer of the central server, all existing structural condition evaluation algorithms can be employed in this data processing strategy. However, in this strategy, the amount of wireless communication required in the network becomes costly in terms of excessive communication times and the associated power it consumes as the network size increases. For example, a wireless sensor network implemented on the Golden Gate Bridge that generated 20 MB of data (1600

seconds of data, sampling at 50 Hz on 64 sensor nodes) took over nine hours to complete the communication of the data back to a central server [42, 60].

Because of power requirements and bandwidth limitations, transferring all the measured information to a central server using WSN is difficult. Furthermore, the high data load and low efficiency of centralized processing cannot meet the demand of timely identifying structural damage. So processing data locally or dispersedly through the sensor's embedded microprocessor has received considerable attention. This strategy is also a radical departure from the conventional approach to monitoring structures.

3.3.2. Independent Processing. Independent processing, as shown in Figure 17(b), utilizes the computational power of every local sensor node to process collected data and requires no communication between sensors. The embedded algorithms on local wireless sensors collect and process raw measurement data available at each sensor with the processed results transmitted one by one to a central server. The central server further extracts useful parameters from different processed results and can also send them back to the wireless sensors when necessary. Using the data exchange between wireless sensors and the central server, the complicated damage diagnosis algorithms would be realized. Because of no data fusing, the implement of independent processing is relatively simple. The biggest challenge is how to modify the algorithms so that they can be realized in a computational core with limited power and executed in the special OS.

Early in 2002, the Cooley-Tukey implementation of the FFT was successfully embedded in the computational core of a wireless sensing unit by Lynch et al. [29, 61, 62]. The embedded FFT is utilized during field deployment of

the wireless monitoring system to provide the frequency response functions (FRFs) of instrumented structures. The wireless sensor is shown to provide identical results compared to those generated by MATLAB using the same time-history data. Then, the FFT has been coded to be executed by both the Motorola MPC555 and Atmel AVR microcontrollers and used to accurately identify the primary model frequencies of various laboratory and field structures. In addition, the peak-picking (PP) scheme that can identify modal frequencies from peaks in the Fourier spectra was also embedded in the wireless sensor. The following year, they executed the autoregressive (AR) model and autoregressive model with exogenous inputs (ARX) prediction (AR-ARX) model in the wireless sensing unit computational core to automatically detect damage of a structure [62–64]. The AR-ARX model takes the residual error of the fitted AR model to compare it with the database of AR-ARX model pairs previously calculated as a damage sensitive feature. In this strategy, only the AR or ARX model coefficients were wirelessly transmitted, and, therefore, the energy consumed for transmission was considerably reduced. The laboratory example shows that the computational core of the wireless sensing unit has successfully executed the AR-ARX model for detecting the possible existence and location of damage in the system. The algorithm of AR coefficients estimation was also embedded in another wireless sensor unit by Kiremidjian et al. [65].

Caffrey et al. [66] have proposed an algorithm to detect damage of a structure by assessing change in modal frequencies and signal energy contained in each corresponding mode. Fourier spectra of structural acceleration time histories are calculated in each wireless sensor unit. After the modal frequencies and modal signal energy contributions are determined in the wireless sensor units, they are transmitted to the host computer to perform damage assessment. The proposed approach is verified by detecting the presence of damage of the IASC-ASCE SHM Benchmark Structure. Hashimoto et al. [67] have embedded a wavelet-based damage detection method in a wireless sensor unit. The continuous wavelet transform is used as an algorithm of data processing. But their strategy is only fit for a single-degree-of-freedom (SDOF) system. Additionally, Chintalapudi et al. [68] embedded a distributed damage detection algorithm in wireless sensors by identifying frequency shifts caused by damage.

Cho et al. [69, 70] have explored a vibration-based tension force estimation method proposed by Zui et al. [71] using a PP algorithm and embedded it in the computational core of a wireless sensor. Welch's method to average Fourier spectra from the segments of a whole time-history signal is employed to remove the nonstationarity of a short-duration acceleration record, which is a limit of the memory-constrained wireless sensor. A series of laboratory tests are conducted on a slender braided steel cable with a variety of cable sags and tension forces. Excellent agreements have been found between the actual tensions and those estimated by the present wireless system. However, the vibration-based tension force estimation method derived by Zui et al. utilizes three lower natural frequencies of a cable. The method may be impractical if vibration of the resisting structure is exciting

the cable, which is called cable-deck interaction. The cable-deck interaction is dominant in the lower natural frequency region, which may distort the vibration signal of a cable, disabling reliable automated peak-picking.

Castaneda et al. [72] and Hackmann et al. [73] have tried to detect damage of a structure by the damage location assurance criterion (DLAC) method. The DLAC method is based on a correlation analysis between identified natural frequencies from measured data and analytical ones in each simulated damage pattern. Acceleration time-history records are transformed to frequency domain by applying the FFT. PSD functions are then calculated. Finally, a curve fitting technique is applied to the PSD function to determine resonant frequencies locations. A set of intermediate curve fitting parameters calculated on a local wireless sensor unit are then transmitted wirelessly to the base station where final roots extraction is finished and DLAC values are reported. It is demonstrated that the decentralized DLAC method can identify damage effectively. But the DLAC method has some limitations because it is not applicable to multiple damage scenarios or symmetrical structures.

Spencer Jr. et al. [60, 70, 74] have provided a library of numerical functions that are common to many SHM algorithms including FFT, singular value decomposition (SVD), Eigenvalue analysis, PSD estimation, and PP. All of those algorithms were modified to be used on the Imote2 and formed different open-source services. Researches all over the world can download them for free, which releases a lot of elementary work for performing high-level decentralized data processing strategies and damage diagnoses. For example, Sim et al. [75] have embedded the *cable tension estimation* that autonomously interrogates cable tensions in the Imote2 platform based on the PSD algorithm and the PP algorithm. This method of cable tension estimation uses the closed form relationship between natural frequencies and the tension force proposed by Shimada [76], which only requires the natural frequencies of a high model of the cable to avoid the cable-deck interaction.

Most recently, an agent-based computing paradigm has emerged in which all wireless sensor units in a homogenous WSN are utilized in a completely parallel and decentralized manner in order to solve complex engineering problems autonomously and without the need for any higher-level coordination. This type of in-network computation has been applied to various SHM problems including modal estimation, model updating, and task scheduling. Chen and Liu [49] presented a mobile agent middleware that allows a sensor network moving computational programs to the data source. The mobile agent code is a regular C program. The AR-ARX is used for damage diagnosis. The validation example shows that the presented mobile agent approach can successfully deploy the AR-ARX damage diagnosis algorithm on distributed sensor nodes.

Hsu et al. [77] embedded a frequency response function change method (FRFCM) in the computational core of the wireless sensing units to realize online damage localization and quantification of a structure. After the acceleration time history $y_i(t)$ is measured in the i th wireless sensor unit (WSU), the Fourier spectrum $Y_i(\omega)$ is calculated by

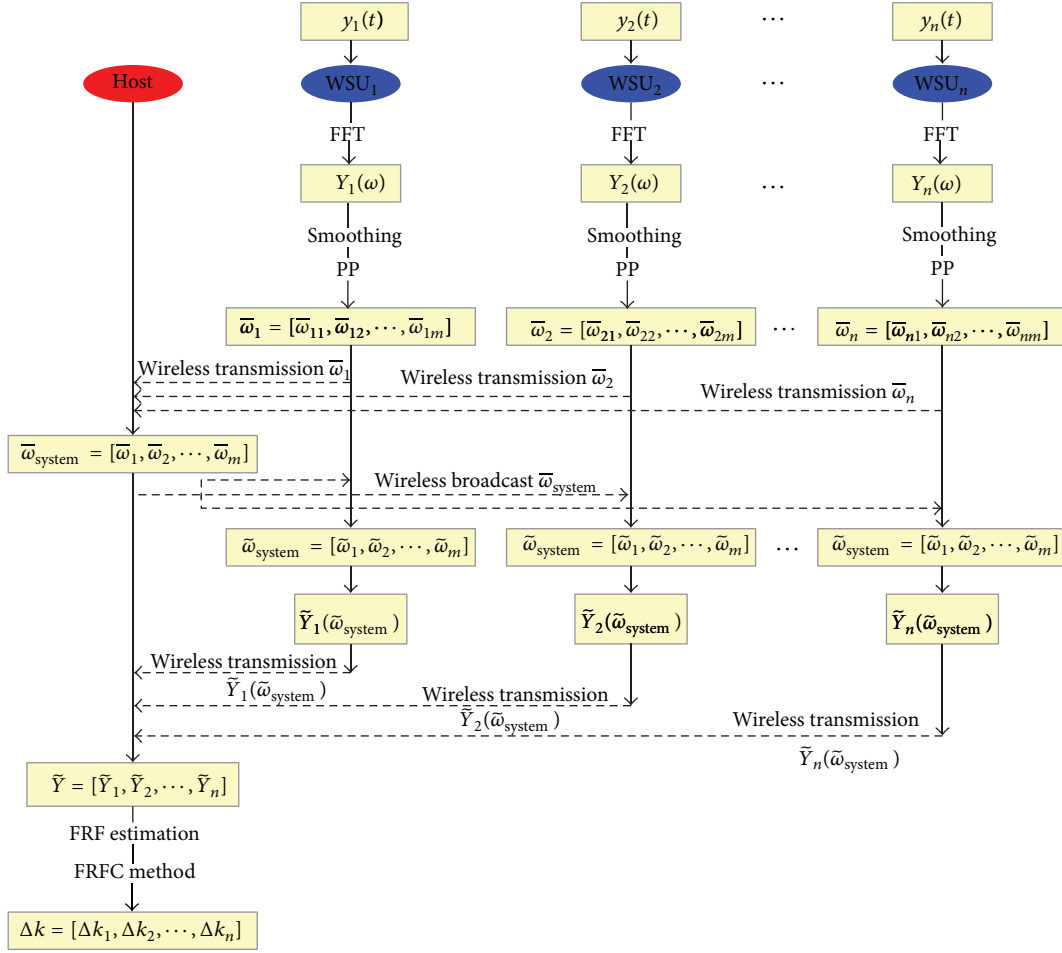


FIGURE 18: Implementation of the FRFCM in a wireless sensing system [77].

an embedded FFT algorithm and a set of eigenfrequencies of the structure in the i th WSU is determined by the embedded smoothing algorithm and PP algorithm. The frequency set selected in each WSU is then transmitted wirelessly to the host computer. The most probable set of the system eigenfrequencies is decided by taking the median of each set of peaks in the host computer and then broadcasted to all the n WSUs. The i th WSU then transmits a set of Fourier spectra around the system's eigenfrequencies back to the host computer. After the host computer receives the selected frequency spectrum segments from all the WSUs, the FRF segments are estimated by dividing the cross-power spectrum between the structural response and input excitation. With the system matrices and FRFs of the structure in the reference state written in the host computer, the variations of stiffness matrices can be calculated. The procedure of implementation of the FRFCM on a wireless sensing system is displayed in Figure 18. The laboratory test results demonstrate that, by taking advantage of collocated computing resources in wireless sensors, the proposed FRFCM can locate and quantify damage with acceptable accuracy and moderate energy efficiency.

Kim and Lynch [78] have proposed a system identification strategy for subspace system identification based

on Markov parameters (MPs). The method is specifically customized for embedment within the decentralized computational framework of a wireless sensor, Narada, proposed by Swartz et al. [35]. First, individual wireless sensor nodes perform local data processing to identify the MPs of a structural system. Then, the estimated MPs are wirelessly communicated to a central server where the global structural properties are assembled by execution of the Eigensystem realization algorithm (ERA). The difference of the modal characteristics autonomously extracted by the in-network data processing was found to be within 2% of those extracted offline by subspace identification for the first four models.

Yun et al. [79] have suggested a *RemoteSensingDP* module to implement decentralized damage identification in Imote2. The *RemoteSensingDP* module conducts data analysis capability using wavelet transformation and is written by the nesC language. The wavelet used in this implementation is the Haar wavelet. The onboard microprocessors conduct wavelet transformations to compute wavelet coefficients corresponding to the accelerations. The wavelet coefficients are transmitted wirelessly to the central server, which is connected to the laptop computer. Then the wavelet energy and entropy can be computed. Finally, the damage can be

identified through wavelet entropy indices. The proposed method was conducted using a bench-scale three-story shear building and a three-dimensional truss bridge structure in a laboratory. It was verified that the damage identification method with wireless sensor nodes could successfully locate damage in a laboratory benchmark truss structure.

The Hilbert-Huang transform (HHT) is an adaptive signal processing technique that produces signal decomposition in both time and frequency domains, providing instantaneous frequencies, phase, and damping for extracting damage sensitive features from the processed and decomposed data. Zhang [80] proposed a new distributed SHM scheme based on HHT for the implementation in the intrinsically decentralized computing environment in WSNs. The HHT-based decentralized data processing approach has been verified with both simulation and experiment. The results show that the proposed method achieves higher accuracy for identifying modal characteristics. The onboard computing features of the proposed system are also proven to be tolerant towards environmental fluctuations in temperature and noise levels.

In the independent processing, measured data are processed by each sensor node independently without communicating with other sensor nodes. After processing, the amount of data wirelessly transferred in the network is significantly reduced. Hence, these embedded data processing methods are relatively power efficient when compared to the transfer of raw data to a central server. However, there is no sharing of sensor data (raw or processed) between nodes, preventing these centralized algorithms from autonomously producing system-wide spatial properties (e.g., model shapes). Additionally, because of their inherently centralized communication architecture, these methods are not scalable to large or spatially diverse sensor networks [37, 81].

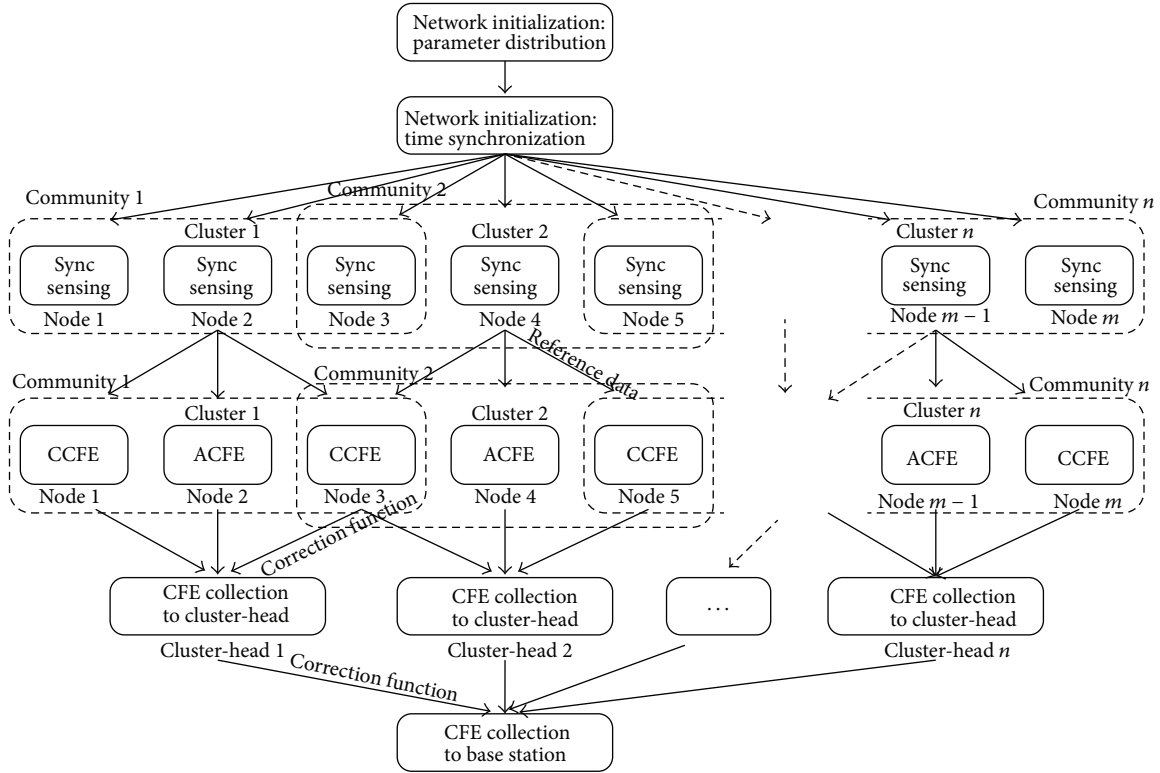
3.3.3. Coordinated Processing. In the coordinated computing strategy (Figure 17(c)), a wireless sensor processes data by a local computational core and exchanges information with other wireless sensors by wireless transmission, which is different from the independent processing. Through cooperation among different wireless sensors, more complicated data processing strategies and damage diagnosis approaches can be realized. Short data transmission distance and highly compressed data volume make the coordinated computing strategy more power efficient. The execution of damage diagnosis using WSNs is more automatic. WSNs employ a coordinated computing strategy to offer a scalable solution that has the potential to dramatically improve SHM efforts. But the coordinated computing strategy requires a more complex network topology, which makes the management of the network difficult.

The most significant contributions in this direction are the one presented by Gao et al. [58] with the introduction of the distributed computing strategy (DCS). Small numbers of wireless sensors are grouped to form different communities so that all sensors in a community are located in the range of a single hop. Although each sensor in Figure 17(c) is included in only one community, in the DCS approach,

wireless sensors can be contained in multiple communities. Each cluster-head collects necessary information and implements the damage detection algorithm for its community. Adjacent cluster-heads interact with each other to exchange information. Once information is aggregated, the cluster-heads determine the information to be sent back to the central server. This coordinated processing allows the sensor nodes to communicate with one another and share information in order to be able to keep spatial information that can be used to produce a global picture of a bridge system. The cluster-head of the community in which damage has not occurred transmits only an "OK" signal to the central server. If damage has occurred, the cluster-head of the community needs to send damage information such as damage location. Thus, the DCS approach requires only limited information which needs to be transferred between sensors throughout the entire sensor network. This approach will significantly reduce the communication traffic in the sensor network. The natural excitation technique (NExT), ERA, and damage locating vector (DLV) method can be utilized as structural analysis techniques to materialize this DCS concept [21].

To verify the DCS concept, Gao and Spencer Jr. [82] have proposed a decentralized flexibility-based damage detection method by extending the DLV method [83]. By utilizing only locally measured information, the damage of the local elements within these communities is detected. The damage detection results in these communities are then communicated with the surrounding communities and sent back to a central server through each community's cluster-head. Continuous online monitoring of a structure can be done without relying on central data processing. This approach will significantly reduce the communication traffic and the associated power demands in the sensor network. Numerical simulation demonstrated that the proposed approach works well for both single and multiple damage scenarios. The experimental results have shown that the proposed DCS approach can successfully monitor local community members only utilizing locally measured information for various damage scenarios [84]. The proposed DCS approach was shown to be promising for application of SHM in a densely distributed sensor network.

Spencer Jr. et al. [21, 85, 86] further established a framework for SHM on the WSN by using DCS. After the first measurement, the cluster-head broadcasts its time history to all the leaf nodes in the community. On receiving the record, each leaf node calculates the spectral density between its own data and the received record. This spectral density estimate is locally stored. After each measurement, the nodes repeat this procedure one time and the stored value is updated by taking a weighted average between the stored value and the current estimate. In this way, cross-spectral density is calculated on each node, and the estimated spectral densities are converted to correlation functions by inverse FFT and sent back to the cluster-head. Subsequently, modal analysis is conducted independently in each sensor group to estimate the local modal information using the ERA or the NExT/ERA. After that, local model shapes are assembled using a least squares approximation to estimate the global modal properties in the base station. Finally, the DLV method or stochastic damage



ACFE: auto-correlation function estimation.
CCFE: cross-correlation function estimation.

FIGURE 19: Information flow for NExT-based coordinated processing [46].

locating vector (SDLV) method [87] is used to localize the damaged element using modal properties identified before and after damage. Figure 19 shows the information flow in the NExT-based coordinated processing scheme. The method is experimentally verified on a steel truss structure using a small number of SHM-H sensor boards as cluster-heads and the SHMA board for the leaf nodes in the sensor network. The results showed that the proposed approach for decentralized modal analysis and damage diagnosis is efficient [46], while the ERA and NExT/ERA can be replaced by other system identification methods such as stochastic subspace identification (SSI) [60] or frequency domain decomposition (FDD) with random decrement technique (RDT) [80]. A similar framework was also employed by Yan et al. [88, 89]. In their method, modal identification is achieved using the FDD method and the PP technique.

Based on the hybrid SHM method proposed by Kim et al. [90], a modified global and local damage detection scheme was designed by Park et al. [43] to monitor prestressed concrete (PSC) bridges. The basic idea of the scheme is that the vibration-based SHM methods that are embedded in the acceleration-based sensor nodes (i.e., Acc-SSNs) are used for alarming damage occurrence at a global structure level and, at the same moment, the impedance-based SHM method that is embedded in the impedance-based sensor nodes (i.e., Imp-SSNs) is used for pinpointing damage occurrence at a local member level. The displacement ratio in

the frequency domain (i.e., frequency-response ratio) between two outputs at different locations is used as the global damage alarming indicator, while the root-mean-square deviation of impedance signatures measured before and after damage is used to quantify the local damage in the structure. From the experimental evaluation, the wireless sensor nodes accurately alarmed the occurrence of damage in the tendon and girder of the PSC girder model.

3.3.4. Parallel Processing. Zimmerman et al. [36] have proposed a distributed data processing strategy, which is named parallelizing processing. The sketch of data flow is described in Figure 17(d). They have adopted and modified three distributed output-only modal identification techniques: the PP method, the FDD method, and the RD method. The first one is the PP method. First, acceleration time-history data is collected at each sensor node and converted to an FRF using an embedded FFT algorithm. Then, each node picks the largest peaks from its FRF. Finally, the central server in the WSN can infer a subset of reasonable modal frequencies from the original PP data provided by wireless sensors. This method is relatively simple to implement in a sensing network. However, PP is always difficult to implement perfectly in a software and does not properly handle closely spaced modes. The second one is the FDD technique. At first, modal frequencies at each node are identified. Then,

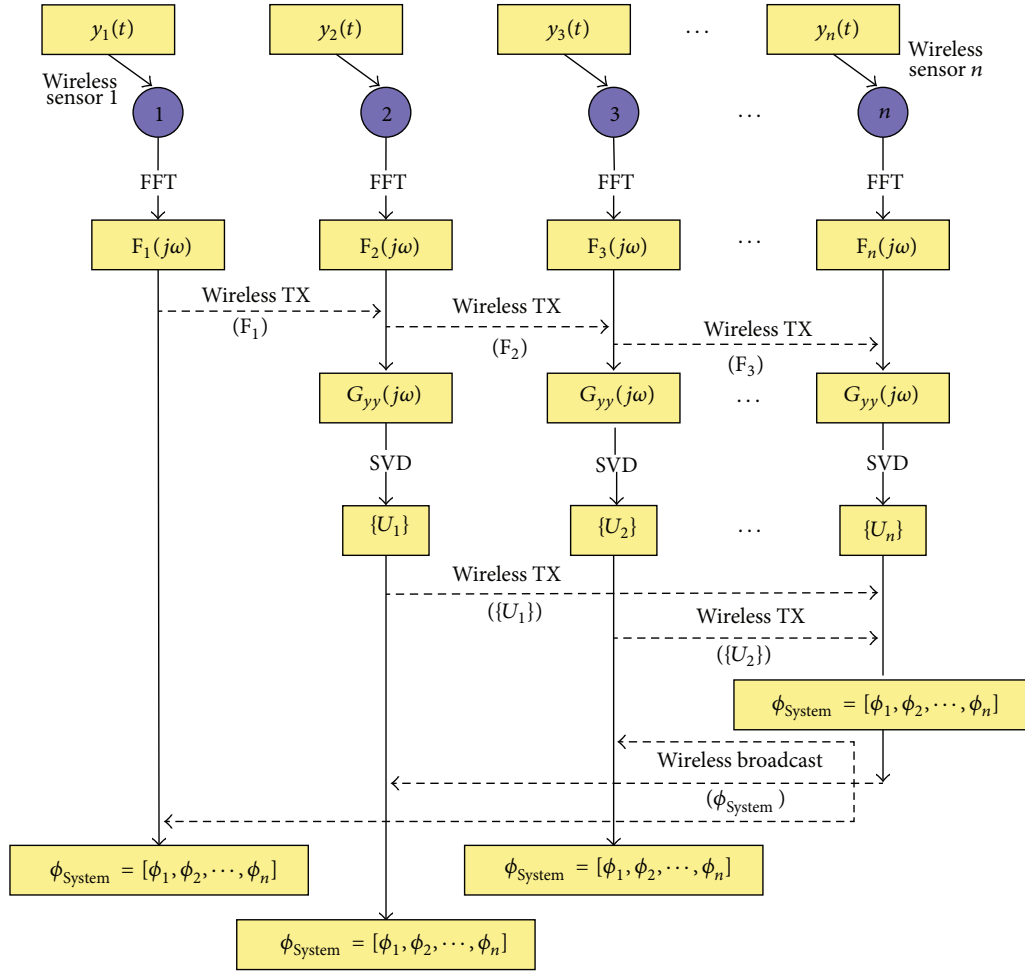


FIGURE 20: Implementation of the FDD method in a network of wireless sensors [36].

every unit in the network transmits its complex FFT results to the next node in a predetermined chain to construct a two-degree-of-freedom PSD matrix. After performing SVD on all of the PSD matrices, a set of two-node model shapes can be extracted at each natural frequency. Finally, all of the two-node model shapes are transmitted to the central server, where they are combined to form the global mode shapes of the structural system. Figure 20 presents the implementation of the FDD method in a network of wireless sensors. Because all FFT and SVD computations are performed simultaneously in a parallel fashion, significant time saving and effective data reduction can be realized. The FDD provides more reliable and robust model shape estimation compared to PP, while this approach requires a linear network topology and may result in substantial accumulation of errors in the global mode shapes. Subsequently, a market-based frequency domain decomposition (MBFDD) technique derived from free-market principles is developed by Zimmerman and Lynch [91] through which an agent-based WSN can autonomously and optimally shift emphasis between improving the accuracy of its mode shape calculations and reducing its dependency on any of the physical limitations of a wireless network, namely, processing time,

storage capacity, wireless bandwidth, or power consumption. In contrast to the FDD method, which uses a predefined chain-like topology through which computational tasks are distributed, the MBFDD technique creates an *ad hoc* tree-like topology through which a set of SVD calculations of varying sizes can be distributed. Numerical results show that the MBFDD is capable of autonomously forming a computational topology that allows a network of wireless sensors to not only improve upon the mode shape estimates of the FDD technique but also optimally distinguish between multiple resource constraints or objectives. The third one is the RD method. Firstly, a set of consistent time-history acceleration data is collected at each sensing node and transferred to the frequency domain. Then, the SDOF free decay impulse response functions are obtained by applying window filter and embedded IFFT. Finally, zero crossing and logarithmic decrement techniques are employed to automatically extract modal frequency and damping information from the impulse response. This method provides accurate estimates of modal damping ratios by taking advantage of the great degree of redundancy available within a sensing network. However, in a multiple-degree-of-freedom system, prior knowledge of the frequency characteristics of the system is required in order to

properly window the Fourier spectrum. This method is also not suited to determining modal properties involving closely spaced modes.

Zimmerman and Lynch [37] have presented novel wireless parallel simulated annealing (WPSA) to update structural models. In the WPSA, a computational task requiring simulated annealing (SA) optimization is first assigned to any one available sensing unit, along with a user-defined initial temperature, T_0 . This first wireless sensor, n_0 , then beacons the network, searching for other sensors available for data processing. If a second sensing node, n_1 , is found, the first sensor, n_0 , will assign the SA search tree starting at the next temperature step, T_1 , to the second sensor, n_1 , passing along its current information regarding the most optimal system state yet visited. This process continues until no sensors remain available for data processing.

3.4. Power Management. Though self-powering of wireless sensors avoids the effect of the AC power-line network on composition of the sensor network and electric surge in the outdoor use, it also causes one of the major challenges in WSNs, sustainable power supply. Wireless sensors typically are battery-powered, and their capacity is still limited although many high capacity batteries were invented like the lithium battery. Once the battery has consumed all of its power, replacement of the battery located remotely can become a very expensive and tedious or even impossible task. Power management is one of the biggest considerations when a large-scale WSN for bridge health monitoring is deployed. There are three relative ways to manage power and prolong WSNs lifetime. The first one is selecting low power consumption hardware. The second one is using power efficiently, termed as power efficiency. And the third one is power harvest from a local place.

3.4.1. Low Power Consumption Hardware. All wireless sensor designers take low power consumption as the most important parameter to be considered when selecting wireless sensor components. With the development of the MEMS technology, the power consumption of wireless sensor components is reduced to a great extent. For example, the microcontroller AT90S8515 consumes 40 mW of power [30], the X-scale processor (PXA27x) consumes 44 mW at a clock rate of 13 MHz [44], the Chipcon CC2420 only consumes 60 mW when receiving and 52 mW when transmitting within the range of 10–75 m [92], and the MaxStream 9XCite wireless modem consumes 250 mW when transmitting, 150 mW when receiving, and less than 5 mW when idle [32]. But a component with low power consumption also implies poor performance. Taking the tradeoff between power consumption and requirement of SHM into account, the power consumption wireless sensor components cannot be decreased illimitably. As a result, the lifetime of the wireless sensor is still very short when comparing with the service life of a bridge. A more effective power strategy is required.

3.4.2. Power Efficiency. Power efficiency is defined as appropriately utilizing limited battery power to maximize lifetime

of WSNs and to achieve the goal of bridge health monitoring at the same time. Three methods are employed generally to consume power efficiently: sleep mode, network optimization, and data compression.

Sleep mode means that most of the components on a wireless sensor are asleep and only the radio transceiver is awake to listen for beacon signals if no monitoring actions are carried out, so the power consumption can be reduced. A lot of components used for wireless sensors are produced with a sleep model, a deep-sleep mode, or different work conditions with different power consumption. Galbreath et al. [93] proposed two low-power monitoring modes. In the first mode, the microcontroller periodically awakes via a watchdog timer interrupt, turns on the telemetry hardware, and listens for a wake command from the central server. In the second mode, the microcontroller remains in the low-power sleep mode until a rising external analog voltage triggers a hardware interrupt. Rice et al. [60] designed two power-efficient management services for sensor nodes, called *SnoozeAlarm* and *ThresholdSentry*. Using the property that the Imote2 allows the processor to be put into a deep-sleep mode with minimal power consumption by making only the processor clock awake, the *SnoozeAlarm* service places the sensor nodes in the deep-sleep state, waking them periodically for a brief time (e.g., 0.6 sec for the single hop and 0.75 sec for multi-hop) to listen for beacon signals sent from the gateway node. Once a signal is heard, the node becomes fully active. The *ThresholdSentry* application runs on the designated sentry nodes periodically executing the sentry's task, that is, collecting data for a given period of time and checking if the threshold value is exceeded. If this threshold is exceeded, the sentry nodes send notification to the gateway node, then the gateway node wakes up the entire network and initiates designated network-wide tasks. But the current implementation of *ThresholdSentry* allows the network only to capture the occurrence of longer-duration, lower-frequency events such as high wind. Besides, the duty-cycle approach, which wakes wireless sensors for a short time in every predetermined period, is a promising method. Whelan and Janoyan [48] stated that, for active sampling at a rate of one minute per hour, the estimated service life of their wireless sensor would be extended to 160 days. Hu et al. [13] demonstrated that the service life of S-Mote is extended to 168 days if the sensor node participates in active sampling for only one hour/day.

Network optimization means finding the optimal node locations or routing so that the power consumption is minimal while the requirement of bridge health monitoring is fulfilled. Zimmerman et al. [94] have developed a resource distribution framework based on a market-based method, which is used to autonomously distribute these scarce network resources (CPU time, wireless bandwidth, storage capacity, battery power, etc.) across various computational tasks with competing objectives and/or resource demands. In this framework, a Pareto-optimal allocation of scarce resources can be reached while completing a set of multiple computational objectives as quickly as possible. And this optimization method can be expanded to other decentralized data processing strategies. Fu et al. [95] have considered

the WSNs deployment problem for finding node locations to reliably diagnose the health of a structure while consuming minimum energy during data collection. A min-max, energy-balanced routing tree and an optimal grid separation formulation that minimize the energy consumption as well as provide fine grain measurements are proposed.

Data compression reduces the volume of transmitted data and shortens the data transmission distance through in-network data processing rather than delivering raw collected data, so that the lifetime of WSNs can be prolonged. Almost all distributed data processing technologies as mentioned in Section 3.3 can compress the volume of transmitted data and alleviate power consumption to some extent. For example, performing the damage detection using the AR-ARX model at the sensor node as compared to wirelessly transmitting the original raw time-history data is shown to be on the order of 50% of data compression [62–64]; the total data to be transmitted when using the ERA to implement modal analysis in the distributed data processing scheme is $N \times n_d + N/2 \times (n_s - 1)$ compared to $N \times n_d \times (n_s - 1)$ in the centralized data collection scheme, where N is data length of each time history, n_d is repeated times of spectral density estimation, and n_s is the number of nodes in the community [22]; over 77% compression was accomplished using local calculation by extracting 105 MPs from 1,200-point response time-history records at 15 wireless sensor nodes [78].

3.4.3. Power Harvest. Though the battery life of a wireless sensor can be extended by efficient power management, data condensation, and in-network processing as mentioned above, the use of ordinary batteries still requires regular battery replacement. Power harvest from a local place is a rational choice. Power harvest is the process of acquiring the energy surrounding a system and converting it into usable electrical energy [96]. Recently, a surge of power harvesting researches has been brought on by the advances in wireless technology and low-power electronics. Thus, many researchers in the SHM and sensing network community have shown interest in power harvesting and have proposed alternative power sources such as sunlight, wind, and vibration [97]. Power harvest can be further classified into three categories: wireless energy transfer, ambient energy harvest, and vibration-based energy harvest. Among them, the harvesting of ambient energy and vibration-based energy is the strongest candidate for application to the bridges.

Wireless energy transfer means power is transmitted wirelessly. Mascarenas et al. [11, 98], for the first time, used wireless RF transmission to deliver electrical energy to power a piezoelectric impedance sensor node by charging the capacitor in the node. A controlled helicopter, which can fly to the wireless sensor node, is used as a central server to send energy to wireless sensors and receive data from wireless sensors. The results showed good performance by transmitting necessary power to the impedance sensor node, and it took about 200 seconds to reach up to the operation voltage level (3.3 V) of the node. However, one of the limitations in microwave transmission is the attenuation of the wave as it travels through space. The loss associated

with this attenuation has been characterized as the square of the distance between the transmitting and receiving antennas. Park et al. [99] proposed an optical system for wireless power and data transmission. It took advantage of optoelectronics for both guided wave generation and sensing. A generated waveform by modulation of a laser is wirelessly transmitted to a photodiode connected to a PZT on the structures. Then, the photodiode converts the light into an electrical signal and excites the PZT and the structure. Finally, the reflected response signal received at the same PZT is reconverted into a laser, which is wirelessly transmitted back to another photodiode located in the data acquisition unit for damage diagnosis. Since the laser emits highly directional and collimated radiation with a low angle of divergence, the energy carried by the laser beam can be transmitted for a long distance without attenuation and focused onto a small area [98].

The main sources of ambient energy are sunlight, thermal gradient, human motion, acoustic noise, and so forth. Multiple articles reviewing the prospects of ambient energy sources for harvesting can be found in the literature [100–104]. From the practical reviews of SHM application, sun energy is perhaps one of the most powerful choices. Raghunathan et al. [105] systematically analyzed the components, design choices, and tradeoffs involved in designing a solar energy harvesting module. The proposed module allows for near-perpetual operation of the Mica2 mote. Jang et al. [106] successfully carried out the validation of solar energy harvesting in the Jindo Bridge deployment using solar panels. The installed solar panel is plotted in Figure 21(a). Chae et al. [9] used a solar cell and rechargeable battery to secure a stable power supply of the WSNs deployed on the Yongjong Grand Bridge. Another promising energy source is wind power in long-span bridges, which are usually located in windy areas. Spencer Jr. and Cho investigated the feasibility of small wind-powered generators to operate wireless sensors located at a cable-stayed bridge to show the maximum output power of a wind turbine is enough [2]. Anant Kishore and Priya [107] provided a 40 cm diameter small wind energy portable turbine (SWEPT), which has rated the power output of 1 W with the rated wind speed of 4.0 m/s and is capable of producing power output up to 2.2 W at the wind speed of 5.5 m/s. Figure 21(b) shows the prototype of SWEPT.

Vibration-based energy harvest represents another important power harvest technology. The most effective method of implementation of vibration-based energy harvest is the use of piezoelectric materials [108]. Piezoelectric materials have a crystalline structure that provides them with the ability to transform mechanical strain energy into electrical charge. This property provides these materials with the ability to transfer ambient vibration into electrical energy that may be stored and used to power other devices. The bridges on which wireless sensors are installed are vibrated continuously, which provides a natural source of vibration-based energy. The concept of utilizing piezoelectric materials for energy generation has been studied by many researchers over the past few decades. It was already developed as an independent subject. Overviews, discussions and comparison of vibration-based energy harvest have recently been given by many

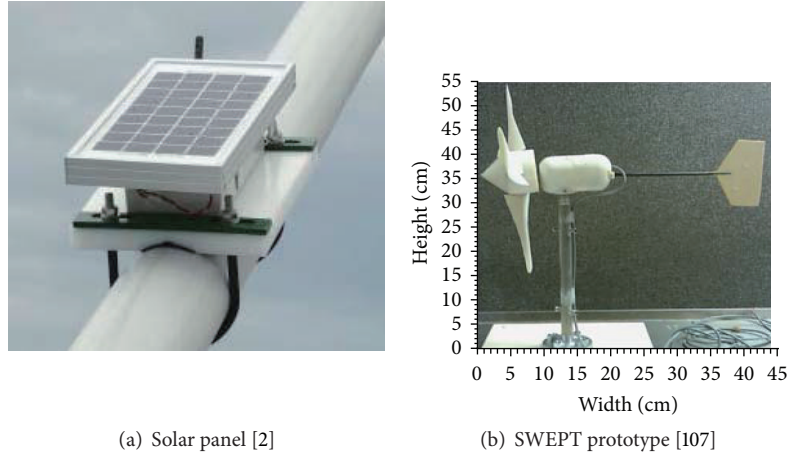


FIGURE 21: Ambient energy harvest.

literatures which include, but are not limited to, Sodano et al. [96], Dutoit et al. [109], Park et al. [110], Gilbert and Balouchi [111], Khaligh et al. [112], and Kim et al. [113]. Because vibration-based energy harvesters are still in the development stage, only a few commercial solutions are available. Most research efforts are still in proof-of-concept demonstrations in a laboratory setting.

3.5. Time Synchronization. Due to the delay of radio transmission or inherent internal sensor clock errors, the collected dates in different wireless sensors in WSNs may initially be unsynchronized. A time synchronization (TS) error in a wireless sensor network can cause inaccuracy in bridge health monitoring applications. The effect of the TS error of the nodes on the accuracy of modal analysis is analyzed by Krishnamurthy et al. The paper shows that a relatively small error in TS (e.g., $30 \mu\text{s}$) can cause a considerable reduction in the reliability of the mode shape reconstruction of higher modes, which are normally better indicators of structural damage. It is concluded that the effect of the TS error is comparable or can even exceed the effect of sensor's noise [20, 22]. Since the appearance of WSNs, TS has been one of the most addressed issues. To date, many TS protocols have been developed. For more detailed information on the TS, it is recommended to refer to those papers by Sivrikaya and Yener [114], Rhee et al. [115], Lasassmeh and Conrad [116], Ranganathan and Nygard [117], and Yang [118], where more than 60 references are cited. Two of the most notable TS protocols are the flooding time synchronization protocol (FTSP) proposed by Maróti et al. [119] and the timing-sync protocol for sensor networks (TPSN) proposed by Ganeriwal et al. [120].

FTSP performs both offset adjustment and estimation of the relative skew of the clocks through a one-way message exchange, decreasing the frequency of transmission of the required TS beacons and hence energy consumption. The FTSP was implemented by Nagayama and Spencer Jr. in the Imote2 [85]. FTSP utilizes time stamps on the senders and receivers. When a beacon node broadcasts a packet to the other nodes, a time stamp, t_{send} , is appended at the end of

the packet. Upon reception of the packet, the receivers stamp the time, t_{receive} , from their own local clocks. The delivery time, t_{delivery} , between these two events is usually not small enough to be ignored, but the variance of t_{delivery} over time is usually small. The offset between the local clock on the receiver and the reference clock on the sender is determined as $t_{\text{receive}} - t_{\text{send}} - t_{\text{delivery}}$. This offset is subtracted from the local time when global time stamps are requested afterward. A group of nine Imote2s was experimented and a TS error of $10 \mu\text{sec}$ is achieved, which is small for SHM applications.

TPSN periodically adjusts the offset of the clocks of the nodes using a two-way message exchange. However, due to a required previous hierarchy formation phase and to the two-way message exchange, it introduces a significant communication overhead, wasting energy and radio channel resources [20]. The first step of the TPSN protocol is to create a hierarchical topology in the network. Each node is assigned a level in this hierarchical structure. A node belonging to level i can communicate with at least one node belonging to level $i - 1$. Only one node is assigned level 0. Once the hierarchical tree structure is established, a node with level i synchronizes to a node with level $i - 1$. After all, every node is synchronized to the root node with level 0 and TPSN achieves network-wide time synchronization [114]. Mica2 motes employing TPSN are reported to synchronize with each other to an accuracy of $50 \mu\text{sec}$ [21].

4. Performance Validation and Application

4.1. Scaled Bridge Test. Performance validation within the well-controlled laboratory environment is the first step towards deployment of WSNs-based bridge health monitoring systems on field bridges. The earlier efforts are bonding several wireless sensors on shaking table or rotator with predetermined input signals; the accuracy and reliability of those wireless sensors are assessed. Those works have been finished after wireless sensors had been designed, which are relatively easy and are not reviewed in this paper. However, more recent studies have begun to deploy complicated WSNs-based bridge health monitoring systems on partial- and full-scale

bridge models, which provide comprehensive insight into the opportunities and challenges of the WSN technologies for bridge monitoring.

Whelan et al. [121] have applied a wireless sensor network platform to perform system identification on a bridge model throughout healthy and damage case states in an effort to assess the performance of the Wireless Sensor Solution developed at Clarkson University [122, 123]. The laboratory bridge features a four-meter span, one-meter wide, steel frame with a steel and cement board deck composed of sheet layers to regulate mass loading and simulate deck wear. A rectangular measurement grid was developed across the steel frame of the bridge model resulting in twenty-eight measurement locations. A wireless node interfaces with a dual-axis LIS2L02AL accelerometer at each measurement location for a total of 56 channels of wireless measurement. These wireless channels are accommodated by two WSNs operating at adjacent carrier frequencies that are synchronously triggered by an external switch wired to interrupt signals at the central network coordinator nodes. Comparison between the acceleration measurement transmitted by the wireless sensor node and the cable-based sensor located at the same place reveals exceptional correlation. The power spectrums contain nearly identical frequency content and magnitudes, thereby validating the transfer function of the wireless sensor signal conditioner and indicating comparable performance between the two data acquisition systems.

Park et al. [43] have verified the proposed autonomous operation schemes using the Acc-SSNs and Imp-SSNs installed on a lab-scaled prestressed concrete girder model. The girder with a T-beam section has the span length of 6 m. Seven Acc-SSNs and seven conventional accelerometers were located on the two symmetrical sides of the test structure. The Imp-SSN was placed on the anchor plate. The impact excitation was applied by an electromagnetic shaker (VTS100) at a location distanced at 1.7 m from the right edge. The vibration-based SHM methods were embedded in the Acc-SSNs and the impedance-based SHM method was embedded in the Imp-SSNs. Frequency responses acquired from the Acc-SSNs and the conventional system show good matches with little difference. Those two impedance signals measured by the Imp-SSN and the commercial analyzer show a great agreement.

Bocca et al. [20] attached eight ISMO-2 nodes to a wooden model bridge to evaluate the capability of the ISMO-2 nodes and proposed a time-synchronized wireless SHM system. The bridge is 420 cm long, 65 cm wide, and 34 cm high, as shown in Figure 22. Sixteen wired accelerometers were also used as reference. The locations of the wireless sensors and wired sensors are plotted in Figure 22. The single-hop star topology was employed to establish the network. All along the tests, the sampling frequency of the wired sensors was set to 1,024 Hz. The sampling frequency of the ISMO-2 nodes was varied, from a minimum of 200 Hz to a maximum of 1 kHz. The measurement period was initially set to 40 seconds and then progressively increased to 2 minutes. Also, different 1-axis, 2-axis, and 3-axis measurement sets were collected. During the tests, the achieved final packets delivery ratio was 99.95%. The modal properties identified

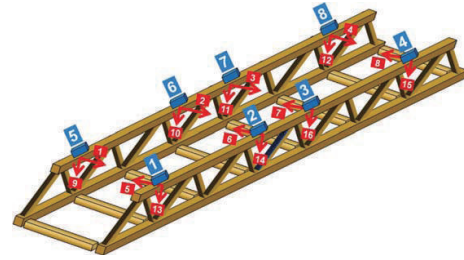


FIGURE 22: The sensors deployed on the wooden model bridge: 16 wired accelerometers (red arrows), 8 ISMO-2 nodes (blue boxes) [20].

with acceleration signals collected by wired sensors and by the wireless nodes have shown 1.035% maximum relative difference.

4.2. Full-Scale Bridge Test. Although the functionality and the stability of many wireless sensors and WSN prototypes have been thoroughly verified by a series of experiments at the laboratory scale bridges, validation of field performance must be done using actual civil bridges for the reason that the noise floor, data transmission distance, network topology, signal interference, and so forth in the practical environment has much difference with those in the laboratory environment. Another attractive benefit is that the WSNs can be further used for the bridge monitoring once their reliability is validated.

Before 2005, only a handful of nodes are instrumented on the actual bridges. Only the feasibility of monitoring the structural response using wireless sensors is validated. Aoki et al. [124] installed only one wireless accelerator on the Tokyo Rainbow Bridge to test the performance of the developed MEMS-based wireless sensor. Galbreath et al. [93] demonstrated the use of a wireless sensor network to monitor the performance of a steel girder composite deck highway bridge. Binns [125] has presented a field validation study of a wireless monitoring system on a highway bridge in Ohio. Lynch et al. [30] deployed seven wireless sensing units interfaced with MEMS-based capacitive accelerometers on the Alamosa Canyon Bridge to validate the performance of the wireless sensing unit in the field. Chung et al. [126] have installed a network of wireless sensors upon a footbridge on the University of California, Irvine, campus to monitor bridge responses under footfall excitation.

In 2006, Heo et al. [39] deployed the improved SWMAS on a self-anchored suspension bridge in Korea to assess the function of the new SWMAS in use of a real flexible structure. The main span and the side span of the bridge are 300 m and 125 m, respectively. Its truss structures are the two-storied Warren trusses. The bridge sustains compressive force and upper eccentric force with its stiffening trusses. The improved SWMAS devices were installed on the hanger rope and at the center of the main span to measure how the bridge reacts to the ambient vibration caused by traffic and wind load. The sampling rate of the wireless sensor unit is set at 80 Hz and the collecting lasted for 100 seconds. The tensile force calculated from the hanger rope differed from the office data by 6.7%.

The main span's natural frequencies remained within a 3% range. The usefulness of the SWMAS for monitoring flexible structure systems was proved.

To quantify the accuracy and robustness of wireless monitoring systems within the complex environment encountered in the field, Lynch et al. [127, 128] installed a network of low-cost wireless sensors in the Geumdang Bridge, Korea. In total, 14 wireless sensors were installed in the concrete box girder span to record acceleration responses of ambient and forced vibrations, and the single-hop network was used for data transmission. The low-cost PCB Piezotronics 3801D1FB3G MEMS capacitive accelerometers were selected for use with the wireless monitoring system. In order to enhance the resolution of the capacitive accelerometers interfaced to the wireless sensors, a signal conditioning circuit that amplifies and filters low-level accelerometer outputs was proposed. The performance of the complete wireless monitoring system was compared to a commercial tethered monitoring system that was installed in parallel. The free-vibration response recorded by the tethered sensor and high-resolution wireless sensor indicates that they are nearly identical. The performance of the wireless monitoring system is shown to be comparable to that of the tethered counterpart. The decentralized FDD is also used to estimate the mode shapes of this bridge. The results have strong agreement with those extracted by the centralized FDD method using MATLAB. So, the effect of the decentralized FDD is validated in real circumstances.

In 2007, Kim et al. [12, 42, 129] deployed the largest WSN at that time for SHM on the Golden Gate Bridge in San Francisco. The Golden Gate Bridge is a cable-supported bridge, with a tower height of 227 m above sea level and a 1280 m long main span. 64 wireless sensor nodes, which were integrated by Crossbow MicaZ motes and new customized accelerometer boards, were distributed over the main span and the tower, collecting ambient vibrations synchronously at 1 kHz rate, with less than 10 μ s jitter, and with an accuracy of 30 μ G. Those nodes formed a 46-hop network, with a bandwidth of 441 B/s at the 46th hop. To provide time synchronization in the network, FTSP is used. The recorded data are transferred from each node to the base station using multihop communication and pipelining. The data on network performance confirmed the effectiveness of spatial reuse of radio bandwidth through pipelining in maintaining a scalable network. The test results showed that the pipelining of data is very effective in providing a constant and reliable effective bandwidth for a large number of hops. Analysis of the ambient vibration data and system identification results demonstrate that high spatial and temporal sensing using the wireless sensor network give a high resolution and confidence in the identified vibration modes. Then, the collected data are used for statistical analysis of vibration modes of this bridge [130]. However, a complete cycle of sampling and data collection for the full network produces 20 MB of data and takes about 9 hours. The efficiency of data collection in this WSN should be improved.

To assess the capabilities of a low-cost wireless structural monitoring system to rapidly collect the dynamic responses of a large-scale civil infrastructure system, Weng et al. [131] employed the rapid-to-deploy wireless sensor prototype by

Wang et al. [34] to monitor the newly retrofitted Gi-Lu cable-stayed bridge (Nantou County, Taiwan) during ambient excitation conditions. Twelve wireless sensors each containing a four-channel sensor interfaced with a high-resolution ADC are used. Transducers interfaced to each wireless sensor node are highly sensitive Tokyo Sokushin VSE-15 velocity meters whose sensitivity constant is 0.25 V/kine (where 1 kine is equal to 1 cm/s). Due to the fact that only 12 wireless sensor-velocity meter pairs are available, the wireless monitoring system is reconfigured during testing to achieve three different test configurations. Data was sampled at 100 points per second on each channel to provide good waveform definition. The wireless monitoring system consists of a distributed network of wireless sensors in direct communication with a high-performance data repository where data is stored and analyzed. During data collection, the wireless monitoring system experienced no data loss as a result of the highly robust communication protocol. The measurement of structural response to ambient levels of wind and traffic has proved to be an effective means of identifying the dynamic properties of a full-scale cable-stayed bridge. Furthermore, the performance of the FDD and SSI is evaluated based on those data.

From 2009 to 2011, the Laboratory for Intelligent Infrastructure and Transportation Technologies (LIITT) at Clarkson University carried out a series of tests on four bridges using the wireless sensor system (WSS). The WSS is based on Tmote Sky mote, which conducts strain- and vibration-based monitoring through a switch. Firstly, a large-scale network consisting of 40 channels of sensor measurements acquired through 20 remote wireless transceiver nodes operating with a sampling rate of 128 Hz was deployed on Wright Road Bridge in St. Lawrence County, NY [48, 122, 123, 132, 133]. Dynamic behavior of the structure from ambient and traffic loads was measured. Successful acquisition of high-rate, lossless data on the highway bridge validates the proprietary wireless network protocol within an actual service environment. Secondly, the STMicroelectronics LIS2L02AL low-noise capacitance-based accelerometers were distributed across the deck surface of the Nine Wells Rail Bridge to record the ambient vibration response due to traffic loading [134]. Then, operational modal analysis was performed based on the measurement data. Thirdly, the deployment of a large-scale, high-density, real-time wireless sensors network for the acquisition of local acceleration measurements across a highway bridge was executed [135]. The deployment consisted of 30 dual-axis accelerometers installed across the girders of the bridge. Output-only system identification of the structure from the experimental data is presented to provide estimates of natural frequencies, damping ratios, and operational mode shapes. Fourthly, a WSS, which is composed of 30 dual-axis LIS2L02AL MEMS accelerometers for a total of 60 channels and 30 strain transducers, was configured on the RT345 Bridge [4, 14, 136]. Modal and strain-based characteristics of the superstructure were acquired through measurements taken from those sensors over a 2-day period. That deployment demonstrates that the developed wireless sensor network has matured to the degree that modal analysis of large civil structures with a distributed network is a currently feasible and comparable alternative to cable-based

measurement approaches. But the single-hop star topology wireless communication makes it difficult to be extended to large-scale bridges.

The hardware and software developed by Spencer Jr. et al. [2, 47, 106] have been validated through full-scale deployment on the 2nd Jindo Bridge test-bed in Korea. The bridge is a cable-stayed bridge with a main span of 344 m. The Jindo Bridge test-bed is constructed as an international collaborative research effort between the USA (University of Illinois at Urbana-Champaign), South Korea (KAIST and Seoul National University), and Japan (University of Tokyo). The collaborative project resulted in the first long-term and the world's largest deployment of wireless sensors to monitor civil infrastructure. The 1st deployment on the bridge test-bed was carried out in 2009. The 70 sensor nodes were installed and divided into two subnetworks: one on the Jindo island side and the other on the Haenam side. The Jindo subnetwork consists of 33 nodes (22 deck nodes, 3 pylon nodes, and 8 cable nodes). The Haenam subnetwork consists of 37 nodes (27 deck nodes, 3 pylon nodes, and 7 cable nodes). One base station was used to collect data for each subnet using a gateway node. Each gateway node consists of an Imote2, interface board, and antenna. Each leaf node is composed of an Imote2, battery board, sensor board, antenna, and environmentally hardened enclosure. 3D-cell batteries were used to power most of the leaf nodes; 8 nodes of the 70 were self-powered using solar panels and rechargeable batteries. SHM-A boards were used to measure acceleration, temperature, humidity, and light for most of nodes; the SHM-W sensor board was used to measure the signal from the 3D ultrasonic anemometer. The 2nd deployment of advanced hardware and software was implemented on the test-bed bridge in 2010. Energy harvesting strategies were employed for all sensor nodes based on the satisfactory performance during 2009; additionally, a miniwind turbine was installed on one node to assess the potential for wind energy harvesting. The network size was also increased to a total of 669 channels on 113 sensor nodes and has been divided into four subnetworks, which is currently the world largest WSN for SHM. For better understanding of wind environment, two more 3D ultrasonic anemometers were installed with newly developed SHM-DAQ boards. Ten SHM-H boards were implemented as cluster-heads of DCS. The wireless sensor locations are displayed in Figure 23. The estimated modal properties based on collected acceleration data are consistent with those from the wired sensor system [137]. The measured wind data are accordant well with the records of the Korea Meteorological Administration. Both results verified that the installed WSN is reliable. Successful deployment of this WSN demonstrates the suitability of the Imote2 sensor platform, the proposed sensor board, and the developed software for full-scale, continuous, autonomous bridge health monitoring. At the same time, the tremendous potential of WSN technology for bridge health monitoring was demonstrated.

To illustrate the suitability of wireless sensors for short-term monitoring of highway bridges, Kim et al. [138] installed a wireless monitoring system upon the Grove Street Bridge to monitor structural responses during static and dynamic load testing. A heterogeneous array of wireless sensing transducers

was installed on the bridge including metal foil strain gages, accelerometers, and linear variable differential transducers. First, the acceleration response of the bridge was monitored during routine traffic loading. Modal parameters are calculated by the wireless sensors so that an analytical model of the bridge constructed in a standard commercial finite element package can be updated offline. Next, the bridge was closed to traffic and trucks of known weight were parked on the bridge to induce static deformations. The results of static load testing were used to validate the behavior of a novel jointless bridge deck constructed from a high-performance fiber reinforced cementitious composite (HPFRCC) material.

Kim et al. [139] installed a wireless sensor network on the 180 m long Yeondae Bridge (Korea) to measure the dynamic response of the bridge to controlled truck loading. To attain a high nodal density with a small number (20) of Narada wireless sensors, the wireless sensor network was installed three times with each installation concentrating sensors in one portion of the bridge. Intentional nodal overlapping of the three different sensor installations allows mode shapes from each installation to be stitched together into global mode shapes. The system is reconfigured with ease due to the fact that the sensors are wireless. During testing, the wireless monitoring system is found to be reliable (with no data loss encountered) and provided accurate response measurements. Using forced and free-vibration response data from the three installations, the modal properties of the bridge are accurately identified. The estimated modes are consistent with modes predicted by the finite element model.

To evaluate the potential of WSNs for use in bridge management, a network of seven sensor nodes was installed on the Ferriby Road Bridge by Hoult et al. [140, 141]. Three displacement transducer nodes were placed across cracks on the soffit of the bridge to measure the change in crack width. Three inclinometer sensor nodes were mounted on two of the elastomeric bearing pads to measure the change in inclination of the bearing pads while a final node monitored temperature in the box that contained the gateway. Due to the isolated location of the Ferriby Road Bridge, the gateway was powered by a 120 Ah-12 V battery, which was in turn charged by a 64 W solar panel attached to the side of the bridge. The test results indicate that the wireless sensor networks represent a useful tool that can be used to supplement, but not replace, visual inspection. It is discovered that commercial offerings of WSNs are still geared towards research prototypes and are currently not yet mature for deployment in practical scenarios.

Kurata et al. [142-144] developed a novel wireless structural monitoring system specifically tailored for large-scale civil infrastructure systems by architecturally combining dense wireless sensor networks with a suite of information technologies remotely accessible by the Internet. The monitoring-system architecture is divided into two major layers: a lower layer consisting of low-power WSNs installed to record the environmental loading and corresponding response of the structure and an upper Internet-enabled layer offering a complete cyberinfrastructure framework for the management and interrogation of bridge response data. A wireless cellular modem is used to communicate between

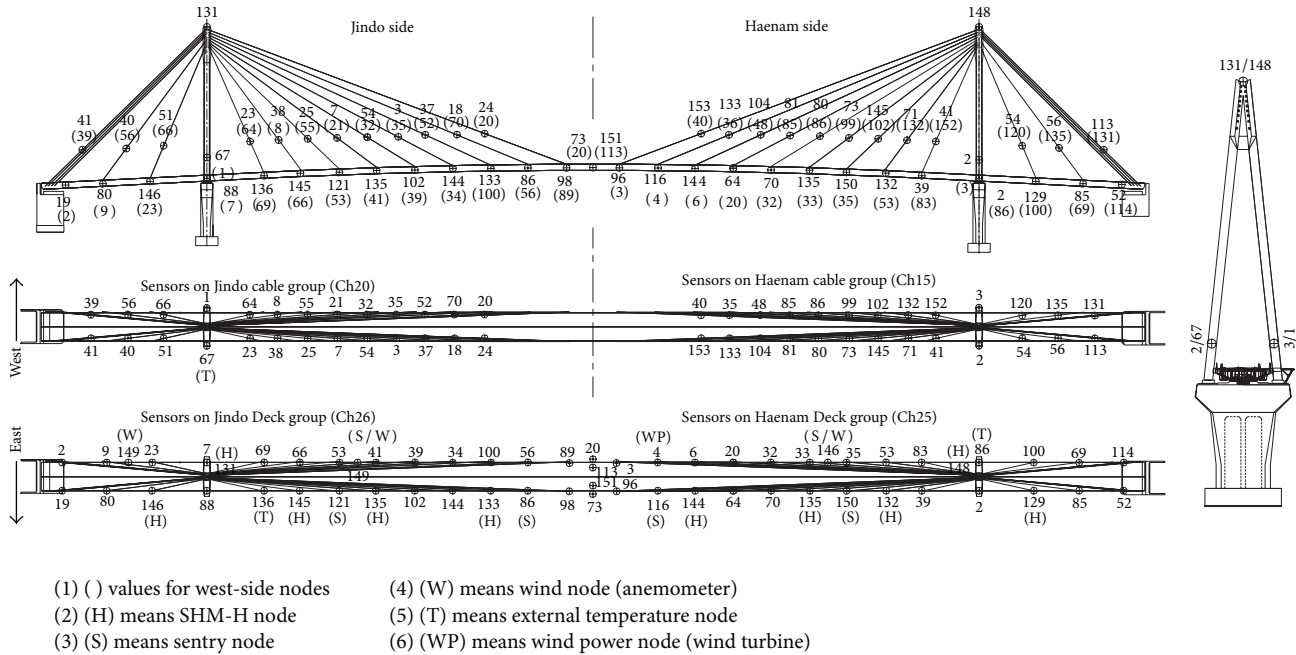


FIGURE 23: Wireless sensor locations [2].

the WSN servers and the upper levels of the monitoring-system architecture. To validate the long-term performance of the cyberenabled wireless structural monitoring system, the system was permanently installed on the New Carquinez Bridge (NCB). Prior to the installation of the permanent wireless system, the performance of the Narada wireless sensor nodes was evaluated on the NCB through a series of short-term deployment carried out in 2009 [145]. The permanent wireless monitoring system consists of 28 Narada nodes collecting data from 81 channels. Figure 24 presents the layout of the Narada WSN. To enhance longevity of the system, a power management strategy based on solar energy is adopted. The role of the wireless monitoring system is to drive a model-updating process to ensure that the existing finite element model of the bridge is suitable for the evaluation of the bridge immediately following a seismic event. Modal properties calculated from the data collected by the wireless monitoring system have been found to be in agreement with those extracted from the wired seismic monitoring system as well as those predicted by a high-fidelity finite element model of the bridge. The Internet-enabled wireless structural monitoring system has been proved to be scalable to a large number of nodes and has thus far proven stable and reliable over long-term use.

Kim and Lynch [146] installed a dense network of wireless sensors on the Yeondae Bridge and a multi-axle truck to identify vehicle-bridge interaction. Twenty Narada nodes, each with an integrated single-axis capacitive accelerometer (Silicon Designs SD2012), were installed permanently along the length of the bridge. The accelerometers were oriented in the vertical direction to record the vertical acceleration of the bridge. A single-axis ± 10 g accelerometer (Analog Devices ADXL105) was installed vertically at each axle and a ± 2 g

accelerometer (Crossbow CXL02) was installed vertically at the center-of-gravity of the truck body. To capture the rotation of the truck body, a MEMS gyroscope (Analog Devices ADXR5624) was also installed at the center-of-gravity of the truck body. In addition, a second ± 2 g accelerometer (Crossbow CXL02) was installed in the horizontal direction at the truck center-of-gravity to measure the inertial acceleration of the truck. Each sensor installed on the truck was interfaced to a Narada wireless sensor; this allowed the truck-based sensors to freely communicate with the permanent wireless monitoring system installed on the bridge. The truck was driven across the bridge at a constant velocity with bridge and vehicle responses measured. All wireless sensor nodes use a sample rate of 100 Hz. Time-synchronized vehicle-bridge response data is used within a two-stage system identification methodology. At first, the time-invariant properties of the bridge are estimated using the free-vibration response of the bridge. And then, the vehicle bouncing motion and the truck position history were combined with the bridge forced vibration response to estimate the time variant load matrix of the system model. Excellent system identification results were obtained with the model predicting closely the measured system response.

Chae et al. [9] deployed the ubiquitous sensor network (USN) based bridge SHM system including the u-Nodes, u-Gateways, application software, and integrating wireless network configurations on the Yongjong Grand Bridge. ZigBee (IEEE 802.15.4) is used for short-distance communications among sensors and code division multiple access (CDMA) for long-distance wireless communications with remote locations. Five types of sensors are integrated in the system. The force balanced type accelerometer was selected to carry out the measurement of stiffening truss vibration, and

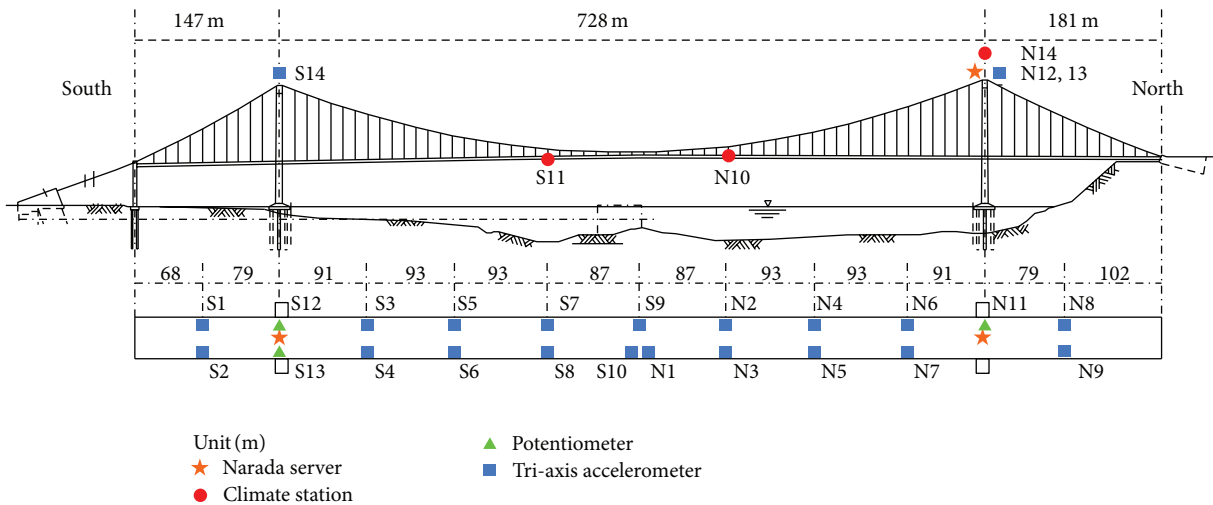


FIGURE 24: Long-term wireless monitoring system installed on the NCB: sensor types and locations [144].

the MEMS-type accelerometer was chosen to measure hanger cable tension. The electrical resistance sensor was applied onto the stiffening truss, a horizontal member, to measure strain. The propeller type wind gauge and the Thermistor type thermometer were also used. A stable power supply is secured by using a solar cell and rechargeable battery. But the solar cell is too large to be used extensively. A total of 45 u-Nodes have been installed in some of the major locations of the stiffening truss structure and in the suspension hanger cables to conduct bridge health monitoring. The USN spends about 50% of its entire system installation costs on cable installation work and data loggers. Overall, the transmission rates were found to be within a stable 90% range. Most data were lost in CDMA modems rather than in a u-Node to u-Gateway ZigBee communication. Although there are some data losses, the data were correctly analyzed by FFT and the tensions of hangers were calculated successfully. The test was operated successfully for about three months, which shows the wireless communication stability and sensor data reliability.

Hu et al. [13] deployed six wireless acceleration sensors and twenty-four strain sensors on the Zhengdian Highway Bridge in Wuhan, China. The Zhengdian Highway Bridge is a prestressed, concrete structure, simply supported slab bridge. The main bridge is 296.54 m long, which consists of 18 spans of 16 m each and two bridge abutments. The sampling rate is set as 100 Hz. The network topology uses multihops, with up to four hops in the WSN. The test takes about an hour and a half. Packet loss was observed during the tests. The final packet delivery ratio is nearly 99.96%. The mode shapes derived from six vertical acceleration measurements with the use of the multivariate ARX method correlate in terms of frequency and shape with finite element analysis. The feasibility of the proposed wireless monitoring system to capture data, transmit data via multihop wireless communication, and analyze monitoring data has been validated.

In addition, a number of other research teams have explored the performance validation and application of WSNs on real bridges. Lei et al. [147] installed a wireless structural

monitoring system on the Wuyuan Bridge in China to monitor the vertical and transverse responses of the bridge riders and arch ribs. Bischoff et al. [148] deployed a WSN, which consisted of 8 nodes supplied with resistance strain gages and the root node, on critical elements to catch the real loading during the passage of heavy freight trains so as to assess the performance of the Keräsjojk Railway Bridge in Sweden. Meyer et al. [149] equipped six cable stays of the Stork Bridge with wireless accelerometers to record the cable vibration, which shows that cable stay force monitoring based on WSNs is feasible. Ye et al. [150] deployed eleven Imote2 sensor nodes on a 30-meter-long railway overpass bridge to verify the decentralized approach for the modal test. Yun and Min [97] installed 46 sensors including 16 wireless accelerometers for vibration monitoring and 5 wireless impedance sensor nodes to investigate the long-term behaviors of the Han River Railroad Bridge. Spencer Jr. and Cho [2] implemented a WSN consisting of 22 leaf nodes in the 115-year-old steel truss Government Bridge to monitor the vibration during operation.

5. Conclusions

WSNs with dense wireless sensors provide a potential solution for long-term, scalable SHM of bridges by providing easier installation and efficient data management at a lower cost than that of traditional tethered monitoring systems. The researchers mentioned previously have dedicated their efforts to promote the WSNs-based bridge health monitoring system with the aim of replacing wired structural monitoring systems. Many available wireless sensor systems are already quite capable and can be expected to replace the traditional wired sensor systems for bridge monitoring. However, wireless sensing technology is still in its infancy; much work remains for bringing this promising technology to fulfill the requirement of complex bridges monitoring and evaluation. The technological improvements require

multidisciplinary researches among the engineers in civil, mechanical, electrical, and computer science engineering to facilitate the comprehensive developments for wireless SHM. Now, the main technological limitations are the power supply, data transmission reliability, and network bandwidth. Some of the existing problems and promising efforts for future research are discussed as follows.

(1) *Power Supply.* Each operation of the wireless sensors impacts their lifetime and consequently the lifetime of the entire WSN. Most WSN-based monitoring systems suffer from high power consumption and are generally equipped with a small power supply. Although extensive research work has been focused on energy harvest and power consumption optimization, the lifetime of a wireless sensor often falls below the levels needed for active sensing systems of bridge health monitoring. Power supply is still considered as one of the most important challenges that should be addressed for the WSNs to be more widely adopted in bridge health monitoring.

(2) *Design Criteria.* The hardware and software of both academic and commercial wireless monitoring systems are proposed personally, which makes extensive expertise required to master those systems. General researchers become incompetent when facing so many complicated operations, so the application of WSNs technology for monitoring bridges is severely limited. Therefore, establishing design specifications of hardware and friendly software development environment is significant so that researchers can focus on improving the performance of the WSNs-based bridge health monitoring system instead of studying elementary knowledge about WSNs.

(3) *Data Management.* WSNs technology enables the deployment of a dense array of sensors to monitor complicated bridges. A tremendous amount of data would be recorded every minute. But the employed low-power radio transceivers only provide a limited bandwidth. An inappropriate data management strategy may induce a large-scale WSN monitoring system collapse. On the other hand, data architecture is the key issue related to the algorithm of structural assessment which can be implemented in real time.

(4) *Optimal Sensor Placement.* Comparing with the needs of understanding bridge performance extensively, the sensor coverage is undoubtedly insufficient, even though the cheap wireless sensors make the installation of a lot of sensors on structures possible. Sensor placement optimization is an inevitable problem when deploying a sophisticated WSNs-based health monitoring system on a large-scale bridge. The limited radio transmission range makes the placement optimization of wireless sensors more complex than that of wired sensors.

(5) *Concept.* As a novel technology emerging about 15 years ago, the WSNs-based bridge health monitoring system is still an illusory thing in the concept of many administrators of bridges. Although a lot of demonstrations indicate that the reliability of the WSNs is comparable with the traditional wired sensor system, the invisible data transmission path

makes this technology not extensively accepted. More effort should be contributed to strengthening the convincingness of WSNs technology in the application of bridge health monitoring.

Acknowledgments

This research work was jointly supported by the Science Fund for Creative Research Groups of the NSFC (Grant no. 51121005), the National Natural Science Foundation of China (Grants nos. 51308186, 51222806, and 51278104), the Natural Science Foundation of Jiangsu Province of China (Grant no. BK20130850), and the Research Fund of the Key Laboratory of Concrete and Prestressed Concrete Structure of the Ministry of Education (Grant no. CPCSM2012-02).

References

- [1] K. Wardhana and F. C. Hadipriono, "Analysis of recent bridge failures in the United States," *Journal of Performance of Constructed Facilities*, vol. 17, no. 3, pp. 144–150, 2003.
- [2] B. F. Spencer Jr. and S. Cho, "Wireless smart sensor technology for monitoring civil infrastructure: technological developments and full-scale applications," in *Proceedings of the World Congress on Advances in Structural Engineering and Mechanics (ASEM '11)*, Seoul, Republic of Korea, 2011.
- [3] M. Bocca, E. I. Cosar, J. Salminen, and L. M. Eriksson, "A reconfigurable wireless sensor network for structural health monitoring," in *Proceedings of International Society for Structural Health Monitoring of Intelligent Infrastructures (ISHMII '09)*, Zurich, Switzerland, 2009.
- [4] M. V. Gangone, M. J. Whelan, and K. D. Janoyan, "Wireless monitoring of a multispan bridge superstructure for diagnostic load testing and system identification," *Computer-Aided Civil and Infrastructure Engineering*, vol. 26, no. 7, pp. 560–579, 2011.
- [5] B. M. Phares, D. D. Rolander, B. A. Graybeal, and G. A. Washer, "Studying the reliability of bridge inspection," *Public Roads*, vol. 64, no. 3, pp. 15–19, 2000.
- [6] J. M. Ko and Y. Q. Ni, "Technology developments in structural health monitoring of large-scale bridges," *Engineering Structures*, vol. 27, no. 12, pp. 1715–1725, 2005.
- [7] T. H. Yi and H. N. Li, "Methodology developments in sensor placement for health monitoring of civil infrastructures," *International Journal of Distributed Sensor Networks*, vol. 2012, Article ID 612726, 11 pages, 2012.
- [8] M. Çelebi, "Real-time seismic monitoring of the New Cape Girardeau Bridge and preliminary analyses of recorded data: an overview," *Earthquake Spectra*, vol. 22, no. 3, pp. 609–630, 2006.
- [9] M. J. Chae, H. S. Yoo, J. Y. Kim, and M. Y. Cho, "Development of a wireless sensor network system for suspension bridge health monitoring," *Automation in Construction*, vol. 21, no. 1, pp. 237–252, 2012.
- [10] J. P. Lynch, A. Partridge, K. H. Law, T. W. Kenny, A. S. Kiremidjian, and E. Carryer, "Design of piezoresistive MEMS-based accelerometer for integration with wireless sensing unit for structural monitoring," *Journal of Aerospace Engineering*, vol. 16, no. 3, pp. 108–114, 2003.
- [11] D. L. Mascarenas, M. D. Todd, G. Park, and C. R. Farrar, "Development of an impedance-based wireless sensor node for structural health monitoring," *Smart Materials and Structures*, vol. 16, no. 6, pp. 2137–2145, 2007.

- [12] S. Kim, S. Pakzad, D. Culler et al., "Health monitoring of civil infrastructures using wireless sensor networks," in *Proceedings of the 6th International Symposium on Information Processing in Sensor Networks (IPSN '07)*, pp. 254–263, April 2007.
- [13] X. Hu, B. Wang, and H. Ji, "A wireless sensor network-based structural health monitoring system for highway bridges," *Computer-Aided Civil and Infrastructure Engineering*, vol. 28, no. 3, pp. 193–209, 2013.
- [14] M. J. Whelan, M. V. Gangone, and K. D. Janoyan, "Highway bridge assessment using an adaptive real-time wireless sensor network," *IEEE Sensors Journal*, vol. 9, no. 11, pp. 1405–1413, 2009.
- [15] J. P. Lynch, K. H. Law, A. S. Kiremidjian, T. W. Kenny, E. Carryer, and A. Partridge, "The design of a wireless sensing unit for structural health monitoring," in *Proceedings of the 3rd International Workshop on Structural Health Monitoring*, pp. 12–14, 2001.
- [16] B. F. Spencer Jr., M. E. Ruiz-Sandoval, and N. Kurata, "Smart sensing technology: opportunities and challenges," *Structural Control and Health Monitoring*, vol. 11, no. 4, pp. 349–368, 2004.
- [17] N. Kurata, B. F. Spencer Jr., and M. Ruiz-Sandoval, "Risk monitoring of buildings with wireless sensor networks," *Structural Control and Health Monitoring*, vol. 12, no. 3-4, pp. 315–327, 2005.
- [18] E. G. Straser and A. S. Kiremidjian, "A modular, wireless damage monitoring system for structure," Report 128, John A. Blume Earthquake Center, CE Department, Stanford University, Stanford, Calif, USA, 1998.
- [19] J. P. Lynch and K. J. Loh, "A summary review of wireless sensors and sensor networks for structural health monitoring," *Shock and Vibration Digest*, vol. 38, no. 2, pp. 91–130, 2006.
- [20] M. Bocca, L. M. Eriksson, A. Mahmood, R. Jäntti, and J. Kullaa, "A synchronized wireless sensor network for experimental modal analysis in structural health monitoring," *Computer-Aided Civil and Infrastructure Engineering*, vol. 26, no. 7, pp. 483–499, 2011.
- [21] T. Nagayama, S. H. Sim, Y. Miyamori, and B. F. Spencer Jr., "Issues in structural health monitoring employing smart sensors," *Smart Structures and Systems*, vol. 3, no. 3, pp. 299–329, 2007.
- [22] V. Krishnamurthy, K. Fowler, and E. Sazonov, "The effect of time synchronization of wireless sensors on the modal analysis of structures," *Smart Materials and Structures*, vol. 17, no. 5, Article ID 055018, 2008.
- [23] S. Cho, C. B. Yun, J. P. Lynch, A. T. Zimmerman, B. F. Spencer Jr., and T. Nagayama, "Smart wireless sensor technology for structural health monitoring of civil structures," *International Journal of Steel Structures*, vol. 8, no. 4, pp. 267–275, 2008.
- [24] T. Nagayama, B. F. Spencer Jr., and J. A. Rice, "Structural health monitoring utilizing Intel's Imote2 wireless sensor platform," in *Proceedings of the Sensors and Smart Structures Technologies for Civil, Mechanical, and Aerospace Systems*, Yokohama, Japan, March 2007.
- [25] H. Jo, J. A. Rice, B. F. Spencer Jr., and T. Nagayama, "Development of high-sensitivity accelerometer board for structural health monitoring," in *Sensors and Smart Structures Technologies for Civil, Mechanical, and Aerospace Systems*, vol. 7647 of *Proceedings of SPIE*, March 2010.
- [26] M. Ruiz-Sandoval, T. Nagayama, and B. F. Spencer Jr., "Sensor development using Berkeley Mote platform," *Journal of Earthquake Engineering*, vol. 10, no. 2, pp. 289–309, 2006.
- [27] J. P. Lynch, K. H. Law, A. S. Kiremidjian, T. Kenny, and E. Carryer, "A wireless modular monitoring system for civil structures," in *Proceedings of the International Modal Analysis Conference (IMAC '02)*, February 2002.
- [28] J. P. Lynch, K. H. Law, A. S. Kiremidjian et al., "Validation of a wireless modular monitoring system for structures," in *SPIE's 9th Annual International Symposium on Smart Structures and Materials*, Proceedings of SPIE, pp. 124–135, March 2002.
- [29] J. P. Lynch, A. Sundararajan, K. H. Law et al., "Field validation of a wireless structural monitoring system on the Alamosa Canyon Bridge," in *Smart Structures and Materials. Smart Systems and Nondestructive Evaluation for Civil Infrastructures*, Proceedings of SPIE, pp. 267–278, March 2003.
- [30] J. P. Lynch, A. Sundararajan, and K. H. Law, "Design and performance validation of a wireless sensing unit for structural health monitoring applications," *Structural Engineering and Mechanics*, no. 173, pp. 393–408, 2004.
- [31] J. P. Lynch, G. Parra-Montesinos, B. A. Canbolat, and T. C. Hou, "Real-time damage prognosis of high-performance fiber reinforced cementitious composite structures," in *Proceeding of Advances in Structural Engineering and Mechanics (ASEM '04)*, Seoul, Republic of Korea, 2004.
- [32] Y. Wang, J. P. Lynch, and K. H. Law, "Wireless structural sensors using reliable communication protocols for data acquisition and interrogation," in *Proceedings of the 23rd International Modal Analysis Conference (IMAC '05)*, 2005.
- [33] Y. Wang, J. P. Lynch, and K. H. Law, "Design of a low-power wireless structural monitoring system for collaborative computational algorithms," in *Nondestructive Evaluation for Health Monitoring and Diagnostics*, Proceedings of SPIE, pp. 106–117, March 2005.
- [34] Y. Wang, J. P. Lynch, and K. H. Law, "A wireless structural health monitoring system with multithreaded sensing devices: design and validation," *Structure and Infrastructure Engineering*, vol. 3, no. 2, pp. 103–120, 2007.
- [35] R. A. Swartz, D. Jung, J. P. Lynch, Y. Wang, D. Shi, and M. Flynn, "Design of a wireless sensor for scalable distributed in-network computation in a structural health monitoring system," in *Proceedings of the 5th International Workshop on Structural Health Monitoring*, pp. 1570–1577, 2005.
- [36] A. T. Zimmerman, M. Shiraishi, R. A. Swartz, and J. P. Lynch, "Automated modal parameter estimation by parallel processing within wireless monitoring systems," *Journal of Infrastructure Systems*, vol. 14, no. 1, pp. 102–113, 2008.
- [37] A. T. Zimmerman and J. P. Lynch, "A parallel simulated annealing architecture for model updating in wireless sensor networks," *IEEE Sensors Journal*, vol. 9, no. 11, pp. 1503–1510, 2009.
- [38] G. Heo, W. Lee, G. Lee, and D. Lee, "Identifying dynamic characteristics of structures to estimate the performance of a smart wireless MA system," in *Smart Structures and Materials. Smart Sensor Technology and Measurement Systems*, Proceedings of SPIE, pp. 373–380, March 2005.
- [39] G. Heo, W. Lee, G. Lee, J.-R. Jeon, and C. Kim, "Field validation of a wireless sensor unit using self-anchored suspension bridge," in *Smart Structures and Materials*, Proceedings of SPIE, March 2006.
- [40] C. Park, Q. Xie, P. H. Chou, and M. Shinozuka, "DuraNode: wireless networked sensor for structural health monitoring," in *Proceedings of the 4th IEEE Conference on Sensors*, pp. 277–280, November 2005.

- [41] H. Joshi, B. Burlacu, M. Prabhu et al., "Wireless structural health monitoring system design, implementation and validation," Research Report 06-02, Constructed Facilities Lab (CFL), North Carolina State University (NCSU), Raleigh, NC, USA, 2006.
- [42] S. N. Pakzad, G. L. Fenves, S. Kim, and D. E. Culler, "Design and implementation of scalable wireless sensor network for structural monitoring," *Journal of Infrastructure Systems*, vol. 14, no. 1, pp. 89–101, 2008.
- [43] J.-H. Park, J.-T. Kim, D.-S. Hong, D. Mascarenas, and J. Peter Lynch, "Autonomous smart sensor nodes for global and local damage detection of prestressed concrete bridges based on accelerations and impedance measurements," *Smart Structures and Systems*, vol. 6, no. 5-6, pp. 711–730, 2010.
- [44] J. A. Rice and B. F. Spencer Jr., "Structural health monitoring sensor development for the Imote2 platform," in *Sensors and Smart Structures Technologies for Civil, Mechanical, and Aerospace Systems*, vol. 6932 of *Proceedings of SPIE*, March 2008.
- [45] N. Kurata, S. Saruwatari, and H. Morikawa, "Ubiquitous structural monitoring using wireless sensor networks," in *Proceedings of the International Symposium on Intelligent Signal Processing and Communications (ISPACS '06)*, pp. 99–102, December 2006.
- [46] H. Jo, S. H. Sim, T. Nagayama, and B. F. Spencer Jr., "Development and application of high-sensitivity wireless smart sensors for decentralized stochastic modal identification," *Journal of Engineering Mechanics*, vol. 138, no. 6, pp. 683–694, 2012.
- [47] H. Jo, S.-H. Sim, K. A. Mechitov et al., "Hybrid wireless smart sensor network for full-scale structural health monitoring of a cable-stayed bridge," in *Sensors and Smart Structures Technologies for Civil, Mechanical, and Aerospace Systems*, *Proceedings of SPIE*, March 2011.
- [48] M. J. Whelan and K. D. Janoyan, "Design of a robust, high-rate wireless sensor network for static and dynamic structural monitoring," *Journal of Intelligent Material Systems and Structures*, vol. 20, no. 7, pp. 849–863, 2009.
- [49] B. Chen and W. Liu, "Mobile agent computing paradigm for building a flexible structural health monitoring sensor network," *Computer-Aided Civil and Infrastructure Engineering*, vol. 25, no. 7, pp. 504–516, 2010.
- [50] M. L. Wang, H. Gu, G. M. Lloyd, and Y. Zhaok, "A multichannel wireless PVDF displacement sensor for structural monitoring," in *Proceedings of the International Workshop on Advanced Sensors, Structural Health Monitoring and Smart Structures*, Tokyo, Japan, 2003.
- [51] K. J. Loh, J. P. Lynch, and N. A. Kotov, "Passive wireless sensing using SWNT-based multifunctional thin film patches," *International Journal of Applied Electromagnetics and Mechanics*, vol. 28, no. 1-2, pp. 87–94, 2008.
- [52] T. Harms, B. Banks, S. S. Sarvestani, and F. Bastianini, "Design and testing of a low-power wireless sensor network for structural health monitoring of bridges," in *Sensors and Smart Structures Technologies for Civil, Mechanical, and Aerospace Systems*, *Proceedings of SPIE*, 72920U-8, March 2009.
- [53] C. O. Yang, M. Yen, and N. Weng, "The development of an on-line structural health monitoring system based on wireless sensor networks," *Electronic Journal of Structural Engineering*, 2010.
- [54] S. G. Taylor, K. M. Farinholt, G. Park, M. D. Todd, and C. R. Farrar, "Multi-scale wireless sensor node for health monitoring of civil infrastructure and mechanical systems," *Smart Structures and Systems*, vol. 6, no. 5-6, pp. 661–673, 2010.
- [55] J. Min, S. Park, C.-B. Yun, and B. Song, "Development of a low-cost multifunctional wireless impedance sensor node," *Smart Structures and Systems*, vol. 6, no. 5-6, pp. 689–709, 2010.
- [56] S. Zakikhani, A. Bagchi, and A. Hammad, "Design criteria of wireless sensors in structural health monitoring systems," in *Proceedings of the International Conference on Computing in Civil and Building Engineering*, vol. 30, p. 445, 2010.
- [57] J. P. Lynch, K. H. Law, A. S. Kiremidjian, T. W. Kenny, E. Carryer, and A. Partridge, "The design of a wireless sensing unit for structural health monitoring," in *Proceedings of the 3rd International Workshop on Structural Health Monitoring*, pp. 12–14, 2001.
- [58] Y. Gao, B. F. Spencer Jr., and M. Ruiz-Sandoval, "Distributed computing strategy for structural health monitoring," *Structural Control and Health Monitoring*, vol. 13, no. 1, pp. 488–507, 2006.
- [59] J. Lian, K. Naik, and G. B. Agnew, "Data capacity improvement of wireless sensor networks using non-uniform sensor distribution," *International Journal of Distributed Sensor Networks*, vol. 2, no. 2, pp. 121–145, 2006.
- [60] J. A. Rice, K. Mechitov, S.-H. Sim et al., "Flexible smart sensor framework for autonomous structural health monitoring," *Smart Structures and Systems*, vol. 6, no. 5-6, pp. 423–438, 2010.
- [61] J. P. Lynch, *Decentralization of wireless monitoring and control technologies for smart civil structures [Ph.D. thesis]*, Department of Civil and Environmental Engineering, Stanford University, Stanford, Calif, USA, 2002.
- [62] J. P. Lynch, A. Sundararajan, K. H. Law, A. S. Kiremidjian, T. Kenny, and E. Carryer, "Embedment of structural monitoring algorithms in a wireless sensing unit," *Structural Engineering and Mechanics*, vol. 15, no. 3, pp. 285–297, 2003.
- [63] J. P. Lynch, A. Sundararajan, K. H. Law, A. S. Kiremidjian, and E. Carryer, "Power-efficient data management for a wireless structural monitoring system," in *Proceedings of the 4th International Workshop on Structural Health Monitoring*, vol. 1, pp. 15–17, Stanford University, November 2003.
- [64] J. P. Lynch, A. Sundararajan, K. H. Law, A. S. Kiremidjian, and E. Carryer, "Embedding damage detection algorithms in a wireless sensing unit for operational power efficiency," *Smart Materials and Structures*, vol. 13, no. 4, pp. 800–810, 2004.
- [65] A. S. Kiremidjian, G. Kiremidjian, and P. Sarabandi, "A wireless structural monitoring system with embedded damage algorithms and decision support system," *Structure and Infrastructure Engineering*, vol. 7, no. 12, pp. 881–894, 2011.
- [66] J. Caffrey, R. Govindan, and E. Johnson, "Networked sensing for structural health monitoring," in *Proceedings of the 4th International Workshop on Structural Control*, pp. 57–66, Columbia University, 2004.
- [67] Y. Hashimoto, A. Masuda, and A. Sone, "Prototype of sensor network with embedded local data processing," in *Smart Structures and Materials 2005. Sensors and Smart Structures Technologies for Civil, Mechanical, and Aerospace Systems*, *Proceedings of SPIE*, pp. 245–252, March 2005.
- [68] K. Chintalapudi, E. A. Johnson, and R. Govindan, "Structural damage detection using wireless sensor-actuator networks," in *Proceedings of the IEEE International Symposium on, Mediterranean Conference on Control and Automation*, pp. 322–327, June 2005.
- [69] S. Cho, J. P. Lynch, and C.-B. Yun, "Development of a low-cost automated tension estimation system for cable-stayed bridges," in *Proceedings of the ASME Conference on Smart Materials, Adaptive Structures and Intelligent Systems (SMASIS '08)*, pp. 279–287, October 2008.

- [70] S. Cho, J. P. Lynch, J.-J. Lee, and C.-B. Yun, "Development of an automated wireless tension force estimation system for cable-stayed bridges," *Journal of Intelligent Material Systems and Structures*, vol. 21, no. 3, pp. 361–376, 2010.
- [71] H. Zui, T. Shinke, and Y. Namita, "Practical formulas for estimation of cable tension by vibration method," *Journal of Structural Engineering*, vol. 122, no. 6, pp. 651–656, 1996.
- [72] N. Castaneda, F. Sun, S. Dyke, C. Lu, A. Hope, and T. Nagayama, "Implementation of a correlation-based decentralized damage detection method using wireless sensors," in *Proceedings of the ASEM Conference*, 2008.
- [73] G. Hackmann, F. Sun, N. Castaneda, C. Lu, and S. Dyke, "A holistic approach to decentralized structural damage localization using wireless sensor networks," in *Proceedings of the Real-Time Systems Symposium (RTSS '08)*, pp. 35–46, December 2008.
- [74] S. H. Sim and B. F. Spencer Jr., "Decentralized strategies for monitoring structures using wireless smart sensor networks," *NSEL Report Series*, no. 19, 2009.
- [75] S. H. Sim, J. Li, S. Cho et al., "Automated cable tension monitoring using smart sensors," in *Proceedings of the World Congress on Advances in Structural Engineering and Mechanics (ASEM '11)*, 2011.
- [76] T. Shimada, "Estimating method of cable tension from natural frequency of high mode," *Proceedings of the Japan Society of Civil Engineers*, no. 501, pp. 163–171, 1994.
- [77] T.-Y. Hsu, S.-K. Huang, K.-C. Lu, C.-H. Loh, Y. Wang, and J. P. Lynch, "On-line structural damage localization and quantification using wireless sensors," *Smart Materials and Structures*, vol. 20, no. 10, Article ID 105025, 2011.
- [78] J. Kim and J. P. Lynch, "Autonomous decentralized system identification by Markov parameter estimation using distributed smart wireless sensor networks," *Journal of Engineering Mechanics*, vol. 138, no. 5, pp. 478–490, 2011.
- [79] G. J. Yun, S.-G. Lee, J. Carletta, and T. Nagayama, "Decentralized damage identification using wavelet signal analysis embedded on wireless smart sensors," *Engineering Structures*, vol. 33, no. 7, pp. 2162–2172, 2011.
- [80] J. Zhang, "On-board computing for structural health monitoring with smart wireless sensors by modal identification using Hilbert-Huang transform," *Mathematical Problems in Engineering*, vol. 2013, Article ID 509129, 9 pages, 2013.
- [81] S.-H. Sim, J. F. Carbonell-Mrquez, B. F. Spencer Jr., and H. Jo, "Decentralized random decrement technique for efficient data aggregation and system identification in wireless smart sensor networks," *Probabilistic Engineering Mechanics*, vol. 26, no. 1, pp. 81–91, 2011.
- [82] Y. Gao and B. F. Spencer Jr., "Online damage diagnosis for civil infrastructure employing a flexibility-based approach," *Smart Materials and Structures*, vol. 15, no. 1, pp. 9–19, 2006.
- [83] D. Bernal, "Load vectors for damage localization," *Journal of Engineering Mechanics*, vol. 128, no. 1, pp. 7–14, 2002.
- [84] Y. Gao and B. F. Spencer Jr., "Structural health monitoring strategies for smart sensor networks," *University of Illinois at Urbana-Champaign*, 2005.
- [85] T. Nagayama and B. F. Spencer Jr., "Structural health monitoring using smart sensors," Newmark Structural Engineering Laboratory (NSEL) Report Series 1, University of Illinois at Urbana-Champaign, Urbana, Ill, USA, 2007.
- [86] S. H. Sim, B. F. Spencer Jr., M. Zhang, and H. Xie, "Automated decentralized modal analysis using smart sensors," *Structural Control and Health Monitoring*, vol. 17, no. 8, pp. 872–894, 2010.
- [87] D. Bernal, "Flexibility-based damage localization from stochastic realization results," *Journal of Engineering Mechanics*, vol. 132, no. 6, pp. 651–658, 2006.
- [88] G. Yan, W. Guo, S. J. Dyke, G. Hackmann, and C. Lu, "Experimental validation of a multi-level damage localization technique with distributed computation," *Smart Structures and Systems*, vol. 6, no. 5-6, pp. 561–578, 2010.
- [89] G. Hackmann, W. Guo, G. Yan, C. Lu, and S. Dyke, "Cyber-physical codesign of distributed structural health monitoring with wireless sensor networks," in *Proceedings of the 1st ACM/IEEE International Conference on Cyber-Physical Systems (ICCCPS '10)*, pp. 119–128, April 2010.
- [90] J.-T. Kim, J.-H. Park, D.-S. Hong, and W.-S. Park, "Hybrid health monitoring of prestressed concrete girder bridges by sequential vibration-impedance approaches," *Engineering Structures*, vol. 32, no. 1, pp. 115–128, 2010.
- [91] A. T. Zimmerman and J. P. Lynch, "Market-based frequency domain decomposition for automated mode shape estimation in wireless sensor networks," *Structural Control and Health Monitoring*, vol. 17, no. 7, pp. 808–824, 2010.
- [92] E. Sazonov, K. Janoyan, and R. Jha, "Wireless intelligent sensor network for autonomous structural health monitoring," in *Smart Structures and Materials. Smart Sensor Technology and Measurement Systems*, Proceedings of SPIE, pp. 305–314, usa, March 2004.
- [93] J. H. Galbreath, C. P. Townsend, and S. W. Mundell, "Civil structure strain monitoring with power-efficient high-speed wireless sensor networks," in *Proceedings International Workshop for Structural Health Monitoring*, vol. 3, Stanford, Calif, USA, 2003.
- [94] A. T. Zimmerman, J. P. Lynch, and F. T. Ferrese, "Market-based resource allocation for distributed data processing in wireless sensor networks," *ACM Transactions on Embedded Computing Systems*, vol. 12, no. 3, article 84, 2013.
- [95] T. S. Fu, A. Ghosh, E. A. Johnson, and B. Krishnamachari, "Energy-efficient deployment strategies in structural health monitoring using wireless sensor networks," *Structural Control and Health Monitoring*, vol. 20, pp. 971–986, 2013.
- [96] H. A. Sodano, D. J. Inman, and G. Park, "A review of power harvesting from vibration using piezoelectric materials," *Shock and Vibration Digest*, vol. 36, no. 3, pp. 197–205, 2004.
- [97] C. B. Yun and J. Min, "Smart sensing, monitoring, and damage detection for civil infrastructures," *KSCE Journal of Civil Engineering*, vol. 15, no. 1, pp. 1–14, 2011.
- [98] D. D. L. Mascarenas, E. Flynn, K. Lin et al., "Demonstration of a roving-host wireless sensor network for rapid assessment monitoring of structural health," in *Smart Sensor Phenomena, Technology, Networks, and Systems*, Proceedings of SPIE, 69330K-1, March 2008.
- [99] H.-J. Park, H. Sohn, C.-B. Yun, J. Chung, and I. I.-B. Kwon, "A wireless guided wave excitation technique based on laser and optoelectronics," *Smart Structures and Systems*, vol. 6, no. 5-6, pp. 749–765, 2010.
- [100] P. Glynne-Jones and N. M. White, "Self-powered systems: a review of energy sources," *Sensor Review*, vol. 21, no. 2, pp. 91–97, 2001.
- [101] S. Roundy, P. K. Wright, and J. M. Rabaey, *Energy Scavenging for Wireless Sensor Networks: With Special Focus on Vibrations*, Springer, 2004.
- [102] M. A. Qidwai, J. P. Thomas, J. C. Kellogg, and J. Baucom, "Energy harvesting concepts for small electric unmanned systems," in *Smart Structures and Materials. Active Materials:*

- Behaviour and Mechanics*, Proceedings of SPIE, pp. 84–85, March 2004.
- [103] L. Mateu and F. Moll, “Review of energy harvesting techniques and applications for microelectronics,” in *VLSI Circuits and Systems II*, vol. 5837 of *Proceedings of SPIE*, pp. 359–373, May 2005.
- [104] J. A. Paradiso and T. Starner, “Energy scavenging for mobile and wireless electronics,” *IEEE Pervasive Computing*, vol. 4, no. 1, pp. 18–27, 2005.
- [105] V. Raghunathan, A. Kansal, J. Hsu, J. Friedman, and M. Srivastava, “Design considerations for solar energy harvesting wireless embedded systems,” in *Proceedings of the 4th International Symposium on Information Processing in Sensor Networks (IPSN '05)*, vol. 64, pp. 457–462, IEEE Press, April 2005.
- [106] S. Jang, H. Jo, S. Cho et al., “Structural health monitoring of a cable-stayed bridge using smart sensor technology: deployment and evaluation,” *Smart Structures and Systems*, vol. 6, no. 5-6, pp. 439–459, 2010.
- [107] R. Anant Kishore and S. Priya, “Design and experimental verification of a high efficiency small wind energy portable turbine (SWEPT),” *Journal of Wind Engineering and Industrial Aerodynamics*, vol. 118, pp. 12–19, 2013.
- [108] W. K. G. Seah, A. E. Zhi, and H.-P. Tan, “Wireless sensor networks powered by ambient energy harvesting (WSN-HEAP)—survey and challenges,” in *Proceedings of the 1st International IEEE Conference on Wireless Communication, Vehicular Technology, Information Theory and Aerospace and Electronic Systems Technology, Wireless (VITAE '09)*, pp. 1–5, May 2009.
- [109] N. E. Dutoit, B. L. Wardle, and S. G. Kim, “Design considerations for MEMS-scale piezoelectric mechanical vibration energy harvesters,” *Integrated Ferroelectrics*, vol. 71, no. 1, pp. 121–160, 2005.
- [110] G. Park, T. Rosing, M. D. Todd, C. R. Farrar, and W. Hodgkiss, “Energy harvesting for structural health monitoring sensor networks,” *Journal of Infrastructure Systems*, vol. 14, no. 1, pp. 64–79, 2008.
- [111] J. M. Gilbert and F. Balouchi, “Comparison of energy harvesting systems for wireless sensor networks,” *International Journal of Automation and Computing*, vol. 5, no. 4, pp. 334–347, 2008.
- [112] A. Khaligh, P. Zeng, and C. Zheng, “Kinetic energy harvesting using piezoelectric and electromagnetic technologies: state of the art,” *IEEE Transactions on Industrial Electronics*, vol. 57, no. 3, pp. 850–860, 2010.
- [113] D. G. Kim, S. N. Yun, Y. B. Ham, and J. H. Park, “Energy harvesting strategy using piezoelectric element driven by vibration method,” *Wireless Sensor Network*, vol. 2, no. 2, pp. 100–107, 2010.
- [114] F. Sivrikaya and B. Yener, “Time synchronization in sensor networks: a survey,” *IEEE Network*, vol. 18, no. 4, pp. 45–50, 2004.
- [115] I.-K. Rhee, J. Lee, J. Kim, E. Serpedin, and Y.-C. Wu, “Clock synchronization in wireless sensor networks: an overview,” *Sensors*, vol. 9, no. 1, pp. 56–85, 2009.
- [116] S. M. Lasassmeh and J. M. Conrad, “Time synchronization in wireless sensor networks: a survey,” in *Proceedings of the IEEE SoutheastCon Conference: Energizing our Future (SoutheastCon '10)*, pp. 242–245, March 2010.
- [117] P. Ranganathan and K. Nygard, “Time synchronization in wireless sensor networks: a survey,” *International Journal of UbiComp*, vol. 1, no. 2, pp. 92–102, 2010.
- [118] Y. Yang, *Time Synchronization in Wireless Sensor Networks: A Survey*, Mid Sweden University, 2012.
- [119] M. Maróti, B. Kusy, G. Simon, and Á. Lédeczi, “The flooding time synchronization protocol,” in *Proceedings of the 2nd International Conference on Embedded Networked Sensor Systems (SenSys '04)*, pp. 39–49, ACM, November 2004.
- [120] S. Ganeriwal, R. Kumar, and M. B. Srivastava, “Timing-sync protocol for sensor networks,” in *Proceedings of the 1st International Conference on Embedded Networked Sensor Systems (SenSys '03)*, pp. 138–149, ACM, November 2003.
- [121] M. J. Whelan, M. V. Gangone, K. D. Janoyan, and R. Jha, “Wireless vibration monitoring for damage detection of highway bridges,” in *Smart Sensor Phenomena, Technology, Networks, and Systems*, Proceedings of SPIE, 69330J-1, March 2008.
- [122] M. J. Whelan, M. P. Fuchs, M. V. Gangone, and K. D. Janoyan, “Development of a wireless bridge monitoring system for condition assessment using hybrid techniques,” in *Sensor Systems and Networks: Phenomena, Technology, and Applications for NDE and Health Monitoring*, vol. 6530 of *Proceedings of SPIE*, 65300H-1, March 2007.
- [123] M. J. Whelan, M. V. Gangone, K. D. Janoyan, K. Cross, and R. Jha, “Reliable high-rate bridge monitoring using dense wireless sensor arrays,” in *Proceedings of the International Workshop on Structural Health Monitoring*, 2007.
- [124] S. Aoki, Y. Fujino, and M. Abe, “Intelligent bridge maintenance system using MEMS and network technology,” in *Smart Structures and Materials 2003: Smart Systems and Nondestructive Evaluation for Civil Infrastructures*, Proceedings of SPIE, pp. 37–42, Virginia Polytechnic Institute and State University, San Diego, Calif, USA, March 2003.
- [125] J. Binns, “Technology: bridge sensor system delivers results quickly,” *Civil Engineering-ASCE*, vol. 74, no. 9, pp. 30–31, 2004.
- [126] H.-C. Chung, T. Enotomo, K. Loh, and M. Shinozuka, “Real-time visualization of bridge structural response through wireless MEMS sensors,” in *Testing, Reliability, and Application of Micro and Nano-Material Systems II*, Proceedings of SPIE, pp. 239–246, March 2004.
- [127] J. P. Lynch, Y. Wang, K. H. Law, J. H. Yi, C. G. Lee, and C. B. Yun, “Validation of a large-scale wireless structural monitoring system on the Geumdang Bridge,” in *Proceedings of 9th International Conference on Structural Safety and Reliability*, pp. 19–23, 2005.
- [128] J. P. Lynch, Y. Wang, K. J. Loh, J.-H. Yi, and C.-B. Yun, “Performance monitoring of the Geumdang Bridge using a dense network of high-resolution wireless sensors,” *Smart Materials and Structures*, vol. 15, no. 6, article 008, pp. 1561–1575, 2006.
- [129] S. N. Pakzad, “Development and deployment of large scale wireless sensor network on a long-span bridge,” *Smart Structures and Systems*, vol. 6, no. 5-6, pp. 525–543, 2010.
- [130] S. N. Pakzad and G. L. Fenves, “Statistical analysis of vibration modes of a suspension bridge using spatially dense wireless sensor network,” *Journal of Structural Engineering*, vol. 135, no. 7, pp. 863–872, 2009.
- [131] J.-H. Weng, C.-H. Loh, J. P. Lynch, K.-C. Lu, P.-Y. Lin, and Y. Wang, “Output-only modal identification of a cable-stayed bridge using wireless monitoring systems,” *Engineering Structures*, vol. 30, no. 7, pp. 1820–1830, 2008.
- [132] M. J. Whelan, M. V. Gangone, K. D. Janoyan, and R. Jha, “Real-time wireless vibration monitoring for operational modal analysis of an integral abutment highway bridge,” *Engineering Structures*, vol. 31, no. 10, pp. 2224–2235, 2009.
- [133] M. V. Gangone, M. J. Whelan, K. D. Janoyan, and R. Jha, “Field deployment of a dense wireless sensor network for condition

- assessment of a bridge superstructure,” in *Smart Sensor Phenomena, Technology, Networks, and Systems*, Proceedings of SPIE, 69330L-9, March 2008.
- [134] M. J. Whelan, M. V. Gangone, K. D. Janoyan, N. A. Hoult, C. R. Middleton, and K. Soga, “Wireless operational modal analysis of a multi-span prestressed concrete bridge for structural identification,” *Smart Structures and Systems*, vol. 6, no. 5-6, pp. 579–593, 2010.
- [135] M. J. Whelan, M. V. Gangone, K. D. Janoyan, and R. Jha, “Operational modal analysis of a multi-span skew bridge using real-time wireless sensor networks,” *JVC/Journal of Vibration and Control*, vol. 17, no. 13, pp. 1952–1963, 2011.
- [136] M. J. Whelan and K. D. Janoyan, “In-service diagnostics of a highway bridge from a progressive damage case study,” *Journal of Bridge Engineering*, vol. 15, no. 5, pp. 597–607, 2010.
- [137] S. Cho, H. Jo, S. Jang et al., “Structural health monitoring of a cable-stayed bridge using wireless smart sensor technology: data analyses,” *Smart Structures and Systems*, vol. 6, no. 5-6, pp. 461–480, 2010.
- [138] J. Kim, R. A. Swartz, J. P. Lynch, J.-J. Lee, and C.-G. Lee, “Rapid-to-deploy reconfigurable wireless structural monitoring systems using extended-range wireless sensors,” *Smart Structures and Systems*, vol. 6, no. 5-6, pp. 505–524, 2010.
- [139] J. Kim, J. P. Lynch, D. Zonta, J.-J. Lee, and C.-B. Yun, “Reconfigurable wireless monitoring systems for bridges: validation on the Yeondae Bridge,” in *Sensors and Smart Structures Technologies for Civil, Mechanical, and Aerospace Systems*, Proceedings of SPIE, March 2009.
- [140] N. A. Hoult, P. R. A. Fidler, P. G. Hill, and C. R. Middleton, “Long-term wireless structural health monitoring of the ferryby road bridge,” *Journal of Bridge Engineering*, vol. 15, no. 2, pp. 153–159, 2010.
- [141] F. Stajano, N. Hoult, I. Wassell, P. Bennett, C. Middleton, and K. Soga, “Smart bridges, smart tunnels: transforming wireless sensor networks from research prototypes into robust engineering infrastructure,” *Ad Hoc Networks*, vol. 8, no. 8, pp. 872–888, 2010.
- [142] M. Kurata, J. P. Lynch, G. W. Van Der Linden, P. Hipley, and L.-H. Sheng, “Application of an automated wireless structural monitoring system for long-span suspension bridges,” in *Proceedings of the AIP Conference*, vol. 1335, pp. 33–40, July 2010.
- [143] M. Kurata, J. Kim, Y. Zhang et al., “Long-term assessment of an autonomous wireless structural health monitoring system at the new Carquinez Suspension Bridge,” in *Smart Structures and Materials Nondestructive Evaluation and Health Monitoring*, Proceedings of SPIE, 798312-9, March 2011.
- [144] M. Kurata, J. Kim, J. P. Lynch et al., “Internet-enabled wireless structural monitoring systems: development and permanent deployment at the new Carquinez suspension bridge,” *Journal of Structural Engineering*, vol. 39, no. 10, pp. 1688–1702, 2013.
- [145] M. Kurata, J. P. Lynch, G. W. van der Linden, V. Jacob, and P. Hipley, “Preliminary study of a wireless structural monitoring system for the new Carquinez suspension bridge,” in *Proceedings of the 5th World Conference on Structural Control and Monitoring*, 2010.
- [146] J. Kim and J. P. Lynch, “Experimental analysis of vehicle-bridge interaction using a wireless monitoring system and a two-stage system identification technique,” *Mechanical Systems and Signal Processing*, vol. 28, pp. 3–19, 2012.
- [147] Y. Lei, W. A. Shen, Y. Song, and J. P. Lynch, “Application of wireless monitoring system for the ambient vibration study of the Wuyuan steel arch bridge,” in *Proceedings of the World Forum on Smart Materials and Smart Structures Technology (SMSST ’07)*, pp. 149–150, Nanjing, China, May 2007.
- [148] R. Bischoff, J. Meyer, O. Enochsso, G. Feltrin, and L. Elfgren, “Event-based strain monitoring on a railway bridge with a wireless sensor network,” in *Proceedings of 4th International Conference on Structural Health Monitoring of Intelligent Infrastructure*, 2009.
- [149] J. Meyer, R. Bischoff, G. Feltrin, and M. Motavalli, “Wireless sensor networks for long-term structural health monitoring,” *Smart Structures and Systems*, vol. 6, no. 3, pp. 263–275, 2010.
- [150] X. Ye, T. Zhu, Q. Yan, and W. Wang, “Experimental verification of decentralized approach for modal identification based on wireless smart sensor network,” *Advanced Materials Research*, vol. 291–294, pp. 3–11, 2011.

Research Article

Safety Monitoring Index of High Concrete Gravity Dam Based on Failure Mechanism of Instability

Shaowei Wang,^{1,2,3} Chongshi Gu,^{1,2,3} and Tengfei Bao^{1,2,3}

¹ State Key Laboratory of Hydrology-Water Resources and Hydraulic Engineering, Hohai University, Nanjing 210098, China

² National Engineering Research Center of Water Resources Efficient Utilization and Engineering Safety, Hohai University, Nanjing 210098, China

³ College of Water-Conservancy and Hydropower, Hohai University, Nanjing 210098, China

Correspondence should be addressed to Shaowei Wang; shaowei2006nanjing@163.com

Received 8 September 2013; Revised 14 November 2013; Accepted 14 November 2013

Academic Editor: Xiao-Wei Ye

Copyright © 2013 Shaowei Wang et al. This is an open access article distributed under the Creative Commons Attribution License, which permits unrestricted use, distribution, and reproduction in any medium, provided the original work is properly cited.

Traditional methods of establishing dam safety monitoring index are mostly based on the observation data. According to the performance of dam-foundation system under the experienced loads, alarm values and extreme values are predicted for monitoring quantities. As for some dams, the potential most unfavorable loads may not yet have appeared, and dam bearing capacity may also decrease over time. Therefore, monitoring index determined by these methods can not reflect whether the dam will break or not. Based on the finite element method, to study the progressive instability failures of high concrete gravity dams under the failure modes of material strength degradation or uncertainty and extreme environmental loads during operation, methods of strength reduction and overloading are, respectively, used. Typical stages in the instability processes are identified by evaluation indicators of dam displacement, the connectivity of yield zones, and the yield volume ratio of dam concretes; then instability safety monitoring indexes are hierarchically determined according to these typical symptoms. At last, a case study is performed to give a more detailed introduction about the process of establishing safety monitoring index for high concrete gravity dams based on the failure mechanism of instability, and three grades of monitoring index related to different safety situations are established for this gravity dam.

1. Introduction

With the implementation of the National West to East Power Transmission Project, a large number of high dams are constructed or under construction in western China, in which concrete gravity dams are frequently adopted. The special mountain valleys in western China provide advantageous topographic conditions for the construction of high dams. However, dam safety becomes an important issue in the western area due to the complicated geological conditions as well as strong earthquakes of high frequency.

Structure safety monitoring is more frequently designed and implemented on civil engineering structures, such as dams, bridges, and high buildings. Meanwhile, analysis and back-analysis of the monitoring data are performed to evaluate the performance of these structures in time [1–5]. As for dams, dam failure is a progressive process, in which local

damages accumulate firstly, then lead to the deterioration of dam safety situation, and finally cause the dam failure. Therefore, to avoid dam failure, it is necessary to monitor the dams and their foundations and timely detect and analyze dam abnormal symptoms according to the observation data [6]. To ensure the normal operation, monitoring quantity should not exceed its allowable value, namely, the safety monitoring index. Hence, monitoring index is defined as the extreme value of each monitoring quantities before dam failure, which is used to evaluate and monitor dam safety [7]. Before the nineteen sixties, engineers had not realized the importance of observation data in dam safety management so that further analyses were ignored, let alone the establishment of monitoring index and temperature alarm, so dam safety monitoring system was not fully utilized. The failures of Malpasset arch dam and Vajont arch dam are both closely related to the absence of monitoring index [8]. The measured

displacement of Malpasset arch dam four months before its failure is significantly larger than the theoretical value, and the closer to dam bottom the more serious. Landslides on the left bank of Vajont arch dam began to creep slowly after the impoundment of upstream reservoir in 1960; the measured total displacement at the dam crest came up to 429 cm on October 7, 1963, and increased at an amazing speed of 48.3 mm/d during the last 12 days before failure. Ternperatwre alarms were not made for the occurrence of abnormalities so that both dam failures occurred without any engineering or nonengineering measures, so the absence of monitoring index for Malpasset arch dam and Vajont arch dam restricted the function of their safety monitoring systems. The situation that monitoring quantity exceeds its monitoring index probably means the abnormality of dam safety, so it is a key problem for managers to determine the monitoring index scientifically.

As for gravity dams, dam failures are mainly caused by the instability of dam-foundation systems, and the failure process depends on failure modes [9, 10]. Due to the complexity and specificity of each dam-foundation system, failure mechanisms and failure processes are different from dam to dam even if under the same failure mode. Therefore, it is necessary to simulate the real failure process and study the failure mechanism of instability under different failure modes, and the instability safety monitoring index of high concrete gravity dams should be determined according to the typical symptoms in the simulated failure process.

This paper firstly makes a brief summary about the current theories and methods of establishing dam safety monitoring indexes, in which disadvantages of each method are analyzed. Then, based on the traditional finite element structural analysis method, considering the most probable potential failure modes of material degradation or uncertainty and extreme external environmental loads during dam operation, methods of strength reduction and overloading are, respectively, used in this paper to study the progressive instability failure process of high concrete gravity dams. Typical stages in the instability processes are identified by evaluation indicators of dam displacement, the connectivity of yield zones, and the yield volume ratio of dam concretes; then instability safety monitoring index of high concrete gravity dams is determined according to these typical symptoms. At last, the proposed method for establishing instability safety monitoring index of high concrete gravity dams is studied in detail with a practical engineering.

2. Research Situation of Dam Safety Monitoring Index

Current dam safety monitoring items are deformation, stress, uplift pressure, seepage, crack opening, and so on. Monitoring indexes for dam stress, uplift pressure, and seepage are determined according to the hydraulic specifications, and these items are often established for local areas where the monitoring quantities should be controlled strictly. Especially for dam stress, the stress-controllable areas, such as dam heel and dam toe, are also the stress concentration areas in

the finite element method (FEM), so it is difficult to determine a reasonable stress control standard for these areas by FEM simulation [11]. As for the crack opening, it is not easy to determine the monitoring index by hydraulic specifications due to the complex opening mechanism of cracks. However, crack opening is the same as other monitoring items that only local damages may appear when its monitoring index is exceeded, and obvious abnormality will be directly reflected on dam deformation even if the rapid development of these local damages will result in the dam failure. Among all these monitoring items, deformation can directly reflect the global safety and the progressive failure process of dam-foundation system, so monitoring index for dam deformation is mostly determined as dam safety monitoring index [12].

The reasonable monitoring index can be used in analyzing and evaluating the situation of dam safety. However, due to the complexity of dam structures and the different material variation characteristics, comprehensive demonstration by different methods should be conducted to determine dam safety monitoring index. The mostly used methods for establishing the monitoring index at present are confidence interval method, typical low probability method, limit state method, and structural analysis method [13]. These methods are all without taking dam failure modes into consideration, let alone the instability mechanism and the progressive failure process under different failure modes. Therefore, advantages and disadvantages of these methods are analyzed before establishing the safety monitoring index of high concrete gravity dam based on failure mechanism of instability.

2.1. Confidence Interval Method. The basic principle of confidence interval method is the little probability event in statistics. According to the observation data, mathematical models (such as statistical model, hybrid model, and deterministic model) are established between monitoring effect quantities and environmental variables, and these models are used in calculating the deviations ($\hat{y} - y$) between the calculated values (\hat{y}) and the measured values y of monitoring effect quantities in the domain of dam experienced loads. If the deviations are within the confidence band of $\Delta = \pm \beta\sigma$ with the probability of $1 - \alpha$ (α is the significance level, which is frequently determined as 1%~5%) and no obvious tendency variations are reflected on the monitoring effect quantities, then this dam is considered to be in normal condition. Therefore, dam monitoring index is established as follows:

$$\delta_m = \hat{y} + \Delta = \hat{y} \pm \beta\sigma, \quad (1)$$

where β is related to the significance level α and σ is the residual standard deviation of the mathematical model.

The frequently used confidence interval method and typical low probability method are both based on the observation data. According to the performance of dam-foundation system under the experienced loads, bearing capacities under the potential loads are evaluated, and the corresponding alarm values and extreme values are predicted for different monitoring effect quantities. However, dam safety information contained in the observation data varies from dam to dam due to the different experienced loads, especially for

some dams which have never experienced the potential most unfavorable loads [14]. Meanwhile, the bearing capacity of dam-foundation system is changing during dam operation. Therefore, monitoring index based on the observation data is without considering the real condition of dam safety, instead of really reflecting whether the dam will break or not, it only can be used as the warning index to identify the abnormality of monitoring quantities [15–17].

Based on the aforementioned analyses, disadvantages of the confidence interval method are as follows. (1) If the observation data under the most unfavorable load combination are absent, monitoring index based on the confidence interval method may be unreliable; it is just the alarming value for the experienced loads rather than the extreme values for dam failure. (2) The residual standard deviation σ of the mathematical model varies with the selected observation data sequences for the same monitoring points, and the significance level is determined with arbitrariness more or less. (3) Instead of associating with dam structural state and failure mechanism, the confidence interval method is totally dependent on statistical theories, so it is lack of physical concepts.

2.2. Typical Low Probability Method. The typical low probability method is the same as the confidence interval method that totally depends on the observation data; differences are that the former qualitatively associates with the controlling conditions of strength and stability by selecting the monitoring effect quantity (y_{mi}) or its component in mathematical models under the unfavorable load conditions (namely, the typical monitoring effect quantities). According to different dam types and the actual situation, y_{mi} is selected annually, and a random sample is constituted as $y = \{y_{m1}, y_{m2}, \dots, y_{mn}\}$. Characteristics of the sample are described as follows:

$$\bar{y} = \frac{1}{n} \sum_{i=1}^n y_{mi}, \quad (2)$$

$$\sigma_E = \sqrt{\frac{1}{n-1} \left(\sum_{i=1}^n y_{mi}^2 - n\bar{y}^2 \right)}. \quad (3)$$

The probability density function $f(y)$ (such as normal distribution, logarithmic normal distribution, and extreme-I distribution) of sample y is determined by statistical tests. Assuming that y_m (y_{\max} or y_{\min}) is the extreme value of the monitoring quantity or its loading component, dam abnormality occurs if $y > y_{\max}$ or $y < y_{\min}$, and the probability is

$$P(y > y_{\max}) = P_a = \int_{y_{\max}}^{+\infty} f(y_{(\max)}) dy \quad \text{upper limit}, \quad (4)$$

or

$$P(y < y_{\min}) = P_a = \int_{-\infty}^{y_{\min}} f(y_{(\min)}) dy \quad \text{lower limit}. \quad (5)$$

Dam failure probability P_a is determined according to the importance of each dam. Then, dam safety monitoring

indexes are established according to P_a and $f(y)$ ($f(y_{(\max)})$ or $f(y_{(\min)})$).

Monitoring indexes established by the typical low probability method can be determined as the extreme value of the whole dam operation period just on the condition that the dam has experienced all kinds of unfavorable conditions (including unfavorable load combinations and material degradation). Another problem is that the controlling conditions of strength and stability are only qualitatively associated, while quantitative analysis is ignored.

2.3. Limit State Method. It is assumed by the limit state method that each dam failure modes are corresponding to a certain load combination, and dam failures are mainly boiled down to the failure modes of strength, stability, cracks, and so on. The limit state equation is defined as follows:

$$Z = R - S \geq 0, \quad (6)$$

where R is the structure resistance, which is defined as material tension strength, compression strength, and shear strength for the evaluation of strength, and the antisliding force and fracture toughness for the evaluation of stability and cracking, respectively; S is the load effect, which is determined as extreme stress, sliding force, and stress intensity factor for the evaluation of strength, stability, and cracking, respectively.

The limit state method shows a relatively clear physical concept by quantificationally contacting with dam strength and stability. However, dam strength is based on the point failure criterion, which cannot reflect the global safety of dam-foundation system; as for dam stability, sliding surface should be assumed in advance for the overall sliding failure criterion, and the stability cannot be directly reflected by the monitoring quantities.

2.4. Traditional Structural Analysis Method. As for the traditional structural analysis method, it, respectively, connects the three safety states (normal, abnormal, and dangerous) in dam safety monitoring standard with three structural behaviors (linear elastic, elastic-plastic, and failure), and three levels of safety monitoring index are established as follows.

Monitoring index of grade one:

$$\delta_1 = F\left(\sigma_t < [\sigma_t], \sigma_c < [\sigma_c], K = \frac{R_{m1}}{S} \geq [K]\right). \quad (7)$$

Monitoring index of grade two:

$$\delta_2 = F\left(\sigma_t < \sigma_{tR}, \sigma_c < \sigma_{cR}, S \leq R_{m2}, K_c \leq [K_c]\right). \quad (8)$$

Monitoring index of grade three:

$$\delta_3 = F\left(\sigma_t < \sigma_{tm}, \sigma_c < \sigma_{cm}, S \leq R_{m3}\right), \quad (9)$$

where σ_t and σ_c are tensile stress and compression stress of controlling areas; $[\sigma_t]$, σ_{tR} , and σ_{tm} are the allowable stress, yield strength, and ultimate strength of dam materials in the state of tension, respectively; $[\sigma_c]$, σ_{cR} , and σ_{cm} are the allowable stress, yield strength, and ultimate strength of

dam materials in the state of compression, respectively; S is the sliding force on the assumed sliding surface; K and $[K]$ are antisliding stability safety coefficients of the actual value and the allowable value, respectively; R_{m1} , R_{m2} , and R_{m3} are antisliding forces, which are, respectively, calculated by material shear strength of sliding surface in states of proportion limit, yield limit, and the peak value; K_c and $[K_c]$ are stress intensity factor and fracture toughness, respectively.

It is the same as the limit state method that the aforementioned three levels of dam safety monitoring index are all based on the point failure criterion and the prior assumed sliding surface. However, due to the huge volume of dam body as well as the complicated geological condition in foundation, structural behaviors for each parts of the dam-foundation system are not the same. If fixed proportions of dam material in stages of linear elastic, elastic-plastic, and failure are used to decide the global structural behavior of dams, it is not easy to determine the proportions reasonably for different complex constructions. Therefore, it is unreasonable to determine the dam safety monitoring index based on the mechanical property of materials, and the failure mechanism of instability under different failure modes cannot be reflected by the traditional structural analysis method.

3. Simulation of the Progressive Failure of High Concrete Gravity Dam

The key problem of high concrete gravity dams is the stability. Practical experiences show that instability failure of gravity dams on rock foundation may occur in two modes [18]: (1) strength degradation caused by seepage, or some original weak structural surfaces, so dam failure occurs once the resistance force along some weak surfaces cannot stand up to the sliding force. Here, the sliding surfaces are usually the foundation plane, construction interfaces in dam body, and some weak structural surfaces in bedrocks. (2) Under the action of extreme environmental loads, pull broken areas and crushed areas in bedrocks of dam heel and dam toe are, respectively, performed, and dam failure of instability occurs accompanied with toppling. The construction interfaces in dam body can be avoided if dam concretes are poured in good quality, namely, the probability of instability failure in dam body is mostly decreased. As for the sliding along weak structural surfaces in bedrocks or the toppling-sliding failure, it mainly depends on the geological conditions. The special mountain valleys provide advantageous topographic conditions for the construction of high dams. However, these dams are often threatened by the complicated geological conditions as well as strong earthquakes of high frequency. Therefore, monitoring index for these high gravity dams must be determined according to the failure mechanism of instability under different potential failure modes.

Due to the complexity of bedrocks, sliding modes of gravity dams cannot be identified directly. Different combinations of foundation weak surfaces result in different sliding modes. According to the spatial distribution of foundation weak surfaces, sliding modes of gravity dams can be summarized into four types, which are single inclined plane sliding, double

inclined plane sliding, crushed failure or bulged failure of the tail rock resistance block [19]. According to the dip angle of foundation weak surfaces, the aforementioned four modes can be summarized into two types, namely, the double or potential double inclined plane sliding and the translational sliding, which is shown in Figure 1. If the foundation weak structural surfaces, respectively, incline to the upstream and downstream directions and intersect at the bedrocks just below the foundation plane, the double inclined plane sliding occurs along the surface of ABC. As for the single inclined weak surface, such as the upstream direction inclined of B'C or the downstream direction inclined of AB'', failure areas of tension-shear or compression-shear may firstly appear at dam heel and dam toe, and the potential double inclined plane sliding occurs along the surface of AB'C and AB''C, respectively. The translational sliding occurs on the condition that the nearly horizontal gentle inclined weak structural surfaces are contained in bedrocks. Dam body and parts of bedrocks above the weak surface slide to the downstream integrally, and the tail rock resistance block tends to be crushed or bulged according to the buried depth of the weak surfaces and the mechanical property of upper rocks.

The stress field and displacement field of dam-foundation system can be calculated by FEM, and it is more reasonable to automatically search the sliding surface according to dam deformation. On the other hand, methods of strength reduction and overloading can be, respectively, used to simulate material degradation or uncertainty and extreme external environmental loads during the service period. Hence, the FEM simulation is frequently used in studying the global safety of gravity dams [19, 20] and arch dams [21–23].

3.1. Overloading Method. To study the overloading capacity of gravity dam-foundation systems, overloading method is conducted under the assumption of unchangeable material properties of dam concretes and bedrocks. Under the normal load combination, external loads are increased until the dam failure by elevating the upstream water level or increasing the upstream reservoir water density, in which water density overloading method is commonly used by engineers. With the enlargement of upstream reservoir water density to K_p times (for normal load condition, the overloading parameter $K_p = 1$), stress field and displacement field are calculated by FEM, and the variation of dam safety is identified by the development of displacement and stress of typical points as well as the connectivity of plasticity yield zones of dam-foundation system. Hence, the overloading method can better simulate dam failures under the potential abnormal environmental loads, which are caused by overtopping, super earthquake, and the landslide of reservoir bank.

Taking a gravity dam section of unit width as an example, the dam height is 160 m and the widths at dam crest and bottom are 16 m and 125 m, respectively. The unit width dam section is designed with a vertical upstream dam surface and the downstream surface at a gradient of 1 : 0.75. According to the current Chinese specifications for seismic design of hydraulic structures DL5073-2000 [24], as for the traditional pseudo-static method, earthquake hydrodynamic pressure and inertial force are, respectively, calculated and

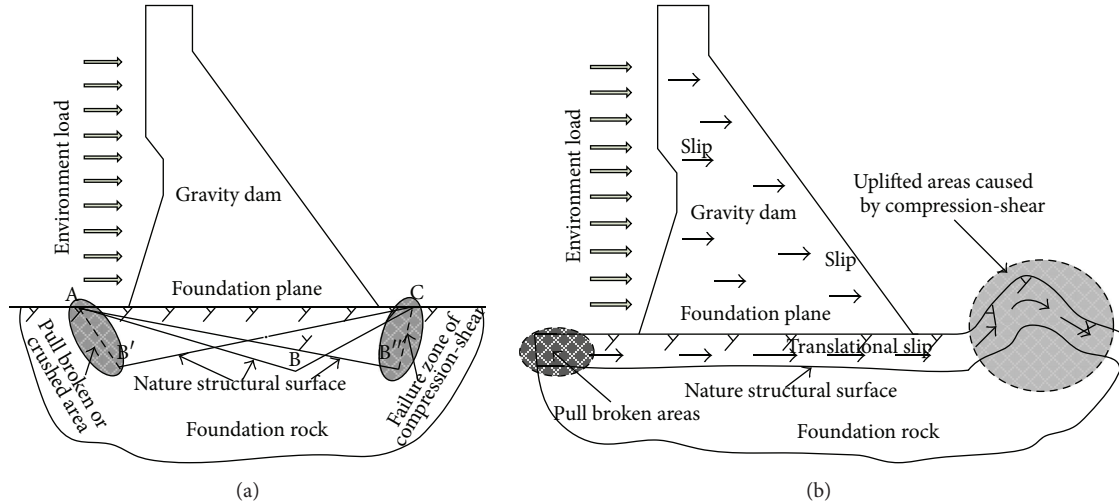


FIGURE 1: Sliding modes of gravity dam: (a) double or potential double inclined plane sliding; (b) translational sliding.

TABLE 1: The equivalent water density overloading parameter of earthquakes.

Peak acceleration of design earthquakes	0.1 g	0.2 g	0.4 g
Static water pressure of upstream (10^7 N)		11.6	
Earthquake hydrodynamic pressure (10^7 N)	0.38	0.76	1.51
Earthquake inertial force (10^7 N)	1.13	2.26	4.51
The total dynamic force/static water pressure	0.13	0.26	0.52
Overloading parameter of water density K_p	1.13	1.26	1.52

Notes: g is the gravitational acceleration, the normal water depth of upstream reservoir is 154 m.

shown in Table 1. It can be seen that the equivalent water density overloading parameter K_p comes up to 1.52 when the peak acceleration of earthquakes reaches 0.4 g. As for the actual situation, extreme external loads caused by strong earthquakes or landslides may be more serious than this, such as the failure of Vajont arch dam; later studies show that the huge water pressure caused by the landslide of reservoir bank is about 8 times of the designed loads.

3.2. Strength Reduction Method. Strength reduction method mainly considers the strength degradation during the service period and the uncertainty of material strength. Under the normal load combination, strengths of dam concretes and bedrocks are gradually reduced until the dam failure. Especially for bedrocks, due to the complexity of rock genesis and geotectonic movement, various faults, joints, and cracks are distributed complicatedly, so it is possible to make big differences of material properties in local small areas that cannot be systematically represented in the geological survey. Based on the Drucker-Prager yield criterion, the original shear strength parameters are denoted as c and f for cohesion and friction angle, respectively. Hence, the reduced parameters are denoted as c/K_s and f/K_s (for normal condition, the strength reduction parameter $K_s = 1$), and the gradually

reduced shear strength is used by FEM simulation until the dam failure.

3.3. Comprehensive Method. Instead of the single action of overloading or strength degradation, dam failure is a progressive process from local damage to global failure under the comprehensive action of these two actors. The comprehensive method is the combination of overloading and strength reduction, so it seems more reasonable to simulate the dam failure. However, due to the specificity of dam projects, how to reasonably combine these two methods is still an unfathomed problem for engineers, and this situation limits the development of the comprehensive method in the studying of dam global safety.

3.4. Dam Safety Evaluation Indicators in the Progressive Failure

3.4.1. Dam Displacement. The global instability failure of gravity dams mainly resulted from the rapid development of infinite deformation caused by material strength degradation or abnormal environmental loads. No matter the sliding modes of inclined plane sliding or the translational sliding, dam displacements are all gradually increased before the dam failure. On the other hand, the progressive failure process of gravity dams under different failure modes can be simulated by FEM, and the theoretical displacements of typical stages in dam failure process can be determined as the instability safety monitoring indexes of gravity dams. The comparison of the observation displacement and its monitoring index shows the current situation of dam safety as well as the safety margin.

The simulation of dam failure by the geomechanical model test shows that when the parameters of strength reduction or overloading come up to a large amplitude, the rapidly increased nonlinear deformation results in the catastrophe of dam displacement, and the bearing capacity of dam-foundation system loses immediately. The development of dam displacement in the FEM simulation is similar to this,

so the catastrophe of dam displacement can be defined as the sign of losing bearing capacity for gravity dam-foundation systems, and the theoretical displacement at this moment is determined as the safety monitoring index of dam failure.

3.4.2. The Connectivity of Yield Zones. With the strength reduction or overloading, yield zones of dam-foundation system extend and join, and these yield zones are finally connected in dam body, along the foundation plane or in bedrocks. Here, yield zones are defined as the zones where the equivalent plastic strain is larger than a certain magnitude, and the equivalent plastic strain is defined as follows [25]:

$$\bar{\varepsilon}^p = \int \dot{\varepsilon}^p dt = \int \left(\frac{2}{3} \dot{\varepsilon}_{ij}^p \dot{\varepsilon}_{ij}^p \right)^{1/2} dt, \quad (10)$$

where $\dot{\varepsilon}^p$ is the equivalent plastic strain rate.

Plastic strain of tension, compression, and shear are all included in the equivalent plastic strain by integrating the equivalent plastic strain rate. Research results [21, 23] show that it is more suitable to set the amplitude of the total equivalent plastic strain at 10^{-4} to determine whether the concrete and bedrock are yielding or not.

Instead of the elastic-perfectly plastic material, both bedrock and dam concrete have the potential bearing capacity after yielding, so there is no obvious relationship between the connectivity of yield zones and the dam failure. Zheng et al. [26] pointed out that the connectivity of yield zones in soil is the necessary condition of soil sliding failure, not the sufficient condition, and the sign of soil sliding failure is identified as the rapid development of infinite deformation. Although the connectivity of yield zones does not immediately result in the dam failure, it still means the approach of ultimate bearing capacity. If engineering or nonengineering measures are not taken immediately to stop the deterioration of dam safety, dam deformation will increase sustainably and result in the dam failure at last.

3.4.3. The Yield Volume Ratio of Dam Body. Various disadvantageous weak structural surfaces are frequently distributed in dam foundation, and the working principle of gravity dams is that using the friction force caused by dam self-weight to resist the upstream horizontal water pressure to guarantee the stability. Meanwhile, yield zones of dam concretes mainly appeared at local areas of dam heel, dam toe, or the turning points of dam upstream and downstream surfaces. Therefore, if dam concretes are poured in good quality to ensure the designed strength and stiffness, global failure of gravity dams is unlikely to be caused by the yield of dam concretes. However, as for some high concrete dams which are constructed on the ideal bedrocks that the strength and stiffness are both guaranteed, dam concrete degradation or the abnormal environmental loads may result in a large proportion of yield concretes, and the rapidly increased infinite deformation of dam body determines the loss of bearing capacity of dam-foundation systems. For these high concrete gravity dams, catastrophe of the yield volume ratio of dam concretes can be determined as the sign of losing bearing capacity.

4. Determination of Instability Safety Monitoring Index of Gravity Dams

To establish the instability safety monitoring index for high concrete gravity dams, according to the actual conditions, such as the geological condition, environmental condition, and the degradation of dam concretes, it is necessary to firstly study the failure mechanism of instability under different potential failure modes. By simulating the progressive failures, typical stages in the instability failure process are identified by evaluation indicators of dam displacement, the connectivity of yield zones, and the yield volume ratio of dam concretes. Then, considering the condition that some of the failure conditions may not appear during dam operation, so these typical stages are analyzed and compared, and from the view of most unfavorable for dam safety, several typical stages are selected for hierarchically determining dam instability safety monitoring indexes. Finally, according to dam displacement fields at these typical stages, safety monitoring indexes are established for different dam safety grades. The flow chart of establishing safety monitoring index for high gravity dams based on the failure mechanism of instability is shown in Figure 2.

5. Case Study

A concrete gravity dam is located in the west of China, with a maximum dam height of 160.0 m, a crest elevation of 1424.0 m, and a crest axis length of 640.0 m. The highest dam section on the riverbed is selected to study the failure mechanism of instability and establish safety monitoring index. There are two nearly horizontal weak interlayers distributed in foundation bedrocks with the average buried depths of 30 m and 80 m, and the thicknesses of 1.65 m and 2.33 m, which are, respectively, denoted as $t1_b$ and $t1_a$. According to the boundaries of $t1_b$ and $t1_a$, foundation rocks are divided into three categories, which are, respectively, denoted as rock I, rock II, and rock III, from the ground surface to the deeper. The range of the FEM model is about two times of the maximum dam height in the upstream, downstream, and downward directions according to the dam heel and dam toe. Thicknesses of the weak interlayer in the FEM model are determined as the actual value. The gravity dam-foundation system is discretized into eight-node and six-node solid elements, with 15932 elements and 19056 nodes, in which the dam body contains 3549 elements and 4432 nodes. The FEM model is shown in Figure 3(a). Material parameters for dam body and its foundation are listed in Table 2.

To study the failure mechanism of instability by methods of strength reduction, overloading and the comprehensive method, evaluation indicators of dam displacement, the connectivity of yield zones, and the yield volume ratio of dam body are used to identify the safety variation of this high concrete gravity dam-foundation system in the progressive failure process. Five observation points of the plumb line in the monitoring system are determined as the typical points of dam displacement, and the elevations are 1424.0 m (dam crest) 1359.0 m, 1320.0 m, 1292.0 m, and 1264.0 m (foundation

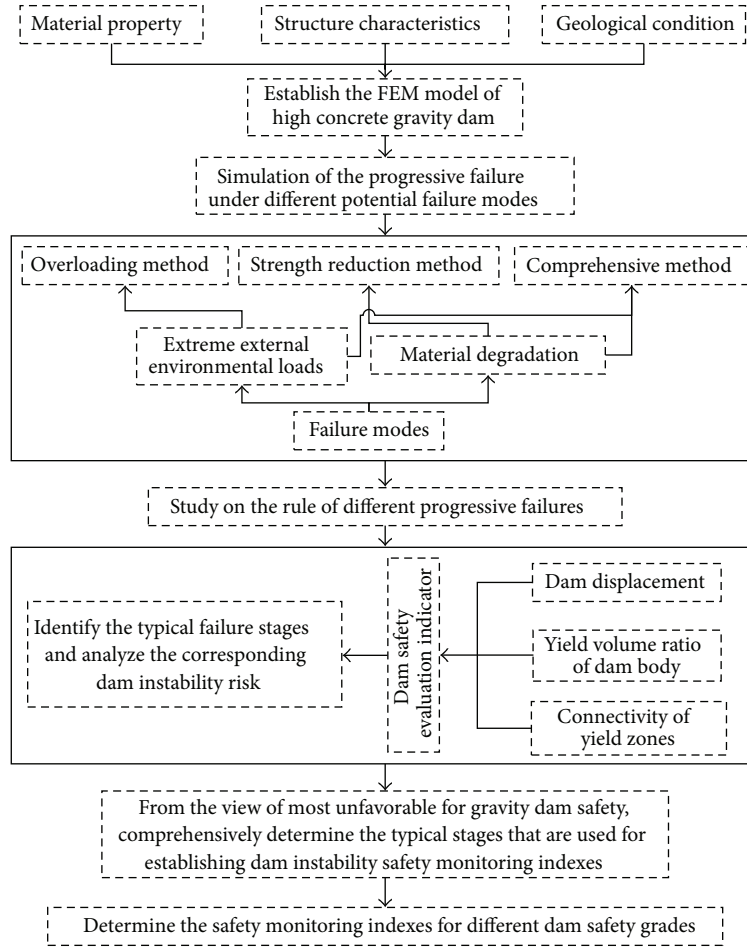


FIGURE 2: The flow chart of establishing safety monitoring index for high concrete gravity dams based on the failure mechanism of instability.

TABLE 2: Material parameters for dam body and its foundation.

	Elastic modulus E (GPa)	Poisson's ratio ν	Density ρ (kg/m^3)	Cohesion c (MPa)	Friction angle f
Dam body	25	0.167	2400	2.7	1.33
Rock I	4	0.27	2600	0.7	0.95
Rock II	8	0.27	2600	1.0	1.15
Rock III	10	0.27	2600	1.3	1.35
Weak interlayer	2	0.3	2500	0.4	0.73

plane), respectively. Distribution of the typical points is shown in Figure 3(b).

5.1. Material Model and Yield Criterion. Drucker-Prager yield criterion is commonly used for concretes and rocks as it can yield a smooth failure surface and is determined corresponding to the hydrostatic stress. Hence, the Drucker-Prager yield criterion is adopted in studying the failure mechanism of instability of high concrete gravity dams, which is presented as follows:

$$f = \alpha I_1 + \sqrt{J_2} - K = 0, \quad (11)$$

where I_1, J_2 are the first invariant of stress tensor and the second invariant of deviatoric stress tensor, respectively. α and K are parameters related to the material shear strength as follows:

$$\alpha = \frac{\sin \varphi}{\sqrt{3} \sqrt{3 + \sin^2 \varphi}}, \quad (12)$$

$$K = \frac{3c \cos \varphi}{\sqrt{3} \sqrt{3 + \sin^2 \varphi}}. \quad (13)$$

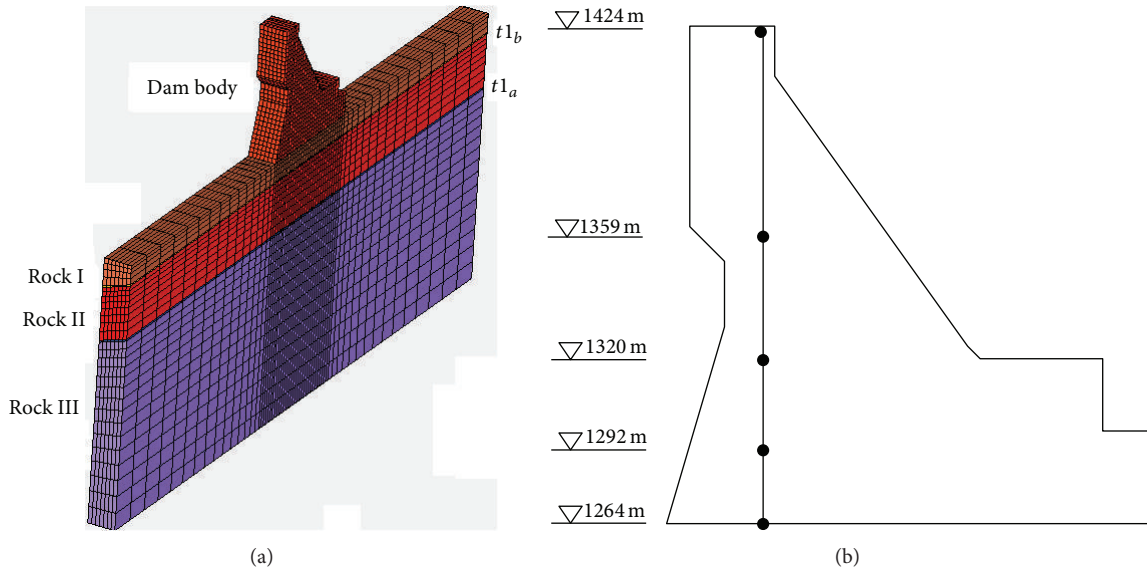


FIGURE 3: Integral FEM model and the typical points: (a) FEM model; (b) typical displacement points.

5.2. Simulation of the Progressive Failure under Different Failure Modes. Considering that the most probable potential failure modes are material degradation and extreme external environmental loads during the service period, hence, to establish dam safety monitoring index based on the risk of dam failure, methods of strength reduction and overloading are used in studying the failure mechanism of instability and the progressive failure process at first. Then, safety monitoring indexes are hierarchically determined according to the typical stages of the progressive failure and the actual dam situation.

5.2.1. Analysis Results of the Strength Reduction Method. The strength reduction method is used to simulate the material strength degradation and uncertainty. The constant load condition is the combination of upstream hydrostatic pressure (with the normal water level of 1418.0 m), dam self-weight, silt pressure, and uplift pressure. The elevation of silt sedimentation is 1335.0 m; the silt submerged unit weight and the friction angle are 12 kN/m^3 and 23° , respectively. The uplift pressure reduction coefficient of dam foundation impervious curtain is 0.25.

The progressive failure process of this gravity dam-foundation system under the simulation method of strength reduction is shown in Figure 4, in which the black zones are the failure regions where the total equivalent plastic strain is beyond the amplitude of 10^{-4} , and it has the same meaning in Figure 7.

Due to the existence of the stream direction horizontal weak interlayer, under the normal load condition, yield zones firstly appeared at the dam toe and its nearby bedrocks of the shallowly buried $t1_b$ interlayer. When the reduction parameter K_s reaches 1.2, the connectivity of yield zones is formed at the dam toe between the foundation plane and the $t1_b$ interlayer; namely, the potential downstream sliding surface is developed. With the continual increments of

the reduction parameter, yield zones rapidly extend towards the upstream direction along the foundation plane and the $t1_b$ interlayer. When $K_s = 2.0$, the connectivity of yield zones from upstream to downstream is partly formed at the shallowly buried $t1_b$ interlayer on the right side of this dam section, and when $K_s = 2.2$, this yield zones are totally connected between the foundation plane and the $t1_b$ interlayer from dam heel to dam toe. Therefore, one of the potential sliding modes of this gravity dam is the translational sliding with three sliding surfaces, which are composed of the tension-shear crack zones at the dam heel, the $t1_b$ interlayer, and the compression-shear crushed zones at the dam toe. When $K_s = 3.0$, the connected yield zones extend to the $t1_a$ interlayer which is deeply buried with a depth of 80 m. Meanwhile, the strength reduction results in the connectivity of dam concretes between the dam heel and the turning point of the downstream dam surface. Thus, the connectivity of yield zones both appeared in dam body and foundation rocks, and the rapidly increased infinite deformation results in the catastrophe of dam displacement and the loss of bearing capacity at last.

The developments of dam displacement and dam body yield volume ratio with the strength reduction parameter are shown in Figures 5 and 6, and it is perfectly in accordance with the aforementioned progressive failure process. It can be seen from Figure 5 that when K_s is less than 2.2, the stream displacement of the selected five typical points remains largely unchanged, and yield zones rarely appeared in dam body. The relatively stable relationship between dam displacement and the reduction parameter indicates the unchanged stable status of this gravity dam. Then, dam concrete yields over a large area, while dam displacement slowly increases with a small amplitude. Reasons may be concluded as follows: the first one is that the connectivity of yield zones in dam body is not formed before K_s reaches 3.0. The other important reason is that the translational sliding

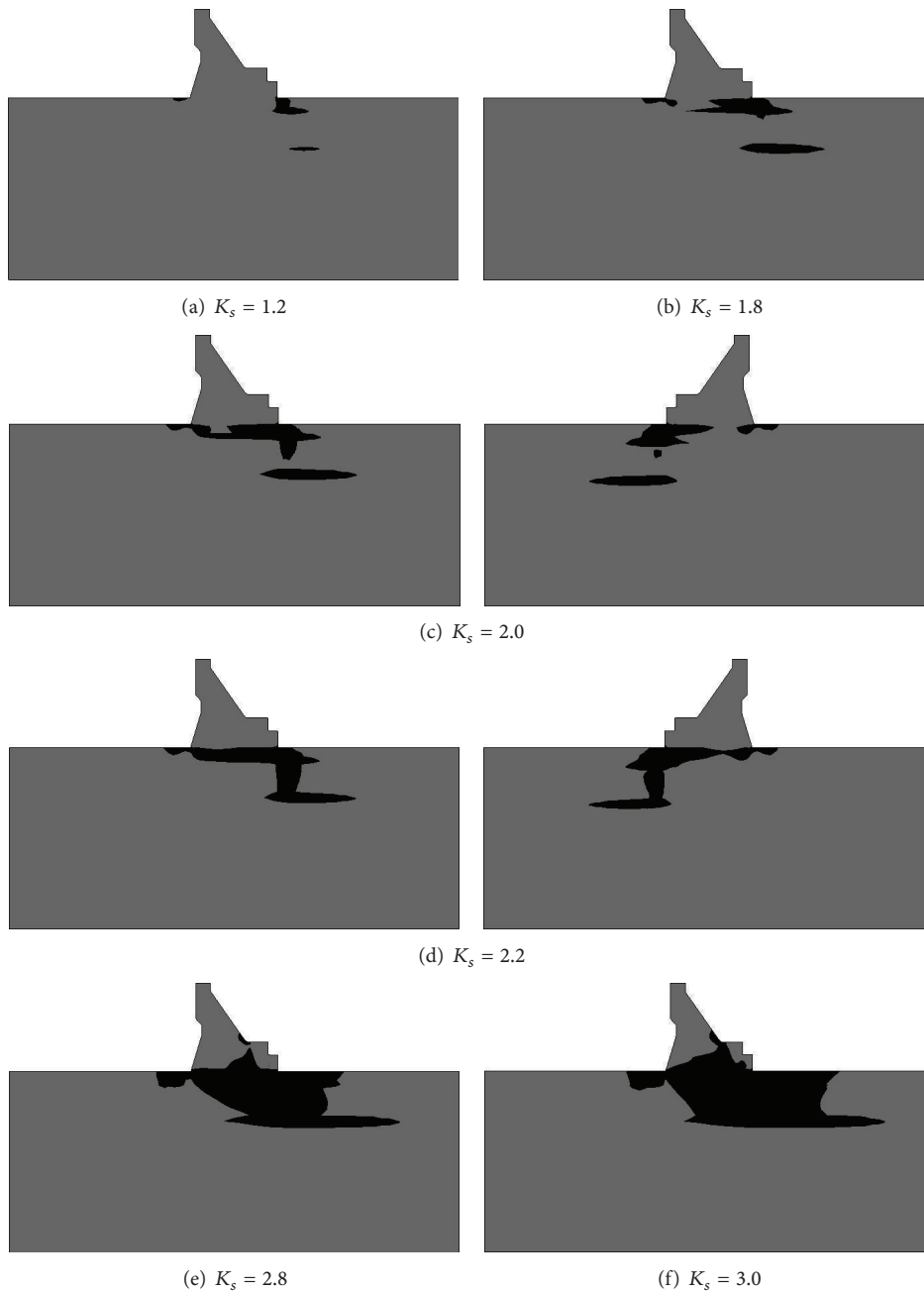


FIGURE 4: The progressive failure process of dam-foundation system under strength reduction.

along the weak interlayer is restricted by the downstream bedrocks. It seems that the totally connected yield zones between the foundation plane and the $t1_b$ interlayer from dam heel to dam toe will result in the rapid development of translational sliding of dam body and parts of the bedrocks after K_s reaches 2.2. However, the $t1_b$ interlayer is buried at an average depth of 30 m and horizontally distributed in the stream direction, so the development of the translational sliding is largely limited by the tail rock resistance blocks, and this phenomenon is better explained by one of the selected typical points which is on the foundation plane. When K_s exceeds 3.0, due to the existence of the downstream free

surface of dam body, the connected yield zones in dam body result in the rapidly increased deformation at the upper of this dam. Therefore, catastrophes are shown on the displacement relation curves of the upper located typical points.

5.2.2. Analysis Results of the Overloading Method. Material strength of dam concretes and bedrocks are designed as the original values in the overloading method. Load condition is the same as that of the strength reduction method; the only difference is that the water density of upstream reservoir is increased to K_p times when the overloading parameter K_p is larger than 1.0; namely, only the upstream water pressure

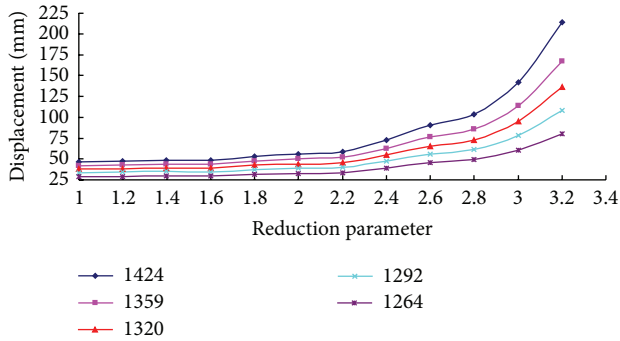


FIGURE 5: Relation curves between the stream displacement of dam body and the strength reduction parameter.

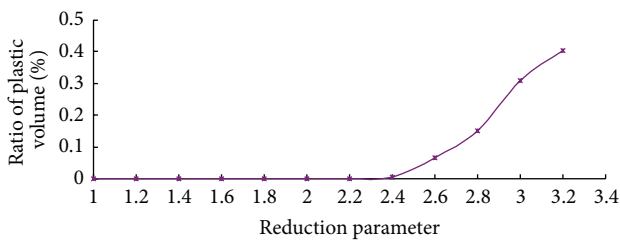


FIGURE 6: Relation curve between the yield volume ratio of dam body and the strength reduction parameter.

is increased when overloading. The overloading simulation process is that dam self-weight is firstly applied to model the pouring of dam concretes; then water pressure, silt pressure, and uplift pressure under the normal load condition are added, and the overloading is finally conducted by the continual increments of water density at an interval of 0.2 times.

The progressive failure process under the overloading method is shown in Figure 7, which is similar to the strength reduction method. As for the dam deformation of typical stages, such as the connectivity of plastic yield zones in bedrocks along the $t1_b$ interlayer from upstream to downstream, dam displacement by the overloading method is obviously larger than that of the strength reduction method at the same stage. When $K_p = 2.0$, the connectivity of yield zones completely appeared between the foundation plane and the $t1_b$ interlayer. Due to the existence of the folded slope of dam upstream surface, the total water weights on the upstream dam surface are also increased with the increments of upstream water density, which results in that the compression-shear yield zones are largely distributed in the bedrocks right below the dam heel. The strength of dam concretes is significantly higher than that of bedrocks; hence, except for some small parts of dam concretes close to the foundation plane, yield zones in dam body firstly appeared at the dam toe and the turning points of the upstream and downstream dam surface until K_p comes up to 2.8. With the continual increments of the overloading parameter, yield zones extend to the internal of dam body, and dam concretes at the turning point of the upstream dam surface yield rapidly.

When $K_p = 3.6$, yield zones are connected in dam body from upstream to downstream.

Figure 8 shows the relation curves between the stream displacement of dam body and the overloading parameter. It can be seen that dam stream displacements of typical points at the elevation of 1424.0 m and 1359.0 m increase rapidly after K_p reaches 3.6. Reasons are that the connectivity of yield zones is formed in dam body when $K_p = 3.6$, and this yield zone works as a plastic hinge for the existence of the downstream dam free surface. Hence, the nonlinear deformation develops rapidly at the upper of the dam body.

It can be concluded from Figures 7 and 8 that the connectivity of yield zones already completely appeared between the foundation plane and the $t1_b$ interlayer when $K_p = 2.0$. However, displacement increasing rate of the five selected typical points is smaller until K_p reaches 3.0 (dam concretes begin to yield rapidly when $K_p = 3.0$). Therefore, for this concrete gravity dam, the connectivity of yield zones in dam foundation does not mean the loss of bearing capacity.

The relation curve between the yield volume ratio of dam body and the overloading parameter is shown in Figure 9. It can be seen that when $K_p = 2.4$, the yield volume ratio begins to increase with a smaller increasing rate. When $K_p = 3.0$, dam concretes yield rapidly, and the yield volume ratio has increased from 0.12 to 0.77 with the overloading parameter that ranges from 3.0 to 4.6. Water pressure on the top of the upstream dam surface increases slowly in the water density overloading method, so yield zones extend slowly to the dam crest after $K_p = 4.6$, and the yield volume ratio of dam body remains largely unchanged.

5.2.3. Analysis Results of the Comprehensive Method. To study the failure mechanism of instability under the comprehensive condition of abnormal environmental loads and material strength degradation or uncertainty, the comprehensive method has been conducted, and the simulation analysis results are concluded as follows.

Relation curves of stream displacement-overloading parameter at the foundation plane and dam crest are shown in Figures 10 and 11, respectively. The bigger strength reduction, the smaller overloading parameter is allowed when nonconvergence occurs, so these curves only reflect dam displacements before the overloading parameter K_p reaches 3.4. The development rule of displacement of the other three typical points are similar to this. Although for different strength reduction parameters, dam displacement changes stably and keeps almost the same values before K_p reaches 2.0. Therefore, under the comprehensive condition of abnormal environmental loads and a certain percentage of material strength degradation, displacement of this gravity dam will increase at a certain amplitude, while dam failure will not directly occur if the strength degradation and environmental loads are properly controlled.

Relation curves between the yield volume ratio of dam body and the overloading parameter under different strength reduction parameters are shown in Figure 12. It can be seen that strength reduction results in a reduced bearing capacity and the earlier occurrence of the catastrophe of concrete

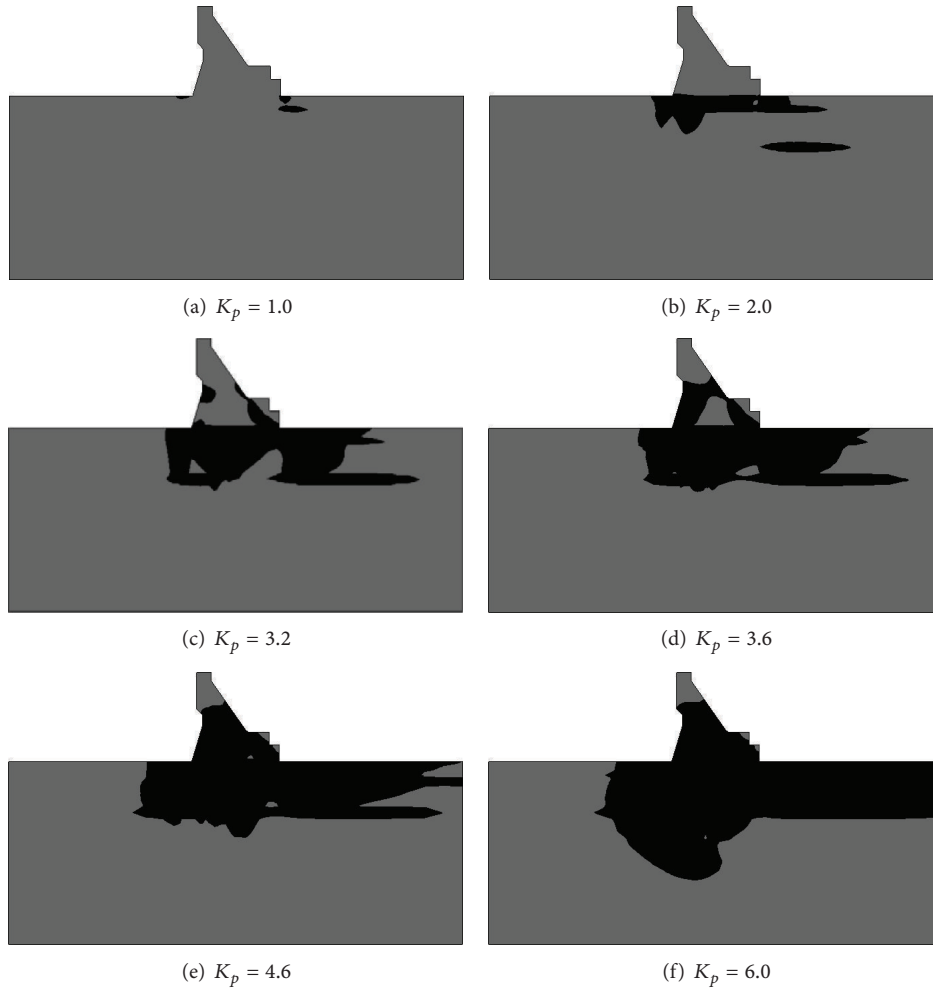


FIGURE 7: The progressive failure process of dam-foundation system under overloading.

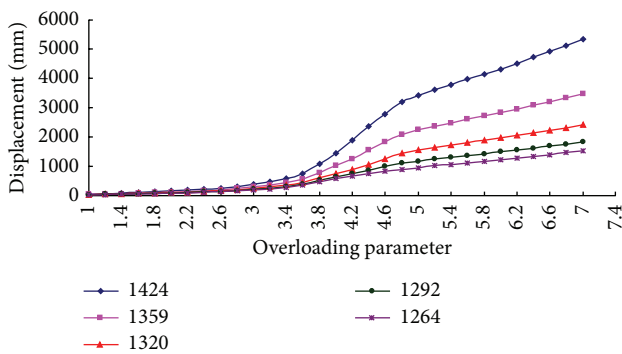


FIGURE 8: Relation curves between the stream displacement of dam body and the overloading parameter.

yield volume ratio. Dam overloading failures under different strength reduction conditions show that catastrophes of the yield volume ratio of dam concretes all appeared next to the connectivity of plastic yield zones between the foundation plane and the $t1_b$ interlayer and before the catastrophe of dam displacement. Therefore, catastrophe of the yield volume ratio

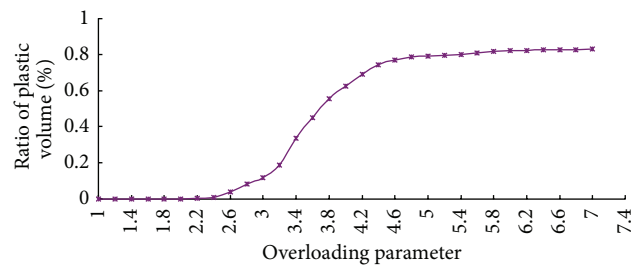


FIGURE 9: Relation curve between the yield volume ratio of dam body and the overloading parameter.

of dam concretes does not mean the loss of bearing capacity for this concrete gravity dam, which should be determined according to whether the excessive plastic deformation will result in the catastrophe of dam displacement or not.

5.3. *Instability Safety Monitoring Indexes.* The progressive failure processes of this gravity dam section under the simulation methods of strength reduction and water density overloading are both represented as follows: plastic yield

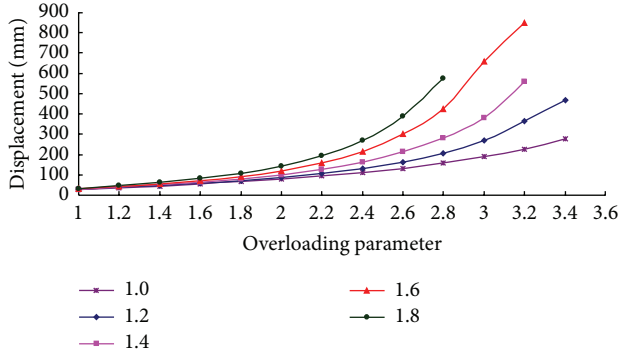


FIGURE 10: Relation curves between the stream displacement of the foundation plane and the overloading parameter under different strength reduction parameters.

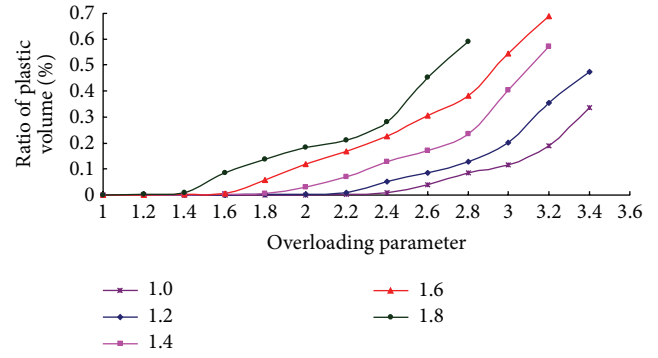


FIGURE 12: Relation curves between the yield volume ratio of dam body and the overloading parameter under different strength reduction parameters.

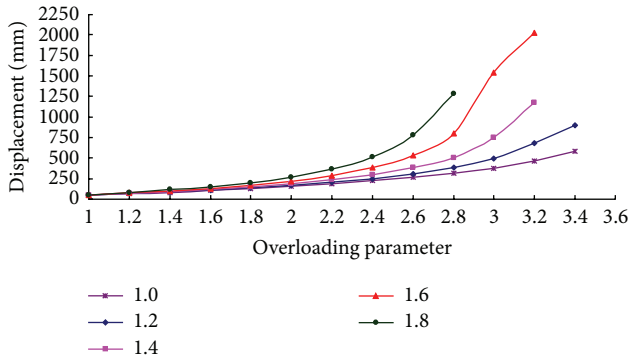


FIGURE 11: Relation curves between the stream displacement of the dam crest and the overloading parameter under different strength reduction parameters.

zones are firstly connected in bedrocks along the $t1_b$ weak interlayer; then, yield zones rapidly extend to dam body and result in the catastrophe of yield volume ratio of dam concretes; the rapidly increased excessive plastic deformation in dam body and foundation rocks results in the catastrophe of dam displacement, and the gravity dam loses the bearing capacity due to the failure of instability finally.

The aforementioned analyses show that catastrophes of the yield volume ratio of dam concretes in both simulation methods all appeared closely next to the connectivity of plastic yield zones between the foundation plane and the $t1_b$ interlayer. Therefore, there are two typical stages that can be defined in both failure processes: the first one is the connectivity of plastic yield zones along the $t1_b$ weak interlayer in bedrocks; the second one is the catastrophe of dam displacement.

During the designed service period, the potential most unfavorable conditions of dams are concluded as material strength degradation and extreme external environmental loads. Hence, methods of strength reduction and overloading can be, respectively, used in studying the failure mechanism of high concrete gravity dams under these two unfavorable conditions. Based on the dam safety monitoring system, dam theoretical displacements of typical points at

the aforementioned two typical stages can be determined as the safety monitoring indexes. Dam failure mechanism under the comprehensive method is similar to that of just overloading, and differences are only represented on the deformation that it is bigger for the same environmental loads when the material strength is reduced. Therefore, from the view of safety, the smaller displacement at the same typical stage is determined as the dam safety monitoring index; namely, monitoring indexes are hierarchically determined according to the theoretical results of strength reduction and overloading.

Research results of the strength reduction method show that the resisting force of the tail rock resistance block can be ensured due to the buried depth of 30 m and 80 m for $t1_b$ and $t1_a$, respectively. Therefore, although there are two weak interlayers distributed in bedrocks, the connectivity of plastic yield zones along the $t1_b$ interlayer will not result in the rapid development of the translational sliding. Dam displacements tend to be rapidly increased until dam concretes yield over large areas when K_s reaches 3.0. However, material property of dam concretes is easy to be identified and varies slightly for the better construction quality, so it is not inconsistent with the actual situation that the strength of all dam concretes can be determined as 1/3 of the original value due to the strength degradation or uncertainty. On the other hand, strength of bedrocks is usually weaker than that of dam concretes, and the strength degradation of bedrocks and weak structural surfaces are more serious than dam concretes for the obvious seepage in dam foundation. Theoretically speaking, dam failure of instability caused by material strength degradation or uncertainty will occur in dam foundation firstly. Therefore, based on the aforementioned analyses, catastrophe of dam displacement in the strength reduction method is not identified as the sign of losing bearing capacity for this concrete gravity dam.

Due to the complexity of rock genesis and geotectonic movement, various faults, joints, and cracks are complicatedly distributed in dam foundation, so big differences of material properties may appear in local small areas that cannot be systematically represented in geological survey. Therefore, under the normal condition, large deformation

TABLE 3: Monitoring indexes of dam stream displacement (unit: mm).

Elevation	Dam instability safety monitoring indexes		
	Grade one	Grade two	Grade three
1424 m	26.06	76.16	399.61
1359 m	18.89	44.86	213.60
1320 m	12.79	25.68	102.83
1292 m	7.00	12.43	45.26

which seems abnormal may also take place due to the uncertainty of rock properties, especially for the strength of weak structural surfaces, and dam safety will be threatened if and only if this uncertainty is beyond the range of acceptable. Therefore, the connectivity of yield zones along the t_{1b} interlayer in the strength reduction method is defined as the variation sign of normal operation for this concrete gravity dam, and the corresponding dam displacement is determined as dam instability safety monitoring index of grade one. As for the connectivity of yield zones along the t_{1b} interlayer caused by overloading, if engineering or nonengineering measures are not taken to stop the rapidly increased deformation (caused by the continual increments of environmental loads or the creep effect of bedrocks and dam concretes), it may result in the instability sliding of this gravity dam-foundation system. For the same typical stage of the connectivity of yield zones along the t_{1b} interlayer, the risk level under overloading is more serious than that of strength degradation, so the second dam instability safety monitoring index is determined by the overloading method at the aforementioned dam failure stage.

Based on the aforementioned failure mechanism of instability, three grades of instability safety monitoring indexes are hierarchically determined for this high concrete gravity dam. The corresponding typical stages in the simulated dam failure process are identified as follows: (1) the first grade, the connectivity of plastic yield zones along the t_{1b} interlayer from dam heel to dam toe by the strength reduction method with $K_s = 2.2$; (2) the second grade, the connectivity of plastic yield zones along the t_{1b} interlayer from dam heel to dam toe by the overloading method with $K_p = 2.0$; (3) the third grade, catastrophe of dam displacement by the overloading method with $K_p = 3.6$. Monitoring indexes for the observation points of the plumb line are shown in Table 3. Here, the monitoring indexes of dam displacement are determined in terms of the foundation plane.

6. Conclusions

Aiming at the potential failure modes of material strength degradation and extreme external environmental loads during the service period, based on the FEM structural analysis method, failure mechanisms and the progressive failure process of high concrete gravity dams are studied in this paper by methods of strength reduction and overloading. Typical stages in the failure process are identified by evaluation indicators of dam displacement, the connectivity of yield

zones, and the yield volume ratio of dam concretes; then instability safety monitoring index of high concrete gravity dams is determined according to these typical symptoms. At last, failure mechanism of a high concrete gravity dam is studied, and according to different dam safety situations, three grades of dam instability safety monitoring index of dam displacement are hierarchically established, which are, respectively, at the stages of the connectivity of yield zones along the weak interlayer by methods of strength reduction and overloading, and the catastrophe of dam displacement by the overloading method.

Acknowledgments

This work was supported by the Research Fund for the Doctoral Program of Higher Education of China (Grants nos. 20120094110005 and 20120094130003), the National Natural Science Foundation of China (Grants nos. 51379068, 51139001, 51279052, 51209077, and 51179066), the Program for New Century Excellent Talents in University (Grant no. NCET-11-0628), and the Ministry of Water Resources Public Welfare Industry Research Special Fund Project (Grants nos. 201201038 and 201101013).

References

- [1] C. S. Gu, B. Li, G. L. Xu, and H. Yu, "Back analysis of mechanical parameters of roller compacted concrete dam," *Science China Technological Sciences*, vol. 53, no. 3, pp. 848–853, 2010.
- [2] H. Yu, Z. R. Wu, T. F. Bao, and L. Zhang, "Multivariate analysis in dam monitoring data with PCA," *Science China Technological Sciences*, vol. 53, no. 4, pp. 1088–1097, 2010.
- [3] Y. Q. Ni, X. W. Ye, and J. M. Ko, "Monitoring-based fatigue reliability assessment of steel bridges: analytical model and application," *Journal of Structural Engineering*, vol. 136, no. 12, pp. 1563–1573, 2010.
- [4] X. W. Ye, Y. Q. Ni, K. Y. Wong, and J. M. Ko, "Statistical analysis of stress spectra for fatigue life assessment of steel bridges with structural health monitoring data," *Engineering Structures*, vol. 45, pp. 166–176, 2012.
- [5] X. W. Ye, Y. Q. Ni, and Y. X. Xia, "Distributed strain sensor networks for in-construction monitoring and safety evaluation of high-rise building," *International Journal of Distributed Sensor Networks*, vol. 2012, Article ID 685054, 13 pages, 2012.
- [6] C. S. Gu, E. F. Zhao, Y. Jin, and H. Z. Su, "Singular value diagnosis in dam safety monitoring effect values," *Science China Technological Sciences*, vol. 54, no. 5, pp. 1169–1176, 2011.
- [7] L. Chen, *Mechanics Performance With Parameters Changing in Space and Monitoring Models of Roller Compacted Concrete Dam*, College of Water Conservancy and Hydropower Engineering, Hohai University, Nanjing, China, 2006 (Chinese).
- [8] P. Lei, *Study on the Theory and Method of Deformation Monitoring Index of Concrete Dam*, College of Water Conservancy and Hydropower Engineering, Hohai University, Nanjing, China, 2008 (Chinese).
- [9] H. Z. Su, J. Hu, J. Y. Li, and Z. R. Wu, "Deep stability evaluation of high-gravity dam under combining action of powerhouse and dam," *International Journal of Geomechanics*, vol. 13, no. 3, pp. 257–272, 2013.

- [10] H. Z. Su, J. Hu, and Z. P. Wen, "Service life predicting of dam systems with correlated failure modes," *Journal of Performance of Constructed Facilities*, vol. 27, no. 3, pp. 252–269, 2013.
- [11] S. L. Fan, J. Y. Chen, and J. Y. Guo, "Application of finite element equivalent stress method to analyze the strength of gravity dam," *Journal of Hydraulic Engineering*, vol. 38, no. 6, pp. 754–766, 2007 (Chinese).
- [12] H. Z. Su, Z. R. Wu, Y. C. Gu, J. Hu, and Z. P. Wen, "Game model of safety monitoring for arch dam deformation," *Science in China E*, vol. 51, no. 2, pp. 76–81, 2008.
- [13] C. S. Gu and Z. R. Wu, *Safety Monitoring of Dams and Dam Foundations-Theories & Methods and Their Application*, Hohai University Press, Nanjing, China, 2006 (Chinese).
- [14] Z. Z. Shen, M. Ma, and X. X. Tu, "Early warning index of deformation for gravity dam based on discontinuous deformation analysis," *Journal of Hydraulic Engineering*, vol. 38, supplement, pp. 94–99, 2007 (Chinese).
- [15] D. J. Zheng, Z. Y. Huo, and B. Li, "Arch-dam crack deformation monitoring hybrid model based on XFEM," *Science China Technological Sciences*, vol. 54, no. 10, pp. 2611–2617, 2011.
- [16] P. Lei, X. L. Chang, F. Xiao, G. J. Zhang, and H. Z. Su, "Study on early warning index of spatial deformation for high concrete dam," *Science China Technological Sciences*, vol. 54, no. 6, pp. 1607–1614, 2011.
- [17] Y. C. Gu and S. J. Wang, "Study on the early-warning threshold of structural instability unexpected accidents of reservoir dam," *Journal of Hydraulic Engineering*, vol. 40, no. 12, pp. 1467–1472, 2009 (Chinese).
- [18] C. S. Shen, S. X. Wang, Y. C. Lin, and X. Q. Liu, *Hydraulic Structure*, China Water Power Press, Beijing, China, 2008 (Chinese).
- [19] X. L. Chang, H. Wang, W. Zhou, and C. B. Zhou, "Mechanism of two sliding failure modes in gravity dam and method for safety evaluation," *Journal of Hydraulic Engineering*, vol. 40, no. 10, pp. 1189–1195, 2009 (Chinese).
- [20] F. Jin, W. Hu, J. W. Pan, J. Yang, J. T. Wang, and C. H. Zhang, "Failure analysis of high-concrete gravity dam based on strength reserve factor method," *Computers and Geotechnics*, vol. 35, no. 4, pp. 627–636, 2008.
- [21] F. Jin, W. Hu, J. W. Pan, J. Yang, J. T. Wang, and C. H. Zhang, "Comparative study procedure for the safety evaluation of high arch dams," *Computers and Geotechnics*, vol. 38, no. 3, pp. 306–317, 2011.
- [22] G. X. Zhang, Y. Liu, and Q. J. Zhou, "Study on real working performance and overload safety factor of high arch dam," *Science in China E*, vol. 51, no. 2, pp. 48–59, 2008.
- [23] D. J. Zheng and T. Lei, "Instability criteria for high arch dams using catastrophe theory," *Chinese Journal of Geotechnical Engineering*, vol. 33, no. 1, pp. 23–27, 2011 (Chinese).
- [24] State Economic and Trade Commission of China [SETCC]. Specifications for seismic design of hydraulic structures DL5073-2000, 2001 (in Chinese).
- [25] MSC, *Software Corporation. MSC. Marc Vol. A: Theory and User Information*, MSCSoftware Corporation, Santa Ana, Calif, USA, 2005.
- [26] Y. R. Zheng, S. Y. Zhao, W. X. Kong, and C. J. Deng, "Geotechnical engineering limit analysis using finite element method," *Rock and Soil Mechanics*, vol. 26, no. 1, pp. 163–168, 2005 (Chinese).

Research Article

Construction of Stiffness and Flexibility for Substructure-Based Model Updating

Shun Weng,¹ Hong-Ping Zhu,¹ Yong Xia,² Ling Ye,¹ and Xian-Yan Hu³

¹ School of Civil Engineering & Mechanics, Huazhong University of Science and Technology, Wuhan, Hubei 430074, China

² Department of Civil and Environmental Engineering, The Hong Kong Polytechnic University, Hung Hom, Kowloon, Hong Kong

³ Department of Architecture and Materials, Hubei University of Education, Wuhan, Hubei 430074, China

Correspondence should be addressed to Hong-Ping Zhu; hpzhu@mail.hust.edu.cn

Received 18 September 2013; Accepted 23 October 2013

Academic Editor: Xiao-Wei Ye

Copyright © 2013 Shun Weng et al. This is an open access article distributed under the Creative Commons Attribution License, which permits unrestricted use, distribution, and reproduction in any medium, provided the original work is properly cited.

In substructuring methods, the substructures are independently analyzed under free-free conditions. For a free-free substructure, its stiffness matrix is singular and rank deficient due to rigid body motion. The variables associated with the inverse of the stiffness matrix are not easy to be accurately determined in the usual manner. This study expands on the previous research on the substructuring methods by taking a deeper look at the analysis of a free-free substructure. A well-conditioned stiffness matrix is constructed for the analysis of a free-free structure. Some difficulties associated with the analysis of the free-free substructures can be solved in a simple and effective way. The substructural eigensolutions and eigensensitivity are solved from the well-conditioned stiffness matrix, other than the singular stiffness matrix. The proposed well-conditioned eigenequation is accurate and efficient to calculate the substructural eigensolutions and eigensensitivity. The properties addressed in this paper are not limited to be used for the analysis of a free-free substructure in many substructuring methods, and they are promising to be generalized to a range of analysis relevant to a free-free structure.

1. Introduction

In the past several decades, a large number of long-term structural health monitoring (SHM) systems have been designed and implemented worldwide on civil engineering structures such as large-scale bridges and high-rise buildings [1–4]. The accurate and efficient model updating and damage detection are significant for the long-term SHM systems. The substructuring methods have proved to be accurate and efficient for the analysis of large-scale structure, and they have been extensively utilized in a large number of applications, such as the model updating, system identification, and structural control [5]. The substructuring methods possess more advantages than the traditional global methods which analyze a structure as a whole. First, as the global structure is replaced by smaller and more manageable substructures, it is much easier and quicker to analyze the small system matrices. Second, the substructuring methods allow for the analysis of local parts. When the substructuring method is applied in model updating or damage identification, only one or more

substructures are involved in an optimization procedure. The size of the model and the number of the uncertain parameters are much smaller than those of the global structure. Finally, in practical testing, the experimental instruments can be saved if it is necessary to measure the whole structure only for one or more substructures [5].

In general, the substructuring approach can be utilized in the forward and inverse manners, respectively. The forward substructuring approach is frequently found in the eigenanalysis of a structure [5–14]. The partitioned substructures are analyzed independently to obtain their designated solutions, such as the substructural eigensolutions and eigensensitivity. The substructural solutions are then assembled to recover the solutions of the global structure by imposing constraints on the interfaces. On the other hand, the substructuring approach can be used in an inverse manner to disassemble the properties of the global structure to the substructure level by satisfying the constraints at the interfaces [15–21]. After eliminating the rigid body components, the independent substructures can be singled out to be used for the static analysis,

dynamic analysis, nonlinear analysis, fatigue analysis, and so forth.

The substructuring methods require dividing the global structure into independent free or fixed substructures. After partition, the substructures are usually analyzed independently under the free-free constraints. Since a free-free structure includes the rigid body motion, its stiffness matrix \mathbf{K} is singular and rank deficient, and hence the inverse of the stiffness (\mathbf{K}^{-1}) does not exist [22, 23]. In consequence, the variables associated with the inverse of the singular stiffness matrix, such as the modal flexibility, residual flexibility, eigensolutions, and eigensensitivity, are not easy to be determined. Some researchers avoided the rigid body modes (zero-frequency modes) by introducing a small shift in the singular and rank-deficient stiffness matrix [23, 24]. This inevitably introduces some errors. For example, the rigid body modes computed by a shift eigensolver are not perfect 0.0 Hz frequencies, and the computed mode shapes are not “clean” rigid body modes. In consequence, the obtained deformational modes which are orthogonal to the “unclean” rigid body modes are inaccurate. The variables relating to the zero-frequency modes, such as the eigensolutions and modal flexibility, are thereby not accurate [24].

When the modal flexibility of a free-free structure is required, the modal flexibility was sometimes computed by extracting the Moore-Penrose pseudoinverse of the stiffness matrix [6, 24]. Due to the numerical roundoffs, the frequencies and mode shapes of the rigid body modes are not accurate. This kind of analysis is not only computationally expensive, but also significantly sensitive to the rank condition when carried out in floating-point arithmetic [25].

This paper addresses some frequently encountered difficulties associated with the analysis of the free-free substructures when the authors studied the substructuring methods in the previous research [5, 9–16]. A new full-rank stiffness matrix is proposed, which leads to a well-conditioned eigenequation. Based on the well-conditioned eigenequation, the substructural flexibility, residual flexibility, eigensolutions, and eigensensitivity of a free-free structure are solved in an effective and efficient way. The formulae proposed in this paper are not only useful for the analysis of a free-free substructure in many substructuring methods but also generally applicable in the analysis of a free-free structure.

2. Construction of Free-Free Stiffness and Flexibility Matrices

2.1. Basic Theory for Eigenanalysis. A structure with N degrees of freedom (DOF) has the eigenequation of

$$\mathbf{K} \{\phi_i\} = \lambda_i \mathbf{M} \{\phi_i\}, \quad (1)$$

where \mathbf{K} and \mathbf{M} are the stiffness and mass matrices. λ_i is the i th eigenvalue of the structure, and $\{\phi_i\}$ is the corresponding eigenvector. They are determined by the physical property of a structure, such as Young's modulus, density, Poisson ratio, and geometric dimension. The eigensolutions of (1) consist of the eigenvalues $\Lambda = \text{Diag}(\lambda_1 \ \lambda_2 \ \cdots \ \lambda_N)$ and the corresponding eigenvectors $\Phi = [\phi_1 \ \phi_2 \ \cdots \ \phi_N]$. The

eigenvectors are mass-normalized such that they satisfy the following relation:

$$\Phi^T \mathbf{K} \Phi = \Lambda, \quad \Phi^T \mathbf{M} \Phi = \mathbf{I}. \quad (2)$$

The stiffness matrix can be written by the mass-normalized eigenmodes as

$$\mathbf{K} = \sum_{i=1}^N \lambda_i (\mathbf{M} \phi_i) (\mathbf{M} \phi_i)^T = \mathbf{M} \Phi \Lambda \Phi^T \mathbf{M}. \quad (3)$$

A flexibility matrix has a very straightforward physical interpretation: the displacement response caused by an applied unit load [26]. The flexibility matrix can also be written by the mass-normalized eigenmodes as

$$\mathbf{F} = \sum_{i=1}^N \frac{1}{\lambda_i} \phi_i \phi_i^T = \Phi \Lambda^{-1} \Phi^T. \quad (4)$$

For a fixed structure, the stiffness matrix and flexibility matrix normally formed a dual inverse of each other as

$$\mathbf{K} \mathbf{F} = \mathbf{I}, \quad \mathbf{F} = \mathbf{K}^{-1}, \quad \mathbf{K} = \mathbf{F}^{-1}. \quad (5)$$

The displacement $\{x\}$ of a free-free structure can be written as a superposition of the deformational and rigid body motions,

$$\{x\} = \{x_d\} + \{x_r\} = \Phi_d \{q\} + \mathbf{R} \{\alpha\}, \quad (6)$$

where $\{x_d\}$ is the displacement due to the deformational motion and $\{x_r\}$ is the displacement due to the rigid body motion. Φ_d is the linear orthogonal deformational modes, \mathbf{R} is the orthogonal rigid body modes, and $\{q\}$ and $\{\alpha\}$ are the participation factors of the orthogonal modes. The subscripts “ d ” and “ r ” hereinafter, respectively, represent the variables associated with the deformational motion and rigid body motion.

Accordingly, eigenequation (1) for a free-free structure has two kinds of eigenpairs.

- (1) N_r zero eigenvalues pertaining to the rigid body motions: the associated eigenvectors span the null space of the stiffness matrix \mathbf{K} , which contribute to the columns of \mathbf{R} . N_r is equal to the number of the statically determinate constraints required to prevent all rigid body motion [24].
- (2) $N_d = N - N_r$ nonzero eigenvalues λ_i ($i = 1, 2, \dots, N_d$): the associated orthogonal deformational eigenvectors $\Phi_d = [\phi_1 \ \phi_2 \ \cdots \ \phi_{N_d}]$ span the range space of \mathbf{K} .

The rigid body modes, and deformational modes satisfy the orthogonal condition of

$$\mathbf{R}^T \mathbf{M} \mathbf{R} = \mathbf{I}, \quad \Phi_d^T \mathbf{M} \Phi_d = \mathbf{I}, \quad \mathbf{R}^T \mathbf{M} \Phi_d = \mathbf{0}. \quad (7)$$

In this research, the rigid body modes are proposed to be formulated by the geometric node locations of the structure, other than being extracted from a shift eigensolver or determined by the null space of the rank deficient stiffness matrix.

For a two-dimensional structure having N nodes, the three independent rigid body modes are the x translation ($\mathbf{R}_x = 1$, $\mathbf{R}_y = 0$), the y translation ($\mathbf{R}_x = 0$, $\mathbf{R}_y = 1$), and the z rotation ($\mathbf{R}_x = -y$, $\mathbf{R}_y = x$); that is,

$$\mathbf{R}^T = \begin{bmatrix} 1 & 0 & 0 & 1 & \cdots & 0 & 0 \\ 0 & 1 & 0 & 0 & \cdots & 1 & 0 \\ -y_1 & x_1 & 1 & -y_2 & \cdots & x_N & 1 \end{bmatrix}. \quad (8)$$

The columns of \mathbf{R} can be orthogonalized and be normalized with respect to mass matrix [24].

2.2. The Formulation of a Well-Conditioned Eigenequation. As the eigenvalues associated with the rigid body modes are zeros, the stiffness matrix (3) of a free-free structure is rewritten by the deformational eigenmodes as

$$\mathbf{K} = \sum_{i=1}^N \lambda_i (\mathbf{M}\phi_i) (\mathbf{M}\phi_i)^T = \sum_{i=1}^{N_d} \lambda_i (\mathbf{M}\phi_i) (\mathbf{M}\phi_i)^T. \quad (9)$$

Mathematically, the flexibility matrix of a structure is defined as the inverse of the stiffness matrix, and it is expressed as $\mathbf{F} = \sum_{i=1}^N (1/\lambda_i) \phi_i \phi_i^T = \Phi \Lambda^{-1} \Phi^T$ (as (4)). Since the rigid body eigenvalues are zeros, the flexibility matrix is positive infinity for a free-free structure. Physically, the flexibility is defined as the displacement response of a structure when a unit force is applied to it. A unit force applied to a free-free structure will make the structure move freely. In this viewpoint, the flexibility matrix of a free-free structure does not exist and cannot be determined like the usually fixed structure in civil engineering [26]. Here, a modal flexibility matrix is employed which is contributed by the deformational modes solely as

$$\mathbf{F} = \sum_{i=1}^{N_d} \frac{1}{\lambda_i} \phi_i \phi_i^T = \Phi_d \Lambda_d^{-1} \Phi_d^T. \quad (10)$$

The stiffness matrix and modal flexibility matrix are orthogonal to the rigid body modes

$$\begin{aligned} \mathbf{K}\mathbf{R} &= \mathbf{R}^T \mathbf{K} = \mathbf{0}, \\ \mathbf{F}\mathbf{M}\mathbf{R} &= \mathbf{R}^T \mathbf{M}\mathbf{F} = \mathbf{0}. \end{aligned} \quad (11)$$

The stiffness matrix and modal flexibility matrix satisfy the relation of

$$\mathbf{K}\mathbf{F} = (\mathbf{M}\Phi_d \Lambda_d \Phi_d^T \mathbf{M}) (\Phi_d \Lambda_d^{-1} \Phi_d^T) = \mathbf{M}\Phi_d \Phi_d^T = \mathbf{I} - \mathbf{M}\mathbf{R}\mathbf{R}^T. \quad (12)$$

Mathematically, the stiffness matrix and modal flexibility matrix, which are formed from the deformational eigenmodes, are singular and rank deficient for a free-free structure. The stiffness matrix and modal flexibility matrix are Moore-Penrose pseudoinverse of each other. The extraction

of Moore-Penrose pseudoinverse is computationally expensive and not accurate. Herein, a new form of the stiffness and flexibility matrices is defined as

$$\begin{aligned} \bar{\mathbf{K}} &= \mathbf{K} + \alpha (\mathbf{M}\mathbf{R}) (\mathbf{M}\mathbf{R})^T = \mathbf{M} \left(\sum_{i=1}^{N_d} \lambda_i \phi_i \phi_i^T + \sum_{r=1}^{N_r} \alpha_r \phi_r \phi_r^T \right) \mathbf{M}, \\ \bar{\mathbf{F}} &= \mathbf{F} + \beta \mathbf{R}\mathbf{R}^T = \sum_{i=1}^{N_d} \frac{1}{\lambda_i} \phi_i \phi_i^T + \sum_{r=1}^{N_r} \beta_r \phi_r \phi_r^T, \end{aligned} \quad (13)$$

where $\bar{\mathbf{K}}$ and $\bar{\mathbf{F}}$ are well conditioned and full rank, and they are hereinafter called the generalized stiffness matrix and the generalized flexibility matrix, respectively. α_r and β_r are the participation factors of the rigid body modes to the generalized stiffness and flexibility matrices, with $\alpha_r > 0$ and $\beta_r > 0$ ($r = 1, 2, \dots, N_r$).

The generalized stiffness and flexibility matrices are related to the rigid body modes by

$$\begin{aligned} \bar{\mathbf{K}}\mathbf{R} &= \mathbf{R}^T \bar{\mathbf{K}} = \alpha \mathbf{M}\mathbf{R}, & \bar{\mathbf{F}}\mathbf{M}\mathbf{R} &= \mathbf{R}^T \mathbf{M}\bar{\mathbf{F}} = \beta \mathbf{R}, \\ \mathbf{R}^T \bar{\mathbf{K}}\mathbf{R} &= \alpha \mathbf{I}, & \mathbf{R}^T \mathbf{M}\bar{\mathbf{F}}\mathbf{M}\mathbf{R} &= \beta \mathbf{I}, \end{aligned} \quad (14)$$

$$\bar{\mathbf{K}}\bar{\mathbf{F}} = (\mathbf{K} + \alpha (\mathbf{M}\mathbf{R}) (\mathbf{M}\mathbf{R})^T) (\mathbf{F} + \beta \mathbf{R}\mathbf{R}^T) = \mathbf{K}\mathbf{F} + \alpha \beta \mathbf{M}\mathbf{R}\mathbf{R}^T. \quad (15)$$

In particular, if the participation factors are chosen as $\alpha_r = 1$, $\beta_r = 1$, ($r = 1, 2, \dots, N_r$), that is,

$$\bar{\mathbf{K}} = \mathbf{K} + (\mathbf{M}\mathbf{R}) (\mathbf{M}\mathbf{R})^T = \mathbf{M} \left(\sum_{i=1}^{N_d} \lambda_i \phi_i \phi_i^T + \sum_{r=1}^{N_r} \phi_r \phi_r^T \right) \mathbf{M} \quad (16a)$$

$$\bar{\mathbf{F}} = \mathbf{F} + \mathbf{R}\mathbf{R}^T = \sum_{i=1}^{N_d} \frac{1}{\lambda_i} \phi_i \phi_i^T + \sum_{r=1}^{N_r} \phi_r \phi_r^T, \quad (16b)$$

the generalized stiffness and flexibility matrices are related to the rigid body modes as

$$\bar{\mathbf{K}}\mathbf{R} = \mathbf{R}\bar{\mathbf{K}} = \mathbf{M}\mathbf{R}, \quad \bar{\mathbf{F}}\mathbf{M}\mathbf{R} = \mathbf{R}\mathbf{M}\bar{\mathbf{F}} = \mathbf{R} \quad (17)$$

$$\mathbf{R}\bar{\mathbf{K}}\mathbf{R} = \mathbf{I}, \quad \mathbf{R}\mathbf{M}\bar{\mathbf{F}}\mathbf{M}\mathbf{R} = \mathbf{I} \quad (18)$$

$$\begin{aligned} \bar{\mathbf{K}}\bar{\mathbf{F}} &= (\mathbf{K} + (\mathbf{M}\mathbf{R}) (\mathbf{M}\mathbf{R})^T) (\mathbf{F} + \mathbf{R}\mathbf{R}^T) \\ &= \mathbf{M}\Phi_d \Phi_d^T + \mathbf{M}\mathbf{R}\mathbf{R}^T = \mathbf{I}. \end{aligned} \quad (19)$$

Considering (19), the generalized stiffness matrix $\bar{\mathbf{K}}$ and generalized flexibility matrix $\bar{\mathbf{F}}$ are dual inverse of each other as

$$\begin{aligned} (\mathbf{K} + (\mathbf{M}\mathbf{R}) (\mathbf{M}\mathbf{R})^T)^{-1} &= \mathbf{F} + \mathbf{R}\mathbf{R}^T = \sum_{i=1}^{N_d} \frac{1}{\lambda_i} \phi_i \phi_i^T, \\ (\mathbf{F} + \mathbf{R}\mathbf{R}^T)^{-1} &= \mathbf{K} + (\mathbf{M}\mathbf{R}) (\mathbf{M}\mathbf{R})^T = \mathbf{M} \left(\sum_{i=1}^N \lambda_i \phi_i \phi_i^T \right) \mathbf{M}. \end{aligned} \quad (20)$$

The modal flexibility matrix is determined from the stiffness matrix by

$$\mathbf{F} = (\mathbf{K} + (\mathbf{MR})(\mathbf{MR})^T)^{-1} - \mathbf{RR}^T, \quad (21)$$

and the modal flexibility can be transformed into the stiffness matrix in the form of

$$\mathbf{K} = (\mathbf{F} + \mathbf{RR}^T)^{-1} - (\mathbf{MR})(\mathbf{MR})^T. \quad (22)$$

The generalized stiffness and flexibility matrices render a simple and effective transformation between the stiffness and modal flexibility matrices, avoiding the expensive pseudoinverse.

2.3. A Well-Conditioned Eigenproblem. The generalized stiffness matrix $\bar{\mathbf{K}}$ leads to the eigenequation

$$(\bar{\mathbf{K}} - \lambda \mathbf{M}) \boldsymbol{\Phi} = \mathbf{0}. \quad (23)$$

Equation (23) has the identical eigenvectors to those of (1), and only the eigenvalues of the rigid body modes are changed from 0 to 1. This well-conditioned eigenequation inherently avoids the zero eigenvalues, which leads to a faster and more accurate extraction of eigensolutions than the traditional strategy with a shift eigensolver [23]. Equation (23) extracts the real eigenvalues and eigenvectors of a free-free structure, whereas the eigenvalues of the rigid body modes are changed to 1.

The well-conditioned eigenequation can also be employed for the calculation of the eigenvalue derivatives and eigenvector derivatives using Nelson's method [27] or the modal method [28]. For the sake of simplicity, the detailed calculation of eigensensitivity will not be demonstrated here. The proposed method for eigensensitivity could be more efficient and accurate than the traditional method which introduces a small shift in the stiffness matrix to calculate the eigensensitivity of a free-free structure [23].

2.4. Calculation of Residual Flexibility and Its Derivative. In some forward substructuring methods [3–14], only a few lower modes of a substructure are calculated to assemble the global structure while the residual flexibility matrix is required for the compensation of the higher modes. In consequence, the residual flexibility and its derivative matrices are required for the calculation of the eigensolutions and eigensensitivity [9–12]. The detailed substructuring method will be described in the next section. Based on the proposed well-conditioned stiffness and flexibility matrices, the general formulation of the first-order and high-order residual flexibility matrices and their derivatives is derived in this section for a free-free structure.

2.4.1. Residual Flexibility. The complete eigenmodes of a structure are divided into the N_m master modes $\boldsymbol{\Phi}_m$, which are usually the lower modes of a structure, and the residual N_s slave modes $\boldsymbol{\Phi}_s$. For a free-free structure, the master modes $\boldsymbol{\Phi}_m$ include the N_r rigid body modes \mathbf{R} and the

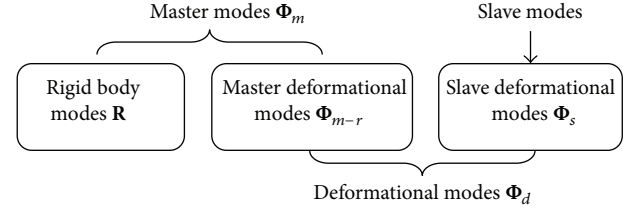


FIGURE 1: Division of master and slave modes in a substructure.

$(N_m - N_r)$ deformational master modes $\boldsymbol{\Phi}_{m-r}$. The relation between the master modes, slave modes, rigid body modes and deformational modes is described in Figure 1.

In the substructuring methods, only some master modes are calculated, while the slave modes are discarded and compensated with a residual flexibility. According to (21), the first-order residual flexibility matrix can be expressed by the generalized stiffness matrix and master modes as

$$\begin{aligned} \mathbf{G}_{(1)} &= \boldsymbol{\Phi}_s \boldsymbol{\Lambda}_s^{-1} \boldsymbol{\Phi}_s^T = (\mathbf{K} + (\mathbf{MR})(\mathbf{MR})^T)^{-1} - \boldsymbol{\Phi}_{m-r} \boldsymbol{\Lambda}_{m-r}^{-1} \boldsymbol{\Phi}_{m-r}^T \\ &\quad - \mathbf{RR}^T = \bar{\mathbf{K}}^{-1} - \boldsymbol{\Phi}_{m-r} \boldsymbol{\Lambda}_{m-r}^{-1} \boldsymbol{\Phi}_{m-r}^T - \mathbf{RR}^T. \end{aligned} \quad (24)$$

The second-order residual flexibility matrix can be expressed in terms of the generalized stiffness matrix and master modes as

$$\begin{aligned} \mathbf{G}_{(2)} &= \boldsymbol{\Phi}_s \boldsymbol{\Lambda}_s^{-2} \boldsymbol{\Phi}_s^T = (\boldsymbol{\Phi}_s \boldsymbol{\Lambda}_s^{-1} \boldsymbol{\Phi}_s^T) \mathbf{M} (\boldsymbol{\Phi}_s \boldsymbol{\Lambda}_s^{-1} \boldsymbol{\Phi}_s^T) \\ &\quad = \bar{\mathbf{K}}^{-1} \mathbf{M} \bar{\mathbf{K}}^{-1} - \boldsymbol{\Phi}_{m-r} \boldsymbol{\Lambda}_{m-r}^{-2} \boldsymbol{\Phi}_{m-r}^T - \mathbf{RR}^T. \end{aligned} \quad (25)$$

In general, the k -order residual flexibility is given by

$$\begin{aligned} \mathbf{G}_{(k)} &= \boldsymbol{\Phi}_s \boldsymbol{\Lambda}_s^{-k} \boldsymbol{\Phi}_s^T = (\boldsymbol{\Phi}_s \boldsymbol{\Lambda}_s^{-1} \boldsymbol{\Phi}_s^T) (\mathbf{M} (\boldsymbol{\Phi}_s \boldsymbol{\Lambda}_s^{-1} \boldsymbol{\Phi}_s^T))^{k-1} \\ &\quad = \bar{\mathbf{K}}^{-1} (\mathbf{M} \bar{\mathbf{K}}^{-1})^{k-1} - \boldsymbol{\Phi}_{m-r} \boldsymbol{\Lambda}_{m-r}^{-k} \boldsymbol{\Phi}_{m-r}^T - \mathbf{RR}^T, \end{aligned} \quad (26)$$

where the subscript k indicates the k th-order residual flexibility.

Due to the orthogonal properties of the eigenmodes, the k th-order residual flexibility can also be generally expressed by the lower-order residual flexibility matrices as

$$\mathbf{G}_{(k)} = \mathbf{G}_{(1)} \mathbf{M} \mathbf{G}_{(k-1)} = \mathbf{G}_{(1)} (\mathbf{M} \mathbf{G}_{(1)})^{k-1} \quad (27a)$$

or

$$\mathbf{G}_{(k)} = \mathbf{G}_{(c)} \mathbf{M} \mathbf{G}_{(k-c)} = \mathbf{G}_{(c)} (\mathbf{M} \mathbf{G}_{(1)})^{k-c} \quad (c = 1, 2, \dots, k). \quad (27b)$$

2.4.2. Derivative of the Residual Flexibility. Differentiating (24) with respect to an elemental parameter a , the derivative

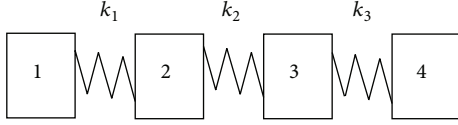


FIGURE 2: The spring-mass model under free-free condition.

matrix of the first-order residual flexibility can be expressed by the generalized stiffness matrix and master modes as

$$\begin{aligned} \frac{\partial \mathbf{G}_{(1)}}{\partial a} &= \frac{\partial (\Phi_s \Lambda_s^{-1} \Phi_s^T)}{\partial a} \\ &= \frac{\partial (\mathbf{K} + (\mathbf{MR})(\mathbf{MR})^T)^{-1}}{\partial a} - \frac{\partial (\Phi_{m-r} \Lambda_{m-r}^{-1} \Phi_{m-r}^T)}{\partial a} \\ &= -\bar{\mathbf{K}}^{-2} \frac{\partial \mathbf{K}}{\partial a} - \left(2\Phi_{m-r} \Lambda_{m-r}^{-1} \frac{\partial (\Phi_{m-r}^T)}{\partial a} \right. \\ &\quad \left. + \Phi_{m-r} \frac{\partial (\Lambda_{m-r}^{-1})}{\partial a} \Phi_{m-r}^T \right). \end{aligned} \quad (28)$$

In general, the k th-order residual flexibility (26) has the derivative matrix

$$\begin{aligned} \frac{\partial \mathbf{G}_{(k)}}{\partial a} &= \frac{\partial (\Phi_s \Lambda_s^{-k} \Phi_s^T)}{\partial a} \\ &= \frac{\partial (\bar{\mathbf{K}}^{-1} (\mathbf{M}\bar{\mathbf{K}}^{-1})^{k-1})}{\partial a} \\ &\quad - \left(2\Phi_{m-r} \Lambda_{m-r}^{-k} \frac{\partial (\Phi_{m-r}^T)}{\partial a} + \Phi_{m-r} \frac{\partial (\Lambda_{m-r}^{-k})}{\partial a} \Phi_{m-r}^T \right). \end{aligned} \quad (29)$$

According to (27a), the derivative of the k th-order residual flexibility can also be obtained by those of the lower order residual flexibility matrices as

$$\begin{aligned} \frac{\partial \mathbf{G}_{(k)}}{\partial a} &= \frac{\partial \mathbf{G}_{(1)}}{\partial a} \mathbf{M} \mathbf{G}_{(k-1)} + \mathbf{G}_{(1)} \mathbf{M} \frac{\partial \mathbf{G}_{(k-1)}}{\partial a}, \\ \frac{\partial \mathbf{G}_{(k)}}{\partial a} &= \frac{\partial \mathbf{G}_{(c)}}{\partial a} \mathbf{M} \mathbf{G}_{(k-c)} + \mathbf{G}_{(c)} \mathbf{M} \frac{\partial \mathbf{G}_{(k-c)}}{\partial a} \end{aligned} \quad (30)$$

$(c = 1, 2, \dots, k).$

2.5. Illustrative Example: Spring-Mass Model. A four-DOF spring-mass model without constraint (Figure 2) is employed to illustrate the formulation of the modal flexibility and residual flexibility from the proposed well-conditioned stiffness matrix.

The stiffness parameters of the three springs are set to $k_1 = k_2 = k_3 = 20$ N/m. The four masses are set to $m_1 = 1$ kg, $m_2 = 2$ kg, $m_3 = 2$ kg, and $m_4 = 1$ kg. The stiffness matrix of the model is

$$\mathbf{K} = \begin{bmatrix} 20 & -20 & 0 & 0 \\ -20 & 40 & -20 & 0 \\ 0 & -20 & 40 & -20 \\ 0 & 0 & -20 & 20 \end{bmatrix}. \quad (31)$$

The stiffness matrix is singular and rank deficient. To form the proposed full-rank stiffness matrix, the mass normalized rigid body mode is constructed according to (8) and is given by

$$\mathbf{R}^T = [0.4082 \quad 0.4082 \quad 0.4082 \quad 0.4082]. \quad (32)$$

In consequence, the generalized stiffness matrix is formed as

$$\begin{aligned} \bar{\mathbf{K}} &= \mathbf{K} + (\mathbf{MR})(\mathbf{MR})^T \\ &= \begin{bmatrix} 20.1667 & -19.6667 & 0.3333 & -0.1667 \\ -19.6667 & 40.6667 & -19.3333 & 0.3333 \\ 0.3333 & -19.3333 & 40.6667 & -19.6667 \\ 0.1667 & 0.3333 & -19.6667 & 20.1667 \end{bmatrix}. \end{aligned} \quad (33)$$

The eigenequation $(\bar{\mathbf{K}} - \lambda \mathbf{M})\Phi = \mathbf{0}$ leads to the eigenvalues and eigenvectors

$$\begin{aligned} \Lambda &= \begin{bmatrix} 1 & 0 & 0 & 0 \\ 0 & 10 & 0 & 0 \\ 0 & 0 & 30 & 0 \\ 0 & 0 & 0 & 40 \end{bmatrix}, \\ \Phi_d &= \begin{bmatrix} 0.4082 & -0.5774 & 0.5774 & 0.4082 \\ 0.4082 & -0.2887 & -0.2887 & -0.4082 \\ 0.4082 & 0.2887 & 0.2887 & 0.4082 \\ 0.4082 & 0.5774 & -0.5774 & -0.4082 \end{bmatrix}. \end{aligned} \quad (34)$$

The eigenequation formulated by the generalized stiffness matrix $\bar{\mathbf{K}}$ is full rank and well conditioned. The eigenvalue of the rigid body mode is 1 as expected.

If the first three modes are chosen as the master modes, the residual flexibility is formulated by the generalized stiffness matrix as

$$\begin{aligned} \mathbf{G} &= \bar{\mathbf{K}}^{-1} - \sum_{i=2,3} \frac{1}{\lambda_i} \phi_i \phi_i^T - \mathbf{R} \mathbf{R}^T \\ &= \begin{bmatrix} 0.0042 & -0.0042 & 0.0042 & -0.0042 \\ -0.0042 & 0.0042 & -0.0042 & 0.0042 \\ 0.0042 & -0.0042 & 0.0042 & -0.0042 \\ -0.0042 & 0.0042 & -0.0042 & 0.0042 \end{bmatrix}. \end{aligned} \quad (35)$$

3. Substructure-Based Model Updating

In the sensitivity-based model updating procedure, the general objective function combining the modal properties of

the frequencies and the mode shapes is usually denoted by [29, 30]

$$J(r) = \sum_i W_{\lambda_i}^2 [\lambda_i(\{a\})^M - \lambda_i^E]^2 + \sum_i W_{\phi_i}^2 \sum_j [\phi_{ji}(\{a\})^M - \phi_{ji}^E]^2, \quad (36)$$

where λ_i^E represents the i th experimental frequencies and ϕ_{ji}^E is the i th experimental mode shape at the j th point. λ_i^M and ϕ_{ji}^M denote the corresponding frequencies and mode shapes from the analytical FE model, which are expressed as the function of the uncertain physical parameters $\{a\}$. $W_{\lambda_i}^2$ and $W_{\phi_i}^2$ are the weight coefficients due to the different measurement accuracy of the frequencies and mode shapes.

The eigensolutions are used to form the objective function. The objective function, formed from the residuals between the eigensolutions of the FE model and the modal properties of the practical structures, is minimized by adjusting continuously the parameters $\{a\}$ of the initial FE model through the optimization searching techniques. The eigensensitivity calculates the changes in the eigensolutions caused by the perturbations of the design parameters of a structural model. It serves for indicating the searching direction of an optimization algorithm, which endows the more sensitive parameter (with respect to the objective function) a higher priority.

3.1. Substructure Method to Eigensolutions. The global structure with N DOF is divided into N_s substructures. Treating the j th substructure of $n^{(j)}$ DOF ($j = 1, 2, \dots, N_s$) as an independent structure, it has the stiffness matrix $\mathbf{K}^{(j)}$ and mass matrix $\mathbf{M}^{(j)}$. If the j th substructure is a free-free structure after division, the stiffness matrix $\mathbf{K}^{(j)}$ is singular and rank deficient. Then the generalized stiffness matrix $\bar{\mathbf{K}}^{(j)}$ is used for the free-free substructure, replacing the stiffness matrix $\mathbf{K}^{(j)}$. The eigenequation for the j th substructure is written as

$$(\mathbf{K}^{(j)} - \lambda^{(j)}\mathbf{M}^{(j)})\Phi^{(j)} = \mathbf{0}. \quad (37)$$

It is noted that $\bar{\mathbf{K}}^{(j)}$ is used in (37) for a free-free substructure, replacing the stiffness matrix $\mathbf{K}^{(j)}$. Hereinafter, only $\mathbf{K}^{(j)}$ is used in the formula for clearance, and it means the proposed generalized stiffness matrix ($\bar{\mathbf{K}}^{(j)}$) for a free-free substructure. The substructural eigenequation has $n^{(j)}$ pairs of eigenvalues and eigenvectors, which are orthogonal to the stiffness and mass matrices as [5]

$$\begin{aligned} \Lambda^{(j)} &= \text{Diag} [\lambda_1^{(j)}, \lambda_2^{(j)}, \dots, \lambda_{n^{(j)}}^{(j)}], \\ \Phi^{(j)} &= [\phi_1^{(j)}, \phi_2^{(j)}, \dots, \phi_{n^{(j)}}^{(j)}], \\ [\Phi^{(j)}]^T \mathbf{K}^{(j)} \Phi^{(j)} &= \Lambda^{(j)}, \\ [\Phi^{(j)}]^T \mathbf{M}^{(j)} \Phi^{(j)} &= \mathbf{I}^{(j)}, \\ (j &= 1, 2, \dots, N_s). \end{aligned} \quad (38)$$

Based on the principle of virtual work and geometric compatibility, the substructuring method [5, 8] reconstructs the eigensolutions of the global structure by imposing the constraints at the interfaces as

$$\begin{bmatrix} \Lambda^P - \bar{\lambda}\mathbf{I} & -\Gamma \\ -\Gamma^T & \mathbf{0} \end{bmatrix} \begin{Bmatrix} \mathbf{z} \\ \boldsymbol{\tau} \end{Bmatrix} = \begin{Bmatrix} \mathbf{0} \\ \mathbf{0} \end{Bmatrix}. \quad (39a)$$

In this equation,

$$\Gamma = [\mathbf{C}\Phi^P]^T,$$

$$\Lambda^P = \text{Diag} [\Lambda^{(1)}, \Lambda^{(2)}, \dots, \Lambda^{(N_s)}], \quad (39b)$$

$$\Phi^P = \text{Diag} [\Phi^{(1)}, \Phi^{(2)}, \dots, \Phi^{(N_s)}],$$

where \mathbf{C} is a rectangular connection matrix constraining the interface DOF of the adjacent substructures to move jointly [5]. $\boldsymbol{\tau}$ is the internal connection forces of the adjacent substructures. $\bar{\lambda}$ is the eigenvalue of the global structure. \mathbf{z} acts as the participation factor of the substructural eigenmodes, and the eigenvectors of the global structure can be recovered by $\bar{\Phi} = \Phi^P \{\mathbf{z}\}$. Superscript “ p ” denotes the diagonal assembly of the independent substructural matrices before constraining the independent substructures at the interfaces.

From the viewpoint of energy conservation, all modes of the substructures contribute to the eigenmodes of the global structure; that is, the complete eigensolutions of all substructures are required to assemble the primitive form of Λ^P and Φ^P . It is inefficient and not worthwhile to calculate all modes of the substructures, as only a few eigenmodes are generally of interest for a large-scale structure. To overcome this difficulty, only the master modes, corresponding to the lower vibration modes, are calculated to assemble the eigenequation of the global structure, while the slave modes (residual higher modes) are discarded and compensated by the residual flexibility in the later calculations. From here on, subscripts “ m ” and “ s ” will denote the “master” and “slave” modes, respectively.

Eigenequation (39a) and (39b) is rewritten according to the master modes and slave modes as

$$\begin{bmatrix} \Lambda_m^P - \bar{\lambda}\mathbf{I} & \mathbf{0} & -\Gamma_m \\ \mathbf{0} & \Lambda_s^P - \bar{\lambda}\mathbf{I} & -\Gamma_s \\ -\Gamma_m^T & -\Gamma_s^T & \mathbf{0} \end{bmatrix} \begin{Bmatrix} \mathbf{z}_m \\ \mathbf{z}_s \\ \boldsymbol{\tau} \end{Bmatrix} = \begin{Bmatrix} \mathbf{0} \\ \mathbf{0} \\ \mathbf{0} \end{Bmatrix}, \quad (40)$$

where $\Gamma_m = [\mathbf{C}\Phi_m^P]^T$, $\Gamma_s = [\mathbf{C}\Phi_s^P]^T$, Λ_m^P and Φ_m^P include the master eigenvalues and eigenvectors of the independent substructures, Λ_s^P and Φ_s^P include the slave eigenvalues and eigenvectors of the independent substructures, and \mathbf{z}_m and \mathbf{z}_s are the mode participation factors of the master modes and slave modes.

With the second line of (40), the slave part of the mode participation factor can be expressed as

$$\mathbf{z}_s = (\Lambda_s^P - \bar{\lambda}\mathbf{I})^{-1} \Gamma_s \boldsymbol{\tau}. \quad (41)$$

Substituting (41) into (40) gives

$$\begin{bmatrix} \Lambda_m^p - \bar{\lambda}\mathbf{I} & -\Gamma_m \\ -\Gamma_m^T & -\Gamma_s^T(\Lambda_s^p - \bar{\lambda}\mathbf{I})^{-1}\Gamma_s \end{bmatrix} \begin{Bmatrix} \mathbf{z}_m \\ \tau \end{Bmatrix} = \begin{Bmatrix} \mathbf{0} \\ \mathbf{0} \end{Bmatrix}. \quad (42)$$

In (42), Taylor expansion of the nonlinear item $(\Lambda_s^p - \bar{\lambda}\mathbf{I})^{-1}$ has

$$(\Lambda_s^p - \bar{\lambda}\mathbf{I})^{-1} = (\Lambda_s^p)^{-1} + \bar{\lambda}(\Lambda_s^p)^{-2} + \bar{\lambda}^2(\Lambda_s^p)^{-3} + \dots. \quad (43)$$

In general, the required eigenvalues $\bar{\lambda}$ correspond to the lowest modes of the global structure and are far less than the values in Λ_s^p when the master modes are appropriately chosen. In that case, retaining only the first item of the

Taylor expansion gives $\Gamma_s^T(\Lambda_s^p - \bar{\lambda}\mathbf{I})^{-1}\Gamma_s \approx \Gamma_s^T(\Lambda_s^p)^{-1}\Gamma_s$. In consequence, (42) is reduced into [5]

$$[(\Lambda_m^p - \bar{\lambda}\mathbf{I}_m) + \Gamma_m\zeta^{-1}\Gamma_m^T]\mathbf{z}_m = \mathbf{0}, \quad (44a)$$

$$\zeta = \Gamma_s^T(\Lambda_s^p)^{-1}\Gamma_s. \quad (44b)$$

The size of the reduced eigenequation (44a) and (44b) is equal to the number of the retained master modes $NP_m \times NP_m$, which is much smaller than the original one of $NP \times NP$ in (39a) and (39b). $\bar{\lambda}$ and \mathbf{z}_m can be solved from this reduced eigenequation using the common eigensolvers. As before, the eigenvalues of the global structure are $\bar{\lambda}$, and the eigenvectors of the global structure are recovered by $\bar{\Phi} = \Phi_m^p \mathbf{z}_m$. $\zeta = \Gamma_s^T(\Lambda_s^p)^{-1}\Gamma_s$ is associated with the first-order residual flexibility that can be calculated using the master modes of the substructures as

$$\Gamma_s^T(\Lambda_s^p)^{-1}\Gamma_s = \mathbf{C}\Phi_s^p(\Lambda_s^p)^{-1}[\Phi_s^p]^T\mathbf{C}^T,$$

$$\Phi_s^p(\Lambda_s^p)^{-1}[\Phi_s^p]^T = \begin{bmatrix} (\mathbf{K}^{(1)})^{-1} - \Phi_m^{(1)}(\Lambda_m^{(1)})^{-1}[\Phi_m^{(1)}]^T & \mathbf{0} & \mathbf{0} \\ \mathbf{0} & \ddots & \mathbf{0} \\ \mathbf{0} & \mathbf{0} & (\mathbf{K}^{(N_s)})^{-1} - \Phi_m^{(N_s)}(\Lambda_m^{(N_s)})^{-1}[\Phi_m^{(N_s)}]^T \end{bmatrix}. \quad (45)$$

3.2. Eigensensitivity with Substructuring Method. The eigensensitivity of the i th mode ($i = 1, 2, \dots, N$) with respect to an elemental parameter will be derived in this section. The elemental parameter is chosen to be the stiffness parameter, such as the bending rigidity of an element, and denoted by parameter a in the A th substructure. The reduced eigenequation (44a) and (44b) is rewritten for the i th mode as

$$[(\Lambda_m^p - \bar{\lambda}_i\mathbf{I}_m) + \Gamma_m\zeta^{-1}\Gamma_m^T]\{\mathbf{z}_i\} = \{\mathbf{0}\}. \quad (46)$$

Equation (46) is differentiated with respect to parameter a as

$$\begin{aligned} & [(\Lambda_m^p - \bar{\lambda}_i\mathbf{I}_m) + \Gamma_m\zeta^{-1}\Gamma_m^T] \frac{\partial\{\mathbf{z}_i\}}{\partial a} \\ & + \frac{\partial[(\Lambda_m^p - \bar{\lambda}_i\mathbf{I}_m) + \Gamma_m\zeta^{-1}\Gamma_m^T]}{\partial a} \{\mathbf{z}_i\} = \{\mathbf{0}\}. \end{aligned} \quad (47)$$

Since $[(\Lambda_m^p - \bar{\lambda}_i\mathbf{I}_m) + \Gamma_m\zeta^{-1}\Gamma_m^T]$ is symmetric, premultiplying $\{\mathbf{z}_i\}^T$ on both sides of (47) gives the eigenvalue derivative of the i th mode as

$$\frac{\partial\bar{\lambda}_i}{\partial a} = \{\mathbf{z}_i\}^T \left[\frac{\partial\Lambda_m^p}{\partial a} + \frac{\partial(\Gamma_m\zeta^{-1}\Gamma_m^T)}{\partial a} \right] \{\mathbf{z}_i\}, \quad (48)$$

where

$$\frac{\partial(\Gamma_m\zeta^{-1}\Gamma_m^T)}{\partial a} = \frac{\partial\Gamma_m}{\partial a}\zeta^{-1}\Gamma_m^T - \Gamma_m\zeta^{-1}\frac{\partial\zeta}{\partial a}\zeta^{-1}\Gamma_m^T + \Gamma_m\zeta^{-1}\frac{\partial\Gamma_m^T}{\partial a}. \quad (49)$$

In this equation, the derivative matrices $\partial\Lambda_m^p/\partial a$, $\partial\Gamma_m/\partial a$, and $\partial\zeta/\partial a$ are formed using the eigenvalue derivatives, eigenvector derivatives, and residual flexibility derivatives of the substructures. Since the substructures are independent, these derivative matrices are calculated within the A th substructure solely, while those in other substructures are zeros; that is,

$$\frac{\partial\Lambda_m^p}{\partial a} = \begin{bmatrix} \mathbf{0} & \mathbf{0} & \mathbf{0} \\ \mathbf{0} & \frac{\partial\Lambda_m^{(A)}}{\partial a} & \mathbf{0} \\ \mathbf{0} & \mathbf{0} & \mathbf{0} \end{bmatrix},$$

$$\frac{\partial\Gamma_m^T}{\partial a} = \mathbf{C} \frac{\partial\Phi_m^p}{\partial a} = \mathbf{C} \begin{bmatrix} \mathbf{0} & \mathbf{0} & \mathbf{0} \\ \mathbf{0} & \frac{\partial\Phi_m^{(A)}}{\partial a} & \mathbf{0} \\ \mathbf{0} & \mathbf{0} & \mathbf{0} \end{bmatrix}$$

$$\frac{\partial\zeta}{\partial a} = \mathbf{C}$$

$$\begin{aligned} & \times \text{Diag} \begin{bmatrix} \mathbf{0} & \mathbf{0} & \mathbf{0} \\ \mathbf{0} & \frac{\partial((\mathbf{K}^{(A)})^{-1} - \Phi_m^{(A)}(\Lambda_m^{(A)})^{-1}[\Phi_m^{(A)}]^T)}{\partial a} & \mathbf{0} \\ \mathbf{0} & \mathbf{0} & \mathbf{0} \end{bmatrix} \\ & \times \mathbf{C}^T. \end{aligned} \quad (50)$$

$\{\mathbf{z}_i\}$, Γ_m , and ζ^{-1} have been computed in the previous section for eigensolutions and can be reused here directly. $\partial\Lambda_m^{(A)}/\partial a$ and $\partial\Phi_m^{(A)}/\partial a$ are the eigensolution derivatives of the master

modes in the A th substructures. They can be calculated with common methods, such as Nelson's method [27], by treating the A th substructure as one independent structure. Subsequently, the eigenvalue derivative of the global structure can be obtained from (48), and it solely relies on a particular substructure (the A th substructure).

The eigenvectors of the global structure are recovered by $\bar{\Phi} = \Phi_m^p \mathbf{z}_m$. Hence, the i th eigenvector of the global structure can be expressed as

$$\bar{\Phi}_i = \Phi_m^p \{\mathbf{z}_i\}. \quad (51)$$

Differentiating (51) with respect to the elemental parameter a , one can obtain the eigenvector derivative of the i th mode as

$$\frac{\partial \bar{\Phi}_i}{\partial a} = \frac{\partial \Phi_m^p}{\partial a} \{\mathbf{z}_i\} + \Phi_m^p \left\{ \frac{\partial \mathbf{z}_i}{\partial a} \right\}. \quad (52)$$

In (52), Φ_m^p and $\{\mathbf{z}_i\}$ have been obtained when calculating the eigensolutions. $\partial \Phi_m^p / \partial a$ is associated with the eigenvector derivatives of the A th substructure as (50). $\{\partial \mathbf{z}_i / \partial a\}$ can be obtained from the reduced eigenequation (47), as described in the following.

$\{\partial \mathbf{z}_i / \partial a\}$ is separated into the sum of a particular part and a homogeneous part as

$$\left\{ \frac{\partial \mathbf{z}_i}{\partial a} \right\} = \{v_i\} + c_i \{\mathbf{z}_i\}, \quad (53)$$

where c_i is a participation factor. Substituting (53) into (47) gives

$$\Psi \{v_i\} = \{Y_i\}, \quad (54a)$$

where

$$\Psi = [(\Lambda_m^p - \bar{\lambda}_i \mathbf{I}_m) + \Gamma_m \varsigma^{-1} \Gamma_m^T], \quad (54b)$$

$$\{Y_i\} = -\frac{\partial [(\Lambda_m^p - \bar{\lambda}_i \mathbf{I}_m) + \Gamma_m \varsigma^{-1} \Gamma_m^T]}{\partial a} \{\mathbf{z}_i\}.$$

Since the items in Ψ and $\{Y_i\}$ are available when calculating the eigenvalue derivatives, the vector $\{v_i\}$ can be solved from (54a) and (54b) effortlessly.

The eigenvector $\{\mathbf{z}_i\}$ of the reduced eigenequation (44a) and (44b) satisfies the orthogonal condition of

$$\{\mathbf{z}_i\}^T \{\mathbf{z}_i\} = 1. \quad (55)$$

Differentiating (55) with respect to a gives

$$\frac{\partial \{\mathbf{z}_i\}^T}{\partial a} \{\mathbf{z}_i\} + \{\mathbf{z}_i\}^T \frac{\partial \{\mathbf{z}_i\}}{\partial a} = 0. \quad (56)$$

Substituting (53) into (56), the participation factor c_i is therefore obtained as

$$c_i = -\frac{1}{2} \left(\{v_i\}^T \{\mathbf{z}_i\} + \{\mathbf{z}_i\}^T \{v_i\} \right). \quad (57)$$

After the vector $\{v_i\}$ and the factor c_i have been achieved, the eigenvector derivative of the global structure can be calculated from (52). Since the reduced eigenequation (44a) and (44b) is smaller in size compared to that of the global structure, calculation of $\{\partial \mathbf{z}_i / \partial a\}$ can be processed much faster than that in the conventional Nelson's method [27]. As calculation of the eigenvector derivatives dominates the whole model updating process, the substructuring method will improve the computational efficiency significantly [9, 11, 12].

With the proposed substructuring method, the eigenvalue and eigenvector derivatives with respect to an elemental parameter are computed solely within the substructure that contains the element, whereas the derivative matrices of all other substructures with respect to the parameter are zero, thus allowing a significant reduction in computational cost.

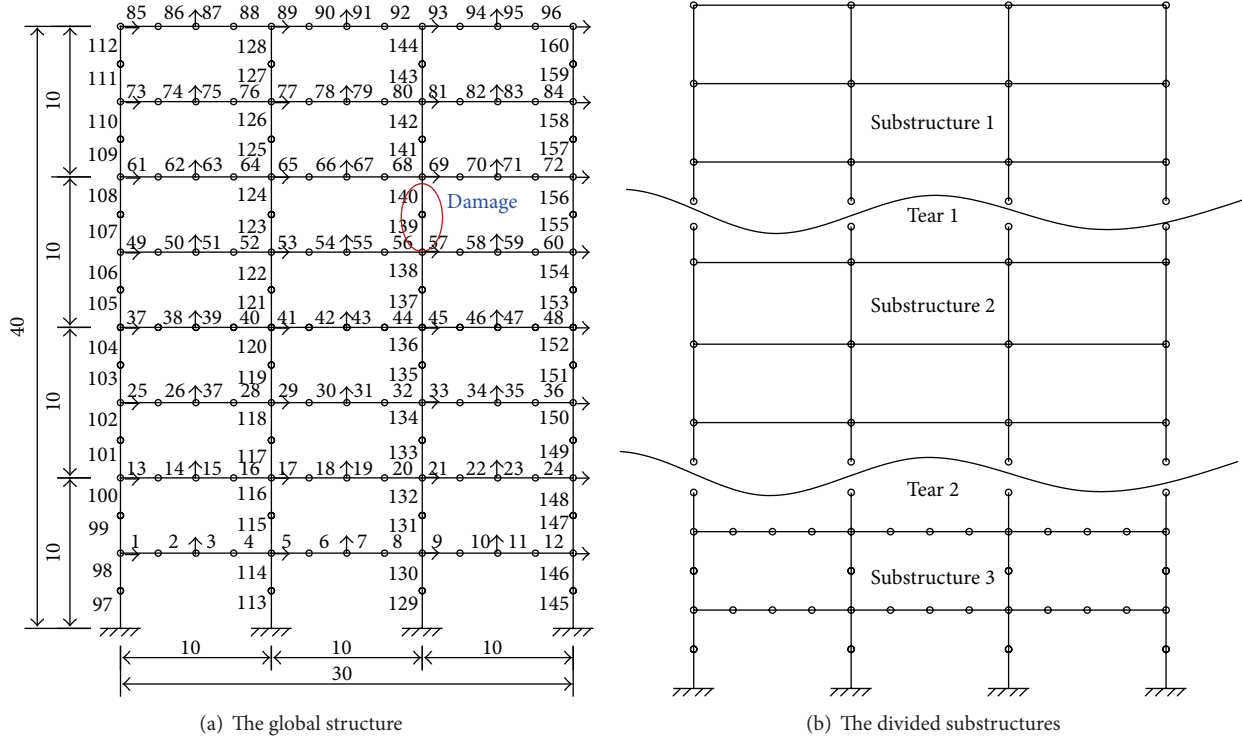
Based on the proposed full-rank well-conditioned substructural eigenequation, the substructure-based model updating is proceeded by the following procedure.

- (1) Divide the global structure into several manageable substructures.
- (2) Calculate the rigid body modes (\mathbf{R}) for the free-free substructures according to (8).
- (3) Construct the generalized stiffness matrix for the free-free substructures by $\bar{\mathbf{K}} = \mathbf{K} + (\mathbf{MR})(\mathbf{MR})^T$.
- (4) Construct the full-rank well-conditioned substructural eigenequation for the free-free substructures as (23). Based on the full-rank well-conditioned substructural eigenequation, the substructural eigensolutions and eigensensitivity of the master mode are calculated for the free-free substructures.
- (5) Calculate the generalized flexibility for the free-free substructures by $\bar{\mathbf{F}} = \mathbf{F} + \mathbf{RR}^T$. Based on the generalized flexibility matrix, the residual flexibility and its derivatives are calculated for the free-free substructures.
- (6) Based on the substructural eigensolutions, eigensensitivity, and residual flexibility, the eigensolutions of the global structure is calculated by (44a) and (44b), and eigensensitivity of the global structure are calculated by (48) and (52). The eigensolutions of the global structure are used to construct the objective function in the model updating process, while the eigensensitivity is used for indicating the searching direction of the optimization process.

The accuracy and efficiency of the full-rank well-conditioned substructural eigenequation in substructure-based model updating will be investigated by two examples in the following section.

4. Case Studies

4.1. Three-Span Frame Structure. The accuracy of the proposed well-conditioned eigenequation for calculation of substructural residual flexibility, eigensolutions, and eigensensitivity will be illustrated by a frame structure. The global frame


 FIGURE 3: The frame structure. \rightarrow : the points and directions of experimental measurement.

is shown in Figure 3. The material constants are chosen as bending rigidity (EI) = $170 \times 10^6 \text{ Nm}^2$, axial rigidity (EA) = $2500 \times 10^6 \text{ N}$, mass per unit length (ρA) = 110 kg/m , and Poisson's ratio = 0.3 . The frame is discretized into 160 two-dimensional beam elements each 2.5 m long, which results in 140 nodes and 408 DOF ($N = 408$). The frame is disassembled into three substructures ($N_s = 3$) when it is torn at 8 nodes as shown in Figure 3. After division, there are 51, 55, and 42 nodes in the three substructures with the DOF of $n_1 = 153$, $n_2 = 165$, and $n_3 = 114$, respectively.

In this example, the first substructure is analyzed to investigate the accuracy of the proposed well-conditioned eigensolver in calculation of substructural eigensolutions and eigensensitivity for a free-free substructure. The first substructure has 153 DOF. The first 30 modes are calculated as the master modes to assemble the eigenequation of the global structure, and the other slave modes are compensated by the residual flexibility. As the first substructure is free after partition, the system matrices of the first substructure are singular and rankdeficient. Traditionally, the Moore-Penrose pseudoinverse is usually used for the analysis of rank-deficient eigenequation to avoid the ill-conditioned eigenproblem. In the following, the results of the proposed well-conditioned eigenequation will be compared with the two traditional methods to investigate its accuracy in analysis of the free-free substructures.

First, the substructural eigensolutions and eigensensitivity are calculated from the proposed well-conditioned eigenequation. The mode shapes of the rigid body modes are

calculated from the geometric node locations of the first substructure according to (8). The well-conditioned eigenequation is formulated from (23). Based on the well-conditioned eigenequation, the eigensolutions of the first substructure are calculated. Since the zero-frequency eigensolutions are usually difficult to be accurately calculated, only the zero-frequency eigensolutions are listed in Table 1. The two-dimension substructure contains three rigid body modes. The eigenvalues of all the three rigid body modes are exactly 1 as expected. The proposed stiffness matrix $\bar{\mathbf{K}}^{(1)}$ is well conditioned and full rank, based on which the residual flexibility is calculated from $G = (\bar{\mathbf{K}}^{(1)})^{-1} - \Phi_m^{(1)}(\Lambda_m^{(1)})^{-1}[\Phi_m^{(1)}]^T$. For comparison, all the eigensolutions of the first substructure are calculated, and the residual flexibility directly from the slave modes $\tilde{G} = \Phi_s^{(1)}(\Lambda_s^{(1)})^{-1}[\Phi_s^{(1)}]^T$ is regarded as exact. The accuracy of the proposed substructure method in calculation of the residual flexibility is evaluated by the difference of the residual flexibility in terms of

$$\text{diff}(G) = \frac{\text{norm}(G - \tilde{G})}{\text{norm}(\tilde{G})}, \quad (58)$$

where G is the residual flexibility calculated from the substructural stiffness matrix and master modes and \tilde{G} is the actual residual flexibility calculated from the slave modes. The difference of the residual flexibility between the proposed method and the exact one is 0.0% as shown in Table 1. The proposed method is exact in calculation of the substructural

TABLE 1: Accuracy of the rigid body eigenvalues and the residual flexibility of the first substructure.

	With the proposed well-conditioned eigenequation		With Moore-Penrose pseudo-inverse for rank-deficient matrix		With a small shift for rank-deficient matrix	
	Eigenvalue	Inverse of eigenvalue	Eigenvalue	Inverse of eigenvalue	Eigenvalue	Inverse of eigenvalue
Rigid body modes	1.00	1.00	$1.48E - 09$	$6.74E + 08$	0.1	10
	1.00	1.00	$4.62E - 09$	$2.17E + 08$	0.1	10
	1.00	1.00	$1.64E - 08$	$6.07E + 07$	0.1	10
Error of residual flexibility	0.00%		0.30%		1.60%	

residual flexibility and eigensolutions. Based on the accurate eigensolutions and residual flexibility, the substructural eigensensitivity can be accurately calculated by common methods [10, 27].

Afterwards, the substructural solutions are calculated from the rank-deficient eigenequation directly by MATLAB eigensolver, in which the Moore-Penrose pseudoinverse is used for the singular and rank-deficient matrix. The eigensolutions are obtained and the zero-frequency eigensolutions are listed in Table 1. Due to the numerical roundoffs, the rigid body modes are not perfect 0.0 Hz frequencies, and the rigid body eigenvalue is about 10^{-8} . The inverse of the rigid body eigenvalues $(\Lambda_m^{(1)})^{-1}$ is a large value with order of 10^8 . The residual flexibility is calculated by $G = (\mathbf{K}^{(1)})^+ - \Phi_m^{(1)}(\Lambda_m^{(1)})^{-1}[\Phi_m^{(1)}]^T$, in which the inverse of the stiffness matrix is calculated from Moore-Penrose pseudoinverse. In consequence, the residual flexibility is calculated based on the Moore-Penrose pseudoinverse of the stiffness matrix and the inaccurate inverse of the eigenvalues. The difference in the residual flexibility between the proposed method and the exact ones is 0.3% in terms of (58). The accuracy of the eigensolutions and residual flexibility is significantly sensitive to the rank condition when carried out in floating-point arithmetic.

Finally, the substructural eigensolutions and eigensensitivity are calculated from the rank-deficient eigenequation with a small shift introduced. The small shift is set to be 0.1, and the eigenvalues for the rigid body modes are 0.1 as shown in Table 1. The residual flexibility is calculated by

$$\begin{aligned} \Phi_s \Lambda_s^{-1} \Phi_s^T &\cong \Phi_s (\Lambda_s + \varepsilon)^{-1} \Phi_s^T \\ &= (\mathbf{K} + \varepsilon \mathbf{M})^{-1} - \Phi_m (\Lambda_m + \varepsilon)^{-1} \Phi_m^T. \end{aligned} \quad (59)$$

Since the small shift is far less than the slave eigenvalues ($\varepsilon \ll \Lambda_s$), it is acceptable to be used to calculate the substructural residual flexibility. The difference between the calculated residual flexibility and the exact residual flexibility in terms of (58) is 1.6%. The small shift introduces a small error in the calculation of residual flexibility, and it will inevitably influence the accuracy of the global eigensolutions and eigensensitivity.

The substructural eigensolutions and eigensensitivity are assembled to the objective function and sensitivity matrix of

the global structure for model updating. The model updating process is performed based on the eigensolutions and eigensensitivity by the above three methods. In model updating, the simulated ‘‘experimental’’ modal data are obtained by intentionally introducing damages on some elements, and then the analytical model is updated to identify these damages [10, 30]. In the present paper, the simulated frequencies and mode shapes, which are treated as the ‘‘experimental’’ data, are calculated from the FE model by intentionally reducing the bending rigidity of Element 139 and Element 140 by 25% (denoted in Figure 3(a)). The first 10 ‘‘experimental’’ modes are available, and the measurements are obtained at the points and directions denoted in Figure 3(a). Both the ‘‘experimental’’ frequencies and mode shapes are utilized to update the analytical model. The mode shapes have been normalized with respect to the mass matrix.

The first 30 modes are retained as master modes in each substructure to calculate the first 10 eigensolutions and eigensensitivities of the global structure. It is noted that using the proposed substructuring method, the eigensolutions and eigensensitivities are calculated based on the reduced equation (15) with size of 90×90 , rather than on the original global system matrices with size of 408×408 . The bending rigidities of all column elements are chosen as the updating parameters. Accordingly, there are 64 updating parameters in total. The optimization is processed with the trust-region method provided by the MATLAB Optimization Toolbox [29–33]. The algorithm can automatically select the steps and searching directions according to the objective function (discrepancy of eigensolutions) and the provided eigensensitivity matrices. To compare the accuracy of the above three methods, the model updating process stops when 12 iterations are performed for all the three methods.

The identified changes of the elemental stiffness parameters are displayed in Figure 4. The stiffness parameters of Element 139 and Element 140 are reduced by 25%, which agree with the simulated reduction in the elemental parameters. The three methods have different accuracy in calculation of the residual flexibility, eigensolutions, and eigensensitivity of the free-free substructure. Some small values observed in other elements are due to the errors in calculation of the substructural eigensolutions and eigensensitivity by the three methods.

Figure 4(a) shows that the proposed well-conditioned eigenequation is accurate to be used in substructure-based

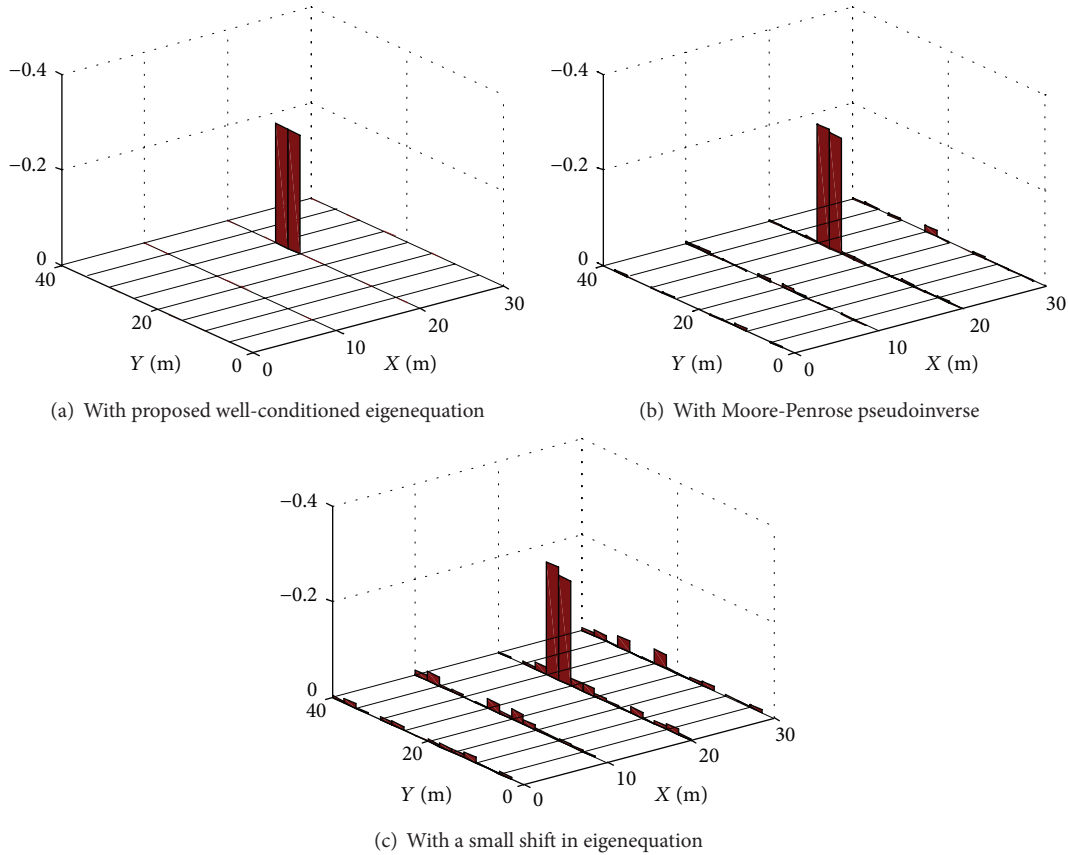


FIGURE 4: Location and severity of identified stiffness changes by the substructure-based model updating.

model updating, as it calculates the substructural residual flexibility, eigensolutions, and eigensensitivity with a high accuracy. The stiffness of Element 139 and Element 140 is identified as -25% . The identified changes of the elemental parameters are exactly consistent with the simulated damage. The proposed method has invisible values in other undamaged elements. On the other hand, the model updating results from traditional methods, which employ the Moore-Penrose pseudoinverse or a small shift for the rank-deficient eigenequation, introduce some small changes of undamaged elements as shown in Figures 4(b) and 4(c). And the introduction of a small shift for the rank-deficient eigenequation is less accurate than the use of Moore-Penrose pseudoinverse in calculation of substructural residual flexibility and eigensolutions. It is noted that a small shift 0.1 is introduced in this example. The selection of 0.1 in this example is not necessarily the best case, and a different selection of the shift value might contribute to better computational accuracy.

Table 1 and Figure 4 show that the proposed well-conditioned eigenequation has high accuracy in calculation of substructural eigensolutions and eigensensitivity for the free-free substructure, and it is accurate to be used in substructure-based model updating. The accurate calculation of eigensolutions and eigensensitivity is significant and helpful for the convergence of the model updating process. The efficiency of the proposed method in substructure-based model updating will be illustrated in the following case study.

4.2. Canton Tower. To illustrate the computational efficiency of the proposed substructuring method in large-scale structures, the FE model of the Canton Tower is employed here. The Canton Tower is a supertall structure of 610 m height. It consists of a main tower (454 m) and an antennary mast (156 m), as shown in Figure 5(a). The main tower comprises a reinforced concrete inner tube and a steel outer tube of concrete-filled-tube (CFT) columns [34]. The outer tube consists of 24 CFT columns, uniformly spaced in an oval while being inclined in the vertical direction. The columns are interconnected transversely by steel ring beams and bracings. The analytical finite element (FE) model of the structure (Figure 5(b)) includes 8,738 three-dimensional elements, 3,671 nodes (each of which has six DOF), and 21,690 DOF.

The global structure is divided into 10 substructures along the vertical direction as in Figure 5(c). The “experimental” frequencies and mode shapes are simulated on the global structure by intentionally reducing the bending rigidity of 48 column elements of the outer tube in the local area (denoted in Figure 5) by 30%. The first 10 “experimental” modes are generated from the structure. The mode shapes are normalized to the mass matrix.

The analytical model is updated by employing the substructuring method. The first 20 modes of the independent substructures are selected as the master modes to calculate the eigensolutions and eigensensitivity of the global structure.

TABLE 2: Computation time for substructure-based model updating.

	With the proposed well-conditioned eigenequation	With Moore-Penrose pseudo-inverse for rank-deficient matrix	With a small shift for rank-deficient matrix
Calculation of substructural eigensolution (seconds)	4.1590	16.6342	4.1433
Calculation of substructural eigensensitivity (seconds)	655.59	1683.21	642.77
One iteration of model updating (hours)	0.3103	0.7328	0.3087
Entire time of substructure-based model updating (hours)	3.8	11.5	5.9

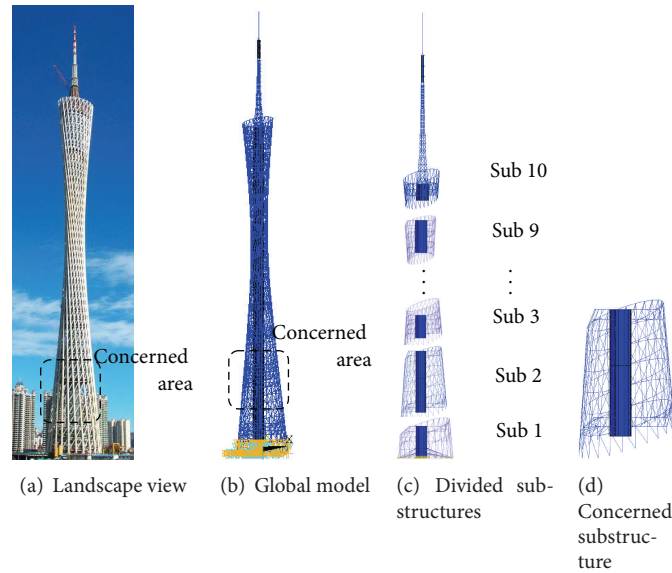


FIGURE 5: Canton Tower and the FE model.

The bending rigidities of all the column elements of the outer tube in the concerned local area (the second substructure) are chosen as the updating parameters. Accordingly, there are a total of 144 updating parameters. The second substructure to the tenth substructure are free-free substructures after partition, and the system matrices of the nine substructures are singular and rank deficient. Three methods are utilized to handle the rank-deficient eigenproblem, namely, with the construction of the proposed well-conditioned eigenequation, with the Moore-Penrose pseudoinverse of rank-deficient matrix, and with a small shift for rank-deficient matrix.

In each iteration, the substructural residual flexibility, eigensolutions, and its derivative matrix are calculated from the independent substructural model. The second substructure is taken as an example to illustrate the computation efficiency of the above three methods for the analysis of the rank-deficient eigenproblem. The system matrices of the second substructure take the size $2,736 \times 2,736$. Table 2 shows the computation time of the substructure-based model updating process by the three methods for the analysis of rank-deficient eigenproblem. With the construction of the proposed well-conditioned eigenequation, it costs about 4.1590 seconds to calculate the first 20 eigensolutions of

the second substructure via an ordinary personal computer with a 3.40 GHz CPU and 16 GB memory. The calculation of the substructural eigensensitivity with respect to the 144 updating parameters costs 655.59 seconds. The substructural eigensolutions and eigensensitivity are assembled to form the eigensolutions and eigensensitivity of the global structure for model updating process. One iteration of model updating consumes about 0.31 hours. Since the proposed full-rank well-conditioned eigenequation is accurate for the calculation of the substructural residual flexibility, eigensolutions, and eigensensitivity, the norm of objective function reaches 10^{-7} after 13 iterations as in Figure 6. The whole model updating process takes about 3.8 hours.

Calculation of Moore-Penrose pseudoinverse for rank-deficient matrix is usually computationally expensive. If the Moore-Penrose pseudoinverse is used for the rank-deficient system matrix, the calculation of substructural eigensolution costs about 16.6342 seconds, and the calculation of substructural eigensensitivity with respect to 144 updating parameters costs about 16.6342 seconds as in Table 2. One iteration of model updating consumes 0.7328 hours. The whole model updating process takes about 11.5 hours until the norm of objective function reaches 10^{-6} after 16 iterations

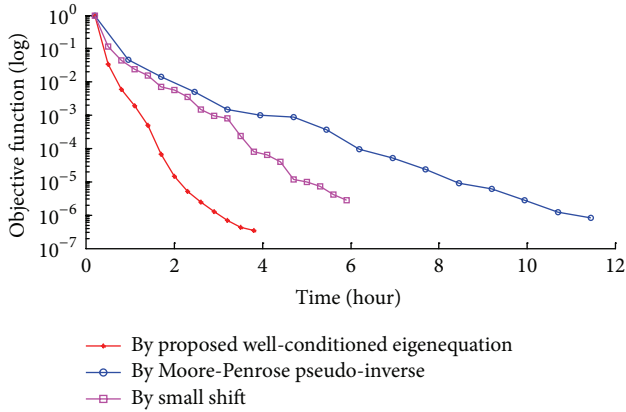


FIGURE 6: Convergence of substructure-based model updating by three methods.

as in Figure 6. The computation time is about 2.5 times of that consumed by the proposed method. The calculation of Moore-Penrose pseudoinverse of the rank-deficient system matrix is computationally expensive, while the results are not as accurate as those of the construction of the proposed well-conditioned eigenequation.

Finally, the substructural residual flexibility, eigensolutions, and eigensensitivity of the free substructures are calculated by introducing a small shift for rank-deficient eigenequation. The small shift is selected to be 0.1. Calculation of the substructural eigensolutions of the second substructure costs about 4.1433 seconds, and the calculation of substructural eigensensitivity costs about 642.77 seconds. The computation time is a little shorter than the method of the proposed well-conditioned eigenequation. However, the small shift in the original eigenequation inevitably introduces some errors. These errors hinder the convergence of model updating process. In Figure 6, the norm of objective function reaches 10^{-5} after 20 iterations. It is noted that the convergence is difficult to achieve the precision of 10^{-7} , as the small shift introduces errors in calculation of substructural solutions and hinders the convergence of model updating. To reach the insufficient accurate results, the model updating process costs 5.9 hours, which is longer than the proposed well-conditioned eigenequation.

In consequence, the construction of the proposed well-conditioned eigenequation for the free-free substructure is accurate and efficient for the calculation of substructural residual flexibility, eigensolutions, and eigensensitivity and is thus efficient for the substructure-based model updating process. The proposed well-conditioned eigenequation is more accurate and efficient than the traditional Moore-Penrose pseudoinverse method for the analysis of the free-free substructures. As compared to the introduction of a small shift, the proposed well-conditioned eigenequation achieves a similar efficiency in calculation of substructural eigensolutions and eigensensitivity, but it has much higher accuracy. The proposed method is more efficient than that of the introduction of a small shift when they are utilized in the substructure-base model updating.

5. Conclusions

This paper provides a deep look at the properties of a free-free structure. It addresses the difficulties associated with the analysis of a free-free substructure that were frequently encountered in the substructuring methods.

The well-conditioned stiffness and flexibility matrices are formulated to overcome the difficulty in analyzing singular stiffness and flexibility matrices. The generalized stiffness and flexibility matrices are constructed to be the dual inversion of each other, such that the stiffness matrix and modal flexibility matrix are transformed into each other efficiently and effectively avoiding the expensive pseudoinverse. The proposed generalized stiffness matrix is full rank, which is helpful for the analysis of a free-free structure in many aspects, such as the analysis of eigenequation with singular stiffness matrix and the calculation of the modal flexibility, residual flexibility, and their derivatives.

The accuracy of the proposed method for the analysis of the free-free substructures and its accuracy in the substructure-based model updating are verified through application to a frame structure. The construction of the proposed well-conditioned eigenequation is accurate in calculation of the substructural residual flexibility, eigensolutions, and eigensensitivity, and the substructure-based model updating results are exactly in agreement with the predefined damaged cases. The efficiency of the proposed method is illustrated through a supertall structure. The proposed full-rank well-conditioned eigenequation is more accurate and efficient than the Moore-Penrose pseudoinverse and the introduction of a small shift for the analysis of the free-free substructural model. The proposed full-rank well-conditioned eigenequation is accurate and efficient to be used in substructure-based model updating.

Although the present research intends to assist the analysis of the free-free substructures in substructuring methods, the proposed well-conditioned eigenequation can be generalized to the analysis of a general free-free structure.

Acknowledgments

This work is supported by a Grant from the National Natural Science Foundation of China (NSFC, no. 51108205), National Basic Research Program of China (973 Program: 2011CB013804), and Huazhong University of Science and Technology (no. 2012QN018).

References

- [1] Y. Q. Ni, X. W. Ye, and J. M. Ko, "Modeling of stress spectrum using long-term monitoring data and finite mixture distributions," *Journal of Engineering Mechanics*, vol. 138, no. 2, pp. 175–183, 2011.
- [2] Y. Q. Ni, X. W. Ye, and J. M. Ko, "Monitoring-based fatigue reliability assessment of steel bridges: analytical model and application," *Journal of Structural Engineering*, vol. 136, no. 12, pp. 1563–1573, 2010.
- [3] T.-H. Yi, H.-N. Li, and M. Gu, "Optimal sensor placement for structural health monitoring based on multiple optimization

- strategies," *Structural Design of Tall and Special Buildings*, vol. 20, no. 7, pp. 881–900, 2011.
- [4] T.-H. Yi, H.-N. Li, and M. Gu, "Recent research and applications of GPS-based monitoring technology for high-rise structures," *Structural Control and Health Monitoring*, vol. 20, no. 5, pp. 649–670, 2012.
- [5] S. Weng, Y. Xia, Y.-L. Xu, X.-Q. Zhou, and H.-P. Zhu, "Improved substructuring method for eigensolutions of large-scale structures," *Journal of Sound and Vibration*, vol. 323, no. 3-5, pp. 718–736, 2009.
- [6] K. C. Park and Y. H. Park, "Partitioned component mode synthesis via a flexibility approach," *AIAA Journal*, vol. 42, no. 6, pp. 1236–1245, 2004.
- [7] R. R. Craig Jr., "Coupling of substructures for dynamic analyses: an overview," in *Proceedings of the 41st AIAA/ASME/ASCE/AHS/ASC 41st Structures, Structural Dynamics, and Materials Conference*, pp. 3–14, Atlanta, Ga, USA, April 2000.
- [8] N. S. Sehmi, *Large Order Structural Eigenanalysis Techniques*, Ellis Horwood, Chichester, UK, 1989.
- [9] Y. Xia, S. Weng, Y.-L. Xu, and H.-P. Zhu, "Calculation of eigenvalue and eigenvector derivatives with the improved Kron's substructuring method," *Structural Engineering and Mechanics*, vol. 36, no. 1, pp. 37–55, 2010.
- [10] S. Weng, Y. Xia, Y.-L. Xu, and H.-P. Zhu, "Substructure based approach to finite element model updating," *Computers and Structures*, vol. 89, no. 9-10, pp. 772–782, 2011.
- [11] S. Weng, H. P. Zhu, Y. Xia, X. Q. Zhou, and L. Mao, "Substructuring approach to the calculation of higher-order eigensensitivity," *Computers & Structures*, vol. 117, pp. 23–33, 2013.
- [12] S. Weng, Y. Xia, Y.-L. Xu, and H.-P. Zhu, "An iterative substructuring approach to the calculation of eigensolution and eigensensitivity," *Journal of Sound and Vibration*, vol. 330, no. 14, pp. 3368–3380, 2011.
- [13] S. Weng, Y. Xia, and Y. L. Xu, "Model updating with improved substructuring method," in *Proceedings of the 3rd International Conference of Integrity, Reliability and Failure*, p. 175, Porto, Portugal, 2009.
- [14] Y. Xia, S. Weng, and Y.-L. Xu, "A substructuring method for calculation of eigenvalue derivatives and eigenvector derivatives," in *Proceedings of the 4th International Conference on Structural Health Monitoring on Intelligent Infrastructure (SHMII '09)*, Zurich, Switzerland, 2009.
- [15] S. Weng, H. P. Zhu, Y. Xia, and L. Mao, "Damage detection using the eigenparameter decomposition of substructural flexibility matrix," *Mechanical Systems and Signal Processing*, vol. 34, no. 1-2, pp. 19–38, 2013.
- [16] S. Weng, Y. Xia, X. Zhou, Y. Xu, and H. Zhu, "Inverse substructure method for model updating of structures," *Journal of Sound and Vibration*, vol. 331, no. 25, pp. 5449–5468, 2012.
- [17] J. Li and S. S. Law, "Damage identification of a target substructure with moving load excitation," *Mechanical Systems and Signal Processing*, vol. 30, pp. 78–90, 2012.
- [18] J. H. Gordis, "On the analytic disassembly of structural matrices," in *Proceedings of the 15th International Modal Analysis Conference (IMAC '97)*, pp. 1292–1297, Bethel, Conn, USA, February 1997.
- [19] K. F. Alvin and K. C. Park, "Extraction of substructural flexibility from global frequencies and mode shapes," *AIAA journal*, vol. 37, no. 11, pp. 1444–1451, 1999.
- [20] M. J. Terrell, M. I. Friswell, and N. A. J. Lieven, "Constrained generic substructure transformations in finite element model updating," *Journal of Sound and Vibration*, vol. 300, no. 1-2, pp. 265–279, 2007.
- [21] S. W. Doebling, L. D. Peterson, and K. F. Alvin, "Experimental determination of local structural stiffness by disassembly of measured flexibility matrices," *Journal of Vibration and Acoustics*, vol. 120, no. 4, pp. 949–957, 1998.
- [22] K. J. Bathe, *Finite Element Procedures in Engineering Analysis*, Prentice-Hall, Englewood Cliffs, NJ, USA, 1982.
- [23] R. M. Lin and M. K. Lim, "Eigenvector derivatives of structures with rigid body modes," *AIAA Journal*, vol. 34, no. 5, pp. 1083–1085, 1996.
- [24] A. A. Abdallah, A. R. Barnett, and T. W. Widrick, "Stiffness-generatd rigid-body mode shapes for Lanczos eigensolution with suport DOF via a MSC/Nastran dmap alter," in *Proceedings of the MSC Word Users' Conference*, Lake Buena Vista, Fla, USA, 1994.
- [25] P. Courrieu, "Fast computation of moore-penrose inverse matrices," *Neural Information Processing*, vol. 8, pp. 25–58, 2005.
- [26] S. W. Doebling, *Measurement of structural flexibility matrices for experiments with incomplete reciprocity [Ph.D. thesis]*, University of Colorado, 1995.
- [27] R. B. Nelson, "Simplified calculation of eigenvector derivatives," *Journal of American Institute of Aeronautics and Astronautics*, vol. 14, no. 9, pp. 1201–1205, 1976.
- [28] R. L. Fox and M. P. Kapoor, "Rate of change of eigenvalues and eigenvectors," *AIAA Journal*, vol. 6, pp. 2426–2429, 1968.
- [29] B. Jaishi and W.-X. Ren, "Damage detection by finite element model updating using modal flexibility residual," *Journal of Sound and Vibration*, vol. 290, no. 1-2, pp. 369–387, 2006.
- [30] J. M. W. Brownjohn, P.-Q. Xia, H. Hao, and Y. Xia, "Civil structure condition assessment by FE model updating: methodology and case studies," *Finite Elements in Analysis and Design*, vol. 37, no. 10, pp. 761–775, 2001.
- [31] K. F. Tee, C. G. Koh, and S. T. Quek, "Numerical and experimental studies of a substructural identification strategy," *Structural Health Monitoring*, vol. 8, no. 5, pp. 397–410, 2009.
- [32] J. Li, S. S. Law, and Y. Ding, "Substructure damage identification based on response reconstruction in frequency domain and model updating," *Engineering Structures*, vol. 41, pp. 270–284, 2012.
- [33] S.-E. Fang, R. Perera, and G. De Roeck, "Damage identification of a reinforced concrete frame by finite element model updating using damage parameterization," *Journal of Sound and Vibration*, vol. 313, no. 3–5, pp. 544–559, 2008.
- [34] Y. Q. Ni, Y. Xia, W. Y. Liao, and J. M. Ko, "Technology innovation in developing the structural health monitoring system for Guangzhou New TV Tower," *Structural Control and Health Monitoring*, vol. 16, no. 1, pp. 73–98, 2009.

Research Article

Real-Time Dry Beach Length Monitoring for Tailings Dams Based on Visual Measurement

Jun Hu,¹ Shan Hu,¹ Fei Kang,² and Jianhua Zhang³

¹ School of Mining Engineering, University of Science and Technology Liaoning, Anshan, Liaoning 114051, China

² Faculty of Infrastructure Engineering, Dalian University of Technology, Dalian, Liaoning 116024, China

³ College of Computer Science and Technology, Zhejiang University of Technology, Hangzhou, Zhejiang 310023, China

Correspondence should be addressed to Jun Hu; kdhj1977@126.com

Received 18 August 2013; Accepted 4 October 2013

Academic Editor: Xiao-Wei Ye

Copyright © 2013 Jun Hu et al. This is an open access article distributed under the Creative Commons Attribution License, which permits unrestricted use, distribution, and reproduction in any medium, provided the original work is properly cited.

The length of dry beach is an important factor that influences the safety of tailings dams. However, there still is no accurate and reliable method that can conveniently measure the length of dry beach. In this paper, the authors focus on developing a novel method for dry beach length determination. The proposed method can effectively measure the dry beach length through an ordinary camera and four marking rods placed on the dry beach. Experimental results show that the proposed method can conveniently measure the dry beach length with high accuracy, and therefore it can be adopted as an effective method in tailings dam real-time health monitoring.

1. Introduction

Increased awareness of the economic and social effects of aging, deterioration, and extreme events on civil infrastructure has been accompanied by recognition of the need for advanced structural health monitoring and damage detection tools [1]. Structural health monitoring is a technology that allows the estimation of the structural state and detection of structural change that affects the performance of a structure [2, 3]. Recently, many advanced measurement methods such as global positioning systems (GPS) [4, 5], wireless sensor networks [6, 7], and fiber Bragg grating sensing [8] have been adopted for health monitoring of engineering structures. Meanwhile, various signal processing methods such as particle filtering algorithm [9], wavelet thresholding [10], particle swarm optimization [11, 12], artificial bee colony algorithm [13], and neural networks [14] are developed to deal with the data obtained by the sensor systems to reflect the status of structures.

Tailings pond is formed by damming at valley interception or damming at all sides, which is used to store tailings and other industrial waste produced by metal and nonmetal mines. Tailings dams are a particular type of dam built to store mill and waste tailings from mining activities, and a tailings

dam is an important part of a tailings pond, which refers to the initial dam and later fill dam. Tailings storage facilities are complex geotechnical structures. A number of singular characteristics make tailings dams more vulnerable than other types of retention structures. Many tailings dam failure cases have been reported [15]. The failure of a tailings dam may cause grave disasters such as floods [16] and groundwater pollution [17]. Therefore, in the design and operation stages of a tailings project, the stability of the tailings dam, the control capacity for flood, and the reliability of the drainage and safety monitoring facilities should be fully evaluated [18]. Some works of the literature have focused on the static and dynamic stability analysis of tailings structures [19–22]. Reinforced terraced fields method for fine tailings disposal was proposed in [23]. Statistical source identification method for groundwater downward the tailings dam was studied in [24], considering that identifying the possible sources of potential harmful metals in groundwater systems plays a crucial role in evaluating the potential risks to residents and local plant cover.

Recently, the safety monitoring of tailings dams has become a hot topic. Security monitoring items of tailings dams include displacement, saturation line, reservoir level, and dry beach [25]. Sjö Dahl et al. [26] proposed an internal erosion

process and anomalous seepage detection method for tailings dams based on resistivity measurements. Security monitoring systems for tailings dams based on global positioning system are discussed in [27, 28]. Several online monitoring strategies for tailings dams also have been researched and developed [25, 29–31]. Blight et al. [32] proposed a freshly deposited surfaces measurement method for two platinum tailings dams.

The length of dry beach is an important index affecting the safe operation of the tailings pond, because it not only affects the height of the tailings dam saturation line and the safety of the tailings dam but also decides the flood control ability of the dam. The shortage of the beach length will seriously affect the safety of the tailings ponds. With the injecting of the tail slurry, the dry beach length changes in real time. Researching and developing the real-time automatic measurement method for the dry beach length monitoring becomes an essential content of the tailings dam safety monitoring system.

Conventional instruments for dry beach length measurement are hard to obtain accurate results in real time. Two methods commonly used are described as follows. In the first approach, controlling the water level as low as possible before the rainy season to keep enough dry beach length, and setting red flags on the dry beach every 50 meters from the highest secondary dam based on the specific conditions of the dry beach. In the flood season, the dry beach length can be determined by cruise visual check. In the second approach, the dry beach slope is assumed to be uniform, and the length of dry beach can be calculated by the difference of reservoir water level elevation and the beach elevation. The disadvantage of the previous two approaches is obvious. The first method cannot achieve automatic measurement. As for the second method, the measurement error can be very large, because the dry beach slope is not evenly made. There also exist automatic noncontact measurement technology and equipment for dry beach length measurement, such as deploying multiple automatic altimeters in the center of ponds to measure the dry beach elevation automatically. An altimeter is consisted of grating measuring system, wireless data transmission modules, solar panels, battery, and so forth. But as a result of constant injection of slurry and changing of beach surface, altimeters need to be made regular layout again, otherwise they will be buried and cannot work normally.

In this paper, a novel online measurement method for dry beach length is proposed based on photogrammetric monitoring. The main work is divided into two parts. The first part refers to the measurement preparation work, and the second part refers to dry beach length calculation by the vision measurement technology. Preparation works mainly include camera calibration and place markers at the scene of the measurement. In the vision measurement process, firstly, an image taken by the camera is isolated as the dry beach area and the reservoir water surface area through image processing. Then the locations of the markers in the image are extracted, and finally, the dry beach length is calculated according to the parameters extracted.

2. Basic Principles of Photogrammetric Monitoring for Dry Beach Length

Pinhole imaging model is shown in Figure 1 [33]. The focal length of the camera is set to f , and the origin of coordinates is set as the optical center of the camera. The coordinates of the point in Q space are (X, Y, Z) and its corresponding points on the imaging plane are (x, y, f) . According to the principle of pinhole imaging, the following equation can be obtained:

$$x = \frac{fX}{Z}, \quad y = \frac{fY}{Z}. \quad (1)$$

Assume that two points in Q space are (X_1, Y_1, Z_1) , (X_2, Y_2, Z_2) , and their coordinates in the image plane are (x_1, y_1) and (x_2, y_2) , respectively. In Q space, the distance between two points can be calculated as

$$D = \sqrt{(X_1 - X_2)^2 + (Y_1 - Y_2)^2 + (Z_1 - Z_2)^2}. \quad (2)$$

When $Z_1 \approx Z_2 = Z$, from (1) and (2), the following equations can be obtained:

$$D = \frac{Z\sqrt{(x_1 - x_2)^2 + (y_1 - y_2)^2}}{f}, \quad (3)$$

$$f = \frac{Z\sqrt{(x_1 - x_2)^2 + (y_1 - y_2)^2}}{D}, \quad (4)$$

$$Z = \frac{Df}{\sqrt{(x_1 - x_2)^2 + (y_1 - y_2)^2}}. \quad (5)$$

When the space distance between two points, distances from two points to the camera, and the image of the two points in the image plane are known, the camera focal length can be calculated from (4). According to (5), when the focal length of the camera, the actual size of the measured object, and the size in the image plane of the measured object are already known, the distance from the camera to the object can be calculated.

The method adopted is assisted by four marking rods in dry beach area. It should ensure that the four marking rods form a rectangle and keep the camera lens in the middle of the rectangle formed by the marking rods. Because the actual dry beach surface can be approximated as a plane, you can determine the water line by the points of four bars, and the dry beach is approximately thought to be in the same plane. Figure 2 shows the layout of the marker rods and the camera. The red points represent the marking rods, and the blue line is called water line, which represents the boundary of the dry beach and the water surface. LP1, LP2, RP1, RP2, dry beach, and the water line are in the same plane. By the points LP1 and LP2, we can define line LL, and the line LL intersects with the water line at point CL. By the points RP1 and RP2, we can define line RL, and the line RL intersects with the water line at the point CR. The distance between CL and CR is equal to the distance between RP1 and LP1.

According to the invariance of X-ray imaging, a point in space is still a point on the imaging plane, and a straight line

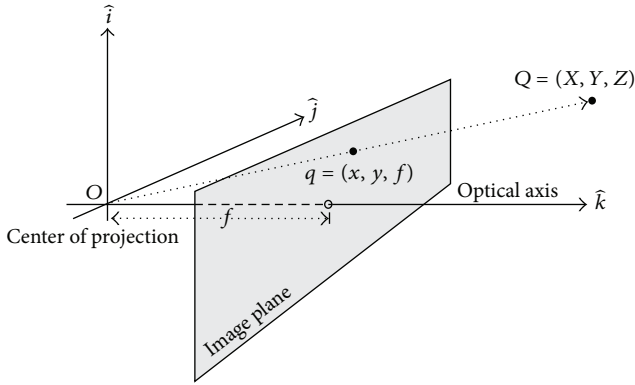


FIGURE 1: Pinhole imaging model.

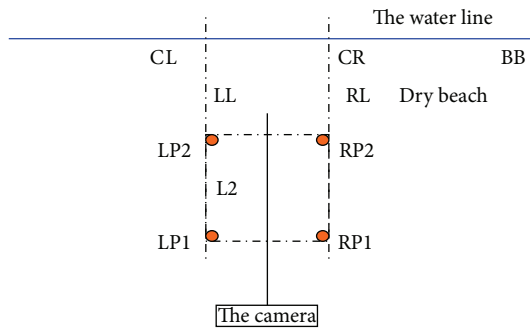


FIGURE 2: Measurement schemes.

in space is still a straight line on the imaging plane. Therefore, two points in the space corresponds to two image points, which determine a straight line on the imaging plane [34]. The principle can be described as follows.

Theorem 1. *Supposing that P1 and P2 are two points in the space and p1 and p2 are two points in the camera image plane, the image of the space straight line between P1, P2 is necessarily the straight line between p1 and p2 on the imaging plane.*

Figure 3 is a picture corresponding to the layout of Figure 2. In this figure, l1 and l2 are corresponding to LP1 and LP2 in Figure 2, and r1 and r2 are corresponding to RP1 and RP2 in Figure 2. According to Theorem 1, l1 and l2 determine the line corresponding to the line LL, and r1 and r2 determine the line corresponding to the line RL in the schematic diagram. Therefore, CL and CR correspond to the imaging points cl and cr, respectively. Because LL and RL are parallel to each other, the distance between CL and CR is equal to the distance between LP1 and RP1. This distance must be determined and measured when setting up marking rods. To calculate the distance between the camera and the boundary line, the critical problems are determination of the camera focal length and calculation of the pixel coordinates of cl and cr. Through (4), the camera focal length can be calculated, and through image processing technique, the pixel distance between cl and cr can be obtained. Then the distance



FIGURE 3: Layout of the mark poles.

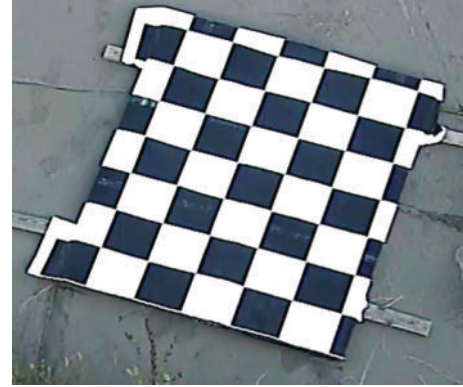


FIGURE 4: International chess calibration plate.

between the camera and the boundary can be calculated from (5).

3. Measurement Steps

3.1. Camera Intrinsic Parameter Calibration. In image measurement process and machine vision applications, in order to determine the interrelation between the object surface geometry in three-dimensional space with the corresponding points in the image, it is necessary to establish the camera imaging geometric model, and the geometric model is determined by the camera parameters.

These parameters must be obtained through experiments and calculation, and the process of solving these parameters is called camera calibration. Both in image measurement and machine vision applications, camera parameter calibration work is a critical factor that influences the calibration results. Calibration precision and stability of the calibration algorithm directly affect the results accuracy of camera work. Therefore, completing the camera calibration is a premise to proceed to the next steps, and improving the calibration accuracy is the key of scientific research work.

The distortion of the camera in the process of imaging is usually unavoidable, and radial distortion is the main part of camera lens distortion. Taking optical axis as the center and its image coordinate as the reference point, radial distortion is proportional to the square of the distance from the point to the reference point. Only considering the second order of lens distortion, radial distortion can be described as

$$\begin{aligned} u - u_0 &= (u' - u_0)(1 + k_u r^2), \\ v - v_0 &= (v' - v_0)(1 + k_v r^2), \end{aligned} \quad (6)$$

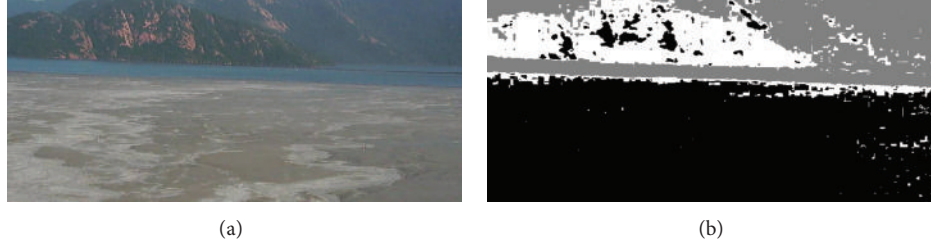


FIGURE 5: Example of image segmentation by k -means clustering algorithm: (a) original image; (b) image after segmentation.

where (u', v') is the ideal arthroscopic image coordinate without distortion, (u, v) is the actual image coordinate, (u_0, v_0) is the image coordinates of the optical axis center, r is the distance between the image point to the reference point, and k_u, k_v are the second-order distortion coefficients along the directions u and v . Camera distortion parameters can be obtained by calibration to the camera intrinsic parameters.

This paper adopts the camera calibration method proposed by Zhang [35]. The plane calibration method proposed by Zhang is a kind of method between the traditional calibration methods and self-calibration methods. It avoids some disadvantages of the traditional methods, such as the high requirement for equipment and complicated operation. Meanwhile, like the self-calibration method, it has the advantage of high accuracy. The steps for camera calibration procedure are described as follows. (1) Make a pane of a chess board template with the size $20\text{ cm} \times 20\text{ cm}$ for each cell and stick it on a flat surface, as shown in Figure 4. (2) Take several template images from different angles. (3) Detect the feature points in the international chess calibration plate. (4) Calculate the inner and outer parameters of the camera. (5) Calculate the distortion coefficient. (6) Optimization and refinement. The camera distortion parameters are obtained after camera calibration, and the distortion parameters can be used to correct the images taken by the camera.

3.2. Dry Beach and the Water Surface Areas Extraction. Due to the characteristics of dry beach area images differ from the characteristics of the water surface area images. Therefore, we can take advantages of regional segmentation method to extract the dry beach area and water surface area in the digital image. The edge of the water surface area is the boundary of the dry beach and the water. The intention of digital image segmentation is to segment the areas with different particular meanings. These areas are mutually disjoint, and each area meets the consistency of a particular area. Areas segmented by an excellent segmentation algorithm should satisfy the following conditions. (1) The partition of the image area should satisfy the requirement for uniformity and connectivity. The uniformity refers to the pixels, which should satisfy all the pixels in the same kind of similarity criterion based on the texture, color, and other characteristics. Connectivity refers to there exist paths for connecting any two points in the area. (2) There are notable differences between adjacent segmented regions. (3) The boundary of

segmentation regions should be neat, and at the same time positioning accuracy of the edges should be ensured.

The image segmentation method based on k -means clustering algorithm is adopted. Because the clustering algorithm is concise and efficient, it is widely used in all kinds of clustering problems. Given a set of data points and the number of clusters k , k -means algorithm can classify the data points into k clusters based on a certain distance function. The parameter k is specified by the user. The steps of k -means clustering algorithm for image segmentation are described as follows.

(1) Transform the camera image from RGB color space to $L \times A \times B$ space. The $L \times A \times B$ space of the image can describe the regional characteristics better than RGB color space, and the values of A and B in the $L \times A \times B$ space are regarded as the characteristic values for each point in the image.

(2) Set the number of clusters to be $k = 3$, and initialize the cluster centers. When camera is adopted to monitor the length of dry beach, the camera image area is mainly composed of dry beach, water, and other areas. Therefore, the number of clusters is set to be $k = 3$ when using the k -means clustering algorithm for image segmentation.

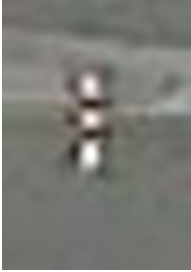
(3) Calculate the distance between each pixel and the clustering center. Each pixel is classified in accordance with the principle of minimum distance to the nearest clustering center. The clustering centers are calculated as mean values of cluster samples in each cluster.

(4) Repeat step (3) until the clustering centers no longer change.

Figure 5 is an example of image segmentation by k -means clustering algorithm. In Figure 5(a), the original image of tailings areas is taken by a camera. The k -means clustering algorithm for image segmentation is adopted to extract different regions. In Figure 5(b), the black part represents the dry beach area, the gray part represents the water surface area, and the white part represents the other area. It can be seen that the water surface area can distinguish different parts clearly. So the pixels of the water surface area can be adopted to extract the boundary.

3.3. Marking Rods Extraction. Marking rods are adopted in the visual measurement to determine two parallel lines. Then the distance from the camera to the dry beach can be measured by using the principle of that the distances between two parallel lines are equal. The positions of the marking rods should be extracted from the image accurately. We use

TABLE 1: Image templates of four marking rods.

Marking rods	1	2	3	4
Sign				

the method of digital image template matching to locate the position of marking rods in the image. The image template is a small image already known. Template matching is a method used to search the goals in a big image. We can find the target and determine its location via calculating under the condition that the target has the same size, direction, and image with the template.

The principle of image template matching is described as follows. Firstly, the image template T ($m \times n$ pixels) is translated into the search graph S ($W \times H$ pixels), and the area that is covered by the image template is called subgraph S_{ij} . The indexes i and j are the coordinates in the search graph S . The search scope is $1 \leq i \leq W - m$ and $1 \leq j \leq H - n$. By comparing the similarity between T and S_{ij} , we can complete the template matching process. Similarity between image template T and subgraph S_{ij} can be measured as

$$D(i, j) = \sum_{p=1}^m \sum_{q=1}^n |S_{ij}(p, q) - T(p, q)|. \quad (7)$$

The procedure for images template matching has the following steps. (1) Extract the required image templates. Table 1 shows the image templates of four marking rods. (2) Calculate the similarity $D(i, j)$ between images and the template by (7). (3) Find the minimum similarity $D(i, j)$, and (i, j) is the position of the marker rod that we want to find.

The installation diagram of high-definition camera is shown in Figures 6 and 7. Figure 8 shows the positions of marking rods detected by template matching method.

3.4. Dry Beach Length Calculation. The water surface area and coordinates of marking rods can be obtained by regional segmentation of the image and identification of marking rods. As shown in Figure 9, the white color represents the water surface area, the red dots represent the marking rods, and the green lines are two parallel lines determined by marking rods. The intersection points of the two parallel lines with the water surface area are cl and cr , as shown in Figure 3. After calculating the distance between the two pixels, by using (5), we can calculate the dry beach length, which equals the distance from the boundary to the camera.



FIGURE 6: Installation diagram.



FIGURE 7: High-definition camera.

4. Experimental Results

Three experiments are performed to verify the proposed method for dry beach length measurement. In the three experiments, the distance between the camera and water line is set at 150 m, 200 m, and 300 m. This is achieved by moving the camera and marking rods. The measurement results of the experiments are shown in Table 2. It can be seen that when the distance is small, the error is also small, and

TABLE 2: The measurement results.

The actual distance (m)	The measured distance (m)	Relative error
150	147.8	1.46%
200	194.6	2.7%
300	309.7	3.2%



FIGURE 8: Extraction of marking rods.

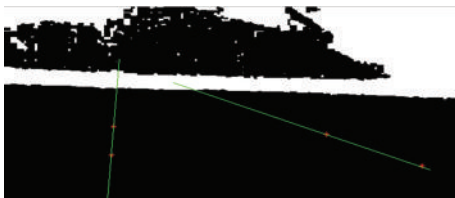


FIGURE 9: Water surface area and parallel lines determined by marking rods.

the error will increase with the rising of distance. When the actual distance is 300 m, the relative error is only 3.2%. Therefore, it still satisfies the requirement of measurement accuracy.

5. Conclusion

The dry beach length of a tailings dam is hard to be accurately measured automatically. In this paper, we propose a method for measuring real-time length of dry beach length by using an ordinary camera assisted with marking rods. When using the method, we should pay special attention to two items. (1) In order to meet the requirement of the measurement model, the four marking rods should be placed as a rectangle. Meanwhile, the optical axis of the camera should be placed at the axis of the rectangular. Then the assumption $Z_1 = Z_2$ in (1) can be satisfied. (2) In the paper, only two marking rods are used to determine a straight line, but in order to improve the measuring reliability and robustness, more marking rods can be used to determine the straight line. After extracting the positions of marking rods from the image, a curve fitting method can be applied to determine the straight line. Experimental results show that the proposed method has the advantages of convenient, accurate, and reliable performance, and the cost of measurement equipments is low.

Acknowledgments

This research was supported by National Natural Science Foundation of China under Grant nos. 51274053, 51109028,

the State ‘‘Twelve Five’’ Science and Technology Support Projects under Grant no. 2013BAB02B00, the Natural Science Foundation of Liaoning Province under Grant no. L2011040, the State Scholarship Fund of China to pursue study in USA as a visiting scholar under Grant no. 201208210208, and Scientific Research Foundation of University of Science and Technology Liaoning

References

- [1] P. C. Chang, A. Flatau, and S. C. Liu, ‘‘Review paper: health monitoring of civil infrastructure,’’ *Structural Health Monitoring*, vol. 2, no. 3, pp. 257–267, 2003.
- [2] Y. Q. Ni, X. W. Ye, and J. M. Ko, ‘‘Monitoring-based fatigue reliability assessment of steel bridges: analytical model and application,’’ *Journal of Structural Engineering*, vol. 136, no. 12, pp. 1563–1573, 2010.
- [3] Y. Q. Ni, X. W. Ye, and J. M. Ko, ‘‘Modeling of stress spectrum using long-term monitoring data and finite mixture distributions,’’ *Journal of Engineering Mechanics*, vol. 138, no. 2, pp. 175–183, 2011.
- [4] T. H. Yi, H. N. Li, and M. Gu, ‘‘Recent research and applications of GPS-based monitoring technology for high-rise structures,’’ *Structural Control and Health Monitoring*, vol. 20, no. 5, pp. 649–670, 2013.
- [5] T. H. Yi, H. N. Li, and M. Gu, ‘‘Wavelet based multi-step filtering method for bridge health monitoring using GPS and accelerometer,’’ *Smart Structures And Systems*, vol. 11, no. 4, pp. 331–348, 2013.
- [6] J. P. Lynch and K. J. Loh, ‘‘A summary review of wireless sensors and sensor networks for structural health monitoring,’’ *Shock and Vibration Digest*, vol. 38, no. 2, pp. 91–130, 2006.
- [7] S. N. Pakzad, G. L. Fenves, S. Kim, and D. E. Culler, ‘‘Design and implementation of scalable wireless sensor network for structural monitoring,’’ *Journal of Infrastructure Systems*, vol. 14, no. 1, pp. 89–101, 2008.
- [8] X. W. Ye, Y. Q. Ni, and J. H. Yin, ‘‘Safety Monitoring of railway tunnel construction using FBG sensing technology,’’ *Advances in Structural Engineering*, vol. 16, no. 8, pp. 1401–1410, 2013.
- [9] T. H. Yi, H. N. Li, and M. Gu, ‘‘Characterization and extraction of global positioning system multipath signals using an improved particle-filtering algorithm,’’ *Measurement Science and Technology*, vol. 22, no. 7, Article ID 075101, 2011.
- [10] T. H. Yi, H. N. Li, and X. Y. Zhao, ‘‘Noise smoothing for structural vibration test signals using an improved wavelet thresholding technique,’’ *Sensors*, vol. 12, no. 8, pp. 11205–11220, 2012.
- [11] F. Kang, J. J. Li, and S. Liu, ‘‘Combined data with particle swarm optimization for structural damage detection,’’ *Mathematical Problems in Engineering*, vol. 2013, Article ID 416941, 10 pages, 2013.
- [12] F. Kang, J. Li, and Q. Xu, ‘‘Damage detection based on improved particle swarm optimization using vibration data,’’ *Applied Soft Computing Journal*, vol. 12, no. 8, pp. 2329–2335, 2012.
- [13] F. Kang, J. Li, and Q. Xu, ‘‘Structural inverse analysis by hybrid simplex artificial bee colony algorithms,’’ *Computers and Structures*, vol. 87, no. 13–14, pp. 861–870, 2009.
- [14] X. Wang, F. Kang, J. J. Li, and X. Wang, ‘‘Inverse parametric analysis of seismic permanent deformation for earth-rockfill dams using artificial neural networks,’’ *Mathematical Problems in Engineering*, vol. 2012, Article ID 383749, 19 pages, 2012.

- [15] M. Rico, G. Benito, A. R. Salgueiro, A. Díez-Herrero, and H. G. Pereira, "Reported tailings dam failures. A review of the European incidents in the worldwide context," *Journal of Hazardous Materials*, vol. 152, no. 2, pp. 846–852, 2008.
- [16] M. Rico, G. Benito, and A. Díez-Herrero, "Floods from tailings dam failures," *Journal of Hazardous Materials*, vol. 154, no. 1–3, pp. 79–87, 2008.
- [17] R. S. Sharma and T. S. Al-Busaidi, "Groundwater pollution due to a tailings dam," *Engineering Geology*, vol. 60, no. 1–4, pp. 235–244, 2001.
- [18] T. Wang, Y. Zhou, Q. Lv, Y. Zhu, and C. Jiang, "A safety assessment of the new Xiangyun phosphogypsum tailings pond," *Minerals Engineering*, vol. 24, no. 10, pp. 1084–1090, 2011.
- [19] G. Yin, G. Li, Z. Wei, L. Wan, G. Shui, and X. Jing, "Stability analysis of a copper tailings dam via laboratory model tests: a Chinese case study," *Minerals Engineering*, vol. 24, no. 2, pp. 122–130, 2011.
- [20] A. T. Özer and L. G. Bromwell, "Stability assessment of an earth dam on silt/clay tailings foundation: a case study," *Engineering Geology*, vol. 151, pp. 89–99, 2012.
- [21] M. T. Zandarín, L. A. Oldecop, R. Rodríguez, and F. Zabala, "The role of capillary water in the stability of tailing dams," *Engineering Geology*, vol. 105, no. 1–2, pp. 108–118, 2009.
- [22] X. Jianbin, F. Jing, L. Wenlian et al., "Dynamic stability of the tailings dam under high intensity seismic load coupled with the effect of seepage," *Disaster Advances*, vol. 5, no. 4, pp. 816–821, 2012.
- [23] Z. Wei, G. Yin, G. Li, J. G. Wang, L. Wan, and L. Shen, "Reinforced terraced fields method for fine tailings disposal," *Minerals Engineering*, vol. 22, no. 12, pp. 1053–1059, 2009.
- [24] M. Kargar, N. Khorasani, M. Karami, G. Rafiee, and R. Naseh, "Statistical source identification of major and trace elements in groundwater downward the tailings dam of Miduk Copper Complex, Kerman, Iran," *Environmental Monitoring and Assessment*, vol. 184, no. 10, pp. 6173–6185, 2012.
- [25] G. Yu, C. Song, J. Zou et al., "Applications of online monitoring technology for tailings dam on digital mine," *Transactions of Nonferrous Metals Society of China*, vol. 21, supplement 3, pp. s604–s609, 2011.
- [26] P. Sjö Dahl, T. Dahlin, and S. Johansson, "Using resistivity measurements for dam safety evaluation at Enemossen tailings dam in southern Sweden," *Environmental Geology*, vol. 49, no. 2, pp. 267–273, 2005.
- [27] J. Hu and X. Liu, "Design and implementation of tailings dam security monitoring system," in *Proceedings of the 1st International Symposium on Mine Safety Science and Engineering (ISMSSE '11)*, vol. 26, pp. 1914–1921, October 2011.
- [28] W. Li and C. Wang, "GPS in the tailings dam deformation monitoring," in *Proceedings of the 1st International Symposium on Mine Safety Science and Engineering (ISMSSE '11)*, vol. 26, pp. 1648–1657, October 2011.
- [29] Q. Li, Y. Wang, and G. Li, "Tailings dam breach disaster online monitoring method and system realization," in *Proceedings of the 1st International Symposium on Mine Safety Science and Engineering (ISMSSE '11)*, vol. 26, pp. 1674–1681, October 2011.
- [30] E. Sun, X. Zhang, and Z. Li, "The internet of things (IOT) and cloud computing (CC) based tailings dam monitoring and pre-alarm system in mines," *Safety Science*, vol. 50, no. 4, pp. 811–815, 2012.
- [31] Z. H. Ouyan, "Research, development and application of surface displacement automatic monitoring system of tailings dam," *Advanced Materials Research*, vol. 422, pp. 304–309, 2012.
- [32] G. Blight, A. Copeland, P. Jardine et al., "Measurements on freshly-deposited surfaces of two platinum tailings dams," *Journal of the Southern African Institute of Mining and Metallurgy*, vol. 112, no. 11, pp. 911–917, 2012.
- [33] G. J. Zhang, *Visual Measurement*, Science press, Beijing, China, 2008.
- [34] R. Hartley and A. Zisserman, *Multiple View Geometry in Computer Vision*, Cambridge University Press, Cambridge, UK, 2004.
- [35] Z. Zhang, "Flexible camera calibration by viewing a plane from unknown orientations," in *Proceedings of the Seventh IEEE International Conference on Computer Vision (ICCV '99)*, vol. 1, pp. 666–673, September 1999.

Research Article

Experimental Study of Aerodynamic Damping of Typical Tall Buildings

Peng Huang, Yong Quan, and Ming Gu

State Key Laboratory of Disaster Reduction in Civil Engineering, Tongji University, Shanghai 200092, China

Correspondence should be addressed to Ming Gu; minggu@tongji.edu.cn

Received 19 August 2013; Accepted 24 September 2013

Academic Editor: Ting-Hua Yi

Copyright © 2013 Peng Huang et al. This is an open access article distributed under the Creative Commons Attribution License, which permits unrestricted use, distribution, and reproduction in any medium, provided the original work is properly cited.

Aerodynamic damping in certain conditions appears to have a negative value, which increases the dynamic response of a tall building. Six single-degree-of-freedom (SDOF) aeroelastic models of tall buildings with typical cross sections (square, square with concave or bevel corners, and rectangular) are tested in a wind tunnel with a suburban terrain flow field condition. The along-wind and across-wind aerodynamic damping ratios of the tall buildings are identified by using the eigensystem realization algorithm (ERA) method in conjunction with the random decrement technique (RDT). The effects of wind speed, corner modifications (concave or bevel corner), side ratio, and wind direction on the aerodynamic damping are studied. The results indicate that in most cases the along-wind aerodynamic damping is positive and gradually increases with the increase of reduced wind speed (U_r). The across-wind aerodynamic damping is likewise a positive value at low U_r in most cases, but suddenly becomes negative when U_r becomes greater than 10.5 for the square cross-section building.

1. Introduction

With the application of new materials and advanced technologies, modern tall buildings are becoming lighter and more slender than their predecessors, and thereby more sensitive to wind excitation. Aerodynamic damping may play an important role in estimating the dynamic response, especially in the wind excited across-wind dynamic response of tall buildings. Aerodynamic damping appears to have a negative value in certain conditions, which increases the dynamic response of the building.

Davenport [1], Holmes [2, 3], and Gabbai and Simiu [4] proposed a few methods to calculate the aerodynamic damping of high-rise structures for specific cases based on the quasi-steady assumption. The aerodynamic damping of tall buildings were mainly identified through wind tunnel tests because the along-wind and across-wind vibrations of tall buildings are highly complicated in the turbulent flow field, and the drastic change of the aerodynamic damping occurs at a high reduced velocity.

Kareem [5] pointed out that the effect of aerodynamic damping on the wind-induced vibration of high-rise buildings is not always negligible. He compared the responses of

the buildings that were calculated in terms of the pressure distributions obtained from the wind tunnel tests of their rigid models with those from aeroelastic model tests. The across-wind aerodynamic damping of buildings appeared to have a negative value sometimes, which significantly increases the vibration amplitude of the building.

A number of studies on aerodynamic damping were then performed. Most of the researchers focused on the aerodynamic damping of square cross-section buildings [6–11]. Watanabe et al. [9] proposed an empirical aerodynamic damping function for tall buildings and prisms, including the effects of the tip amplitude, aspect ratio, shapes of cross-section, and turbulence intensity of the flow field. Quan et al. [11] studied the effects of the reduced wind velocity, terrain type, and structural damping ratio on the aerodynamic damping, which allowed the researchers to derive the formulas of across-wind and along-wind aerodynamic damping ratios of the square super high-rise building.

The cross-section shape highly impacts the aerodynamic damping of tall buildings. As such, Hayashida et al. [12], Marukawa et al. [8], Cheng and Chiang [10], and as some other researchers studied the aerodynamic damping of nonsquare cross-section buildings. Marukawa et al. [8]

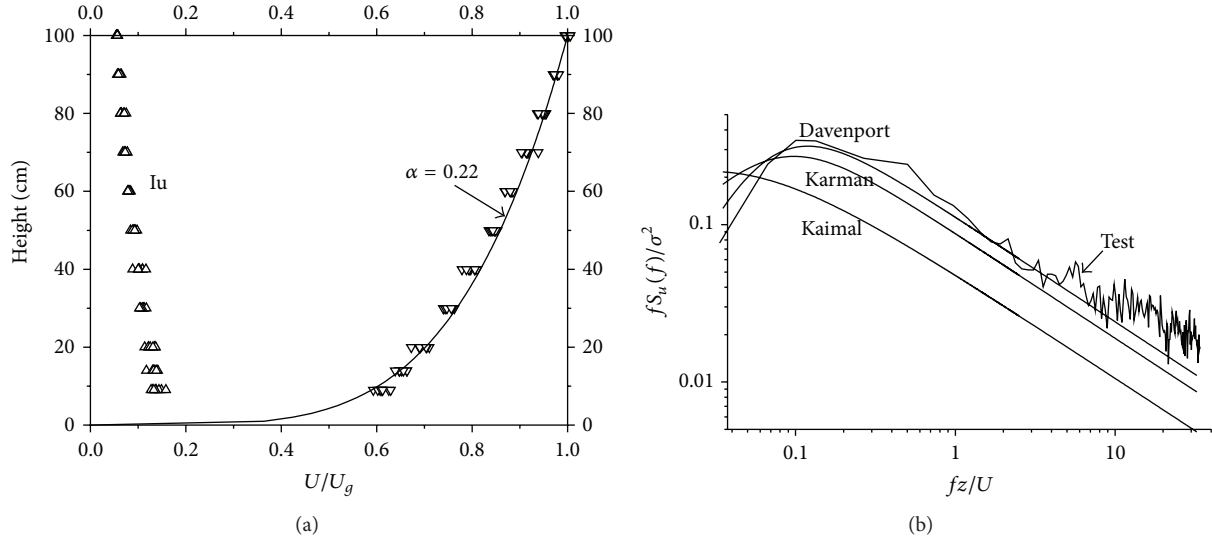


FIGURE 1: Simulated wind parameters of the suburban terrain: (a) profiles of mean wind velocity and turbulent intensity; and (b) power spectral density of fluctuating wind velocity.

investigated the aerodynamic damping characteristics of high-rise buildings with a rectangular cross-section (side ratio of 0.33 to 3) by using wind tunnel tests. An aeroelastic stick model and the random decrement technique (RDT) were applied to estimate the damping ratios. RDT is widely used to evaluate aerodynamic damping ratios from the random vibration responses of structures excited by random wind loads [11, 13–15], but the accuracy of this technique may not be satisfactory if data length is insufficient or if the structural modes of the models are not well-separated during vibration [16]. In the current paper, a time domain method, eigensystem realization algorithm (ERA) is used in conjunction with the RDT technique to identify the aerodynamic damping ratios. The ERA does not require excessively long data and the experiment results demonstrate that the ERA + RDT approach is efficient and can provide more precise results.

Studies on the aerodynamic damping of tall buildings are generally limited, and only discrete test results were presented. In the present research, six single-degree-of-freedom (SDOF) aeroelastic models of tall buildings with typical cross-sections (square, square with concave or bevel corners, and rectangular) were tested in a wind tunnel with a suburban terrain flow field condition. The effects of wind speed, concave or bevel corner, side ratio, and wind direction on the along-wind and across-wind aerodynamic damping are studied by using the ERA + RDT method to evaluate the aerodynamic damping ratios. Several conclusions were eventually obtained.

2. Experimental Setup

2.1. Simulation of Wind Characteristic. The test was carried out in the TJ-1 Boundary Layer Wind Tunnel with a working section of 1.8 m in width and 1.8 m in height as well as a wind speed ranging from 3 m/s to 32 m/s. A 1:500 scaled

wind model of the natural wind flow over a suburban terrain (terrain category C based on the Chinese load code GB50009-2012) was simulated in the wind tunnel. The exponent of the mean wind profiles for the suburban terrain was 0.22, and the corresponding gradient height was 450 m. The wind characteristic was achieved by combining turbulence generating spires, a barrier at the entrance of the wind tunnel, and roughness elements along the wind tunnel floor upstream of the model. Figure 1 shows the simulated mean wind velocity profile, turbulent intensity profile, and power spectral density of the fluctuating wind velocity at the model height in the wind tunnel.

2.2. Building Models. The building models had a height of 60 cm, which represents a height of 300 m for real buildings (i.e., a length scale of 1:500). The wind velocity scale of the wind tunnel test was set as 1:8. The other scales, such as for structural mass and frequency, were correspondingly determined based on the above basic scales C_V and C_L . Therefore, the mass and frequency as well as time scales were $C_m = 1.25 \times 10^8$, $C_f = 62.5$, and $C_t = 1/62.5$, respectively.

The structural parameters of the typical super high-rise building should be initially determined to reasonably investigate the effects of the factors on aerodynamic damping. Firstly, in terms of investigations of a great number of tall buildings in Japan [17], the first translation mode natural frequency (f_1) of common high-rise buildings with a height of 300 m is estimated to be

$$f_1 = \frac{1}{0.015H} \sim \frac{1}{0.02H} = 0.167 \sim 0.222 \text{ Hz} \quad (1)$$

In addition, average mass densities of common high-rise buildings are usually 160 kg/m^3 to 240 kg/m^3 . The mass density of a typical building in this paper was set as 180 kg/m^3 because super high-rise buildings were prone to being light.

TABLE 1: Dimensions of the models.

Case	Height of model (cm)	Cross section (cm)	Corner modified	Frequency (Hz)	
				f_x	f_y
A	60	10 × 10	—	20.0	12.2
B	60	10 × 10	Concave corner 10%	20.0	12.2
C	60	10 × 10	Bevel corner 10%	20.0	12.2
D	60	10 × 15	—	19.0	11.7
E	60	10 × 20	—	17.8	11.2
F	60	10 × 30	—	16.1	10.4

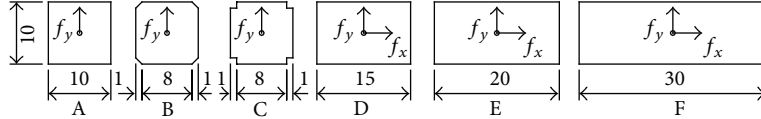


FIGURE 2: Cross sections of the six models (unit: cm).

In this study, the parameters of the six SDOF aeroelastic models (A to F) are listed in Table 1, and the cross sections are presented in Figure 2. Six kinds of cross sections, namely, square, square with concave or bevel corners, and rectangular (side ratio D/B of 0.3 to 3) were tested to study the aerodynamic damping of typical tall buildings.

The square prism model (Case A) is the basic one of the six models. This model had dimensions of 0.1 m (B) × 0.1 m (B) × 0.6 m (H), which represents a real building with a height of 300 m and a breadth of 50 m. The mass densities of the buildings (ρ_s) were all set as 180 kg/m³. The critical structural damping ratio (ζ_s) of the model was set as 1.2%, whereas the critical structural damping ratios (ζ_s) of the other models were set as 1.1%. The first mode frequencies for free vibrations at the x and y directions are shown in Table 1.

Figure 3 shows the specially designed supporting base of the aeroelastic model, where the rigid building model could vibrate in two perpendicular directions under wind actions [11, 18, 19]. The required mass and stiffness can be achieved by selecting appropriate mass blocks and springs, respectively. Structural damping ratios can be simulated by selecting damping cards of proper size and depth for immersion into the oil pool. In the wind tunnel test, the damping cards were bent toward their vibration direction in the oil pool to ensure that the structural damping ratios are independent from their vibration amplitudes. Two mini-accelerometers were perpendicularly mounted on top of the model to measure the along-wind and across-wind responses. The testing wind velocity at the level of the model height (U_H) ranged from 4 m/s to 16 m/s. The data were recorded for a sampling duration of 87.38 seconds at a sampling rate of 375 Hz; that is, 32768 data were recorded for each channel.

3. Methods for Identifying Aerodynamic Damping

The methods for estimating damping from a time history of random vibration responses can be classified into two

categories: frequency and time domain approaches. The frequency-domain approaches are those related to spectral analysis, such as the spectra-based half-power and the spectral moment methods. The time-series approaches include the autocorrelation decay, RDT, maximum entropy estimates, autoregressive (AR), and the moving averages (ARMA).

The RDT is widely used to evaluate aerodynamic damping ratios from the random vibration responses of structures that are excited by random wind loads [11, 13–15, 20]. In the RDT method, the measured structural responses are averaged by using a common initial or triggering condition, where a random decrement function is gained and which can be considered as the free vibration responses of the structures. Structural damping ratios and frequencies can be easily acquired based on the assumption of the free vibration response.

RDT extracts free-decay responses from a series of samples but requires very long data to average. The average number of the RDT method is over 5,000 times in order to attain better results, which reveals the necessity of a large amount of data in applying the RDT technique [14]. When exponential functions are used to fit the diminishing processes of the free-decay responses, only several peak data are used to obtain the structural damping ratios and frequencies [21]. The accuracy of RDT may not be satisfactory in certain conditions, such as the nonstationary time histories of measured responses, or when the structural modes of a model are densely distributed [16].

3.1. ERA + RDT Method. The RDT is a time domain procedure and is considered in association with the time domain modal identification algorithm, such as the ERA method, to improve precision in identification. In this study, a time domain method, namely, ERA [22], is used in conjunction with the RDT technique (ERA + RDT), to evaluate the aerodynamic damping ratios based on the random vibration responses of the aeroelastic model tests. The ERA + RDT method has a higher precision than RDT and could identify the high-order mode parameters of the models with

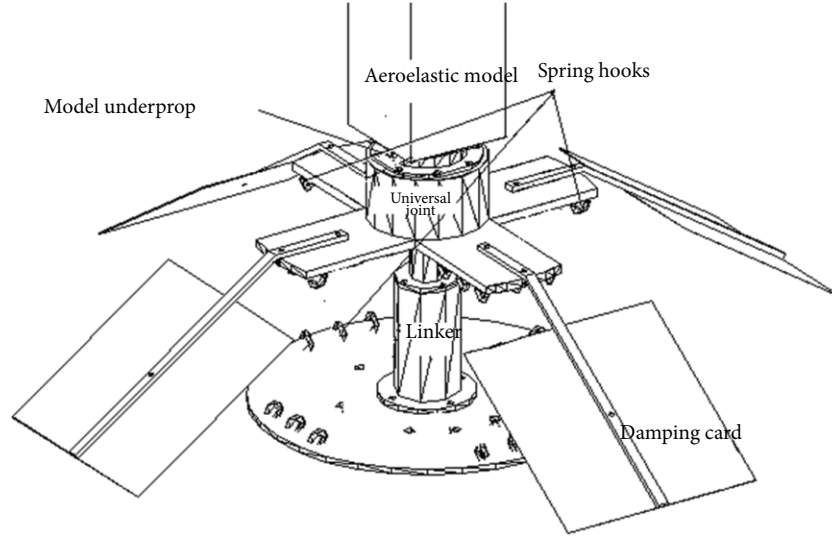


FIGURE 3: Base of the SDOF aeroelastic model [11].

satisfactory accuracy. The ERA + RDT method likewise does not require very long data from tests.

The ERA is based on the system impulse response or free decay response. In the discrete-time space, the motion of an N -degree-of-freedom system with the action of $\{u\}$ can be expressed by the state equation as follows:

$$\begin{aligned} \{x(k+1)\} &= A\{x(k)\} + B\{u(k)\}, \\ \{y(k)\} &= C\{x(k)\}, \end{aligned} \quad (2)$$

where A , B , and C are the state, input, and output matrices, respectively; $\{x(k+1)\}$ and $\{x(k)\}$ are the states at time instant $(k+1)\Delta t$ and $k\Delta t$; $\{y(k)\}$ is the response at time $k\Delta t$; and Δt is the sampling time interval.

The response $\{y(k)\}$ of the system is related to the state, input, and output matrices A , B , and C are based on the random vibration theory:

$$\{y(k)\} = CA^{k-1}B, \quad (k > 0). \quad (3)$$

By forming the block Hankel matrix,

$$\begin{aligned} &H_{rs}(k-1) \\ &= \begin{bmatrix} \{y(k)\} & \{y(k+1)\} & \cdots & \{y(k+s)\} \\ \{y(k+1)\} & \{y(k+2)\} & \cdots & \{y(k+s+1)\} \\ \vdots & \vdots & & \vdots \\ \{y(k+r)\} & \{y(k+r+1)\} & \cdots & \{y(k+s+r)\} \end{bmatrix}. \end{aligned} \quad (4)$$

The state matrix (A) can be determined by using ERA:

$$A = S^{-1/2}P^T H_{rs}(1)QS^{-1/2}, \quad (5)$$

where r and s are the numbers of row and column shifts of the Hankel matrix, respectively; P , S , and Q are the matrices used to construct the pseudoinverse of $H_{rs}(0)$, which are

determined by the singular value decomposition (SVD) of the matrix $H_{rs}(0)$:

$$H_{rs}(0) = PSV^T. \quad (6)$$

The modal parameters of the system (building) can be determined by solving the eigenvalue problem of the state matrix A and by converting the eigen pairs into a continuous-time space.

The ERA method could only identify the modal parameters of the system impulse responses or free decay responses. These are obtained by using the RDT technique, such that the random decrement functions gained by the RDT can be considered as the free vibration responses of structures.

3.2. Definition of the Aerodynamic Damping Ratio. When a building model is under the action of a random wind load in a wind tunnel, the damping ratio identified with this method includes not only the structural damping ratio, but also the aerodynamic damping ratio. The aerodynamic damping ratios can be obtained after the structural damping ratio is subtracted from the total damping ratio:

$$\zeta_a = \zeta_T - \zeta_s, \quad (7)$$

where

ζ_a is the aerodynamic damping ratio;

ζ_T is the total damping ratio;

ζ_s is the structural damping ratio of the model.

3.3. Validation of the ERA + RDT Method. The proposed method is validated through a comparison of the aerodynamic damping ratios of the square building model obtained by the ERA + RDT with short-term (87.38 s) data (current paper) and those of the same model estimated only by the RDT technique with long-term data [11]. Quan et al. [11]

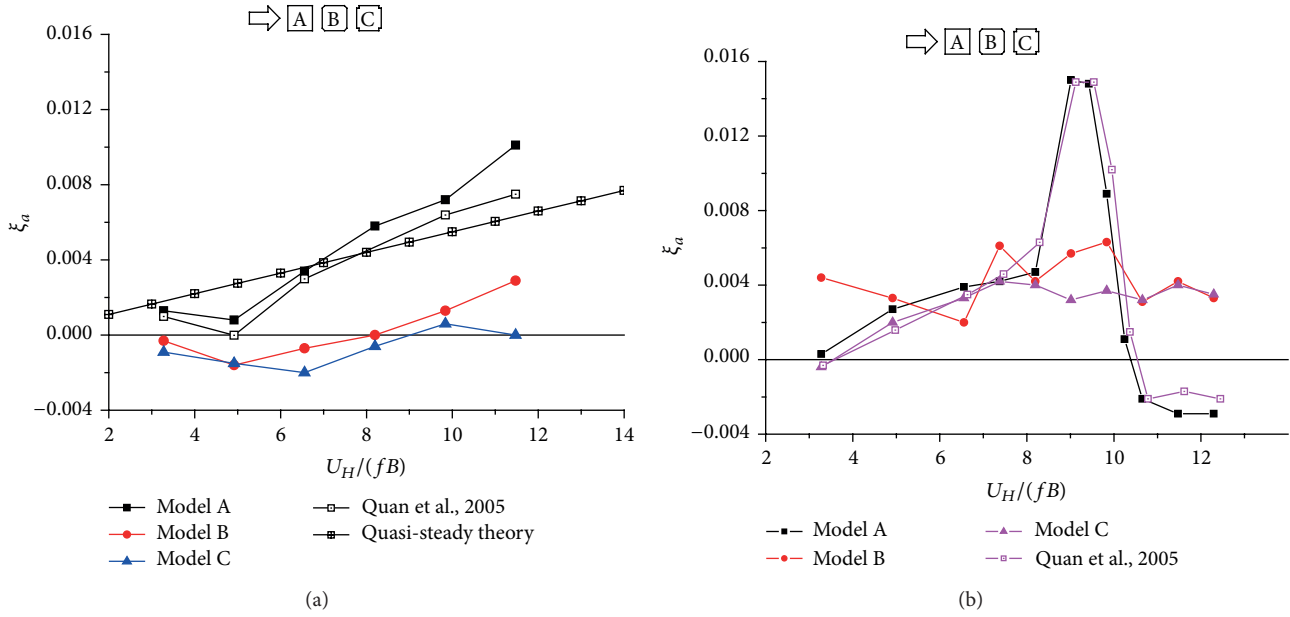


FIGURE 4: Effect of corner-modified shape: (a) along-wind; and (b) across-wind.

studied the aerodynamic damping ratios by using several structural damping ratios and terrain types. Data were recorded given a sampling duration of 825 s because only the RDT technique was applied. The average numbers of the random decrement function using the RDT method were 7,500 to 11,000. Figure 4 shows the results, and the ratios identified by the ERA + RDT method were almost the same as those based on the long-term data, which indicates that the ERA + RDT method used in this paper is valid and accurate. At the same time, the identified results are compared with the calculated aerodynamic damping ratios based on the quasi-steady theory [4], whose values are similar and have the same tendency.

4. Experimental Results and Discussions

Six kinds of cross sections of tall buildings, namely, square, square with concave or bevel corners, and rectangular (side ratio D/B is 0.3 to 3), were tested to study the effects of wind speed, corner modifications (concave or bevel corner), side ratio, and wind direction on the aerodynamic damping of typical tall buildings. The along-wind aerodynamic damping was generally positive in most cases and gradually increased with the increase of reduced wind speed (U_r). The across-wind aerodynamic damping was likewise positive at low U_r in most cases, but suddenly becomes negative when the U_r is greater than 10.5 for the square cross-section building. Further experimentation is necessary on rectangular cross-section buildings to obtain results when the U_r is greater than 10.

4.1. Effect of Modified Corner. Figure 4 shows the identified aerodynamic damping ratios of square buildings with and without modified corners.

4.1.1. Square Building without Modified Corners. In the along-wind direction, aerodynamic damping ratios are generally positive and increase with an increase of wind speed. In the across-wind direction, aerodynamic damping ratios are likewise positive and slowly increase with wind speed when the U_r is

$$U_r = \frac{U_H}{f\sqrt{BD}} \leq 8. \quad (8)$$

When U_r steadily increases from 8, the across-wind aerodynamic damping ratios increase rapidly and attain peak values at U_r of approximately 9 to 10. When wind speed further increases, the aerodynamic damping ratios suddenly decrease and become negative at U_r greater than 10.5.

4.1.2. Square Building with Modified Corners. The aerodynamic damping ratios of corner-modified square cross-section buildings (10% concave corner and 10% bevel corner) tend to be similar to those of square buildings without modified corners. In the along-wind direction, aerodynamic damping ratios appear to have negative values when the U_r is less than or equal to 7. However, the absolute values are small and the influence of these ratios could be negligible for practical purposes. When wind speed increases, the aerodynamic damping ratios increase to positive values, which are much smaller than those of the square building. In the across-wind direction, all aerodynamic damping ratios are positive and are almost the same as those of the square building when U_r is smaller than or equal to 8. When U_r is greater than 8, the aerodynamic damping ratios of the corner-modified square buildings retain the same variation tendency as those when U_r is less than 8. The damping characteristics seem to indicate that the effects of the aerodynamic damping in both the along-wind and across-wind directions of the

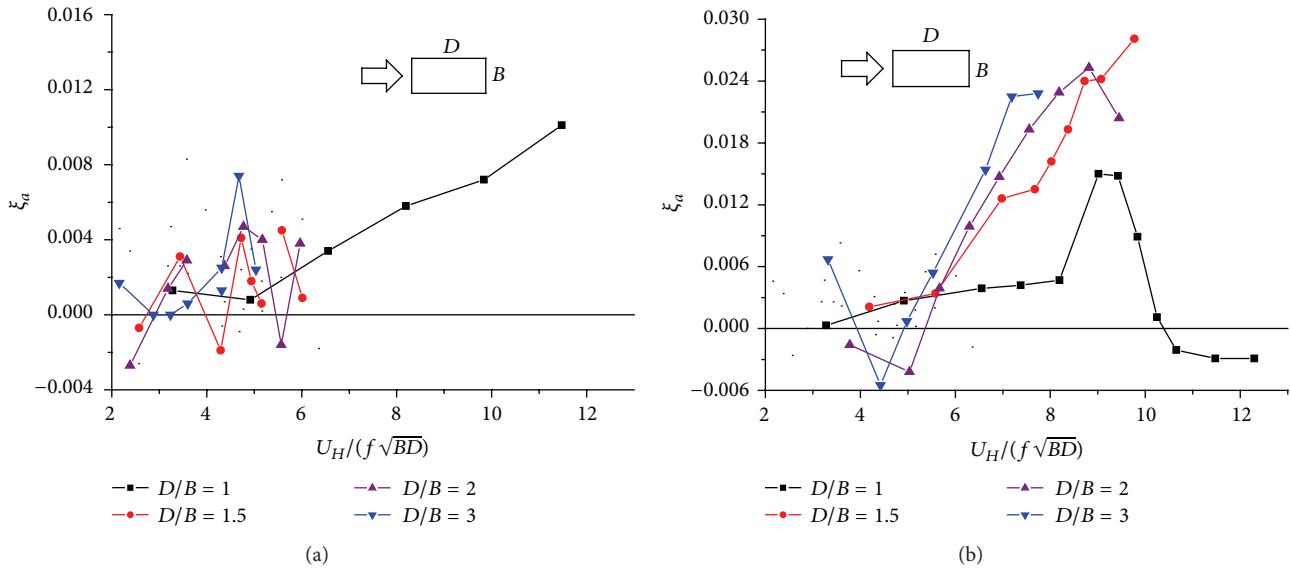


FIGURE 5: Effect of the side ratio ($D/B \geq 1$): (a) along-wind; and (b) across-wind.

buildings with corner modifications could be neglected for engineering purposes.

4.2. Effect of Side Ratios (D/B)

4.2.1. D/B is Greater Than or Equal to 1. The effect of the side ratios (D/B is equal to 1, 1.5, 2, and 3) on the aerodynamic damping of rectangular cross-section tall buildings is presented in Figure 5. In the along-wind direction, the aerodynamic damping ratios of the rectangular buildings (D/B of greater than 1) tend to be similar to those of the square building (D/B equal to 1) when U_r is less than or equal to 6. When U_r is greater than 6, further experimentation is necessary.

In the across-wind direction, the aerodynamic damping ratios of rectangular cross-section buildings (D/B equal to 1.5, 2, and 3) have a similar variation tendency with the wind speed, which increases more rapidly than those of the square building. The aerodynamic damping ratios of the rectangular buildings appear to have negative values when the U_r is less than or equal to 5, with a minimum value of -0.55% . The further increase of reduced wind velocity from 6 causes the aerodynamic damping ratios of rectangular buildings to generally increase with a side ratio. All the aerodynamic damping ratios are much larger than those of the square building.

The across-wind aerodynamic damping ratios of the square building suddenly decrease and become negative values when U_r is greater than 10.5. Further experimentation is necessary to obtain results for rectangular cross-section buildings with U_r greater than 10.

4.2.2. D/B Is Smaller Than or Equal to 1. Figure 6 shows the effect of the side ratios (D/B equal to 1, 0.67, 0.5, and 0.33) on the aerodynamic damping of rectangular cross-section tall buildings. In the along-wind direction, the aerodynamic

damping ratios of the four kinds of side ratios are positive. The aerodynamic damping ratios of rectangular buildings generally decrease with the side ratio but are larger than those of the square building.

In the across-wind direction, the aerodynamic damping ratios of buildings with a D/B equal to 0.67 have a similar variation tendency as those of the square building when the U_r is less than or equal to 6. The aerodynamic damping ratios of buildings with D/B s equal to 0.5 and 0.33 are small, and finding the variation laws with the wind speed is difficult. The aerodynamic damping ratios of rectangular buildings with D/B s equal to 1 also appeared to have some negative values, but the absolute values were very small. Further experimentation is necessary for U_r that is greater than 6.

4.2.3. Comparison between the Present Study and Marukawa. Marukawa et al. [8] identified the along-wind and across-wind aerodynamic damping ratios of square and rectangular cross-section buildings by using the RDT from a SDOF aeroelastic model wind tunnel test. The side ratios of the models ranged from 0.33 to 3 with a basic aspect ratio of 6. The simulated wind flow was the flow over the open terrain, where the exponent of the wind profile and the turbulent intensity at the top of the model were 0.167 and 10.7%, respectively. The structural damping ratio of the building model was 1%.

The comparisons of the aerodynamic damping ratios between the present study and Marukawa are shown in Figure 7. The aerodynamic damping ratios of the two studies revealed a common tendency, despite the differences in the values of the aerodynamic damping ratios that may have been caused by the different simulated terrain conditions.

4.3. Effect of Wind Direction. Studying the effect of wind direction on aerodynamic damping is important for practical purposes because wind flow is not always normal to the building facades. The variations of the aerodynamic damping

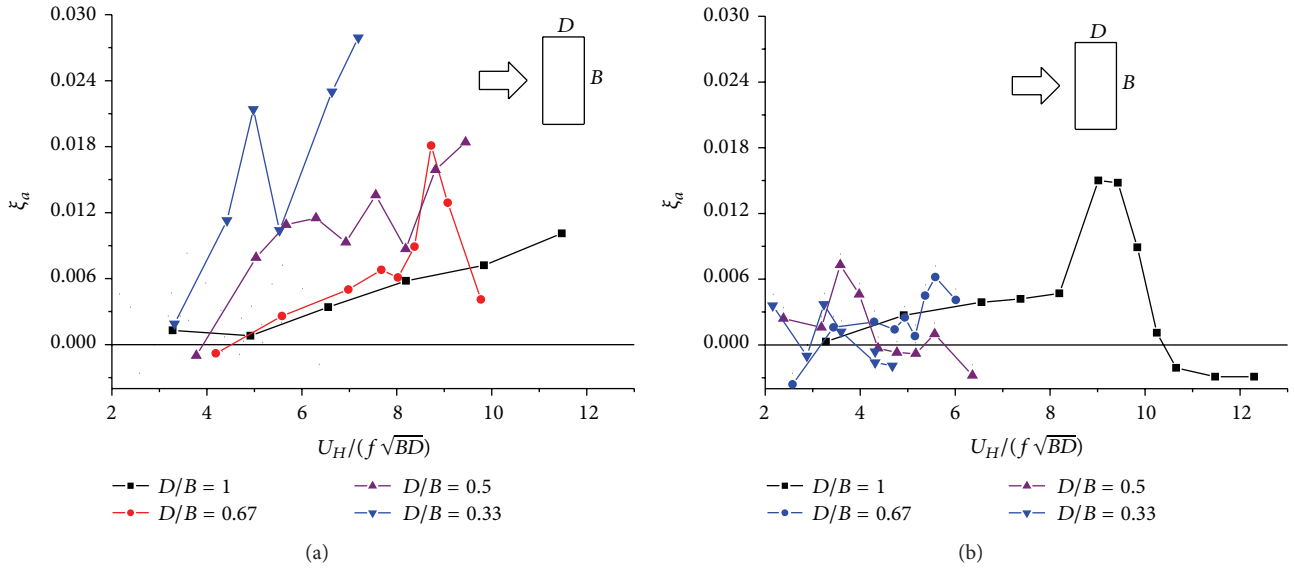


FIGURE 6: Effect of the side ratio ($D/B \leq 1$): (a) along-wind; and (b) across-wind.

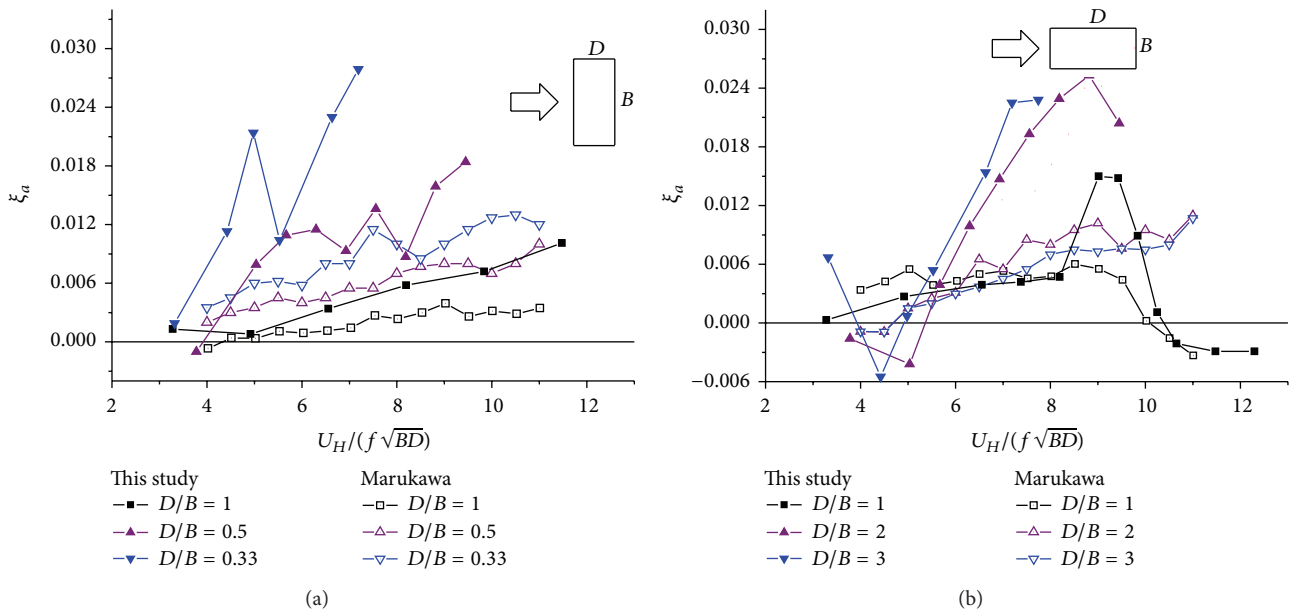


FIGURE 7: Comparison between the present study and that of Marukawa et al. [8]: (a) along-wind ($D/B \leq 1$); and (b) across-wind ($D/B \geq 1$).

ratios of the rectangular cross-section buildings (D/B s of 1.5 and 3) with the wind direction are illustrated in Figure 8.

The aerodynamic damping ratio for the rectangular building with a D/B of 1.5 tends to increase with the increase of wind angle. The minimum value was -0.55% at a 0° angle (i.e., across-wind direction) and U_r of 4.4. The maximum value was 3.0% at an 80° angle and U_r of 6.6.

The aerodynamic damping ratios for the building with a D/B of 3 were all positive with the maximum value of 2.9% at a 0° angle (across-wind direction) and U_r of 9.8. The aerodynamic damping ratios of the two rectangular buildings likewise have the common tendency to roughly increase with the increase of wind speed.

5. Concluding Remarks

The conclusions on the along-wind and across-wind aerodynamic damping ratios of different cross-sections of tall buildings as obtained by using the wind tunnel experiment are as follows.

- (1) The aerodynamic damping ratios identified by the ERA + RDT method were almost the same as those based on the long-term data, which indicates that the ERA + RDT method used in this paper is valid and accurate.
- (2) The along-wind aerodynamic damping is positive in most cases and gradually increases with the increase

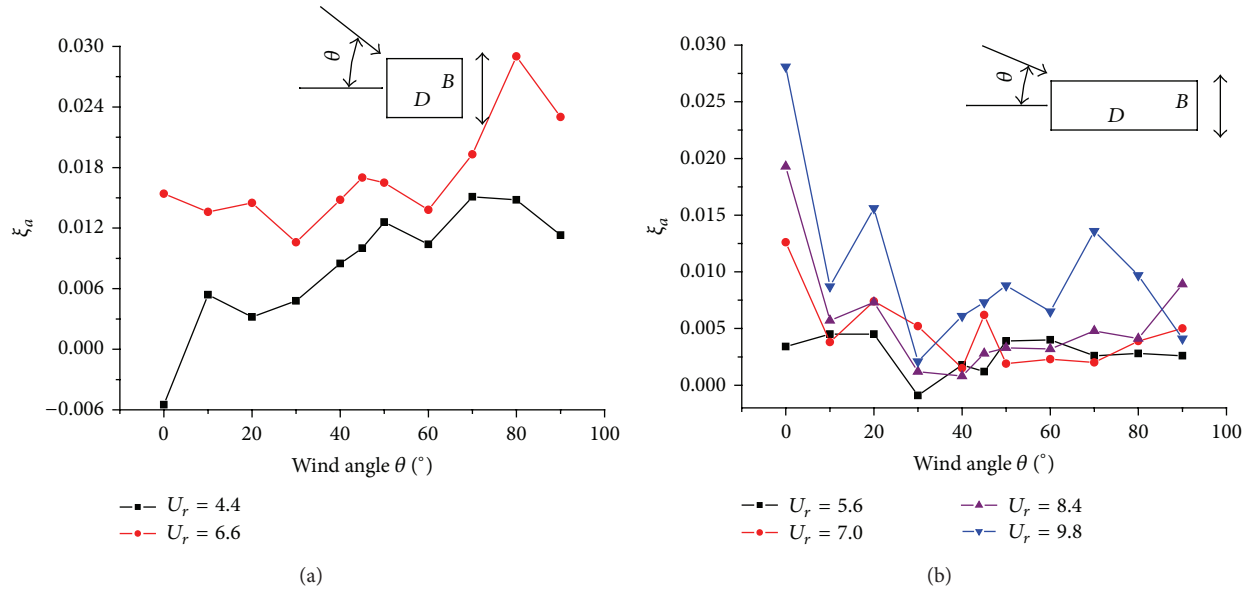


FIGURE 8: Variations of the aerodynamic damping ratios with the wind angle: (a) $D/B = 1.5$; and (b) $D/B = 3$.

- of U_r . The across-wind aerodynamic damping was likewise positive at low U_r , in most cases, but suddenly became negative when the U_r is greater than 10.5 for the square cross-section building. Further experimentation on rectangular cross-section buildings is necessary to obtain results when U_r is greater than 10.
- (3) The along-wind aerodynamic damping ratios for tall buildings with a corner-modified square cross-section (10% concave corner and 10% bevel corner), appeared to have some negative and small absolute values at a low wind speed. The across-wind aerodynamic damping ratios were all positive and small. These results indicate that the effects of aerodynamic damping in the along-wind and across-wind directions of buildings with corner modifications may be neglected for engineering purposes.
 - (4) Both the along-wind and across-wind aerodynamic damping ratios for the rectangular cross-section buildings with a D/B greater than 1 appeared to have some negative values at a low wind speed. The across-wind aerodynamic damping ratios at a high wind speed were large, reaching 2.9%.
 - (5) All of the along-wind aerodynamic damping ratios for the rectangular cross-section buildings with a D/B smaller than 1 were positive, and the across-wind aerodynamic damping ratios appeared to have some negative values at a low wind speed. The across-wind aerodynamic damping ratios at a high wind speed were large, reaching 2.3% to 2.8%.

Acknowledgment

This project is supported by Chinese National Natural Science Foundation (nos. 51178352, 90715040, and 91215302), which is gratefully appreciated.

References

- [1] A. G. Davenport, *The Influence of Turbulence on the Aeroelastic Responses of Tall Structures to Wind*, University of Karlsruhe, Karlsruhe, Germany, 1979.
- [2] J. D. Holmes, "Along-wind response of lattice towers—II. Aerodynamic damping and deflections," *Engineering Structures*, vol. 18, no. 7, pp. 483–488, 1996.
- [3] J. D. Holmes, *Wind Loading of Structures*, E & FN Spon, London, UK, 2001.
- [4] R. D. Gabbai and E. Simiu, "Aerodynamic damping in the along-wind response of tall buildings," *Journal of Structural Engineering*, vol. 136, no. 1, pp. 117–119, 2010.
- [5] A. Kareem, *Wind excited motion of buildings [Ph.D. thesis]*, Colorado State University at Fort Collin, Colorado, Colo, USA, 1978.
- [6] A. Steckley, *Motion-induced wind forces on chimneys and tall buildings [Ph.D. thesis]*, University of Western Ontario, Ontario, Canada, 1989.
- [7] H. Nishimura and Y. Taniike, "Unsteady wind force on a square prism in a turbulent boundary layer," in *Proceedings of the 9th International Conference on Wind Engineering: Retrospect and Prospect (ICWE '95)*, pp. 195–203, New Delhi, India, 1995.
- [8] H. Marukawa, N. Kato, K. Fujii, and Y. Tamura, "Experimental evaluation of aerodynamic damping of tall buildings," *Journal of Wind Engineering and Industrial Aerodynamics*, vol. 59, no. 2-3, pp. 177–190, 1996.
- [9] Y. Watanabe, N. Isyumov, and A. G. Davenport, "Empirical aerodynamic damping function for tall buildings," *Journal of Wind Engineering and Industrial Aerodynamics*, vol. 72, no. 1–3, pp. 313–321, 1997.
- [10] C. M. Cheng and Y. C. Chiang, "Acrosswind aerodynamic damping of rectangular tall buildings," in *Proceedings of the 2nd International Symposium on Wind and Structures*, Busan, Republic of Korea, 2002.
- [11] Y. Quan, M. Gu, and Y. Tamura, "Experimental evaluation of aerodynamic damping of square super high-rise buildings," *Wind and Structures*, vol. 8, no. 5, pp. 309–324, 2005.

- [12] H. Hayashida, Y. Mataki, and Y. Iwasa, "Aerodynamic damping effects of tall building for a vortex induced vibration," *Journal of Wind Engineering and Industrial Aerodynamics*, vol. 43, no. 1-3, pp. 1973-1983, 1992.
- [13] S. R. Ibrahim, "Random decrement technique for modal identification of structures," *Journal of Spacecraft and Rockets*, vol. 14, no. 11, pp. 696-700, 1977.
- [14] Y. Tamura and S. Suganuma, "Evaluation of amplitude-dependent damping and natural frequency of buildings during strong winds," *Journal of Wind Engineering and Industrial Aerodynamics*, vol. 59, no. 2-3, pp. 115-130, 1996.
- [15] A. Kareem and K. Gurley, "Damping in structures: its evaluation and treatment of uncertainty," *Journal of Wind Engineering and Industrial Aerodynamics*, vol. 59, no. 2-3, pp. 131-157, 1996.
- [16] A. P. Jeary, "Damping in tall buildings-a mechanism and predictor," *Earthquake Engineering and Structural Dynamics*, vol. 14, no. 5, pp. 733-759, 1986.
- [17] Y. Tamura, K. Suda, and A. Sasaki, "Damping in buildings for wind resistant design," in *Proceedings of the International Symposium on Wind and Structures for the 21st Century*, pp. 115-129, Cheju, Republic of Korea, January 2000.
- [18] T. H. Yi, H. N. Li, and X. D. Zhang, "Sensor placement on Canton Tower for health monitoring using asynchronous-climb monkey algorithm," *Smart Materials and Structures*, vol. 21, no. 12, Article ID 125023, pp. 1-12, 2012.
- [19] T. H. Yi, H. N. Li, and X. Wang, "Multi-dimensional sensor placement optimization for Canton Tower focusing on application demands," *Smart Structures And Systems*, vol. 12, no. 3-4, pp. 235-250, 2013.
- [20] H. F. Bai, T. H. Yi, H. N. Li, and L. Ren, "Multisensors on-site monitoring and characteristic analysis of UHV transmission tower," *International Journal of Distributed Sensor Networks*, vol. 2012, Article ID 545148, 10 pages, 2012.
- [21] R. W. Clough and J. Penzien, *Dynamics of Structures*, Computers & Structures, Berkeley, Calif, USA, 3rd edition, 2003.
- [22] J. Juang and R. S. Pappa, "An Eigensystem Realization Algorithm for modal parameter identification and model reduction," *Journal of Guidance, Control, and Dynamics*, vol. 8, no. 5, pp. 620-627, 1985.

Research Article

An Improved Negative Pressure Wave Method for Natural Gas Pipeline Leak Location Using FBG Based Strain Sensor and Wavelet Transform

Qingmin Hou,¹ Liang Ren,² Wenling Jiao,¹ Pinghua Zou,¹ and Gangbing Song^{2,3}

¹ School of Municipal and Environmental Engineering, Harbin Institute of Technology, Harbin 150090, China

² Faculty of Infrastructure Engineering, Dalian University of Technology, Dalian 116024, China

³ Department of Mechanical Engineering, University of Houston, Houston, TX 77004, USA

Correspondence should be addressed to Wenling Jiao; jiaowenling62@163.com

Received 24 August 2013; Accepted 27 September 2013

Academic Editor: Ting-Hua Yi

Copyright © 2013 Qingmin Hou et al. This is an open access article distributed under the Creative Commons Attribution License, which permits unrestricted use, distribution, and reproduction in any medium, provided the original work is properly cited.

Methods that more quickly locate leakages in natural gas pipelines are urgently required. In this paper, an improved negative pressure wave method based on FBG based strain sensors and wavelet analysis is proposed. This method takes into account the variation in the negative pressure wave propagation velocity and the gas velocity variation, uses the traditional leak location formula, and employs Compound Simpson and Dichotomy Searching for solving this formula. In addition, a FBG based strain sensor instead of a traditional pressure sensor was developed for detecting the negative pressure wave signal produced by leakage. Unlike traditional sensors, FBG sensors can be installed anywhere along the pipeline, thus leading to high positioning accuracy through more frequent installment of the sensors. Finally, a wavelet transform method was employed to locate the pressure drop points within the FBG signals. Experiment results show good positioning accuracy for natural gas pipeline leakage, using this new method.

1. Introduction

Nowadays, pipelines have become ubiquitous for natural gas transportation. Therefore, natural gas pipelines play a vital role in modern enterprises and economies. However, leakage from natural gas pipelines occurs due to inevitable factors such as pipeline aging, erosion, natural disaster, and third party intrusion. Without proper and immediate fixing, leakage can lead to serious pollution and the danger of explosion due to the poisonous and explosive properties of natural gas. Therefore, effective ways to detect the exact position of leakage accidents are important, so that losses and danger can be greatly reduced.

Over recent years, the number of techniques for leak location of natural gas pipeline has been grown [1]. Presently, methods based on control theory and signal processing are popular, such as the methods based on model detection, pressure gradient, and methods based on negative pressure waves [2, 3]. With the advantage of quick response speeds, the

negative pressure wave method based on pressure sensors is the most widely used leak location technology [4]. However, the installation of pressure sensors required for this method necessitates localized deconstruction of the pipeline. So pressure sensors are usually installed at input and output points of a pipeline and seldom anywhere in between. This leads to large signal attenuation and interference, leading to high rates of false alarms whilst reducing the precision of locating algorithms. In addition, the traditional leak location formula often assumes that the propagation velocity of the negative pressure wave and the velocity of natural gas in the pipeline are constants, even ignoring the velocity of natural gas. This does not match with the actual situation and will inevitably result in a large positioning error. Therefore, research is required into developing an improved method to overcome these shortcomings.

Distributed fiber optical sensors have been widely used for leak detection and location of natural gas pipeline [5–7]. The simple principle of this method is that a leak in a

natural gas pipeline will lead to temperature variation or vibration, which can be detected by a distributed fiber optical sensor. The position of leakage point can be obtained by processing the captured signal. Temperature variation or vibration can be caused by other factors such as environment temperature change or random vibration of fiber optical. Thus vulnerable to interference and high false positive rate are main drawbacks of this method.

Fiber Bragg grating (FBG) sensor offers a number of advantages over traditional sensor, including immunity to electromagnetic interference, being light weight and durable, having small size, incorporating multiplexing capabilities, and is easy to install [8–14]. Due to the above attractive application features, FBG sensors have been playing an increasingly important role in the sensing community and have been widely used in structural health monitoring, damage detection, aviation, and other fields [15–21]. However, FBGs have not been extensively adopted in natural gas pipeline leakage location. While a kind of swellable polymer based FBG strain sensor has been proposed for oil pipeline leak detection and location [22]. The main component of natural gas is methane, the chemical properties of methane are very stable, and only a scarce number of polymer types swell when encountering methane. Therefore, this method is not suitable for natural gas pipeline. It is necessary to develop a FBG sensor applicable to natural gas pipelines.

In this paper, firstly, a modified leakage location formula was proposed based on the principle of negative pressure wave location, and Compound Simpson formula and Dichotomy Searching were employed to solve this formula. Secondly, a FBG based strain sensor for collecting the negative pressure wave signals was developed and experimentally tested. Finally, in order to get accurate time difference for that formula, a wavelet transform method was demonstrated to identify the pressure drop point within the FBG signals.

2. Modified Leak Location Formula

2.1. Principle of Negative Pressure Wave Leak Location and Traditional Leak Location Formula. When leaks develop in a natural gas pipeline, the gas density near the leaking point will decrease rapidly. This phenomenon results in a negative pressure wave, which propagates through the pipeline from the leak point. Pressure sensors installed upstream and downstream can collect such negative pressure wave signals. According to time difference for detected signals and propagation velocity in the medium, the exact position of the leakage can be calculated [23]. The principle for negative pressure wave propagation is now described, in relation to Figure 1.

In regard to Figure 1, assume that the distance between two sensors is L , the propagation velocity of negative pressure wave in the pipeline is v , the distance between the leak point and upstream sensor is x , the times when the wave is detected by the two sensors are t_1, t_2 , and the velocity of natural gas in the pipeline is u .

As the pipeline diameter and gas transportation velocity increase, the velocity of natural gas cannot be ignored compared with that of the negative pressure wave. With the velocity of natural gas taken into consideration in our study,

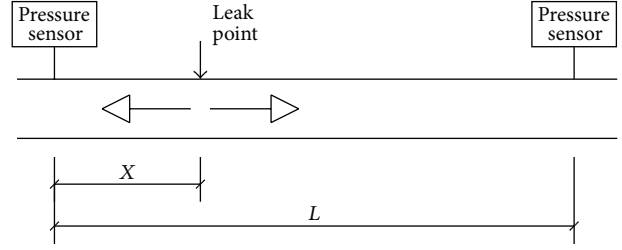


FIGURE 1: Schematic of negative pressure wave propagation.

the relations between the length and time variables can be developed as follows:

$$\begin{aligned} t_1 &= \frac{x}{(v - u)}, \\ t_2 &= \frac{(L - x)}{(v + u)}, \\ \Delta t &= t_1 - t_2. \end{aligned} \quad (1)$$

The distance between the leak point and upstream sensor can be obtained from (1):

$$x = \frac{1}{2v} [L(v - u) + \Delta t (v^2 - u^2)]. \quad (2)$$

Equation (2) is the traditional leak location formula.

2.2. Modification of Leak Location Formula. The traditional formula assumes that the propagation velocity of the negative pressure wave, v , and the velocity of natural gas in the pipeline, u , are constants. In fact, v and u are related with the temperature, pressure, density, and specific heat of the surrounding medium, and the formulas of these two velocities can be obtained by thermal and hydraulics analysis. Treating the propagation velocity of the negative pressure wave and natural gas as variable parameters, the leak location formula can be rewritten as

$$t_1 = \int_0^x \frac{1}{v(x) - u(x)} dx, \quad (3)$$

$$t_2 = \int_x^L \frac{1}{v(x) + u(x)} dx, \quad (4)$$

$$\Delta t = t_1 - t_2. \quad (5)$$

Since the expressions for $v(x)$ and $u(x)$ are complex, the integral above is not a simple definite integral. Therefore, numerical integral was chosen for determining t_1, t_2 . The Compound Simpson formula was employed to calculate the variable integral as given above.

As can be seen from the above equations, if a value for the leak position, x , is assumed, the propagation velocity of negative pressure wave $v(x)$ and the velocity of natural gas in the pipeline $u(x)$ can be calculated. Finally, the time difference Δt can be determined, from which the leak position x can be improved. This is a recursive formula, as x cannot be solved deterministically. Therefore, a Dichotomy Searching was employed to solve this problem.

2.3. The Methods of Solving the Modified Formula

2.3.1. Compound Simpson Formula. The integral domain $[a, b]$ is divided into n equal parts. The approximate integral value of the function $f(x)$ in this domain can be obtained by

$$\int_a^b f(x) dx = \frac{h}{6} \sum_{i=0}^{n-1} [f(x_i) + 4f(x_{i+1/2}) + f(x_{i+1})], \quad (6)$$

where $x_i = a + ih$ ($i = 0, 1, \dots, n$) and $h = (b - a)/n$, which is the step length.

Equation (6) is the Compound Simpson formula. Using this formula to solve (3) and (4), the time difference Δt can be obtained as

$$\begin{aligned} \Delta t &= t_1 - t_2 \\ &= \int_0^x \frac{1}{v(x) - u(x)} dx - \int_x^L \frac{1}{v(x) - u(x)} dx \\ &\approx \frac{h}{6} \sum_{i=x}^{x-1} \left[\frac{1}{v(x_i) - u(x_i)} + 4 \left(\frac{1}{v(x_{i+1/2}) - u(x_{i+1/2})} \right) \right. \\ &\quad \left. + \frac{1}{v(x_{i+1}) - u(x_{i+1})} \right] \\ &\quad - \frac{h}{6} \sum_{i=x}^{L-1} \left[\frac{1}{v(x_i) + u(x_i)} + 4 \left(\frac{1}{v(x_{i+1/2}) + u(x_{i+1/2})} \right) \right. \\ &\quad \left. + \frac{1}{v(x_{i+1}) + u(x_{i+1})} \right]. \end{aligned} \quad (7)$$

2.3.2. Dichotomy Searching. In order to locate the leaking point, Dichotomy Searching was used to determine x . Dichotomy Searching is explained below in reference to Figure 2.

As shown in Figure 2, the midpoint t_2 of domain $[t_0, t_4]$ is obtained to calculate $f(t_2)$, then $f(t_0)$, $f(t_2)$, and $f(t_4)$ are compared (in case of $f(t_0) < 0$, $f(t_4) > 0$).

- (1) If $f(t_2) > 0$, then $[t_2, t_4]$ is rejected, and Dichotomy Searching is going in the domain of $[t_0, t_2]$. The next computational point is the midpoint of domain $[t_0, t_2]$.
- (2) If $f(t_2) < 0$, then $[t_0, t_2]$ is rejected, and Dichotomy Searching is going in the domain of $[t_2, t_4]$. The next computational point is the midpoint of domain $[t_2, t_4]$.

In order to use this method to calculate the leak position, a function $f(x)$ is defined as follows:

$$f(x) = \frac{h}{6} \sum_{i=0}^{x-1} \left[\frac{1}{v(x_i) - u(x_i)} + 4 \left(\frac{1}{v(x_{i+1/2}) - u(x_{i+1/2})} \right) \right. \\ \left. + \frac{1}{v(x_{i+1}) - u(x_{i+1})} \right]$$

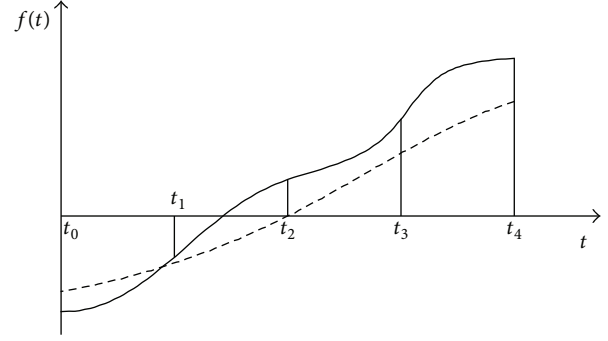


FIGURE 2: Sketch map of the Dichotomy Searching.

$$\begin{aligned} & - \frac{h}{6} \sum_{i=x}^{L-1} \left[\frac{1}{v(x_i) + u(x_i)} \right. \\ & \quad \left. + 4 \left(\frac{1}{v(x_{i+1/2}) + u(x_{i+1/2})} \right) \right. \\ & \quad \left. + \frac{1}{v(x_{i+1}) + u(x_{i+1})} \right] - \Delta t. \end{aligned} \quad (8)$$

The root of equation $f(x) = 0$ is just the leak position, and the flow chart of solving process is shown in Figure 3.

2.4. Critical Factors of Follow-Up Work. From (8), it can be clearly observed that the actual detection time difference plays an important role in leak location. Two critical factors for precise measurements of the time difference have been identified as follows:

- (1) sensors that can be easily installed, such that the spacing between sensors can be kept small,
- (2) accurate identification of the pressure drop point (t_1, t_2) from the sensor pressure trace, as this directly influences the sensitivity and reliability of leakage locating.

The following two sections address these critical factors.

3. FBG Based Strain Sensor and Experiment

3.1. Principle of FBG Based Strain Sensor. FBG based strain sensors are wrapped around the wall of a pipeline, as shown in Figure 4. A change in pressure within the pipeline leads to its expansion or contraction with the hoop (circumferential) strain of the pipeline changing accordingly. The FBG strain sensors detect pressure changes within the pipe by sensing the hoop strain. The hoop strain within a pipeline system can be expressed as

$$\varepsilon_y = \frac{\sigma_y - \nu \sigma_z}{E}, \quad (9)$$

where ε_y is the pipeline hoop strain, ν is the pipeline Poisson ratio, σ_y is the pipeline hoop stress, σ_z is the pipeline axial stress, and E is the pipeline elasticity modulus.

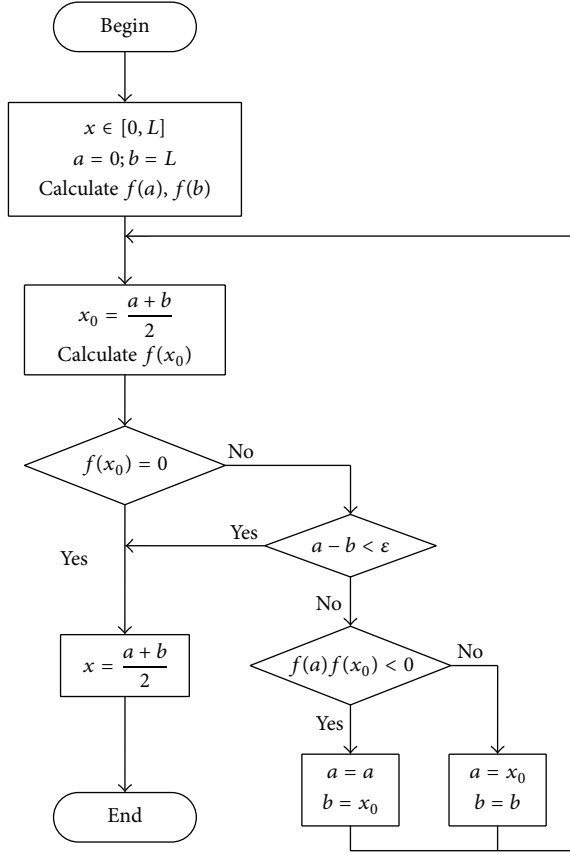


FIGURE 3: Flow chart of solving process.

Using (9), a relationship can be derived to relate the hoop strain with the pipeline pressure and pipe wall thickness. First, it is assumed that the pipeline is infinitely long, so that axial stress can be neglected; that is $\sigma_z = 0$. Meanwhile, as $\sigma_y = pR/h$, the values for σ_y and σ_z can be substituted into (9), which gives

$$\varepsilon_y = \frac{pR}{hE}, \quad (10)$$

where p is the pressure in the pipeline, R is the pipeline internal radius, and h is the pipeline wall thickness. As seen from (10), as the pressure in the pipeline changes, the pipeline hoop strain also changes linearly. Therefore FBG based strain sensors can detect the pressure variation by monitoring the hoop strain of the pipe wall.

3.2. Experimental Setup. The proposed methodology for detecting and locating gas pipeline leakage was tested on an experimental pipeline. The schematic for this gas pipeline is shown in Figure 5(a). Two air tanks and a section of pipeline were used to simulate a realistic gas transfer main. The pipeline in this experiment is made of steel, with a diameter of 273 mm as frequently used in practice. The pipeline length was 11 m due to lab space limitations. A leak point was simulated by manually opening valve at locations. As shown

in Figure 5(b), a rotameter was located at the leak point for measuring the leak rate, and two FBG strain sensors (L1, L2) were installed.

Briefly, the experimental process followed these steps: First, air is compressed into air tank 1 by air compressor. Air tank 1 plays the role of stabilizing the pressure in the pipeline. Second, when the pressure is stable, a valve is opened to simulate a leak in the pipeline. In the meantime, all the sensors gather data.

3.3. Experimental Results. The signals from FBG based strain sensors were captured to determine their ability to sense negative pressure waves caused by sudden leaks. A leakage was simulated by opening the valve at the leak point as shown in Figure 6(a). Sensors set upstream and downstream collected the hoop (circumferential) strain response, and the pipeline pressure was calculated from this signal. As seen in Figure 6, the pressure was steady before the leak occurred. A sudden pressure drop developed in the waveform that resulted from the leak. Because the duration of the leak was limited, so the pipeline finally returned to a steady but lower pressure due to the loss of gas. Furthermore, the waveforms recorded at L1 and L2 are similar, as shown in Figures 6(a) and 6(b); this was expected due to the propagation of the negative pressure wave on either side of the leak. These results indicate that the FBG based strain sensors can accurately detect the negative pressure wave produced by leakage events.

4. Identify the Pressure Drop Points Using Wavelet Transform

4.1. Definition of Wavelet Transform. The wavelet transform method was used to find the sharp transition in the FGB trace, corresponding to the movement of the negative pressure wave passes through the FBG sensor location. This method was used because this method can scale up the signal to find the sharp transition simply.

The definition of wavelet transform for a function $x(t)$ is given in [24–26]

$$\begin{aligned} WT_x(a, b) &= \int x(t) \psi^* \frac{[(t-b)/a]}{\sqrt{a}} dt \\ &= \int x(t) \psi_{a,b}^*(t) dt = \langle x(t), \psi_{a,b}(t) \rangle. \end{aligned} \quad (11)$$

In this equation, a , b , and t are continuous variables, which is also the reason why (11) is called the continuous wavelet transform. If the wavelet coefficients are computed on all possible scales, the computational burden is large. With the consideration of practical feasibility in numerical computation and simplicity of theoretical analysis, wavelet transforms are normally discretized in practice. The relevant discrete wavelet transform is described by

$$C_{j,k} = \int_{-\infty}^{+\infty} f(t) \psi_{j,k}^*(t) dt = \langle f, \psi_{j,k} \rangle, \quad (12)$$

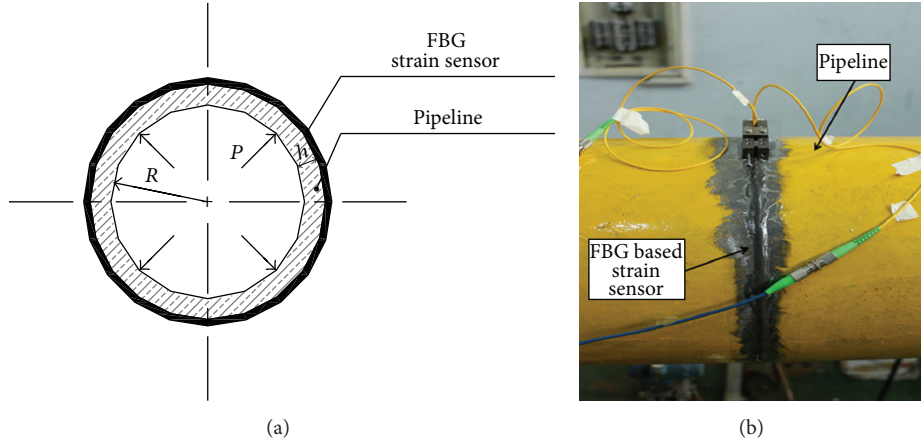


FIGURE 4: (a) Schematic of a FBG based strain sensor as installed on a pipeline; (b) photo of the sensor installed on an experimental pipeline.

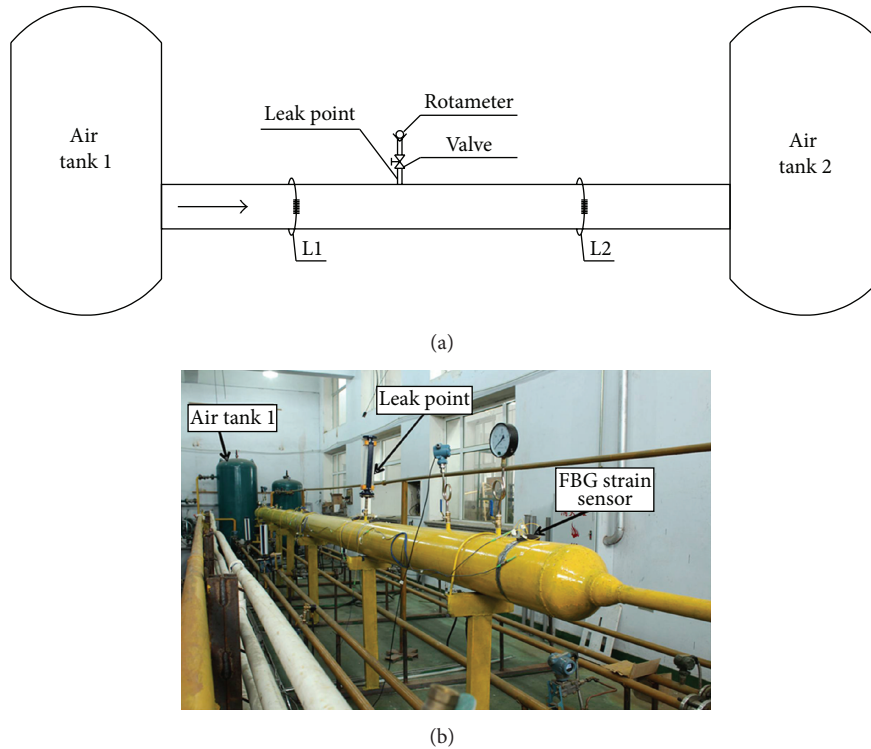


FIGURE 5: (a) Schematic diagram of experiment setup; (b) photo of experiment setup.

where $\psi_{j,k}(t)$ can be expressed in the following form:

$$\begin{aligned} \psi_{j,k}(t) &= \frac{a_0 \psi(t - ka_0^j b_0)}{a_0^j} \\ &= a_0^{-1/2} \psi(a_0^{-j} t - kb_0). \end{aligned} \quad (13)$$

In practice, wavelet in (13) is usually dyadic, which means that

$$\psi_{j,k} = 2^{-j/2} \psi(2^{-j} t - k) j, \quad k \in z. \quad (14)$$

4.2. The Application of Wavelet Transform and Positioning Results. The wavelet transform maxima in modulus on all possible transform scales correspond to the positions where the signals have sharp transition [27]. So the singularity can be obtained by detecting the wavelet transform maxima. Further, the wavelet transform modulus of real singularity is almost fixed value on all scales. In contrast, the modulus of faked singularities is inversely proportional to the scale. Consequently, it is reasonable to determine the real singularity by using this property. However, the detection of singularity is more accurate on a small scale, but this process is likely to be interrupted by noise, As a result, the faked singularity may

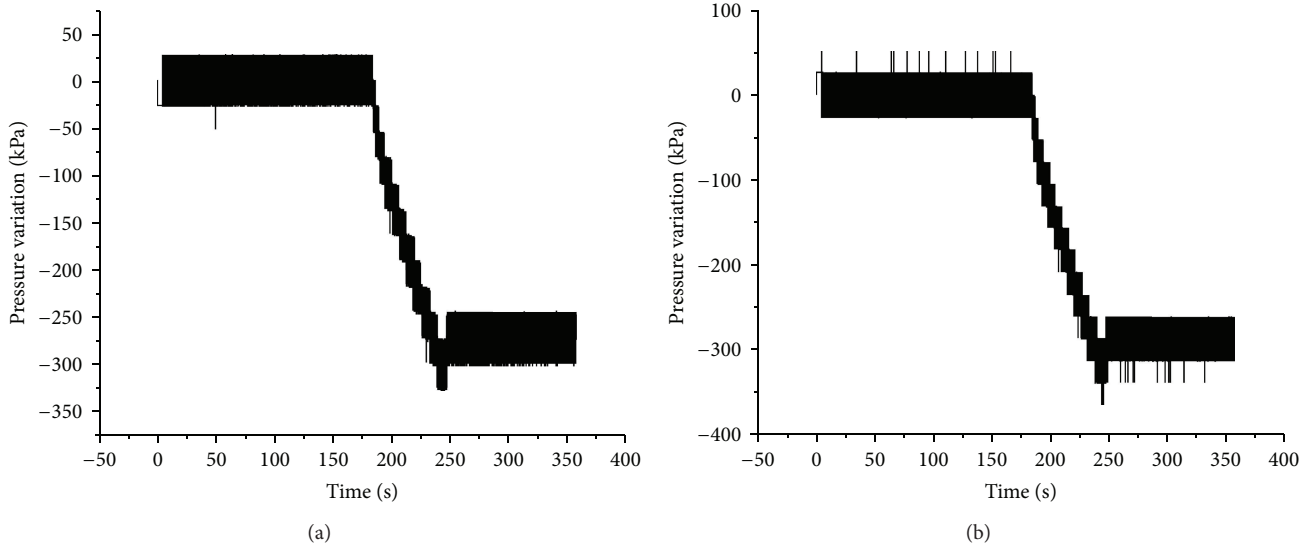


FIGURE 6: (a) Pressure measured by FBG based strain sensor L1; (b) pressure measured by FBG based strain sensor L2.

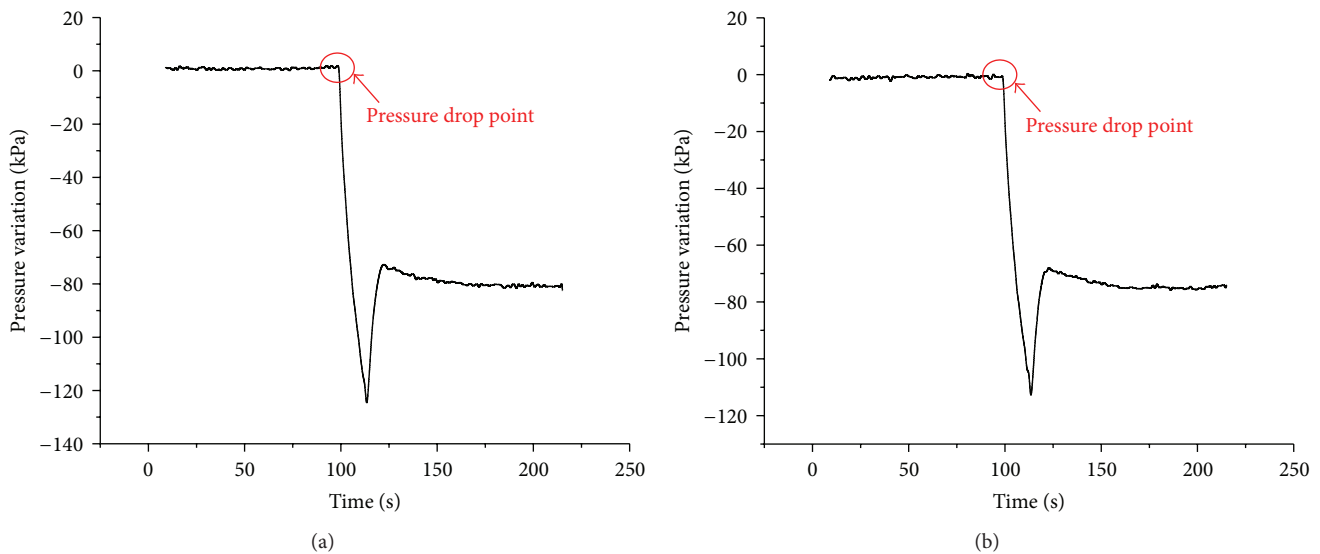


FIGURE 7: (a) Denoised pressure signal measured by FBG based strain sensor L1; (b) denoised pressure signal measured by FBG based strain sensor L2.

appear. On the other hand, in the large scale, although noise has little influence on the detection, the deviation between the real singularity and the detective one is large. Since practical pressure signals are mixed with noise even after filtering, it is beneficial to consider multiscale transforms to find the real singularity. Therefore, this study used the following procedure to determine the location of singularities. Firstly, the approximate range wherein the singularity was located was determined by large scales. Secondly, the real singularity was located within this range by taking advantage of the small scales.

In this experiment, the negative pressure wave was produced by opening a valve to simulate a leakage, and the magnitude of the pressure wave was measured by FBG based

strain sensors over time. The FBG sensors trace at L1 and L2 were chosen to calculate the leakage position, and the distance between them is 8 m. The denoised signals at L1 and L2 are shown in Figure 7. The pressure drop points at both L1 and L2 are marked in Figure 7, and these points were used to determine the time difference using the methodology as describe above.

Figure 8 shows the wavelet analysis of the signal measured at L1 and L2. The pressure drop points in Figure 8 are the singularities. In Figure 8(a) the detail signals at L1 after wavelet transform from scales of 9 to 12 are shown. Similarly, the results from applying wavelet transforms to the pressure signals from L2 are shown in Figure 8(b). When scale = 9, it can be clearly observed that there are many fake singularities

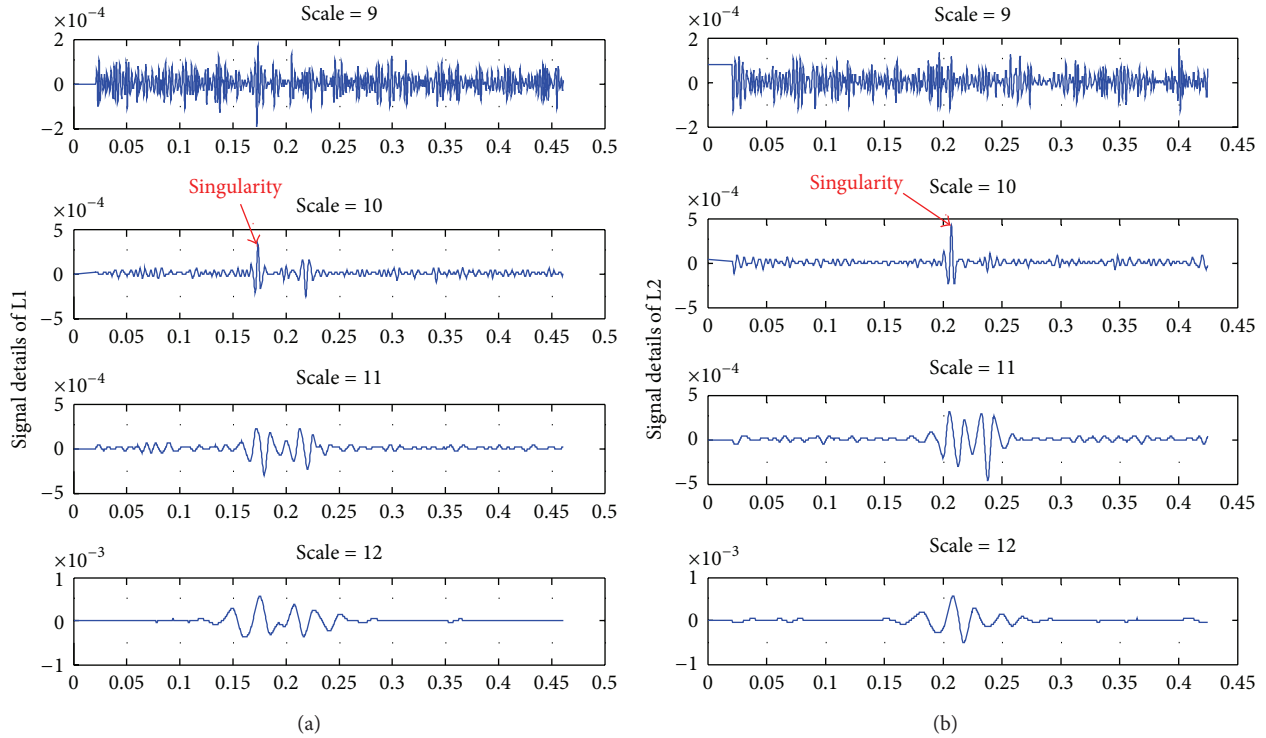


FIGURE 8: (a) Wavelet analysis of denoised signal measured by L1; (b) wavelet analysis of denoised signal measured by L2.

in the detail signal, and this phenomenon also happens when the scale is less than 8. On the other hand, as the scale increases, the fake singularities become less frequent, and the real singularities become more conspicuous, although singularity deviation may happen. Taking advantage of the multiscale transform, the singularities can be identified; therefore, the difference between the arrival time of the negative pressure wave between L1 and L2 can be determined. For this case study, this time difference was calculated to be $\Delta t \approx -1.24 \times 10^{-4}$ s. By substituting this value of Δt into (8), the distance between the leak point and L1 was calculated as $x = 3.98$ m, whilst the actual distance was 3.6 m, yielding an absolute error of 0.38 m and a relative error of 4.8%. Because the distance between L1 and L2 in this experiment is very short (8 m), t_1 and t_2 are very similar, so small deviations in determining Δt cause large errors in relative positioning accuracy. However, this limitation would not apply to systems where the distance between L1 and L2 were greater as would be the case in practice. Therefore, the authors have reason to believe that this method can locate the leakage with good accuracy.

5. Conclusion

At present, the negative pressure wave method based on pressure sensors is the most widely used leak location technology. In this study, this method is enhanced through incorporating the variation of negative pressure wave and natural gas velocities into the negative pressure wave leak location formula. The Compound Simpson formula and Dichotomy Searching

were employed to solve this modified formula. In order to overcome the installation difficulty of traditional pressure sensors, a FBG based strain sensor for collecting the negative pressure wave signals was developed and experimentally tested. Compared to conventional pressure sensors, FBG based strain sensors have favorable properties, such as high sensitivity, cheap cost, and ease of installation. Furthermore, a wavelet transform based method for identifying the pressure drop points within the FBG signals was proposed to calculate the leak position. Utilizing the above methods to calculate the leak position, an absolute error of 0.38 m was obtained in this experiment. This result demonstrated good positioning accuracy using this improved method.

Acknowledgment

This work was partially supported by the Science Fund for Creative Research Groups from the National Science Foundation of China under Grant no. 51121005.

References

- [1] R. A. Silva, C. M. Buiatti, S. L. Cruz, and J. A. F. R. Pereira, "Pressure wave behaviour and leak detection in pipelines," *Computers and Chemical Engineering*, vol. 20, no. 1, pp. S491–S496, 1996.
- [2] T.-H. Yi, H.-N. Li, and M. Gu, "Characterization and extraction of global positioning system multipath signals using an improved particle-filtering algorithm," *Measurement Science and Technology*, vol. 22, no. 7, Article ID 075101, 2011.
- [3] T.-H. Yi, H.-N. Li, and X.-Y. Zhao, "Noise smoothing for structural vibration test signals using an improved wavelet

- thresholding technique,” *Sensors*, vol. 12, no. 8, pp. 11205–11220, 2012.
- [4] I. R. Ellul, “Advances in pipeline leak detection techniques,” *Pipes and Pipelines International*, vol. 34, no. 3, pp. 7–12, 1989.
 - [5] B. Vogel, C. Cassens, A. Graupner, and A. Trostel, “Leakage detection systems by using distributed fiber optical temperature measurement,” in *Smart Structures and Materials 2001: Sensory Phenomena and Measurement Instrumentation for Smart Structures and Materials*, Proceedings of SPIE, pp. 23–34, Newport Beach, Calif, USA, March 2001.
 - [6] E. A. Mendoza, R. A. Lieberman, J. Prohaska, and D. Robinson, “Distributed fiber optic chemical sensors for detection of corrosion in pipelines and structural components,” in *Nondestructive Evaluation of Utilities and Pipelines II*, Proceedings of SPIE, pp. 136–143, San Antonio, Tex, USA, April 1998.
 - [7] D. S. McKeehan, R. W. Griffiths, and J. E. Halkyard, “Marine applications for a continuous fiber optic strain monitoring system,” in *Proceedings of the 18th Annual Offshore Technology Conference*, pp. 342–345, Houston, Tex, USA, 1986.
 - [8] K. T. V. Grattan and B. T. Meggitt, *Optical Fiber Sensor Technology*, vol. 2, Chapman and Hall, London, UK, 1998.
 - [9] K. T. V. Grattan and B. T. Meggitt, *Optical Fiber Sensor Technology*, vol. 3-4, Kluwer Academic, Boston, Mass, USA, 1999.
 - [10] B. Culshaw and J. Dakin, *Optical Fiber Sensors*, vol. 1–4, Artech House, Boston, Mass, USA, 1988–1997.
 - [11] A. Dandridge and C. Kirkendall, “Passive fiber optic sensor networks,” in *Handbook of Optical Fiber Sensing Technology*, J. M. Lopez-Higuera, Ed., pp. 433–448, Wiley, New York, NY, USA, 2002.
 - [12] A. Kersey, “Distributed and multiplexed fiber optic sensors,” in *Fiber Optic Sensors: An Introduction for Engineers and Scientists*, E. Udd, Ed., pp. 325–368, Wiley, New York, NY, USA, 1991.
 - [13] S. Yin, P. B. Ruffin, and F. T. S. Yu, *Fiber Optic Sensors*, CRC Press, Boca Raton, Fla, USA, 2nd edition, 2008.
 - [14] O. S. Wolfbeis, “Fiber-optic chemical sensors and biosensors,” *Analytical Chemistry*, vol. 78, no. 12, pp. 3859–3873, 2006.
 - [15] S. Yashiro, T. Okabe, and N. Takeda, “Damage identification in a holed CFRP laminate using a chirped fiber Bragg grating sensor,” *Composites Science and Technology*, vol. 67, no. 2, pp. 286–295, 2007.
 - [16] T.-H. Yi and H.-N. Li, “Methodology developments in sensor placement for health monitoring of civil infrastructures,” *International Journal of Distributed Sensor Networks*, vol. 2012, Article ID 612726, 11 pages, 2012.
 - [17] H. Tsuda, J.-R. Lee, and Y. Guan, “Fatigue crack propagation monitoring of stainless steel using fiber Bragg grating ultrasound sensors,” *Smart Materials and Structures*, vol. 15, no. 5, article no. 032, pp. 1429–1437, 2006.
 - [18] D. C. Betz, G. Thursby, B. Culshaw, and W. J. Staszewski, “Advanced layout of a fiber Bragg grating strain gauge rosette,” *Journal of Lightwave Technology*, vol. 24, no. 2, pp. 1019–1026, 2006.
 - [19] H.-J. Park and M. Song, “Linear FBG temperature sensor interrogation with Fabry-Perot ITU multi-wavelength reference,” *Sensors*, vol. 8, no. 10, pp. 6769–6776, 2008.
 - [20] N. Takeda, Y. Okabe, J. Kuwahara, S. Kojima, and T. Ogisu, “Development of smart composite structures with small-diameter fiber Bragg grating sensors for damage detection: quantitative evaluation of delamination length in CFRP laminates using Lamb wave sensing,” *Composites Science and Technology*, vol. 65, no. 15-16, pp. 2575–2587, 2005.
 - [21] T.-H. Yi, H.-N. Li, and H.-M. Sun, “Multi-stage structural damage diagnosis method based on “energy-damage” theory,” *Smart Structures and System*, vol. 12, no. 3-4, pp. 345–361, 2013.
 - [22] R. M. López, V. V. Spirin, M. G. Shlyagin et al., “Coherent optical frequency domain reflectometry for interrogation of bend-based fiber optic hydrocarbon sensors,” *Optical Fiber Technology*, vol. 10, no. 1, pp. 79–90, 2004.
 - [23] X. Lu, Y. Sang, J. Zhang, and Y. Fan, “A pipeline leakage detection technology based on wavelet transform theory,” in *Proceedings of IEEE International Conference on Information Acquisition (ICIA '06)*, pp. 1432–1437, Shandong, China, August 2006.
 - [24] I. Daubechies, “The wavelet transform, time-frequency localization and signal analysis,” *IEEE Transactions on Information Theory*, vol. 36, no. 5, pp. 961–1005, 1990.
 - [25] H. Li, T. Yi, M. Gu, and L. Huo, “Evaluation of earthquake-induced structural damages by wavelet transform,” *Progress in Natural Science*, vol. 19, no. 4, pp. 461–470, 2009.
 - [26] T.-H. Yi, H.-N. Li, and M. Gu, “Wavelet based multi-step filtering method for bridge health monitoring using GPS and accelerometer,” *Smart Structures and Systems*, vol. 11, no. 4, pp. 331–348, 2013.
 - [27] Y. Hao, W. Guizeng, and F. Chongzhi, “Application of wavelet transform to leak detection and location in transport pipelines,” *Engineering Simulation*, vol. 13, no. 6, pp. 1025–1032, 1996.